DOCTORAL THESIS

Innovative Smart Probes for

Molecular Imaging Applications

ROSA PUJALES PARADELA

A CORUÑA, 2019

UNIVERSIDADE DA CORUÑA

Innovative Smart Probes for

Molecular Imaging Applications

Rosa Pujales Paradela

Doctoral Thesis 2019

Directores/Advisors:

Dr. Carlos Platas Iglesias

Dr. David Esteban Gómez

Departamento de Química, Facultade de Ciencias
Centro de Investigacións Científicas Avanzadas (CICA)
Universidade da Coruña (UDC)

Programa regulado por el RD 99/2001: Programa Oficial de Doctorado en Química Ambiental y Fundamental

Memoria presentada en la Facultade de Ciencias de la Universidade da Coruña por Rosa Pujales Paradela para optar al **Grado de Doctora en Química con Mención Internacional** por la Universidade da Coruña.

A Coruña, Febrero de 2019.

Doctoranda

Rosa Pujales Paradela

Directores

Dr. Carlos Platas Iglesias   Dr. David Esteban Gómez

A mi familia
y a mis seres queridos

Dr. Carlos Platas Iglesias y **Dr. David Esteban Gómez**, Profesores Titulares de Universidad, pertenecientes al Área de Química Inorgánica del Departamento de Química de la Universidad de A Coruña.

HACEN CONSTAR

Que el presente trabajo titulado "*Innovative Smart Probes for Molecular Imaging Applications*", presentado por **Dña. Rosa Pujales Paradela** para optar al Grado de Doctora en Química con Mención Internacional, ha sido realizado bajo su dirección en los laboratorios del Área de Química Inorgánica dependientes del Departamento de Química de la Facultade de Ciencias y en el Centro de Investigaciones Científicas Avanzadas (CICA) de la Universidade da Coruña y, habiendo sido concluída,

AUTORIZAN

su presentación.

Y para que así conste, firman la presente.

A Coruña, Febrero de 2019.

Dr. Carlos Platas Iglesias   Dr. David Esteban Gómez

Acknowledgements

En primeiro lugar querería expresar o máis sincero agradecemento aos meus directores de tese, Carlos Platas Iglesias e David Esteban Gómez. Grazas por acollerme no voso grupo e permitirme aprender ao voso carón. Grazas pola vosa dedicación e paixón contaxiosa pola ciencia. Grazas polas vosas explicacións e ensinanzas. Grazas pola vosa presenza e alento. Grazas pola vosa guía. Tamén querería darlle as grazas a Mónica, por ser tan comprensiva con Carlos e aturar todas as súas adicións (ao traballo).

Grazas á Unidade de Espectroscopia Molecular e Análise Estructural dos Servizos de Apoio á Investigación (SAI) da Universidade da Coruña por toda a axuda prestada na medición e caracterización das mostras. Particularmente a Jorge Otero e Miriam Vieites, por toda a súa axuda e atención, por sempre escoitar todas as peticións que facía. Grazas por estar sempre dispoñibles e por preocuparvos de que as cousas saíran ben. Grazas, Miriam, pola túa compañía en moitos momentos na sala de RMN do SAI, entre experimento e experimento.

Grazas ao CESGA, Centro de Supercomputación de Galicia, polos seus servizos e soporte informático, sobre todo a Pablo Rey Mayo, pola rapidez en responder dúbidas e resolver problemas.

During my stay at the *Max Planck Institute for Biological Cybernetics* I had the immense honour of being supervised by Priv.-Doz. Dr. Goran Angelovski. It was a wonderful experience and I will preserve those memories during my whole life. He provided me the best environment to learn. We shared ideas, discussed about Science, methods, research, life… His attitude was always remarkable, his attention, sharing knowledge, support… I could not ask for more. Thank you very much, Goran, sincerely.

As well, I had the pleasure of being hosted by Dr. Mauro Botta during my stay at the *Università del Piemonte Orientale "Amedeo Avogrado"*. It was a pleasure to be welcomed into his group and to learn from him. We could not share many moments, but I was amazed by his closeness and kindness. Thank you for all your attention and suggestions. Thank you very much for giving me the chance to be there, learning and collecting experiences. Thank you for always replying to our petitions with that short notice.

Además, también querría agradecer su presencia y apoyo a mis compañeros de laboratorio. En especial, no podría obviar a Israel Carreira Barral, por ayudarme en mis inicios; a Antonella Gayoso Padula, por ser una amiga, por nuestros debates sobre naturaleza y medioambiente, por su ayuda con el monopatín, por permitirme ser yo misma y por todos nuestros momentos juntas; a Rocío Uzal Varela, porque ¡ojalá hubiera llegado antes!, por ser una bellísima persona y por todo su apoyo, comprensión y ayuda, por todas las cosas que compartimos y porque puedes contar conmigo; a Aurora Rodríguez Rodríguez, porque aunque hace poquito que se reincorporó al grupo, se ha ganado un lugar en mi corazón y recuerdos, por su increíble actitud: gracias por toda la ayuda, consejos y ánimos, y por ofrecerme tu portátil cuando el mío se empeñaba en morir

cada poco en esta recta final (¡ojalá tú también hubieras llegado antes!). También querría mencionar a Zarai Jiménez Prieto, por compartir tanto, y a Fran Ferreiro Rey (Franchi) y Ángela Arnosa Prieto (Angie) por ser como son, por sus bromas y cariño.

También quería agradecer su presencia y convivencia a mis compañeros del CICA: desde los que empezamos en los laboratorios del Área de Inorgánica de la Universidade de A Coruña a los que ahora compartimos las dependencias del CICA. En especial querría mencionar a mis amigas Lorena Alonso Marañón y Rosa RMN Nieto Prieto. Gracias por vuestra amistad, por entenderme sin prejuicios, por vuestros consejos, vuestros oídos, vuestras palabras, vuestros ánimos, vuestra alegría, vuestra felicidad. Gracias por ser como sois y por estar ahí. También no podría dejar de agradecer su ayuda y consejos a Diana Martínez Matamoros, sobre todo por su introducción a las técnicas de purificación mediante HPLC. Porque si no me hubiese ayudado en ese momento crítico, en Marzo de 2017, ¿quién sabe dónde estaría ahora? También le doy las gracias por su explicación sobre el funcionamiento de las bombonas de butano, sin el cual no podría haber sobrellevado el invierno pasado sin haberme congelado, y por introducirme en el mundo de los complejos vitamínicos de *dm*. Gracias también a Alicia Latorre, cuya sonrisa ilumina el CICA entero. Por su corazón, por su actitud, por escucharme y por su optimismo. Gracias a Juan Manuel Bermúdez García, por sentar precedente en la presentación de tesis doctorales. También por su profesionalidad, por sus consejos, por escuchar. A Alberto García Fernández, por sus abrazos y por su actitud admirable. A Jorge Lado Sanjurjo, por su buena voluntad.

Además, también querría agradecer su cariño y presencia a mis amigos del máster en Ciencia y Tecnología de Materiales, en la Universidad de Santiago de Compostela. Porque a pesar de la distancia y del tiempo sin vernos o sin hablar, siempre han estado ahí y siempre lo han demostrado. A Vhi (Víctor Gómez) por todas las aventuras, historias, relatos, consejos, risas, bailes,… porque ahora eres Vhi, mi amigo. A Daniel Sóñora (pitufo), porque pase o tempo que pase, nada cambia. Porque o tempo pasa voando cando nos xuntamos, e espero que o próximo reencontro sexa pronto. A Alberto Pardo Montero (Tuco), por facerme rir, por non deixarme no olvido, polas mensaxes de felicitación de cumpreanos de cada ano, por ser un poeta.

A mis compañeros del *Centro de Linguas* de la UDC, sobre todo a Aitor García Tomillo. Por sus mensajes, por sus motes, porque aunque sea un *Grumpy* y esté en contra de subir andando las escaleras mecánicas, siempre te saca una sonrisa.

También al profesorado de la Facultade de Ciencias de la Universidade da Coruña que han formado parte de mi formación y con los que he seguido interactuando a lo largo de estos años. En especial, a Suqui y a Dini. A Suqui, porque ella fue la que me introdujo en la investigación, proponiéndome en 3º de carrera una práctica de nanopartículas de magnetita. Así fue que mis elecciones posteriores me llevaron a la técnica de imagen por resonancia magnética, aunque no concretamente en el empleo de nanopartículas magnéticas como agentes de contraste T_2, como cabría esperar. A Dini, por su humor, por sus bromas y por su ironía. También querría agradecer a Jaime Rodríguez González, coordinador del CICA, su vitalidad, optimismo, su pasión por la investigación y su preocupación por todos los formamos parte del CICA. Por su carisma, su sonrisa y su inconformismo.

Also during my stays I had the immense fortune to meet many people who have carved a place for themselves in my memories. I would like to thank Djordje Toljić for sharing his hood with me, for all the paintings and his irony. He has a quite serious countenance but he hides a sensitive soul. Thanks for your attitude and your help. Also I would like to thank Liam Connah, for all the good memories, good talks, good company and good feeling. Sorry for being that good defensive player and not letting you score when we

And, finally, to Ioannis. For opening my eyes and keep my thoughts raised high, without the presence of Laistrygonians, Cyclops or the wild Poseidon. For his support, his advises. For making me see that part of me. For challenging me. For making me evolve and getting better. For sharing with me his voyage, full of adventure and discovery, to Ithaka. Thank you for all that you have shared with me so far, for continuing to fill our "basket" with incredible memories and adventures. Thank you for believing in me. Thank you for your trust, for your company. Ευχαριστώ πάρα πολύ.

Moitas grazas. Muchas gracias. Thank you very much.

Пуно вам хвала. *Vielen dank. Grazie tanti.* Ευχαριστώ πολύ.

Abstract

The main purpose of the present doctoral thesis is the development of new systems based on metal complexes for their application as contrast agents in Magnetic Resonance Imaging (MRI).

To achieve this aim, this study encompasses the design, synthesis and characterisation of new metal complexes of the lanthanide ions or transition metal ions (Mn^{2+} or Ni^{2+}), as well as a detailed investigation of their structures and physicochemical properties, both in solution and in the solid state. In addition, *in vitro* studies have also been carried out to assess their potential as contrast agents in MRI applications. Theoretical studies were performed using density functional theory (DFT) providing structural information of the complexes in solution, as well as information at the molecular level on the mechanisms that provide MRI response. The complexes presented in this work provide response at different frequencies (^{1}H or ^{19}F), either following the classical mechanism of longitudinal relaxation enhancement (Mn^{2+}, Gd^{3+}), or through the chemical exchange saturation transfer mechanism.

This project was executed within the framework of the European COST Action CA15209 ("*European Network on NMR Relaxometry*"), funded by the European Science Foundation. Furthermore, it has been funded by the Research Projects "*New Generation of Contrast Agents for Magnetic Resonance Imaging (MRI) Alternative to Gadolinium Derivatives*" (CTQ2016-76756-P), "*Innovative Smart Probes for Molecular Imaging Applications*" (CTQ2013-43243-P) and the grant for predoctoral contracts for doctoral training associated to this Project (FPI grant, BES-2014-068399), funded by the Ministerio de Economía y Competitividad (Ministry of Economy and Competitiveness). The results achieved during this project lays the foundations for providing new products for medical application with competitive advantages over the current state-of-art.

Resumen

El objetivo principal de la presente tesis doctoral es el desarrollo de nuevos sistemas basados en complejos metálicos para su aplicación como agentes de contraste en la técnica de imagen por resonancia magética (IRM).

Para alcanzar este objetivo, este estudio engloba el diseño, síntesis y caracterización de nuevos complejos metálicos de los iones lantánidos o iones de transición (Mn^{2+} o Ni^{2+}), así como un estudio detallado de sus estructuras y propiedades fisicoquímicas, tanto en disolución como en estado sólido. Además, también se ha llevado a cabo el estudio *in vitro* de su capacidad para actuar como agentes de contraste. Los estudios teóricos realizados mediante la teoría del funcional de densidad (DFT) proporcionaron información estructural de las sustancias en disolución, así como información a nivel molecular, sobre los mecanismos que proporcionan respuesta mediante IRM. Los compuestos estudiados en este trabajo proporcionan respuesta a frecuencias diferentes (^{1}H o ^{19}F), bien mediante el mecanismo clásico de relajación longitudinal (Mn^{2+}, Gd^{3+}), o mediante el mecanismo de transferencia de saturación por intercambio químico.

Este proyecto fue realizado en el marco de la acción europea COST CA15209 ("*European Network on NMR Relaxometry*"), financiada por la Fundación Europea de la Ciencia, y ha sido subvencionada con cargo a los proyectos de investigación "*Nueva Generación de Agentes de Contraste Para Imagen por Resonancia Magnética (IRM)*"

Alternativos a los Derivados de Gadolinio" (CTQ2016-76756-P), "*Nuevas Sondas Inteligentes para Aplicación en Imagen Molecular*" (CTQ2013-43243-P) y la ayuda para contratos predoctorales para la formación de doctores asociada a este proyecto (Ayuda FPI, BES-2014-068399), financiadas por el Ministerio de Economía y Competitividad. El trabajo realizado durante este proyecto sienta las bases para la obtención de nuevos productos de aplicación médica con ventajas competitivas respecto a los compuestos utilizados en la actualidad.

Resumo

O obxectivo principal da presente tese de doutoramento é o desenvolvemento de novos sistemas baseados en complexos metálicos para a súa aplicación como axentes de contraste na técnica de imaxe por resonancia magnética (IRM).

Para acadar este obxectivo, o estudo engloba o deseño, síntese e caracterización de novos complexos metálicos dos ións lantánidos ou ións de transición (Mn^{2+} ou Ni^{2+}), así como un estudo detallado das súas estruturas e propiedades fisicoquímicas, tanto en disolución coma no estado sólido. Ademais, tamén se levou a cabo o estudo *in vitro* da súa capacidade para actuar como axentes de contraste. Os estudos teóricos realizados coa teoría do funcional de densidade (DFT) proveron información estrutural dos complexos en disolución, así como información a nivel molecular, dos mecanismos que proporcionan resposta mediante IRM. Os compostos estudados neste traballo proporcionan resposta a frecuencias diferentes (^{1}H ou ^{19}F), ben mediante o mecanismo clásico de relaxación lonxitudinal (Mn^{2+}, Gd^{3+}), ou mediante o mecanismo de transferencia de saturación por intercambio químico.

Este proxecto realizouse no marco da acción europea COST CA15209 ("*European Network on NMR Relaxometry*"), financiada pola Fundación Europea da Ciencia, e foi subvencionada con cargo aos proxectos de investigación "*Nova Xeración de Axentes de Contraste Para Imaxe por Resonancia Magnética (IRM) Alternativos aos Derivados de Gadolinio*" (CTQ2016-76756-P), "*Novas Sondas Intelixentes para Aplicación en Imaxe Molecular*" (CTQ2013-43243-P) e a axuda para contratos predoutorais para a formación de doutores asociada a este proxecto (Axuda FPI, BES-2014-068399), financiadas polo Ministerio de Economía e Competitividade. O traballo realizado durante este proxecto senta as bases para a obtención de novos produtos de aplicación médica con vantaxes competitivas respecto os compostos utilizados na actualidade.

Preface

The exceptional progress that medicine has experienced in recent times has been strongly supported by the emergence of new technologies and methods that provide the foundations of biomedical imaging.[1] These techniques allow exploring the human body providing anatomical, physiological and molecular information, thereby helping to provide not only an accurate diagnosis and suitable treatment, but also to get insight into pathological and normal behaviour of cells, tissues and organs, offering the possibility of monitoring the progress of a treatment.[2]

Among the different molecular imaging techniques, which can be classified into three main groups according to the nature of the radiation used (ionising, non-ionising and hybrid), magnetic resonance imaging (MRI) has emerged as a powerful tool in medical diagnosis, as it provides high-resolution images with limitless penetration depth and the use of non-ionising radiation.[2] MRI provides the possibility of obtaining three-dimensional images of practically the whole body. Based on the physics of proton nuclear magnetic resonance (NMR), this technique is able to provide information regarding different pathological processes or lesions due to their different properties in comparison to healthy tissues and organs.[3] To obtain high quality images with an improved resolution and sensitivity, it is a common practise the use of exogenous agents, known as contrast agents, which contribute to the enhancement of the intrinsic properties of the water molecules that constitute around 60% of the human body.[4] These agents, usually gadolinium complexes, must present high kinetic inertness and thermodynamic stability in order to prevent the release of the metal ion into the body, which is very toxic.[4] In spite of the enormous contribution of these contrast agents to diagnostic medical imaging, they also present important limitations and drawbacks:

i) The presence of sizeable background signal, which is related to their mechanism as contrast enhancing agents: They alter an already existing signal of water molecules within the body, but they are unable to provide a specific and quantifiable response to know the concentration of the agent.

ii) Toxicity problems associated to the release of the metal ion *in vivo*, which was directly related to the appearance of a new disease, nephrogenic systemic fibrosis (NSF), in patients with renal impairment, and the localisation of gadolinium in the brain and other organs.

The scientific community is currently gathering efforts focused on the development of new platforms that provide a solution to overcome these limitations.[4] Several approaches are being taken under consideration, like the design of new platforms and systems that provide contrast through alternative mechanisms, combine the information extracted from diverse mechanisms in a single probe, or improve the efficiency, inertness and stability of the complexes by improving the ligand design. Moreover, in the last few years another alternative has emerged with promising results: the use of other paramagnetic metal ions characterised for their inferior toxicity.[4]

Two of the most promising alternative mechanisms that are being explored in the context of MRI contrast agents are: 1) The use of Chemical Exchange Saturation Transfer (CEST) probes, which contain groups with exchangeable protons (–NH or –OH), or even a water molecule coordinated to a metal ion, in slow-to-intermediate exchange with bulk water;[4,5] and 2) probes allowing direct detection. The direct detection approach relies on the use of nuclei that can be easily detected by multinuclear probes or with small adjustments on the resonance frequency of the clinical

scanners. These nuclei may be either ^{1}H nuclei providing paramagnetically shifted signals well separated from resonances of endogenous nuclei (the PARASHIFT approach),[4,6] or nuclei that are not present in the body.[4,7] These type of contrast agents can be measured and provide the concentration of the agent *in vivo*. Among the altenative nuclei, ^{19}F presents the most promising features due to its high NMR sensitivity, the highest after ^{1}H, and its 100% abundance and non-quadrupolar nature. The enclosure of a paramagnetic centre in the structure of a fluorinated compound at the appropriate distance enables to accelerate the relaxation rates of the fluorinated nuclei, leading to faster acquisitions.[4,8]

Another family of contrast agents, based on the traditional relaxation enhancement mechanism, which has emerged in the last two decades, is that of the so-called smart or responsive contrast agents.[9] These agents present a specific response to a biomarker or parameter in the physiological environment (pH, temperature, light, concentration of an ion or molecule…) that alters the MR signal of the probe. Although they present a more specific response, they are still limited by the lack of signal quantification due to the unknown probe concentration. Therefore, the combination of the CEST mechanism or fluorine detection with pH response, response to the concentration of metal ions (i.e. Ca^{2+}, Zn^{2+}) or a metabolic reaction, to name a few, is an attractive approach to achieve quantitative analysis.[4] In spite of the impressive advances reported in this field during the last years, the development of this sort of agents remains a very important and challenging task in molecular imaging.

The present doctoral thesis was conceived to develop alternatives to the classical gadolinium probes that operate either as relaxation enhancement agents (i.e. Mn^{2+}-based complexes), or as dual probes that provide response at the ^{1}H and ^{19}F frequencies. The response at the proton frequency may be provided by the classical T_1 mechanism (Gd^{3+} complexes) or following paraCEST response (for instance Ni^{2+}, Tm^{3+} or Yb^{3+} complexes).[2,4]

The investigations carried out during the project included the synthesis and characterisation of the probes, the investigation of the structures of the compounds in solution and their physicochemical properties, as well as the assessment of their potential as contrast agents in MRI application. Theoretical studies performed using DFT provided structural information of the substances in solution, and also information at the molecular level on the mechanisms that provide MRI response. This project was executed in the framework of the European COST Action CA15209 ("*European Network on NMR Relaxometry*"), which is funded by the European Science Foundation. The results achieved during this project laid foundations for providing new industrial products for application in radiology with significant advantages over the current state-of-art. Besides the work developed at the University of A Coruña (synthesis, physicochemical characterisation, computational studies and data analysis), the PhD work reported here also involves MRI and CEST studies carried out at the *MR Neuroimaging Agents*, *Max Planck Institute for Biological Cybernetics*, Tübingen, Germany, under the supervision of Dr. Goran Angelovski. Nuclear magnetic relaxation dispersion (NMRD) and ^{17}O NMR measurements were recorded at the *Dipartimento di Scienze e Innovazione Tecnologica* (DiSIT), *Università degli Studi del Piemonte Orientale "Amedeo Avogadro"*, Alessandria, Italy, under the supervision of Prof. Mauro Botta.

The first chapter of this thesis (**Chapter 1**) presents a general overview of the different molecular imaging methods, with particular emphasis in MRI and the different strategies reported in the literature to generate contrast with the use of exogenous agents. The specific scientific goals of the thesis are collected in the subsequent chapters, which were organised according to the different types of mechanisms involved in the generation of contrast (**Chapters 2-6**). Each of these Chapters contains a brief *Introduction*, a *Results and Discussion* section and an *Experimental* part that provides the details of the experimental and theoretical methods used. Furthermore, a *Conclusions* section summarises the main results and the conclusions that followed each piece of work. All these sections are conveniently supported by appropriate literature references.

- **Chapter 2 and 3** describe the development of Mn^{2+}-based contrast agents and a detailed relaxometric study to analyse the parameters governing the efficiency of these systems as contrast agents for MRI. **Chapter 2** reports complexes derived from the triacyclononane platform, while **Chapter 3** describes a non-macrocyclic ligand derived from 2,2'-azanodiyldiacetic acid functionalised with a picolinate group in the nitrogen atom (H_3paada) and its lipophilic derivative, functionalised with a dodecylxyl group in the pyridylic ring position 4 (H_3C_{12}Opaada). The systems described in **Chapter 2** were designed to modulate the steric compression around the water binding site, to assess the influence of steric hindrance on the approach of the incoming water molecule during the exchange reaction. **Chapter 3** discloses the analysis of two manganese(II) complexes with pentadentate ligands. In one of the complexes, the insertion of an aliphatic chain on the chelate was used to promote the formation of micelles above a certain concentration (critical micellar concentration, *cmc*) due to intermolecular hydrophobic forces. The *cmc* was determined by relaxometric measurements and confirmed by fluorescence studies. The formation of micelles slows down the rotation of the complex in solution, which affects very significantly the relaxation properties. In addition, the interaction of the lipophilic complex with bovine serum albumin (BSA) was also examined as a potential approach to improve the relaxation ability of the complex.

- **Chapter 4** presents novel Gd^{3+} contrast agents with dual detection at the ^1H and ^{19}F frequencies. These systems were designed to generate contrast to both proton and fluorine frequencies, in particular through optimisation of the distance between the paramagnetic ion from the ^{19}F nuclei. This chapter provides a detailed study of the diverse parameters that affect proton relaxivity at different fields and temperature, as well as an analysis on the distances between the paramagnetic centre and the fluorinated nuclei that result in optimal response at the ^{19}F frequency.

- **Chapter 5** reports innovative lanthanide-based contrast agents with multiple response. Three different ligand systems presenting different amount of fluorinated nuclei and providing different Ln···F distances are described. This allowed performing a very detailed analysis of the different physicochemical parameters that control the ^{19}F relaxation efficiency of these agents. Furthermore, some of the complexes were studied for their potential as ^1H CEST probes, combining the fluorinated signal with the CEST effect afforded by the presence of an amide –NH group and the paramagnetism of the lanthanide ion.

- **Chapter 6** shows potential Ni^{2+} cross-bridged derivatives as promising contrast agents presenting dual response thanks to the ^1H CEST mechanism and ^{19}F frequency output. Due to the current concern regarding the toxicity issues of Gd^{3+}-based contrast agents, transition metal ion complexes have arisen as a solid alternative to be consider on the MRI field. The strong paramagnetism of the Ni^{2+} ion provides an enhancement effect on the relaxation experienced by fluorinated nuclei, allowing faster acquisition times of the MR images. Furthermore, the use of a reinforced platform as the cross-bridged cyclam, offers an ideal cavity for the metal ion designed to prevent the release of the metal ion *in vivo*. Besides, the presence of an –NH group in one of the pendant arms yields a highly-shifted amide resonance beneficial for the CEST mechanism.

Finally, **Chapter 7** gathers the main conclusions of this doctoral thesis work, summarizing the most remarkable results and the main contributions that this thesis provides to the field of MRI contrast agents. Furthermore, **Annexes A– E** include additional information such as NMR spectra and other details that support the results presented in **Chapters 2– 6**.

Following the regulations established by the *Escola Internacional de Doutoramento da Universidade da Coruña (EIDUDC, International Doctoral School of University of A Coruña)*, this thesis contains a summary in Spanish, included in **Annexe F**.

References

1. R. Weissleder, U. Mahmood, *Radiology,* 2001, **219**, 316.

2. (a) L. Fass, *Molecular Oncology 2* 2008, 115. (b) M. Rudin and R. Weissleder, *Nature Reviews Drug Discovery*, 2003, **2**, 123. (c) R. Weissleder and M. J. Pittet, *Nature,* 2008, **452,** 580. (d) M. A. Stammes, S. L. Bugby, T. Porta, K. Pierzchalski, T. Devling, C. Otto, J. Dijkstra, A. L. Vahrmeijer, L.-F. de Geus-Oei and J. S. D. Mieog, *Br. J. Surg.*, 2018, **105**, e69-e83.

3. P. Lam, Medical News Today. MediLexicon, Intl.,"What to know about MRI scans." 24 July 2018. Accessed 24 December. 2018, https://www.medicalnewstoday.com/articles/146309.php

4. (a) C. F. G. C. Geraldes and S. Laurent, *Contrast Media Mol. Imaging*, 2009, **4**, 1. (b) J. Lohrke, T. Frenzel, J. Endrikat, F. Caseiro-Alves, T. M. Grist, M. Law, J. M. Lee . T. Leiner, K.-C. Li, K. Nikolaou, M. R. Prince, H. H. Schild, J. C. Weinreb, K. Yoshikawa and H. Pietsch, *Adv. Ther.*, 2016, **33**, 1. (c) Y.-D. Xiao, R. Paudel, J. Liu, C. Ma, Z.-S. Zhang, S.-K. Zhou, *Inter. J. Mol. Med.*, 2016, **38**, 1319. (d) J. Wahsner, E. M. Gale, A. Rodríguez-Rodríguez and P. Caravan, *Chem. Rev.* 2019, **119**, 957.

5. K. M. Ward, A. H. Aletras and R. S. Balaban, *J. Magn. Reson*, 2000, **143**, 79.

6. P. Harvey, A. M. Blamire, J. I. Wilson, K.-L. N. A. Finney, A. M. Funk, P. K. Senanayake, D. Parker, *Chem. Sci*., 2013, **4**, 4251.

7. (a) T. Tanaka, R. Araki, T. Saido, R. Abe and S. Aoki, *Eur. J. Inorg. Chem*., 2016, 3330. (b) L. Calucci, G. Ciofani, D. De Marchi, C. Forte, A. Menciassi, L. Menichetti and V. Positano, *J. Phys. Chem. Lett*., 2010, **1**, 2561. (c) S. Capuania, P. Porcaria, F. Fasano, R. Campanella and B. Maraviglia, *Magn. Reson. Imag.*, 2008, **26**, 987.

8. (a) K. L. Peterson, K. Srivastava, V. C Pierre, *Front. Chem*., 2018, **6**, 160. (b) J. Blahut, P. Hermann, A. Gálisová, V. Herynek, I. Císařová, Z. Tošnerc, J. Kotek, *Dalton Trans*., 2016, **45**, 474. (c) M. Yu, D. Xie, K. P. Phan, J. S. Enriquez, J. J. Luci, E. L. Que, *Chem. Commun*., 2016, **52**, 13885. (d) J. Blahut, K. Bernasek, A. Galisova, V. Herynek, I. Cisarova, J. Kotek, J. Lang, S. Matejkova, P. Hermann, *Inorg. Chem*., 2017, **56**, 13337. (e) K. H. Chalmers, E. De Luca, N. H. M. Hogg, A. M. Kenwright, I. Kuprov, D. Parker, M. Botta, J. I. Wilson, A. M. Blamire, *Chem. Eur. J.*, 2010, **16**, 134. (f) K. H. Chalmers, M. Botta, D. Parker, *Dalton Trans*., 2011, **40**, 904.

9. D. V. Hingorani, A. S. Bernstein and M. D. Pagel, *Contrast Media & Molecular Imaging*, 2014, **10**, 245.

Contents

Chapter 3

Chapter 4

Chapter 5

Chapter 6

Chapter 7

Controlling water exchange rates in potential Mn^{2+}-based MRI agents derived from NO2A^{2-}

A Pentadentate Member of the Picolinate Family for Mn(II) Complexation and an Amphiphilic Derivative

Gadolinium(III) based Dual ^{1}H/^{19}F MRI Probes

Lanthanide Complexes with ^{1}H paraCEST and ^{19}F Response for MRI Applications

Reinforced Ni(II)-cyclam derivatives as dual ^{1}H/^{19}F MRI probes

Spanish Summary

CURRICULUM VITAE Rosa Pujales Paradela

$\Delta\omega_m$	Chemical shift difference between bound and bulk water
Δ^2	Mean square zero-field-splitting energy
τ_M	Residence time of a water molecule in the metal ion inner-sphere
τ_{RG}	Correlation time describing global motions
τ_{RL}	Correlation time describing local motions
τ_V	Correlation time for the modulation of the ZFS energy
$D_{H_2O}^{298}$	Self-diffusion of water
T_{1m}^H	Relaxation time of the proton nuclei of inner-sphere water molecules
τ_R^{298}	Rotational correlation times
$1/T_{2r}$	Reduced transverse relaxation rates
^{1}H NMRD	Proton Nuclear Magnetic Relaxation Dispersion
a_{GdH}	Distance of closest approach for the outer-sphere contribution
$A_O/\hbar$	^{17}O Hyperfine coupling constant
B_0	External magnetic field
B_1	Radiofrequency power applied
BM	Bloch-McConnell equations
BMS	Bulk Magnetic Susceptibility method
BSA	Bovine Serum Albumin
CA	Contrast Agent
CASSCF	Complete Active Space Self-Consistent Field
CEST	Chemical Exchange Saturation Transfer (Cest)
cmc	Critical Micellar Concentration
CT or CAT	Computed Tomography or Computed Axial Tomography
DD	Dipole-Dipole mechanism
DFT	Density Functional Theory
DOSY	Diffusion-Ordered NMR SpectroscopY
EMA	European Medicines Agency

ESI-TOF	Electrospray-Ionisation Time-Of-Flight
E_v	Activation energy for the modulation of the zero field splitting interaction
FA	Flip Angle
FID	Free Induction Decay
FLASH	Fast Low Angle Single Shot Pulse Sequence
FONAR	Field Focussed Nuclear Magnetic Resonance
FOV	Field Of View
FRI	Fluorescence reflectance imaging
FW	Molecular Weight
GdCA	Gd^{3+}-based Contrast Agent
HSA	Human Serum Albumin
hybrid meta-GGA	Hybrid Meta-Generalised Gradient Approximation
IEFPCM	Integral Equation Formalism Variant Of The Polarizable Continuum Model
I_F	Fluorescence at a given ligand
$I_{F\infty}$	Protein fluorescence "saturated" of ligand
I_{Fo}	Fluorescence in the absence of ligand
IRM	Imagen Por Resonancia Magnética
k_{ex}	Water exchange rate of the coordinated water molecule
LCRECP	Large-Core Quasi-Relativistic Effective Core Potential
MEMRI	Manganese-Enhanced Magnetic Resonance Imaging
MnDPDP	Teslascan^{tm} (mangafordipir trisodium)
MPIO	Micron-Sized Particles of Iron Oxide
MPLC	Medium Performance Liquid Chromatography
MRI	Magnetic Resonance Imaging
MTX	Matrix Size
NEVPT2	N-Electron Valence Perturbation Theory To Second Order
NEX	Number Of Excitations
NSF	Nephrogenic Systemic Fibrosis
NMR	Nuclear Magnetic Resonance
NMRD	Nuclear Magnetic Relaxation Dispersion

NS	Nuclear Scan or Radionuclide Scan
OI	Optical Imaging
PET	Positron Emission Tomography
PET-CT	Positron Emission Tomography-Computed Tomography
PRE	Proton Relaxation Enhancement
q	Water Molecules Coordinated To The Metal Ion
QDPT	Quasi-Degenerate Perturbation Theory
r_{1p}	Longitudinal Relaxivity
r_{2p}	Transverse Relaxivity
r_{MH}	Distance between the proton nuclei of inner-sphere water molecules and the metal ion (M)
SAP	Square Antiprismatic Isomer
SC	Scalar mechanism
SIPP	Superparamagnetic Iron Platinum Particles
SMD	Solvation Model based on solute electron Density
SNR	Signal-To-Noise Ratio
SPECT	Single-Photon Emission Tomography
SPIOs	Superparamagnetic Iron Oxides
T_1	Longitudinal (spin-lattice) relaxation time
T_{1e}	Longitudinal electronic relaxation time
T_2	Transverse (spin-spin) relaxation time
T_2^*	T_2 considering magnetic field inhomogeneity
T_{2e}	Transverse electronic relaxation time
TA	Total Acquision time
TE	Echo Time
TR	Repetition Time
TSAP	Twisted Square Antiprismatic Isomers
US	Ultrasound
USPIO	Ultrasmall Superparamagnetic Iron Oxide
WHO	World Health Organisation
ZPEs	Zero-Point Energies

Introduction
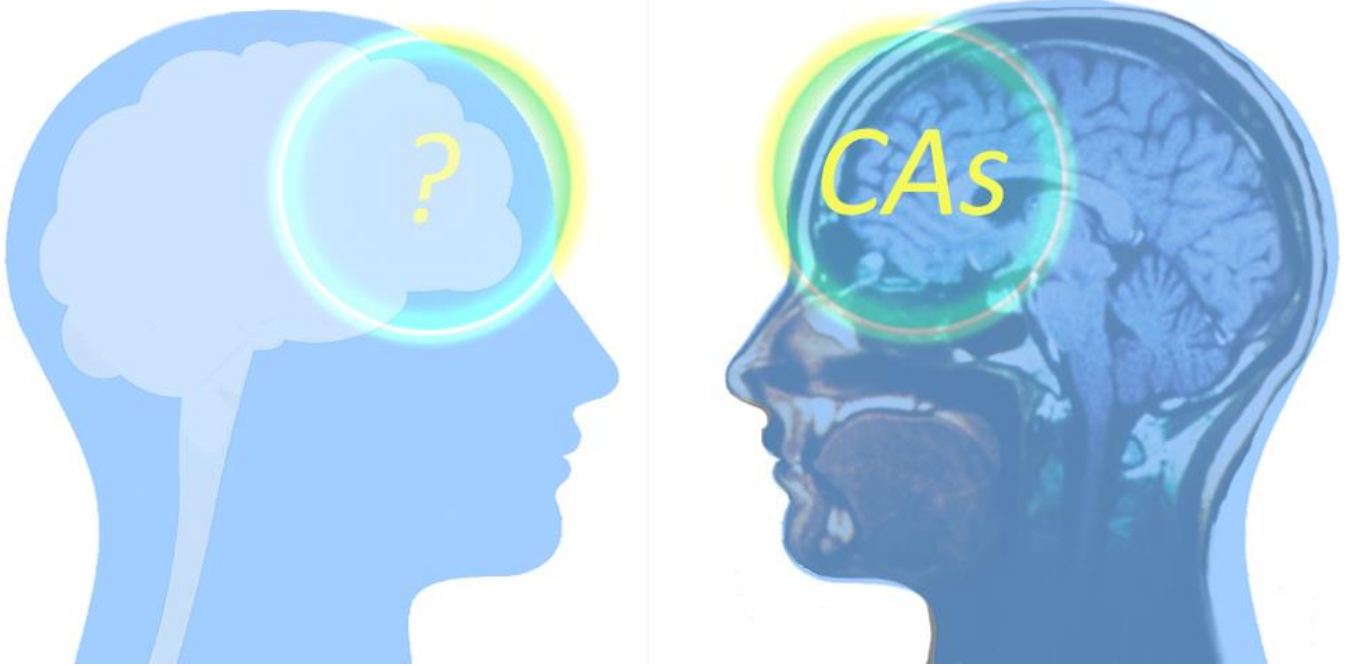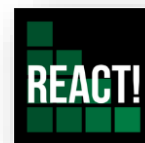
Chapter 1

Innovative Smart Probes for Molecular Imaging Application.

1.1.   Introduction.

The technological advances achieved in the last decades are undeniable. The knowledge and capabilities accumulated by the human race are almost limitless, which allowed developing new methods, new systems, new techniques and even new equipment that fulfil our requirements quite easily. The target of all these developments is mainly increasing the comfort and wellness of the human being. Although all these efforts are conceptualised to improve the quality of life, people should have the availability and health conditions to take advantage of it. Even though the purchasing power around the world is quite unequally distributed,[1] the average life expectancy in general terms has increased without the presence of worldwide wars. Although expected lifespan increases, new factors that were not present in former times, as for instance higher levels of pollution, bigger exposure to radiation or even stress, are now conditioning people's life and lifestyle.[2] All these new challenges that the society faces everyday are tackled through different approaches, but one of the most important ways of action is to maintain and improve physical and mental health, especially through the provision of medical services.[3]

Given aside some factors as the geographical location, access to preventive care or the quality of the healthcare system,[3] research, development and innovation have improved the average health condition of the different societies, reaching the point in which many diseases have been eradicated so far.[4] The support of new techniques and methods turned once fatal illnesses into chronic diseases through palliative treatments. Nevertheless, in order to give the right treatment to a patient, new methods have been developed to detect and provide the accurate diagnosis.[5] According to the World Health Organisation (WHO),[6] the top 10 causes of death worldwide are: ischemic heart diseases, stroke, chronic obstructive pulmonary diseases, lung cancer (along with trachea and bronchus cancers), diabetes, dementias, lower respiratory infections, diarrheal diseases, tuberculosis and road injuries. Noteworthy, most of the deadliest illnesses are preventable or treatable. Providing an early diagnosis, screening, treatment and palliative care improve the likelihood of survival from these illnesses.[7] Furthermore, over the last decades and after noticing its huge impact on our society, the scientific community has been focusing a huge effort on the development of methods to detect the presence of some of these deathliest diseases, as well as monitoring the treatments or progress of the illnesses. The designated tool for this purpose is **Medical Imaging**, a set of non-invasive techniques or modalities that provide detailed pictures with not only anatomical information, but also insight into molecular and cellular processes that take place inside a body.[8] These images help physicians to give a successful diagnosis and appropriate treatment.

1.2.   Molecular Imaging.

The different imaging modalities can be classified according the radiation used in the examination, which may have or not ionising character:[9]

- **Diagnostic techniques based on ionising radiation.**

i) **Computed Tomography (CT) scan or Computed Axial Tomography (CAT):**[10,11] A series of detailed pictures of the organs taken from different angles (cross-sectional pictures) are obtained from an X-ray machine controlled by a computer. Afterwards the computer combines these pictures in order to furnish a 3-dimensional image that reveals any abnormality or tumour.

ii) **Nuclear scan or radionuclide scan (NS):**[11] This technique requires the use of a tracer. A tracer is a substance characterised by its radioactive properties. A small amount of the tracer is injected through the bloodstream and it is accumulated in certain organs or bones. A scanner detects and measures its radioactivity inside the body and creates pictures on a computer screen. The radioactive substance is excreted quickly from the body.

iii) **Positron Emission Tomography (PET):**[12] Analogous to NS, this diagnostic technique uses a positron-emitting radionuclide (also called radiopharmaceutical, radionuclide or radiotracer). A detector collects the γ-ray emissions that are emitted into the body as a result of the annihilation of a positron and an electron when they collide. The most common used radiotracer is a compound analogous to glucose, fluorodeoxyglucose (F-18 FDG), which targets areas of high metabolic activity (as cancer), since they metabolise sugar into energy.

iv) **Single-Photon Emission Tomography (SPECT):**[9g,12] This modality uses a similar basis and technology than PET. The difference between these two modalities relies on the tracer used: The SPECT radionuclide emits gamma radiation directly, while a PET radiotracer emits the radiation indirectly (when an emitted positron and an electron collide).

Table 1. Important properties of the different imaging modalities.[9b,c]

Imaging Modality	Spatial Resolution	Depth	Time	Quantitative	Multichannel	Target	Cost	Primary small-animal use	Clinical Use
CT	50 µm	No limit	Minutes	Yes	No	Anatomical, physiological	€€	Lung and bone imaging	Yes
PET	1-2 mm	No limit	Minutes to hours	Yes	No	Physiological, molecular	€€€	Versatile imaging modality with many different tracers	Yes
SPECT	1-2 mm	No limit	Minutes to hours	Yes	No	Physiological, molecular	€€	Commonly used to image labelled antibodies, peptides and so on	Yes
PET-CT		No limit				Anatomical, physiological, molecular	€€€		Yes
US	50 µm	cm	Seconds to minutes	Yes	No	Anatomical, physiological	€€	Vascular and interventional imaging	Yes
MRI	10-100 µm	No limit	Minutes to hours	Yes	No	Anatomical, physiological, molecular	€€€	Versatile imaging modality with high soft-tissue contrast	Yes
OI / Fluorescence reflectance Imaging (FRI)	2-5 mm (Visible to NIR)	< 1 cm	Seconds to minutes	No	Yes	Physiological, molecular	€	Rapid screening of molecular events in surface-based tumours	Development
PET-MRI		No limit				Anatomical, physiological, molecular	€€€		Development

v) Positron Emission Tomography-Computed Tomography (PET-CT):[13,14] Hybrid technique which combines PET and CT imaging modalities under one single instrument. The CT technique provides anatomical details while PET imaging presents locations with high metabolic activity. The combination of these two techniques offers a more accurate diagnosis and a more precise monitoring of the disease.

- Diagnostic techniques based on non-ionising radiation.

i) Ultrasound (US):[15] This technique, also called sonography or ultrasonography, is based on high-frequency sound waves to obtain pictures of internal organs. A transducer transforms into images the collected sound waves after colliding with the organs or soft-tissues. Abnormal and healthy tissues bounce off differently and this is traduced as diverse contrast on the images, which facilitates the diagnosis.

ii) Magnetic Resonance Imaging (MRI):[16] Detailed pictures of organs and tissues are produced by the action of strong magnets and radio waves. Magnets generate magnetic fields that lift the degeneracy of the nuclear spin levels of water molecules within the body. The absorption of radiofrequency radiation results in the population of the excited nuclear-spin states, which return to their initial state with different rates. The contrast generated in MRI depends on proton density of the particular tissue/organ and the longitudinal and transverse relaxation rates of water proton nuclei. For instance, cancerous tissues have dissimilar

rates from healthy tissues and these discrepancies can be seen as a distinctive contrast (darker or brighter areas) on the images.

iii) Optical Imaging (OI):[17] Photophysical processes as absorption, scattering and emission of light can be used for optical imaging, analysing the interaction of light with biological tissues in order to get insight about specific cells or tissues. The photons emitted as result of the excitation of fluorescent molecules, or as a consequence of a biochemical reaction that takes place into the body, are recorded.

- Hybrid diagnostic techniques. PET-MRI:[12b,18] A recent interest has emerged on the development of multimodal imaging, unifying two different modalities into a single instrument. These hybrid techniques are present on the aforementioned PET-CT modality, combining two ionising radiation techniques. In order to eliminate an additional radiation dose from CT a newer attention has been introduced over the last years: PET-MRI systems. MRI improves soft tissue imaging in comparison to the CT technique, providing an accurate localisation of the PET tracer within the body for a better diagnosis and treatment.

The different imaging modalities have their associated strengths and drawbacks, including the resolution of the images, the sensitivity of the technique, its penetration limit, scanning time and cost. **Table 1** summarises the main characteristics of the different imaging modalities. Hybrid techniques aim at combining the strengths of two different and complementary techniques. For instance, PET-MRI

combines the sensitivity of PET with the superb spatial resolution of MRI.

This PhD thesis is focused in developing efficient contrast agents for application in MRI. Thus, the next sections will describe the basic principles of this technique, with particular emphasis on the different mechanisms used to generate contrast and the types of contrast agents that have been developed so far. Some of these contrast agents entered the clinical practice already three decades ago, but a great effort is being currently devoted to find alternatives (i. e. with a better toxicity profiles or with a specific response).

1.3. Magnetic Resonance Imaging

Among the different methods available in the molecular imaging palette, MRI is one of the most versatile and promising ones, as it allows obtaining images of tissues and organs of the body and identifying anomalies on them at the anatomical, physiological and molecular levels.[9,10b,16] MRI provides images with a very high resolution and unlimited penetration depth, which makes this imaging modality ideal to study many diseases as ischemic heart diseases, strokes, chronic obstructive pulmonary diseases, cancer, lower respiratory infections, multiple sclerosis, diseases of the liver, inflammatory bowel diseases or malformations and abnormalities within the body.[19] MRI has a plethora of applications not only in medical diagnosis, but also in biomedical research using animal models, and can be applied to virtually any part of the body.[16b,19] Furthermore, MRI can be used to check the health state of the organs, as breast, ovaries, prostate, liver, kidneys, pancreas…

MRI is based on the same principles as an NMR spectrometer (Figure 1), recording the NMR signal of water proton nuclei present in the body. In the presence of an external magnetic field (B_0), ^{1}H nuclear spins can be aligned either parallel or antiparallel with respect to that field, which corresponds to two different energy states. The population of the ground energy level (parallel to B_0) is higher than that of the excited level according to Boltzmann equation, which results in a net magnetisation of the sample M_0 parallel to B_0. The acquisition of an NMR experiment starts by application of an oscillating electromagnetic field B_1 (a radiofrequency pulse) perpendicular to B_0. The duration of the excitation pulse is calculated to tilt M_0 by 90° or a flip angle α. Once the excitation pulse finishes, the magnetisation returns to equilibrium, so that the magnetisation along the z axis raises exponentially with a time constant T_1 and the magnetisation in the xy plane decreases exponentially with a time constant T_2. These time constants are called longitudinal (spin-lattice) relaxation time (T_1) and transverse (spin-spin) relaxation time (T_2). During the return to equilibrium the magnetisation precesses around the z axes, generating an electric current in a receiver coil situated in the xy plane that is converted into a Free Induction Decay (FID). The FID is converted into a conventional NMR spectrum through a Fourier transform.[16]

J. R. Singer at Berkeley University was the first one to propose in 1959 the use of NMR to measure in vivo blood flow.[20] The first applications of MRI to study tissues and tumours were reported by Damadian already in 1971.[21] He introduced the first acronym to denote what nowadays is known as MRI, calling this modality FONAR (Field fOcussed Nuclear mAgnetic Resonance).[16a] Moreover, the first human body image obtained by NMR is attributed to him and his colleagues from State University of New York, which required developing their own superconductor magnet.[16a]
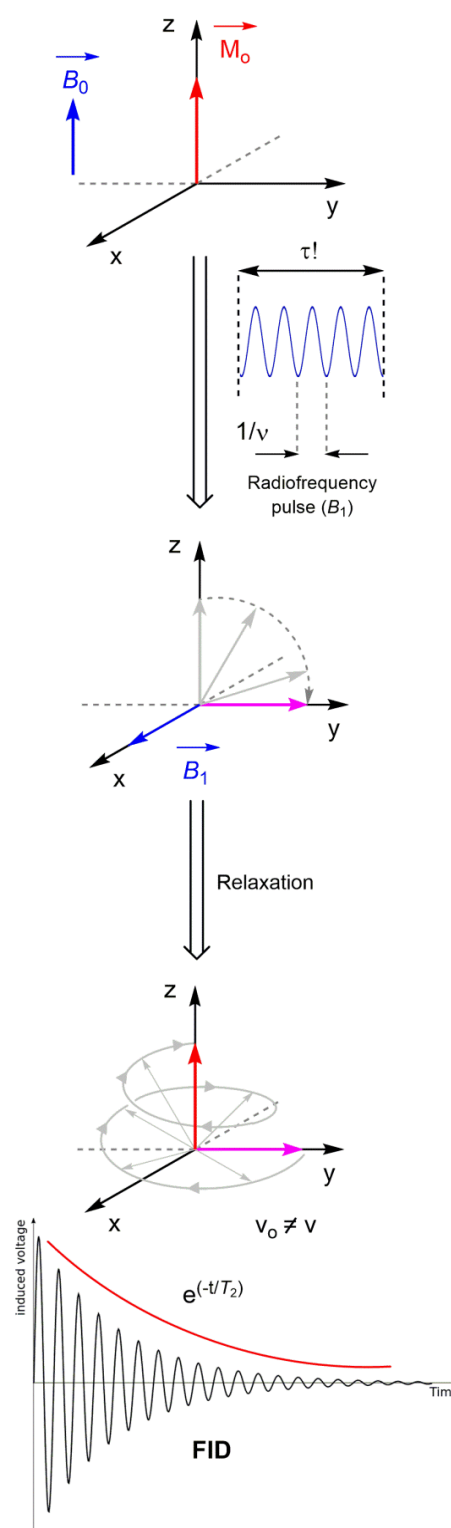
Figure 1. Acquisition of an NMR experiment. Application of a radiofrequency pulse perpendicular to B₀ flips the magnetisation into the xy plane. An electric current is induced in a receiver coil placed in the xy plane due to the precession of the magnetisation around the z axis (relaxation). This electric current is converted into a FID that is transformed into an NMR spectrum by Fourier transform.
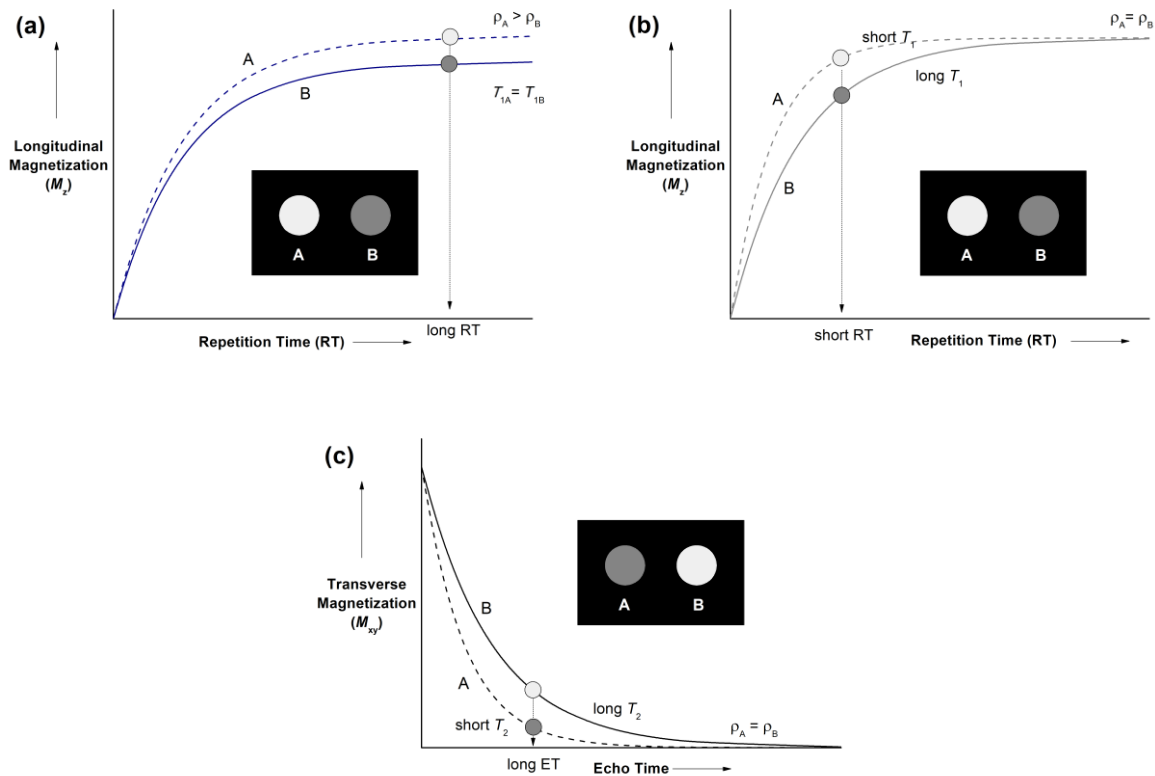
Figure 2. (a) Evolution of the longitudinal magnetisation for two hypothetical tissues A and B characterised by different proton densities and identical relaxation times. (b) Evolution of the longitudinal magnetisation for two hypothetical tissues A and B characterised by different T_1 and identical proton densities. (c) Evolution of the transverse magnetisation for two hypothetical tissues A and B characterised by different T_2 and identical proton densities.[16b]

The MRI scanners used in clinical practice and biomedical research are equipped with a magnet, with current clinical MRI scanners generally incorporating a 1.5 or 3 T magnet. However, 7 T magnets are starting to be used in some countries for both research and clinical practice.[22] Besides the magnet, MRI scanners incorporate radiofrequency coils (usually constituted by transmitter, body and receiver coils) to produce and collect the MR signals, a set of gradient coils, which are controlled by pulse sequences and allow faster acquisition and improve the contrast in the recorded images, and a console and computer system to send the instructions and collect the data.[16a] The use of MRI grew very quickly since the first scan of a human head was recorded in 1978, becoming the preferred method for non-trauma neurological scanning already in the late 1980s and reaching more than 10,000 MRI scanners operating worldwide by 1996.[16a] Nowadays, approximately 50,000 MRI scanners exist around the world,[23] performing more than 75 million clinical examinations per year.[24]

The contrast observed in MRI is generated by taking advantage of: 1) differences in proton density (the number of proton nuclei present in a certain unit volume) of tissues and organs, or 2) differences in the longitudinal and/or transverse relaxation times of the different tissues.[16a] The water content of most tissues is rather similar, and thus the contrast achieved by taking advantage of differences in proton densities is rather poor (Figure 2).[16] Furthermore, the contrast generated by differences in proton densities requires using long repetition times (the time from the

application of an excitation pulse to the application of the next pulse), which results in longer acquisition times.[16a]

Images generated by taking advantage of differences in longitudinal relaxation of diverse tissues are called T_1-weighed images (Figure 2b).[16b] T_1-weighed images are obtained by using short repetition times, and generally provide very bright spots of fat-based tissues due to their short relaxation times, while water-based tissues and fluids are mid-grey and very dark, respectively.[16a] Finally, differences in T_2 can be also exploited to generate contrast by using appropriate pulse sequences. In T_2-weighed images tissues with short T_2 are observed as dark regions in the image, in contrast to T_1-weighed images.[16] T_2-weighed images generally require rather long repetition times and echo times involved in the commonly used spin echo pulse sequence.

The energy difference between the ground and excited levels in NMR experiments is low, and thus relaxation is not spontaneous and need to be stimulated.[25] Longitudinal relaxation is facilitated by the movement of neighbouring nuclei, which creates an oscillating magnetic field generating a distribution of frequencies that contains the resonance frequency of the excited nucleus. The introduction of species containing unpaired electrons accelerates the relaxation process, as the magnetic moment of the electron is 658 times higher than that of ^{1}H.[26] Thus, it became obvious already in the early times of MRI that the use of paramagnetic systems can alter relaxation times and thus generate contrast in MRI. These paramagnetic agents enhance the contrast effect and the intensity of the region of interest, usually inducing changes in the relaxation times of water

nuclei in their surroundings.[16,27-30] These paramagnetic compounds are known as **contrast agents** (CAs).

1.3.1. Contrast agents

Currently, contrast agents are used in about one third of the clinical scans obtained with this technique.[30,31] These chemical substances are used in order to improve the specificity, quality and resolution of the images. They can be classified according to the effect that they produce in the magnetic resonance image. The most common CAs are those producing a shortening on the relaxation times.[27-30] This shortening can affect the longitudinal relaxation times (T_1), resulting in an increase of the signal intensity, or altering the transverse relaxation times (T_2), leading to a decrease of the signal intensity.[16,27-30] The CAs based on the modification of the T_1 are called traditional contrast agents or T_1-weighted, and they produce brighter images. Typically these agents are complexes of paramagnetic ions, the mostly spread and commonly used being based on the gadolinium ion (Gd^{3+}).[27-30] On the other hand, those CAs that affect T_2 are known

as T_2 or T_2* (pronounced as "*tee two star*", when they consider T_2 and field inhomogeneity), providing darker images.[16a] These CAs are fundamentally superparamagnetic particles, namely magnetite particles with a size of around 50-150 nm in diameter, also known as superparamagnetic iron oxides (SPIOs), and they were developed more recently than the classical Gd^{3+} agents.[16a] The main drawbacks concerning T_2 agents are usually the poor specificity and the longer scan times in comparison with T_1 agents,[32] but the stronger paramagnetism affects to broader zones and the amount of CA required to the examinations is lower than using gadolinium contrast agents.[16a] This is related to the stronger paramagnetism of the particles that spread the inhomogeneity on larger volumes, meanwhile gadolinium contrast agents affect mainly the protons located at very short distances. In fact, bigger amounts of SPIOs can produce huge shortenings on T_2, which may be counterproductive for recording the images, as signal intensity can decrease to the point that is hardly observed.[16a]
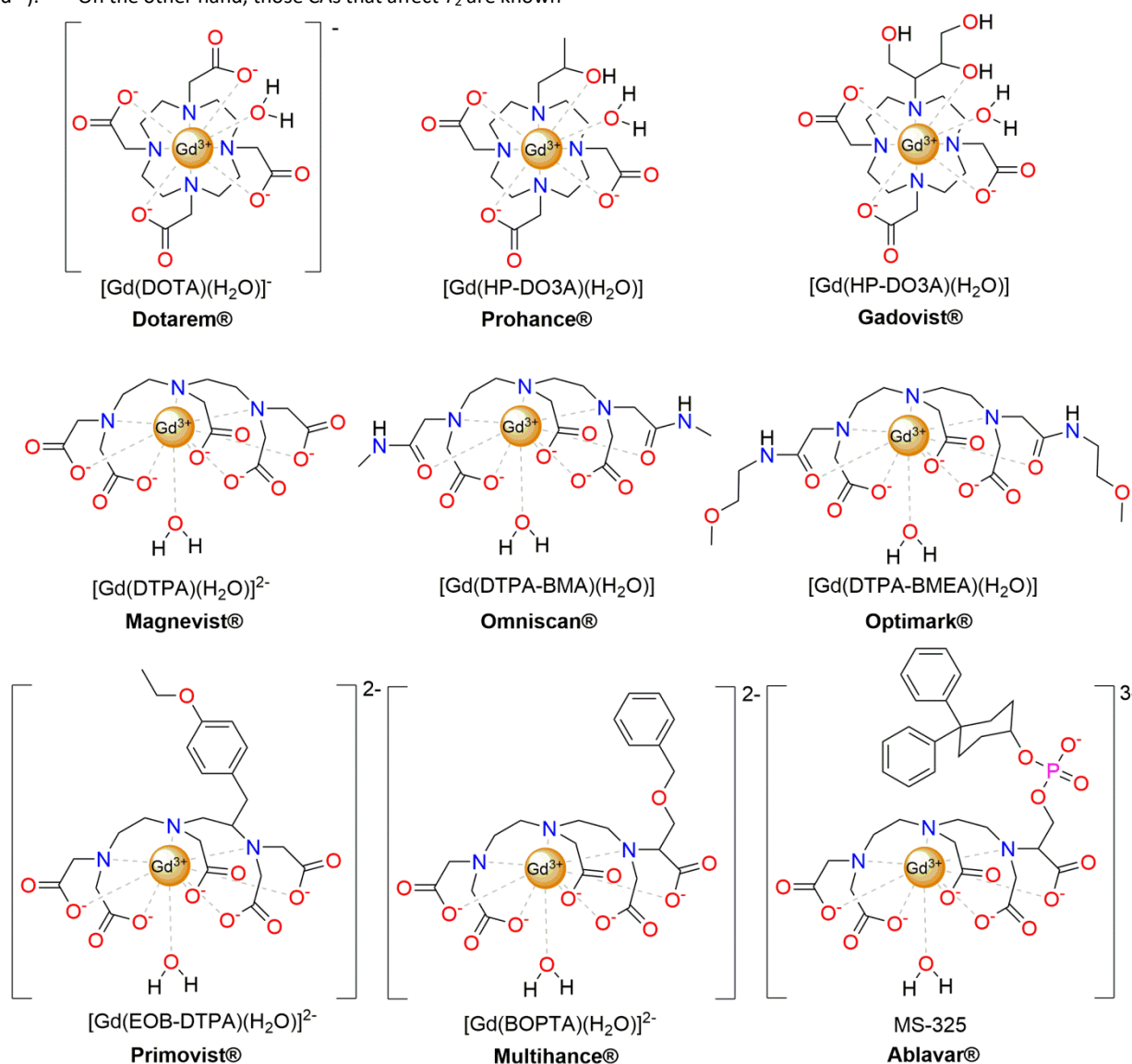
Figure 3. The nine Gd^{3+}-based contrast agents approved for clinical practice.[33]

Another class of CAs relies on the accumulation of these substances in specific locations within the body. These agents or probes give a differentiating response to some MR parameters, as radiofrequency, saturation pulses or magnetic field, or to some physiological parameters like substance concentration, pH or the presence of endogenous anions or cations, enzymatic or redox activity…[27,30,34] Due to the specific response that they provide, it is possible to locate these CAs and get contrast enhancement for an accurate diagnosis and later treatment.[30,35]

Traditional (T_1) contrast agents. Some paramagnetic transition metal ions like Mn^{2+} and Fe^{3+} played a very important role in the history and evolution of MRI. These metal ions were used as T_1 shortening agents to investigate their binding to DNA.[36-38] Pioneering MRI studies reported by Lauterbur and Goldman[28,36-38] in the 1970s used a Mn^{2+} salt to differentiate normal myocardial tissue and infracted zones in dogs.[28,38] This was achieved because normal myocardial tissue accumulates Mn^{2+}, resulting in brighter (more intense) spots in the images compared with infarcted regions. Subsequently, $FeCl_3$ was used to enhance the gastrointestinal track in humans.[36b] Some years later, it was discovered that a Gd^{3+} complex, $[Gd(DTPA)](H_2O)]^{2-}$, was very efficient in enhancing cerebral tumours in humans after intravenous injection of the agent.[5,28] This astonishing discovery prompted a very intense research on Gd^{3+}-based CAs, which eventually led to the commercialisation of several Gd^{3+} agents.[16,27-33]

The first Gd^{3+}-based contrast agent (GdCA) approved for clinical use was gadopentetate dimeglumine or gadopentetic acid, a salt of $[Gd(DTPA)](H_2O)]^{2-}$ known by its commercial name Magnevist®, which was authorised in 1988.[28-33] Subsequently, a number of Gd^{3+}-based CAs entered the market, reaching a total number of nine gadolinium complexes (Figure 3).[33]

Traditional T_1 contrast agents were conceived to reduce the longitudinal relaxation times of bulk water molecules producing a positive effect, giving rise to bright images.[16] The use of Gd^{3+} for this purpose is related to its optimal magnetic properties, which make this exogenous paramagnetic metal ion an ideal relaxation agent. The $[Xe]4f^7$ electron configuration of Gd^{3+} results in a high effective magnetic moment associated to the presence of seven unpaired electrons (μ^2= 63 BM^2).[39] Furthermore, the symmetrical ^8S ground state results in a very slow relaxation of the electron spin, making Gd^{3+} a very powerful relaxation agent. The paramagnetism of Gd^{3+} modifies both the longitudinal (spin-lattice) and the transverse (spin-spin) relaxation times. When the concentration used for the examinations is low (around 0.1 mmol Gd/kg of body weight) the effect on the longitudinal relaxation predominates over transverse relaxation, while at higher doses (around 1 mmol/kg of body weight), transverse relaxation dominates over longitudinal relaxation.[16a]

These Gd^{3+} chelates used in clinical practice can be classified in linear and macrocyclic by considering the structural features of the ligand (Figure 3). This classification is relevant, as the stability of these chelates is directly related to their structure. Indeed, it has been demonstrated that macrocyclic complexes are kinetically more inert than linear ones,[40] which reduces the possibility that the toxic Gd^{3+} ion is released *in vivo*. The toxicity of Gd^{3+} is an important issue, as it was related to a new disease, nephrogenic systemic fibrosis (NSF), allergies and other side effects problems. NSF is a potentially fatal disease that was discovered in 2006 and associated to the administration of Gd^{3+}-based CAs to patients having renal impairment, particularly after the administration of several doses.[41] NSF was correlated to the release of the metal ion in the body. More recently, several studies evidenced deposits of gadolinium (the metal ion and/or the complexed form) accumulating in the brain and other tissues, although no side effects were yet described associated to these deposits.[41] Presently, the most widely used CA is the Gd^{3+}-based complex DOTAREM®, which consist in a macrocyclic ligand containing four acetate groups to ensure a firm coordination of the metal ion within the ligand cavity.[42] Other Gd^{3+}-based CAs as Gadovist® (gadobutrol) and Prohance® (gadoteridol) are also derived from macrocyclic structures, while others like Ablavar® (formerly known as Vasovist®, gadofosveset trisodium), Magnevist® (gadopentetic acid), Multihance® (gadobenic acid), Omniscan® (gadodiamide), Optimark® (gadoversetamide) and Primovist® (gadoxetic acid), are linear complexes derived from a DTPA or DTPA-bisamide framework (Figure 3).[27-30,33,35]

As a consequence of the aforementioned side effects and health problems, on December 2017 the European Medicines Agency (EMA) introduced some restrictions and revoked some authorisations for the use of linear CAs.[43] Meanwhile, all the macrocyclic agents maintain their authorisations, as they were demonstrated to be kinetically more inert than linear systems. Indeed, the authorisations for intravenous administration of Omniscan®, Optimark® and Magnevist® have been suspended, while the intravenous administration of Multihance® has been restricted to liver scans. The authorisations for intra-articular administration of Magnevist® and intravenous administration of Primovist® were both maintained.[43,44]

Another family of traditional T_1 contrast agents is based on manganese complexes. The high-spin Mn^{2+} ion possesses five unpaired d electrons that provides a high effective magnetic moment, as well as a long electronic relaxation time.[45] Manganese-enhanced magnetic resonance imaging (MEMRI) is an imaging technique of growing interest for biomedical research using animal models. MEMRI was introduced almost 30 years ago for evaluation of Mn^{2+} toxicity in rats[46], and generally uses $MnCl_2$ to generate contrast. Manganese is present in trace amounts within the body, and can be found in human tissues, bones and organs.[47] This ion is required for the normal brain and nerve functions, and for other metabolism purposes. As a result, the body can assimilate small amounts of this metal ion for its daily function, and developed strategies to manage small excesses.[46,48] Thus, manganese agents are regarded as having a better toxicity profile compared with the Gd^{3+} counterparts. Nevertheless, big amounts or a chronic exposure to this metal ion can cause manganism, a progressive neurodegenerative disease. Furthermore, overexpose to this ion may lead to cardiac toxicity or even hepatic failure.[47]

Only two manganese(II)-based probes were clinically approved for human use, Teslascan™ (mangafordipir trisodium, MnDPDP) and LumenHance™ (a liposomal-matrix of polygalacturonic acid and xanthan gum-encapsulated manganese(II) chloride tetrahydrate) (Figure 4).[27-30,33] Teslascan™ was designed as a liver-specific contrast agent, while LumenHance™ was used as an oral contrast for gastrointestinal imaging.[49] Both of them have been suspended for human administration, although LumenHance™ (free ionic manganese) can still be used for animal MRI studies.[50] The role of the ligand present in MnDPDP is to promote a slow release of Mn^{2+} in the liver, rather than providing a very stable complex (Figure 4).[51]
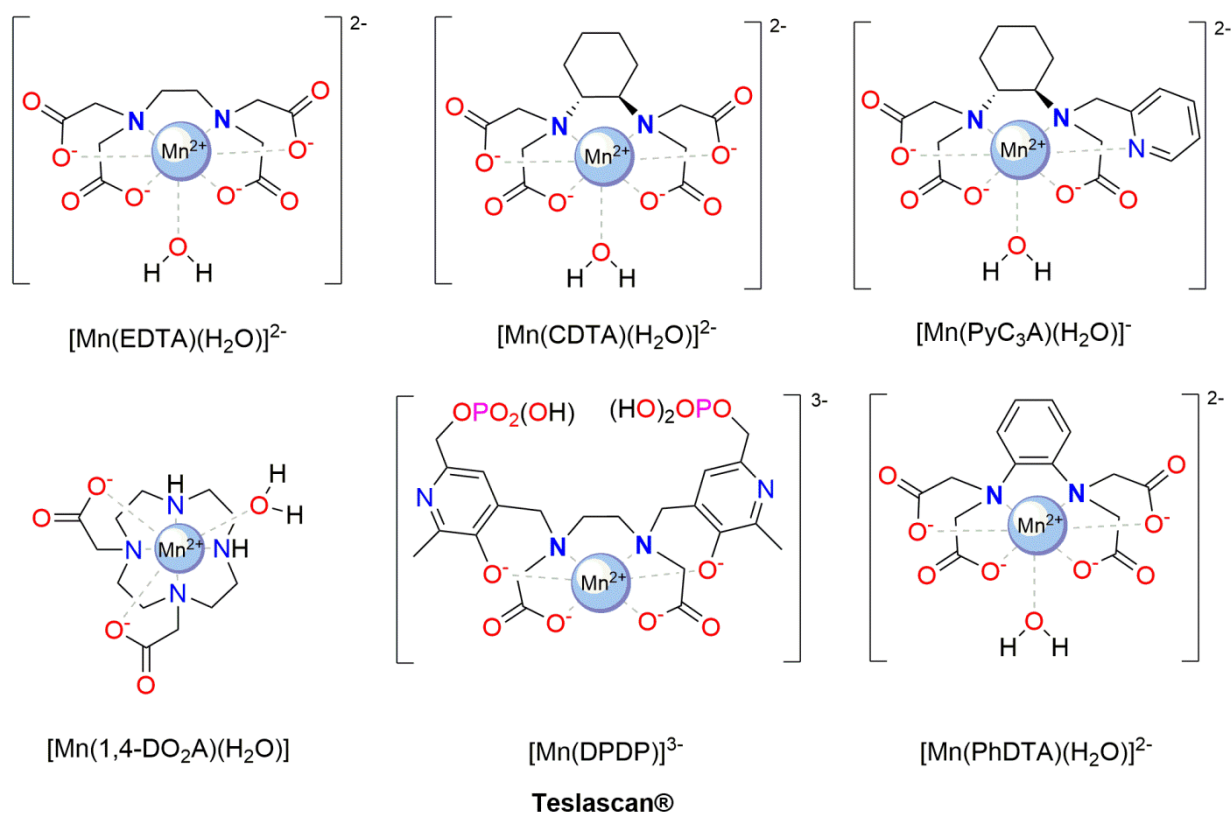
Figure 4. Structures of Mn^{2+} complexes proposed as contrast agents.

The toxicity problems associated with the administration of some Gd^{3+} agents triggered a renewed interest in Mn^{2+} agents. For instance, a not yet clinical approved manganese-based contrast agent, [MnPyC3A]$^-$, was proposed as an alternative to Gd^{3+}-based CAs in 2015.[52] This CA candidate is derived from a rigid platform containing three acetate arms, which guarantee a strong coordination of the metal ion. The ligand leaves a vacant coordination site available for a water molecule, which results in a relaxation enhancement of water proton nuclei comparable to those presented in small Gd^{3+} agents.[53] A recent study reported by Gale *et al.*[52] in 2018 presents some encouraging results for this system, corroborating the potential of this probe as an alternative to Gd^{3+} probes. This study claimed the highly stability of the system, so any potential release of the metal ion will be within the threshold of its tolerability.

A number of Mn^{2+} complexes were reported to possess relaxation properties similar to those of small monohydrated Gd^{3+} chelates.[54] Some of the CA candidates reported so far are [Mn(EDTA)]$^{2-}$ and [Mn(1,4-DO2A)] derivatives (Figure 4), which were found to present rather high thermodynamic stability.[16b,45,55] The rigidified [Mn(EDTA)]$^{2-}$ derivatives [Mn(PhDTA)]$^{2-}$ and [Mn(CDTA)]$^{2-}$ present slower dissociation kinetics when compared with the parent EDTA complex.[56] Bis-amide derivatives of [Mn(1,4-DO2A)] were also found to be more inert respect to complex dissociation when compared to the parent complex.[55] Nevertheless, the design of inert Mn^{2+} complexes for application in MRI remains a challenging task for coordination chemists.

The ability of a Gd^{3+} or Mn^{2+} complex to promote the relaxation of surrounding water molecules depends on a relatively large number of physicochemical parameters. The efficiency of the CA is generally assessed *in vitro* in terms of relaxivity, r_{1p}, which is defined

as the relaxation enhancement of water protons induced by the paramagnetic agent at 1 mM concentration of the paramagnetic metal ion. The observed relaxivity contains both inner and outer-sphere contributions, which are originating from the water molecules directly bound to the metal ion and water molecules freely diffusing in the vicinity of the paramagnetic metal ion, respectively.
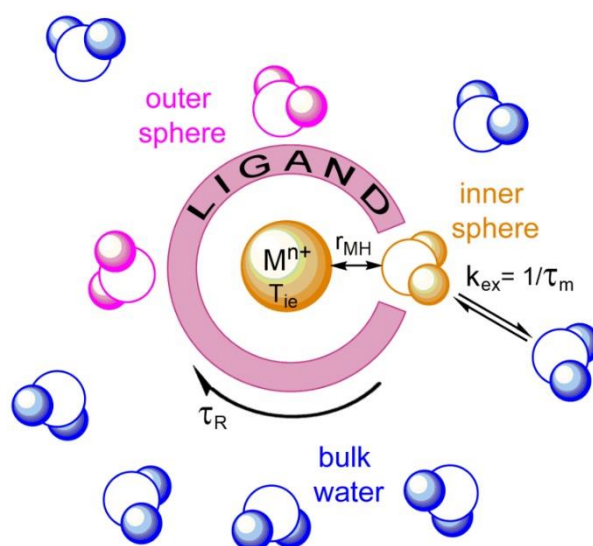
Figure 5. Schematic representation of a T_1 contrast agent. M^{n+} represents a paramagnetic ion (Gd^{3+} or Mn^{2+}) coordinated by a ligand and an inner-sphere water molecule (orange) involved in fast exchange with bulk water (blue).

The inner-sphere contribution to relaxivity is directly proportional to the number of water molecules coordinated to the metal ion (q), and depends on the mean residence time of a water molecule in the metal ion inner-sphere (τ_M) and the relaxation time of the proton nuclei of inner-sphere water molecules (T_{1m}^H), as shown in Eq (1). The term $1/1000 \times 55.55$ normalises the relaxivity to a mM concentration of the paramagnetic agent.[16b,57]

This relaxation time considers the dipole-dipole (DD) and the scalar (SC) mechanisms, which are proportional to $S(S+1)$, with the electron spin S being 7/2 and 5/2 for Gd^{3+} and Mn^{2+}, respectively.

$$r_{1p,is} = \frac{1}{1000} \times \frac{q}{55.55} \times \frac{1}{T_{1m}^H + \tau_m} \tag{1}$$

The relaxation time of inner-sphere proton nuclei are dominated by the dipole-dipole (DD) mechanism, involving the interaction of the electron and nuclear spins, which can be expressed according to the following equations:

$$\left(\frac{1}{T_{1m}^H}\right)^{DD} = \frac{2}{15}\left(\frac{\mu_0}{4\pi}\right)^2 \frac{\gamma_I^2 g^2 \mu_B^2}{r_{MH}^6} S(S+1)\left(\frac{3\tau_{d1}}{1+\omega_I^2\tau_{d1}^2} + \frac{7\tau_{d2}}{1+4\omega_s^2\tau_{d2}^2}\right) \tag{2}$$

$$\frac{1}{\tau_{di}} = \frac{1}{\tau_R} + \frac{1}{\tau_m} + \frac{1}{T_{ie}}, \text{with } i = 1,2 \tag{3}$$

Where S is the electron spin, γ_I is the nuclear gyromagnetic ratio, g is the electron g factor, μ_B is the Bohr magneton, r_{MH} is the distance between the electron and nuclear spins, and ω_I and ω_S are the nuclear and electron Larmor frequencies, respectively. The terms τ_{di} (i = 1 or 2) include the rotational correlation time τ_R, the aforementioned mean water residence time, τ_M, and the electronic relaxation times T_{ie}.

The outer-sphere contribution is commonly defined by Freed's model,[58] which describes the long range dipolar coupling between the nuclear spin of water molecules diffusing nearby the paramagnetic ion and the electron spin of the paramagnetic centre:

$$r_{1p,OS} = \frac{32N_A\pi}{405}\left(\frac{\mu_0}{4\pi}\right)^2 \frac{\hbar^2\gamma_S^2\gamma_I^2}{a_{MH}D_{MH}} S(S+1)[3J_{OS}(\omega_I; T_{1e}) + 7J_{OS}(\omega_I; T_{2e})] \tag{4}$$

The term $J_{OS}(\omega_I; T_{je})$ in Eq. 4 is described by the following expression:

$$J_{OS}(\omega_I; T_{je}) = Re\left[\frac{1+\frac{1}{4}\left(i\omega\tau_{MH}+\frac{\tau_{MH}}{T_{je}}\right)^{1/2}}{1+\left(i\omega\tau_{MH}+\frac{\tau_{MH}}{T_{je}}\right)^{1/2}+\frac{4}{9}\left(i\omega\tau_{MH}+\frac{\tau_{MH}}{T_{je}}\right)+\frac{1}{9}\left(i\omega\tau_{MH}+\frac{\tau_{MH}}{T_{je}}\right)^{3/2}}\right] \tag{5}$$

With $\tau_{MnH} = \frac{a_{MnH}^2}{D_{MnH}}$ (6)

In Eqs (4)-(6) N_A is the Avogadro constant, a_{MH} is the distance of closest approach of an outer-sphere water molecule to the paramagnetic metal ion, T_{1e} and T_{2e} are the longitudinal and transverse relaxation times of the electron spin and γ_S the electron gyromagnetic ratio. The relative diffusion coefficient D_{MH} is the sum of the self-diffusion coefficients of the metal complex and water molecules. The longitudinal (T_{1e}) and transverse (T_{2e}) electronic relaxation times are generally described by Eqs (7)-(8), where τ_V is the correlation time characterising the modulation of the zero-field-splitting (ZFS) interaction, Δ^2 is the mean square ZFS energy and ω_S is the electron Larmor frequency.

$$\frac{1}{T_{2e}} = \frac{1}{25}\Delta^2\tau_v\{4S(S+1)-3\}\left(\frac{1}{1+\omega_s^2\tau_v^2}+\frac{4}{1+4\omega_s^2\tau_v^2}\right) \tag{7}$$

$$\frac{1}{T_{2e}} = \frac{1}{50}\Delta^2\tau_v\{4S(S+1)-3\}\left(3+\frac{5}{1+\omega_s^2\tau_v^2}+\frac{2}{1+4\omega_s^2\tau_v^2}\right) \tag{8}$$

The electronic relaxation affects the inner-sphere relaxivity at low fields (< 20 MHz), while at the imaging fields the main parameters affecting r_{1p} are τ_M and τ_R. The main differences between the efficiency of Gd^{3+} and Mn^{2+} complexes are related to the different $S(S+1)$ terms, which take values of 15.75 and 8.75, respectively. Thus, if all other parameters were similar, the relaxivity of a Gd^{3+} complex is expected to be about 1.8 times higher than that of a Mn^{2+} complex. However, this can be compensated in part by the shorter r_{MnH} distance (~2.8 Å) compared to the r_{GdH} one (3.1 $\pm$ 0.1 Å). As a result, some Mn^{2+} complexes present relaxivities comparable or higher than those of commercially available Gd^{3+} agents.[59]

T_2-weighted contrast agents. This category of contrast agents are mainly used as blood-pool agents,[60] providing imaging of the venous system. As result of the larger size of this agents in comparison with the molecular T_1 probes, the diffusion occurs into the intravascular circulation without crossing the endothelial membrane into the extracellular space.[61] These contrast agents are fundamentally superparamagnetic iron oxides (SPIOs), usually magnetite (Fe_3O_4) or maghemite (γ-Fe_2O_3) –type nanoparticles, providing a negative contrast.[16,60] The first SPIOs that reached the market were Endorem™ (called in USA Feridex) and Resovist™.[27-30,60,61] Endorem™ is composed by magnetite crystals of 4.3-4.8 nm radius, while Resovist™ is a suspension of 4.2 nm radius nanoparticles of both iron oxides.[62] In both cases the particles are coated with a biocompatible shell to prevent their agglomeration. According to their size they can be classified in micron-sized particles of iron oxide (MPIO), superparamagnetic iron oxides or in ultrasmall superparamagnetic iron oxides (USPIOs).[16] MPIO are particles with a diameter of several microns that due to their large size are only conceived for oral administration. They are used to explore the gastrointestinal tract and also to observe individual cells. Nanoparticles with a size inferior to 50 nm are known as USPIOs, and a new generation with sizes below 10 nm are starting to be considered as T_1 contrast agents due to their extraordinary T_1-enhancing properties, as the r_2/r_1 ratio for a SPIO particles decreases with decreasing particle size.[16,27]
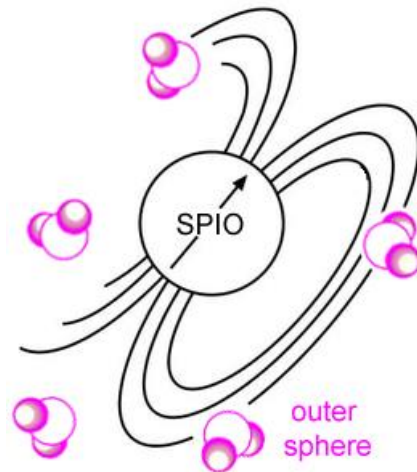
Figure 6. Schematic representation of the outer-sphere effect on T_2 provided by superparamagnetic iron oxide nanoparticles.

The physics behind the behaviour of these superparamagnetic particles is related to the absence of magnetic domain walls from a certain nanoparticle size (depending on the material),[63,64] so every crystal is composed by a single domain of thousands of magnetic spins susceptible to be magnetised in the presence of the external magnetic field, creating a single and large magnetic moment.[63] It has been shown that the inner-sphere contribution to the relaxivities of iron oxide particles is negligible, and thus relaxivities are generally explained by the outer-sphere mechanism (Figure 6).[39,64] In the case of magnetite and maghemite nanoparticles, this mono-domain size is 128 and 166 nm respectively, so below that diameter and under a specific temperature (blocking temperature, where the resistance to the alignment of the spins to the field is overcome) the nanoparticles are presenting superparamagnetism.[39,63,64] SPIOs and USPIOs are formulated for the diagnosis of liver tumours, as they are assimilated preferentially by Kupffer cells in the spleen and liver.[27,39,60-62] Although the progress of these CAs to the market was initially slow, several compounds were approved for clinical use: Endorem (Feridex I.V., Ferumoxide, AMI-25), Resovist (Cliavist), Sinerem (Combidex, Ferumoxtran, AMI-227), Clariscan (PEG-Fero, Feruglose NC100150) and Lumirem (GastroMARK, ferumoxsil, AMI-121)[62b]. However, they were later withdrawn from the market.[65] Even though SPIOs have exhibited very low or no cytotoxic activity in doses below the 100 mg/mL threshold, coated and uncoated SPIOs have presented in *in vivo* and *in vitro* studies some modifications in cell behaviour through diverse mechanisms, for instance disruption of cytoskeletons, inducement of oxidative stress, generation of free radicals, impairment of mitochondrial function, damage of DNA, and altering of cell signalling pathways among others.[66]

In addition to the SPIOs, some other compounds based on the lanthanide dysprosium or on superparamagnetic iron platinum particles (SIPP) are being considered as T_2 contrast agents. The Dy^{3+} metal ion possesses four unpaired electrons and a fast electron spin relaxation time that render a negligible T_1 effect, whereas its high magnetic moment (10.6 BM) makes this ion the most powerful T_2 susceptibility contrast agent.[60,67] Studies employing the same DTPA platform present in Magnevist for Gd^{3+} complexation explored the use of the Dy^{3+} as a T_2 agent. These studies found out [Dy(DTPA)]$^{2-}$ problematic for clinical development due to the high dosages needed to observe a useful decrease on signal intensity, higher than those used for [Gd(DTPA)]$^{2-}$. Later on, it was shown that the non-ionic complex [Dy(DTPA-BMA)] (Sprodyamide) increases visual contrast producing darker images by intravenous administration.[67a] However, given the toxicity concerns related to the use of DTPA and DTPA-bisamide Gd^{3+} complexes, it is unlikely that any of these complexes will have practical relevance. Nowadays, the dysprosium-based systems that are receiving more attention are solid state probes that may be combined with other metal ions (gadolinium, thulium,…) to obtain multimodal probes.[68,69]

Other superparamagnetic contrast agents being rediscovered during the last years are the SIPPs, although they have not been tested in humans so far. These compounds offer better T_2 relaxivity in comparison with SPIOs and USPIOs.[29,65] They are presented as micelles encapsulated with phospholipids and are designed for specifically target human prostate cancer cells.[60,65]
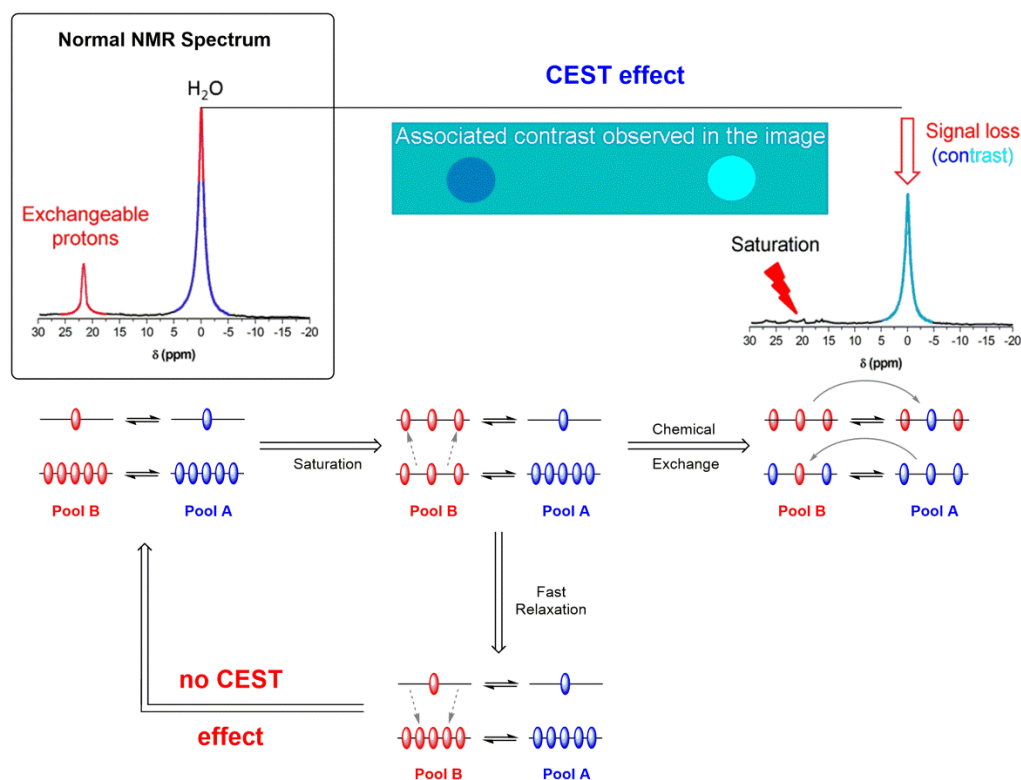
Figure 7. Illustration of the Chemical Exchange Saturation Transfer (CEST) mechanism. Saturation of a pool of exchangeable protons with a radiofrequency pulse results in the magnetisation of bulk water protons through chemical exchange. For the CEST effect to be efficient, chemical exchange should be faster than relaxation.[70]

CEST contrast agents. Another group of contrast agents takes advantage of the chemical exchange saturation transfer (CEST) mechanism. This technique provides a selective response to a particular radiofrequency pulse, which offers the possibility to modulate the contrast on demand.[71] CEST agents contain a pool of exchangeable protons, typically –NH or –OH groups of the molecule or even a water molecule coordinated to a metal ion. Application of a radiofrequency pulse at the spectral frequency of the exchangeable protons (Figure 7) results in the transfer of some magnetisation to proton nuclei of the bulk water signal, hence the intensity of the water signal is decreased.[71-73] The enhancement produced on the image is perceived as a negative contrast. This innovative technique was introduced around 20 years ago by Ward, Aletras and Balaban,[71] and conceived initially for direct application on different metabolites present in the body that contain exchangeable protons (amino acids, proteins, sugars, nucleotides; diamagnetic CEST or diaCEST).

One of the most relevant requirements for the effectiveness of the CEST effect is the slow-to-intermediate exchange regime between the pool of exchangeable protons and bulk water, a condition that is fulfilled when the exchange rate k_{ex} is lower or similar than the chemical shift difference between the exchanging protons and bulk water $\Delta\omega$ ($k_{ex} \leq \Delta\omega$).[71-73] In the case of metabolites acting as endogenous agents, the chemical shift difference is generally small (less than 6 ppm), so that the slow exchange rates required to fulfil the $k_{ex} \leq \Delta\omega$ condition represent an important limitation for the application of this technique.[71] Furthermore, the broadening of the bulk water signal *in vivo* due the inhomogeneities on the local magnetic field, hinders the selective saturation of exchangeable protons at their specific magnetic resonance frequency.[73] This problem can be attenuated by increasing the magnetic field (high field MRI scanners)[74] or by incorporating a paramagnetic centre to the probe, yielding paramagnetic CEST or paraCEST probes.[73]

Some paramagnetic ions induce important paramagnetic shifts in the proton signals of nuclei close to the paramagnetic centre without causing excessive line-broadening.[75] This increases the $\Delta\omega$ values, therefore the slow-to-intermediate exchange regime can be achieved with faster exchange rates. Nevertheless, once this condition is satisfied, the exchange rates between the two pools should ideally present high values.[71-73] The reason for this is that relaxation processes compete with the CEST mechanism, as illustrated in Figure 7. In case that the relaxation of protons in the exchangeable pool is faster than chemical exchange the system would recover the Boltzmann distribution before the exchange takes place. Similarly, if the relaxation of the protons of bulk water is too fast, the new spin distribution resulting from saturation transfer would not be maintained long enough to be observed in the NMR spectrum. Consequently, an optimal CEST effect requires that the relaxation times of the protons involved are long compared with those characterising chemical exchange. Furthermore, the CEST effect is affected by the applied field, which modifies the frequency separation between the pools involved in chemical exchange. Moreover, the CEST efficiency is related to the concentration of exchangeable protons and the radiofrequency power applied (B_1), which increases the saturation transfer observed.[72,73] However, high saturation powers should be avoided for *in vivo* applications.[76] Two small molecules are already approved for their use as CEST contrast agent for intravenous administration. One of them is glucose, used for its –OH exchangeable group, and another is iopamidol, a contrast agent currently used for X-ray that contains a –NH exchangeable group. Both of them are being used in human clinical trials.[30]

The most common paramagnetic metal ions used to obtain paraCEST agents are lanthanide ions such as Eu^{3+},[72] Tm^{3+}[78] or Yb^{3+}[79,77] and transition metals like Ni^{2+},[80] Fe^{2+}[81] and Co^{2+}.[82,83,84] The influence of the paramagnetic centre in the signal of the labile protons of the exogenous agent shifts the ^1H resonance with respect to bulk water. Figure 8 shows some typical paraCEST agents based on different paramagnetic metal ions and exchangeable protons. For instance $[Eu(DOTAMGly)(H_2O)]^-$ displays CEST effect upon saturation of the signal of the coordinated water molecule shifted by about 55 ppm with respect to the water peak.[77a,85,86] In the case of $[Eu(C_{18}Py_2)]^{3+}$ [87] the CEST effect is provided by the hydroxyl protons of the ligand. Another type of labile protons that often provide CEST effect are protons of amide groups, such as those of the Ni^{2+} and Fe^{2+} complexes shown in Figure 8. Some of the paramagnetic CEST contrast agents can present a smart response to some physiological conditions, such as pH, temperature, concentration of endogenous metal ions, redox potential or enzymatic activity.[77,81a,82b,84d,88]

$[Eu(DOTAMGly)(H_2O)]^-$

$[Eu(C_{18}Py_2)]^{3+}$

$[Fe(DOTAMGlyOEt)]^{2+}$

$[Ni(NOTAM)]^{2+}$
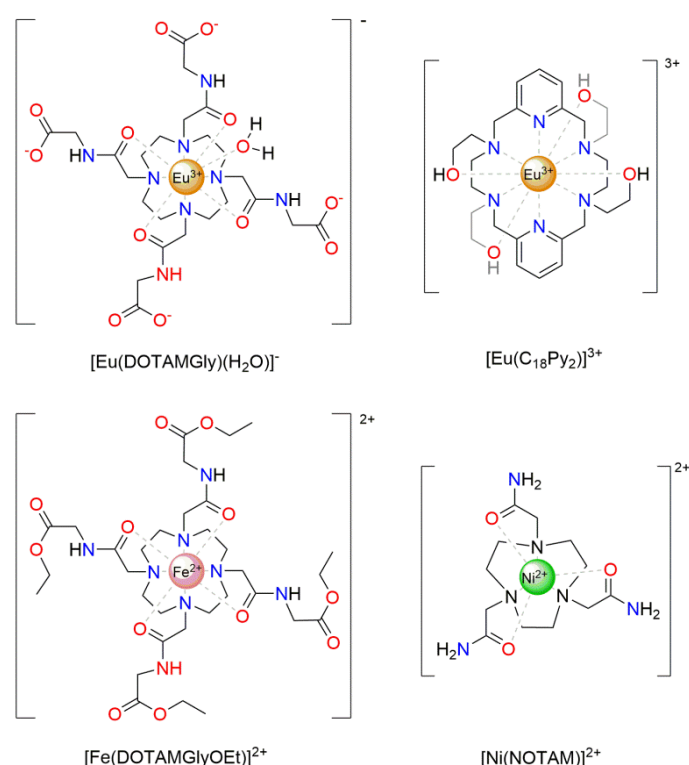
Figure 8. Typical paraCEST agents.

Direct detection contrast agents. One of the major disadvantages of traditional T_1 and T_2 contrast agents and also CEST agents is that they produce an effect in the bulk water signal.[27,30] Since the human body is composted on around 60% of water, these contrast agents are affected by a considerable background signal. This background signal can be improved by the use of diverse radiofrequency pulse-sequences to increase the signal-to-noise (SNR) ratio, as well as refining the design of the probes to ensure a better T_2/T_1 ratio.[16a]

Different groups have proposed the use of nuclei different than proton ^1H, such as ^{19}F or ^{11}B,[89] as they allow a selective detection at their specific resonance frequency without providing background signal.[90] Among these types of agents, ^{19}F is likely the most promising one. Fluorinated nuclei offer a similar sensitivity to ^1H (83%) and its isotope is present at 100% natural abundance.[91] The high

gyromagnetic ratio (40.05 MHz/T) makes the detection of the nuclei simple with small adjustments on the Larmor frequency from the current ^1H MRI scanners. Its wide chemical shift range (~350 ppm) and the non-quadrupolar nature (I = ½) turns this nucleus into an element of special interest for its incorporation in contrast agents.[90-92]

One of the requirements for the success of these nuclei as direct detection contrast agent is the presence of a single major resonance involving as many equivalent nuclei as possible, so that the intensity of the signal is maximised at lower concentration of the probe. Indeed, the disadvantage of these agents is the necessity of high amounts of these molecules in order to get a high-resolution and high-quality image, which likely could be turned into an increase in the toxicity or limitations related to the solubility of the contrast agent.[30,91,92] Emulsions containing perfluorocarbon molecules such as hexafluorobenzene (HFB) or perfluoro-15-crown-5 ether (PFCE) have been proposed as ^{19}F contrast agents.[30] However, fluorinated compounds possess relatively long relaxation times, which elongate acquisition times.[91] Thus, paramagnetic fluorinated probes were proposed as ^{19}F MRI agents, as the relaxation enhancement (PRE) provided by the paramagnetic centre located in the vicinity of ^{19}F nuclei shortens the relaxation times and thus MRI acquisition.[90b,92] Both transition metals and lanthanide metal ions were used to promote T_1 and T_2 relaxation of the ^{19}F signal, notably by the groups of D. Parker and V. Pierre (Figure 9). The final resolution of the collected images is dictated by the optimal design of the probes, both in terms of the metal–^{19}F nuclei distance and the election of the appropriate metal ion with its effective magnetic moment.[91e,93] These fluorinated agents can combine different approaches in one single probe, for instance providing response to diverse frequencies (^1H and ^{19}F, for instance)[91ac,92h,93,94ab] or to a specific frequency and a certain physiological biomarker (i.e. ^{19}F and metabolic function)[91ac,94c]. Usually it is sought to merge a more specific response with the traditional one, so one can determine the location and concentration of the labelled agents or cells with the positive contrast due to the effect in proton relaxation of water.
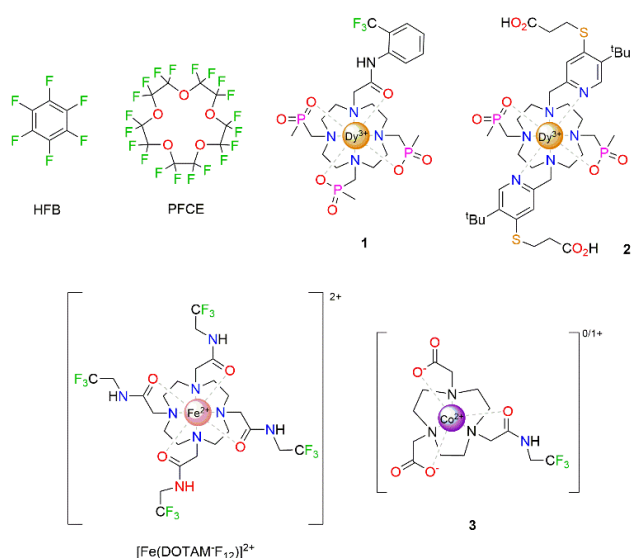
Another class of probes suitable for direct detection are paraSHIFT probes. These paramagnetic complexes, typically with lanthanide ions, present signals arising from a large number of magnetically equivalent nuclei that are shifted outside the conventional ^1H chemical shift range by effect of the paramagnetic shift.[88,95] Typically the shifted signals arise from *tert*-butyl groups, which can be shifted in opposite directions depending on the chosen lanthanide ion. Both the bulk water signal and the signal of *tert*-butyl groups can be used for dual-frequency MRI, with the chemical shift of the *tert*-butyl group being very sensitive to temperature.

Responsive contrast agents. Any contrast agent providing response to a change in a physiological biomarker is included in this category.[96] The response of these agents to this change depends on the modification of physicochemical factors like water exchange rate, electron spin state, superparamagnetism of the agent, accessibility of water to the agent, modifications of the tumbling time or magnetic resonance frequency, among others. Usually these factors are modified by changes in pH, temperature, light, concentration of metal ions, metabolites, proteins, nucleic acids, activity of enzymes or changes in redox state.[97]

One of the most interesting responsive probes are pH-sensitive agents. Tumour tissue is known to possess different pH than normal tissue.[98] Depending on the type of tumour the pH range varies. The response to pH changes usually is achieved by including groups in the ligands that undergo protonation in the physiological pH window. Those groups can affect the hydration number of the metal complex, modify the accessibility of bulk water to the agent or its exchange rate.[27-30,33] Another interesting example is the response to light of some contrast agents.[27-30,33,96] Based on the stimulation of the fluorescence of many proteins by a light source that could be external to the biological system, from the catalysis of luciferin by luciferase or via Cerenkov radiation,[96] these probes can experience isomeric conformation changes after light irradiation. These changes can modify the water exchange rate of the agent by the accessibility of the bulk water to the coordination environment of the system, or the water coordination at the paramagnetic centre.[99] Most of the responsive contrast agents present a change in the conformation, geometrical or electronical disposition in the presence of these microenvironmental factors. For instance, in the case of contrast agents that detect metal ions (i.e. Zn^{2+},[100] Ca^{2+},[101] Mg^{2+},[102] Na^+,[103] Cu^+[104] or Cu^{2+} [89]), the ligand that conforms the system can present certain affinity to bind these metal ions and produce a change on the T_1 relaxation due to the water accessibility to the coordinated metal ion,[96] usually the Gd^{3+} metal ion. Metabolite-responsive contrast agents are generally based on the same principle, reducing the water access to the central metal ion. For instance, an increased T_1 relaxation time can be observed when a noncovalent adduct with sugars and pyrophosphate is formed and hinders water accessibility.[96] For protein, nucleic acid or enzyme responsive probes it is observed the same trend, producing a modification on T_1 relaxation time or on chemical shift. The drawback of contrast agents for nucleic acid detection is the low concentration of DNA, which represents an important limitation for MRI detection.[30,96] Regarding redox contrast agents, their detection is based on physiological processes. These physiological processes are regulated by metabolites providing a redox environment that can modify the oxidation state of the metal ion or of the ligand, giving rise to changes on the observed relaxation times or chemical shifts.[96]

Figure 9. Compounds proposed as ^{19}F and paraSHIFT MRI probes.

1.4.   References

1. International Monetary Fund. World Economic Outlook: Challenges to Steady Growth. Washinton DC, October 2018.
2. Y. Li, A. Pan, D. D. Wang, X. Liu, K. Dhana, O. H. Franco, S. Kaptoge , E. Di Angelantonio, M. Stampfer, W. C. Willett and F. B. Hu, *Circulation*, 2018, **138**, 345.
3. (a) F. Carinci, K. Van Gool, J. Mainz, J. Veillard, E. C. Pichora, J. M. Januel, I. Arispe, S. M. Kim and N.S. Klazinga, *International Journal for Quality in Health Care*, 2015, **27**, 137. (b) The psychological and social needs of patients. British Medical Association, Arts & Health South West, Oxford. 2011. Accessed: 15 December 2018. https://www.ahsw.org.uk/userfiles/Other_Resources/Health__Social_Care_Wellbeing/psychologicalsocialneedsofpatients_tcm41-202964_copy.pdf
4. OECD (2017), Health at a Glance 2017: OECD Indicators, OECD Publishing, Paris, https://doi.org/10.1787/health_glance-2017-en. ISBN 978-92-64-28040-3.
5. Diagnostic Imaging. Geneva, World Health Organization, 2018. Accessed: 15 December 2018. https://www.who.int/diagnostic_imaging/en/
6. Global Health Estimates 2016: Deaths by Cause, Age, Sex, by Country and by Region, 2000-2016. Geneva, World Health Organization, 2018.
7. Global Action Plan for Prevention and Control of Noncommunicable diseases 2013-2020. Geneva, World Health Organization, 2018. ISBN 978 92 4 150623 6
8. R. Weissleder, U. Mahmood, Radiology, 2001, 219, 316.
9. (a) L. Fass, *Molecular Oncology 2* 2008, 115. (b) M. Rudin and R. Weissleder, *Nature Reviews Drug Discovery*, 2003, **2**, 123. (c) R. Weissleder and M. J. Pittet, *Nature* 2008, **452,** 580. (d) M. A. Stammes, S. L. Bugby, T. Porta, K. Pierzchalski, T. Devling, C. Otto, J. Dijkstra, A. L. Vahrmeijer, L.-F. de Geus-Oei and J. S. D. Mieog, *Br J Surg*, 2018, **105**, e69-e83. (e) Medical Imaging and Technology Alliance 2018, Medical Imaging Modalities, MITA, Arlington, VA, Accessed 28 January 2019, https://www.medicalimaging.org/about-mita/medical-imaging-primer/ (f) World Health Organization 2018, Diagnostic Imaging, WHO, Geneva, Accessed 28 January 2019, https://www.who.int/diagnostic_imaging/imaging_modalities/en/ (g) M. L. Gregory, V. J.Burton, Bruce K. Shapiro, Chapter 3 - Developmental Disabilities and Metabolic Disorders, Neurobiology of Brain Disorders, Biological Basis of Neurological and Psychiatric Disorders, 2015, 18.
10. (a) L. De Chiffre, S. Carmignato, J.-P. Kruth, R. Schmitt, A. Weckenmann, *CIRP Annals - Manufacturing Technology* 2014, **63** 655. (b) R. Weissleder, B. D. Ross, A. Rehemtulla and S. S. Gambhir, Molecular imaging: principles and practice, People's Medical Pub. House, Shelton, 2010.
11. (a) H. Jadvar, Cancer Theranostics, Chapter 4, Radionuclide Imaging of Cancer Therapy, 2014, Ed. X. Chen and S. Wong, 45-54. (b) National Cancer Institute at the National Institutes of Health, Diagnosis and Staging, Accessed 14 December 2018, https://www.cancer.gov/about-cancer/diagnosis-staging/diagnosis.
12. (a) M. J. Zigmond, J. T. Coyle and L. P. Rowland, Neurobiology of Brain Disorders: Biological Basis of Neurological and Psychiatric Disorders, San Diego, US, 2015. (b) A. Signore, A. W. J. M. Glaudemans, F. Galli and F. Rouzet, *Biomed Res Int.* 2015, **2015**, 615150.
13. A. T. Soderlund, J. Chaal, G. Tjio, J. J. Totman, M. Conti and David W. Townsend, *J Nucl Med* 2015, **56**, 1285.
14. SPECT-CT. O. Ferrando, A. Chimenz, F. Foppiano, A. Ciarmiello, *J. Diagn. Imaging Ther*. 2018, **5**, 32.
15. D. Komljenovic and T. Bäuerle, Cancer Theranostics, Chapter 8, Ultrasound Imaging of Cancer Therapy, 2014, Ed. X. Chen and S. Wong, 127-137.
16. (a) D. W. McRobbie, E. A. Moore, M. J. Graves and M. R. Prince, MRI: from picture to proton, 2nd Edition, Cambridge, 2007. (b) A. Merbach, L. Helm and É. Tóth, The Chemistry of Contrast Agents in Medical Magnetic Resonance Imaging, 2nd Edition, West Sussex, 2013.
17. (a) M. Solomon, Y. Liu, M. Y. Berezin and S. Achilefu, *Med Princ Pract* 2011, **20**, 397. (b) R. Pleijhuis, L. Crane, M. van Oosten, G. van Dam and V. Ntziachristos, Cancer: Cares, Treatments and Preventions, Chapter Optical imaging applications in cancer research and treatment, 2014. (c) T. Imamura, T. Saitou and R. Kawakami, *Cancer Sci.* 2018, **109**, 912. (d) C. G. Hadjipanayis, H. Jiang, D. W. Roberts and L. Yang, *Semin Oncol.* 2011, **38**, 109.
18. F. Nensa, F. Bamberg, C. Rischpler, L. Menezes, T. D. Poeppel, C. la Fougère, D. Beitzke, S. Rasul, C. Loewe, K. Nikolaou, J. Bucerius, A. Kjaer, M. Gutberlet, N. H. Prakken, R. Vliegenthart, R. H. J. A. Slart, S. G. Nekolla, M. L. Lassen, B. J. Pichler, T. Schlosser, A. Jacquier, H. H. Quick, M. Schäfers and M. Hacke, *European Journal of Hybrid Imaging*, 2018, **2**, 14.
19. P. Lam, Medical News Today. MediLexicon, Intl.,"What to know about MRI scans." 24 July 2018. View 24 December. 2018, https://www.medicalnewstoday.com/articles/146309.php
20. J. R. Singer, *Science*, 1959, **130**, 1652.
21. R. Damadian, *Science*, 1971, **171**, 1151.
22. A. Nowogrodzki, *Nature*, 2018, **563**, 24.
23. OECD (2019), Magnetic Resonance Imaging exams, total. Definitions, Sources and Methods per country. View 29 January 2019, http://stats.oecd.org/wbos/fileview2.aspx?IDFile=8d3b4c1f-0ccd-4d36-954a-9a81bea235d0
24. OECD (2019), Magnetic resonance imaging (MRI) units (indicator). doi: 10.1787/1a72e7d1-en. Accessed 24 December 2018.
25. F. Bloch, *Phys. Rev.*, 1946, **70**, 460.
26. E. Belorizky, P. H. Fries, L. Helm, J. Kowalewsky, D. Kruk, R. R. Sharp, P.-O. Westlund, *J. Chem. Phys.*, 2008, **128**, 052315.
27. C. F. G. C. Geraldes and S. Laurent, *Contrast Media Mol. Imaging*, 2009, **4**, 1.
28 J. Lohrke, T. Frenzel, J. Endrikat, F. Caseiro-Alves, T. M. Grist, M. Law, J. M. Lee . T. Leiner, K.-C. Li, K. Nikolaou, M. R. Prince, H. H. Schild, J. C. Weinreb, K. Yoshikawa and H. Pietsch, *Adv. Ther.*, 2016, **33**, 1.
29 Y.-D. Xiao, R. Paudel, J. Liu, C. Ma, Z.-S. Zhang, S.-K. Zhou, *Inter. J. Mol. Med.*, 2016, **38**, 1319.
30 J. Wahsner, E. M. Gale, A. Rodríguez-Rodríguez and P. Caravan, *Chem. Rev.* 2019, **119**, 957.
31 N. Ferris, S. Goergen, Gadolinium Contrast Medium (MRI Contrast agents), InsideRadiology, The Royal Australian and New Zealand College of Radiologist, Sydney, Accessed 24 December 2018, https://www.insideradiology.com.au/gadolinium-contrast-medium/
32 J. Kurhanewicz, D. Vigneron, P. Carroll and F. Coakley, *Current Opinion in Urology*, 2008, **18**, 71.
33 D. Gaynor and D. M. Griffith, *Dalton Trans.*, 2012, **41**, 13239.
34 S. Sinharay and M. D. Pagel, *Annu. Rev. Anal. Chem*., 2016, **9**, 95.
35 Y. Jeong, H. Sook Hwang and K. Na, *Biomaterials Research*, 2018, **22**, 20.
36 (a) M. H. Mendonça-Dias, E. Gaggelli, P. C. Lauterbur, *Semin Nucl Med.* 1983, **13**, 364. (b) I.R. Young, G. J. Clarke, D. R. Bailes, J. M. Pennock, F. H. Doyle and G. M. Bydder*, J Comput Tomogr.* 1981, **5**, 543

37 (a) P. C. Lauterbur, *Nature*, 1973, **242**, 190. (b) P. C. Lauterbur, M. H. M. Dias and A. M. Rudin, Augmentation of tissue water proton spin-lattice relaxation rates by in vivo addition of paramagnetic ions. Ed. P. Dutton. Electrons to tissues. London: Academic Press; 1978. p. 752–9.

38 (a) T. J. Brad, M. R. Goldman, I. L. Pykett, F. S. Buonanno, J. P. Kistler, J. H. Newhouse, C. T. Burt, W. S. Hinshaw and G. M. Pohost, *Radiology*, 1982, **144**, 343. (b) M. R. Goldman, T. J. Brady, I. L. Pykett, C. T. Burt, F. S. Buonanno, J. P. Kistler, J. H. Newhouse, W. S. Hinshaw, G. M. Pohost, *Circulation*, 1982, **66**, 1012.

39 L. M. De León-Rodríguez, A. F. Martins, M. C. Pinho, N. M. Rofsky, A.D. Sherry, *J. Magn. Reson. Imaging* 2015, **42**, 545.

40 Z. Baranyai, Z. Palinkas, F. Uggeri, A. Maiocchi, S. Aime, E. Brücher, *Chem. Eur. J*. 2012, **18**, 16426.

41 (a) M. Rogosnitzky, S. Branch, *Biometals* 2016, **29**, 365. (b) L. Caschera, A. Lazzara, L. Piergallini, D. Ricci, B. Tuscano, A. Vanzulli, *Pharmacol. Res*. 2016, **110**, 65.

42 H. U. Rashid, M. A. U. Martines, J. Jorge, P. M. de Moraes, M. N. Umar, K. Khan, H. U. Rehman, *Bioorg. Med. Chem*. 2016, **24**, 5663.

43 I. A. Dekkers, R. Roos, A. J. van der Molen, *Eur. Radiol*. 2018, **28**, 1579.

44 European Medicines Agency, Gadolinium-containing contrast agents, London, UK, Accessed 30 November 2018, https://www.ema.europa.eu/en/medicines/human/referrals/gadolinium-containing-contrast-agents

45 (a) D. Pan, A. H. Schmieder, S. A. Wickline and G. M. Lanza, *Tetrahedron*, 2011, **67**, 8431. (b) B. Drahos, I. Lukes and É. Tóth, *Eur. J. Inorg. Chem*., 2012, 1975. (c) M. Kueny-Stotz, A. Garofalo and D. Felder-Flesch, *Eur. J. Inorg. Chem*., 2012, 1987.

46 C. A. Massaad and R. G. Pautler, *Methods Mol Biol*. 2011, **711**, 145.

47 J. M. Malheiros, F. F. Paiva, B. M. Longo, C. Hamani and L. Covolan, *Front. Neurol.*, 2015, **6**, 161.

48 (a) A. Geiger and J. Cooper, Overview of Airborne Metals Regulations, Exposure Limits, Health Effects, and Contemporary Research DRAFT, 2010, Cooper Environmental Services LLC, Portland. (b) J. A. Roth, *Biological Research*, 2006, **39**, 45.

49 D. Regge, S. Cirillo, A. Macera and G. Galatola, *Reports in Medical Imaging,* 2009, **2**, 55.

50 H. Liu and X.-A. Zhang, Encyclopedia of Inorganic and Bioinorganic Chemistry, 2018 John Wiley & Sons, Ltd. DOI: 10.1002/9781119951438.eibc2626.

51 (a) K. Islam, S. Kim, H.-K. Kim, S. Park, G.-H. Lee, H. J. Kang, J.-C. Jung, J.-S. ParkO, T.-J. Kim and Y. Chang, *J. Med. Chem*. 2017, **60**, 2993. (b) I. Bertini, C. Luchinat, G. Parigi and E. Ravera, Relaxometry and contrast agents for MRI. Solution NMR of Paramagnetic Molecules, 2nd Edition, 2017, **2**, pp.313-345.

52 E. M. Gale, H.-Y. Wey, I. Ramsay, Y.-F. Yen, D. E. Sosnovik and P. Caravan, *Radiology*, 2018, **286**, 865.

53 A. L. Thompson, D. Parker, D. A. Fulton, J. A. K. Howard, S. U. Pandya, H. Puschmann, K. Senanayake, P. A. Stenson, A. Badari, M.Botta, S. Avedano, S. Aime, *Dalton Trans*. 2006, **47**, 5605.

54 (a) A. Forgacs, M. Regueiro-Figueroa, J. L. Barriada, D. Esteban-Gomez, A. de Blas, T. Rodriguez-Blas, M. Botta and C. Platas-Iglesias, *Inorg. Chem*., 2015, **54**, 9576; (b) A. Forgács, L. Tei, Z. Baranyai, D. Esteban-Gómez, C. Platas-Iglesias and M. Botta, *Dalton Trans*., 2017, **46**, 8494. (c) R. Pujales-Paradela, F. Carniato, R. Uzal-Varela, I. Brandariz, E. Iglesias, C. Platas-Iglesias, M. Botta and D. Esteban-Gomez, *Dalton Trans*., 2019, **48**, 696.

55 R. Pujales-Paradela, M. Regueiro-Figueroa, D. Esteban-Gómez and C. Platas-Iglesias, Contrast Agents for MRI. Experimental Methods, ed. V. C. Pierre and M. J. Allen, Royal Society of Chemistry, Croydon, UK, 2018, ch. 5.

56 (a) F. K. Kálmán and G. Tircsó, *Inorg. Chem*., 2012, **51**, 10065. (b) K. Pota, Z. Garda, F. K. Kalman, J. L. Barriada, D. Esteban-Gomez, C. Platas-Iglesias, I. Toth, E. Brucher and G. Tircso, *New J. Chem.,* 2018, **42**, 8001.

57 E. M. Gale, J. Zhu and P. Caravan, *J. Am. Chem. Soc*., 2013, **135**, 18600.

58 J. H. Freed, *J. Chem. Phys*., 1978, **68**, 4034.

59 M. Regueiro-Figueroa, G. A. Rolla, D. Esteban-Gomez, A. de Blas, T. Rodriguez-Blas, M. Botta and C. Platas-Iglesias, *Chem. Eur. J*., 2014, **20**, 17300.

60 R. Weissleder, A. Rehemtulla and S. S. Gambhir, Molecular imaging: principles and practice. Ed. Shelton, Connecticut, People's Medical Publishing House, 2010.

61 I. S. Oliveira, S. S. Hedgire, W. Li, S. Ganguli, A. M. Prabhakar, *Cardiovasc Diagn Ther*., 2016, **6**, 508.

62 (a) H. B. Na, I. C. Song and T. Hyeon, *Adv. Mater.*, 2009, **21**, 2133. (b) Y.-X. J. Wang, *Quant Imaging Med Surg* 2011, **1**, 35.

63 (a) L. E. Smart and E. A. Moore, Solid state chemistry: an introduction. 3rd edition. Taylor & Francis CRC Press. 2005. (b) R. M. Cornell, The iron oxides : structure, properties, reactions, occurrences, and uses. 2nd edition. Weinheim, Cambridge, Wiley-VCH, 2003.

64 N. Lee and T. Hyeon, *Chem. Soc. Rev*., 2012, **41**, 2575.

65 A. L Fymat, *Curr. Trends Clin. Med. Imaging*, 2017, **1**.

66 R. A. Revia and M. Zhang, *Materials Today*, 2016, **19**, 157.

67 (a) A. D. Watson, *Journal of Alloys and Compounds*, 1994, **207-208**, 14. (b) P. Caravan, M. T. Greenfield and J. W. Bulte, *Magn Reson Med*., 2001, **46**, 917.

68 K. Kattel, J. Y. Park, W. Xu, H. G. Kim, E. J. Lee, B. A. Bony, W. C. Heo, S. Jin, J. S. Baeck, Y. Chang, T. J. Kim, J. E. Bae, K. S. Chae and G. H. Lee, *Biomaterials*, 2012, **33**, 3254.

69 T. Tegafaw, W. Xu, W. Ahmad, J. S. Baeck, Y. Chang, J. E. Bae, K. S. Chae, T. J. Kim and G. H. Lee, *Nanotechnology*, 2015, **26**, 365102.

70 M. Woods, D. E. Woessner, A. D. Sherry, *Chem Soc Rev*., 2006, **35**, 500.

71 K. M. Ward, A. H. Aletras and R. S. Balaban, *J. Magn. Reson*, 2000, **143**, 79.

72 S. Zhang, P. Winter, K. Wu and A. D. Sherry, *J. Am. Chem. Soc.* 2001, **123**, 1517.

73 A. D. Sherry and M. Woods, *Annu. Rev. Biomed. Eng*., 2008, **10**, 391. (b) S. Viswanathan, Z. Kovacs, K. N. Green, S. J. Ratnakar and A. D. Sherry, *Chem. Rev.*, 2010, **110**, 2960.

74 N. D. Fichtner, I.-A. Giapitzakis, N. Avdievich, R. Mekle, D. Zaldivar, A. Henning and R. Kreis, *Magn. Reson. Med.*, **79**, 2863.

75 (a) S. Goerke, J. Breitling, M. Zaiss, J. Windschuh, P. Kunz, P. Schuenke, D. Paech, D. L. Longo, K. D. Klika, M. E. Ladd and P. Bachert, *NMR in Biomedicine*, 2018, **31**, e3920. (b) A. J. Pella, G. Pintacuda, C. P. Grey, *Progress in Nuclear Magnetic Resonance Spectroscopy*, 2018, pp. 1-825

76 K. M. Jones, A. C. Pollard and M. D. Pagel, *J. Magn. Reson. Imag.*, 2018, **47**, 11.

77 (a) S. Aime, A. Barge, D. Delli Castelli, F. Fedeli, A. Mortillaro, F. U. Nielsen and E. Terreno, *Magn. Reson. Med*., 2002, **47**, 639. (b) M. Suchý, A. X. Li, Y. Liu, Q. Feng, R. Bartha and R. H. E. Hudson, *Canadian Journal of Chemistry*, 2016, **94**, 715. (c) S. J. Ratnakar, M. Woods, A. J. M. Lubag, Z. Kovacs and A. D. Sherry, *J. Am. Chem. Soc.*, 2008, **130**, 6. (d) S. J. Ratnakar, T. C. Soesbe, L. L. Lumata, Q. N. Do, S. Viswanathan, C.-Y. Lin, A. D. Sherry and Z. Kovacs, *J. Am. Chem. Soc*., 2013, **135**, 14904.

78 (a) M. Suchý, M. Milne, A. A. H. Elmehriki, N. McVicar, A. X. Li, R. Bartha and R. H. E. Hudson, *J. Med. Chem*., 2015, **58**, 16, 6516. (b) K. Srivastava, G. Ferrauto, S. M. Harris, D. L. Longo, M. Botta, S. Aime and V. C. Pierre. *Dalton Trans*., 2018, **47**, 11346.

79 A. C. L. Opina, Y. Wu, P. Zhao, G. Kiefer and A. D. Sherry, *Contrast Media Mol Imaging*., 2011, **6**, 459.

80 (a) L. Caneda-Martínez, L. Valencia, I. Fernández-Pérez, M. Regueiro-Figueroa, G. Angelovski, I. Brandariz, D. Esteban-Gómez and C. Platas-Iglesias, *Dalton Trans*., 2017, **46**, 15095. (b) A. O. Olatunde, S. J. Dorazio, J. A. Spernyak and J. R. Morrow, *J. Am. Chem. Soc*., 2012, 134, **45**, 18503. (c) S. M. Abozeid, E. M. Snyder, A. P. Lopez, C. M. Steuerwald, E. Sylvester, K. M. Ibrahim, , R. R Zaky, H. M. Abou-El-Nadar, and J. R. Morrow, *Eur. J. Inorg. Chem*., 2018, 1902.

81 (a) P. B. Tsitovich, J. M. Cox, J. R. Morrow, *Inorg. Chem*., 2016, **55**, 12001. (b) P. B. Tsitovich, F. Gendron A. Y. Nazarenko, B. N. Livesay, A. P. Lopez, M. P. Shores, J. A. Autschbach, J. R. Morrow, *Inorg. Chem*., 2018, **57**, 8364.

82 (a) P. B. Tsitovich, T. Y. Tittiris, J. M. Cox, J. B. Benedict and J. R. Morrow, *Dalton Trans*., 2018, **47**, 916. (b) P. B. Tsitovich, J. M.Cox, J. B. Benedict, J. A. Spernyak, J. R. Morrow, *Inorg. Chem.*, 2015, **55**, 700.

83 S. M.Abozeid, E. M. Snyder, T. Y. Tittiris, C. M. Steuerwald, A. Y. Nazarenko, J. R. Morrow, *Inorg. Chem*., 2018, **57**, 2085.

84 (a) S. J. Dorazio, A. O. Olatunde, P. B. Tsitovich, J. R. Morrow, *J. Biol. Inorg. Chem*., 2014, **19**, 191. (b) A. O. Olatunde, J. M. Cox, M. D. Daddario, J. A. Spernyak, J. B. Benedict, J. R. Morrow, *Inorg. Chem*., 2014, **53**, 8311. (c) P. J.Burns, J. M.Cox, J. R. Morrow, *Inorg. Chem*., 2017, **56**, 4545. (d) A. O. Olatunde, C. J. Bond, S. J. Dorazio, M. D. Daddario, J. A. Spernyak, J. M. Cox, J. B. Benedict and J. R. Morrow, *Chem. Eur. J*., 2015, **21**, 18290.

85 E. Terreno, D. Delli Castelli, G. Cravotto, M. Milone and S. Aime, *Invest. Radiol*, 2004, **39**, 235.

86 E. Terreno, D. Delli Castelli and S. Aime, *Contrast Media Mol. Imaging* 2010, **5**, 78.

87 G. Castro, M. Regueiro-Figueroa, D. Esteban-Gómez, R. Bastida, A. Macías, P. Pérez-Lourido, C. Platas-Iglesias and L. Valencia, *Chem. Eur. J*., 2015, **21**, 18662.

88 (a) P. B. Tsitovich, P. J. Burns, A. M. McKay and J. R. Morrow, *J. Inorg. Biochem*., 2014, **133**, 143. (b) M. Yu, D. Xie, K. P. Phan, J. S. Enriquez, J. J. Luci and E. L. Que, *Chem. Commun*., 2016, **52**, 13885.

89 (a) T. Tanaka, R. Araki, T. Saido, R. Abe and S. Aoki, *Eur. J. Inorg. Chem*., 2016, 3330. (b) L. Calucci, G. Ciofani, D. De Marchi, C. Forte, A. Menciassi, L. Menichetti and V. Positano, *J. Phys. Chem. Lett*., 2010, **1**, 2561. (c) S. Capuania, P. Porcaria, F. Fasano, R. Campanella and B. Maraviglia, *Magn. Reson. Imag.*, 2008, **26**, 987.

90 (a) J. Ruiz-Cabello, B. P. Barnett, P. A. Bottomley, J. W. Bulte, *NMR Biomed*., 2011, **24**, 114. (b) J-X. Yu, R. R. Hallac, S. Chiguru, R. P. Mason, *Progress in Nuclear Magnetic Resonance Spectroscopy*, 2013, **70**, 25.

91 (a) K. L. Peterson, K. Srivastava, V. C Pierre, *Front. Chem*., 2018, **6**, 160. (b) J. Blahut, P. Hermann, A. Gálisová, V. Herynek, I. Císařová, Z. Tošnerc, J. Kotek, *Dalton Trans*., 2016, **45**, 474. (c) M. Yu, D. Xie, K. P. Phan, J. S. Enriquez, J. J. Luci, E. L. Que, *Chem. Commun*., 2016, **52**, 13885. (d) J. Blahut, K. Bernasek, A. Galisova, V. Herynek, I. Cisarova, J. Kotek, J. Lang, S. Matejkova, P. Hermann, *Inorg. Chem*., 2017, **56**, 13337. (e) K. H. Chalmers, E. De Luca, N. H. M. Hogg, A. M. Kenwright, I. Kuprov, D. Parker, M. Botta, J. I. Wilson, A. M. Blamire, *Chem. Eur. J*., 2010, **16**, 134. (f) K. H. Chalmers, M. Botta, D. Parker, *Dalton Trans*., 2011, **40**, 904.

92 (a) K. H. Chalmers, A. M. Kenwright, D. Parker, A. M. Blamire, *Magn. Reson. Med*., 2011, **66**, 931. (b) P. Harvey, I. Kuprov, D. Parker, *Eur. J. Inorg. Chem*., 2012, 2015. (c) P. K. Senanayake, A. M. Kenwright, D. Parker, S. K. van der Hoorn, *Chem. Commun*., 2007, 2923. (d) A. M. Kenwright, I. Kuprov, E. De

Luca, D. Parker, S. U. Pandya, P. K. Senanayake, D. G. Smith, *Chem. Commun*., 2008, 2514. (e) K. Srivastava, E. A. Weitz, K. L. Peterson, M. Marjanska, V. C. Pierre, *Inorg. Chem*., 2017, **56**, 1546. (f) K. Srivastava, G. Ferrauto, V. G. Young, Jr., S. Aime, V. C. Pierre, *Inorg. Chem*., 2017, **56**, 12206. (g) P. Kadjane, C. Platas-Iglesias, P. Boehm-Sturm, V. Truffault, G. E. Hagberg, M. Hoehn, N. K. Logothetis, G. Angelovski, *Chem. Eur. J*., 2014, **20**, 7351. (h) N. Cakic, T. Savic, J. Stricker-Shaver, V. Truffault, C. Platas-Iglesias, C. Mirkes, R. Pohmann, K. Scheffler, G. Angelovski, *Chem. Commun*., 2016, **52**, 9224. (i) N. Cakić, B. Tickner, M. Zaiss, D. Esteban-Gómez, C. Platas-Iglesias, G. Angelovski, *Inorg. Chem*., 2017, **56**, 7737.

93 R. Pujales-Paradela, T. Savić, D. Esteban-Gomez, G. Angelovski, F. Carniato, M. Botta and C. Platas-Iglesias, *Chem. Eur. J*., 2019, doi: 10.1002/chem.201806192.

94 (a) S. Mizukami, R. Takikawa, F. Sugihara, Y. Hori, H. Tochio, M. Wälchli, M. Shirakawa and K. Kikuchi, *J. Am. Chem. Soc*., 2008, **130**, 794. (b) S. Mizukami, R. Takikawa, F. Sugihara, F., M. Shirakawa and K. Kikuchi, *Angew. Chem. Int. Ed*., 2009, **48**, 3641. (c) L. A. Basal, M. D. Bailey, J. Romero, M. Ali, L. Kurenbekova, J.Yustein, R. G. Pautler and M. J. Allen, *Chem. Sci*., 2017, **8**, 8345. (d) J.-X. Yu, V. D. Kodibagkar, L. Liu, Z. Zhang, L. Liu, J. Magnussona and Y. Liu, *Chem. Sci*., 2013, **4**, 2132.

95 P. Harvey, A. M. Blamire, J. I. Wilson, K.-L. N. A. Finney, A. M. Funk, P. K. Senanayake, D. Parker, *Chem. Sci*., 2013, **4**, 4251.

96 D. V. Hingorani, A. S. Bernstein and M. D. Pagel, *Contrast Media & Molecular Imaging*, 2014, **10**, 245.

97 C. Tu, E. A. Osborne and A. Y. Louie, *Ann Biomed Eng*., 2011, **39**, 1335.

98 X. Zhang, Y. Lin and R. J. Gillies, *J Nucl Med*., 2010, **51**, 1167.

99 G.-L. Davies, I. Krambergera and J. J. Davis, *Chem Commun*, 2013, **49**, 9704.

100 (a) M. Isaac, A. Pallier, F. Szeremeta, P.-A. Bayle, L. Barantin, C. S. Bonnet and O. Sénèque, *Chem. Commun*., 2018, **54**, 7350. (b) C. S. Bonnet, *Coordination Chemistry Reviews*, 2018, **369**, 91. (c) M. Regueiro-Figueroa, S. Gündüz, V. Patinec, N. K. Logothetis, D. Esteban-Gómez, R. Tripier, G. Angelovski and C. Platas-Iglesias, *Inorg. Chem*., 2015, **54**, 10342.

101 (a) S. Okada, B. B. Bartelle, N. Li, V. Breton-Provencher, J. J. Lee, E. Rodriguez, J. Melican, M. Sur and A. Jasanoff, *Nature Nanotechnology*, 2018, **13**, 473. (b) K. Dhingra, P. Fousková, G. Angelovski, M. E. Maier, N. K. Logothetis and É. Tóth, *J. Biol. Inorg. Chem*., 2008, **13**, 35.

102 S. Abada, A. Lecointre, M. Elhabiri, D. Esteban-Gómez, C. Platas-Iglesias, G. Tallec, M. Mazzanti and L. J. Charbonnière, *Chem. Commun*., 2012, **48**, 4085.

103 (a) N. K. Paschke, W. Neumann, T. Uhrig, M. Winkler, E. Neumaier-Probst, M. Fatar, L. R. Schad, F. G. Zöllner, *Investigative Radiology*, 2018, **53**, 555. (b) R. Ouwerkerk, *J. Am. Coll. Radiol*., 2007, **4**, 739. (c) M. Hammon, S. Grossmann, P. Linz, C. Kopp, A. Dahlmann, C. Garlichs, R. Janka, A. Cavallaro, F. C. Luft, M. Uder and J. Titze, *PLoS One*., 2015, **10**, e0141336. (d) T. Platt, R. Umathum, T. M. Fiedler, A. M. Nagel, A. K. Bitz, F. Maier, P. Bachert, M. E. Ladd, M. O. Wielpütz, H.-U. Kauczor and N. G. R. Behl, *Magn. Reson. Med*., 2018, **80**, 1005.

104 (a) E. L. Que, E. J. Newa and C. J. Chang, *Chem Sci*., 2012, 1, **3**, 1829. (b) E. L. Que, E. Gianolio, S. L. Baker, S. Aime and C. J. Chang, *Dalton Trans*., 2010, **39**, 469.

Controlling water exchange rates
in potential Mn^{2+}-based MRI agents
derived from NO2A^{2-}
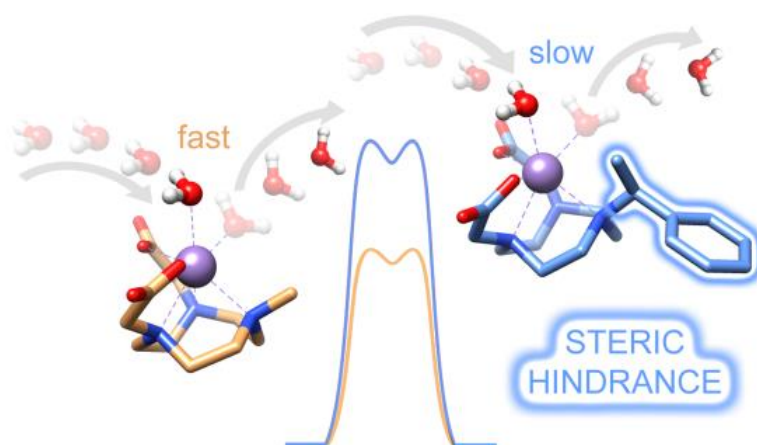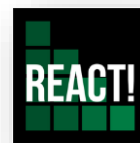
Controlling water exchange rates in potential Mn²⁺-based MRI agents derived from NO2A²⁻

We report a series of pentadentate ligands based on a 1,4,7,-triazacyclononane-1,4-diacetic acid (H_2NO2A) containing different substituents attached to the third nitrogen atom of the macrocyclic unit. A detailed [1]H Nuclear Magnetic Relaxation Dispersion (NMRD) characterisation of the corresponding Mn²⁺ complexes suggest the formation of six-coordinate species in solution containing an inner-sphere water molecule. This was confirmed by recording transverse [17]O relaxation time and chemical shift measurements. The water exchange rate of the coordinated water molecule was found to be strongly influenced by the nature of the substituent R at position 7 of the triazacyclononane unit (R = Me, k_{ex}^{298} = 62.6×10⁷ s⁻¹; R = Bz, k_{ex}^{298} = 4.4×10⁷ s⁻¹; R = 1-phenylethyl, k_{ex}^{298} = 2.6×10⁷ s⁻¹). The decreasing exchange rates are explained by the increasing bulkiness of the substituent, which hinders the approach of the entering water molecule in an associatively activated water exchange mechanism. This is supported by DFT calculations (M062X/TZVP), which confirm the associative nature of the water exchange reaction. A potentially decadentate ligand containing two NO2A units linked by a xylenyl spacer in the *meta* position was also synthesised. The corresponding binuclear Mn²⁺ complex contains two metal ions with different hydration numbers, as evidenced by ¹H NMRD and ¹⁷O NMR measurements. DFT calculations show that this is related to the presence of a bridging bidentate μ-η¹-carboxylate group connecting the two metal centers. The results reported in this work provide a straightforward strategy to control the exchange rate of the coordinated water molecule in this family of MRI contrast agent candidates.

2.1. Introduction

Magnetic Resonance Imaging (MRI) has emerged during the last few decades as one of the most successful and widely used diagnostic imaging modalities, which nevertheless is under continuous development and improvement. Contrast agents (CA) are broadly used during the MRI scans in order to improve the contrast in the recorded images of organs and tissues, increasing the sensitivity and decreasing the acquisition times.[1] These agents are usually paramagnetic metal complexes with good water solubility that increase the relaxation rates of water proton nuclei in their vicinity.[1,2] One of the most common and widespread CAs used in clinical practice is DOTAREM®, a Gd³⁺ macrocyclic complex that presents high stability and relaxivity.[1] In the last few years, a renewed interest has emerged to find alternatives to the already used Gd³⁺ chelates, because of the raising concerns about some health risks associated with their use.[3] Although none of the studies reported so far demonstrated a clinically relevant toxic effect directly attributed to gadolinium deposition in brain and other tissues,[4] gadolinium contrast agents are related to the onset of nephrogenic systemic fibrosis (NSF) in patients with abnormal and even normal renal function, or that have experienced liver transplantation.[3] Several suspensions of marketing authorisations and restrictions in the use of linear gadolinium based-contrast agents have been executed recently by some international regulatory health authorities,[5] and these restrictions are likely to be expanded in the nearly future.

In this renewed interest on alternatives to gadolinium contrast agents, high-spin manganese(II) complexes are playing a strong leading position,[6-9] due to a number of optimal features: high effective magnetic moment associated with the presence of five unpaired *d* electrons, long electronic relaxation time and fast water exchange kinetics.[6] In recent papers, we have reported several manganese systems that present relatively high relaxivities, comparable to those of small monohydrated Gd³⁺ complexes.[10] These chelates should guarantee a high thermodynamic and kinetic stability to avoid the release of the Mn²⁺ ion *in vivo*,[11] and they should present one free coordination site to the metal ion for at least one water molecule. Besides, the ligands should provide a good redox stability to avoid the oxidation of Mn²⁺ to Mn³⁺, which commonly furnishes lower relaxivities.[12] Noteworthy, it has been proven that contrast agents based on macrocyclic metal complexes are generally kinetically more inert than linear analogues.[13]

Among the different parameters that affect the efficiency (relaxivity) of Mn²⁺-based contrast agents, the exchange rate of the coordinated water molecule(s) plays an important key role.
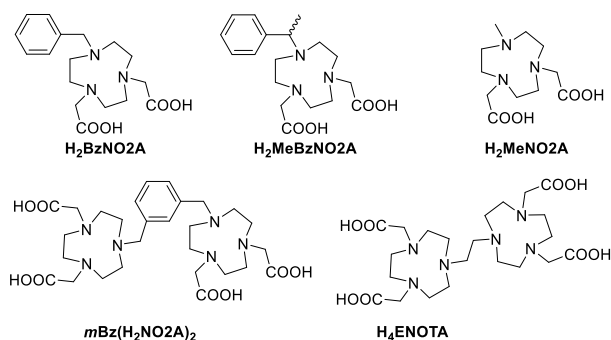
Scheme 1. Chemical structure of the ligands studied in this work.

Some time ago, É. Tóth and co. reported a detailed characterisation of the NO2A derivative [Mn₂(ENOTA)] (Scheme 1), which was found to possess a rather slow water exchange rate of the coordinated water molecule ($k_{ex}^{298} = 5.5 \times 10^7$ s⁻¹),[14] comparable to that of the aquated [Mn(H₂O)₆]²⁺ ion ($k_{ex}^{298} = 2.8 \times 10^7$ s⁻¹).[15] In a subsequent study, we investigated the [Mn(MeNO2A)] complex, which was found to present a water exchange rate one order of magnitude higher ($k_{ex}^{298} = 62.6 \times 10^7$ s⁻¹).[16] Other [Mn(NO2A)] derivatives containing different pendant arms attached to the third N atom of the macrocyclic unit presented k_{ex}^{298} values in the range 1.3-2.7×10⁷ s⁻¹.[17]

The motivation of this study was to analyse the effect that steric hindrance provokes in the water exchange rate of [Mn(NO2A)] derivatives. We hypothesised that the presence of bulky groups on the vicinity of the water binding site may hinder the approach of a water molecule from the bulk, following an associatively activated mechanism. To this aim, we prepared

the H₂BzNO2A and H₂MeBzNO2A ligands (Scheme 1) and performed a full relaxometric characterisation of the corresponding Mn²⁺ complexes using Nuclear Magnetic Relaxation Dispersion (NMRD)[18] and ¹⁷O NMR studies. The different bulkiness of the groups attached to the secondary amine of NO2A and the comparison with [Mn(MeNO2A)] allows to rationalise the water exchange dynamics in this family of complexes. Furthermore, we also report here the binuclear complex [*m*Bz(MnNO2A)₂)], in an attempt to increase the observed relaxivity by slowing down the molecular tumbling of the complex in solution.

2.2. Results and discussion

2.2.1. Synthesis

The triazacyclononane-based ligands H₂BzNO2A, H₂MeBzNO2A and *m*Bz(H₂NO2A)₂ were prepared by alkylation of the bis-protected triazacyclononane derivative di-*tert*-butyl 2,2'-(1,4,7-triazacyclononane-1,4-diyl)diacetate (NO2A*t*Bu) with alkyl bromide derivatives **1a**, **1b** or **1c** (Scheme 2). The protected ligands were isolated in quantitative yields, and then treated with TFA to remove the *tert*-butyl protecting groups. The final ligands were isolated in nearly quantitative amounts.

The preparation of the Mn²⁺ complexes was carried out by a solvothermal approach using n-butanol as solvent and DIPEA as base. The complexes were purified by reverse-phase medium performance liquid chromatography (MPLC). The high-resolution mass spectra (Annexe A, Figures S13-S15) confirm the formation of the complexes.
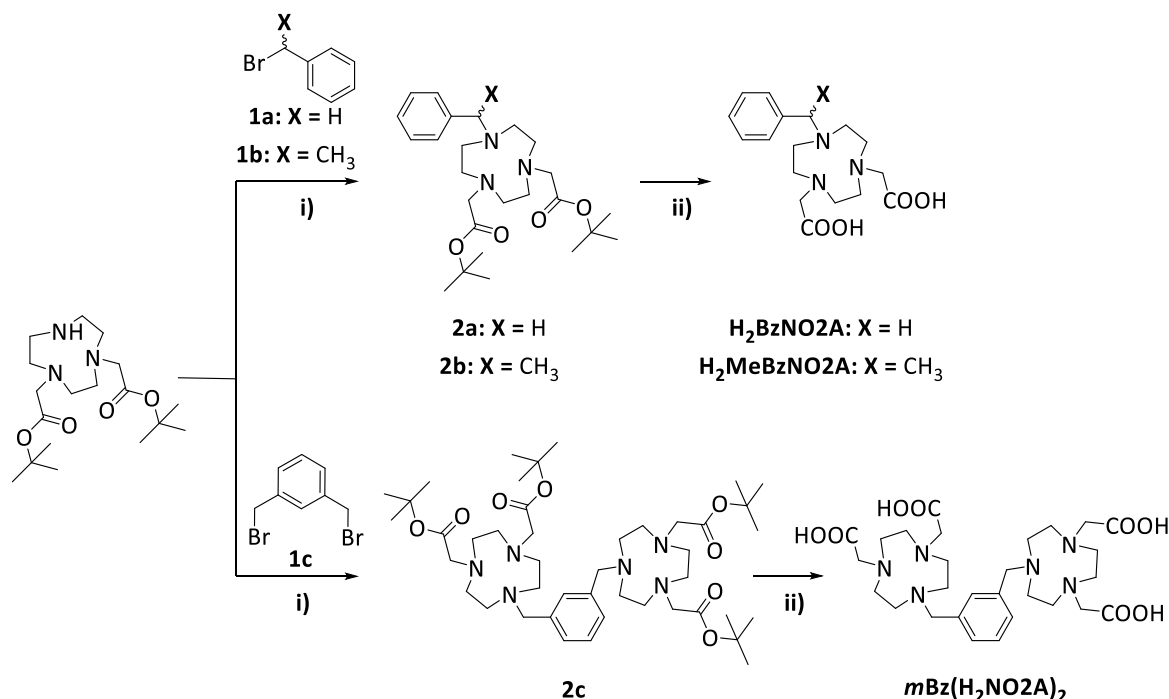
Scheme 2. Synthesis of the ligands discussed in this work. Conditions: i) K₂CO₃ in CH₃CN, 48 h, 100%; ii) TFA:CH₂Cl₂, RT, 48h, 88-100%.
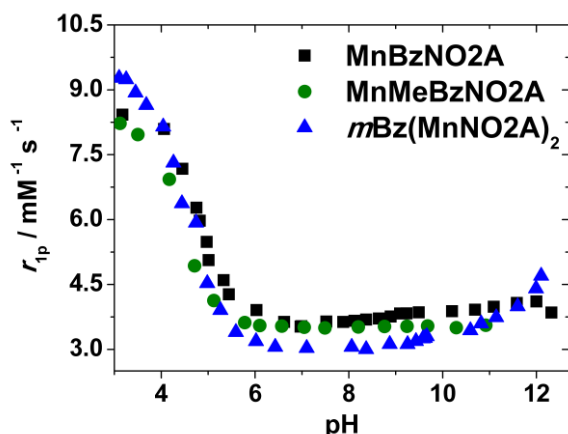
Figure 1. Plot of the ¹H relaxivities at 20 MHz and 298 K as a function of pH.

2.2.2. pH dependence of ¹H relaxivity (r_{1p})

The assessment of the efficiency of a paramagnetic complex as a contrast agent *in vitro* is determined by its relaxivity, r_{1p}, defined as the relaxation enhancement of water protons induced by the paramagnetic agent at 1 mM concentration (based on the paramagnetic metal ion).

The relaxivity determined for [Mn(BzNO2A)] at pH 6.47 (25 °C, 20 MHz) is 3.43 mM⁻¹ s⁻¹, a value that is close to that reported for monohydrated complexes of similar size, such as [Mn(EDTA)]²⁻ (3.3 mM⁻¹ s⁻¹ at pH 7.4, 25 °C and 20 MHz).[19] The r_{1p} value measured for [Mn(MeBzNO2A)] under the same conditions (3.54 mM⁻¹ s⁻¹) is very similar, indicating a low impact of the added methyl group on the observed relaxivity. These relaxivity values suggest the presence of a water molecule coordinated to the metal ion in both [Mn(BzNO2A)] and [Mn(MeBzNO2A)], indicating that the presence of the methyl group does not affect the hydration state of the complex. Meanwhile, the relaxivity measured for the dinuclear chelate [mBz(MnNO2A)₂)] (2.58 mM⁻¹ s⁻¹) is decidedly lower than those of the related mononuclear complexes. However, this relaxivity is still higher than the one observed for non-hydrated Mn²⁺ complexes such as [Mn(DO3A)]⁻,[19] but close to the r_{1p} values reported for complexes with 0 < q < 1 (q is the number of coordinated water molecules).[20] Thus, the relaxivity measured for [mBz(MnNO2A)₂)] suggests that the coordination environment of at least one of the Mn²⁺ ions differs with respect to those of the mononuclear analogues.

The relaxivities of the three complexes (25 °C, 20 MHz) were measured over a broad pH range, from 3 to 12, to assess their stability around physiological pH (Fig 1). The observed relaxivities are constant in the pH range ~6.0-9.0. Below that range relaxivity increases due to the stepwise dissociation of the complex and formation of [Mn(H₂O)₆]²⁺, which presents a relaxivity of 8.6 mM⁻¹s⁻¹ under these conditions.[15b] Above pH ~9 r_{1p} experiences a significant increase, which might be related to an acceleration of the water exchange process by a base-catalysed mechanism. A relaxivity increase at high pH values was observed previously for lanthanide complexes presenting slow water exchange thanks to the prototropic base-catalysed mechanism.[21,22] Since water exchange in these [Mn(NO2A)] derivatives is rather fast and does not limit relaxivity at 298 K

(see below), the relaxivity increase at basic pH must be related to a different effect. It has been shown that [Mn(NO2A)] complexes form hydroxo species at basic pH.[17] Thus, the formation of hydroxo species is most likely responsible for the observed behaviour, either by affecting the number of proton nuclei in the vicinity of the metal ion, the Mn⋯H distance or the rotational dynamics of the complex.

2.2.3. ¹H NMRD measurements

Proton Nuclear Magnetic Relaxation Dispersion (¹H NMRD) profiles were recorded at 10, 25 and 37 °C in the proton Larmor Frequency range from 0.01 to 70 MHz. The analysis of the ¹H NMRD profiles provides additional information on the different mechanisms and physicochemical parameters that affect the observed relaxivity (Figure 2). The NMRD profiles recorded for [Mn(BzNO2A)] and [Mn(MeBzNO2A)] are nearly identical in the whole range of ¹H Larmor frequencies, which suggests that the two complexes present very similar structures and dynamics. The relaxivities of the dinuclear complex [mBz(MnNO2A)₂)] are clearly lower, again suggesting a lower hydration number. The NMRD profiles recorded for the three complexes present a single dispersion in the range ~ 2 – 20 MHz and two plateaus at low (< 2 MHz) and high (> 20 MHz) fields. The relaxivity at high field decreases with increasing temperature in all cases, a situation typical of small Mn²⁺ chelates presenting fast rotation (short rotational correlation times, τ_R).[18] It is also worth mentioning that the NMRD profiles do not show a second dispersion at low field (~0.3-0.02 MHz), which is characteristic of complexes that present a sizeable scalar contribution to relaxivity. This second dispersion was so far only observed for the aquated ion [Mn(H₂O)₆]²⁺ and [Mn₂(ENOTA)].[14,15]

Recently, Peters and Geraldes have proposed a method to determine the hydration number of Mn²⁺ complexes from ¹H NMRD measurements.[23] These authors proposed a correlation of the hydration number q with the relaxivity observed at 0.01 MHz (and 25 °C) and the molecular weight (*FW*) of the complex:

$$q = \frac{r_{1p}}{9.16\left\{1-e^{(-2.97\times FW\times 10^{-3})}\right\}} \quad (1)$$

The relaxivities at 0.01 MHz and 25 °C were determined to be 4.97, 6.63, 6.88 and 4.38 mM⁻¹ s⁻¹ for [Mn(MeNO2A)], [Mn(BzNO2A)], [Mn(MeBzNO2A)] and [mBz(MnNO2A)₂)], which correspond to q values of 0.9, 0.9, 1.1 and 0.5. The estimated uncertainty of the method was determined to be ±0.4 units. These results point to the formation of monohydrated species for all mononuclear complexes of this series, while the dinuclear complex [mBz(MnNO2A)₂)] likely presents a lower effective hydration number.

2.2.4. ¹⁷O NMR measurements

Transverse ¹⁷O NMR relaxation rate measurements were recorded at 11.75 T to obtain information regarding the hydration number and water exchange rate of the coordinated water molecule ($k_{ex} = 1/\tau_m$). The paramagnetic ¹⁷O transverse relaxation rates $1/T_{2p}$ can be approximated by:

$$\frac{1}{T_{2p}} = \frac{1}{T_{2,obs}} - \frac{1}{T_{2,ref}} = \frac{q[\text{Mn}^{2+}]}{[\text{H}_2\text{O}]}\frac{1}{\tau_m}\frac{T_{2m}^{-2}+\tau_m^{-1}T_{2m}^{-1}+\Delta\omega_m^2}{(\tau_m^{-1}+T_{2m}^{-1})^2+\Delta\omega_m^2} \quad (2)$$

where $1/T_{2,obs}$ and $1/T_{2,ref}$ are the observed relaxation rates for the solution of the paramagnetic complex and of the diamagnetic reference, respectively, while $1/T_{2m}$ is the relaxation rate of the bound water molecule. By neglecting the chemical shift difference between bound and bulk water ($\Delta\omega_m$), the $1/T_{2p}$ values can be approximated as:

$$\frac{1}{T_{2p}} = \frac{q[\text{Mn}^{2+}]}{[\text{H}_2\text{O}]}\frac{1}{\tau_m + T_{2m}} \qquad (3)$$

The ^{17}O transverse relaxation rate of the coordinated water molecule is dominated by the scalar mechanism according to:

$$\frac{1}{T_{2m}} \cong \frac{1}{T_{2,sc}} = \frac{S(S+1)}{3}\left(\frac{A}{\hbar}\right)^2 \tau_{s1} \qquad (4)$$

Here, A/$\hbar$ is the scalar hyperfine coupling constant and S is the electron spin ($S = 5/2$ for a high-spin Mn²⁺ complex). $1/\tau_{s1}$ is the sum of the exchange rate constant and the electron spin relaxation rate:

$$\frac{1}{\tau_{s1}} = \frac{1}{\tau_m} + \frac{1}{T_{1e}} \qquad (5)$$

Caravan et al.[24] noticed that at high magnetic fields $T_{1e} \gg \tau_m$, so that τ_m is the correlation time that dominates in Eq (4). As a result, at the maximum of the temperature dependence of $1/T_{2p}$, where $T_{2m} = \tau_m$, one can obtain Eq (6) by combining Eqs (3) and (4):

$$q = r_{2p,max}[\text{H}_2\text{O}]\left(\frac{2}{\sqrt{\frac{S(S+1)}{3}\frac{A_o}{\hbar}}}\right) \qquad (6)$$

In Eq (6) r_{2p} stands for the transverse ^{17}O relaxivity, defined as:

$$\frac{1}{T_{2p}} = r_{2p}[\text{Mn}^{2+}] \qquad (7)$$

The temperature dependence of r_{2p} measured for the three complexes shows that [Mn(BzNO2A)] and [Mn(MeBzNO2A)] present very similar transverse relaxivities at the maximum of the temperature dependence ($r_{2p}\sim300$ mM⁻¹ s⁻¹, Figure 3), while the relaxivity measured for [mBz(MnNO2A)₂)] is about one half of those observed for the mononuclear complexes ($r_{2p}\sim150$ mM⁻¹ s⁻¹). Thus, these results indicate that the binuclear [mBz(MnNO2A)₂)] complex presents a lower hydration number than the mononuclear analogues. By assuming a A/$\hbar$ value of -33×10⁶ rad s⁻¹, Caravan proposed that each coordinated water molecule should provide a contribution of 510 mM⁻¹ s⁻¹ to r_{2p}. This results in hydration numbers of $q = 0.6$ for the mononuclear complexes and $q = 0.3$ for [mBz(MnNO2A)₂)]. Since the proton relaxivities point to the presence of a coordinated water molecule in [Mn(BzNO2A)] and

[Mn(MeBzNO2A)], we conclude that our ^{17}O r_{2p} measurements underestimate the hydration number of these complexes. Taking together, the ^{17}O and ^{1}H data are compatible with $q = 1$ mononuclear complexes and a $q = 0.5$ dinuclear [mBz(MnNO2A)₂)] complex. Our DFT calculations presented below provide support to this hypothesis.

With the hydration numbers in hand, we obtained the reduced transverse relaxation rates ($1/T_{2r}$), which are normalised for the molar fraction of bound water P_m:

$$\frac{1}{T_{2r}} = \frac{1}{P_m}\left[\frac{1}{T_{2,obs}} - \frac{1}{T_{2,ref}}\right] \approx \frac{1}{\tau_m + T_{2m}} \qquad (8)$$

The temperature dependence of T_{2m} and τ_m are generally opposite, so that the residence time of the coordinated water molecule is shortened on increasing temperature (i. e. k_{ex} increases), while T_{2m} becomes longer. Thus, the plots of $1/T_{2r}$ versus reciprocal temperature present different slopes depending on the term that dominates the denominator of Eq (2). A positive slope is then expected in the plots of $1/T_{2r}$ versus 1/T for systems in the fast exchange regime, while the opposite behaviour should be observed for complexes within the slow exchange regime. In the case of the complexes investigated here, the $1/T_{2r}$ data present a maximum that point to a changeover from the low water exchange regime at low temperatures to a fast water exchange at high temperatures (Figure 2). This temperature dependence of $1/T_{2r}$ is in clear contrast with that observed for [Mn(MeNO2A)], which was characterised by a very fast water exchange.[16] We also noticed that the maximum of the $1/T_{2r}$ is shifted towards higher temperatures for [mBz(MnNO2A)₂)] and [Mn(MeBzNO2A)] with respect to [Mn(BzNO2A)], which anticipates a slightly faster water exchange in the latter.

2.2.5. Fittings of the ^{17}O NMR and ^{1}H NMRD data

The quantitative analysis of the ^{17}O and ^{1}H NMRD data was carried out using the Solomon-Bloembergen-Morgan theory to describe the inner-sphere contribution[25] and Freed's model[26] to account for the outer-sphere contribution to relaxivity. The complete set of equations used, together with those describing the ^{17}O NMR data, are given in the Annexe A.These equations depend upon a large number of parameters, hence to achieve a reliable analysis some of them had to be fixed to standard values during the fitting procedure: The distances between the proton nuclei of inner-sphere water molecules and the metal ion (r_{MnH}) were fixed to the average values obtained from DFT calculations (Table 1), while the distance of closest approach of outer-sphere water molecules a_{MnH} was set at 3.6 Å. Finally, the diffusion coefficient D_{MnH}^{298} and its activation energy E_{DMnH} were fixed to established values.[19] Table 1 shows the parameters obtained from the fittings, which are compared with those reported previously for [Mn(MeNO2A)] and [Mn₂(ENOTA)].[14,16]
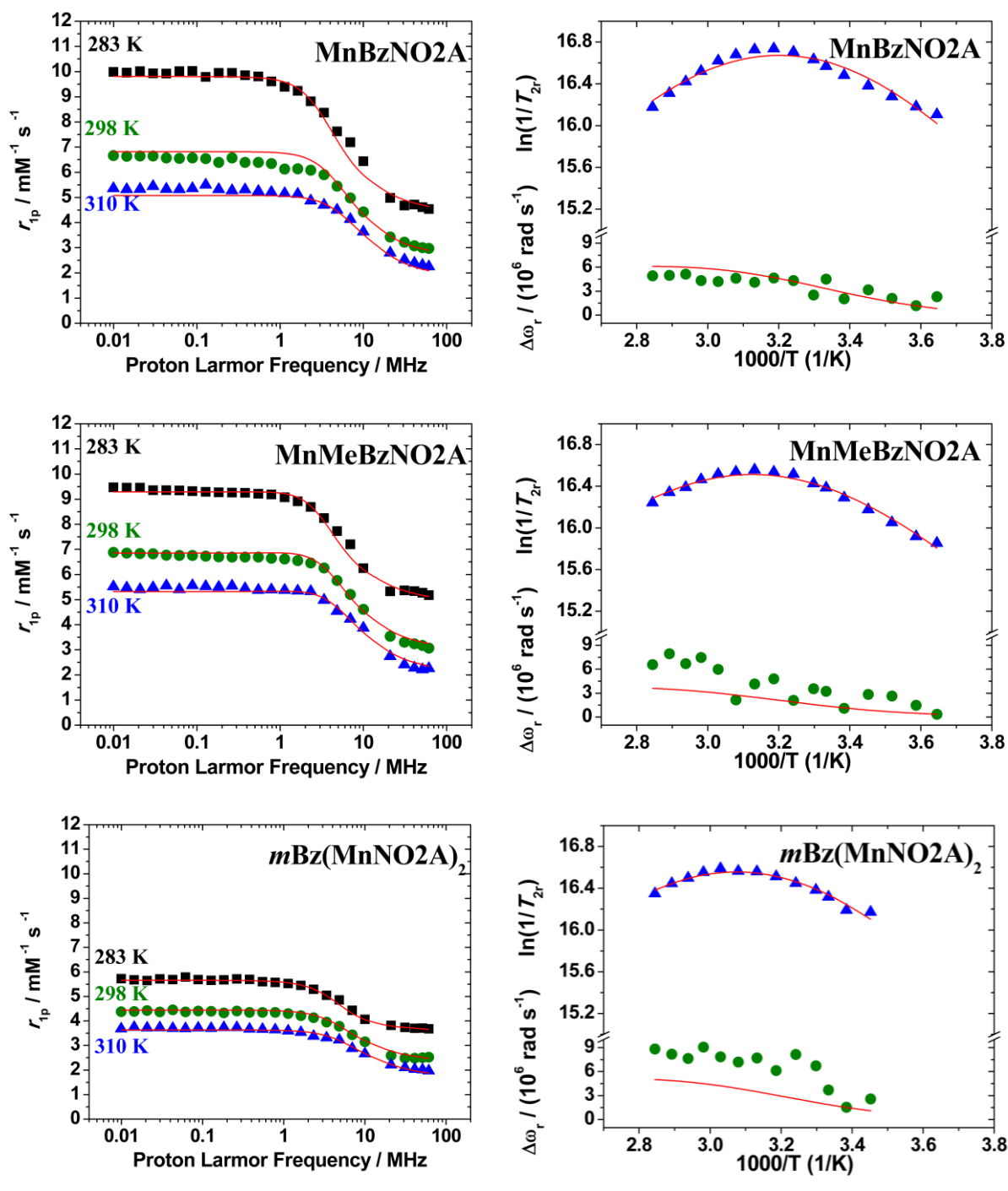
Figure 2. Left panel: ¹H NMRD profiles recorded at different temperatures for [Mn(BzNO2A)], [Mn(MeBzNO2A)] and [*m*Bz(MnNO2A)₂)]. Right panel: Reduced transverse ¹⁷O NMR relaxation rates and chemical shifts versus reciprocal temperature. The red lines represent the fits of the data as explained in the text.

The ¹⁷O hyperfine coupling constants ($A_O/\hbar$) are in the upper part of the range typically observed for small Mn²⁺ complexes (25× 10⁶ to 47 × 10⁶ rad s⁻¹).[27] Furthermore, they are in very good agreement with the values estimated by DFT calculations (see below), which confirms that the hydration numbers used in the analysis are correct.

The rotational correlation times (τ_R^{298}) obtained for [Mn(BzNO2A)] and [Mn(MeBzNO2A)] are very similar, but somewhat longer than the value reported previously for [Mn(MeNO2A)], as would be expected on the basis of their molecular weights. The τ_R^{298} value obtained for [*m*Bz(MnNO2A)₂)] is about 50% longer than that of [Mn(MeNO2A)], matching rather well that of [Mn₂(ENOTA)] (Table 1).

The parameters related to the relaxation of the electron spin of the Mn²⁺ ion (the mean square zero-field-splitting energy (Δ^2) and its associated correlation time (τ_V) are similar to the values reported for other Mn²⁺ complexes. The mononuclear

complexes [Mn(BzNO2A)] and [Mn(MeBzNO2A)] present very similar parameters, which suggests very similar coordination environment of the metal ion in the two complexes. The value of Δ^2 obtained for [mBz(MnNO2A)$_2$)] is somewhat higher, but very similar to that of [Mn(MeNO2A)].

The water exchange rates determined for this family of complexes match the qualitative analysis presented in the previous section. The water exchange rate determined for [Mn(BzNO2A)] (k_{ex}^{298} = 4.4×10⁷ s⁻¹) is one order of magnitude lower than the one obtained for [Mn(MeNO2A)] (k_{ex}^{298} = 63×10⁷ s⁻¹). This very different k_{ex}^{298} values highlight the impact that an increasing steric hindrance has on the water exchange rate. Increasing further the steric hindrance by introducing a methyl group at the benzylic carbon reduces further the water exchange rate (k_{ex}^{298} = 2.6×10⁷ s⁻¹ for [Mn(MeBzNO2A)]). Finally, the binuclear complex [mBz(MnNO2A)$_2$)] displays a water exchange rate similar to that of [Mn(MeBzNO2A)].
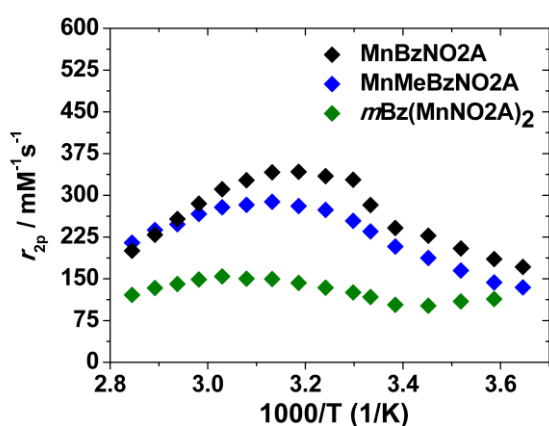
Figure 3. Plot of the transverse ¹⁷O relaxivity as a function of temperature recorded at 11.75 T.

2.2.6. Theoretical calculations

DFT calculations (M062X/TZVP) were carried out to gain information on the structures of the complexes described in this work and their water exchange kinetics. The [Mn(MeNO2A)] complex was studied with DFT calculations in a previous work including a coordinated water molecule and a variable number of explicit second-sphere water molecules.[16] These studies showed that the inclusion of two second-sphere water molecules was critical for an adequate description of the Mn-O$_{water}$ distances and scalar hyperfine coupling constants $A_O/\hbar$. We therefore included two explicit second-sphere water molecules in our models. In the case of the complex of mBz(MnNO2A)$_2$ the experimental ¹H NMRD and ¹⁷O NMR data suggest the presence of a water molecule coordinated to one of the Mn²⁺ ions, while the second one does not contain a coordinated water molecule. We hypothesised that a carboxylate group of one of the NO2A units of the ligand could coordinate simultaneously to the two Mn²⁺ ions, as bridging carboxylate groups were observed previously in the solid state structures of Mn²⁺ complexes with polyaminopolycarboxylate ligands.[28] The optimised geometry of the [mBz(MnNO2A)(MnNO2A)(H$_2$O)]·2H$_2$O system (Figure 4) supports the different hydration numbers of the two Mn²⁺ ions, as a result of the presence of a bridging bidentate μ-η¹-carboxylate group.

The Mn-O$_{water}$ distances calculated for [Mn(MeNO2A)(H$_2$O)]·2H$_2$O, [Mn(BzNO2A)(H$_2$O)]·2H$_2$O and [Mn(MeBzNO2A)(H$_2$O)]·2H$_2$O are virtually identical (2.183-2.185 Å), while for the [mBz(MnNO2A)(MnNO2A)(H$_2$O)]·2H$_2$O system this distance is slightly shorter (2.141 Å). The scalar hyperfine coupling constants $A_O/\hbar$ obtained with DFT for [Mn(MeNO2A)(H$_2$O)]·2H$_2$O, [Mn(BzNO2A)(H$_2$O)]·2H$_2$O and [Mn(MeBzNO2A)(H$_2$O)]·2H$_2$O are also very similar (~-50×10⁶ rad s⁻¹), and show a satisfactory agreement with the experimental values, though the deviation is more important in [Mn(MeBzNO2A)(H$_2$O)]·2H$_2$O. These results confirm that the hydration numbers assumed for the analysis of the ¹H NMRD and ¹⁷O NMR data are correct, and that the bulkiness of the substituents attached to position 7 of the triazacyclononane unit does not significantly influence the strength of the Mn-O$_{water}$ bonds.

Table 1. Parameters obtained from the simultaneous analysis of ¹⁷O NMR and ¹H NMRD data.[a]

	[Mn(BzNO2A)]	[Mn(MeBzNO2A)]	[mBz(MnNO2A)$_2$]	[Mn(MeNO2A)] [b]	[Mn$_2$(ENOTA)] [c]
r_{1p} at 10/25/37 °C / mM⁻¹ s⁻¹ [b]	5.0/3.4/2.8	5.3/3.5/2.7	3.8/2.6/2.2	3.3/2.8	
k_{ex}^{298}/ 10⁷ s⁻¹	4.4 ± 0.1	2.6 ± 0.1	2.4 ± 0.1	62.6 ± 2.3	5.5
$\Delta H^\ddagger$ / kJ mol⁻¹	32.17 ± 1.5	25.4 ± 0.9	31.1 ± 1.6	11 ± 1.0	20.5
τ_R^{298} / ps	52.8 ± 0.1	67.2 ± 0.6	78.7 ± 0.7	36 ± 3	85
E_r / kJ mol⁻¹	26.7 ± 0.8	24.6 ± 0.5	20.8 ± 0.6	22.8 ± 0.7	18
τ_V^{298} / ps	51 ± 4	52 ± 4	25 ± 2	21.4 ± 3.8	7.7
E_v / kJ mol⁻¹	1.0[a]	1.0[a]	1.0[a]	1.0[a]	24.8
D_{MnH}^{298} / 10⁻¹⁰ m² s⁻¹	20.0[a]	20.0[a]	20.0[a]	26.9 ± 4.0	23.0[a]
E_{DMnH} / kJ mol⁻¹	20	20	20	17.3 ± 2.4	18
Δ^2 / 10¹⁹ s⁻²	1.69 ± 0.08	2.26 ± 0.11	6.9 ± 0.4	7.2 ± 1.5	0.47
$A_O/\hbar$/ 10⁶ rad s⁻¹ [d]	-49.6 ± 2.3	-32.6 ± 0.9	-44.1 ± 2.7	-46.0 ± 0.2	-32.7
$A_O/\hbar$/ 10⁶ rad s⁻¹ [e]	-51.3	-52.0		-52.3	
r_{MnH}/Å	2.85[a]	2.865[a]	2.85[a]	2.77[a]	2.75
a_{MnH}/Å	3.6[a]	3.6[a]	3.6[a]	3.6[a]	3.2
q^{298}	1[a]	1[a]	0.5[a]	1[a]	1

[a] Parameters fixed during the fitting procedure. [b] Data from Ref 16. [c] Data from ref 14. [d] Experimental values obtained from ¹⁷O NMR measurements. [e] Obtained with DFT calculations.
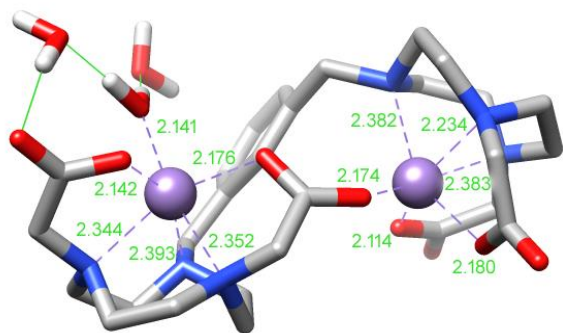
Figure 4. Structure of the [mBz(MnNO2A)(MnNO2A)(H₂O)]·2H₂O system obtained with DFT calculations (M062X/TZVP). Bond distances are provided in Å.
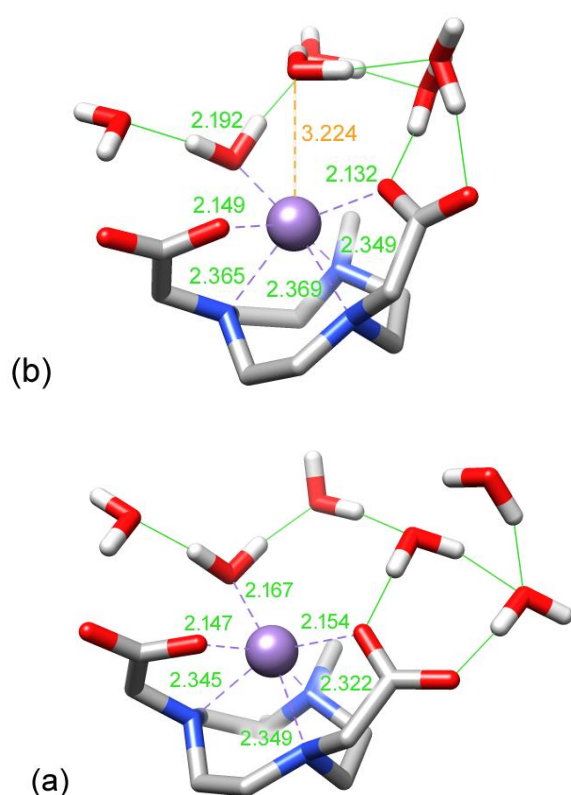
Figure 5. Structures of the energy minimum (a) and transition state (b) characterising the associative water exchange mechanism in [Mn(MeNO2A)(H₂O)]·5H₂O (M062X/TZVP). Bond distances are provided in Å.

Additional DFT calculations were performed to gain insight into the mechanism responsible for the water exchange reaction in this family of complexes.[29] For this purpose, we used a model of the [Mn(MeNO2A)] complex including six explicit water molecules. We then optimised the geometries of the [Mn(MeNO2A)(H₂O)]·5H₂O and [Mn(MeNO2A)(H₂O)₂]·4H₂O systems (Fig 5), which turned out to correspond to local energy minima of the potential energy surface. Our calculations predict that the monohydrated complex is more stable than the q = 2

complex, with a Gibbs free energy difference of 7.2 kJ mol⁻¹. Thus, our calculations with the M062X functional predict the correct hydration number for the [Mn(MeNO2A)] complex, in line with recent findings.[30] Next we located the transition state connecting the two energy minima, which provided an activation free energy of $\Delta G^{\#298}$ = 7.6 kJ mol⁻¹. The distance between the metal ion and the entering water molecule decreases from 6.01 to 3.22 Å to reach the transition state, while the Mn-O distance involving the coordinated water molecule experiences only a slight increase from 2.17 to 2.19 Å, in line with an associatively activated mechanism. The calculated activation entropy is negative ($\Delta S^{\#}$ = -47.3 J mol⁻¹ K⁻¹), as would be expected for an associative mechanism,[31] representing the main contribution to the free energy barrier at 298 K.

2.3. Experimental section

2.3.1. Materials and methods

NO2A*t*Bu was purchased from CheMatech (Dijon, France). All other reagents and solvents were commercial and used without further purification. ¹H and ¹³C NMR spectra were recorded at 25 °C on Bruker Avance 300 MHz and Bruker Avance 500 MHz spectrometers. High resolution electrospray-ionisation time-of-flight (ESI-TOF) mass spectra were obtained in the positive mode using a LC-Q-q-TOF Applied Biosystems QSTAR Elite spectrometer. Elemental analyses were carried out on a ThermoQuest Flash EA 1112 elemental analyser. Medium performance liquid chromatography (MPLC) was carried out using a Puriflash XS 420 instrument equipped with a reverse-phase Puriflash 15C18HP column (60 Å, spherical 15 μm, 20 g) and UV-DAD detection at 210 and 254 nm, and operating at a flow rate of 10 mL/min. Aqueous solutions were lyophilised using a Telstar Cryodos-80 apparatus.

2.3.2. Synthetic procedures

General procedure for synthesis of the ligands.

Triazacyclononane derivative NO2A*t*Bu was dissolved in CH₃CN (20 mL) in the presence of K₂CO₃. A solution of the corresponding bromide precursor in CH₃CN (20 mL) was added dropwise to the suspension and the mixture was stirred during 48 h at room temperature. Once the alkylation was completed, the reaction mixture was filtered and the filtrate concentrated in vacuum at low temperature (30 °C) to afford yellowish oils that were characterised by ¹H and ¹³C NMR and mass spectrometry (see details below), and used in the next step without further purification. The protected ligands were hydrolysed using a 1:1 TFA:CH₂Cl₂ mixture (8 mL), stirring at room temperature for 48 h. Once the deprotection was completed, the solution was concentrated *in vacuo* and washed several times with water (5x10 mL). The product was redissolved in water and lyophilised to obtain the final ligands.

Synthesis of di-*tert*-butyl 2,2'-(7-benzyl-1,4,7-triazonane-1,4-diyl)diacetate (H₂BzNO2A*t*Bu, 2a). This compound was obtained by using NO2A*t*Bu (0.2059 g, 0.5759 mmol), benzyl bromide (**1a**, 68.5 μL, 1 eq) and K₂CO₃ (0.138 g, 1.73 eq). Yellowish oil (0.260 g, quantitative). ¹H NMR (300 MHz, CDCl₃): δ_H (ppm): 7.31-7.25 (5H, m, CH_Ph), 3.67 (2H, m, CH₂), 3.30-3.24 (4H, m, CH₂), 2.93-2.80 (2H, m, CH₂), 1.45-1.38 (18H, m, CH₂);

¹³C NMR (75 MHz, CDCl₃): δ_C (ppm) 171.46 (COOtBu), 139.94 (C$_{Ph}$), 129.01 (C$_{Ph}$), 128.11 (C$_{Ph}$), 126.76 (C$_{Ph}$), 80.58 (-OC(CH₃)₃), 62.54 (CH₂), 59.85 (CH₂), 55.35 (CH₂), 55.15 (CH₂), 28.19 (CH₃). Mass spectrometry (ESI⁺) *m/z* (%BPI): 448.32 (100) ([C₂₄H₄₂N₃O₄]⁺).

Synthesis of 2,2'-(7-benzyl-1,4,7-triazonane-1,4-diyl)diacetic acid (H₂BzNO2Ac). Yellowish solid (0.3363 g, quantitative). ¹H NMR (300 MHz, D₂O): δ_H (ppm) 8.28 (3H, s, CH$_{Ph}$), 7.60 (1H, s, CH$_{Ph}$), 7.58 (2H, s, CH$_{Ph}$), 4.53 (4H, s, CH₂), 3.64-3.58 (8H, d, CH₂), 3.22 (6H, s, CH₂); ¹³C NMR (75 MHz, D₂O): δ_C (ppm) 174.73 (COOH), 166.01 (C$_{Ph}$), 131.02 (C$_{Ph}$), 130.30 (C$_{Ph}$), 129.46 (C$_{Ph}$), 60.54 (CH₂), 57.55 (CH₂), 50.69 (CH₂), 50.45 (CH₂), 49.22 (CH₂). Mass spectrometry (ESI⁺) *m/z* (%BPI): 336.19 (100) ([C₁₇H₂₆N₃O₄]⁺), 358.17 (10) ([C₁₇H₂₅N₃NaO₄]⁺), 374.15 (7) ([C₁₇H₂₅KN₃NaO₄]⁺). HR-MS (ESI⁺) *m/z*: [M+Na]⁺, calculated: 336.1917, found: 336.1931.

Synthesis of di-*tert*-butyl 2,2'-(7-(1-phenylethyl)-1,4,7-triazonane-1,4-diyl)-diacetate (H₂MeBzNO2A*t*Bu, 2b). This compound was obtained using NO2A*t*Bu (0.2066 g, 0.578 mmol), α-methylbenzyl bromide (1b, 81.3 μL, 1 eq) and K₂CO₃ (0.121 g, 1.5 eq). Yellowish oil (0.267 g, quantitative). ¹H NMR (300 MHz, CDCl₃): δ_H (ppm) 7.34-7.32 (2H, d, CH$_{Ph}$), 7.27-7.22 (2H, t, CH$_{Ph}$), 7.18-7.13 (1H, t, CH$_{Ph}$), 3.79 (1H, s, CH), 3.24 (4H, s, CH₂), 2.90-2.69 (12H, m, CH₂), 1.40 (18H, s, CH₃), 1.32-1.31 (4H, d, CH₃). ¹³C NMR (75 MHz, CDCl₃): δ_C (ppm) 171.48 (COOtBu), 144.60 (C$_{Ph}$), 127.97 (C$_{Ph}$), 127.83 (C$_{Ph}$), 126.52 (C$_{Ph}$), 80.50 (-OC(CH₃)₃), 63.17 (CH), 59.58 (CH₂), 55.93 (CH₂), 55.20 (CH₂), 52.71 (CH₂), 28.18 (-OC(CH₃)₃). Mass spectrometry (ESI⁺) *m/z* (%BPI): 462.33 (100) ([C₂₆H₄₄N₃O₄]⁺), 406.27 (12) ([C₂₂H₃₆N₃O₄]⁺).

Synthesis of 2,2'-(7-(1-phenylethyl)-1,4,7-triazonane-1,4-diyl)diacetic acid (H₂MeBzNO2A). Yellowish solid (0.200 g, quantitative). ¹H NMR (300 MHz, D₂O)): δ_H (ppm) 7.57-7.53 (5H, m, CH$_{Ph}$), 3.65 (16H, m, CH₂), 3.18 (1H, s, CH), 1.79-1.77 (3H, d, CH₂). ¹³C NMR (75 MHz, D₂O): δ_C (ppm) 174.77 (COOH), 135.36 (C$_{Ph}$), 132.13 (C$_{Ph}$), 131.16 (C$_{Ph}$), 130.56 (C$_{Ph}$), 67.96 (CH), 57.75 (CH₂), 51.72 (CH₂), 50.86 (CH₂), 15.66 (CH₃). Mass spectrometry (ESI⁺) *m/z* (%BPI): 350.21 (100) ([C₁₈H₂₈N₃O₄]⁺), 372.19 (17) ([C₁₈H₂₇N₃NaO₄]⁺), 388.15 (12) ([C₁₈H₂₇KN₃O₄]⁺). HR-MS (ESI⁺) *m/z*: [M+Na]⁺, calculated: 350.2074, found: 350.2071.

Synthesis of tetra-*tert*-butyl 2,2',2'',2'''-((1,3-phenylenebis(methylene))bis(1,4,7-triazonane-7,1,4-triyl))tetraacetate (*m*Bz(NO2A*t*Bu)₂, 2c). This compound was obtained using NO2A*t*Bu (0.3022 g, 0.8453 mmol), α,α'-dibromo-m-xylene (1c, 0.1151 g, 0.5 eq) and K₂CO₃ (0.294 g, 5 eq). Yellow oil (0.345 g, quantitative). ¹H NMR (300 MHz, CDCl₃): δ_H (ppm) 7.42 (1H, t, CH$_{Ph}$), 7.28-7.26 (2H, d, CH$_{Ph}$), 7.06-7.04 (1H, d, CH$_{Ph}$), 3.97 (2H, s, CH₂), 3.01-2.52 (30H, m, CH₂), 1.72-1.69 (4H, s, CH₂), 1.13-1.11 (36H, d, CH₃). ¹³C NMR (75 MHz, CDCl₃): δ_C (ppm) 170.53 (COOtBu), 131.54 (C$_{Ph}$), 129.95 (C$_{Ph}$), 129.00 (C$_{Ph}$), 116.45 (C$_{Ph}$), 81.00 (-OC(CH₃)₃), 59.86 (CH₂), 57.72 (CH₂), 52.48 (CH₂), 27.86 (-OC(CH₃)₃). Mass spectrometry (ESI⁺) *m/z* (%BPI): 817.58 (15) ([C₄₄H₇₇N₆O₈]⁺), 409.29 (100) ([C₄₄H₇₈N₆O₈]²⁺).

Synthesis of 2,2',2'',2'''-((1,3-phenylenebis(methylene))bis(1,4,7-triazonane-7,1,4-triyl))tetraacetic acid (*m*Bz(H₂NO2A)₂). Reddish solid (0.250 g, quantitative). ¹H NMR (300 MHz, D₂O): δ_H (ppm) 7.66 (4H, m, CH$_{Ph}$), 3.67-3.13 (32H, m, CH₂), 1.21 (4H, s, CH₂); ¹³C NMR (75 MHz, D₂O): δ_C (ppm) 165.37-165.02 (COOH), 135.25 (C$_{Ph}$), 134.48 (C$_{Ph}$), 132.15 (C$_{Ph}$), 61.95 (CH₂), 52.33 (CH₂), 51.95 (CH₂), 50.81 (CH₂). Mass spectrometry (ESI⁺) m/z (%BPI): 631.27 (100) ([C₂₈H₄₄KN₆O₈]⁺), 593.33 (20) ([C₂₈H₄₅N₆O₈]⁺), 669.22 (33) ([C₂₈H₄₃K₂N₆O₈]⁺). HR-MS (ESI⁺) *m/z*: [M+Na]⁺, calculated: 593.3293, found: 593.3268.

General procedure for synthesis of the complexes.

The corresponding triazacyclononane ligand derivative was dissolved in *n*-BuOH (10 mL) in the presence of DIPEA (5 eq.) with the assistance of an ultrasound bath. The solution was purged with an argon flow and afterwards the solid manganese salt, MnCl₂·4H₂O, was added. The reaction was maintained at 112 ºC for 6 h. The reaction was stopped and allowed to cool down to room temperature. The reaction mixture was concentrated in vacuum and redissolved in dichloromethane. The product was extracted with water (4x5 mL) and the aqueous phase was evaporated to furnish a yellowish solid. The solid was purified by MPLC using a reverse-phase C18 column. An aqueous solution of the compound in the eluting conditions (CH₃CN:H₂O, *v:v*, containing 0.1% triethylamine) was prepared and filtered through a cellulose filter (0.20 μm pore size) before injection. The purification method was carried out in gradient of solvent B (CH₃CN, 5 to 10%) in solvent A (H₂O). The fractions containing the complex were combined and the solvent was removed in vacuum. The final product was redissolved in water and lyophilised to furnish the final complexes.

Synthesis of [Mn(BzNO2A)]. Yellowish solid (0.066 g, 34%). Mass spectrometry (ESI⁺) *m/z* (%BPI): 411.1 (100) ([C₁₇H₂₃N₃O₄NaMn]⁺). HR-MS (ESI⁺) *m/z*: [M+Na]⁺, calculated: 411.0961, found: 411.0954.

Synthesis of [Mn(MeBzNO2A)]. Yellowish solid (0.086 g, 37%). Mass spectrometry (ESI⁺) *m/z* (%BPI): 425.11 (100) ([C₁₈H₂₅N₃O₄NaMn]⁺), 403.13 (17) ([C₁₈H₂₆N₃O₄Mn]⁺). HR-MS (ESI⁺) *m/z*: [M+Na]⁺, calculated: 425.1117, found: 425.1113.

Synthesis of [*m*Bz(MnNO2A)₂]. Yellowish solid (0.090 g, 39%). Mass spectrometry (ESI⁺) *m/z* (%BPI): 721.16 (100) ([C₂₈H₄₀N₆O₈NaMn₂]⁺), 699.18 (8) ([C₂₈H₄₁N₆O₈Mn₂]⁺). HR-MS (ESI⁺) *m/z*: [M+Na]⁺, calculated: 721.1560, found: 721.1551.

2.3.3. ¹H NMRD and ¹⁷O NMR measurements

The proton $1/T_1$ NMRD profiles were measured on a fast field-cycling Stelar SmartTracer relaxometer (Mede, Pv, Italy) over a continuum of magnetic field strengths from 0.00024 to 0.25 T (corresponding to 0.01-10 MHz proton Larmor frequencies). The relaxometer operates under computer control with an absolute uncertainty in $1/T_1$ of ± 1%. The temperature control was carried out using a Stelar VTC-91 airflow heater equipped with a calibrated copper–constantan thermocouple (uncertainty of ±0.1 K). Additional data points in the range 20-60 MHz were obtained on a Stelar Relaxometer equipped with a Bruker WP80 NMR electromagnet adapted to variable-field measurements (15-80 MHz proton Larmor frequency). The exact complex concentration was determined by the BMS shift method at 11.7 T.[33] ¹⁷O NMR measurements were recorded on a Bruker Avance III spectrometer (11.7 T) equipped with a 5 mm probe and standard temperature control unit. Aqueous solution of the complexes (ca. 6-10 mM) containing 2.0% of the ¹⁷O

isotope (Cambridge Isotope) were used. The observed transverse relaxation rates were calculated from the signal width at half-height.

2.3.4. pH stability range

Solutions of [Mn(BzNO2A)], [Mn(MeBzNO2A)] and [*m*Bz(MnNO2A)₂] (1 mM) were prepared in the pH range 1.72–10.5. The longitudinal relaxation rates were measured at 20 MHz and 298 K. The measurements were carried out in a BrukerMinispec MQ 20.

2.3.5. Computational details

Full geometry optimisations of the [Mn(MeNO2A)(H₂O)]·xH₂O (x = 2, 5), [Mn(BzNO2A)(H₂O)]·2H₂O, [Mn(MeBzNO2A)(H₂O)]·2H₂O and [*m*Bz(MnNO2A)₂]·3H₂O systems were performed employing DFT calculations at the M06-2X/TZVP[34,35] level employing the Gaussian 09 package (Revision E.01).[36] Solvent effects (water) were introduced by using the integral equation formalism variant of the polarizable continuum model (IEFPCM).[37] No symmetry constraints have been imposed during the optimisations. All stationary points found as a result of geometry optimisation were confirmed to represent energy minima on the potential energy surfaces via frequency analysis. ¹⁷O hyperfine coupling constants were calculated using the M06-2X functional in combination with aug-cc-pVTZ-J basis set for Mn[38] and the EPR-III[39] basis set for the ligand atoms.

The potential energy surface of the [Mn(MeNO2A)(H₂O)]·5H₂O system was investigated by performing relaxed potential energy surface scans, which were generated by either: i) increasing the distance between Mn and the oxygen atom of the coordinated water molecule in steps of 0.1 Å, and ii) Shortening the distance between a second-sphere water molecule and the Mn atom in steps of 0.1 Å. The geometries generated from these calculations were subsequently used to calculate the transition state characterising the associative water exchange mechanisms with the aid of the synchronous transit-guided quasi-Newton approach.[40] Saddle points were characterised using frequency calculations, which also provided zero-point energies (ZPEs), enthalpies (*H*) and free energies (*G*) at 298.15 K and 1 atm.

2.4. Conclusions

In this work, we have presented a family of Mn²⁺ complexes with ligands containing a NO2A²⁻ chelating unit functionalised with different substituents at the third nitrogen atom of the triazacyclononane moiety. A detailed relaxometric study showed demonstrated that the water exchange process becomes slower upon increasing the steric hindrance around the water binding site. This can be accounted for by the associative mechanism followed by the water exchange process. The increased bulkiness of the substituent hinders the approach of the entering water molecule, causing a destabilisation of the seven-coordinated transition state. DFT calculations provided support for the associative water exchange mechanism.

The results reported here give insight at the molecular level on important parameters that control the efficiency of Mn²⁺ complexes as MRI contrast agents. In the case of Gd³⁺ MRI contrast agents the studies reported during the last two decades provide a plethora of data that enable a rational control of some key physicochemical parameters. For instance, steric compression around the water coordination site was found to accelerate the water exchange process, by facilitating the dissociative water exchange reaction.[32] In the case of Mn²⁺ complexes the amount of data accumulated is far lower, so that the design of potential MRI contrast agent on a rational basis is more difficult. We have shown here that increasing the steric compression around the water coordination site may have opposite effects on the water exchange rates of Gd³⁺ and Mn²⁺ complexes.

2.5. Notes

The work presented in this chapter has been submitted for publication as communication in a scientific journal.

2.6. References

1 (a) J. Wahsner, E. M. Gale, A. Rodríguez-Rodríguez and P. Caravan, *Chem. Rev.,* 2019, **DOI:** 10.1021/acs.chemrev.8b00363. (b) A. Merbach, L. Helm and E. Tóth, The Chemistry of Contrast Agents in Medical Magnetic Resonance Imaging, John Wiley & Sons, Chichester, Second Ed., 2013.

2 (a) L. Helm, J. R. Morrow, C. J. Bond, F. Carniato, M. Botta, M. Braun, Z. Baranyai, R. Pujales-Paradela, M. Regueiro-Figueroa, D. Esteban-Gómez, C. Platas-Iglesias and T. J. Scholl, Contrast Agents for MRI. Experimental Methods, ed. V. C. Pierre and M. J. Allen, Royal Society of Chemistry, Croydon, UK, 2018, ch. 3. (b) B. Phukan, C. Mukherjee, U. Goswami, A. Sarmah, S. Mukherjee, S. K. Sahoo and S. Ch. Moi, *Inorg. Chem.*, 2018, **57**, 2631.

3 (a) S. Cheng, L. Abramova, G. Saab, G. Turabelidze, P. Patel, M. Arduino, T. Hess, A. Kallen and M. Jhung, *J. Am. Med. Assoc.,* 2007, **297**, 1542; (b) T. H. Darrah, J. J. Prutsman-Pfeiffer, R. J. Poreda, M. E. Campbell, P. V. Hauschka and R. E. Hannigan, *Metallomics*, 2009, **1**, 479.

4 (a) D. R. Roberts, S. M. Lindhorst, C. T. Welsh, K. R. Maravilla, M. N. Herring, K. A. Braun, B. H. Thiers and W. C. Davis, *Invest. Radiol.,* 2016, **51**, 280; (b) M. Birka, K. S. Wentker, E. Lusmöller, B. Arheilger, C. A. Wehe, M. Sperling, R. Stadler and U. Karst, *Anal. Chem.,* 2015, **87**, 3321; (c) T. Kanda, T. Fukusato, M. Matsuda, K. Toyoda, H. Oba, J. Kotoku, T. Haruyama, K. Kitajima and S. Furui, *Radiology,* 2015, **276**, 228; (d) E. Kanal and M. F. Tweedle, *Radiology,* 2015, **275**, 630. (e) T. J. Fraum, D. R. Ludwig, M. R. Bashir and K. J. Fowler, *J. Magn. Reson. Imaging,* 2017, **46**, 338.

5 V. M. Runge, *Invest. Radiol.,* 2018, **53**, 571.

6 (a) D. Pan, A. H. Schmieder, S. A. Wickline and G. M. Lanza, *Tetrahedron,* 2011, **67**, 8431. (b) B. Drahos, I. Lukes and E. Toth, *Eur. J. Inorg. Chem.,* 2012, 1975; (c) M. Kueny-Stotz, A. Garofalo and D. Felder-Flesch, Eur. J. Inorg. Chem., 2012, 1987.

7 J. R. Morrow and E. Toth, *Inorg. Chem.*, 2017, **56**, 6029.

8 E. M. Gale, I. P. Atanasova, F. Blasi, I. Ay and P. Caravan, *J. Am. Chem. Soc.*, 2015, **137**, 15548.

9 (a) J. Zhu, E. M. Gale, I. Atanasova, T. A. Rietz and P. Caravan, *Chem. Eur. J.*, 2014, **20**, 14507; (b) B. Phukan, A. B. Patel and C. Mukherjee, *Dalton Trans.*, 2015, **44**, 12990; (c) H. Su, C. Wu, J. Zhu, T. Miao, D. Wang, C. Xia, X. Zhao, Q. Gong, B. Song and H. Ai, *Dalton Trans.*, 2012, **41**, 14480.

10 (a) M. Regueiro-Figueroa, G. A. Rolla, D. Esteban-Gomez, A. de Blas, T. Rodriguez-Blas, M. Botta and C. Platas-Iglesias, *Chem. Eur. J.*, 2014, **20**, 17300; (b) A. Forgacs, M. Regueiro-Figueroa, J. L. Barriada, D. Esteban-Gomez, A. de Blas, T. Rodriguez-Blas, M. Botta and C. Platas-Iglesias, *Inorg. Chem.*, 2015, **54**, 9576; (c) A. Forgács, L. Tei, Z. Baranyai, D. Esteban-Gómez, C. Platas-Iglesias and M. Botta, *Dalton Trans.*, 2017, **46**, 8494; (d) R. Pujales-Paradela, F. Carniato, R. Uzal-Varela, I. Brandariz, E.

Iglesias, C. Platas-Iglesias, M. Botta and D. Esteban-Gomez, *Dalton Trans.,* **2019**, *48*, 696.

11 G. F. Kwakye, M. M.B. Paoliello, S. Mukhopadhyay, A. B. Bowman and M. Aschner, *Int. J. Environ. Res. Public Health*, 2015, **12**, 7519.

12 (a) G. L. Loving, S. Mukherjee and P. Caravan, *J. Am. Chem. Soc.*, 2013, **135**, 4620; (b) E. M. Gale, S. Mukherjee, C. Liu, G. S. Loving and P. Caravan, *Inorg. Chem.*, 2014, **53**, 10748.

13 (a) Z. Baranyai, Z. Palinkas, F. Uggeri, A. Maiocchi, S. Aime and E. Brucher, *Chem. Eur. J.,* 2012, **18**, 16426; (b) Z. Baranyai, E. Brucher, F. Uggeri, A. Maiocchi, I. Toth, M. Andrasi, A. Gaspar, L. Zekany and S. Aime, *Chem. Eur. J.,* 2015, **21**, 4789.

14 E. Balogh, Z. He, W. Hsieh, S. Liu and É. Tóth, *Inorg. Chem.*, 2007, **46**, 238–250.

15 (a); Y. Ducommun, K. E. Newman and A. E. Merbach, *Inorg. Chem.,* 1980, **19**, 3696; (b) D. Esteban-Gómez, C. Cassino, M. Botta and C. Platas-Iglesias, *RSC Adv.,* 2014, **4**, 7094.

16 V. Patinec, G. A. Rolla, M. Botta, R. Tripier, D. Esteban-Gomez and C. Platas-Iglesias, *Inorg. Chem.*, 2013, **52**, 11173-11184.

17 A. de Sá, C. S. Bonnet, C. F. G. C. Geraldes, É. Tóth, P. M. T. Ferreira and J. P. André, *Dalton Trans.*, 2013, **42**, 4522-4532.

18 S. Aime, M. Botta, D. Esteban-Gómez and C. Platas-Iglesias, *Mol. Phys.,* 2018, DOI: 10.1080/00268976.2018.1516898.

19 G. A. Rolla, C. Platas-Iglesias, M. Botta, L. Tei and L. Helm, *Inorg. Chem.,* 2013, **52**, 3268.

20 L. Tei, G. Gugliotta, M. Fekete, F. K. Kalman and M. Botta, *Dalton Trans.,* 2011, **40**, 2025.

21 S. Aime, A. Barge, J. I. Bruice, M. Botta, J. A. K. Howard, J. M. Moloney, D. Parker, A. S. de Sousa and M. Woods, *J. Am. Chem. Soc.,* 1999, **121**, 576; (b) S. Aime, A. Barge, M. Botta, D. Parker and A. S. De Sousa, *J. Am. Chem. Soc.,* 1997, **119**, 4767; (c) A. Rodriguez-Rodriguez, M. Regueiro-Figueroa, D. Esteban-Gomez, T. Rodriguez-Blas, V. Patinec, R. Tripier, G. Tircso, F. Carniato, M. Botta and C. Platas-Iglesias, *Chem. Eur. J.,* 2017, **23**, 1110.

22 S. Aime, A. Barge, J. I. Bruce, M. Botta, J. A. K. Howard, J. M. Moloney, D. Parker, A. S. de Sousa and M. Woods, *J. Am. Chem. Soc.,* 1999, **121**, 5762.

23 J. A. Peters and C. F. G. C. Geraldes, *Inorganics,* 2018, **6**, 116.

24 E. M. Gale, J. Zhu and P. Caravan, *J. Am. Chem. Soc.,* 2013, **135**, 18600.

25 (a) I. Solomon and N. Bloembergen, *J. Chem. Phys.*, 1956, **25,** 261; (b) N. Bloembergen and L. O. Morgan, *J. Chem. Phys.*, 1961, **34**, 842.

26 J. H. Freed, *J. Chem. Phys.*, 1978, **68**, 4034.

27 R. Pujales-Paradela, M. Regueiro-Figueroa, D. Esteban-Gómez and C. Platas-Iglesias, Contrast Agents for MRI. Experimental Methods, ed. V. C. Pierre and M. J. Allen, Royal Society of Chemistry, Croydon, UK, 2018, ch. 5.

28 (a) E. Molnar, N. Camus, V. Patinec, G. A. Rolla, M. Botta, G. Tircso, F. K. Kalman, T. Fodor, R. Tripier and C. Platas-Iglesias, *Inorg. Chem.*, 2014, **53**, 5136; (b) M. Khannam, T. Weyhermüller, U. Goswami and C. Mukherjee, *Dalton Trans.,* 2017, **46**, 10426.

29 L. Leone, D. Esteban-Gomez, C. Platas-Iglesias, M. Milanesio and L. Tei, *Chem. Commun.,* 2019, **55**, 513.

30 K. Pota, Z. Garda, F. K. Kalman, J. L. Barriada, D. Esteban-Gomez, C. Platas-Iglesias, I. Toth, E. Brucher and G. Tircso, *New J. Chem.,* 2018, *42*, 8001.

31 (a) C. D. Hubbard and R. van Eldik, *Inorg. Chim. Acta,* 2010, **363**, 2357; (b) L. Helm and A. E. Merbach, *Chem. Rev.,* 2005, **105**, 1923.

32 (a) S. Laus, R. Ruloff, E. Toth and A. E. Merbach, *Chem. Eur. J.,* 2003, *9*, 3555; (b) L. Tei, G. Gugliotta, Z. Baranyai and M. Botta, *Dalton Trans.,* 2009, 9712; (c) E. Balogh, M. Mato-Iglesias, C. Platas-Iglesias, E. Toth, K. Djanashvili, J. A. Peters, A. de Blas and T. Rodríguez-Blas, *Inorg. Chem.,* 2006, *45*, 8719; (d) J. Kotek, P. Lebduskova, P. Hermann, L. Vander Elst, R. N. Muller, C. F. G. C. Geraldes, T. Maschmeyer, I. Lukes and J. A. Peters, *Chem. Eur. J.*, 2003, *9*, 5899.

33 D. M. Corsi, C. Platas-Iglesias, H. van Bekkum and J. A. Peters, *Magn. Reson. Chem.,* 2001, **39**, 723.

34 Y. Zhao and D. G. Truhlar, *Theor. Chem. Acc.*, 2008, **120**, 215.

35 A. Schaefer, C. Huber and R. Ahlrichs, *J. Chem. Phys.,* 1994, **100**, 5829.

36 Gaussian 09, Revision E.01, M. J. Frisch, G. W. Trucks, H. B. Schlegel, G. E. Scuseria, M. A. Robb, J. R. Cheeseman, G. Scalmani, V. Barone, G. A. Petersson, H. Nakatsuji, X. Li, M. Caricato, A. Marenich, J. Bloino, B. G. Janesko, R. Gomperts, B. Mennucci, H. P. Hratchian, J. V. Ortiz, A. F. Izmaylov, J. L. Sonnenberg, D. Williams-Young, F. Ding, F. Lipparini, F. Egidi, J. Goings, B. Peng, A. Petrone, T. Henderson, D. Ranasinghe, V. G. Zakrzewski, J. Gao, N. Rega, G. Zheng, W. Liang, M. Hada, M. Ehara, K. Toyota, R. Fukuda, J. Hasegawa, M. Ishida, T. Nakajima, Y. Honda, O. Kitao, H. Nakai, T. Vreven, K. Throssell, J. A. Montgomery, Jr., J. E. Peralta, F. Ogliaro, M. Bearpark, J. J. Heyd, E. Brothers, K. N. Kudin, V. N. Staroverov, T. Keith, R. Kobayashi, J. Normand, K. Raghavachari, A. Rendell, J. C. Burant, S. S. Iyengar, J. Tomasi, M. Cossi, J. M. Millam, M. Klene, C. Adamo, R. Cammi, J. W. Ochterski, R. L. Martin, K. Morokuma, O. Farkas, J. B. Foresman, and D. J. Fox, Gaussian, Inc., Wallingford CT, 2016.

37 J. Tomasi, B. Mennucci and R. Cammi, *Chem. Rev.,* 2005, **105**, 2999.

38 E. D. Hedegard, J. Kongsted and S. P. A. Sauer, *J. Chem. Theory Comput.,* 2011, **7**, 4077.

39 N. Rega, M. Cossi and V. Barone, *J. Chem. Phys.,* 1996, **105**, 11060.

40 (a) C. Peng and H. B. Schlegel, *Israel J. of Chem.,* 1993, **33**, 449; (b) C. Peng, P. Y. Ayala, H. B. Schlegel and M. J. Frisch, *J. Comp. Chem.,* 1995, **16**, 49.

A Pentadentate
Member of the Picolinate Family
for Mn(II) Complexation
and an Amphiphilic Derivative
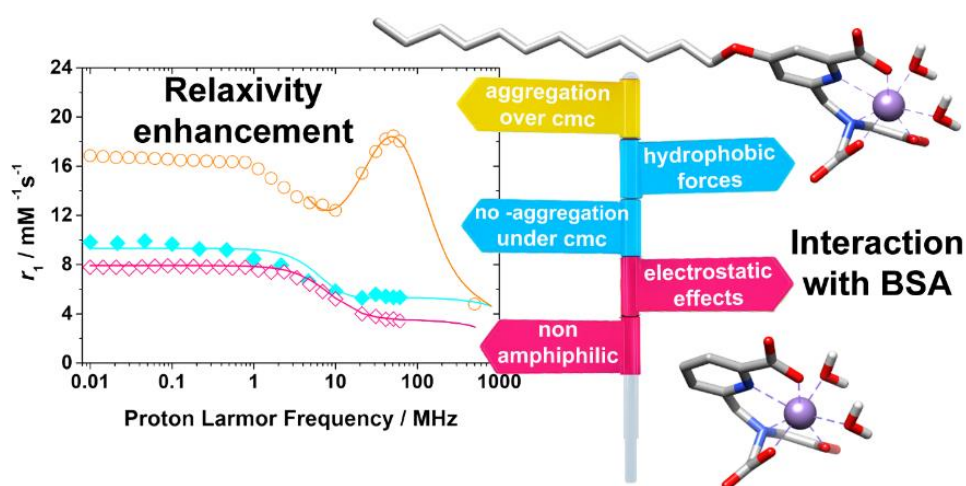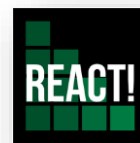
A Pentadentate Member of the Picolinate Family for Mn(II) Complexation and an Amphiphilic Derivative

We report a pentadentate ligand containing a 2,2'-azanediyldiacetic acid moiety functionalised with a picolinate group at the nitrogen atom (H$_3$paada), as well as a lipophylic derivative functionalised with a dodecyloxy group at position 4 of the pyridyl ring (H$_3$C$_{12}$Opaada). The protonation constants of the paada^{3-} ligand and the stability constant of the Mn(II) complex were determined using a combination of potentiometric and spectrophotometric titrations (25 °C, 0.15 M NaCl). A detailed relaxometric characterisation was accomplished by recording ^{1}H Nuclear Magnetic Relaxation Dispersion (NMRD) profiles and ^{17}O chemical shifts and relaxation rates. These studies provide a detailed information on the microscopic parameters that control their efficiency as relaxation agents *in vitro*. For the sake of completeness and to facilitate comparison, we also characterised the related [Mn(nta)]$^-$ complex (nta = nitrilotriacetate). Both the [Mn(paada)]$^-$ and [Mn(nta)]$^-$ complexes turned out to contain two inner-sphere water molecules in aqueous solution. The exchange rate of these coordinated water molecules was slower in [Mn(paada)]$^-$ ($k_{ex}^{298} = 90 \times 10^7$ s^{-1}) than in [Mn(nta)]$^-$ ($k_{ex}^{298} = 280 \times 10^7$ s^{-1}). The complexes were also characterised using both DFT (TPSSh/def2-TZVP) and *ab initio* CAS(5,5) calculations. The lipophylic [Mn(C$_{12}$Opaada)]$^-$ complex forms micelles in solution characterised by a critical micellar concentration (*cmc*) of 0.31±0.01 mM. This complex also forms a rather strong adduct with Bovine Serum Albumin (BSA) with an association constant of 5.5×10^4 M^{-1} at 25 °C. The enthalpy and entropy changes obtained for the formation of the adduct indicate that the binding event is driven by hydrophobic interactions.

3.1. Introduction

Acyclic polydentate ligands containing picolinate groups have been intensively investigated in the last decade due to their ability to form stable complexes with a wide range of metal ions. The most common examples of this ligand class contain a number of amine nitrogen atoms ranging from 1 to 3 functionalised with several 6-methylpicolinate and acetate pendant arms. A judicious choice of the number and type of donor atoms provided ligands with denticity ranging from 5 (i. e. dpaMea^{2-})[1] to 10 (i. e. decapa^{5-} or tpaen^{4-}, Scheme 1).[2,3] The hexadentate ligand dedpa^{2-} and the rigidified derivative *CHX*dedpa^{2-} and lipophilic derivatives were found to be particularly well suited for the complexation of small metal ions relevant in radiopharmaceutical applications, such as Ga(III) and Cu(II),[4,5] as well as Zn(II), Cd(II) and Pb(II).[6] The Ni(II) complexes with the bis-amide derivatives dedpam and *CHX*dedpam were recently investigated as potential contrast agents for application in Magnetic Resonance Imaging (MRI) based on the Chemical Exchange Saturation Transfer (CEST) effect.[7] Another versatile hexadentate ligand is dpaa^{3-}, which was shown to present favourable Ga^{3+} complexation kinetics giving a rather stable complex.[8] The Mn(II) complex was proposed as a potential alternative to Gd^{3+} as contrast agent for application in MRI thanks to the presence of one water molecule directly coordinated to the metal ion.[9,10] The octadentate ligand octapa^{4-} was demonstrated to form stable complexes with larger metal ions such as In^{3+} and the lanthanide ions (Ln^{3+}).[2,11] As a result, octapa^{4-} and the rigidified derivative *CHX*octapa^{4-} were proposed as chelators for the preparation of ^{111}In and ^{177}Lu radiopharmaceuticals[5] and potential Gd^{3+}-based contrast agents for application in MRI.[12] The pentadentate ligand pmpa^{2-} was also proposed recently as a potential MRI contrast agent endowed with high relaxivity thanks to the presence of two coordinated water molecules.[13]

Recently we started a research program aiming to develop Mn(II)-based contrast agents for application in MRI. A potential advantage of Mn(II)-based contrast agents with respect to the Gd^{3+} analogues used in clinical practice is related to the better toxicity profile of Mn(II) compared to Gd^{3+}.[14,15] Currently, the issue of Gd^{3+} toxicity is generating some concerns on the use of non-macrocyclic complexes of this metal ion as CAs, particularly in case of administration of multiple doses.[16] Indeed, recent studies also reported Gd^{3+} deposition in the brain and other tissues following the administration of contrast agents.[17] Thus, there is a need for developing safer contrast agent for MRI. High-spin Mn(II) complexes represent an attractive alternative for this purpose, as the *d*^{5} configuration of the metal ion results in slow relaxation times of the electron spin.[18,19] Furthermore, ligands stabilizing both Mn(II) and Mn^{3+} can be used as redox-responsive MRI probes.[20]

In a recent work we investigated the Mn(II) complexes of the pentadentate ligand dpaMea^{2-} and several derivatives containing lipophilic units or multiple dpaMea^{2-} chelating units.[1,9] These complexes feature two water molecules coordinated to the metal ion and present high relaxivities both in aqueous solution and in plasma, where they reversibly bind to human serum albumin (HSA). The incorporation of an acetate arm into the structure of dpaMea^{2-} decreases the number of water molecules coordinated to Mn(II) from 2 to 1, but results in an enhanced thermodynamic stability.[9] Herein, we complete this family of ligands by reporting the pentadentate ligand paada^{3-}. This ligand was prepared by Cameron *et al.* and used for complexation of Ru(III) in the search for nitric

oxide scavengers.[21] A derivative of paada³⁻ containing a 4-ethynyl-*N*,*N*-dimethyl aniline group at position 4 of the pyridine unit was also developed for complexation of the lanthanide ions.[22] We report in this work an improved synthesis of the ligand. The thermodynamic stability of the corresponding Mn(II) complex was investigated by using potentiometric titrations. A full ¹H and ¹⁷O NMR relaxometric characterisation of the complex was carried out to determine the parameters that control the relaxivity of the [Mn(paada)]⁻ complex. For the sake of comparison, we have also performed a relaxometric study of the related [Mn(nta)]⁻ complex. Finally, we have synthesised and characterised a lipophilic derivative of paada³⁻ that contains a dodecyloxo group in position 4 of the pyridyl unit (H₃C₁₂Opaada, Scheme 1). The ability of this lipophilic derivative to form micelles and bind to BSA was investigated by using relaxometric and spectrofluorometric methods.

3.2. Results and discussion

3.2.1. Synthesis of the ligands

A synthesis of H₃paada with a 29% yield was reported in the literature, which involved the alkylation of dimethyl 2,2'-azanediyldiacetate with methyl 6-(((methylsulfonyl)oxy)methyl)picolinate and subsequent basic hydrolysis of the methyl ester groups.[21] The synthesis of H₃paada reported here (Scheme 2) was achieved by alkylation of di-*tert*-butyl 2,2'-azanediyldiacetate with ethyl 6-(chloromethyl)picolinate (**4**) in acetonitrile using K₂CO₃ as a base. Subsequent hydrolysis of the ester groups using 6 M HCl provided H₃paada as its hydrochloride salt with good overall yield (61%).

The synthesis of the lipophilic derivative H₃C₁₂Opaada started from diethyl 4-hydroxy-2,6-pyridinedicarboxylate, which was converted into diethyl 4-dodecyloxy-2,6-pyridinedicarboxylate (**1**) following the

literature procedure (Scheme 2).[23] Reduction of one of the ethyl ester groups of **1** with NaBH₄ in methanol afforded compound **2**, which was subsequently treated with thionyl chloride to give **3**. Reaction of **3** with di-*tert*-butyl 2,2'-azanediyldiacetate in acetonitrile using K₂CO₃ as a base followed by acid hydrolysis of the ester groups provided the H₃C₁₂Opaada ligand.

3.2.2. Ligand protonation constants and stability constants of the Mn(II) complex

The protonation constants of the paada³⁻ ligand defined as in Eq. (1) were determined by potentiometric titrations in 0.15 M NaCl.

$$K_i^H = \frac{[H_iL]}{[H_{i-1}L][H^+]} \qquad \text{with } i = 1, 2, 3, 4 \qquad (1)$$

The logK_i^H values determined for paada³⁻ are compared to those of the related dpaMea²⁻, dpaa³⁻ and nta³⁻ ligands in Table 1. The four protonation constants determined for paada³⁻ are related to the stepwise protonation of the amine nitrogen atom and all the three carboxylate groups of the ligand. The first protonation constant of paada³⁻ is slightly higher than those of dpaa³⁻ and dpaMea²⁻, but lower than that reported for nta³⁻. Thus, the amine nitrogen atom of the ligand experiences a decreased basicity upon replacing acetate arms of nta³⁻ by picolinate pendants, an effect that is well documented.[25,26] The second protonation constants of the ligands containing picolinate groups are one log$K$ unit higher than that of nta³⁻, which indicates that pyridylcarboxylate groups are more prone to protonate than acetate groups.[27] This effect can also be noticed when compared the logK_3^H values determined for dpaa³⁻ (logK_3^H= 3.29) and paada³⁻ (logK_3^H= 2.34). The paada³⁻ ligand presents an overall basicity ($\sum$logK_i^H, i = 1-4) intermediate between nta³⁻ and dpaa³⁻.
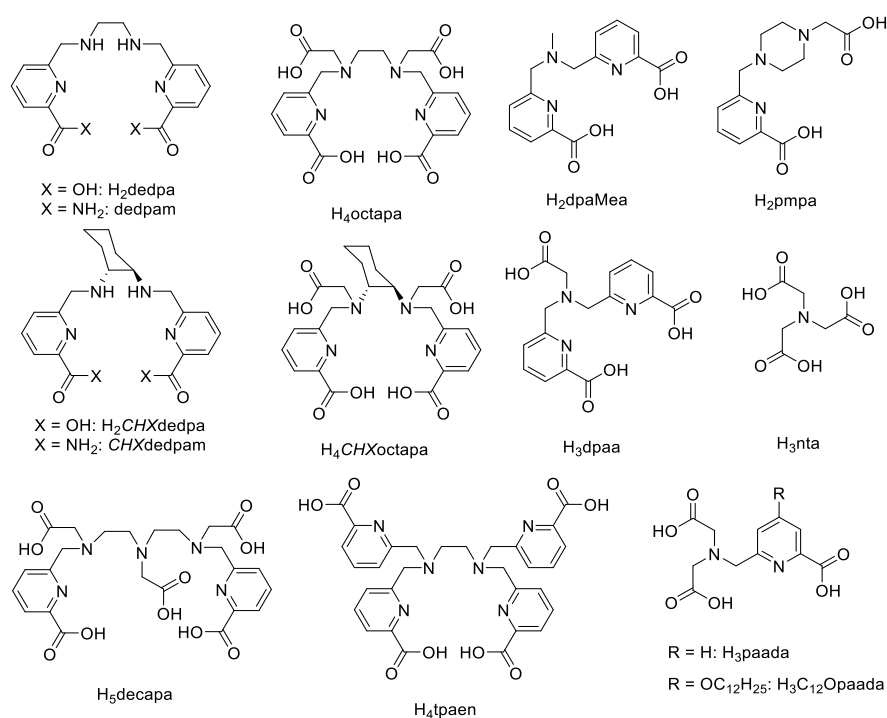
Scheme 1. Structures of the ligands discussed in this work.
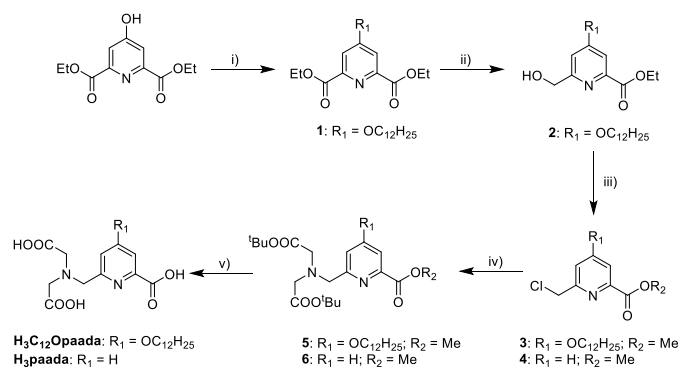
Scheme 2. Synthesis of the ligands. i) K₂CO₃, C₁₂H₂₅Br, acetonitrile; ii) NaBH₄, MeOH; iii) SOCl₂; iv) K₂CO₃, (ᵗBuOOCCH₂)₂NH, acetonitrile; v) 6 M HCl, reflux.

The stability of the Mn(II) complex of paada³⁻ was investigated by using a combination of potentiometric and spectrophotometric experiments at 25 °C in 0.15 M NaCl. The stability constant and protonation constant of the complex are defined in Eqs 2 and 3:

$$K_{MnL} = \frac{[MnL]}{[Mn][L]} \qquad (2)$$

$$K_{MnHL} = \frac{[MnHL]}{[MnL][H^+]} \qquad (3)$$

Table 1. Ligand protonation constants and stability and protonation constants of the corresponding Mn(II) complexes determined using potentiometric titrations (25 °C, 0.15 M NaCl).

	paada³⁻	dpaa³⁻ ᵃ	dpaMea²⁻ ᵇ	nta³⁻ ᶜ
$\log K_1^H$	8.058(2)	7.26	7.82	9.71
$\log K_2^H$	3.462(4)	3.90	3.71	2.49
$\log K_3^H$	2.34(2)	3.29	2.61	1.86
$\log K_4^H$	1.79(9)	1.77		0.8
$\sum \log K_i^H$	15.65	16.22	14.14	14.86
$\log K_{MnL}$	9.59(6)	13.19	10.13	7.44
$\log K_{MnLH}$	2.9(1)ᵉ/3.1ᶠ / 3.0ᵍ	2.90	2.57	
pMn^d	6.93	8.98	7.28	5.21

ᵃ Data from reference 9. ᵇ Data from reference 1b. ᶜ Data in 0.1 M KCl and 20 °C from reference 24. ᵈ Defined as −log[Mn]꜀ᵣₑₑ with pH = 7.4, [Mn(II)] = [L] = 10⁻⁵ M. ᵉ From potentiometric titrations using a 1:1 stoichiometry. ᶠ From potentiometric titrations using a ten-fold excess of Mn(II). ᵍ From spectrophotometric titrations using a 30-fold excess of Mn(II).

The potentiometric titration data obtained using a 1:1 (Mn(II):H₃paada) ratio could be fitted to a model assuming the formation of a single complex species [Mn(paada)]⁻, but the quality of the fit improved when including the protonated complex [Mn(Hpaada)]. To validate the equilibrium model, we carried out potentiometric pH titrations using a ten-fold excess of Mn(II) (1.6×10⁻² M) with respect to the ligand (1.6×10⁻³ M). Under these conditions, the concentration of [Mn(Hpaada)] at equilibrium increases with respect to the free ligand, whose concentration remains very low. The analysis of the data provided logK_MnHL= 3.1, in good agreement with the value obtained from the titrations performed using 1:1 stoichiometry (Table 1).

The formation of a protonated complex species at low pH was further investigated using spectrophotometric experiments. In these experiments a mild acidic solution of the ligand (pH~ 4, 1.7 × 10⁻⁴ M) in the presence of an excess of Mn(II) (5.4×10⁻³ M) was acidified with a standard HCl solution or using trichloroacetic

acid as a buffer. In these conditions the main species in solution is the [Mn(paada)]⁻ complex, which is transformed into the protonated form as the pH decreases (Figure 1). This is causing significant changes in the absorption band due to the picolinate chromophore at 272 nm, with the absorbance at the maximum of the band increasing with decreasing pH. The analysis of the data gives a protonation constant of logK_MnHL= 3.0, a value that increases to 3.2 in the presence of buffer. These values are in excellent mutual agreement and match well the potentiometric results.
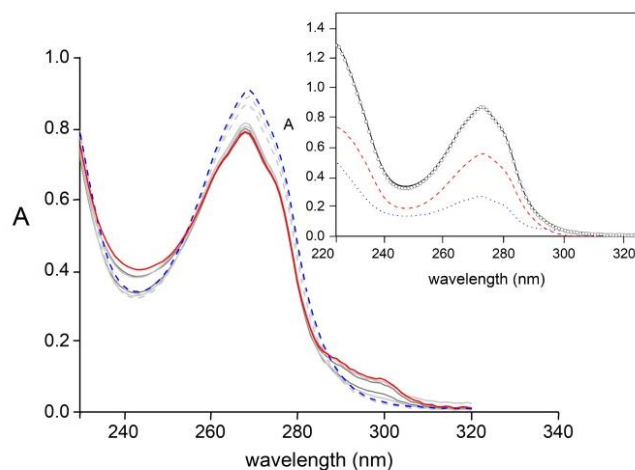
Figure 1. Absorption spectra of H₃paada (1.7×10⁻⁴ M) in the presence of an excess of Mn(II) (5.4×10⁻³ M) at different proton concentrations; pH varies from 4 (solid red line) to 2.2 (blue dashed line). Inset: data at pH=2.6, the open circles are the experimental points, and the lines are the calculated absorbance values: The solid line is the total absorbance, the dashed line is the absorbance of [Mn(Hpaada)] (58% of the total ligand concentration) and the dotted line is the absorbance of [Mn(paada)⁻] (35%).

The stability constant of the [Mn(paada)]⁻ complex lies between those of [Mn(nta)]⁻ and [Mn(dpaa)]⁻, reflecting and intermediate denticity of paada³⁻ with respect to tetradentate nta³⁻ and hexadentate dpaa³⁻. However, the stability of [Mn(paada)]⁻ is also slightly lower than that of [Mn(dpaMea)], in spite of the lower negative charge of the ligand. These results indicate that the 6,6'-(azanediylbis(methylene))dipicolinate unit present in dpaMea²⁻ and dpaa³⁻ is better suited for the coordination to Mn(II). The thermodynamic stabilities of complexes with different ligands are more appropriately assessed by the pMn values (pMn= -log[Mn(II)]꜀ᵣₑₑ) defined using the conditions suggested by Drahos[28] (pH= 7.4, [Mn(II)]= [L]= 10⁻⁵ M). The pMn values follow the same trend observed for the stability constants, with the stability of the complexes decreasing in the order dpaa³⁻ > dpaMea²⁻ > paada³⁻ > nta³⁻ (Table 1). The pMn value calculated for the approved contrast agent mangafodipir trisodium (Na₃[Mn(dpdp)], TESLASCAN®, pMn = 7.2)[29] is only slightly higher than that of the dpaa³⁻ complex. These pMn values are nevertheless considerably lower than that of [Mn(paada)]⁻ (pMn = 8.98) or the bis-hydrated complex [Mn(pmpa)] (pMn = 8.1 calculated from data obtained in 0.1 M KCl).[13] Concerning the pMn values reported for Mn(II) complexes containing at least a coordinated water molecule, they take values generally lower than 8.3,[28,30] which highlights the difficulties in designing very stable Mn(II) complexes for application as MRI contrast agents.
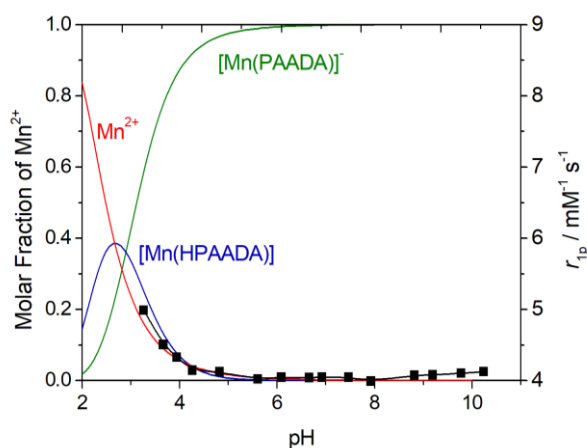
Figure 2. Proton relaxivity (r_{1p}) of [Mn(paada)]⁻ as a function of pH (squares) and species distributions calculated with the stability constants reported in Table 1 (25 °C, 0.15 M NaCl).

3.2.3. ¹H NMRD and ¹⁷O NMR studies

Proton relaxivity (r_{1p}) is a measure of the efficiency in vitro of a paramagnetic probe to enhance the relaxation rate of water proton nuclei normalised to a 1 mM concentration of the agent. The relaxivity of [Mn(paada)]⁻ recorded at pH 7.4 (25 °C, 20 MHz) is 4.0 mM⁻¹ s⁻¹, a value that is somewhat higher than those reported for monohydrated Mn(II) complexes such as [Mn(edta)]²⁻ (3.3 mM⁻¹ s⁻¹) and [Mn(dpaa)]⁻ (3.6 mM⁻¹ s⁻¹, Table 2). The relaxivity determined for [Mn(nta)]⁻ (4.3 mM⁻¹ s⁻¹) is slightly higher than that of [Mn(paada)]⁻. These results represent a clear indication that both [Mn(nta)]⁻ and [Mn(paada)]⁻ contain two water molecules in the inner coordination sphere.

The relaxivity of [Mn(paada)]⁻ remains constant in a broad pH range (ca. 5-11), and increases below pH 5 as a consequence of the dissociation of the complex (Figure 2). This is confirmed by the speciation diagram obtained with the equilibrium constants reported in Table 1, which shows that the dissociation of the complex occurs at pH< ~ 5 (Figure 2).

¹H NMRD (proton Nuclear Magnetic Relaxation Dispersion) profiles of aqueous solutions of [Mn(nta)]⁻ and [Mn(paada)]⁻ (Fig 3) were recorded in the range of proton Larmor frequencies of 0.01–70 MHz, which corresponds to magnetic field strengths from 2.343×10^{-4} to 1.645 T. The relaxivities of the two complexes are rather similar in the range 20-60 MHz, but differ considerably at low fields (< 1 MHz). At low magnetic fields, relaxivity is dominated by the relaxation of the electron spin, which is modulated by fluctuations of the zero field splitting (ZFS) energy.

The ¹⁷O NMR reduced transverse relaxation rates ($1/T_{2r}$) and chemical shifts ($\Delta\omega_r$) of [Mn(nta)]⁻ and [Mn(paada)]⁻ were measured as a function of temperature to gain information on the exchange rate of the coordinated water molecules and the hydration number of the complexes. The $1/T_{2r}$ values increase with decreasing temperature over the full temperature range from approximately 0 to 80 °C, which is typical of systems under the fast exchange regime (Fig 4). Under these conditions the transverse relaxation rates do not provide direct information on the hydration state of the complexes.[31] Thus, we performed a simultaneous fit of the ¹H NMRD and ¹⁷O NMR data to confirm the presence of two coordinated water molecules, and to obtain information on the physicochemical parameters that determine the relaxivity of these complexes. The results of the fits

are shown in Figures 3 and 4, while the fitted parameters are listed in Table 2 and compared with the parameters reported previously for related Mn(II) complexes.

A rather large number of structural and dynamic molecular parameters describe the NMRD and ¹⁷O NMR relaxation data and ¹⁷O NMR chemical shifts. As a result, a reliable analysis requires fixing some of these parameters during the least-squares fit of the data. Thus, we fixed the distance of closest approach for the outer-sphere contribution a_{MnH} at 3.6 Å, while the distances between the Mn(II) ion and the proton nuclei of the coordinated water molecules (r_{MnH}) were fixed at the average values obtained from DFT calculations (2.830 and 2.777 Å for [Mn(paada)]⁻ and [Mn(nta)]⁻, respectively). The diffusion coefficient, D_{MnH}^{298}, and its activation energy, E_{DMnH}, were fixed to common values, while the number of water molecules in the inner coordination sphere of Mn(II) was fixed to q=2 (Table 2).

The water exchange rate determined for [Mn(paada)]⁻ ($k_{ex}^{298} = 90\times10^7$ s⁻¹) is considerably higher than that of [Mn(dpaa)]⁻ ($k_{ex}^{298} = 12.6\times10^7$ s⁻¹), while the water exchange of [Mn(nta)]⁻ is about three times faster than that of [Mn(paada)]⁻. The water exchange obtained for [Mn(nta)]⁻ ($k_{ex}^{298} = 280\times10^7$ s⁻¹) is higher than that reported by Hunt using only ¹⁷O NMR data obtained at low magnetic field ($k_{ex}^{298} = 150\times10^7$ s⁻¹).[32] The values obtained for the rotational correlation time (τ_R^{298}) are typical of small Mn(II) complexes (i.e. [Mn(edta)]⁻).[33]

The ¹⁷O hyperfine coupling constants ($A_O/\hbar$) fall within the range typically observed for small Mn(II) complexes (-25×10⁶ to -47×10⁶ rad s⁻¹).[34] Finally, the parameters related to the electron spin relaxation of the metal ion (the electronic correlation time for the modulation of the zero-field-splitting interaction, τ_V, and the mean square zero-field-splitting energy, Δ^2) are also similar to those obtained for other Mn(II) complexes (Table 2). The fits provide a larger Δ^2 value for [Mn(paada)]⁻ compared to [Mn(nta)]⁻, which might be related to the different coordination environment of the metal ion in the two complexes (see below).

3.2.4. Theoretical calculations

DFT calculations (TPSSh/def2-TZVP, see computational details below) were carried out to gain insight into the structures of the [Mn(paada)]⁻ and [Mn(nta)]⁻ complexes. In these calculations, we included two inner-sphere water molecules and up to four second-sphere water molecules. Additionally, bulk solvent effects were included by using a polarised continuum model (PCM). This mixed cluster-continuum approach was shown to provide accurate Mn-O$_{water}$ distances and ¹⁷O and ¹H hyperfine coupling constants.[35] The optimised structure of the [Mn(nta)(H₂O)₂]⁻·4H₂O system shows a distorted octahedral coordination around the metal ion (Figure 5). The coordinated water molecule in *trans* with respect to the amine nitrogen atom of the ligand presents a significantly shorter Mn-O$_{water}$ distance (Mn-O(2w) = 2.201 Å) than the water molecule in *cis* position (Mn-O(1w) = 2.264 Å). The metal coordination environment in [Mn(paada)(H₂O)₂]⁻·4H₂O can be described as pentagonal bipyramidal, in which the equatorial plane is defined by the donor atoms of the picolinate unit, the amine nitrogen atom, an oxygen atom of a carboxylate group (O2) and an inner-sphere water molecule. An oxygen atom of a carboxylate group of the ligand (O1) and the second coordinated water molecule (O2w) define the apical positions. The bond distances involving apical donor atoms are shorter than those of donor atoms lying in the equatorial plane, as usually observed for pentagonal bipyramidal Mn(II) complexes.[36] Thus, the faster water exchange determined for

[Mn(paada)(H$_2$O)$_2$]$^-$ compared to [Mn(dpaa)(H$_2$O)$_2$]$^-$ is likely related to the presence of a labile water molecule occupying a coordination position at the equatorial plane of the pentagonal bipyramidal coordination polyhedron in the former. In the case of [Mn(nta)(H$_2$O)$_2$]$^-$, the water exchange process likely follows an associatively activated mechanism, given the preference of Mn(II) for coordination numbers 6 and 7.

Table 2. Parameters obtained from the simultaneous analysis of ^{17}O NMR and ^{1}H NMRD data.

	[Mn(paada)]$^-$	[Mn(nta)]$^-$	[Mn(dpaa)]$^{-\,b}$	[Mn(dpaMea)]^c	[Mn(edta)]$^{2-\,d}$
r_{1p} at 25/37 °C / mM^{-1} s$^{-1\,b}$	4.0/3.3	4.3/3.5	3.5/2.7	5.3/4.2	3.3/2.8
k_{ex}^{298}/ 10^7 s^{-1}	90±3	280±10	12.6±0.5	30.6	47.1
$\Delta H^{\ddagger}$ / kJ mol^{-1}	28.3±1.0	20.2±0.9	42.7±1.0	28.1	33.5
τ_R^{298} / ps	40.1±0.5	37.2±0.8	47.6±0.2	47.8	57
E_r / kJ mol^{-1}	22.6±0.5	18.9±0.5	22.8±0.4	25.3	21.8
τ_V^{298}/ ps	12.0±2.0	16.0±4.0	19.4±0.2	39.2	27.9
E_v / kJ mol^{-1}	1.0^a	1.0^a	1.0^a	1.0^a	1.0^a
D_{MnH}^{298} / 10^{-10} m^2 s^{-1}	23^a	23^a	22.4^a	22.4^a	23.1
E_{DMnH} / kJ mol^{-1}	20^a	20^a	17.3^a	17.3^a	18.9
Δ^2 / 10^{19} rad^2 s^{-2}	12.8±3.7	4.1±1.2	5.5±0.2	2.38	6.9
$A_O/\hbar$/ 10^6 rad s^{-1}	-38.6±0.3	-47.5±0.3	-31.5±0.6	-45.8	-40.5
r_{MnH}/Å	2.830^a	2.777^a	2.756^a	2.74^a	2.83^a
a_{MnH}/Å	3.6^a	3.6^a	3.6^a	3.6^a	3.6^a
q^{298}	2^a	2^a	1^a	2^a	1^a

^{a} Parameters fixed during the fitting procedure. ^{b}Data from Ref 9. ^{c}Data from Ref 1b. ^{d} Data from Ref 33.
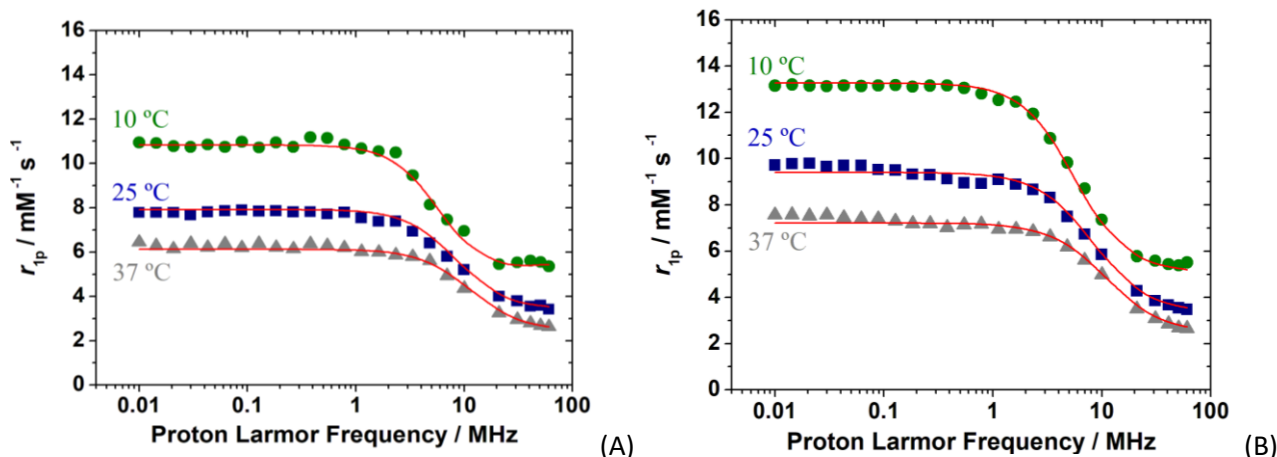
Figure 3. ^{1}H NMRD profiles recorded at different temperatures for [Mn(paada)]$^-$ (A) and [Mn(nta)]$^-$ (B). The lines represent the fit of the data as explained in the text.
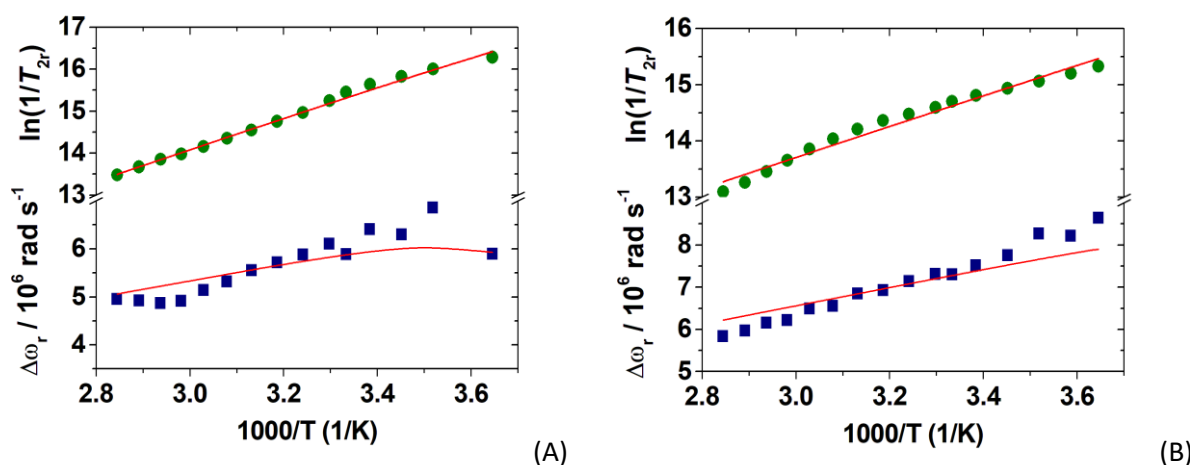
Figure 4. Reduced transverse ^{17}O NMR relaxation rates and chemical shifts versus reciprocal temperature measured for [Mn(paada)]$^-$ (A) and [Mn(nta)]$^-$ (B) at 11.74 T. The lines represent the fit of the data as explained in the text.

The ^{17}O hyperfine coupling constants ($A_O/\hbar$) of the coordinated water molecules were calculated using the methodology described earlier.[35] These calculations yielded average values of $A_O/\hbar$ = -43.9×10^6 and -49.1×10^6 rad s^{-1} for [Mn(nta)(H$_2$O)$_2$]$^-$·4H$_2$O and [Mn(paada)(H$_2$O)$_2$]$^-$·4H$_2$O, respectively. These values are in good agreement with the experimental data obtained from the analysis of the ^{17}O NMR chemical shifts and relaxation data, which confirms that the hydration number of q= 2 assumed for the fit of NMRD and ^{17}O NMR data is correct.The values of the mean square zero field splitting (ZFS) energy obtained from the analysis of the ^{17}O and NMRD data of [Mn(paada)(H$_2$O)$_2$]$^-$ and [Mn(nta)(H$_2$O)$_2$]$^-$ are rather different (Δ^2 = 12.8 and 4.1×10^{19} rad^2 s^{-2}, respectively, Table 2). Different studies have pointed out that the relaxation of the electron spin in both Mn(II) and Gd^{3+} complexes is the result of both the static and transient mechanisms.[37,38] The transient mechanism is expected to dominate for systems with high symmetry, in which the static ZFS is very small. For complexes with lower symmetry of the coordination environment, such as those investigated here, both the static and transient mechanisms likely contribute to the Δ^2 values obtained from relaxation data. The calculation of ZFS parameters of Mn(II) and Gd^{3+} complexes using DFT was found to be problematic, with the results depending critically on the functional employed.[38,39] Thus, we carried out *ab initio* calculations based on the complete active space self-consistent field model, with an active space defined by the five electrons occupying the Mn-based 3d orbitals (CAS(5,5)). The effects of dynamic correlation were subsequently included by using *N*-electron valence perturbation theory to second order (NEVPT2). These CASSCF/NEVPT2 calculations provided very similar ZFS parameters with D= -0.0497 cm^{-1} and E/D= 0.2045 for [Mn(nta)(H$_2$O)$_2$]$^-$·4H$_2$O and D= -0.0526 cm^{-1} and E/D= 0.0908 for [Mn(paada)(H$_2$O)$_2$]$^-$, which result in Δ = 0.043 cm^{-1} and Δ^2 = 6.6×10^{19} rad^2 s^{-2} for the two systems. The agreement between the experimental and calculated values of Δ^2 is very good for [Mn(nta)(H$_2$O)$_2$]$^-$, given the difficulties of calculating accurate ZFS parameters with *ab initio* methods. For [Mn(paada)(H$_2$O)$_2$]$^-$ the experimental ZFS is larger than that estimated with CASSCF/NEVPT2 calculations, which might be related to a more important contribution of the transient mechanism, which arises from fluctuations of the ZFS energy rather than its average value.

3.3.5. Characterisation of the lipophilic derivative [Mn(C$_{12}$Opaada)]$^-$

Typically, the relaxivity of a discrete paramagnetic ion chelate in aqueous media is assessed through the measurement of the water proton relaxation rate, R_1= (1/T_1) as a function of the concentration of the metal ion over a range of about 0-3 mM. The data follows a linear behaviour and the relaxivity of the chelate, r_{1p}, corresponds to the slope of the line. However, in the case of lipophilic complexes able to self-aggregate into supramolecular assemblies, large deviations from this simple behaviour are observed. In the case of [Mn(C$_{12}$Opaada)]$^-$ the experimental data, measured at 20 MHz and 298 K, are reported in Figure 6. In the concentration range 0.8 to 0.3 mM, a linear relationship is observed that corresponds to a high relaxivity value (15.4±0.2 mM^{-1} s^{-1}). By lowering the concentration, a second linear region is then observed (concentration range 300 to 100 μM) characterised by a pronounced change in the slope (5.3±0.1 mM^{-1} s^{-1}). The value of the slope of this line corresponds to relaxivity values typical of rapidly rotating, low molecular weight Mn(II) complexes (Table 2).[33] This behaviour is very similar to that observed

by Forgács and co-workers for Mn(dpac12a), a Mn(II) complex functionalised with a -C$_{12}$ hydrocarbon chain.[9] Similarly, we can attribute the variation of relaxivity to the formation of micelles, which are characterised by a slowed rotational mobility and therefore by an increase in r_{1p}. The point of intersection between the two straight lines defines the critical micelle concentration (*cmc*) that for [Mn(C$_{12}$Opaada)]$^-$ assumes the value of 0.31±0.01 mM, slightly higher than for Mn(dpac12a) (0.096 mM).[9]
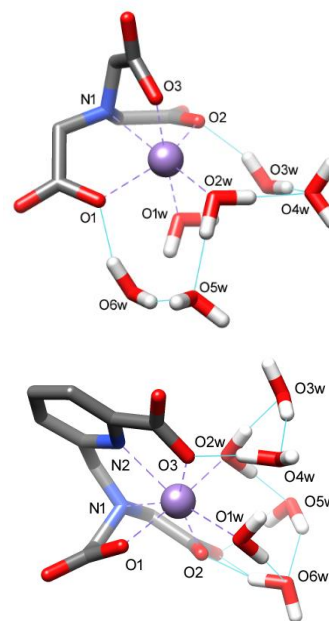
Figure 5. Structures of the [Mn(nta)(H$_2$O)$_2$]$^-$·4H$_2$O (left) and [Mn(paada)(H$_2$O)$_2$]$^-$·4H$_2$O (right) systems obtained with DFT calculations (TPSSh/Def2-TZVP). Calculated bond distances (Å): [Mn(nta)(H$_2$O)$_2$]$^-$·2H$_2$O, Mn-N(1), 2.339; Mn-O(1), 2.171; Mn-O(2), 2.201 ; Mn-O(3), 2.146; Mn-O(1w), 2.264; Mn-O(2w), 2.202. [Mn(paada)(H$_2$O)$_2$]$^-$·4H$_2$O, Mn-N(1), 2.500; Mn-N(2), 2.361; Mn-O(1), 2.132; Mn-O(2), 2.287; Mn-O(3), 2.262 Mn-O(1w), 2.274; Mn-O(2w), 2.217.

In the region above the *cmc*, the relaxation rate is given by the contribution of the monomeric complex (at the concentration corresponding to the *cmc*) and of the micellar aggregate. Therefore, the paramagnetic contribution to the observed relaxation rate assumes the form reported in Eq. 4, where $r_1^{n.a.}$ and r_1^a correspond to the relaxivity values of the non-aggregated and aggregated forms, respectively, R_1^d is the relaxation rate of pure water (0.38 s^{-1} at 20 MHz and 298 K) and C is the analytical concentration of the Mn(II) complex:

$$R_1^{obs} - R_1^d = (r_1^{n.a.} - r_1^a) \times cmc + r_1^a \times C \qquad (4)$$

On the other hand, the relaxivity of the discrete complexes, $r_1^{n.a.}$, is expressed by the following equation:

$$R_1^{obs} - R_1^d = r_1^{n.a.} \times C \qquad (5)$$

By fitting the data to Eqs. 4 and 5 the parameters *cmc*, $r_1^{n.a.}$ and r_1^a can be obtained (Table 3).
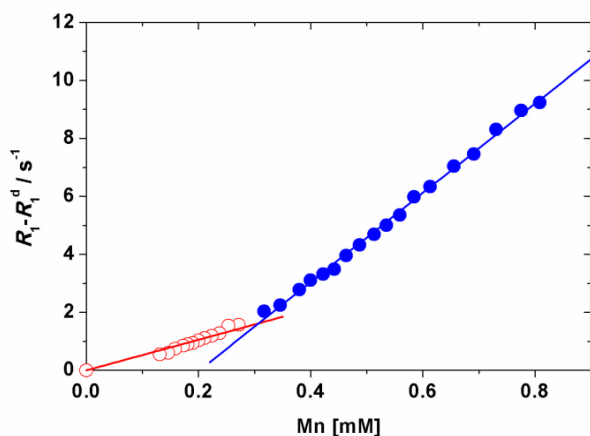
Figure 6. Plot of the water ¹H longitudinal relaxation rate at 20 MHz and 298 K as a function of the total Mn(II) concentration for [Mn(C₁₂Opaada)]⁻ and least-squares fit according to Eqns. 4 and 5.

The method based on the fluorescence emission of pyrene (Py) was also used to determine the *cmc* at ionic strength of 0.15 M (NaCl) and in the absence of NaCl.[40] The monomer fluorescence spectrum of Py shows significant fine vibrational structure. The vibration bands show strong dependence on solvent environment. The ratio of the fluorescence emission intensities due to third and first vibration peaks increases as the polarity of the solvent decreases. In the absence of micelles (bellow *cmc*), Py senses the water environment, where $I_3/I_1 \sim 0.65$; above the *cmc* when micelles are formed, Py molecules are hosted in the interior of the micelles due to the high hydrophobicity of Py, and consequently the I_3/I_1 ratio shows a sharp increase within a narrow range of the surfactant concentration. Taken the *cmc* as the lower surfactant concentration above which micelles form (Figure 7), these measurements provide a *cmc* for [Mn(C₁₂Opaada)]⁻ of 0.32 mM at pH 7.4 and 0.15 M of NaCl, and of 0.56 mM at pH 7.4 in the absence of added salt. The *cmc* obtained at 0.15 M NaCl ionic strength is in excellent agreement with that determined by the relaxometric method (0.31±0.01 mM). Increasing the ionic strength of the solution lowers the *cmc*, as would be expected.

Table 3. Best fit parameters obtained from the analysis of the NMRD profiles of [Mn(C₁₂Opaada)]⁻ below and above the *cmc* (25 °C).

	Below *cmc*	Above *cmc*
r_{1p} at 25 °C / mM⁻¹ s⁻¹ ^{b}	5.3	15.4
k_{ex}^{298} / 10⁷ s⁻¹	90^a	90^a
τ_{RG}^{298} / ps	71±4	1920±110
τ_{RL}^{298} / ps	/	90±5
S^2	/	0.22±0.01
τ_V^{298} / ps	14±1	12.0±2.0
D_{MnH}^{298} / 10⁻¹⁰ m² s⁻¹	23^a	23^a
Δ^2 / 10¹⁹ rad² s⁻²	15.0±1.4	3.1±0.6
r_{MnH}/Å	2.830^a	2.83^a
a_{MnH}/Å	3.6^a	3.6^a
q^{298}	2^a	2^a

^{a} Parameters fixed during the fitting procedure.

The ¹H NMRD profile below *cmc* exhibits the typical shape and amplitude of low molecular weight Mn(II) complexes (Figure 8). It shows a plateau at low fields, followed by a dispersion around 3-4 MHz and then a region of nearly constant relaxivity at higher fields

(≥ 20 MHz). The data analysis was carried out by fixing to two the number of inner sphere water molecules, at a distance of 2.83 Å and with a residence lifetime of 5 ns (298 K). Under these conditions, the relaxivity is largely controlled by the rotational dynamics, which is expressed in terms of the rotational correlation time (τ_R= 71±4 ps). The τ_R value, ca. 77% longer than for [Mn(paada)(H₂O)]⁻, is influenced by the functionalisation of the chelate with the aliphatic chain, which increases the molecular size. On the other hand, the electronic relaxation parameters are quite similar to those of the parent complex, suggesting an analogous coordination geometry: τ_V = 14.2±1.1 ps and Δ^2 = 15.0±1.4×10¹⁹ s⁻².
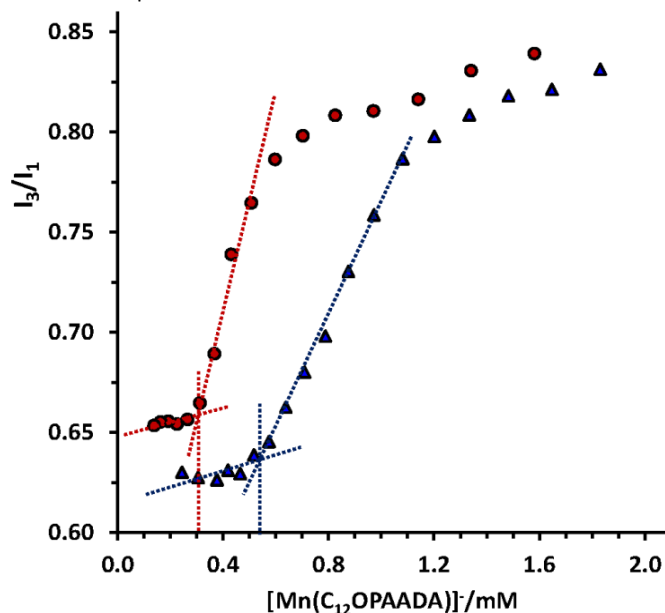
Figure 7. Ratio of the fluorescence emission intensities corresponding to third (I_3) and first (I_1) vibrational bands of pyrene (2.04 μM) as a function of the surfactant concentration [Mn(C₁₂Opaada)]⁻ at: (●) pH 7.46 and [NaCl]= 0.15 M; (▲) pH 7.43 in the absence of sodium chloride.

The NMRD profile of the aggregated form of the complex exhibits a different amplitude and shape, characterised by a broad peak centred at 40 MHz, typical of slowly tumbling systems (Fig 8).[41] The portion of the profile at high fields (> 3 MHz) was fitted considering the occurrence of a local internal rotation superimposed to the global tumbling of the micelle (Lipari-Szabo approach).[42] Given the large number of parameters, some of them were fixed at known or reasonable values according to a well-established procedure. In the best-fit procedure the hydration number *q* was set to two, as for the parent complex, the Mn-H_w distance r_{MnH} was set to 2.83 Å, the distance of closest approach of the outer sphere solvent molecules to Mn(II), *a*, was fixed to 3.6 Å, while for the water-solute relative diffusion coefficient, *D*, a value of 2.3×10⁻⁵ cm² s⁻¹ was used (25 °C). The least-square analysis was carried out by using as adjustable parameters the electron spin relaxation parameters (τ_v and Δ^2), the correlation times describing global (τ_{RG}) and local (τ_{RL}) motions and the order parameter S^2, whose value is comprised between 0 (isotropic internal motion) and 1 (completely restricted motion). The results of the fit yield τ_{RG} = 1.9±0.3 ns and τ_{RL} = 90±6 ps, with S^2 = 0.21±0.01, indicating that relaxivity is limited by the local rotational flexibility (Table 3).
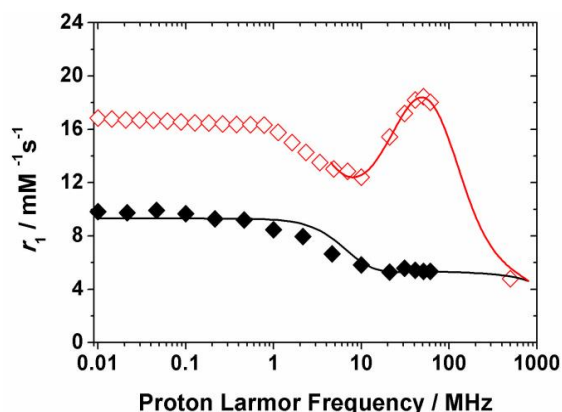
Figure 8. $1/T_1$ ^{1}H NMRD profiles, at 298 K, of the non-aggregated (◆) aggregated (◇) form of [Mn(C$_{12}$Opaada)]$^-$. The solid lines are calculated with the parameters reported in Table 3.

3.2.6. Interaction with BSA

Following a non-covalent binding interaction with a macromolecular substrate, the relaxivity of a paramagnetic chelate shows a marked enhancement (at intermediate fields) because of the pronounced variation (elongation) of τ_R passing from the rapidly rotating Mn(II) complex to the slowly tumbling supramolecular adduct. The Proton Relaxation Enhancement (PRE) technique is a non-separative methodology that enables to assess the binding parameters by measuring and analysing the changes in the NMR relaxation rates of the solvent water protons following the addition of increasing amounts of a macromolecule to a solution of the paramagnetic metal complex.[43]

We have investigated the binding interaction of [Mn(C$_{12}$Opaada)]$^-$ with BSA using the PRE procedure at 20 MHz and 298 K. We have utilised a 0.11 mM aqueous solution of the complex and made several additions of the protein to obtain concentrations in the range ca. 0.02-0.7 mM (Figure 9).
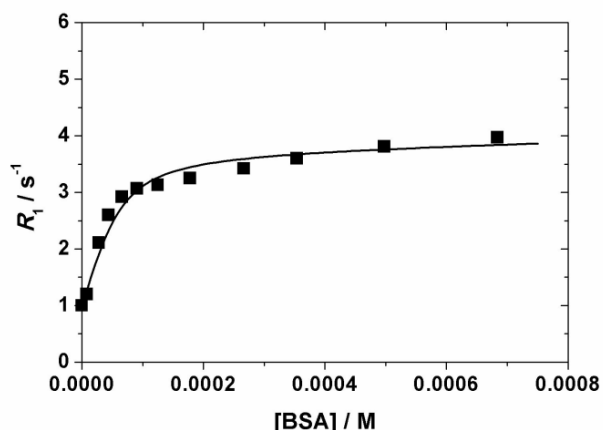
Figure 9. Water proton relaxation rate of a 0.11 mM aqueous solutions of [Mn(C$_{12}$Opaada)]$^-$ as a function of increasing amounts of BSA, measured at 20 MHz and 298 K.

The observed relaxation rate, R_1^{obs}, increases with the concentration of BSA (hence with the fraction of bound complex) and tends to an asymptotic value, which depends on the relaxivity of the bound complex, r_1^b, following a binding isotherm (Figure 9). The nonlinear fitting of the experimental data according to the PRE equations provides a fairly accurate estimation of the relaxivity of r_1^b (30.5±0.6 mM^{-1} s^{-1}) and of the $n \times K_A$ (5.6×10^4 M^{-1}) term, where n represents the number of equivalent and independent binding sites and K_A is the affinity constant. The best results are obtained with n between 1 and 2. These data are in perfect agreement with those obtained by spectrofluorimetric titration (see below). As compared to [Mn(DPAC12A)], a related complex bearing a pendant −C$_{12}$ alkyl chain, the affinity constant is slightly lower whereas the relaxivity of the adduct is twice as large (K_A = 1.3×10^5 M^{-1} and r_1^b = 15.5 mM^{-1} s^{-1} for [Mn(DPAC12A)]).[9] Probably, this difference simply reflects the different state of hydration of the two complexes, q= 1 for [Mn(DPAC12A)] and q= 2 for [Mn(C$_{12}$Opaada)]$^-$. Lower association constants with Human Serum Albumin were reported for Mn(II) macrocyclic ligands functionalised with benzyl groups.[30c]

The interactions of BSA with ligands H$_3$paada and H$_3$C$_{12}$Opaada, either in the absence or in the presence of Mn(II) at 1:1 metal:ligand (Mn:L) ratio, were also investigated by fluorimetric titration at three temperatures (15, 25 and 36 °C) in 10 mM Tris-HCl buffered solutions at pH 7.4. Under these experimental conditions, according to the pK_a values listed in Table 1, both ligands are ionic compounds in the absence of Mn(II). In fact, the concentration of Hpaada^{2-} can be estimated as 4-fold that of paada^{3-}. A similar situation is expected for the hydrophobic ligand H$_3$C$_{12}$Opaada assuming that the presence of a hydrocarbon chain -OC$_{12}$H$_{25}$ has little effect on the pK_a values of the basic or acidic head groups in water. The Mn(II) complexes are negatively charged due to the high stability constant of the [Mn(paada)]$^-$ species.

On the other hand, BSA has two tryptophan residues that possess intrinsic fluorescence and usually dominate the protein fluorescence when the excitation is performed at $\lambda_{ex} \geq$ 290 nm.[44] It is necessary to remark that neither the free ligands nor the Mn(II) complexes show fluorescence. Furthermore, the addition of Mn(II) (e.g. 52 μM) on an aqueous buffered solution of BSA (5.2 μM) has no effect on the emission spectrum of BSA. On the contrary, the fluorescence intensity of BSA decreases as the concentrations of the ligand (H$_3$paada or H$_3$C$_{12}$Opaada) or the corresponding Mn(II) complexes increase. However, the overall effect induced by the addition of the substrate on the intrinsic fluorescence of the protein is quite different.

Figure 10 shows the decrease of the fluorescence intensity, I$_F$, of BSA read at the maximum wavelength emission of 343 nm as a function of ligand concentration varied in the range of 0.07 to 0.8 mM for H$_3$paada and from 13 to 200 μM for the case of H$_3$C$_{12}$Opaada. As a first observation, if the binding of the ligand does not introduce conformational changes in the protein, the value of the fraction θ of the sites of the protein occupied by the ligand can be determined as θ= (I$_{Fo}$-I$_F$)/(I$_{Fo}$-I$_{F∞}$), where I$_{Fo}$ is the fluorescence in the absence of ligand (the quencher, Q); I$_F$ is the fluorescence at a given [Q], and I$_{F∞}$ represents the protein fluorescence "saturated" of quencher.[45]
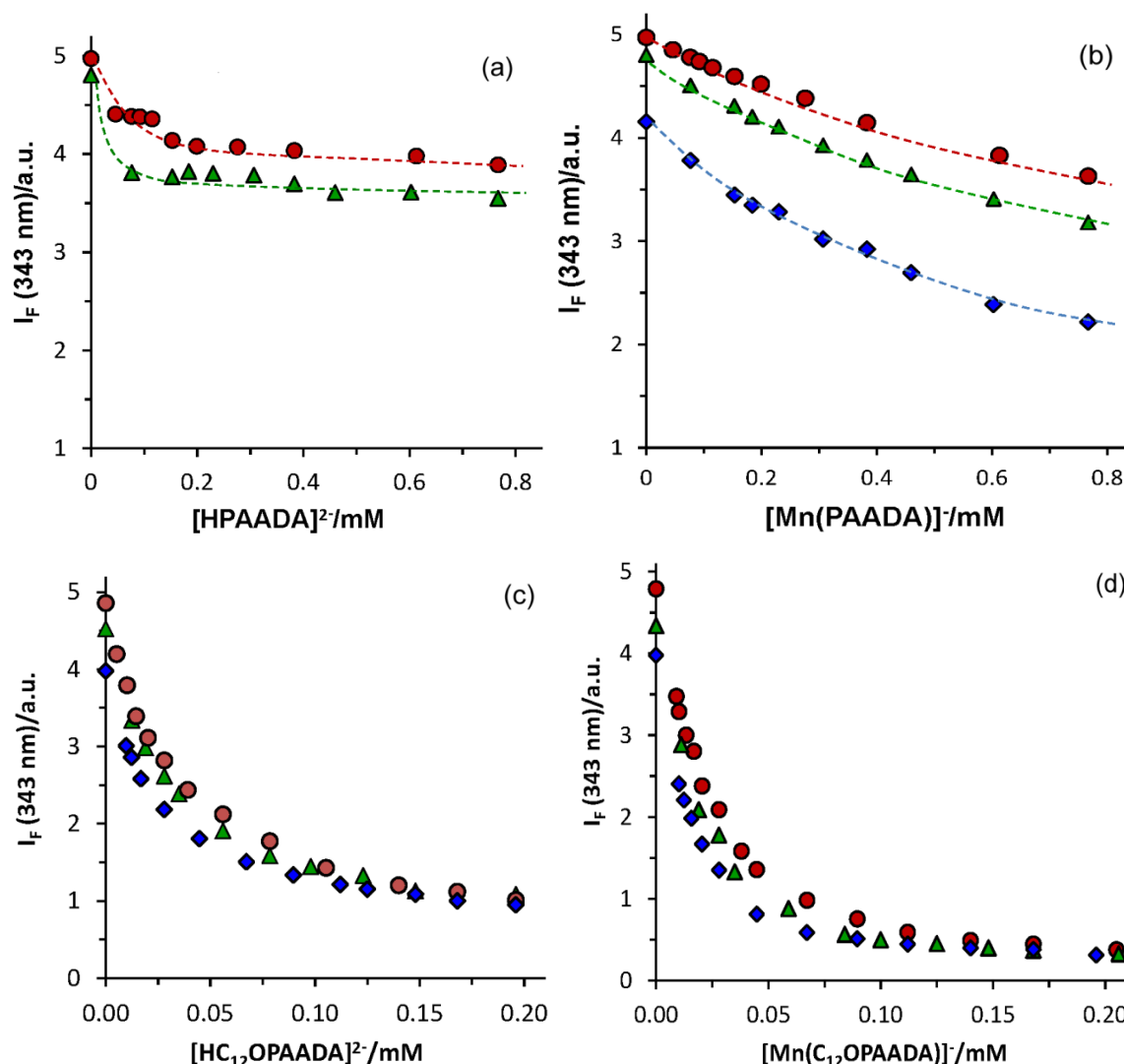
Figure 10. The emission fluorescence intensity of BSA (5.2 µM) as a function of ligand concentration in the absence of Mn(II) (a) and (c), and in the presence of Mn(II) (b) and (d), at pH 7.4 in 10 mM Tris-HCl buffer, measured at 15 (●), 25 (▲), and 36 °C (◆).

Table 4. Binding constants, K_b, and thermodynamic parameters of ligand-BSA complex formation obtained from the analysis of protein fluorescence quenching by the substrate.

T/K	K_b/ M^{-1}	ΔS/ J·mol^{-1}K^{-1}	ΔH/ kJ·mol^{-1}	K_b/ M^{-1}	ΔS/ J·mol^{-1}K^{-1}	ΔH/ kJ·mol^{-1}	K_b/ M^{-1}	ΔS/ J·mol^{-1}K^{-1}	ΔH/ kJ·mol^{-1}
	[Mn(paada)]$^-$			HC$_{12}$Opaada^{2-}			[Mn(C$_{12}$Opaada)]$^-$		
288	705			3.05×10^4			4.55×10^4		
298	1081	174	34.5	3.46×10^4	120	9.7	5.51×10^4	130	11.3
309	1877			4.01×10^4			6.30×10^4		

Taking the last value as I$_{F\infty}$≈ 0.3, see Figure 10, one estimates the fraction of protein sites occupied at 0.10 mM of each ligand and 15 °C as 15, 30, 85, and 100 %, respectively for Hpaada^{2-}, [Mn(paada)]$^-$, HC$_{12}$Opaada^{2-} or [Mn(C$_{12}$Opaada)]$^-$, which follows the normal trend of increasing the quencher hydrophobicity. The ligand complexed with Mn(II) shows stronger binding to the protein than the free ligand, but the presence of the hydrophobic hydrocarbon chain - OC$_{12}$H$_{25}$ determines the hydrophobic interaction with the protein. The fluorescence quenching by Hpaada^{2-} (and/or paada^{3-}) does not show a gradual variation with [Q], which evidences that the ligand interactions with the protein surface are dominated mainly by electrostatic effects; in the other cases, the fluorescence decreases gradually as the ligand concentration increases.

By assuming a 1:1 stoichiometry for the P·Q complex (P and Q stand for the protein and quencher, respectively), the binding equilibrium constant, K_b, is represented in Eq. 6. Given that the measured fluorescence intensity is only due to the protein and taking into account that the protein concentration is much lower than that of the quencher, [P]$_o$<<[Q]$_o$, then I$_{Fo}$= α_o[P]$_o$ (being α_o= 2.3I$_o\phi\epsilon\ell$ the proportionality coefficient between the fluorescence intensity and the protein concentration, i.e. I$_F$= 2.3I$_o\phi\epsilon\ell$[P]$_o$ with I$_o$ the intensity of excitation source, ϕ fluorescence quantum yield, ϵ molar

absorptivity at the excitation wavelength, and ℓ the path length) and $I_F = \alpha_o[P] + \alpha_1[P \cdot Q]$.

$$P + Q \rightleftharpoons P \cdot Q \quad ; \qquad K_b = \frac{[P \cdot Q]}{[P][Q]} \qquad (6)$$

The equilibrium of Eq. 6 and the mass balance on protein concentration, $[P]_o = [P] + [P \cdot Q]$, leads to Eq. 7, which can be rearranged in linear forms, such as the Scatchard plot (where $[(I_{Fo}/I_F)-1]/[Q]_o$ versus I_{Fo}/I_F should be linear)[46] or the Benesi-Hildebrand plot transformation in the form of $[Q]_o/(I_{Fo}-I_F)$ versus $[Q]_o$, where K_b is obtained from the quotient of slope/intercept of the resulting straight line.[47]

$$I_F = \frac{I_F^o + \left(\alpha_1/\alpha_o\right)I_F^o K_b[Q]_o}{1 + K_b[Q]_o} \qquad (7)$$

The experimental data of I_F - $[Q]_o$ were fitted to Eq. 7 using a non-linear method (Figure S5, Annexe B). Furthermore, good linear plots were obtained in both Scatchard or Benesi-Hildebrand plots (Figures S6-S7, Annexe B). The determined values of K_b along with the corresponding thermodynamic parameters are listed in Table 4. The positive values of both entropy and enthalpy changes point to hydrophobic interactions as the main driving force in the complex $P \cdot Q$ formation.[48] The binding of $HC_{12}Opaada^{2-}$ and the corresponding Mn(II) complex are characterised by very similar thermodynamic parameters and association constants, which suggests that the binding of the aliphatic chain of the ligand through hydrophobic forces plays a major role. The $[Mn(paada)]^-$ complex, which lacks the aliphatic moiety, provides a much weaker binding. The binding constant obtained at 25 ºC for $[Mn(C_{12}Opaada)]$ (5.51×10^4 M⁻¹) is in excellent agreement with the one obtained with the PRE method (5.6×10^4 M⁻¹), which provides confidence on the reliability of the two methods.

3.3. Experimental Section

3.3.1. Materials and methods

All reagents and solvents were commercial and used without further purification. SiO₂ (Sigma-Aldrich, pore size 60 Å, 70–230 mesh) was used for preparative column chromatography. ¹H and ¹³C NMR spectra were recorded at 25 °C on Bruker Avance 300 MHz and Bruker Avance III HD 400 MHz spectrometers. ESI-TOF mass spectra were recorded using a LC-Q-q-TOF Applied Biosystems QSTAR Elite spectrometer in the positive mode. Elemental analyses were carried out on a ThermoQuest Flash EA 1112 elemental analyser. FT-IR spectra were recorded using a Thermo Scientific-Nicolet is10 spectrophotometer equipped with an attenuated total reflectance (ATR) accessory.

3.3.2. Synthetic procedure

Methyl 6-(chloromethyl)-4-(dodecyloxy)picolinate (3). Diethyl 4-(dodecyloxy)pyridine-2,6-dicarboxylate (1.20 g, 2.94 mmol) was dissolved in methanol (40 mL) and the mixture was cooled to 0 °C. NaBH₄ (0.557 g, 14,70 mmol) was added in small portions over a period of 4 h. A saturated NaHCO₃ solution (50 mL) was added and the mixture was extracted with CH₂Cl₂ (3x50 mL). The combined organic layers were dried over anhydrous Na₂SO₄ and the solvent was removed under reduced pressure to yield an oily residue. The crude product was purified by column chromatography on SiO₂ using

AcOEt:hexane (40:60) as eluent providing 1.04 g of the white solid compound (**2**). MS (ESI⁺) m/z: 366.26 (20%) $[C_{21}H_{35}NO_4+H]^+$; 388.25 (100%) $[C_{21}H_{35}NO_4+Na]^+$. This intermediate was dissolved in thionyl chloride (5 mL) and the mixture was stirred at 0 °C for 4 h. The mixture was allowed to warm to room temperature and the thionyl chloride was removed in the rotary evaporator. A saturated NaHCO₃ solution (50 mL) was added and the mixture was extracted with CH₂Cl₂ (3×50 mL). The combined organic layers were dried over anhydrous Na₂SO₄ and the solvent was removed under reduced pressure to give a yellow solid. The crude product was purified by column chromatography on SiO₂ (CH₂Cl₂ to CH₂Cl₂:MeOH 95:5) giving 0.221 g of a white solid. Yield 25%. The ethyl ester group of the precursor was converted into methyl ester under the conditions used for chromatographic separation. ¹H NMR (CDCl₃, 400 MHz, 25 °C, TMS): δ 7.53 (d, 1H, py, ⁴J= 2.4 Hz), 7.14 (d, 1H, py, ⁴J= 2.4 Hz), 4.64 (s, 2H, py-CH₂), 4.02 (t, 2H, O-CH₂, ³J= 6.5 Hz), 3.93 (s, 3H, COO-CH₃), 1.75 (m, 2H, CH₂), 1.39 (m, 2H, CH₂), 1.20 (m, 18H, CH₂), 0.81 (t, 3H, CH₃, ²J= 6.7 Hz). ¹³C NMR (CDCl₃, 100.6 MHz, 25 °C, TMS): δ 167.01 (COOCH₃), 165.51 (C$_{py}$-O), 158.65 (C$_{py}$-CH₂Cl), 149.05 (C$_{py}$-COOCH₃), 112.28 (C$_{py}$), 111.26 (C$_{py}$), 68.75 (CH₂-O), 53.10 (COOCH₃), 46.39 (CH₂Cl), 31.91 (CH₂), 29.64 (CH₂), 29.62 (CH₂), 29.56 (CH₂), 29.51 (CH₂), 29.34 (CH₂), 29.27 (CH₂), 28.79 (CH₂), 25.86 (CH₂), 22.68 (CH₂), 14.11 (CH₃) ppm. MS (ESI⁺) m/z: 370.21 (23%) $[C_{20}H_{32}ClNO_3+H]^+$; 392.20 (100%) $[C_{20}H_{32}ClNO_3+Na]^+$. Anal. calcd. for $C_{20}H_{32}ClNO_3$: C, 64.94; H, 8.72; N, 3.79. Found: C, 64.71; H, 8.64; N, 3.65%.

2,2'-(((6-carboxy-4-(dodecyloxy)pyridin-2-yl)methyl)azanediyl) diacetic acid (H₃C₁₂Opaada). Compound **3** (0.1915 g, 0.518 mmol) and di-*tert*-butyl 2,2'-azanediyldiacetate (0.1223 g, 0.499 mmol) were dissolved in acetonitrile (20 mL) and K₂CO₃ (0.1723 g, 1.247 mmol) were added. The mixture was stirred at room temperature for 3 days. The excess K₂CO₃ was removed by filtration and the filtrate concentrated to dryness yielding a deep yellow oil, which was purified by column chromatography on SiO₂ using AcOEt:hexane (20:80) as eluent giving 0.310 g of the ester intermediate **5** an oily product. The oil was dissolved in 6 M HCl (20 mL) and the mixture was stirred at room temperature 24 h. The white precipitate was isolated by filtration and washed with acetone. Addition of acetone to the filtrate provoked the precipitation of a second batch of the product. The combined white solids were dried providing a white solid (0.095 g, 0.160 mmol). Yield 42%. ¹H NMR (CDCl₃, 300 MHz, 25 °C, TMS): δ 7.48 (s, 2H, Py), 4.04 (m, 4H, O-CH₂), 3.92 (s, 2H, Py-CH₂), 3.43 (s, 4H, CH₂-COOH), 1.75 (m, 2H, CH₂), 1.22 (s, 18H, CH₂), 0.83 (t, 3H, CH₃, ²J= 7.1 Hz). ¹³C NMR (CDCl₃, 125.8 MHz, 25 °C, TMS): δ 170.51, 166.96, 166.02, 162.44, 148.82, 111.45, 111.10, 68.46, 60.19, 52.89, 31.95, 29.70, 29.67, 29.61, 29.59, 29.38, 29.35, 28.93, 25.97, 22.72, 14.15 (CH₃) ppm. MS (ESI⁺) m/z: 453.26 (100%) $([C_{23}H_{36}N_2O_7+H]^+)$. IR (ATR): ν 1746 cm⁻¹ (C=O). Anal. calcd. for $C_{23}H_{36}N_2O_7 \cdot 2HCl$: C, 52.57; H, 7.29; N, 5.33. Found: C, 52.86; H, 6.56; N, 5.38%.

di-*tert*-Butyl 2,2'-(((6-(methoxycarbonyl)pyridin-2-yl)methyl)azanediyl)diacetate (6). A solution of methyl 6-(chloromethyl)picolinate (0.1878 g, 1.012 mmol) in CH₃CN (15 mL) was added dropwise to a mixture of di-tert-butyl 2,2'-azanediyldiacetate (0.2475 g, 1.008 mmol) and K₂CO₃ (0.7019 g, 5.079 mmol, 5 eq) in CH₃CN (20 mL) at room temperature. The reaction mixture was stirred at room temperature for 72 h and at 50 °C for another 24 h. After filtration, the residue was washed with CH₂Cl₂ (3×50 mL). The organic layer was dried over anhydrous Na₂SO₄ and the solvent was removed under reduced pressure to yield a solid residue. Quantitative. ¹H NMR (CDCl₃, 300 MHz, 25 °C,

TMS): δ 7.73-7.71 (d, 2H, PyH), 7.61-7.56 (t, 1H, PyH), 3.88 (s, 2H, CH₂), 3.70 (s, 3H, CH₃), 3.22 (s, 4H, CH₂), 1.18 (s, 18H, (CH₃)₃). ¹³C NMR (CDCl₃, 75 MHz, 25 °C, TMS): δ 170.03 (COOtBu), 165.49 (COOCH₃), 160.35 (C-Py), 146.96 (C-Py), 137.30 (CH-Py), 126.02 (CH-Py), 123.39 (CH-Py), 80.69 (C(CH₃)₃), 59.71 (CH₂), 55.63 (CH₂), 52.44 (CH₃), 27.88 ((CH₃)₃). MS (ESI⁺) m/z: 417.20 [C₂₀H₃₀N₂O₆ + Na]⁺.

2,2'-(((6-Carboxypyridin-2-yl)methyl)azanediyl)diacetic acid (H₃paada). Compound **6** (0.3980 g, 1.008 mmol) was dissolved in 6M HCl (10 mL) and heated under reflux for 48 h. After cooling the mixture, the white precipitate formed was collected by filtration, washed with acetone and dried (0.300 g, 0.857 mmol). Yield 85%. ¹H NMR (D₂O, 300 MHz, 25 °C, TMS): δ 7.83-7.78 (t, 1H, PyH), 7.71-7.69 (d, 1H, PyH), 7.56-7.54 (d, 1H, PyH), 3.82 (s, 2H, CH₂), 3.14 (s, 4H, CH₂). ¹³C NMR (D₂O, 75 MHz, 25 °C, TMS): δ 174.08 (CH₂COOH), 172.88 (Py-COOH), 153.49 (C-Py), 152.74 (C-Py), 138.83 (C-Py), 126.16 (C-Py), 123.38 (C-Py), 58.94 (CH₂), 57.24 (CH₂COOH). MS (ESI⁺) m/z: 267.06 [C₁₁H₁₂N₂O₆-H]⁻. Anal. calcd. for C₁₁H₁₂N₂O₆·2HCl·0.5H₂O: C, 37.73; H, 4.32; N, 8.00. Found: C, 37.61; H, 4.50; N, 7.67%.

3.3.3. Equilibrium measurements

The protonation constants of the ligand and the stability constant of the Mn(II) complex with paada³⁻ were determined by potentiometric and spectrophotometric titrations. The necessary amount of sodium chloride was added to all solutions in order to keep the ionic strength at a constant value of 0.15 M, while the temperature was always 25 °C. The Hyperquad program[49] was used to fit potentiometric titration data. The calibration parameters were determined using solutions of known proton concentration, as described below, and were given to the program in order to obtain the equilibrium constants.

The spectrophotometric data were fitted with the pHab program,[50] a program designed to fit spectrophotometrical data of solutions of known pH (with pH= -log[H⁺]). Again, solutions of known proton concentration were used to calibrate the electrode and to find the pH of sample solutions. The UV-vis absorption spectra were recorded with a Uvikon-XS (Bio-Tek Instruments) double-beam spectrophotometer with cells of 1 cm path length. The spectra were recorded in the range 220–320 nm (100 wavelengths). The solutions were prepared one day before the measurements were carried out, to assure that the equilibrium was attained (batch method).

All potentiometric titrations were performed in a dual-wall cell that was kept at a constant temperature by circulating water from a thermostat. Nitrogen was bubbled on the surface of the solution to avoid CO₂ absorption while a magnetic stirrer was used to homogenise the solutions. A Crison microBu 2030 automatic burette equipped with 2.5 mL or 1.0 mL syringes was used to deliver the titrant. The electromotive force (emf) values were read using a Crison micropH 2000 pH-meter connected to a glass electrode (Radiometer pHG211) and a reference electrode (Radiometer REF201). The calibration procedure was described elsewhere.[7] Briefly, the electrode response at constant ionic strength is given by E= E°' + s log[H⁺], with E being the emf, E°' the formal potential, and s the slope. A weak acid (Na₂HPO₄) was titrated with a standard HCl solution and with the known equilibrium constants the proton concentration was found at each point of the titration. A linear regression of E $vs.$ log[H⁺] yielded s and E°'.

Several titrations were performed to obtain the acid-base and the complexation constants of the paada³⁻ ligand with Mn(II). The ligand was in the hydrochloride form, so that it was initially titrated with sodium hydroxide. At the end of this titration, NaOH was added to deprotonate the ligand, and the basic solution was titrated with HCl in order to determine the acid-base equilibrium constants. At the end of the titration in acid media (pH~ 2) Mn(II) was added (at the same concentration of the ligand) and the solution was titrated with NaOH until pH~ 4, before reaching the equivalence point, to preclude precipitation. The concentration of the ligand was in the range 2.0–3.5 mM. The equilibrium was attained quickly in the titrations of the complex except near the equivalence point. Thus, points very near the equivalence point were not used for the fitting (pH> 4).

3.3.4. ¹H NMRD and ¹⁷O NMR measurements

The proton $1/T_1$ NMRD profiles were recorded using a fast field-cycling Stelar SmartTracer relaxometer (Mede, Pv, Italy) over a continuum of magnetic field strengths from 0.00024 to 0.25 T (corresponding to 0.01−10 MHz proton Larmor frequencies). The temperature was controlled with a Stelar VTC-91 airflow heater equipped with a calibrated copper–constantan thermocouple (uncertainty of ±0.1 K). A Stelar Relaxometer equipped with a Bruker WP80 NMR electromagnet adapted to variable-field measurements (15-80 MHz proton Larmor frequency) was used to obtain additional data points in the range 15-70 MHz. The relaxometer is operated under computer control providing $1/T_1$ values with an absolute uncertainty of ±1%.

¹⁷O NMR chemical shifts and transverse relaxation rates were recorded on a Bruker Avance III spectrometer (11.7 T) equipped with a 5 mm probe and standard temperature control unit. The solutions of the complexes were enriched to reach 2.0% of the ¹⁷O isotope (Cambridge Isotope). The transverse relaxation rates were obtained from the signal width at half-height. The exact concentrations of the solutions used for ¹H NMRD and ¹⁷O NMR measurements were determined by the BMS shift method at 11.7 T.[51]

3.3.5. Fluorescence measurements

Steady-state fluorescence measurements were performed on an Amincon-Bowman series 2 spectrofluorimeter equipped with thermostat bath. Excitation and emission slits were fixed at 4 and 2 nm, respectively. The excitation wavelength was set at 290 nm, and the fluorescence emission spectra were recorded at different temperatures (288, 298, and 310 K) in the wavelength range of 300-420 nm; the intensity of fluorescence, I_F, was read at the emission maximum wavelength of 343 nm. Fluorescence titration experiments were performed by keeping the concentration of BSA constant (5.2 μM) in 10 mM Tris-HCl buffer, pH 7.4 while varying either the ligand concentration or both the ligand and Mn(II) concentrations at the Mn:L ratio of 1:1. In the two sets of experiments, the ratio [ligand]/[BSA] was made to vary from 4 to 40, approximately. The reported pH values correspond to the sample mixture. Concentrated aqueous solutions of MnCl₂ were used to simply add small aliquots (i.e. 10-100 μL) to about 3.0 mL of a single sample solution of BSA (in a fluorimetric cuvette) and the ligand in Tris-HCl buffer; that is, the same solution was used to record both the fluorescence spectrum in the absence and presence of Mn(II). Sufficient time was leave between measurements in order to achieve the new equilibration. Corrections for the dilution of the absorbent or fluorescent material were made when necessary. The absorbance values read at the excitation wavelength (335 nm for pyrene or 290 nm for BSA) were always lower than 0.15 absorbance units to avoid inner filter effects.

3.3.6. Computational details

Full geometry optimisations of the [Mn(paada)(H₂O)₂]⁻·4H₂O and [Mn(nta)(H₂O)₂]⁻·4H₂O systems were performed employing DFT calculations at the M06-2X/Def2-TZVP[52,53] level employing the Gaussian 09 package (Revision E.01).[54] Solvent effects were introduced by using the polarizable continuum model (PCM). In particular, we used the integral equation formalism (IEFPCM) variant as implemented in Gaussian 09.[55] No symmetry constraints have been imposed during the optimisations. The stationary points found on the potential energy surfaces as a result of geometry optimisations were confirmed to represent energy minima rather than saddle points via frequency analysis. ¹⁷O hyperfine coupling constants were calculated using the M06-2X functional in combination with the EPR-III[56] basis set for the ligand atoms and the aug-cc-pVTZ-J basis set for Mn.[57]

Complete Active Space Self-Consistent Field (CASSCF)[58] and N-electron valence perturbation theory to second order (NEVPT2)[59] calculations were performed using the ORCA program package (Release 4.0.1.2).[60] The def2-TZVP basis set[53] basis set was used throughout. CASSCF calculations were performed by using an active space including five electrons distributed into the five Mn 3d-based molecular orbitals (CAS(5,5)). The orbitals were optimised by averaging 1 sextet, 24 quartets and 75 doublet roots. NEVPT2 calculations were performed on the top of the CASSCF wave functions to account for dynamic correlation, while SOC effects were introduced by quasi-degenerate perturbation theory (QDPT).[61] Solvent effects were introduced with the universal solvation model based on solute electron density and on a continuum model (SMD).[62]

3.4. Conclusions

In this work, we have reported and discussed the synthesis of the pentadentate picolinate ligand paada³⁻ and the lipophilic derivative C₁₂Opaada³⁻, together with a detailed characterisation of their Mn(II) complexes. The thermodynamic stability of the [Mn(paada)]⁻ complex was found to be intermediate between those of the Mn(II) complexes formed with the hexadentate dpaa³⁻ and the tetradentate nta³⁻ ligands. A detailed ¹H and ¹⁷O relaxometric characterisation of the [Mn(paada)]⁻ complex indicated the presence of two inner-sphere water molecules involved in a rather fast exchange with bulk water. The corresponding lipophilic derivative [Mn(C₁₂Opaada)]⁻ self-assembles into micelles in aqueous solution characterised by a *cmc* of 0.31±0.01 mM, as estimated by the relaxometric method. Fluorescence measurements using pyrene as a fluorescent indicator confirmed the accuracy of the *cmc* obtained by proton relaxometry and revealed a noticeable impact of the ionic strength on the measured *cmc* values.

The [Mn(C₁₂Opaada)]⁻ complex binds with a moderate affinity to BSA, with hydrophobic interactions being the main driving force for the adduct formation. The interaction of the aliphatic chain of the ligand with the protein through hydrophobic forces plays a major role in the binding process. The formation of micelles or binding to BSA provides a straightforward strategy to improve the relaxivity of Mn(II)-based MRI contrast agents.

3.5. Notes

The work presented in this chapter has been published in the following article:

3.6. References

1. (a) M. Regueiro-Figueroa, G. A. Rolla, D. Esteban-Gómez, A. de Blas, T. Rodríguez-Blas, M. Botta and C. Platas-Iglesias, *Chem. Eur. J.* 2014, **20**, 17300; (b) A. Forgács, M. Regueiro-Figueroa, J. L. Barriada, D. Esteban-Gómez, A. de Blas, T. Rodríguez-Blas, M. Botta and C. Platas-Iglesias, *Inorg. Chem.* 2015, **54**, 9576.

2. E. W. Price, J. F. Cawthray, G. A. Bailey, C. L. Ferreira, E. Boros, M. J. Adam and C. Orvig, *J. Am. Chem. Soc.*, 2012, **134**, 8670.

3. N. Chatterton, Y. Bretonnière, J. Pécaut and M. Mazzanti, *Angew. Chem. Int. Ed.*, 2005, **44**, 7595.

4. (a) E. Boros, J. F. Cawthray, C. L. Ferreira, B. O. Patrick, M. J. Adam and C. Orvig, *Inorg. Chem.*, 2012, **51**, 6279; (b) C. F. Ramogida, E. Boros, B. O. Patrick, S. K. Zeisler, J. Kumlin, M. J. Adam, P. Schaffer and C. Orvig, *Dalton Trans.*, 2016, **45**, 13082; (c) C. F. Ramogida, D. Schindler, C. Schneider, Y. L. K. Tan, S. Huh, C. L. Ferreira, M. J. Adam and C. Orvig, *RSC Adv.*, 2016, **6**, 103763; (d) C. F. Ramogida, J. Pan, C. L. Ferreira, B. O. Patrick, K. Rebullar, D. T. T. Yapp, K.-S. Lin, M. J. Adam and C. Orvig, *Inorg. Chem.*, 2015, **54**, 4953; (e) E. Boros, C. L. Ferreira, J. F. Cawthray, E. W. Price, B. O. Patrick, D. W. Wester, M. J. Adam and C. Orvig, *J. Am. Chem. Soc.*, 2012, **132**, 15726-15733.

5. C. F. Ramogida, J. F. Caethray, E. Boros, C. L. Ferreira, B. O. Patrick, M. J. Adam and C. Orvig, *Inorg. Chem.*, 2015, **54**, 2017.

6. R. Ferreirós-Martínez, D. Esteban-Gómez, C. Platas-Iglesias, A. de Blas and T. Rodríguez-Blas, *Dalton Trans.* 2008, 5754.

7. L. Caneda-Martínez, L. Valencia, I. Fernández-Pérez, M. Regueiro-Figueroa, G. Angelovski, I. Brandariz, D. Esteban-Gómez and C. Platas-Iglesias, *Dalton Trans.*, 2017, **46**, 15095.

8. (a) D. M. Weekes, C. F. Ramogida, M. de G. Jaraquemada-Peláez, B. O. Patrick, C. Apte, T. I. Kostelnik, J. F. Cawthray, L. Murphy and C. Orvig, *Inorg. Chem.*, 2016, **55**, 12544; (b) T. W. Price, J. Gallo, V. Kubicek, Z. Böhmová, T. J. Prior, J. Greenman, P. Hermann and G. J. Stasiuk, *Dalton Trans.*, 2017, **46**, 16973.

9. A. Forgács, R. Pujales-Paradela, M. Regueiro-Figueroa, L. Valencia, D. Esteban-Gómez, M. Botta and C. Platas-Iglesias, *Dalton Trans.*, 2017, **46**, 1546.

10. M. Khannam, T. Weyhermüller, U. Goswami and C. Mukherjee, *Dalton Trans.*, 2017, **46**, 10426.

11. (a) C. Platas-Iglesias, M. Mato-Iglesias, K. Djanashvili, R. N. Muller, L. Vander Elst, J. A. Peters, A. de Blas and T. Rodríguez-Blas, *Chem. Eur. J.*, 2004, **10**, 3579; (b) F. K. Kálmán, A. Végh, M. Regueiro-Figueroa, É. Tóth, C. Platas-Iglesias and G. Tircsó, *Inorg. Chem.*, 2015, **54**, 2345.

12. G. Tircsó, M. Regueiro-Figueroa, V. Nagy, Z. Garda, T. Garai, F. K. Kálmán, D. Esteban-Gómez, É. Tóth and C. Platas-Iglesias, *Chem. Eur. J.*, 2016, **22**, 896.

13. B. Phukan, C. Mukherjee, U. Goswani, A. Sarmah, S. Mukherjee, S. K. Sahoo and S. C. Moi, *Inorg. Chem.*, 2018, **57**, 2631.

14. (a) B. Drahos, I. Lukes and E. Toth, *Eur. J. Inorg. Chem.* 2012, 1975; (b) M. Kueny-Stotz, A. Garofalo and D. Felder-Flesch, *Eur. J. Inorg. Chem.* 2012, 1987.

15. D. Pan, A. H. Schmieder, S. A. Wickline and G. M. Lanza, *Tetrahedron* 2011, **67**, 8431.

16. (a) S. Cheng, L. Abramova, G. Saab, G. Turabelidze, P. Patel, M. Arduino, T. Hess, A. Kallen and M. Jhung, *J. Am. Med. Assoc.*,

2007, **297**, 1542; (b) T. H. Darrah, J. J. Prutsman-Pfeiffer, R. J. Poreda, M. E. Campbell, P. V. Hauschka and R. E. Hannigan, *Metallomics,* 2009, **1**, 479.

17 (a) T. Kanda, T. Fukusato, M. Matsuda, K. Toyoda, H. Oba, J. Kotoku, T. Haruyama, K. Kitajima and S. Furui, *Radiology,* 2015, **276**, 228; (b) E. Kanal and M.F. Tweedle, *Radiology,* 2015, **275**, 630: (c) D.R. Roberts, S.M. Lindhorst, C.T. Welsh, K.R. Maravilla, M.N. Herring, K.A. Braun, B.H. Thiers and W.C. Davis, *Invest Radiol.,* 2016, **51**, 280; (d) M. Birka, K.S. Wentker, E. Lusmöller, B. Arheilger, C.A. Wehe, M. Sperling, R. Stadler and U. Karst, *Anal. Chem.,* 2015, **87**, 3321.

18 E. M. Gale, I. P. Atanasova, F. Blasi, I. Ay and P. Caravan, *J. Am. Chem. Soc.,* 2015, **137**, 15548.

19 I. Bertini, F. Briganti, Z. Xia and C. Luchinat, *J. Magn. Reson.,* 1993, **101**, 198.

20 (a) G. S. Loving, S. Mukherjee and P. Caravan, *J. Am. Chem. Soc.,* 2013, **135**, 4620; (b) E. M. Gale, S. Mukherjee, C. Liu, G. S. Loving and P. Caravan, *Inorg. Chem.,* 2014, **53**, 10748.

21 T. Storr, B. R. Cameron, R. A. Gossage, H. Yee, R. T. Skerlj, M. C. Darkes, S. P. Fricker, G. J. Bridger, N. A. Davies, M. T. Wilson, K. P. Maresca, J. Zubieta, *Eur. J. Inorg. Chem.,* 2005, 2685.

22 M. Schäferling, T. Ääritalo and T. Soukka, *Chem. Eur. J.,* 2014, **20**, 5298.

23 C. S. Bonnet, F. Pellagatti, F. Buron, C. M. Shade, S. Villette, V. Kubicek, G. Guillaumet, F. Suzenet, S. Petoud and E. Toth, *Chem. Commun.,* 2010, **46**, 124.

24 G. Anderegg, *Pure Appl. Chem.,* 1982, **54**, 2693.

25 N. Chatterton, C. Gateau, M. Mazzanti, J. Pécaut, A. Borel, L. Helm and A. Merbach, *Dalton Trans.,* 2005, 1129.

26 Nonat, C. Gateau, P. H. Fries and M. Mazzanti, *Chem. Eur. J.,* 2006, **12**, 7133.

27 A. N. Nonat, C. Gateau, P. H. Fries, L. Helm and M. Mazzanti, *Eur. J. Inorg. Chem.,* 2012, 2049.

28 B. Drahos, J. Kotek, P. Hermann, I. Lukes and E. Toth, *Inorg. Chem.,* 2010, **49**, 3224.

29 S. M. Rocklage, W. P. Cacheris, S. C. Quay, F. E. Hahn and K. N. Raymond, *Inorg. Chem.,* 1989, **28**, 477.

30 (a) B. Drahos, J. Kotek, I. Cisarova, P. Hermann, L. Helm, I. Lukes and E. Toth, *Inorg. Chem.,* 2011, **50**, 12785; (b) A. de Sa, C. S. Bonnet, C. F. G. C. Geraldes, E. Toth, P. M. T. Ferreira and J. P. Andre, *Dalton Trans.,* 2013, **42**, 4522; (c) A. Forgacs, L. Tei, Z. Baranyai, D. Esteban-Gomez, C. Platas-Iglesias and M. Botta, *Dalton Trans.,* 2017, **46**, 8494.

31 E. M. Gale, J. Zhu and P. Caravan, *J. Am. Chem. Soc.,* 2013, **135**, 18600.

32 M. S. Zetter, M. W. Grant, E. J. Wood, H. W. Dodgen and J. P. Hunt, *Inorg. Chem.,* 1972, **11**, 2701.

33 G. A. Rolla, C. Platas-Iglesias, M. Botta, L. Tei and L. Helm, *Inorg. Chem.,* 2013, **52**, 3268.

34 L. Tei, G. Gugliotta, M. Fekete, F. K. Kalman, M. Botta, *Dalton Trans.,* 2011, **40**, 2025.

35 (a) V. Patinec, G. A. Rolla, M. Botta, R. Tripier, D. Esteban-Gómez and C. Platas-Iglesias, *Inorg. Chem.,* 2013, **52**, 11173; (b) D. Esteban-Gómez, C. Cassino, M. Botta and C. Platas-Iglesias, *RSC Adv.,* 2014, **4**, 7094.

36 G.-F. Liu, M. Filipovic, F. W. Heinemann and I. Ivanovic-Burmazovic, *Inorg. Chem.,* 2007, **46**, 8825.

37 P. H. Fries and E. Belorizky, *ChemPhysChem,* 2012, **13**, 2074.

38 C. Platas-Iglesias, D. Esteban-Gómez, L. Helm and M. Regueiro-Figueroa, *J. Phys. Chem. A,* 2016, **120**, 6467.

39 (a) S. Khan, R. Pollet, R. Vuilleumier, J. Kowalewski and M. Odelius, *J. Chem. Phys.,* 2017, **147**, 244306; (b) (a) S. Khan, A. Kubica-Misztal, D. Kruk, J. Kowalewski and M. Odelius, *J. Chem. Phys.,* 2015, **142**, 034304.

40 A. Domínguez, A. Fernández, N. González, E. Iglesias and L. Montenegro, *J. Chem. Edu.,* 1997, **74**, 1227.

41 S. Aime, M. Botta, D. Esteban-Gómez and C. Platas-Iglesias, *Mol. Phys.,* 2018, DOI: 10.1080/00268976.2018.1516898.

42 (a) G. Lipari and S. Szabo, *J. Am. Chem. Soc.,* 1982, **104**, 4556; (b) G. Lipari and S. Szabo, *J. Am. Chem. Soc.,* 1982, **104**, 4559.

43 L. Helm, J. R. Morrow, C. J. Bond, F. Carniato, M. Botta, M. Braun, Z. Baranyai, R. Pujales-Paradela, M. Regueiro-Figueroa, D. Esteban-Gómez, C. Platas-Iglesias and T. J. Scholl, Contrast Agents for MRI. Experimental Methods. Ed. V. C. Pierre and M. J. Allen, Royal Society of Chemistry, Croydon, UK, chapter 3.

44 (a) J. R. Lakowicz, Principles of fluorescence Spectroscopy, 3rd ed. Springer, New York, 2006, chap. 16; (b) P. Bourassa, I. Hasni and H. A. Tajmir-Riahi, *Food Chem.,* 2011, **129**, 1148.

45 (a) E. Lissi and E. Abuin, *J. Fluoresc.,* 2011, **21**, 1831; (b) D. V. Naik, W.L. Paul, R.M. Threatte and S. G. Schulman, *Anal. Chem.,* 1975, **47**, 267.

46 (a) G. Scatchard, *Ann. N. Y. Acad. Sci.,* 1949, **61**, 660; (b) T. N. Tikhonova, E. A. Shirshin, G. S. Budylin, V. V. Fadeev and G. P. Petrova, *J. Phys. Chem. B,* 2014, **118**, 6626.

47 K. A. Connors, Binding Constants. The measurement of molecular complex stability, John Wiley, USA, 1987, chaps. 4 and 12.

48 P. D. Ross and S. Subramanian, *Biochemistry,* 1981, **20**, 3096.

49 L. Alderighi, P. Gans, A. Ienco, D. Peters, A. Sabatini and A. Vacca, *Coord. Chem. Rev.,* 1999, **184,** 311.

50 P. Gans, A. Sabatini and A. Vacca, *Annali di Chimica,* 1999, **89**, 45.

51 D. M. Corsi, C. Platas-Iglesias, H. van Bekkum and J. A. Peters, *Magn. Reson. Chem.,* 2001, **39**, 723.

52 Y. Zhao and D. G. Truhlar, *Theor. Chem. Acc.,* 2008, **120**, 215.

53 F. Weigend and R. Ahlrichs, *Phys. Chem. Chem. Phys.,* 2005, **7**, 3297.

54 M. J. Frisch et al. Gaussian, Inc., Wallingford CT, 2009.

55 J. Tomasi, B. Mennucci and R. Cammi, *Chem. Rev.,* 2005, **105**, 2999.

56 N. Rega, M. Cossi and V. Barone, *J. Chem. Phys.,* 1996, **105**, 11060.

57 E. D. Hedegard, J. Kongsted and S. P. A. Sauer, *J. Chem. Theory Comput.,* 2011, **7**, 4077.

58 P.-A. Malqvist and B. O. Roos, *Chem. Phys. Lett.,* 1989, **155**, 189.

59 (a) C. Angeli, R. Cimiraglia and J.-P. Malrieu, *Chem. Phys. Lett.,* 2001, **350**, 297; (b) C. Angeli, R. Cimiraglia and J.-P. Malrieu, *J. Chem. Phys.,* 2002, **117**, 9138; (c) C. Angeli, R. Cimiraglia, S. Evangelisti, T. Leininger and J.-P. Malrieu, *J. Chem. Phys.,* 2001, **114**, 10252; (d) C. Angeli and R. Cimiraglia, *Theor. Chem. Acc.,* 2002, **107**, 313.

60 F. Neese, *Wiley Interdiscip. Rev.: Comput. Mol. Sci.,* 2012, **2**, 73.

61 F. Neese, *J. Chem. Phys.,* 2005, **122**, 034107.

62 A. V. Marenich, C. J. Cramer and D. G. Truhlar, *J. Phys. Chem. B,* 2009, **113**, 6378.
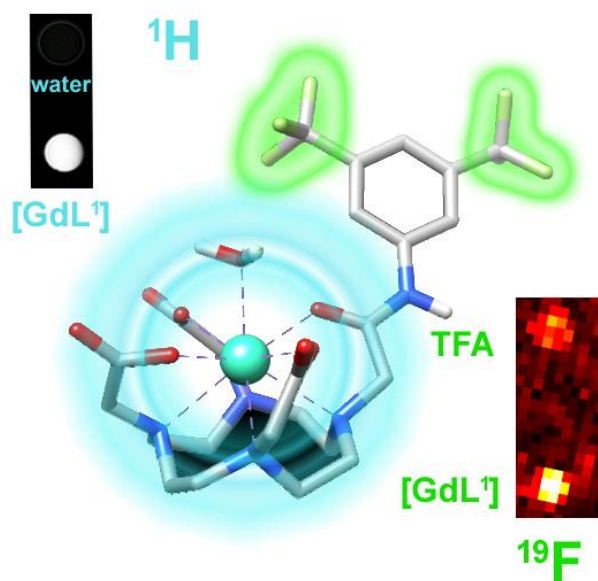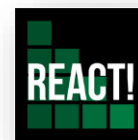
Gadolinium(III)-based
Dual ^{1}H/^{19}F MRI Probes

Gadolinium(III)-based Dual ^{1}H/^{19}F MRI Probes

We present two novel octadentate cyclen-based ligands containing one (L^1) or two (L^2) phenylacetamide pendants that feature two CF$_3$ groups either at positions 3 and 5 (L^1) or 4 (L^2). The corresponding Gd^{3+} complexes possess one coordinated water molecule, as confirmed by the luminescence lifetime measurements recorded on the Eu(III) and Tb(III) analogues. A detailed ^{1}H and ^{17}O relaxometric characterisation revealed the parameters that govern the relaxivities of these complexes. The water exchange rate of the mono-amide derivative GdL^1 (k_{ex}^{298} = 1.52×10^6 s^{-1}) is faster than that determined for the bis-amide complex GdL^2 (k_{ex}^{298} = 0.73×10^6 s^{-1}). ^{1}H and ^{19}F NMR studies indicate that the complexes are present in solution almost exclusively as the square antiprismatic (SAP) isomers. ^{19}F NMR relaxation studies provided Gd⋯F distances of 7.4 $\pm$ 0.1 and 9.1 $\pm$ 0.1 Å for GdL^1 and GdL^2, respectively. Phantom MRI studies revealed the favourable properties of GdL^2 as a dual ^{1}H/^{19}F MRI probe, while the shorter Gd⋯F distance of GdL^1 reduces the signal to noise ratio due to the very short transverse relaxation time of the ^{19}F NMR signal.

4.1. Introduction

Magnetic resonance imaging (MRI) is a non-invasive technique that uses nuclear magnetic resonance principles for generating 3D-anatomical images with very high resolution and unlimited depth penetration.[1] MRI images are based on the alignment of nuclear spins to an external magnetic field, which can be perturbed by applying a radiofrequency pulse. The nuclear spins then return to the initial state at different rates after the application of the pulse (relaxation). Contrast in MRI can be achieved by taking advantage of the differences in relaxation times of water proton nuclei of different tissues. However, image contrast can be improved by manipulating the relaxation times with the so called contrast agents (CAs).[1-3] These substances are designed to improve the sensitivity and quality of the images, usually producing brighter images by shortening the longitudinal relaxation times of water protons (T_1-weighted agents). CAs are usually paramagnetic metal complexes, generally containing the lanthanide ion Gd^{3+}. Gadolinium contrast agents (GdCAs) affect the longitudinal (T_1) and transverse (T_2) relaxation times of water proton nuclei, shortening both components. The choice of Gd^{3+} is related to its electronic properties (seven unpaired electrons, high effective magnetic moment at room temperature - μ^2= 63 BM^2 – and a long relaxation time of the electron spin).[4]

The most robust CAs used in clinical practice are macrocyclic Gd^{3+} complexes such as [Gd(DOTA)]$^-$ (DOTAREM®), as the macrocyclic ligand ensures a high stability and inertness with respect to complex dissociation.[5] Indeed, some toxicity problems have been attributed to the dissociation of GdCAs, most often after administration of non-macrocyclic derivatives.[6] As a consequence of these toxicity issues, restrictions and suspensions of authorisations of some of the linear GdCAs have been executed recently by the European Medicines Agency.[7] These restrictions do not affect macrocyclic agents, which are kinetically more inert than

the linear ones.[8] Another disadvantage of traditional T_1 CAs is the presence of a background signal due to the bulk water. In the last decades, different alternatives were explored to improve the sensitivity and reduce the toxicity and acquisition times of the MRI scans.[9] Among several of the targets set for these improvements are, for instance, the use of other metal ions (i.e Mn^{2+},[10] Fe^{3+},[11] Fe^{2+},[12] Co^{2+},[13] Ni^{2+14}) potentially less harmful than gadolinium in case of release, the development of new modalities of imaging (i.e. paraCEST,[12-16] paraSHIFT,[17] responsive or smart agents[18,19]) or the use of diverse approaches combined on the same probe (i.e. multimodal or multiresponsive probes).[20]

Fluorinated probes are one of the most attractive approaches to overcome the issue associated with the background signal of bulk water.[21,22] Some of the reasons that make these systems quite promising are that fluorinated substances are almost absent in the human body, being present only in teeth and bones as solid salts.[23] Thus, one can obtain images at the frequency of ^{19}F without the background due to this nucleus. This solves the water-background signal problem, improving the signal-to-noise ratio (SNR) on the recorded images. Other properties that make attractive this nucleus is the high gyromagnetic ratio (40.05 MHz/T), its isotopic abundance ratio (100%), its non-quadrupolar nature (I= ½) and wide chemical shift range (~350 ppm), and the similar sensitivity to ^{1}H (83%). Another noteworthy feature is the possibility of using the same scanners than for standard ^{1}H MRI, with just small adjustments on the Larmor frequency for detecting the ^{19}F nuclei (i.e. tuning at 282 MHz for ^{19}F instead of 300 MHz for ^{1}H). Fluorinated compounds have relatively long relaxation rates, and consequently acquisition times would be rather long.[23, 24] This issue can be solved by introducing a paramagnetic centre, either a transition metal[24,25] or lanthanide metal ions,[23,26-29] in the vicinity of ^{19}F nuclei, which shortens both T_1 and T_2 relaxation times through the paramagnetic relaxation enhancement (PRE) effect.[22,27c] While the shortening of the longitudinal relaxation times leads

to a decrease on the acquisition times, reducing T_2 causes line-broadening, and thus decreases signal intensity, sensitivity and the final resolution of the collected images. Hence, optimal probes should present a T_2/T_1 ratio close to the unit.[30]

The ¹⁹F probes based on Ln³⁺ ions so far investigated were designed for the paramagnetic ions of the second part of the lanthanide series (Tb³⁺ to Yb³⁺). These Ln³⁺ ions combine a high effective magnetic moment and relatively long relaxation times of the electron spin, which prevents extensive line-broadening.[31] The detailed work of Parker and co-workers concluded that for these metal ions the optimal distance between the paramagnetic ion and the ¹⁹F nuclei should be in the range 5-7 Å.[26] A typical scaffold used by Parker et al. to achieve this range of Ln···F distances is represented by ligand H_3L^3 (Scheme 1).
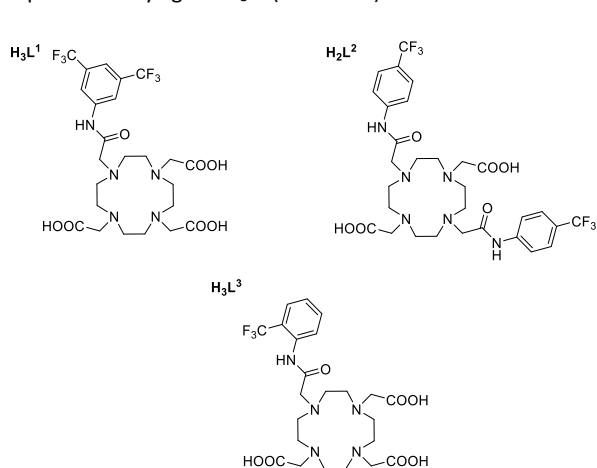
Scheme 1. Chemical structure of the ligands studied in this work.

We hypothesised that a careful selection of the distance between the paramagnetic Gd³⁺ ion and the ¹⁹F nuclei would allow the preparation of genuine dual Gd³⁺-based ¹H/¹⁹F probes. These agents would combine the robustness and sensitivity of traditional T_1 agents with the background-free images provided by ¹⁹F, which should allow for quantification of the probe concentration. Thus, herein we report the synthesis of the cyclen-based ligands H_3L^1 and H_2L^2 (Scheme 1), which contain two CF₃ groups at different positions of the phenylacetamide pendant arms. This allows for a comparison of the effect of the Gd···F distance on the ¹⁹F relaxation times. Furthermore, we present a complete relaxometric study including proton nuclear magnetic relaxation dispersion (¹H NMRD) profiles and ¹⁷O and ¹⁹F chemical shifts and relaxation measurements. In addition, we report a structural study of the Gd³⁺ complexes in solution using DFT calculations in combination with the analysis of the ¹H NMR spectra of the Eu³⁺ analogue and luminescence lifetimes of the Eu³⁺ and Tb³⁺ derivatives. Finally, we also report in vitro MRI studies on tube phantoms at both the ¹H and ¹⁹F frequencies.

4.2. Results and discussion

4.2.1. Synthesis

The synthesis of ligands H_3L^1 and H_2L^2 was undertaken by an alkylation of the tris- or bis-protected cyclen derivatives DO3AtBu or DO2AtBu, respectively, with chloromethyl acetamides **1a** and **1b**

(Scheme 2). These precursors were prepared in one step by reaction of chloroacetyl chloride with the respective fluorinated aniline.[32,33] The ligands were isolated with nearly quantitative overall yields (> 98%) upon cleavage of the *tert*-butyl protecting groups with formic acid.

The preparation of the complexes was undertaken by using a solvothermal method, employing hydrated LnCl₃ (Ln = Eu, Gd or Tb), n-butanol as solvent and DIPEA as a base. The complexation of Ln³⁺ ions by macrocyclic ligands is known to be faster in non-aqueous media.[34] The purification of the complexes was achieved by reverse-phase medium performance liquid chromatography (MPLC). The high-resolution mass spectra (Figures S1-S6, Annexe C) confirm the formation of the complexes.
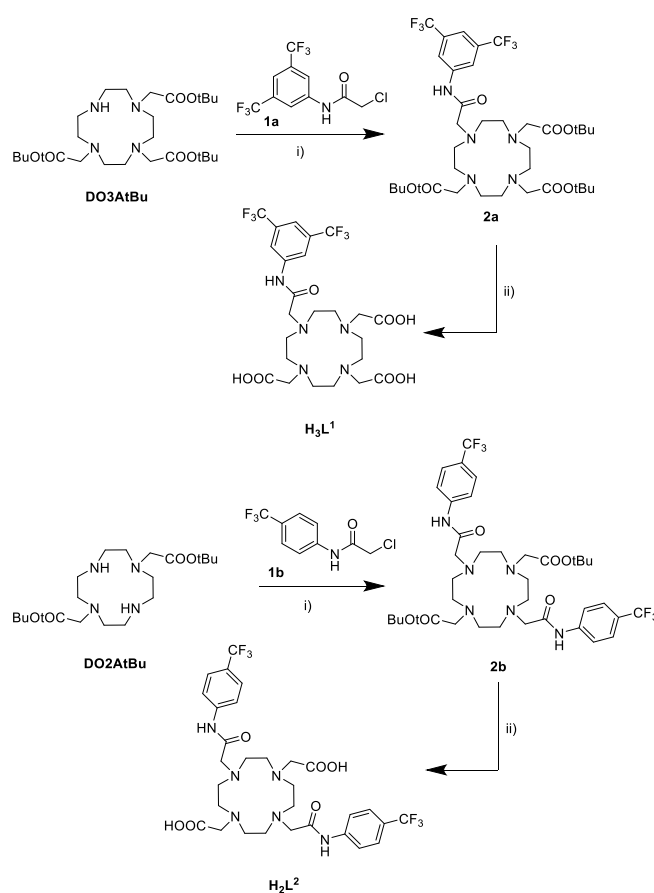
Scheme 2. Synthesis of the ligands reported in this work. Reagents and conditions: i) CH₃CN, K₂CO₃, 45 °C, 9 days; ii) HCOOH, 80 °C, 48 h.

4.2.2. r_{1p} determination and hydration numbers

The relaxation enhancement of water protons induced by the presence of a paramagnetic agent at 1 mM concentration, known as relaxivity (r_{1p}), represents a straightforward measure of the efficiency of a paramagnetic complex as a T_1-weighted contrast agent in vitro.[35] The relaxivities of both gadolinium complexes were measured at 298 K and 300 MHz from aqueous solutions buffered at pH 7.4 (0.05 M HEPES). The measured paramagnetic relaxation enhancements present a linear dependence with Gd³⁺ concentration (measured using 2.5-4.5 mM solutions). The slopes of the straight lines (Figure S7, Annexe C) provide the relaxivities of

the complexes, resulting in values r_{1p} = 4.85 mM^{-1} s^{-1} and 3.97 mM^{-1} s^{-1} for GdL^1 and GdL^2, respectively. These relaxivity values are respectively similar to those of monohydrated neutral and positively charged complexes with similar size, indicating the presence of one water molecule coordinated to the metal ion (q=1) in both systems.[36]

Table 1. Emission lifetimes and hydration numbers obtained for the complexes of L^1 and L^2.

	$\tau(H_2O)$ (ms)	$\tau(D_2O)$ (ms)	q^a
EuL^1	0.607	1.85	1.0
TbL^1	1.85	3.10	0.8
EuL^2	0.663	1.59	0.6
TbL^2	1.71	2.92	0.9

^{a} Obtained using the method proposed by Beeby, ref. 37.

The hydration numbers of the GdL^1 and GdL^2 complexes were further investigated by measuring the emission lifetimes of the excited $^5D_0$ of the Eu^{3+} and the $^5D_4$ of the Tb^{3+} analogues in solutions of the complexes in H$_2$O and D$_2$O (Table 1).[37] The lifetimes of both the Eu^{3+} and Tb^{3+} complexes are typical of mono-hydrated complexes,[38] and the hydration numbers calculated using the methodology proposed by Beeby[37] confirms the formation of q = 1 complexes.

4.2.3. Solution structure

The ^{1}H NMR spectra of the EuL^1 and EuL^2 complexes are rather well resolved, presenting paramagnetically shifted signals in the range ~ -20-35 ppm (Figure 1). The signals of the most shifted axial protons of the macrocyclic unit are observed in the range 27-34 ppm, which is typical of DOTA-like complexes adopting square antiprismatic geometries in solution.[39] The presence of a broad signal at ~10-12 ppm likely reflects the presence of a small amount of the twisted-square antiprismatic isomer. The spectra of the two complexes are very similar, indicating that they present very similar structures in solution. The corresponding ^{19}F NMR spectra present an intense resonance due to the CF$_3$ groups of the ligand at -62.1 and -61.5 ppm for EuL^1 and EuL^2, respectively, indicating the almost exclusive formation of SAP isomers (Figure S8, Annexe C). In the case of EuL^2 a broad resonance at -62.7 ppm identifies the presence of a small fraction of TSAP isomer, with an abundance < 10%. The presence of a single major ^{19}F NMR signal in EuL^1 implies a fast rotation on the NMR time scale about the NH-C bond of the phenyl group. The presence of a single ^{19}F NMR signal is important from the perspective of MRI to maximise the signal intensity provided by the probe.[40]

The emission spectra recorded for the EuL^1 and EuL^2 complexes in H$_2$O present the typical $^5D_0{\rightarrow}^7F_J$ transitions of Eu^{3+} (J = 0-4, Figure S9, Annexe C).[41] The spectra present a single and well-defined $^5D_0{\rightarrow}^7F_0$ transition, which suggests the presence of a single species in solution. The splitting of the two components observed for the $^5D_0{\rightarrow}^7F_1$ transition (158 and 185 cm^{-1} for EuL^1 and EuL^2, respectively), are characteristic of SAP isomers (i. e. 190 and 120 cm^{-1} for the SAP and TSAP isomers of EuDOTA$^-$, respectively).[42]
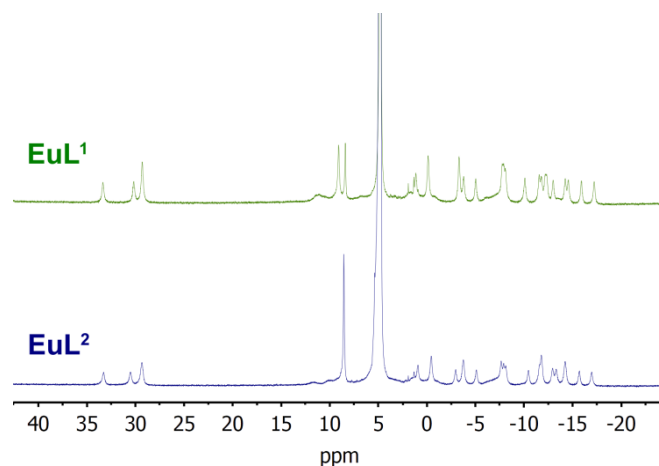
Figure 1. ^{1}H NMR spectra (D$_2$O, 300 MHz, 25 °C) of the EuL^1 and EuL^2 complexes (pH = 6.9 and 7.3, respectively).

The structure of the GdL^1 and GdL^2 complexes was also investigated by DFT calculations using well-established methods (see computational details below).[43] These calculations provide the expected SAP and TSAP isomers as local energy minima. The relative Gibbs free energies obtained with DFT favour the SAP isomer by ~1.9 kJ mol^{-1} for both complexes, which is in perfect agreement with the spectroscopic data. The Gd-O$_{water}$ distance calculated for the SAP isomer of GdL^2 (2.428 Å) is shorter than that of GdL^1 (2.458 Å), which is a consequence of the positive charge of the complex. This anticipates a slower exchange rate of the coordinated water molecule in GdL^2, as a stronger Gd-O$_{water}$ interaction implies a higher energy to reach the octacoordinated transition state following a dissociative mechanism.[44]

4.2.4. ^{1}H NMRD and ^{17}O NMR measurements

^{1}H NMRD profiles were recorded to gain insight regarding the different physicochemical parameters that affect the observed relaxivity on both gadolinium complexes. The NMRD profiles were measured at 10, 25 and 37 °C in the 0.01 to 70 MHz proton Larmor frequencies range. All profiles present shapes that are typical of small and rapidly rotating Gd^{3+} complexes, which generally show a plateau at low fields (< 1 MHz), a dispersion in the range 1-10 MHz, and a fairly constant relaxivity above 20 MHz.[45] The relaxivities of GdL^1 decrease when the temperature is increased, and this effect is typical of complexes in which relaxivity is mainly limited by fast rotation.
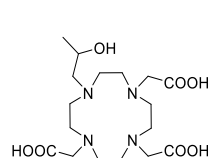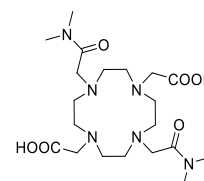
Scheme 3. Chemical structure of the ligands discussed in the text for comparative purposes.

On the other hand, the relaxivity of GdL^2 remains nearly constant with temperature on the range 10-37 ºC, indicating that a low water exchange is limiting relaxivity, particularly at low temperatures.[36,46] The relaxivities of the two complexes at 37 ºC and 20 MHz are however very similar.

^{17}O NMR transverse relaxation rates and chemical shifts were measured to obtain information of the exchange rate of the coordinated water molecule. The relaxation data obtained for GdL^1 present a maximum at ca. 52 ºC that signals a changeover from the slow exchange regime at low temperatures to fast exchange at higher temperatures. For GdL^2 $1/T_2$ increases with temperature over the whole range, indicating a slower water exchange rate. The fit of the transverse relaxation and chemical shift data was performed using the Swift-Connick equations, following a well-established methodology.[47] The scalar hyperfine coupling constants $A/\hbar$ obtained from the fits of the ^{17}O NMR data fall within the typical range observed for Gd^{3+} complexes,[43] confirming the reliability of the analysis. The water exchange rate determined for GdL^1 ($k_{ex}^{298} = 1.5 \times 10^6$ s^{-1}) is somewhat lower than that reported for GdDOTA$^-$.[45a] This is attributed to: i) the almost exclusive

presence of a SAP isomer in solution in GdL^1, as SAP isomers present water exchange rates 40- 800-fold lower than TSAP ones;[48-50] ii) The neutral charge of the GdL^1 complex compared to the negatively charged GdDOTA$^-$, as increasing the positive charge of the complex generally results in lower water exchange rates.[51] This effect is very evident when comparing the k_{ex}^{298} values of GdL^1 and GdL^2, as the two complexes are present in solution almost exclusively as SAP isomers.

The water exchange rate determined for GdL^1 is virtually identical to that reported for the SAP isomer of GdHPDO3A (Table 2, see also Scheme 3).[49] Furthermore, the k_{ex}^{298} value obtained for GdL^2 matches very well that reported for the SAP isomer of [Gd(DOTA-2DMA)]$^+$.[50] The corresponding water exchange rates reported for the minor TSAP isomers present in solution are 112×10^6 and 70.4×10^6 s^{-1} for GdHPDO3A and [Gd(DOTA-2DMA)]$^+$, respectively. These results confirm that the GdL^1 and GdL^2 complexes adopt SAP coordination environments, and that the charge of the complex plays a very important role in the water exchange of the coordinated water molecule.
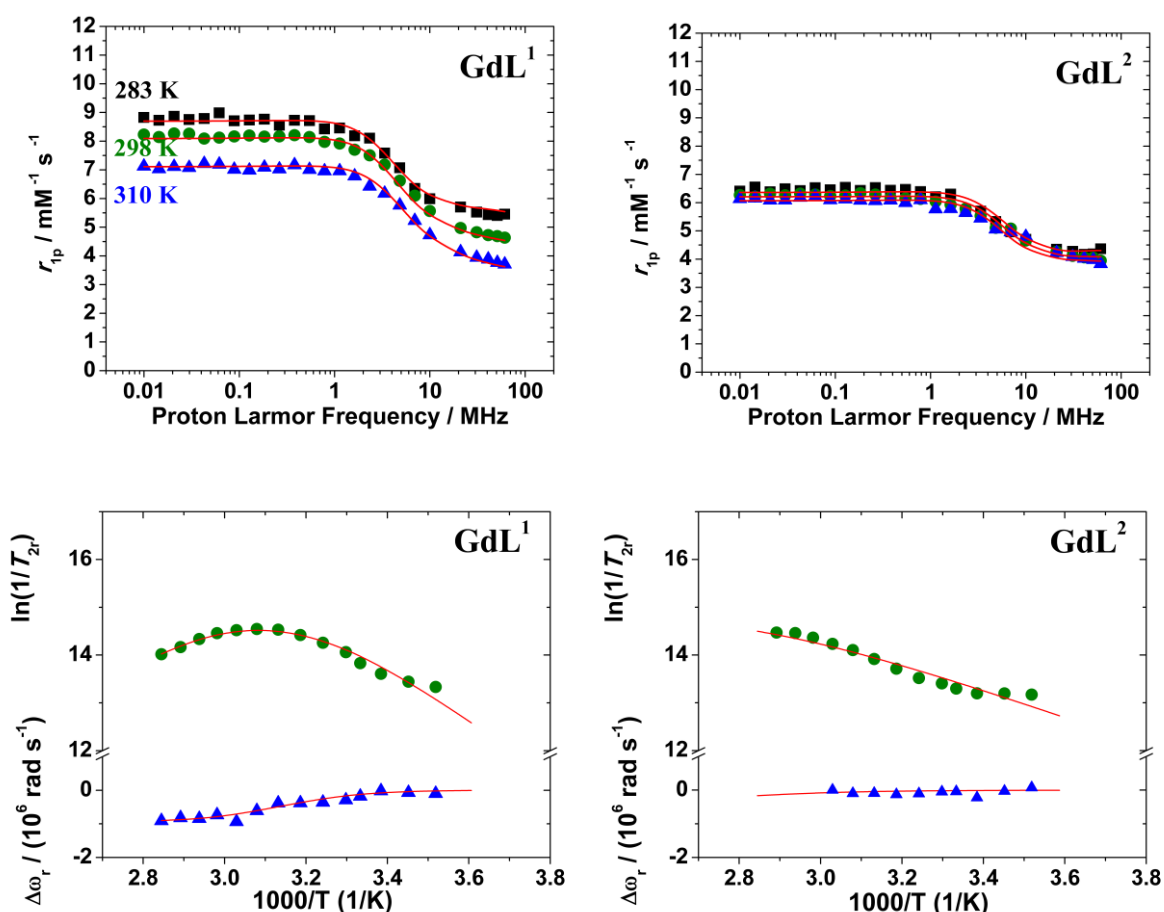
Figure 2. ^{1}H NMRD profiles at different temperatures (top) and ^{17}O transverse relaxation rates and chemical shifts (bottom, 11.75 T) recorded for GdL^1 and GdL^2. The solid lines correspond to the fits of the data as described in the text.

Table 2. Parameters obtained from the analysis of the ^{1}H NMRD and ^{17}O NMR data.

	GdL^1	GdL^2	GdHPDO3A^b	GdDOTA-2DMA^c	GdDOTA^d
r_{1p} (25/37 °C) / mM^{-1} s^{-1}	4.97/4.14	4.26/4.23	4.8/3.7		4.2/3.6
k_{ex}^{298}/ 10^6 s^{-1}	1.52 ± 0.17	0.73 ± 0.04	1.56	0.74	4.1
$\Delta H^{\ddagger}$ / kJ mol^{-1}	49.6 ± 3.5	22.9 ± 2.0	53	50^a	49.8
τ_R^{298} / ps	98.3 ± 2.8	94.0 ± 2	65		77
E_r / kJ mol^{-1}	15.6 ± 1.1	15.6^a			16.1
τ_V^{298}/ ps	24.4 ± 2.0	15.4 ± 0.4	8	9.7	11
E_v / kJ mol^{-1}	1.0^a	1.0^a			1.0^a
D_{GdH}^{298} / 10^{-10} m^2 s^{-1}	24.4 ± 0.1	24.4^a	22.2		22
E_{DGdH} / kJ mol^{-1}	24.5 ± 3.5	15.3± 0.8			20.2
Δ^2 / 10^{19} s^{-2}	2.9 ± 0.3	7.4 ± 0.4	9.9	1.1	1.6
A$_O$/ℏ/ 10^7 rad s^{-1}	-4.1 ± 0.3	-3.8 ± 0.3	-3.5		-3.7
r_{GdH}/Å	3.1^a	3.1^a	3.0^a		3.1^a
a_{GdH}/Å	4.0^a	4.0^a	3.8^a		3.5^a
q^{298}	1^a	1^a	1^a	1^a	1^a

^{a} Parameters fixed during the fitting procedure. ^{b} Data for the SAP isomer from reference 49. ^{c} Data obtained for the SAP isomer from reference 50. ^{d} Data from reference 45a.

The ^{1}H NMRD data was analysed using the standard Solomon-Bloembergen-Morgan theory for the inner-sphere contribution to relaxivity,[52] and Freed's model to account for the outer-sphere contribution.[53] The water exchange rates and their corresponding activation energies were set to the values obtained from ^{17}O NMR data. Following the standard procedure some of the parameters affecting relaxivity were fixed to typical values: the distance between the proton nuclei of the coordinated water molecule and the Gd^{3+} ion r_{GdH} was fixed to 3.1 Å,[54] the number of coordinated water molecules q was set to one, the distance of closest approach of an outer-sphere water molecule was taken as a_{GdH} = 4.0 Å, and the activation energy for the modulation of the zero-field splitting was fixed at E_v = 1 kJ mol^{-1}. In the case of GdL^2 two additional parameters had to be fixed to obtain reasonable fitted parameters as a consequence of the negligible temperature dependence of r_{1p}: the diffusion coefficient D_{GdH}^{298} was fixed to 24.4 × 10^{-10} m^2 s^{-1} and the activation energy for the rotational correlation time E_r was set to 15.6 kJ mol^{-1}. The rotational correlation times (τ_R^{298}) obtained from the fits of the data (~100 ps) are typical of small Gd^{3+} complexes. The same holds for the parameters describing the relaxation of the electron spin (the mean square zero-field-splitting energy, Δ^2, and its correlation time τ_v), which take values that are similar to those determined for Gd^{3+} complexes of DOTA derivatives (Table 2).

4.2.5. ^{19}F measurements

The ^{19}F NMR spectra of GdL^1 and GdL^2 present a single broad resonance at -63.08 and -61.25 ppm, respectively (Figure 3). The signal is clearly broader for GdL^1 as compared to GdL^2. The longitudinal and transverse relaxation rates measured at 7.05, 9.4 and 11.75 T are in line with the trend observed for the linewidths, with GdL^1 being characterised by faster relaxation rates (Figure 3, Table 3). The ^{19}F relaxation rates of Gd^{3+} complexes are dominated by the dipolar contribution, as given by:[55]

$$R_1 = \frac{2}{15} \frac{\gamma_I^2 g^2 \mu_B^2}{r_{GdF}^6} S(S+1) \left(\frac{\mu_0}{4\pi}\right)^2 \left[7 \frac{\tau_{C2}}{1+\omega_S^2\tau_{C2}^2} + 3 \frac{\tau_{C1}}{1+\omega_I^2\tau_{C1}^2}\right] \quad (1)$$

$$R_2 = \frac{1}{15} \frac{\gamma_I^2 g^2 \mu_B^2}{r_{GdF}^6} S(S+1) \left(\frac{\mu_0}{4\pi}\right)^2 \left[13 \frac{\tau_{C2}}{1+\omega_S^2\tau_{C2}^2} + 3 \frac{\tau_{C1}}{1+\omega_I^2\tau_{C1}^2} + 4\tau_{C1}\right] \quad (2)$$

In these equations S is the electron spin (S = 7/2 for Gd^{3+}), γ_I is the nuclear gyromagnetic ratio, g is the electron g factor, μ_B is the Bohr magneton, r_{GdF} is the nuclear-spin-electron-spin distance and ω_I and ω_S are the nuclear and electron Larmor frequencies. τ_{C1} and τ_{C2} are given by:

$$\frac{1}{\tau_{Ci}} = \frac{1}{\tau_R} + \frac{1}{T_{ie}} \qquad i = 1, 2 \qquad (3)$$

At high magnetic fields $T_{1e} >> \tau_R$, so that τ_R is the correlation time that dominates in Eq (3). Thus, the ^{19}F relaxation data were fitted to Eqs (1) and (2), providing the values of τ_R and r_{GdF} shown in Table 4. The longer rotational correlation time obtained for GdL^2 can be ascribed to the higher molecular weight of this complex compared to GdL^1. It is worth noting that the rotational correlation times shown in Table 4 correspond to the rotation of the Gd···F vector. Thus, it is not surprising that they are considerably longer than those obtained from ^{1}H NMRD data (Table 2), which correspond to the rotation of the Gd···H vector involving the proton nuclei of the coordinated water molecule. The local mobility of the coordinated water molecule is responsible for the shorter τ_R values evaluated from ^{1}H NMRD. Longer rotational correlation times were for instance obtained from ^{17}O NMR measurements for the Gd···O vector of coordinated water molecules, compared with those obtained with ^{1}H NMRD.[56]

The ^{1}H NMRD data was analysed using the standard Solomon-Bloembergen-Morgan theory for the inner-sphere contribution to relaxivity,[52] and Freed's model to account for the outer-sphere contribution.[53] The water exchange rates and their corresponding activation energies were set to the values obtained from ^{17}O NMR data. Following the standard procedure some of the parameters affecting relaxivity were fixed to typical values: the distance between the proton nuclei of the coordinated water molecule and the Gd^{3+} ion r_{GdH} was fixed to 3.1 Å,[54] the number of coordinated water molecules q was set to one, the distance of closest approach

of an outer-sphere water molecule was taken as a_{GdH} = 4.0 Å, and the activation energy for the modulation of the zero-field splitting was fixed at E_v = 1 kJ mol^{-1}. In the case of GdL^2 two additional parameters had to be fixed to obtain reasonable fitted parameters as a consequence of the negligible temperature dependence of r_{1p}: the diffusion coefficient D_{GdH}^{298} was fixed to 24.4 × 10^{-10} m^2 s^{-1} and the activation energy for the rotational correlation time E_r was set to 15.6 kJ mol^{-1}. The rotational correlation times (τ_R^{298}) obtained from the fits of the data (~100 ps) are typical of small Gd^{3+} complexes. The same holds for the parameters describing the relaxation of the electron spin (the mean square zero-field-splitting energy, Δ^2, and its correlation time τ_v), which take values that are similar to those determined for Gd^{3+} complexes of DOTA derivatives (Table 2).

Figure 3. Top: longitudinal (R_1, open symbols) and transverse (R_2, closed symbols) relaxation rates recorded for GdL^1 and GdL^2. The solid lines correspond to the fits of the data as described in the text. Bottom: ^{19}F NMR spectra (7.05 T, 25 ^{o}C) of GdL^1 and GdL^2. All measurements were obtained using 5 mM concentrations based on Gd^{3+}.

Table 3. ^{19}F NMR longitudinal (T_1) and transverse (T_2) relaxation times obtained at different magnetic fields (25 °C).

	B (T)	T_1 (ms)	T_2 (ms)	T_2/T_1
GdL^1	7.05	0.80	0.69	0.86
	9.4	0.87	0.71	0.82
	11.75	0.91	0.71	0.78
GdL^2	7.05	2.00	1.60	0.80
	9.4	2.31	1.71	0.74
	11.75	2.62	1.69	0.65

The r_{GdF} distance obtained from ^{19}F NMR data for GdL^1 (7.4 Å) is considerably shorter than that calculated for GdL^2 (9.1 Å), as would be expected considering the different position of the CF$_3$ groups on the phenyl ring(s) of the ligand. This relatively small distance variation (1.7 Å) causes an important effect on the observed R_1 and R_2 values, which is mainly related to the inverse sixth power relationship of r_{GdF} with R_1 and R_2. The DFT structure described above for GdL^2 presents rather different r_{GdF} distances involving the CF$_3$ groups in *cis* (average at 6.83 Å) and *trans* (average at 9.75 Å) with respect to the amide oxygen atom. Thus, the r_{GdF} distance was estimated by averaging the $(1/r_{GdF})^6$ values obtained with DFT calculations, resulting in r_{GdF} = 9.4 Å. The dependence of both R_1 and R_2 on $(1/r_{GdF})^6$ implies that those F nuclei with shorter r_{GdF} distances provide a higher contribution to the observed relaxation rates. Following the same procedure, the DFT structure gives r_{GdF} = 7.3 Å for GdL^1. These values are in excellent agreement with those obtained from ^{19}F relaxation data, which confirms the reliability of the analysis.

Table 4. Parameters obtained from the analysis of the ^{19}F NMR longitudinal and transverse relaxation data.

	τ_{RF} (ps)	r_{GdF} (Å) ^{a}	r_{GdF} (Å) ^{b}
GdL^1	166 ± 19	7.4 ± 0.1	7.3
GdL^2	237 ± 16	9.1 ± 0.1	9.4

^{a}Obtained from relaxation data. ^{b}Obtained from DFT calculations.
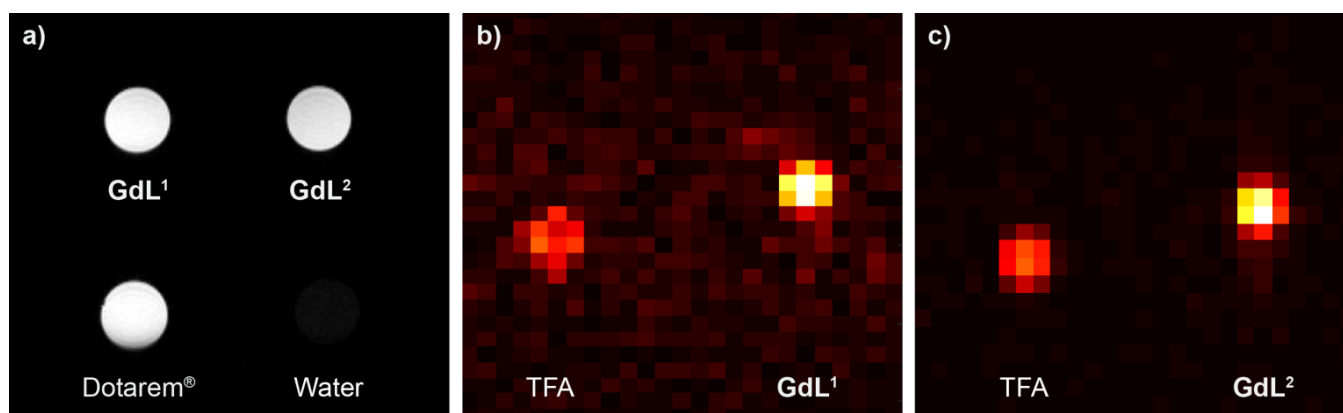
Figure 4. ^{1}H and ^{19}F MRI on tube phantoms (5 mM complex, 7.05 T, RT). a) ^{1}H MRI of GdL$^{1-2}$ along with those obtained for an equimolar amount of GdDOTA$^-$ (Dotarem$^®$) and pure water; b) ^{19}F MRI of GdL^1 and TFA (10 mM) and c) ^{19}F MRI of GdL^2 and TFA (10 mM).

4.2.6. ¹H and ¹⁹F MRI studies

The potential of GdL$^{1-2}$ for their use as dual ¹H / ¹⁹F MRI probes was assessed by means of MRI on tube phantoms at 7.05 T magnetic field, using 5 mM buffered solutions of the complexes (equivalent to 30 mM fluorine). For ¹H MRI, the phantom study consisted of GdL^1, GdL^2, GdDOTA⁻ (Dotarem®) and water, using the latter two samples as controls (Figure 4a). All Gd-containing samples had the same concentration of this paramagnetic ion (5 mM), resulting in comparable MR signal intensities upon performing the T_1-weigthed MRI. This result is indeed expected, given the similar r_{1p} values of GdL$^{1-2}$ (see above) and GdDOTA⁻.[57]

For ¹⁹F MRI, separate experiments were performed for GdL^1 and GdL^2, respectively (Figure 4b,c). Namely, due to the difference in their ¹⁹F T_1 and T_2 relaxation times (Table 3), optimisation of ¹⁹F MRI experimental parameters was performed first for achieving the maximal SNR to the given set of ¹⁹F T_1 and T_2 (see ESI), and thus used different flip angles for the utilised fast low angle single shot (FLASH) pulse sequence. For comparison, in each experiment was used a tube with a solution of TFA (10 mM), which contained the same concentration in fluorine as in the paramagnetic complex (30 mM). The resulting ¹⁹F MR images indicated the affirmative properties of these complexes, especially GdL^2. Namely, the obtained signal-to-noise ratio (SNR) for GdL^2 after 1 hour acquisition time was 103, which was over 50% higher than that of TFA (67). Concurrently, a lower SNR was observed in the experiment with GdL^1, again being doubled relative to TFA (SNR = 22 and 11 for GdL^1 and TFA, respectively). If the SNR=2 is taken as the border-line detection limit of the measurement, we estimate detection limits of ~450 and ~100 μM for GdL^1 and GdL^2, respectively. These estimates suggest an improvement in sensitivity of the measurement with almost twice lower GdL^2 concentration needed for detection compared to the previously reported Gd³⁺ complex containing a fluorinated aryl-phosphonate group.[58] On one hand, both GdL^1 and GdL^2 show that PRE effect of Gd³⁺ reduces the ¹⁹F relaxation times to significant extent, thus resulting in greater SNR values in ¹⁹F MRI experiments for paramagnetic probes relative to diamagnetic samples (TFA). On the other hand, different structural properties of GdL^1 and GdL^2 are clearly reflected on the final ¹⁹F MRI results as well. One should note that a shorter Gd···F distance in GdL^1 results in much stronger PRE effect and thus shorter ¹⁹F T_1 and T_2 relaxation times, with T_2 being over 6 times shorter in GdL^1 than in GdL^2 (Table 3). Consequently, such dramatic shortening of T_2 leads to substantial loss of signal in the ¹⁹F MRI experiments of GdL^1 relative to GdL^2. For GdL^2, the PRE effect of the adjacent Gd³⁺ also shortens both ¹⁹F T_1 and T_2; however, the slightly longer Gd···F distance this time provides an affirmative T_2/T_1 ratio, which is reflected in ¹⁹F MR images with very high SNR. Indeed, considering the obtained SNR values, one could significantly reduce the acquisition times for GdL^2 to the level of 5-10 min, still expecting the SNR>10 in the analogous ¹⁹F MRI experiment.

4.3. Experimental section

4.3.1. Materials and methods

DO3AtBu and DO2AtBu were purchased from CheMatech (Dijon, France). All other reagents and solvents were commercial and used without further purification. ¹H, ¹⁹F and ¹³C NMR spectra were recorded on Bruker Avance 300 MHz, Bruker Avance III HD 400 MHz and Bruker Avance 500 MHz spectrometers.

High-resolution electrospray-ionisation time-of-flight ESI-TOF mass spectra were recorded using a LC-Q-q-TOF Applied Biosystems QSTAR Elite spectrometer in positive and negative mode. Elemental analyses were accomplished on a ThermoQuest Flash EA 1112 elemental analyser. Medium performance liquid chromatography (MPLC) was carried out using a Puriflash XS 420 instrument equipped with a reverse-phase Puriflash 15C18HP column (60 Å, spherical 15 μm, 20 g) and UV-DAD detection at 210 and 254 nm, and operating at a flow rate of 10 mL/min. Aqueous solutions were lyophilised using a Telstar Cryodos-80 apparatus.

4.3.2. Synthetic procedure

2-chloro-N-(3,5-di-trifluoromethyl-phenyl)acetamide (1a). A solution of chloroacetyl chloride (11.5 mmol) in acetic acid (5 mL) was added dropwise to a mixture of 3,5-bis(trifluoromethyl)aniline (9.78 mmol) in acetic acid (35 mL) at 0 °C. The reaction mixture was maintained at room temperature for an additional 4 hours. Subsequently it was slowly poured into 100 mL of ice water. The aqueous solution was extracted with CH₂Cl₂ (4x100 mL). The combined organic phase was dried over anhydrous Na₂SO₄, filtered and the solvent was evaporated to furnish a solid residue. Yield: 92%. ¹H NMR (solvent CDCl₃, 298 K, 400 MHz) δ$_H$ (ppm): 8.52 (s, 1H, NH), 8.07 (s, 2H, CH$_{Ar}$), 7.67 (s, 1H, CH$_{Ar}$), 4.23 (s, 2H, CH₂). ¹³C NMR (solvent CDCl₃, 298 K, 101 MHz) δ$_C$ (ppm): 164.4, (quaternary, CO), 138.1 (quaternary, C$_{Ar}$), 133.1-132.1 (quaternary, CF₃), 127.0 (tertiary, CH$_{Ar}$), 124.3 (tertiary, CH$_{Ar}$), 121.6 (quaternary, CH$_{Ar}$), 119.9 , 118.9, 118.6, 118.6, 118.6, 42.7 (secondary, CH₂). ¹⁹F NMR (solvent CDCl₃, 298 K, 376 MHz) δ$_F$ (ppm): -63.09. Mass spectrometry (ESI⁻) m/z (%BPI): 304.00 (100) ([C₁₀H₅ClF₆NO]⁻); 339.98 (7) (C₁₀H₆ClF₆NO[Cl]⁻). HR-MS (ESI⁻) m/z: [M]⁻, calculated: 303.9958, found: 303.9959.

2-chloro-N-(4-(trifluoromethyl)phenyl)acetamide (1b). Chloroacetyl chloride (12.0 mmol) in dry CH₂Cl₂ (20 mL) was slowly added dropwise to a mixture of 4-(trifluoromethyl)aniline (10.0 mmol) and NaHCO₃ (25.5 mmol) in dry CH₂Cl₂ (30 mL) at 0 °C. The reaction mixture was stirred at 0 °C for an additional 4 hours. At a subsequent stage it was slowly poured into 80 mL of water. The aqueous solution was extracted with CH₂Cl₂ (8x150 mL). The combined organic layer was washed with brine and dried over anhydrous Na₂SO₄. The solvent was evaporated to dryness to afford a solid residue. Yield: 97%. ¹H NMR (solvent CDCl₃, 298 K, 300 MHz) δ$_H$ (ppm): 8.35 (s, 1H, NH), 7.71-7.61 (dd, 4H, CH$_{Ar}$), 4.22 (s, 2H, CH₂). ¹³C NMR (solvent CDCl₃, 298 K, 75 MHz) δ$_C$ (ppm): 164.0 (quaternary, CO), 139.8 (quaternary, C$_{Ar}$), 126.4 (tertiary, C$_{Ar}$), 126.4 (tertiary, CH$_{Ar}$), 119.7 (quaternary, CH$_{Ar}$), 42.8 (secondary, CH₂). ¹⁹F NMR (solvent CDCl₃, 298 K, 282 MHz) δ$_F$ (ppm): -62.26. Mass spectrometry (ESI⁻) m/z (%BPI): 236.02 (100) ([C₉H₆ClF₃NO]⁻); 272.00 (6) (C₉H₇ClF₃NO[Cl]⁻). HR-MS (ESI⁻) m/z: [M]⁻, calculated: 236.0095, found: 236.0099.

General procedure for the preparation of the ligands: The cyclen derivative was dissolved in CH₃CN (25 mL) under basic conditions. A solution of the corresponding 2-chloro-N-substituted-acetamide in CH₃CN (20 mL) was added dropwise to the mixture at ambient temperature. The reaction was heated at 45 °C for several days, until the alkylation was completed. The reaction mixture was

removed from heat and allowed to cool to room temperature, filtered and reduced to dryness *in vacuo*. The yellow oil was redissolved in CH_2Cl_2 and washed with water. The organic layer was concentrated under vacuum pressure to afford a yellowish oil. The product was purified by neutral alumina chromatography, eluting with $CHCl_3$ in gradient up to 5% in MeOH to yield a yellowish foam. Final ligands H_3L^1 and H_2L^2 were achieved by deprotection of the *tert*-butyl groups with formic acid (5 mL), stirred at reflux for 48 h. Subsequently, the acid was removed and the residue was washed several times with water (5x10 mL). The product was redissolved in water and lyophilised to achieve a yellowish solid.

1,4,7-Tris(tert-butoxycarboxymethyl)- 10-((3,5-(trifluoromethylphenyl)acetamide)-1,4,7,10-tetraazacyclododecane (2a). DO3A*t*Bu (0.526 g, 1.02 mmol), 2-chloro-N-(3,5-(trifluoromethyl)phenyl)acetamide (0.360 g, 1.175 mmol, 1.15 equiv), K_2CO_3 (0.353 g, 2.55 mmol, 2.5 equiv), stirred at 45 °C during 9 days. Yellow foam (0.645 g, 81%). ¹H NMR (300 MHz, $CDCl_3$): δ_H (ppm): 12.12 (s, 1H, NH), 8.36 (s, 2H, CH_{Ar}), 7.45 (s, 1H, CH_{Ar}), 3.80 (s, 2H, CH_2), 3.51-1.92 (m, 22H, CH_2), 1.61 (s, 9H, CH_3), 1.46-1.37 (s, 18H, CH_3). ¹³C NMR (solvent $CDCl_3$, 298 K, 75 MHz) δ_C (ppm): 172.6 (quaternary, CO), 172.3 (quaternary, CO), 151.9 (quaternary, CO), 140.8 (quaternary, CH_{Ar}), 131.5 (tertiary, CH_{Ar}), 120.5 (quaternary, CF_3), 116.2 (tertiary, CH_{Ar}), 116.1 (tertiary, CH_{Ar}), 82.4 (quaternary, CCH_3), 56.8 (secondary, CH_2), 55.8 (secondary, CH_2), 55.5 (secondary, CH_2), 29.7 (secondary, CH_2), 27.9 (primary, CH_2), 27.8 (primary, CH_2). ¹⁹F NMR (solvent $CDCl_3$, 298 K, 282 MHz) δ_F (ppm): -63.05. Mass spectrometry (ESI⁺) *m/z* (%BPI): 806.39 (100) ($[C_{36}H_{55}F_6N_5NaO_7]^+$); 784.41 (2) ($[C_{36}H_{56}F_6N_5O_7]^+$).

Triacetic 1,4,7-Tris(carboxymethyl)- 10-((3,5-(trifluoromethylphenyl)acetamide)-1,4,7,10-tetraazacyclododecane acid (H₃L¹). Brownish solid (0.5060 g, quantitative). ¹H NMR (300 MHz, D_2O): δ_H (ppm): 8.36 (s, 1H, CH_{Ar}), 8.06 (s, 2H, CH_{Ar}), 7.84 (s, 1H, NH), 3.89-3.16 (m, 24H, CH_2). ¹³C NMR (solvent D_2O, 298 K, 75 MHz) δ_C (ppm): 174.3 (quaternary, CO), 172.6 (quaternary, CO), 140.0 (quaternary, HN- C_{Ar}), 133.7-132.8 (quaternary, CF_3), 128.2 (quaternary, C_{Ar}), 126.6 (tertiary, CH_{Ar}), 123.0 (quaternary, CF_3), 120.2 (tertiary, CH_{Ar}), 59.1 (secondary, CCH_3), 54.5 (secondary, CH_2), 52.5 (secondary, CH_2), 51.9 (secondary, CH_2), 31.9 (primary, CH_2). ¹⁹F NMR (solvent D_2O, 298 K, 282 MHz) δ_F (ppm): -62.66. Mass spectrometry (ESI⁺) *m/z* (%BPI): 638.20 (96) ($[C_{24}H_{31}F_6N_5NaO_7]^+$); 676.15 (63) ($[C_{24}H_{30}F_6KN_5NaO_7]^+$), 698.13 (100) ($[C_{24}H_{29}F_6KN_5Na_2O_7]^+$); 714.11 (67) ($[C_{24}H_{29}F_6K_2N_5NaO_7]^+$. HR-MS (ESI⁺) m/z: [M+Na]⁺, calculated: 638.2019, found: 638.2014.

1,7-bis(tert-butoxycarboxymethyl)- 4,10-((4-(trifluoromethylphenyl)acetamide)-1,4,7,10-tetraazacyclododecane (2b). Cyclen derivative DO2A*t*Bu (0.117 g, 0.2928 mmol), 2-chloro-N-(4-(trifluoromethyl)phenyl)acetamide (0.165 g, 0.6978 mmol, 2.4 equiv), K_2CO_3 (0.2014 g. 5 equiv). The reaction was heated to reflux for 9 days. Yellow crude solid (0.235 g, quantitative). ¹H NMR (300 MHz, $CDCl_3$): δ_H (ppm): 9.73 (s, 2H, NH), 7.86-7.84 (d, 4H, CH_{Ar}), 7.32-7.30 (d, 4H, CH_{Ar}), 3.47-2.07 (m, 22H, CH_2), 1.32 (s, 9H, CH_3), 1.27 (s, 9H, CH_3). ¹³C NMR (solvent $CDCl_3$, 298 K, 75 MHz) δ_C (ppm): 171.6 (quaternary, CO), 170.8 (quaternary, CO), 141.6 (quaternary, C_{Ar}), 129.5 (tertiary, CH_{Ar}), 125.9-124.6 (quaternary, CF_3), 122.3 (tertiary, CH_{Ar}), 119.7 (secondary, CH_2), 119.3 (secondary, CH_2), 118.7 (secondary, CH_2), 116.5 (secondary, CH_2), 81.8 (quaternary, CCH_3),), 81.5

(quaternary, CCH_3), 58.7 (secondary, CH_2), 58.4 (secondary, CH_2), 57.2 (secondary, CH_2), 56.6 (secondary, CH_2), 52.1 (secondary, CH_2), 27.9 (primary, CH_2). ¹⁹F NMR (solvent $CDCl_3$, 298 K, 282 MHz) δ_F (ppm): -62.33. Mass spectrometry (ESI) m/z (%BPI): 825.38 (100) ($[C_{38}H_{52}F_6N_6NaO_6]^+$); 803.40 (2) ($[C_{38}H_{53}F_6N_6O_6]^+$).

Diacetic 1,7-Bis(carboxymethyl)- 10-((4-(trifluoromethylphenyl)acetamide)-1,4,7,10-tetraazacyclododecane acid (H₂L²). Light yellow solid (0.202 g, quantitative). ¹H NMR (300 MHz, D_2O): δ_H (ppm): 8.42 (s, 2H, CH_{Ar}), 7.66 (s, 2H, NH), 7.41 (s, 6H, CH_{Ar}), 3.53-2.89 (m, 24H, CH_2). ¹³C NMR (solvent D_2O, 298 K, 101 MHz) δ_C (ppm): 172.1 (quaternary, CO), 171.0 (quaternary, CO), 140.1 (quaternary, C_{Ar}), 125.9 (tertiary, CH_{Ar}), 125.4 (quaternary, CF_3), 120.9 (tertiary, CH_{Ar}), 57.2 (quaternary, CCH_3), 55.1 (secondary, CH_2), 51.9 (secondary, CH_2), 50.4 (secondary, CH_2). ¹⁹F NMR (solvent D_2O, 298 K, 282 MHz) δ_F (ppm): -62.05. Mass spectrometry (ESI⁺) *m/z* (%BPI): 713.25 (100) ($[C_{30}H_{36}F_6N_6NaO_6]^+$); 751.20 (40) ($[C_{30}H_{35}F_6KN_6NaO_6]^+$), 729.22 (25) ($[C_{30}H_{36}F_6KN_6O_6]^+$), 691.27 (17) ($[C_{30}H_{37}F_6N_6O_6]^+$). HR-MS (ESI⁺) m/z: [M+Na]⁺, calculated: 713.2492, found: 713.2503.

General procedure for the preparation of the complexes: The corresponding ligand H_3L^1 or H_2L^2 was solved in *n*-butanol in the presence of base (DIPEA) and the solution was homogenised with ultrasound bath assistance. The corresponding hydrated $LnCl_3$ (Ln = Eu, Gd or Tb) were added in solid state to the mixture and heated at 112 °C for 6 h. Subsequently the mixture was allowed to cool down and the solvent was removed by the use of the rotary evaporator to achieve an orange crude. The reaction mixture was purified by reverse-phase medium performance liquid chromatography (MPLC). For the neutral complexes, the purification method was carried out in gradient of solvent B (CH_3CN, 10 to 30%) in solvent A (H_2O). For the charged complexes, the purification was performed in gradient of solvent B (0.01% Et_3N in CH_3CN, 5 to 15%) in solvent A (0.01% Et_3N in H_2O). The fractions containing the complexes were combined and the solvent was removed *in vacuo*. The final product was redissolved in water and lyophilised to furnish the final complexes.

EuL¹. White solid (0.0309 g, 64%). Mass spectrometry (ESI⁺) m/z (%BPI): 788.10 (100) ($[C_{24}H_{28}N_5O_7F_6NaEu]^+$). HR-MS (ESI⁺) m/z: [M+Na]⁺, calculated: 788.0997, found: 788.0994.

GdL¹. White solid (0.0282 g, 56%). Mass spectrometry (ESI⁺) m/z (%BPI): 793.10 (100) ($[C_{24}H_{28}N_5O_7F_6NaGd]^+$). HR-MS (ESI⁺) m/z: [M+Na]⁺, calculated: 793.1026, found: 793.0992.

TbL¹. White solid (0.0479 g, 54%). Mass spectrometry (ESI⁺) m/z (%BPI): 794.10 (100) ($[C_{24}H_{28}N_5O_7F_6NaTb]^+$). HR-MS (ESI⁺) m/z: [M+Na]⁺, calculated: 794.1038, found: 794.1045.

EuL². White solid (0.0291 g, 31%). Mass spectrometry (ESI⁺) m/z (%BPI): 841.17 (100) ($[C_{30}H_{34}N_6O_6F_6Eu]^+$). HR-MS (ESI⁺) m/z: [M]⁺, calculated: 841.1650, found: 841.1651.

GdL². White solid (0.0286 g, 31%). Mass spectrometry (ESI⁺) m/z (%BPI): 846.17 (100) ($[C_{30}H_{34}N_6O_6F_6Gd]^+$). HR-MS (ESI⁺) m/z: [M]⁺, calculated: 846.1679, found: 846.1673.

TbL². White solid (0.0517 g, 56%). Mass spectrometry (ESI⁺) m/z (%BPI): 847.17 (100) ($[C_{30}H_{34}N_6O_6F_6Tb]^+$). HR-MS (ESI⁺) m/z: [M]⁺, calculated: 847.1692, found: 847.1698.

4.3.3. Relaxometric measurements

Relaxivities of the Gd³⁺ complexes were measured at 298 K and 300 MHz using a Bruker Advance III 300 MHz spectrometer and aqueous

solutions buffered at pH 7.4 (0.05 M HEPES) containing 10% D$_2$O for locking purposes. Proton NMRD profiles were measured at 10, 25 and 37 °C over a continuum of magnetic fields from 0.0002 to 0.25 T (corresponding to 0.01-10 MHz proton Larmor frequencies) on a fast field-cycling Stelar SmarTracer relaxometer (Mede, Pv, Italy). The relaxometer operates under computer control with an absolute uncertainty in $1/T_1$ of ± 1%. The temperature control was carried out using a Stelar VTC-91 airflow heater equipped with a calibrated copper–constantan thermocouple (uncertainty of ± 0.1 K). Data points at higher field strengths were measured on a Stelar Spinmaster relaxometer in the range from 0.5 to 1.5 T (20-60 MHz proton Larmor frequencies) equipped with a Bruker WP80 electromagnet adapted to variable-field measurements. A Bruker Advance III spectrometer (11.75 T) equipped with a 5 mm probe and standard temperature control unit was used to perform ^{17}O NMR measurements. Samples in aqueous solution used for the measurements contained 2.0% of the ^{17}O isotope (Cambridge Isotope). The observed transverse relaxation rates were established from the signal width at half-height. The exact concentrations of all solutions used for ^{1}H relaxivity and ^{17}O NMR measurements were determined by the bulk magnetic susceptibility (BMS) method.[59]

4.3.4. Computational details

All the calculations were carried out by using the Gaussian 09 package (Revision E.01).[60] Full-geometry optimisations of the [GdL^1] and [GdL^2]$^+$ complexes were performed in aqueous solution by employing DFT within the hybrid meta-generalised gradient approximation (hybrid meta-GGA) with the TPSSh exchange-correlation functional.[61] The large-core quasi-relativistic effective core potential (LCRECP) developed by Dolg and and co-workers and the associated [5 s4p3d]-GTO valence-basis set was employed for the lanthanides,[62] whereas the ligand atoms were described by using the standard 6–31G(d,p) basis set. The stationary points found on the potential-energy surfaces as a result of geometry optimisations were tested to represent energy minima rather than saddle points by using frequency analysis. Solvent effects were included by using the integral-equation formalism variant of the polarizable continuum model (IEFPCM).[63]

4.3.5. Magnetic resonance imaging

MRI measurements on tube phantoms were performed on Bruker BioSpec 70/30 USR magnet (software version Paravision 5.1) using a Bruker volume coil (RF RES 300 ^{1}H 075/040 QSN TR). ^{1}H and ^{19}F MR images where acquired using Fast Low Angle Single Shot (FLASH) pulse sequence. ^{1}H phantom consisted of 4 x 400 μL vials containing 5 mM of GdL^1, GdL^2, GdDOTA$^-$ (Dotarem®) and water. ^{19}F phantom consisted of a pair of such vials containing either 5 mM of GdL^1 or GdL^2 with equimolar concentration of TFA (calculated per fluorine atoms) as a reference.

 ^{1}H MR image was acquired using following parameters: field of view (FOV) = 31.8 x 31.8 mm^2, matrix size (MTX) = 212 x 212, slice thickness 0.5 mm, flip angle (FA) = 90°, repetition time (TR) = 10 ms, echo time (TE) = 2.746 ms, number of excitations (NEX) = 10, and total acquisition time (TA)= 21.2 sec. ^{19}F MR imaging parameters were: FOV = 32 x 32, MTX = 32 x 32, slice thickness 5 mm, FA = 89° (GdL^1)/ 78° (GdL^2), TR = 3.2 ms, TE = 1.01 ms, NEX = 35156, TA = 60

min. The imaging parameters TR and FA were optimised using Eq. (4).[64]

$$SNR = \frac{\sin(FA)\left(1-\exp^{-\frac{TR}{T_1}}\right)}{\left(1-\exp^{-\frac{TR}{T_1}\cos(FA)}\right)}\sqrt{TR} \qquad (4)$$

4.4. Conclusions

Two cyclen-based Gd^{3+} complexes were designed and synthesised as potential dual ^{1}H/^{19}F MRI contrast agents. The presence of a coordinated water molecule yields ^{1}H relaxivities comparable to those of the commercially available contrast agent GdDOTA$^-$ (Dotarem®), though the slower water exchange in the bis-amide derivative results in a somewhat lower relaxivity. An interesting feature of these complexes is their presence in solution as a single major species, which was characterised as the square antiprismatic (SAP) isomer. The shorter Gd···F distance determined for GdL^1 (7.4 Å) results in considerably shorter T_1 and T_2 relaxation times compared with GdL^2 (Gd···F = 9.1 Å). Phantom studies evidenced that the slightly longer transverse relaxation of GdL^2 yields good SNRs compared to GdL^1. Thus, a Gd···F distance in the range 9-10 Å appears to be optimal for the design of efficient Gd^{3+}-based MRI probes. The study reported here paves the way for the preparation of genuine ^{1}H/^{19}F MRI probes characterised by high stability and inertness.

4.5. Notes

The work presented in this chapter has been published in the following article:

4.6. References

1   B.-T. Doan, S. Meme, J.-C. Beloeil in The Chemistry of Contrast Agents in Medical Magnetic Resonance Imaging, (Eds.: A. Merbach, L. Helm, E. Toth), John Wiley & Sons, Chichester, 2013, pp. 1-23.

2   J. Wahsner, E. M. Gale, A. Rodriguez-Rodriguez, P. Caravan, *Chem. Rev.* 2019, DOI: 10.1021/acs.chemrev.8b00363.

3   S. Faulkner, O. A. Blackburn, in *The Chemistry of Molecular Imaging*, (Eds.: N. Long, W.-T. Wong), John Wiley & Sons, Hoboken, 2015, pp. 179-197.

4   L. M. De León-Rodríguez, A. F. Martins, M. C. Pinho, N. M. Rofsky, A. D. Sherry, *J. Magn. Reson. Imaging* 2015, **42**, 545.

5   H. U. Rashid, M. A. U. Martines, J. Jorge, P. M. de Moraes, M. N. Umar, K. Khan, H. U. Rehman, *Bioorg. Med. Chem.* 2016, **24**, 5663.

6   (a) M. Rogosnitzky, S. Branch, *Biometals* 2016, **29**, 365. (b) L. Caschera, A. Lazzara, L. Piergallini, D. Ricci, B. Tuscano, A. Vanzulli, *Pharmacol. Res.* 2016, **110**, 65.

7   I. A. Dekkers, R. Roos, A. J. van der Molen, *Eur. Radiol.* 2018, **28**, 1579.

8   Z. Baranyai, Z. Palinkas, F. Uggeri, A. Maiocchi, S. Aime, E. Brücher, *Chem. Eur. J.* 2012, **18**, 16426.

9   J. R. Morrow, E. Toth, *Inorg. Chem*. 2017, **56**, 6029.

10 (a) B. Drahos, I. Lukes, E. Toth, *Eur. J. Inorg. Chem.* 2012, 1975. (b) M. Kueny-Stotz, A. Garofalo and D. Felder-Flesch, *Eur. J. Inorg. Chem.* 2012, 1987. (c) G. S. Loving, S. Mukherjee and P. Caravan, *J. Am. Chem. Soc.,* 2013, **135**, 4620. (d) E. M. Gale, S. Mukherjee, C. Liu, G. S. Loving and P. Caravan, *Inorg. Chem.,* 2014, **53**, 10748. (e) M. Regueiro-Figueroa, G. A. Rolla, D. Esteban-Gomez, A. de Blas, T. Rodriguez-Blas, M. Botta, C. Platas-Iglesias, *Chem. Eur. J.* 2014, **20**, 17300.

11 N. Kuznik, M. Wyskocka, *Eur. J. Inorg. Chem.* 2016, 445.

12 (a) S. J. Dorazio, P. B. Tsitovich, K. E. Siters, J. A. Spernyak, J. R. Morrow, *J. Am. Chem. Soc.* 2011, **133**, 14154. (b) P. B. Tsitovich, J. M. Cox, J. A. Spernyak, J. R. Morrow, *Inorg. Chem.* 2016, **55**, 12001. (c) S. J. Dorazio, J. R. Morrow, *Inorg. Chem.* 2012, **51**, 7448. (d) S. J. Dorazio, J. R. Morrow, *Eur. Inorg. Chem.* 2012, 2006.

13 (a) P. B. Tsitovich, J. A. Spernyak, J. R. Morrow, *Angew. Chem. Int. Ed.* 2013, **52**, 13997. (b) S. J. Dorazio, A. Olatunde, J. A. Spernyak, J. R. Morrow, *Chem. Commun.* 2013, **49**, 10025. (c) A. E. Thorarinsdottir, K. Du, J. H. P. Collins, T. D. Harris, *J. Am. Chem. Soc.* 2017, **139**, 15836.

14 (a) A. Olatunde, S. J. Dorazio, J. A. Spernyak, J. R. Morrow, *J Am Chem Soc* 2012, **134**, 18503. (b) L. Caneda-Martínez, L. Valencia, I. Fernandez-Perez, M. Regueiro-Figueroa, G. Angelovski, I. Brandariz, D. Esteban-Gomez and C. Platas-Iglesias, *Dalton Trans.* 2017, **46**, 15095.

15 (a) S. J. Dorazio, A. O. Olatunde, P. B. Tsitovich, J. R. Morrow, *J Biol Inorg. Chem.* 2014, **19**, 191. (b) A. Olatunde, C. J. Bond, S. Dorazio, J. M. Cox, J. B. Benedict, M. D. Daddario, J. A. Spernyak, J. R. Morrow, *Chem. Eur. J.* 2015, **21**, 18290.

16 (a) S. Viswanathan, Z. Kovacs, K. N. Green, S. J. Ratnakar, A. D. Sherry *Chem. Rev.* 2010, **110**, 2960. (b) E. Terreno, D. D. Castelli, S. Aime, *Contrast Media Mol. Imaging* 2010, **5**, 78.

17 (a) P. Harvey, A. M. Blamire, J. I. Wilson, K.-L. N. A. Finney, A. M. Funk, P. K. Senanayake, D. Parker, *Chem. Sci.* 2013, **4**, 4251. (b) P. B. Tsitovich, J. M. Cox, J. B. Benedict, J. R. Morrow, *Inorg. Chem.* 2016, **55**, 700.

18 (a) G. Angelovski, *Acc. Chem. Res.* 2017, **50**, 2215. (b) G. Angelovski, É. Tóth, *Chem. Soc. Rev.*, 2017, **46**, 324.

19 (a) M. C. Heffern, L. M. Matosziuk, T. J. Meade, *Chem. Rev.* 2014, **114**, 4496. (b) J. L. Major, T. J. Meade, *Acc. Chem. Res.* 2009, **42**, 893.

20 (a) S. N. M. Chilla, C. Henoumont, L. Vander Elst, R. N. Muller, S. Laurent, *Isr. J. Chem.* 2017, **57**, 800. (b) E. Debroye, T. N. Parac-Vogt, *Chem. Soc. Rev.* 2014, **43**, 8178.

21 J. Ruiz-Cabello, B. P. Barnett, P. A. Bottomley, J. W. Bulte, *NMR Biomed.* 2011, **24**, 114.

22 J-X. Yu, R. R. Hallac, S. Chiguru, R. P. Mason, *Progress in Nuclear Magnetic Resonance Spectroscopy* 2013, **70**, 25.

23 K. L. Peterson, K. Srivastava, V. C Pierre, *Front. Chem.* 2018, **6**:160.

24 J. Blahut, P. Hermann, A. Gálisová, V. Herynek, I. Císařová, Z. Tošnerc, J. Kotek, *Dalton Trans.*, 2016, **45**, 474.

25 (a) M. Yu, D. Xie, K. P. Phan, J. S. Enriquez, J. J. Luci, E. L. Que, *Chem. Commun.* 2016, **52**, 13885. (b) J. Blahut, K. Bernasek, A. Galisova, V. Herynek, I. Cisarova, J. Kotek, J. Lang, S. Matejkova, P. Hermann, *Inorg. Chem.* 2017, **56**, 13337.

26 K. H. Chalmers, E. De Luca, N. H. M. Hogg, A. M. Kenwright, I. Kuprov, D. Parker, M. Botta, J. I. Wilson, A. M. Blamire, *Chem. Eur. J.*, 2010, **16**, 134.

27 (a) K. H. Chalmers, M. Botta, D. Parker, *Dalton Trans.* 2011, **40**, 904. (b) K. H. Chalmers, A. M. Kenwright, D. Parker, A. M. Blamire, *Magn. Reson. Med.* 2011, **66**, 931. (c) P. Harvey, I. Kuprov, D. Parker, *Eur. J. Inorg. Chem.* 2012, 2015. (d) P. K. Senanayake, A. M. Kenwright, D. Parker, S. K. van der Hoorn,

Chem. Commun., 2007, 2923. (e) A. M. Kenwright, I. Kuprov, E. De Luca, D. Parker, S. U. Pandya, P. K. Senanayake, D. G. Smith, *Chem. Commun.*, 2008, 2514.

28 (a) K. Srivastava, E. A. Weitz, K. L. Peterson, M. Marjanska, V. C. Pierre, *Inorg. Chem.* 2017, **56**, 1546. (b) K. Srivastava, G. Ferrauto, V. G. Young, Jr., S. Aime, V. C. Pierre, *Inorg. Chem.* 2017, **56**, 12206.

29 (a) P. Kadjane, C. Platas-Iglesias, P. Boehm-Sturm, V. Truffault, G. E. Hagberg, M. Hoehn, N. K. Logothetis, G. Angelovski, *Chem. Eur. J.* 2014, **20**, 7351. (b) N. Cakic, T. Savic, J. Stricker-Shaver, V. Truffault, C. Platas-Iglesias, C. Mirkes, R. Pohmann, K. Scheffler, G. Angelovski, *Chem. Commun.* 2016, **52**, 9224. (c) N. Cakić, B. Tickner, M. Zaiss, D. Esteban-Gómez, C. Platas-Iglesias, G. Angelovski, *Inorg. Chem.* 2017, **56**, 14, 7737.

30 A. Keliris, K. Scheffler, J. Engelmann in *Fluorine Magnetic Resonance Imaging*, (Eds.: U. Flogel, E. Ahrens), Pan Stanford Publishing Pte. Ltd., Singapore, 2013, pp. 141-170.

31 A. J. Pella, G. Pintacuda, C. P. Grey, *Paramagnetic NMR in solution and the solid state, Progress in Nuclear Magnetic Resonance Spectroscopy* 2018, 1-825.

32 Q. Ji, D. Yang, X. Wang, C. Chen, Q. Deng, Z. Ge, L. Yuan, X. Yang, F. Liao, *Bioorg. Med. Chem.*, 2014, **22**, 3405.

33 Z. Xiaohe, Q. Yu, Y. Hong, S. Xiuqing, Z. Rugang, *Chem. Biol. Drug Des.* 2010, **76**, 330.

34 A. Rodriguez-Rodriguez, D. Esteban-Gomez, R. Tripier, G. Tircso, Z. Garda, I. Toth, A. de Blas, T. Rodriguez-Blas, C. Platas-Iglesias, *J. Am. Chem. Soc.* 2014, **136**, 17954.

35 L. Helm in *Contrast Agents for MRI. Experimental Methods* (Eds.: V. C. Pierre, M. J. Allen), The Royal Society of Chemistry, Croydon, 2018, p. 122.

36 A. L. Thompson, D. Parker, D. A. Fulton, J. A. K. Howard, S. U. Pandya, H. Puschmann, K. Senanayake, P. A. Stenson, A. Badari, M. Botta, S. Avedano, S. Aime, *Dalton Trans.* 2006, **0**, 5605.

37 A. Beeby, I. M. Clarkson, R. S. Dickins, S. Faulkner, D. Parker, L. Royle, A. S. de Sousa, J. A. G. Williams, M. Woods, *J. Chem. Soc. Perkin Trans. 2* 1999, 493.

38 (a) R. M. Supkowski, W. DeW. Horrocks, Jr., *Inorg. Chim. Acta* 2002, **340**, 44.(b) M. Woods, S. Aime, M. Botta, J. A. K. Howard, J. M. Moloney, M. Navet, D. Parker, M. Port, O. Rousseaux, *J. Am. Chem. Soc.* 2000, **122**, 9781.

39 (a) C. Kumas, W. S. Fernando, P. Zhao, M. Regueiro-Figueroa, G. E. Kiefer, A. F. Martins, C. Platas-Iglesias, A. D. Sherry, *Inorg. Chem.* 2016, **55**, 9297. (b) C. Adair, M. Woods, P. Y. Zhao, A. Pasha, P. M. Winters, G. M. Lanza, P. Athey, A. D. Sherry, G. E. Kiefer, *Contrast Media Mol. Imaging* 2007, **2**, 55. (c) M. Polasek, J. Kotek, P. Hermann, I. Cisarova, K. Binnemans, I. Lukes, *Inorg. Chem.* 2009, **48**, 466. (d) F. A. Dunand, R. S. Dickins, D. Parker, A. E. Merbach, *Chem. Eur. J.* 2001, **7**, 5160.

40 E. De Luca, P. Harvey, K. H. Chalmers, A. Mishra, P. K. Senanayake, J. I. Wilson, M. Botta, M. Fekete, A. M. Blamire, D. Parker, *J. Biol. Inorg. Chem.*, 2014, **19**, 215.

41 K. Binnemans, *Coord. Chem. Rev.* 2015, **295**, 1.

42 R. S. Dickins, D. Parker, J. I. Bruce, D. J. Tozer, *Dalton Trans.* 2003, 1264.

43 D. Esteban-Gomez, A. de Blas, T. Rodriguez-Blas, L. Helm, C. Platas-Iglesias, *ChemPhysChem* 2012, **13**, 3640.

44 M. Regueiro-Figueroa, C. Platas-Iglesias, *J. Phys. Chem. A* 2015, **119**, 6436.

45 (a) D. H. Powell, O. M. Ni Dhubhghaill, D. Pubanz, L. Helm, Y. S. Lebedev, W. Schlaepfer, A. E. Merbach, *J. Am. Chem. Soc.* 1996, **118**, 9333. (b) H. Lammers, F. Maton, D. Pubanz, M. W. van Laren, H. van Bekkum, A. E. Merbach, R. N. Muller, J. A. Peters, *Inorg. Chem.* 1997, **36**, 2527.

46 (a) G. M. Nicolle, F. Yerly, D. Imbert, U. Bottger, J.-C. G. Bünzli, A. E. Merbach, *Chem. Eur. J.* 2003, **9**, 5453. (b) S. Aime, M. Botta, M. Fasano, *Chem Eur J* 1997, **3**, 1499.

47 (a) T. J. Swift, R. E. Connick, *J. Chem. Phys.* 1962, **37**, 307. (b) T. J. Swift, R. E. Connick, *J. Chem. Phys.* 1964, **41**, 2553.

48 (a) F. A. Dunand, R. S. Dickins, D. Parker, A. E. Merbach, *Chem. Eur. J.* 2001, **7**, 5160. (b) F. A. Dunand, S. Aime, A. E. Merbach, *J. Am. Chem. Soc.* 2000, **122**, 1506.

49 D. Delli Castelli, M. C. Caligara, M. Botta, E. Terreno, S. Aime, *Inorg. Chem.* 2013, **52**, 7130.

50 S. Zhang, Z. Kovacs, S. Burgess, S. Aime, E. Terreno, A. D. Sherry, *Chem. Eur. J.* 2001, **7**, 288.

51 J. Henig, E. Toth, J. Engelmann, S. Gottschalk, H. A. Mayer, *Inorg. Chem.* 2010, **49**, 6124.

52 (a) I. Solomon, *Phys. Rev.* 1955, **99**, 559. (b) I. Solomon, N. Bloembergen, *J. Chem. Phys.* 1956, **25**, 261. (c) N. Bloembergen, *J. Chem. Phys.* 1957, **27**, 572. (d) N. Bloembergen, L. O. Morgan, *J. Chem. Phys.* 1961, **34**, 842.

53 J. H. Freed, *J. Chem. Phys.* 1978, **68**, 4034.

54 A. V. Astashkin, A. M. Raitsimring, P. Caravan, *J. Phys. Chem. A* 2004, **108**, 1990.

55 J. A. Peters, J. Huskens, D. J. Raber, *Prog. Nucl. Magn. Reson. Spectrosc.* 1996, **28**, 283.

56 F. A. Dunand, A. Borel, A. E. Merbach, *J. Am. Chem. Soc.* 2002, **124**, 710.

57 J. B. Livramento, C. Weidensteiner, M. I. M. Prata, P. R. Allegrini, C. Geraldes, L. Helm, R. Kneuer, A. E. Merbach, A. C. Santos, P. Schmidt, É. Toth, *Contrast Media Mol. Imaging* 2006, **1**, 30.

58 M. P. Placidi, M. Botta, F. K. Kalman, G. E. Hagberg, Z. Baranyai, A. Krenzer, A. K. Rogerson, I. Toth, N. K. Logothetis, G. Angelovski, *Chem. Eur. J.* 2013, **19**, 11644.

59 D. M. Corsi, C. Platas-Iglesias, H. van Bekkum, J. A. Peters, *Magn. Reson. Chem.* 2001, **39**, 723.

60 Gaussian 09, Revision A.01. M. J. Frisch, G. W. Trucks, H. B. Schlegel, G. E. Scuseria, M. A. Robb, J. R. Cheeseman, G. Scalmani, V. Barone, B. Mennucci, G. A. Petersson, H. Nakatsuji, M. Caricato, X. Li, H. P. Hratchian, A. F. Izmaylov, J. Bloino, G. Zheng, J. L. Sonnenberg, M. Hada, M. Ehara, K. Toyota, R. Fukuda, J. Hasegawa, M. Ishida, T. Nakajima, Y. Honda, O. Kitao, H. Nakai, T. Vreven, J. A. Montgomery Jr., J. E. Peralta, F. Ogliaro, M. Bearpark, J. J. Heyd, E. Brothers, K. N. Kudin, V. N. Staroverov, R. Kobayashi, J. Normand, K. Raghavachari, A. Rendell, J. C. Burant, S. S. Iyengar, J. Tomasi, M. Cossi, N. Rega, N. J. Millam, M. Klene, J. E. Knox, J. B. Cross, V. Bakken, C. Adamo, J. Jaramillo, R. Gomperts, R. E. Stratmann, O. Yazyev, A. J. Austin, R. Cammi, C. Pomelli, J. W. Ochterski, R. L. Martin, K. Morokuma, V. G. Zakrzewski, G. A. Voth. P. Salvador, J. J. Dannenberg, S. Dapprich, A. D. Daniels, O. Farkas, J. B. Foresman, J. V. Ortiz, J. Cioslowski, D. J. Fox in *Gaussian 09, Revision A.01*; Gaussian, Inc., Wallingford, CT, 2009.

61 J. M Tao, J. P. Perdew, V. N. Staroverov, G. E. Scuseria, *Phys. Rev. Lett.* 2003, **91**, 146401.

62 M. Dolg, H. Stoll, A. Savin, H. Preuss, *Theor. Chim. Acta* 1989, **75**, 173.

63 J. Tomasi, B. Mennucci, R. Cammi, *Chem. Rev.* 2005, **105**, 2999.

64 M. A. Bernstein, K. F. King, X. J. Zhou in *Handbook of MRI Pulse Sequences*, Elsevier Academic Press, Burlington, MA; London, 2004, p. 1017.

Lanthanide Complexes with ^{1}H paraCEST and ^{19}F Response for MRI Applications
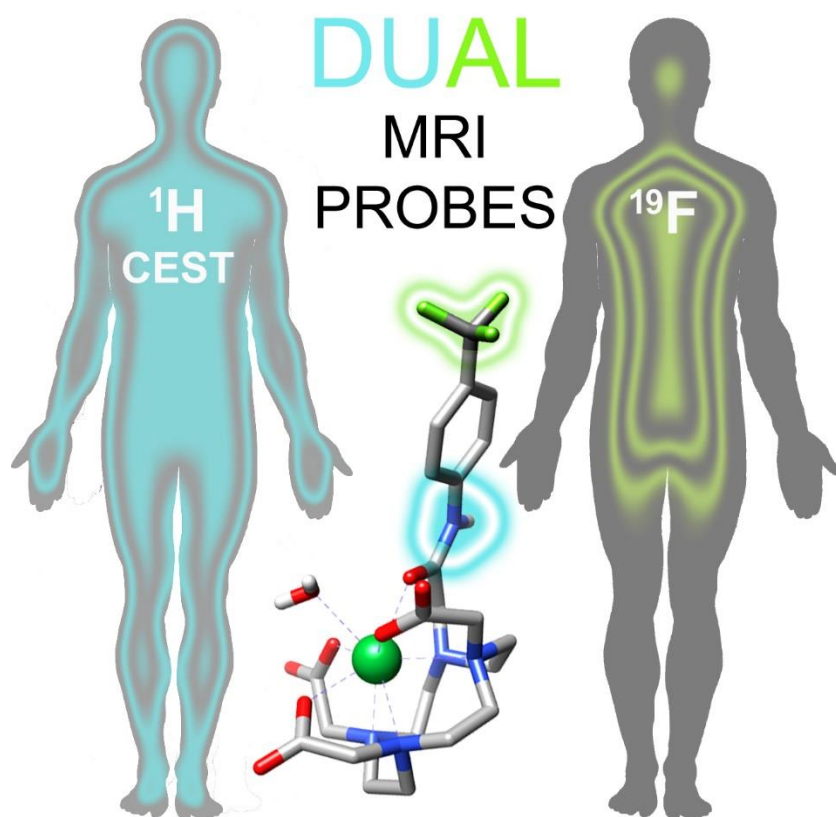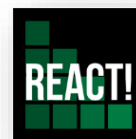
Chapter 5

Lanthanide Complexes with ^{1}H paraCEST and ^{19}F Response for MRI Applications

We present a detailed study of the lanthanide(III) complexes with cyclen-based ligands containing phenylacetamide pendants that incorporate CF$_3$ at different distances from the metal ion. The complexes exhibit square antiprismatic (SAP) coordination in solution, as demonstrated by the analysis of the Yb^{3+} induced paramagnetic shifts and the X ray structure of the [YbL^3] complex. Luminescence lifetime measurements and a detailed ^{1}H and ^{17}O relaxometric characterisation confirmed the presence of an inner-sphere water molecule. The Tm^{3+} complexes provide Chemical Exchange Saturation Transfer (CEST) response upon saturation at the frequency of the amide protons. A ^{19}F relaxation study provided accurate estimates of the Ln···F distances that were used to rationalise the efficiency of the complexes as ^{19}F MRI probes, which was tested in vitro using MRI phantom studies.

5.1. Introduction

Fluorinated probes for application in magnetic resonance imaging (MRI) represent an interesting alternative to the classical ^{1}H contrast agents. The first in vitro ^{19}F MRI study dates from 1977, when Holland reported phantoms of NaF solutions.[1] *In vivo* ^{19}F MRI studies were reported eight years later by using fluorinated anesthetics.[2] The interest on this topic has been reinforced in the last decade, in particular with the use of perfluorocarbon molecules, often as colloidal suspensions or emulsions in aqueous buffer.[3] One of the most interesting and promising properties offered by these fluorinated systems is the absence of a background signal, as fluorine is present *in vivo* in negligible amounts, mainly as solid salts in teeth and bones.[4] Furthermore, the ^{19}F nucleus presents 100% isotopic abundance, a sensitivity only slightly lower with respect to ^{1}H (83%) and a non-quadrupolar nuclear spin (I= ½).[5] The high gyromagnetic ratio of ^{19}F (40.05 MHz·T^{-1}) is very similar to that of ^{1}H (42.55 MHz·T^{-1}), so that ^{19}F detection requires only a small tuning of the conventional MRI scanners.[6]

Another interesting class of contrast agents for application in MRI that have been intensively studied during the last two decades are Chemical Exchange Saturation Transfer (CEST) contrast agents.[7] These probes contain protons involved in slow-to-intermediate chemical exchange with bulk water. Application of a radiofrequency pulse at the frequency of the exchangeable protons results in the transference of some magnetisation to bulk water through chemical exchange, so that the intensity of the bulk water signal decreases.[7,8]

The use of paramagnetic ^{19}F and CEST (paraCEST) probes has some advantages over diamagnetic ones. First, the ^{19}F relaxation times of diamagnetic compounds are relatively long, which may result in rather long acquisition times. The introduction of a paramagnetic ion in the vicinity of the ^{19}F nucleus shortens these relaxation times thanks to the paramagnetic relaxation enhancement effect.[9] This allows using ultrafast pulse sequences that shorten the acquisition times and increase the signal-to-noise ratio (SNR) of the images.[10] Following the pioneering work of Parker on paramagnetic lanthanide complexes,[11] different groups have developed ^{19}F MRI probes using either paramagnetic lanthanide[12,13] or transition metal ions (i. e. Fe^{2+}, Co$^{2+/3+}$, Ni^{2+} or Cu^{+}/Cu^{2+}).[14] paraCEST probes also present some advantages with respect to diamagnetic derivatives, as the paramagnetic chemical shifts induced by the metal ion shift the signal of exchangeable protons away from that of bulk water. As a result, the resonance of exchangeable protons can be saturated selectively and the slow-to-exchange condition can be achieved with faster exchange rates.[15]

In a recent work, we have shown that the [GdL^1]$^+$ and [GdL^2] complexes (Scheme 1) provide dual response at the ^{1}H and ^{19}F frequencies. The ^{1}H response is generated by the classical T_1 effect, thanks to the presence of a water molecule coordinated to the Gd^{3+} ion in fast exchange with bulk water. These complexes also showed interesting ^{19}F NMR relaxation properties, particularly in the case of [GdL^1]$^+$, as the longer Gd···F distance results in slower transverse ^{19}F relaxation, and thus in sharper signals.[16] In this paper we report a detailed study of the potential of the complexes of H$_3$L^1 and H$_2$L^2 with other lanthanide ions as ^{19}F MRI probes. In addition, we present the new cyclen-based ligand H$_3$L^3 and the corresponding complexes with the lanthanide ions. We report a detailed study of the ^{19}F longitudinal and transverse relaxation rates (R_1 and R_2) of these systems at different fields, and analyse the effect of the effective magnetic moment (μ_{eff}) along the lanthanide series to the ^{19}F relaxation rates. Furthermore, we present a structural study of the complexes in solution by using NMR spectroscopy and DFT calculations in combination with the luminescence lifetimes of the Eu^{3+} and Tb^{3+} analogues. In addition, we present the X-ray structure of [YbL^3] complex and a full

relaxometric characterisation of [GdL³] including ¹H NMRD (Proton Nuclear Magnetic Relaxation Dispersion) profiles and ¹⁷O NMR measurements. Besides, we investigated the Z-spectra at different frequency fields and temperatures for the Yb³⁺ and Tm³⁺ analogues. The amide protons of the Tm³⁺ complexes give significant CEST response, which imparts dual-frequency (¹H/¹⁹F) response to these complexes.
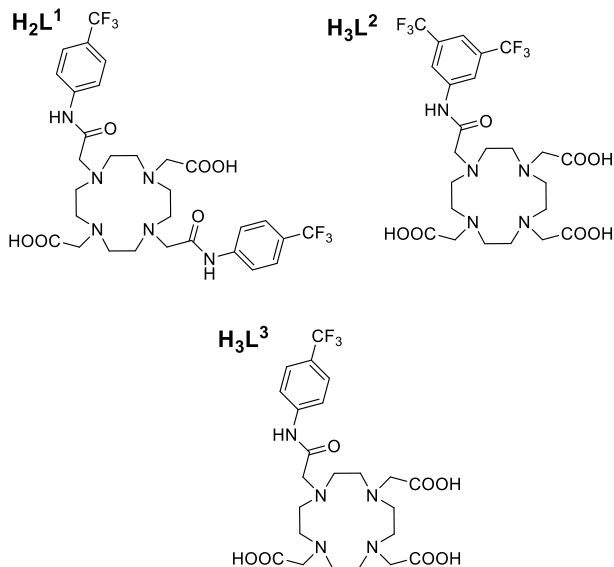
Scheme 1. Structures of the ligands discussed in the present work.

5.2. Results and discussion.

5.2.1. Synthesis and structural characterisation

The synthesis of H_3L^3 was achieved by alkylation of DO3A*t*Bu with 2-chloro-N-(4-(trifluoromethyl)phenyl)acetamide in acetonitrile using NaHCO₃ as a base. Hydrolysis of the *tert*-butyl ester groups using formic acid afforded H_3L^3 in 63% over the two steps. The complexes with different Ln³⁺ ions were prepared by reacting the ligand with the corresponding hydrated LnCl₃ salt in 1-butanol. The charge neutral [LnL¹] complexes (Ln = Eu, Gd, Tb, Tm Yb or Lu) were isolated in ~60-75% yields after purification using reverse-phase chromatogrtaphy. The complexes of ligands H_2L^1 and H_3L^2 were prepared following the same procedures described previously for the Gd³⁺ analogues.[16]

The crystal structure of [YbL³(H₂O)] complex was determined by single crystal X-ray diffraction measurements (Figure 1). The four amine donor atoms of the macrocycle and the four oxygen atoms of the carbonyl groups provides an eight coordination environment to the metal ion, nine coordination being completed by a water molecule. The coordination polyhedron around the Yb³⁺ ion can be described as capped square antiprism (SAP). The nitrogen atoms of the cyclen unit define the lower plane of the polyhedron, the oxygen atoms of the pendant arms the upper plane, and the oxygen atom of the coordinated water molecule occupies the capping position. The metal ion is placed closer to the

upper plane (0.726 Å) than to the plane delineated by the nitrogen atoms (1.595 Å), a general trend observed for the family of lanthanide DOTA derivatives.[17] The mean twist angle of the two square planes is 39.8 ± 1.0°, a value that is close that expected for an ideal square antiprism (45°). The crystal lattice contains the two centrosymmetrically related Δ(λλλλ)/Λ(δδδδ) enantiomers, where Λ and Δ define the two possible orientations of the four pendant arms (clockwise or anti-clockwise) with respect to the C_4 pseudo-symmetry axis of the complex, while δ or λ describe the conformations of the five-membered chelate rings resulting from the coordination of the ethylenediamine units.[18] The cyclen unit adopts a [3333] conformation using the notation proposed by Dale.[19] The Yb-N distances are close to those observed for nine-coordinated Yb³⁺ complexes with cyclen based ligands (2.58-2.64 Å).[17,20-21] The bond distance involving the coordinated water molecule [Yb(1)··O(8), 2.4577(10) Å] is longer than those reported for Yb³⁺ DOTA-tetraamide complexes, which present a rather broad range (2.34-2.44 Å).[21] The longer distance observed for [YbL³(H₂O)] is related to the reduced positive charge of the complex, which weakens the Yb-O_water interaction.[22]
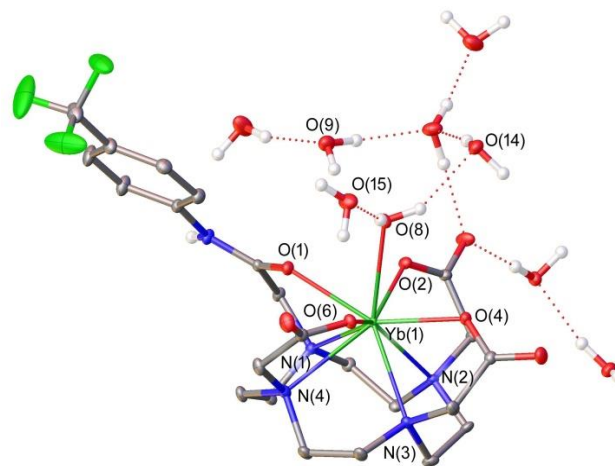
Figure 1. X-ray structure of the [YbL³(H₂O)] complex. Bond distances (Å): Yb(1)··O(1), 2.3368(10), Yb(1)··O(2), 2.2725(9), Yb(1)··O(4), 2.2743(10), Yb(1)··O(6), 2.2420(10), Yb(1)··O(8), 2.4577(10), Yb(1) ·N(1), 2.6430(11), Yb(1)··N(2), 2.6098(11), Yb(1)··N(3), 2.5880(11), Yb(1)··N(4), 2.6512(11). The ellipsoids represent the 50% probability level.

The coordinated water molecule is involved in hydrogen-bonding interactions with up to three second-sphere water molecules. The coordinated water molecule serves as a hydrogen bond donor to O(15) and O(14) [O(8)···O(15) = 2.7716(11) Å, O(8)-H(8D)···O(15) = 1.93 Å, O(8)-H(8D)···O(15) = 159.6°; O(8)···O(14) = 2.8377(12) Å, O(8)-H(8C)···O(14) = 2.04 Å, O(8)-H(8C)···O(14) = 149.8°;]. A weaker hydrogen bond involves a third water molecule of crystallisation acting as a hydrogen bond donor [O(9)···O(8) = 3.0350(11) Å, O(9)-H(9D)···O(8) = 2.25 Å, O(9)-H(9D)···O(8) = 159.0°] and the inner-sphere water molecule. Similar hydrogen bonding patterns were observed in the solid state for several Gd³⁺ complexes in the presence of counterions with poor ability to form hydrogen bonds.[23] Similar second-sphere interactions were also found to be crucial to obtain accurate

Gd-O$_{water}$ distances and ^{17}O spin densities for Gd^{3+} complexes using DFT methods.[24]

The emission spectra of the [LnL^3] complexes (Ln = Eu, Tb) recorded under excitation through the ligand bands at 263 nm present the expected $^5D_0 \rightarrow ^7F_J$ transitions of Eu^{3+} (J = 0-4) or $^5D_4 \rightarrow ^7F_J$ (Tb^{3+}) (Figures S15-S16, Annexe D). The emission lifetimes of $^5D_0$ (Eu) and $^5D_4$ (Tb) excited states recorded in H$_2$O and D$_2$O solutions (Table 1) provide hydration numbers that confirm the presence of a water molecule in the first coordination sphere of the metal ions.[25] Both the lifetimes and emission spectra of [LnL^2] and [LnL^3] are very similar, which points to very similar structures of these complexes in solution. This implies that the different substitution pattern of the phenylacetamide pendant arm of these ligands does not affect significantly the structure of the corresponding complexes.

Table 1. Emission lifetimes and hydration numbers obtained for the [EuL^3] and [EuL^3] complexes.

	τ(H$_2$O) / ms	τ(D$_2$O) / ms	q^a
EuL^1	0.616	1.904	0.9
TbL^1	1.85	3.15	0.8

^{a} Obtained using the method proposed by Beeby, ref. 25.

The ^{1}H NMR spectra of the [EuL^3] and [YbL^3] (pD= 6.8, 10 mM, 25 ^{o}C) present four resonances due to the most shifted axial protons of the cyclen unit in the range ~34 – 29 and 109 – 126 ppm, respectively. These chemical shifts are characteristic of complexes adopting capped square antiprismatic (SAP) coordination.[26,27] The signals of the twisted square antiprismatic isomers (TSAP) are not observed in any of the spectra, indicating that these complexes exists in solution as the SAP isomers almost exclusively.

A more detailed analysis of the structure of the [YbL^3] complex in solution was carried out by analysing the Yb^{3+}-induced pseudocontact shifts. The ^{1}H NMR spectrum of [YbL^3] presents 26 well-resolved signals that could be assigned in part with the aid of ^{1}H-^{1}H COSY spectra and line-width analysis. This provides a straightforward differentiation of the broad axial signals from the sharper equatorial ones, as a result of their different distances to the paramagnetic ions.[28]

The ^{1}H paramagnetic shifts induced by Yb^{3+} are dominated by the pseudocontact mechanism, with contact contributions being generally negligible.[29] The pseudocontact shifts can be expressed as linear combinations of the axial and rhombic components of the susceptibility tensor χ:[30]

$$\delta^{pc} = \frac{1}{2N_A}\left[\left(\chi_{zz} - \chi_{av}\right)\left(\frac{3z^2 - r^2}{r^5}\right) + \left(\chi_{xx} - \chi_{yy}\right)\left(\frac{x^2 - y^2}{r^5}\right)\right] (1)$$

$$r = \sqrt{x^2 + y^2 + z^2} \qquad (2)$$

The paramagnetic shifts of [YbL^3] were analysed by assuming diamagnetic shifts of 7.8 ppm for the signals of aromatic protons and 3.0 ppm for CH$_2$ protons. The paramagnetic shifts were then fitted to Eq (1) by using the Cartesian coordinates obtained from the X-ray structure described above. Since the positions of the magnetic axes are not constrained by symmetry for this complex,

we carried out a fitting procedure involving five paramaters: the axial (χ_{zz} - χ_{av}) and rhombic (χ_{xx} - χ_{yy}) magnetic anisotropies and the three Euler angles that allow the rotation of the complex so that the Cartesian axes match the magnetic axes.[31] The best fit of the data provides calculated pseudocontact shifts in good agreement with the experimental values (Figure 2), with deviations < 6.1 ppm. The calculated axial and rhombic magnetic susceptibilities are χ_{zz} - χ_{av} = 1.34(2) and χ_{xx} - χ_{yy} = -0.51(5) cm^3 K mol^{-1}, indicating that the magnetic anisotropy is dominated by the axial contribution. The orientation of the molecule that results from the analysis such that the z magnetic axis is perpendicular to the best plane defined by the nitrogen donor atoms of the macrocycle, and contains the Yb^{3+} ion and the oxygen atom of the coordinated water molecule (Figure S22, Annexe D). Thus, the analysis of the Yb^{3+} induced shifts shows that the [YbL^3] complex retains in solution the structure observed in the solid state.
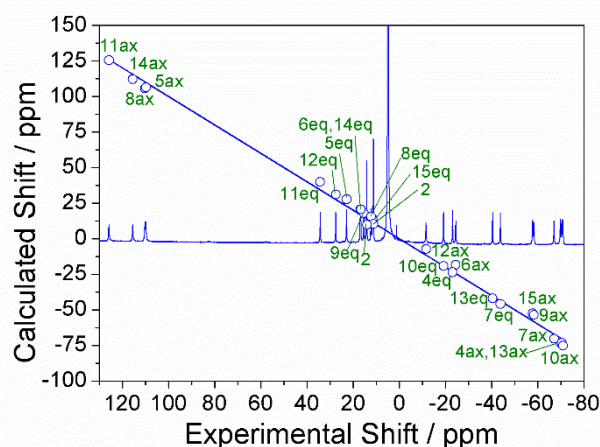
Figure 2. ^{1}H NMR (300 MHz, 298 K) spectrum of [YbL^3] recorded in D$_2$O solution and plot of the experimental shifts versus those calculated with the X-ray structure and pseudocontact contributions. The solid line represents the identity line.

DOSY (diffusion-ordered NMR spectroscopy) experiments were performed on 15 mM H$_2$O solutions of [TmL^3] and selected complexes of L^1 and L^2 ([EuL^2], [TmL^1] and [YbL^1], the latter using 5 mM concentration). These experiments provided diffusion coefficients D at 298 K totaling 3.94(2) × 10^{-10} m^2 s^{-1} for [EuL^2]$^+$, 4.65(1) × 10^{-10} m^2 s^{-1} for [TmL^1], 4.82(1) × 10^{-10} m^2 s^{-1} for [YbL^1] and 4.94 × 10^{-10} m^2 s^{-1} for [TmL^3]. The diffusion coefficients obtained for the complexes of L^1 and L^3 are very similar, as would be expected given their similar size and neutral charge. The D^{298} value determined for [EuL^2]$^+$ is somewhat lower, which is explained by the larger hydrodynamic radius associated to its higher molecular weight and positive charge. Nevertheless, the diffusion coefficients measured for these complexes are similar to those reported for lanthanide complexes with similar size,[32] and higher than the D^{298} value reported for lanthanide DO3A derivatives that form stable dimeric species in solution[33] (for comparative purposes the D^{298} values measured in D$_2$O must be scales by a factor of 1.24 to account for the different viscosities of

H$_2$O and D$_2$O). Thus, we conclude that the complexes investigated here adopt discrete mononuclear structures in H$_2$O solution.

5.2.2. ¹H relaxivity and ¹⁷O NMR studies

In the previous chapter, it was reported a detailed characterisation of the [GdL^1] and [GdL^2]$^+$ complexes using ¹H Nuclear Magnetic Relaxation Dispersion (NMRD) and ¹⁷O NMR studies. For the sake of completeness, it is reported here the characterisation of [GdL^3] using the same techniques.

The relaxivity of [GdL^3] was first assessed at 298 K and 300 MHz from aqueous solutions buffered at pH 7.4 (50 mM HEPES). ¹H relaxivities are a measure of the efficiency of a given paramagnetic probe to enhance the relaxation of water proton nuclei, normalised to a 1 mM concentration of the paramagnetic agent. A linear dependence on measured paramagnetic relaxation enhancement with Gd^{3+} concentration (measured 2.5-4.5 mM solutions) was observed. The slope of the straight line provides a relaxivity of r_{1p} = 4.27 mM^{-1} s^{-1} (Figure S13, Annexe D). This relaxivity is in perfect agreement with the expected values for small mononuclear gadolinium systems, and confirms the presence of a water molecule coordinated to the metal ion.[34]

A more detailed information of the parameters that control the relaxivity of [GdL^3] was obtained by measuring ¹H NMRD profiles at 10, 25 and 37 °C in the range from 0.01 to 70 MHz proton Larmor frequencies (Figure 3). Furthermore, ¹⁷O NMR transverse relaxation rates (T_{2r}) and chemical shifts ($\Delta\omega_r$) were recorded to get insight into the exchange rate of the coordinated water molecule (k_{ex}^{298}).

The relaxivities of [GdL^3] present a trend similar to those of [GdL^1], presenting a plateau at low fields (< 1 MHz), a sizeable dispersion in the range 1-20 MHz, reaching again another reasonably constant plateau above 21 MHz. The relaxivity decreases when the temperature is increased, which indicates that r_{1p} is limited by a fast rotation of the complex in solution characterised by a short rotational correlation time (τ_R).[35,36] The ¹⁷O data obtained for [GdL^3] parallel those reported previously for [GdL^1], indicating that these complexes present similar exchange rates of the coordinated water molecule. In particular, the T_{2r} dependence with inverse temperature presents a maximum at 52 °C that signals a change from the slow exchange regime at low temperature to the fast exchange regime at high temperature. This maximum is virtually at the same position for the two complexes, pointing to very similar water exchange kinetics.

The fitting of the ¹⁷O NMR and ¹H NMRD data of [GdL^3] was carried out using the Swift-Connick equations for the ¹⁷O transverse relaxation and chemical shift data[37] and the Solomon-Bloembergen-Morgan theory[38] and Freed's model[39] for the inner- and outer-sphere contribution to relaxivity, respectively. For this analysis, the number of water molecules coordinated to the Gd^{3+} ion (q) was fixed to 1 as it was predicted through luminescence lifetime measurements and confirmed by the X-ray crystal structure described above. The distance between the Gd^{3+} ion and the H atoms of the coordinated water molecule (r_{GdH}) was fixed to 3.1 Å following the ENDOR studies. Finally, we also fixed the

distance of closest approach for the outer-sphere contribution (a_{GdH}) and the activation energy for the modulation of the zero field splitting interaction (E_v) to common values (4.0 Å and 1 kJ mol^{-1}). All remaining parameters were obtained from the least squares fit of the data (Table 2). Figure 3 presents the fitted curves, which reproduce well the experimental data. The rotational correlation times (τ_R^{298}) and the value for the scalar hyperfine coupling constant ($A/\hbar$) obtained from the fittings of the data are in good agreement with the typical range of values observed for small Gd^{3+} complexes, supporting the consistency of the analysis. The mean square zero-field-splitting energy (Δ^2) and its correlation time (τ_v), parameters, which define the relaxation of the electron spin, subscribe the aforementioned analysis, with values comparable to those determined for Gd^{3+} complexes of DOTA derivatives.[40] The same holds for the diffusion coefficient D_{GdH}^{298} and its activation energy E_{DGdH}, which are close to the values determined for the self-diffusion of water ($D_{H_2O}^{298}$ = 20.3 × 10^{-10} m^2 s^{-1} and E_{DH_2O} = kJ mol^{-1}).[41]
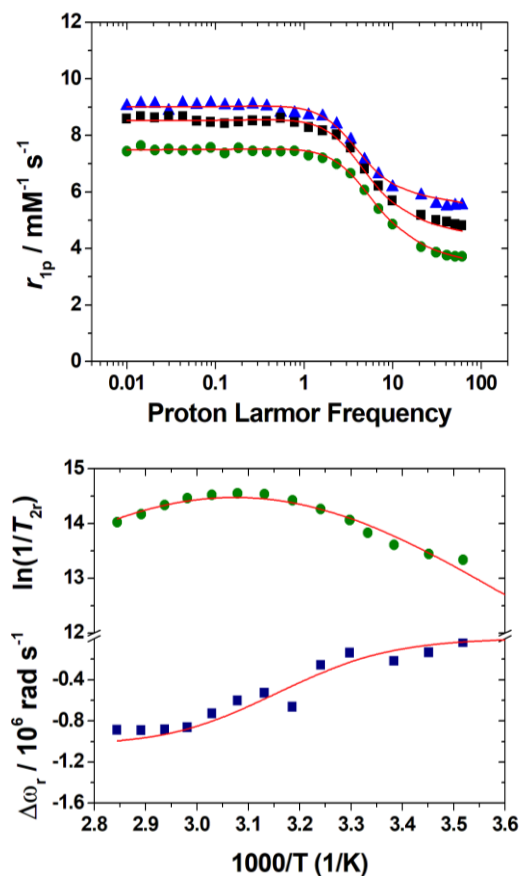
Figure 3. Top: ¹H NMRD profiles recorded at different temperatures for [GdL^3]. Bottom: Reduced transverse ¹⁷O relaxation rates (green ●) chemical shifts (blue ■) measured for [GdL^3] at 11.75 T. The lines represent the fit of the data as explained in the text.

Table 2. Parameters obtained from the simultaneous analysis of ^{17}O NMR and ^{1}H NMRD data.

	[GdL³]	[GdL¹]⁺ [b]	[GdL²] [b]	[GdDOTA]⁻ [c]
r_{1p} at 25/37 °C / mM⁻¹ s⁻¹ [b] (20 MHz)	5.18/4.07	4.97/4.14	4.26/4.23	4.7/3.8
k_{ex}^{298}/10⁶ s⁻¹	1.61 ± 0.18	1.52 ± 0.17	0.73 ± 0.04	4.1
$\Delta H^{\ddagger}$ / kJ mol⁻¹	48.6 ± 1.3	49.6 ± 3.5	22.9 ± 2.0	49.8
τ_{R}^{298} / ps	93.4 ± 4	98.3 ± 2.8	94.0 ± 2	77
E_{r} / kJ mol⁻¹	19.2 ± 1.3	15.6 ± 1.1	15.6 [a]	16.1
τ_{v}^{298}/ ps	26.5 ± 0.5	24.4 ± 2.0	15.4 ± 0.4	11
E_{v} / kJ mol⁻¹	1.0 [a]	1.0 [a]	1.0 [a]	1.0 [a]
D_{GdH}^{298} / 10⁻¹⁰ m² s⁻¹	21.8 ± 0.08	24.4 ± 0.1	24.4 [a]	22
E_{DGdH}/ kJ mol⁻¹	17.9 ± 1.5	24.5 ± 3.5	15.3 ± 0.8	20.2
Δ^{2} / 10¹⁹ s⁻²	2.5 ± 0.4	2.9 ± 0.3	7.4 ± 0.4	1.6
$A/\hbar$ / 10⁶ rad s⁻¹	-4.5 ± 0.3	-4.1 ± 0.3	-3.8 ± 0.3	-3.7
r_{GdH} / Å	3.1 [a]	3.1 [a]	3.1 [a]	Or
a_{GdH} / Å	4.0 [a]	4.0 [a]	4.0 [a]	3.5 [a]
q^{298}	1 [a]	1 [a]	1 [a]	1 [a]

[a] Parameters fixed during the fitting procedure. [b] Data from reference 16. [c] Data from reference 40.

Table 3. Parameters obtained from the analysis of CEST spectra recorded at 7.05 T (complex concentration 15 mM, saturation time 10 s).

	pH	T / °C	δ / ppm	M_z/M_0 / % (B_1 = 10 μT)	M_z/M_0 / % (B_1 = 30 μT)	r_{1p} / mM⁻¹ s⁻¹ [b]	k_{ex} / kHz [c]
[TmL³]	6.9	25	-52	6	9	0.10	1.4 ± 0.3
		37	-49	9	16	0.08	3.7 ± 0.8
[YbL³]	7.3	25	-10	22	-	0.02	4.1 ± 0.2
[TmL¹]	7.6	25	-48	5	21	0.10	12.9 ± 1.2
		37	-42	2	13	0.08	22.7 ± 2.6
[TmL²]⁺ [a]	7.0	25	-21	12	26	0.15	4.6 ± 1.5
		37	-24	6	-	0.15	4.9 ± 0.5

[a] Complex concentration was 8 mM. [b] Proton relaxivity of the bulk water signal. [c] Exchange rate values obtained using the Bloch-McConnell (BM) equations and assuming a 2-pool model (bulk water and one paramagnetically-shifted exchanging pools).

The water exchange rate determined for [GdL³] (k_{ex}^{298} = 1.61 × 10⁶ s⁻¹), is virtually identical to that determined for [GdL¹] (k_{ex}^{298} = 1.5 × 10⁶ s⁻¹), confirming the qualitative analysis described above. These water exchange rates are intermediate between those of the positively charged [GdL²]⁺ and negatively charged [GdDOTA)]⁻.[40] This is expected considering that water exchange in these complexes follows a dissociative mechanism. Thus, an increase in the positive charge of the complex increases the activation energy to reach the eight-coordinated transition state by strengthening the Gd-O$_{water}$ bond.[22] DFT calculations provide Gd-O$_{water}$ distances of 2.428 Å for [GdL²]⁺ and 2.462 Å for [GdL³] (see computational details below), which supports that the slower exchange rate of [GdL²]⁺ is related to a stronger Gd-O$_{water}$ bond.[22]

5.2.3. CEST properties

Chemical exchange saturation transfer studies were first performed for the [YbL³] and [TmL³] complexes (Figure 4). CEST spectra were acquired from 15 mM solutions at 25 and 37 °C by applying different radiofrequency fields (B_1 = 2.5, 5, 10, 15, 20, 25 and 30 μT). The Z-spectra were performed employing a saturation time of 10 s and a 1 ppm frequency resolution. The spectrum obtained for [YbL³] at 25 °C presents a CEST peak at -10 ppm that is better defined at lower saturation powers. This chemical shift is characteristic of amide protons of Yb³⁺ DOTA-monoamide

derivatives,[42] and similar to that observed for DOTA-tetraamides (~-15 ppm).[20b] The CEST effect is hardly visible at 37 °C due to the broadening of both the water and amide signals. The [TmL³] complex presents a better defined CEST feature at ~-50 ppm that is well defined at both 25 and 37 °C, regardless the saturation power applied. This chemical shift is similar to those observed for DOTA-tetraamide Tm³⁺ complexes.[43]

The CEST properties of [TmL²]⁺ and [TmL¹] complexes were also investigated under analogous conditions (Table 3, see also Figures S25, Annexe D). The [TmL¹] complex presents CEST properties comparable to those of [TmL³], providing a CEST peak a similar frequency. This was expected in light of their very similar structures. However, exchange rate values (k_{ex}) determined with the Bloch-McConnell (BM)[44] equations and assuming a 2-pool model (bulk water and one paramagnetically-shifted exchanging pool) were found to be very different (Table 3). Indeed, the exchange rate of amide protons was found to be one order of magnitude faster for [TmL¹] compared to [TmL³]. This is attributed to the combined electron withdrawing effect of two –CF₃ groups in [TmL¹], which increases the acidity of amide protons. Since amide exchange follows a base-catalysed mechanism,[45] an increasing acidity of amide protons is expected to result in faster exchange.
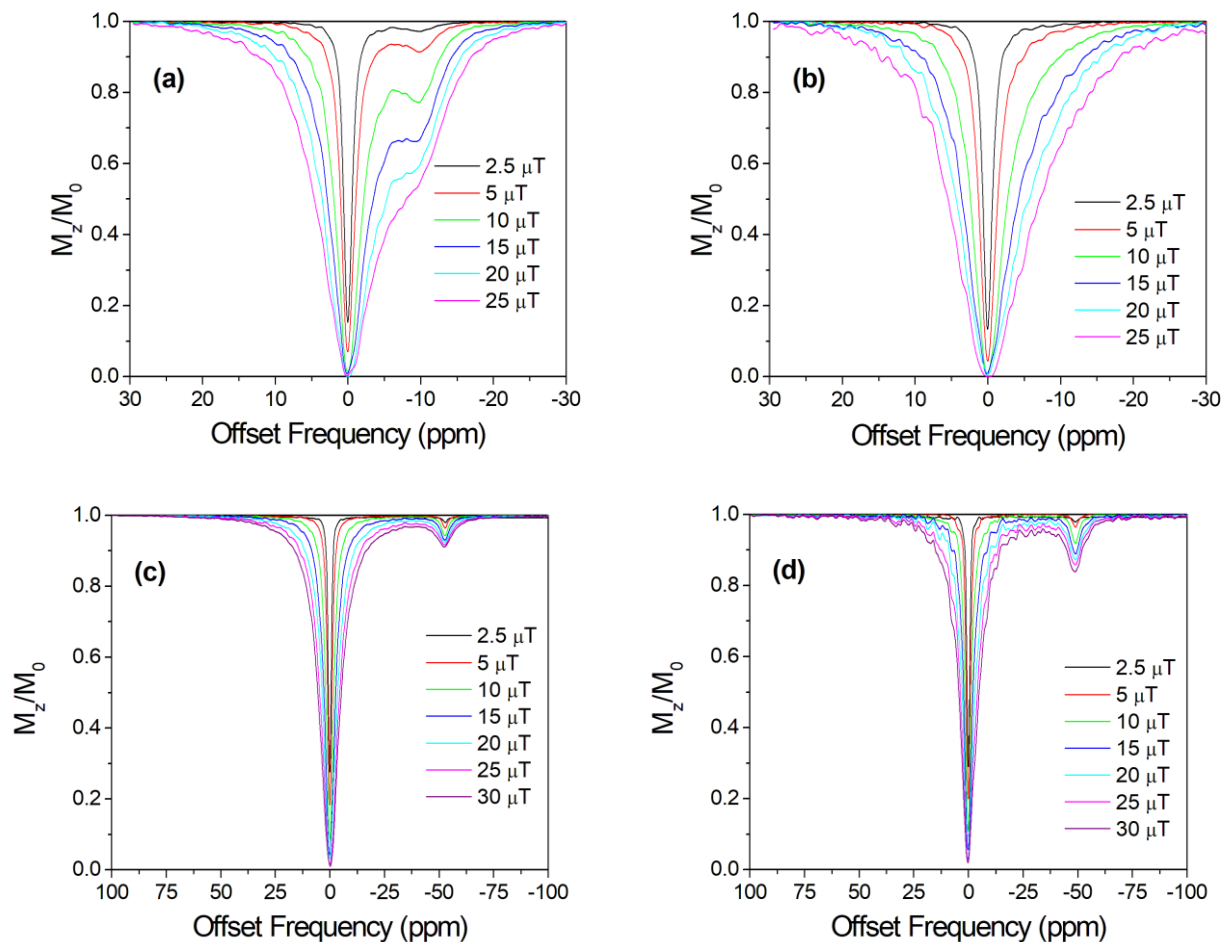
Figure 4. Z-spectra (15 mM in H$_2$O, saturation time 10 s) recorded for (a) [YbL^3] at 25 ^{o}C, (b) [YbL^3] at 37 ^{o}C, (c) [TmL^3] at 25 ^{o}C and (d) [TmL^3] at 37 ^{o}C.

The bis-amide [TmL^2]$^+$ complex presents a somewhat different behavior, as it shows a CEST peak with a considerably smaller shift with respect to bulk water (-21 ppm at 25 ^{o}C, Table 3). Since the paramagnetic shifts induced by Tm^{3+} are dominated by pseudocontact contributions,[46] this different chemical shifts observed for this complex must be related to a different magnetic anisotropy of the system.[47] The exchange rates of amide protons are only slightly higher than those reported for [TmL^3], which contains the same number and position of CF$_3$ groups in the amide pendant arm.

5.2.4. ^{19}F longitudinal and transverse relaxation rates

To assess the effect of the effective magnetic moment of various lanthanides complexes on ^{19}F relaxation times, ^{19}F NMR chemical shifts, longitudinal and transverse relaxation data were measured for [LnL^1], [LnL^2]$^+$ and [LnL^3] at different fields (7.05, 9.4 and 11.74 T, Ln = Eu, Gd, Tb, Tm, Yb or Lu). In the case of the [LnL^1] complexes additional data at 1.43 T could be also recorded (in the remaining cases lower solubility and/or number of ^{19}F nuclei prevented

relaxation measurements at low field). The observed ^{19}F NMR chemical shifts and longitudinal (R_1) and transverse (R_2) relaxation rates are compiled in Table 4.

The ^{19}F NMR spectra along the series of lanthanides present a single and intense resonance due to the CF$_3$ group or groups of the three ligands. The presence of a major single ^{19}F signal demonstrates the presence of a single isomer in solution (the SAP isomer). The observed ^{19}F chemical shifts (δ^{obs}) follow rather well the trend predicted by Bleaney's theory (Figure S21, Annexe D). This indicates that contact contributions are negligible, as expected for remote nuclei with respect to the paramagnetic center (in terms of number of bonds). The slope of the straight line obtained for [LnL^1] is considerably larger than those of [LnL^2]$^+$ and [LnL^3], which is related to a shorter Ln···F distance, as the geometric term present in the expression of the pseudocontact shift is proportional to $1/r_{LnF}$, where r_{LnF} is the Ln···F distance.[48]

The longitudinal (R_1) and transverse (R_2) relaxation rates of the paramagnetic complexes studied in this work follow the trend Gd^{3+} >> Tb^{3+} > Tm^{3+} > Yb^{3+} > Eu^{3+}, with the values observed for the

Eu^{3+} complexes being only slightly higher than those observed for the corresponding diamagnetic Lu^{3+} derivatives (Table 4). The trend observed for the lanthanide ions other than Gd^{3+} follow the order expected on the basis of their effective magnetic moments, although exceptions to this behaviour have been reported.[49] The [LnL^1] complexes present higher ^{19}F relaxation rates, while [LnL^2]$^+$ complexes show slightly higher R_1 and R_2 values than the [LnL^3] analogues.

The longitudinal ^{19}F relaxation rates of Gd^{3+} complexes are dominated by the dipolar contribution, which at the high magnetic field strengths used here (> 7 T) can be approximated by Eq (3), in which the contribution of electron relaxation has been neglected:[9]

$$R_1 = \frac{2}{15} \frac{\gamma_I^2 g^2 \mu_B^2}{r_{GdF}^6} S(S+1) \left(\frac{\mu_0}{4\pi}\right)^2 \left[\frac{7\tau_R}{1 + \omega_S^2 \tau_R^2} + \frac{3\tau_R}{1 + \omega_I^2 \tau_R^2}\right] \quad (3)$$

In this equation $\mu_0/4\pi$ is the magnetic permeability of a vacuum, S is the electron spin (S = 7/2 for Gd^{3+}), γ_I is the nuclear gyromagnetic ratio, g is the electron g factor, μ_B is the Bohr magneton, r_{GdF} is the nuclear-spin-electron-spin distance and ω_S and ω_I are the electron and nuclear Larmor frequencies, respectively. For Ln^{3+} ions other than Gd^{3+} R_1 presents contributions of both the dipolar and Curie spin mechanisms:

$$R_1 = \frac{2}{15} \frac{\gamma_I^2 \mu_{eff}^2 \mu_B^2}{r_{LnF}^6} \left(\frac{\mu_0}{4\pi}\right)^2 \left[\frac{7\tau_c}{1 + \omega_S^2 \tau_c^2} + \frac{3\tau_c}{1 + \omega_I^2 \tau_c^2}\right]$$
$$+ \frac{6}{5} \frac{\gamma_I^2 B_0^2 \mu_{eff}^4 \mu_B^4}{(3kT)^2 r_{LnF}^6} \left(\frac{\mu_0}{4\pi}\right)^2 \left[\frac{\tau_R}{1 + \omega_I^2 \tau_R^2}\right] \quad (4)$$

Where μ_{eff} is the effective magnetic moment of the Ln^{3+} ion, B_0 is the magnetic field strength and τ_c depends on the rotational correlation time and the longitudinal electronic relaxation time (T_{1e}):

$$\frac{1}{\tau_c} = \frac{1}{\tau_R} + \frac{1}{T_{1e}} \quad (5)$$

The first term in Eq (4) accounts for the dipolar interaction and the second term for the Curie spin mechanism, which becomes more important upon increasing the magnetic field strength, particularly for Ln^{3+} ions with high μ_{eff} values.[9]

The relaxation data shown in Table 4 were analysed simultaneously by using Eqs (3)-(5). The Eu^{3+} complexes were not included in the analysis due to the small paramagnetic effect observed in the relaxation rates, which are very similar to those observed for the Lu^{3+} analogues. All R_1 values were corrected for the diamagnetic contribution by using the data obtained for the Lu^{3+} complexes. The transverse relaxation rates were not included in the quantitative analysis due to their higher experimental uncertainties. The experimental data were fitted by assuming that [LnL^1] and [LnL^3] complexes present identical τ_R values and different r_{LnF} distances, which were considered independent of the Ln^{3+} ion for the complexes with a given ligand. Furthermore, the r_{LnF} distance in [LnL^2]$^+$ complexes was considered to be identical to that of [LnL^3], while the τ_R values were assumed to be different. DFT calculations support that the r_{LnF} distances do not change significantly acroos the lanthanide series, providing very similar

values for [LnL^2]$^+$ and [LnL^3] complexes (Figure S23, Annexe D). Finally, we hypothesised that T_{1e} and μ_{eff} values are characteristic of the particular Ln^{3+} ion, but independent of the ligand structure. This approximation is reasonable taking into account the similar coordination geometries of all the complexes studied in this work. The experimental R_1 values could be fitted reasonably well to Eqs (3)-(5) by applying these approximations, as shown in Figure 5 (see also Figure S24, Annexe D).

Table 5. Parameters obtained from the fits of ^{19}F relaxation data.

	μ_{eff} / BM ^{a}	T_{1e} / fs ^{b}
Tb	10.2 ± 0.3 (9.7)	720 ± 35 (203)
Tm	8.4 ± 0.5 (7.6)	400 ± 48 (369)
Yb	4.9 ± 4.0 (4.5)	190 ± 160 (137)
	τ_R / ps	r_{LnF} / Å
[LnL^3]	141 ± 6	9.13 ± 0.05
[LnL^2]$^+$	208 ± 10	9.13 ± 0.05
[LnL^1]	141 ± 6	7.45 ± 0.04

^{a} Theoretical values are provided within parentheses.
^{b} In parentheses the values reported for the aqua ions (see text).

The τ_R and r_{LnF} values obtained from the fits are very similar to those obtained previously using the relaxation data of [GdL^1] and [GdL^2]$^+$ only. However, the values obtained from the simultaneous fit present considerably lower standard deviations. The longer τ_R value obtained for [LnL^2]$^+$ is consistent with a larger hydrodynamic radius associated to the higher molecular weight and charge. The fitted effective magnetic moments present relatively large errors, particularly in the case of Yb^{3+}, but are close to the theoretical values.[50] The same holds for the fitted T_{1e} data, which are reasonably close to those reported for the aqua-ions,[51] providing confidence to the analysis.

5.2.5. ^{19}F MRI studies

A phantom ^{19}F MRI study at 7.05 T was performed for the series of [LnL^1] complexes to gain more precise information on their potential as fluorinated probes. The MR images were recorded using 5 mM buffered solutions of the complexes (30 mM fluorine concentration). The resulting ^{19}F MR images (Figure 6) indicated the affirmative properties of the Tb^{3+} and Tm^{3+} complexes, which present signal-to-noise ratios (SNRs) after 1 hour acquisition time of ca. 10 and 7 times higher than that of the TFA reference. On the contrary, the Yb^{3+} and Gd^{3+} complexes present SNR values similar to that of TFA, a situation that remains similar on increasing the time of acquisition (Table 6). These results show that the Tb^{3+} and Tm^{3+} complexes present a good balance between the relaxation ability of the paramagnetic ion and the Ln···F distance. On the contrary, Yb^{3+} and Eu^{3+} induce very small paramagnetic relaxation enhancement to the ^{19}F signal (Table 4), resulting in a negligible SNR gain with respect to the diamagnetic reference. Finally, the dramatic T_1 relaxation enhancement induced by Gd^{3+} is accompanied by a dramatic shortening of T_2 (~0.7 ms at 7 T), which causes signal loss. Remarkably high SNRs were obtained previously however for [GdL^2]$^+$ with respect to the diamagnetic reference as a result of the longer Ln···F distance.[16]

Table 4. [19]F chemical shifts and R_1 and R_2 values for the lanthanide complexes studied in this work (5 mM in H_2O:D_2O, 9:1 v:v, pH = 7.4, 0.05 M HEPES buffer).

	δ_F / ppm	R_1 / s[-1]			R_2 / s[-1]			T_2/T_1
		7 T	9.4 T	11.7 T	7 T	9.4 T	11.7 T	
EuL[3]	-61.6	1.1	1.3	1.5	4.9	10.5	15.9	0.22
EuL[2]	-61.5	1.3	1.5	1.7	10.8	12.2	14.3	0.12
EuL[1]	-62.2	1.1	1.3	1.6	3.7	7.9	6.8	0.30
GdL[3]	-61.3	370	357	323	435	400	416	0.85
GdL[2 a]	-61.2	500	433	382	625.0	583.1	593.5	0.80
GdL[1 a]	-62.5	1250	1152	1097	1445	1401	1417	0.87
TbL[3]	-67.1	11.3	14.5	18.7	52.0	68.8	68.4	0.22
TbL[2]	-69.8	15.3	18.9	22.7	67.1	71.4	82.3	0.23
TbL[1]	-74.7	35.7	43.8	56.1	52.6	88.5	109.5	0.40
TmL[3]	-58.5	5.7	7.4	9.5	26.4	33.1	82.7	0.22
TmL[2]	-58.2	6.6	8.1	10.3	38.3	42.5	54.6	0.17
TmL[1]	-53.9	17.2	22.3	27.2	37.2	46.9	55.2	0.46
YbL[3]	-60.1	1.7	2.1	2.6	11.8	35.5	37.0	0.14
YbL[2]	-59.9	1.8	2.3	2.7	11.8	20.4	39.9	0.15
YbL[1]	-58.7	3.3	3.9	4.5	23.4	31.1	33.9	0.14
LuL[3]	-62.2	0.8	0.9	1.0	1.5	2.1	2.8	0.53
LuL[2]	-62.2	0.9	1.0	1.1	1.6	1.8	2.3	0.56
LuL[1]	-63.0	0.8	0.9	0.9	5.2	6.5	9.1	0.15

[a] Data from reference 16.
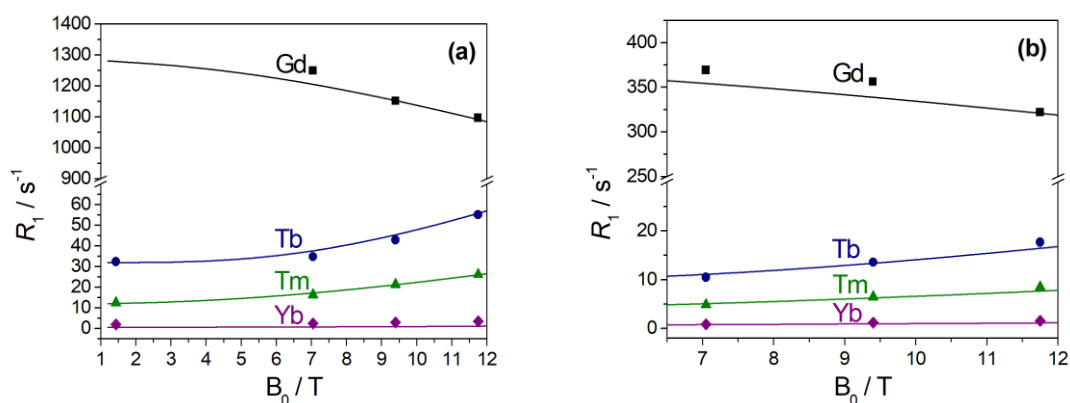
Figure 5. [19]F relaxation rates as a function of the magnetic field strength showing the fits and the experimental data points obtained for [GdL[1]] (a) and [GdL[3]] (b) (5 mM in H_2O:D_2O, 9:1 v:v, pH = 7.4, 0.05 M HEPES buffer).
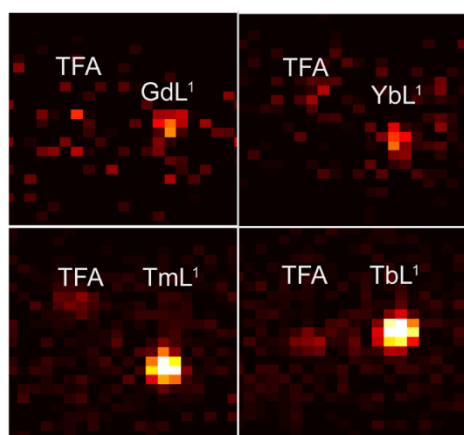
Figure 6. [19]F MRI on tube phantoms (5 mM complex, 7.05 T, RT) and TFA (10 mM).

Table 6. Signal to noise ratios (SNR) obtained with ^{19}F MRI studies for [LnL[1]] complexes using different times of acquisition (TA).

SNR	TA= 60 min	TA= 120 min	TA= 240 min
EuL[1]	4.58	5.69	10.45
YbL[1]	13.94	18.66	31.35
TmL[1]	66.95	75.00	108.67
TbL[1]	100.00	120.99	185.00
GdL[1 a]	12.87	19.31	b
TFA	9.93	20.72	22.78

[a] Acquisition parameters could not be optimised due to the short T_1 and T_2 relaxation times. [b] Not determined.

5.3. Experimental and computational section

5.3.1. Materials

DO3A*t*Bu was purchased from CheMatech (Dijon, France). Ligands H₂L¹ and H₃L² and 2-chloro-N-(4-(trifluoromethyl)phenyl)acetamide were prepared as reported previously. All other reagents and solvents were commercial and used without further purification.

5.3.2. General methods

High resolution electrospray-ionisation time-of-flight (ESI-TOF) mass spectra were recorded using a LC-Q-q-TOF Applied Biosystems QSTAR Elite spectrometer in positive and negative mode. Elemental analyses were accomplished on a ThermoQuest Flash EA 1112 elemental analyser. Medium performance liquid chromatography (MPLC) was carried out using a Puriflash XS 420 instrument equipped with a reverse-phase Puriflash 15C18HP column (60 Å, spherical 15 μm, 20 g) and UV-DAD detection at 210 and 254 nm, and operating at a flow rate of 10 mL/min. Aqueous solutions were lyophilised using a Telstar Cryodos-80 apparatus.

5.3.3. NMR spectroscopy

¹H, ¹⁹F and ¹³C NMR spectra were recorded on Bruker Avance 300 MHz, Bruker Avance III HD 400 MHz and Bruker Avance 500 MHz spectrometers. ¹⁹F chemical shifts were referenced by using sodium triflate on D₂O solvent (δ = 75.6 ppm). CEST spectra were obtained from H₂O solutions of the complexes using saturation times of 10 s. The pH of the solutions was adjusted to ~7 by adding 0.01 to 0.1 M NaOH or HCl solutions.

5.3.4. MRI studies

MRI measurements were performed on a Bruker BioSpec 70/30 USR magnet (software version Paravision 5.1) using Bruker surface (RF SUC 300 ¹H/¹⁹F_20mm LIN TR) and volume (RF RES 300 ¹H 075/040 QSN TR) coils. All data were acquired using the fast low angle single shot (FLASH) pulse sequence. MRI phantoms were obtained using 400 μL vials each containing 5 mM solutions of the [LnL¹] complexes (pH 7.4, 0.05 M HEPES buffer) using aqueous TFA with the same fluorine concentration was used as a reference in all recordings. The following parameters were used for MRI acquisition: FOV = 32 x 32, MTX = 32 x 32, slice thickness 5 mm, FA = 90 ⁰, while TR/TE and NEX were adjusted respect to individual complex in order to result in TA = 1, 2 or 4 hours (see Table S1, Annexe D, TA = 1 and 2 hours for [GdL¹]). The signal intensity scales were adjusted individually for each complex.

5.3.5. Crystal structure determination

A single crystal of [YbL³(H₂O)]·was analysed by X-ray diffraction. Crystallographic data were collected at 100 K using a Bruker D8 Venture diffractometer with a Photon 100 CMOS detector and Mo-Kα radiation (λ = 0.71073 Å) generated by an Incoatec high brilliance microfocus source equipped with Incoatec Helios multilayer optics. The software APEX3[52] was used for collecting frames of data, indexing reflections, and the determination of lattice parameters, SAINT[53] for integrating the intensity of the reflections, and SADABS[54] for scaling and empirical absorption correction. The structure was solved by dual-space methods using the program SHELXT.[55] All non-hydrogen atoms were refined with anisotropic thermal parameters by full-matrix least-squares calculations on F² using the program

SHELXL-2014.[56] Hydrogen atoms were inserted at calculated positions and constrained with isotropic thermal parameters. CCDC 1891733 contains the supplementary crystallographic data for this paper. These data can be obtained free of charge from the Cambridge Crystallographic Data Centre via www.ccdc.cam.ac.uk/data_request/cif. Crystal data and structure refinement details: Formula: $C_{23}H_{45}F_3N_5O_{15}Yb$; MW: 861.68; crystal system: triclinic; space group: P–1; a=9.5512(9) Å; b=10.1528(10) Å; c=17.9472(16) Å; α= 103.418(3)°, β=99.954(3)°, ⬚ = 96.389(3)°; V=1646.4(3) Å³; F(000)=870; Z=2; D_{calc}=1.738 g cm⁻³; μ=2.932 mm⁻¹; θ range=2.70– 30.57⁰; R_{int}=0.0260; 67698 measured reflections, of which 10095 were independent and 9781 were unique with $I > 2\sigma(I)$. GOF on F^2=1.049; $R1$=0.0146; $wR2$ (all data) = 0.0361; Largest differences peak and hole: 1.070 and –0.965 eÅ⁻³.

5.3.6. Computational details

All the calculations were carried out by using the Gaussian 09 package (Revision D.01).[57] Geometry optimisations of the [LnL¹(H₂O)]·2H₂O, [LnL²(H₂O)]⁺·2H₂O and [LnL¹(H₂O)]·2H₂O were performed using the hybrid meta-GGA TPSSh exchange-correlation functional.[58] Two explicit second sphere water molecules were included in the model systems to improve the description of the Ln-O$_{water}$ bonds.[22,59] Bulk solvent effects were considered by using the integral-equation formalism variant of the polarizable continuum model (IEFPCM).[60] The large-core quasi-relativistic effective core potential (LCRECP) approach and the associated [5s4p3d]-GTO valence-basis set was employed for all lanthanides,[61] in combination with the 6–31G(d,p) basis set for ligand atoms. Geometry optimisations were followed by frequency calculations to confirm the nature of the optimised geometries as local minima.

5.3.7. Synthetic procedure

1,4,7-Tris(*tert*-butoxycarboxymethyl)-10-((4-(trifluoromethylphenyl)acetamide)-1,4,7,10-tetraazacyclododecane (1). The cyclen derivative DO3A*t*Bu was dissolved in CH₃CN (25 mL) and NaHCO₃ (0.3345 g, 3.98 mmol, 5.1 eq) was added. A solution of 2-chloro-N-(4-(trifluoromethyl)phenyl)acetamide (0.2421 g, 1.019 mmol, 1.3 eq) in CH₃CN (20 mL) was added dropwise to the mixture at ambient temperature. One the addition was finished the mixture was heated at 46 ⁰C 7 days, until the alkylation was completed. The reaction mixture was removed from heat and allowed to cool to room temperature, filtered and evaporated to dryness in vacuo. The yellow oil was re-dissolved in CH₂Cl₂ and washed with water (20 mL). The organic layer was concentrated under reduced pressure to afford a yellowish oil. The product was purified by column chromatography on neutral alumina (CHCl₃ to CHCl₃:MeOH 95:5 (v:v)) to give a yellow foam (0.4829 g, 87%). ¹H NMR (300 MHz, CDCl₃): δ_H (ppm): 10.43 (s, 1H, NH), 8.07-8.04 (dd, 2H, CH_Ph), 7.43-7.40 (dd, 2H, CH_Ph), 3.77 (s, 2H, CH₂), 3.64-1.92 (m, 22H, CH₂), 1.63 (s, 3H, CH₃), 1.25 (s, 9H, CH₃). ¹³C-RMN (solvent CDCl₃, 298 K, 75 MHz) δ_C (ppm): 172.28 (quaternary, CO), 171.85 (quaternary, CH_Ph), 142.04 (quaternary, CH_Ph), 125.33 (quaternary, CF₃), 119.93 (quaternary, CH_Ph), 82.22 (quaternary, CCH₃), 82.06 (quaternary, CCH₃), 57.25 (secondary, CH₂), 55.73 (secondary, CH₂), 31.90 (secondary, CH₂), 29.63 (secondary, CH₂), 29.33 (secondary, CH₂), 27.94 (primary, CH₂), 27.92 (primary, CH₂), 22.67 (primary, CH₂). ¹⁹F-RMN (solvent CDCl₃, 298 K, 282 MHz) δ_F (ppm): -62.14 (CF₃). Mass spectrometry (ESI⁺) m/z (%BPI): 738.40 (100) ([$C_{35}H_{56}F_3N_5NaO_7$]⁺).

Triacetic 1,4,7-Tris(carboxymethyl)-10-((4-(trifluoromethylphenyl)acetamide)-1,4,7,10-tetraazacyclododecane acid (H$_3$L^3). Compound **1** was dissolved in formic acid (5 mL) and the mixture was refluxed for 48 h. Subsequently, the acid was evaporated and the residue was dissolved in water. The solvent was again evaporated and this process was repeated five times to remove completely formic acid. The product was redissolved in water (10 mL) and lyophilised to provide a yellowish solid (0.2675 g, 72%). ^{1}H NMR (300 MHz, D$_2$O): δ$_H$ (ppm): 8.47 (s, 2H, CH$_{Ph}$), 7.73-7.69 (dd, 2H, CH$_{Ph}$), 3.99-2.83 (m, 24H, CH$_2$). ^{13}C-RMN (solvent D$_2$O, 298 K, 75 MHz) δ$_C$ (ppm): 172.37 (quaternary, CO), 171.04 (quaternary, CH$_{Ph}$), 140.28 (quaternary, CH$_{Ph}$), 126.27 (quaternary, CH$_{Ph}$), 126.26 (quaternary, CF$_3$), 122.84 (quaternary, CH$_{Ph}$), 121.16 (quaternary, CH$_{Ph}$), 59.45 (quaternary, CCH$_3$), 57.52 (secondary, CH$_2$), 55.10 (secondary, CH$_2$), 50.98 (secondary, CH$_2$), 49.93 (secondary, CH$_2$). ^{19}F-RMN (solvent D$_2$O, 298 K, 282 MHz) δ$_F$ (ppm): -61.80 (CF$_3$). Mass spectrometry (ESI$^+$) m/z (%BPI): 548.23 (97) ([C$_{23}$H$_{33}$F$_3$N$_5$O$_7$]$^+$); 570.21 (100) ([C$_{23}$H$_{32}$F$_3$N$_5$NaO$_7$]$^+$), 586.18 (32) ([C$_{23}$H$_{32}$F$_3$KN$_5$O$_7$]$^+$); 608.16 (17) ([C$_{23}$H$_{31}$F$_3$KN$_5$NaO$_7$]$^+$.

General procedure for the preparation of the complexes: The corresponding ligand H$_3$L^1, H$_3$L^2 or H$_2$L^3 was solved in n-butanol in the presence of base (DIPEA) and the solution was homogenised with ultrasound bath assistance. The corresponding solid hydrated LnCl$_3$ salt (Ln = Eu, Gd, Lu, Tb, Tb or Yb) was added and the mixture was heated at 112 °C for 6 h. Subsequently, the mixture was allowed to cool down and the solvent was removed by the use of the rotary evaporator to give an orange crude product. The complexes were purified by reverse-phase medium performance liquid chromatography (MPLC) using UV detection. For the neutral complexes MPLC purification was carried out using a gradient of solvent B (CH$_3$CN, 10 to 30%) in solvent A (H$_2$O). For the charged complexes, purification was achieved with a gradient of solvent B (0.01% HCOOH in CH$_3$CN, 5 to 30%) in solvent A (0.01% HCOOH in H$_2$O). The fractions containing the complexes were combined and the solvent was removed *in vacuo*. The final product was redissolved in water and lyophilised to furnish the final complexes.

EuL^1. White solid (0.0309 g, 64%). Mass spectrometry (ESI$^+$) m/z (%BPI): 788.10 (100) ([C$_{24}$H$_{28}$N$_5$O$_7$F$_6$NaEu]$^+$). HR-MS (ESI$^+$) m/z: [M+Na]$^+$, calculated: 788.0997, found: 788.0994.

GdL^1. White solid (0.0282 g, 56%). Mass spectrometry (ESI$^+$) m/z (%BPI): 793.10 (100) ([C$_{24}$H$_{28}$N$_5$O$_7$F$_6$NaGd]$^+$). HR-MS (ESI$^+$) m/z: [M+Na]$^+$, calculated: 793.1026, found: 793.0992.

LuL^1. White solid (0.0367 g, 43%). Mass spectrometry (ESI$^+$) m/z (%BPI): 810.12 (100) ([C$_{24}$H$_{28}$N$_5$O$_7$F$_6$NaLu]$^+$), 788.14 (7) ([C$_{24}$H$_{29}$N$_5$O$_7$F$_6$Lu]$^+$). HR-MS (ESI$^+$) m/z: [M+Na]$^+$, calculated: 810.1192, found: 810.1190, [M+H]$^+$, calculated: 788.1373, found: 788.1378.

TbL^1. White solid (0.0479 g, 54%). Mass spectrometry (ESI$^+$) m/z (%BPI): 794.10 (100) ([C$_{24}$H$_{28}$N$_5$O$_7$F$_6$NaTb]$^+$). HR-MS (ESI$^+$) m/z: [M+Na]$^+$, calculated: 794.1038, found: 794.1045.

TmL^1. White solid (0.0431 g, 63%). Mass spectrometry (ESI$^+$) m/z (%BPI): 804.11 (100) ([C$_{24}$H$_{28}$N$_5$O$_7$F$_6$NaTm]$^+$), 782.13 (12) ([C$_{24}$H$_{29}$N$_5$O$_7$F$_6$Tm]$^+$). HR-MS (ESI$^+$) m/z: [M+Na]$^+$, calculated: 804.1127, found: 804.1128, [M+H]$^+$, calculated: 782.1307, found: 782.1313.

YbL^1. White solid (0.021 g, 49%). Mass spectrometry (ESI$^+$) m/z (%BPI): 809.12 (100) ([C$_{24}$H$_{28}$N$_5$O$_7$F$_6$NaYb]$^+$), 787.14 (15) ([C$_{24}$H$_{29}$N$_5$O$_7$F$_6$Yb]$^+$). HR-MS (ESI$^+$) m/z: [M+Na]$^+$, calculated: 809.1152, found: 809.1173, [M+H]$^+$, calculated: 787.1354, found: 787.1362.

EuL^2. White solid (0.0291 g, 31%). Mass spectrometry (ESI$^+$) m/z (%BPI): 841.17 (100) ([C$_{30}$H$_{34}$N$_6$O$_6$F$_6$Eu]$^+$). HR-MS (ESI$^+$) m/z: [M]$^+$, calculated: 841.1650, found: 841.1651.

GdL^2. White solid (0.0286 g, 31%). Mass spectrometry (ESI$^+$) m/z (%BPI): 846.17 (100) ([C$_{30}$H$_{34}$N$_6$O$_6$F$_6$Gd]$^+$). HR-MS (ESI$^+$) m/z: [M]$^+$, calculated: 846.1679, found: 846.1673.

LuL^2. White solid (0.0403 g, 51%). Mass spectrometry (ESI$^+$) m/z (%BPI): 863.19 (100) ([C$_{30}$H$_{34}$N$_6$O$_6$F$_6$Lu]$^+$). HR-MS (ESI$^+$) m/z: [M]$^+$, calculated: 863.1846, found: 863.1863.

TbL^2. White solid (0.0517 g, 56%). Mass spectrometry (ESI$^+$) m/z (%BPI): 847.17 (100) ([C$_{30}$H$_{34}$N$_6$O$_6$F$_6$Tb]$^+$). HR-MS (ESI$^+$) m/z: [M]$^+$, calculated: 847.1692, found: 847.1698.

TmL^2. White solid (0.0191 g, 21%). Mass spectrometry (ESI$^+$) m/z (%BPI): 857.18 (100) ([C$_{30}$H$_{34}$N$_6$O$_6$F$_6$Tm]$^+$).

YbL^2. White solid (0.0233 g, 31%). Mass spectrometry (ESI$^+$) m/z (%BPI): 862.18 (100) ([C$_{30}$H$_{34}$N$_6$O$_6$F$_6$Yb]$^+$). HR-MS (ESI$^+$) m/z: [M]$^+$, calculated: 862.1827, found: 862.1817.

EuL^3. White solid (0.0823 g, 62%). Mass spectrometry (ESI$^+$) m/z (%BPI): 720.11 (100) ([C$_{23}$H$_{29}$N$_5$O$_7$F$_3$NaEu]$^+$). HR-MS (ESI$^+$) m/z: [M+Na]$^+$, calculated: 720.1123, found: 720.1127.

GdL^3. White solid (0.0591 g, 73%). Mass spectrometry (ESI$^+$) m/z (%BPI): 725.11 (100) ([C$_{23}$H$_{29}$N$_5$O$_7$F$_3$NaGd]$^+$). HR-MS (ESI$^+$) m/z: [M+Na]$^+$, calculated: 725.1152, found: 725.1139.

LuL^3. White solid (0.0213 g, 46%). Mass spectrometry (ESI$^+$) m/z (%BPI): 742.13 (100) ([C$_{23}$H$_{29}$N$_5$O$_7$F$_3$NaLu]$^+$), 758.12 (43) ([C$_{23}$H$_{29}$N$_5$O$_7$F$_3$KLu]$^+$). HR-MS (ESI$^+$) m/z: [M+Na]$^+$, calculated: 742.1319, found: 742.1315.

TbL^3. White solid (0.0705 g, 54%). Mass spectrometry (ESI$^+$) m/z (%BPI): 726.12 (100) ([C$_{23}$H$_{29}$N$_5$O$_7$F$_3$NaTb]$^+$), 704.13 (10) ([C$_{23}$H$_{30}$N$_5$O$_7$F$_3$Tb]$^+$). HR-MS (ESI$^+$) m/z: [M+Na]$^+$, calculated: 726.1164, found: 726.1158, [M+H]$^+$, calculated: 704.1345, found: 704.1340.

TmL^3. White solid (0.0817 g, 61%). Mass spectrometry (ESI$^+$) m/z (%BPI): 736.13 (100) ([C$_{23}$H$_{29}$N$_5$O$_7$F$_3$NaTm]$^+$), 714.14 (10) ([C$_{23}$H$_{30}$N$_5$O$_7$F$_3$Tm]$^+$). HR-MS (ESI$^+$) m/z: [M+Na]$^+$, calculated: 726.1253, found: 726.1277, [M+H]$^+$, calculated: 714.1434, found: 714.1427.

YbL^3. White solid (0.0536 g, 65%). Mass spectrometry (ESI$^+$) m/z (%BPI): 741.13 (100) ([C$_{23}$H$_{29}$N$_5$O$_7$F$_3$NaYb]$^+$), 719.15 (10) ([C$_{23}$H$_{30}$N$_5$O$_7$F$_3$Yb]$^+$). HR-MS (ESI$^+$) m/z: [M+Na]$^+$, calculated: 741.1300, found: 741.1295.

5.4. Conclusions

We have shown that the properties of potential ^{19}F MRI probes can be conveniently optimised by ligand design in combination with a judicious selection of the optimal Ln^{3+} ion. The complexes investigated in this work have the advantage of providing a single major diastereoisomer in solution, which was identified as the SAP isomer by ^{1}H NMR studies in solution and single-crystal X-ray crystallography in the case of [YbL^3]. The complexes contain the expected inner-sphere water molecule, which results in ^{1}H relaxivities of the Gd^{3+} complexes comparable to those of commercially available contrast agents. An attractive property of the Tm^{3+} complexes is the presence of an amide resonance highly shifted with respect to bulk water, which provides a sizeable CEST signal. These amide protons are in rather fast exchange with bulk water due to the electron-withdrawing effect of the −CF$_3$ substituents. As a

result, the ligand design must be improved to obtain efficient Tm^{3+} probes operating both at the ^{1}H and ^{19}F frequencies.

The detailed analysis of the ^{19}F NMR shifts and ^{19}F longitudinal and transverse relaxation rates (R_1 and R_2) allowed a very accurate determination of the average Ln···F distances in solution and the rotational correlation times associated to the Ln···F vector. The μ_{eff} and T_{1e} values obtained from the fits of the experimental data present larger uncertainties, but are still in agreement with the expected values. The Ln···F distance determined for [LnL^{1}] complexes (7.45 $\pm$ 0.04 Å) is optimal for Ln^{3+} ions such as Tb^{3+}, as confirmed by in vitro MRI studies. The longer distance in [LnL^{3}] and [LnL^{2}]$^{+}$ complexes (9.13 $\pm$ 0.05 Å) is more favourable for Gd^{3+}.

5.5. Notes

The work presented in this chapter is being prepared to be submitted for publication as communication in a scientific journal.

5.6. References

1   G. N. Holland, P. A. Bottomley and W. S. Hinshaw, *J. Magn. Reson.* 1977, **28**, 133.
2   E. McFarland, J. A. Koutcher, B. R. Rosen, B. Teicher and T. J. Brady, *J. Comput. Assist. Tomogr.* 1985, **9**, 8.
3   (a) I. Tirotta, V. Dichiarante, C. Pigliacelli, G. Cavallo, F. Terraneo, B. Bombelli, P. Metrangolo and G. Resnati, *Chem. Rev.*, 2015, **115**, 1106. (b) A. A. Kislukhin, H. Xu, S.R. Adams, K. H. Narsinh and R. Tsien, *Nat. Mater.* 2016, **15**, 662.
4   K. L. Peterson, K. Srivastava and V. C. Pierre, *Front. Chem.*, 2018, **6**, 160.
5   P. Harvey, I. Kuprov and D. Parker, *Eur. J. Inorg. Chem.*, 2012, 2015.
6   P. Kadjane, C. Platas-Iglesias, P. Boehm-Sturm, V. Truffault, G. E. Hagberg, M. Hoehn, N. K. Logothetis and G. Angelovski, *Chem. Eur. J.*, 2014, **20**, 7351.
7   (a) M. T. McMahon, A. A. Gilad, J. W. M. Bulte and P. C. M. van Zijl, Chemical Exchange Saturation Transfer Imaging: Advances and Applications, Pan Stanford Publishing Pte. Ltd., Singapore, 2017, (b) G. Liu, X. Song, K. W. Y. Chan and M. T. McMahon, *NMR Biomed.* 2013, **26**, 810.
8   O. M. Evbuomwan, E. Terreno, S. Aime and A. D. Sherry, CEST and Paracest Agents for Molecular Imaging. In The Chemistry of Molecular Imaging, First Edition (Long, N.; Wong, W.-T. Eds), John Wiley & Sons, 2015.
9   J. A. Peters, J. Huskens and D. J. Raber, *Prog. Nucl. Magn. Reson. Spectrosc.*, 1996, **28**, 283.
10 F. Schmid, C. Höltke, D. Parker and C. Faber, *Magn. Reson. Med.*, 2013, **69**, 1056.
11 (a) K. H. Chalmers, E. De Luca, N. H. M. Hogg, A. M. Kenwright, I. Kuprov, D. Parker, M. Botta, J. I. Wilson and A. M. Blamire, *Chem. Eur. J.*, 2010, **16**, 134-148. (b) K. H. Chalmers, M. Botta and D. Parker, *Dalton Trans.*, 2011, **40**, 904. (c) K. H. Chalmers, A. M. Kenwright, D. Parker and A. M. Blamire, *Magn. Reson. Med.*, 2011, **66**, 931. (d) P. K. Senanayake, A. M. Kenwright, D. Parker and S. K. van der Hoorn, *Chem. Commun.*, 2007, 2923. (e) A. M. Kenwright, I. Kuprov, E. De Luca, D. Parker, S. U. Pandya, P. K. Senanayake and D. G. Smith, *Chem. Commun.*, 2008, 2514.
12 (a) Z.-X. Jiang, Y. Feng and Y. B. Yu, *Chem. Commun.*, 2011, **47**, 7233. (b) K. Srivastava, E. A. Weitz, K. L. Peterson, M. Marjanska and V. C. Pierre, *Inorg. Chem.*, 2017, **56**, 1546. (c) V. Herynek, M. Martiniskova, Y. Bobrova, A. Galisova, J. Kotek, P. Hermann, F. Koucky, D. Jirak and M. Hajek, *Magn. Reson. Mater. Phy.*, 2018, https://doi.org/10.1007/s10334-018-0721-9.
13 (a) N. Cakic, T. Savic, J. Stricker-Shaver, V. Truffault, C. Platas-Iglesias, C. Mirkes, R. Pohmann, K. Scheffler and G. Angelovski,

Chem. Commun. 2016, **52**, 9224. (b) N. Cakić, B. Tickner, M. Zaiss, D. Esteban-Gómez, C. Platas-Iglesias and G. Angelovski, *Inorg. Chem.*, 2017, **56**, 7737.
14 (a) K. Srivastava, G. Ferrauto, V. G. Jr. Young, S. Aime and V. C. Pierre, *Inorg. Chem.*, 2017, **56**, 12206. (b) J. Blahut, P. Hermann, A. Gálisová, V. Herynek, I. Císařová, Z. Tošnerc and J. Kotek, *Dalton Trans.*, 2016, **45**, 474. (c) M. Yu, D. Xie, K. P. Phan, J. S. Enriquez, J. J. Luci and E. L. Que, *Chem. Commun.*, 2016, **52**, 13885. (d) J. Blahut, K. Bernasek, A. Galisova, V. Herynek, I. Cisarova, J. Kotek, J. Lang, S. Matejkova and P. Hermann, *Inorg. Chem.*, 2017, **56**, 13337. (d) M. Yu, B. S. Bouley, J. S. Enriquez and E. L. Que, *J. Am. Chem. Soc.*, 2018, **140**, 10546. (e) D. Xie, S. Kim, V. Kohli, A. Banerjee, M. Yu, J. S. Enriquez, J. J. Luci, J. J. and E. L. Que, *Inorg. Chem.*, 2017, **56**, 6429.
15 (a) S. Aime, S. Geninatti Crich, E. Gianolio, G. B. Giovenzana, L. Tei and E. Terreno, *Coord. Chem. Rev.*, 2006, **250**, 1562. (b) E. Terreno, D. Delli Castelli and S. Aime, Encoding the frequency dependence in MRI contrast media: the emerging class of CEST agents. *Contrast Media Mol. Imaging*, 2010, **5**, 78. (c) E. Vinogradov, A. D. Sherry and R. E. Lenkinski, *J. Magn. Reson.*, 2013, **229**, 155. (d) P. C. M. van Zijl and N. N. Yadav, *Magn. Reson. Med.*, 2011, **65**, 927. (e) S. J. Dorazio and J. R. Morrow, *Eur. J. Inorg. Chem.*, 2012, 2006. (f) P. B. Tsitovich, P. J. Burns, A. M. McKay and J. R. Morrow, *J. Inorg. Biochem.*, 2014, **133**, 143. (g) S. J. Ratnakar, M. Woods, A. J. M. Lubag, Z. Kovacs and A. D. Sherry, *J. Am. Chem. Soc.*, 2008, **130**, 6-7. (h) S. J. Ratnakar, T. C. Soesbe, L. L. Lumata, Q. N. Do, S. Viswanathan, C.-Y. Lin, A. D. Sherry and Z. Kovacs, *J. Am. Chem. Soc.*, 2013, **135**, 14904.
16 (a) R. Pujales-Paradela, T. Savic, D. Esteban-Gómez, G. Angelovski, F. Carniato, M. Botta and C. Platas-Iglesias, *Chem. Eur. J.*, 2019, doi: 10.1002/chem.201806192.
17 D. Parker, H. Puschmann, A. S. Batnasov and K. Senanayake, *Inorg. Chem.*, 2003, **42**, 8646.
18 J. Dale, *Acta Chem. Scand.*, 1973, **27**, 1115.
19 S. Aime, M. Botta, M. Fasano, M. P. M. Marques, C. F. G. C. Geraldes, D. Pubanz and A. E. Merbach, *Inorg. Chem*, 1997, **36**, 2059.
20 (a) M. Milne, K. Chicas, A. Li, R. Bartha and R. H. E. Hudson, *Org. Biomol. Chem.*, 2012, **10**, 287. (b) S. Zhang, L. Michaudet, S. Burgess and A. D. Sherry, *Angew. Chem. Int. Ed.*, 2002, **41**, 1919. (c) A. S. Batnasov, A. Beeby, J. A. Bruce, J. A. K. Howard, A. M. Kenwright and D. Parker, *Chem. Commun.*, 1999, 1011.
21 L. S. Natrajan, N. M. Khoabane, B. L. Dadds, C. A. Muryn, R. G. Pritchard, S. L. Heath, A. M. Kenwright, I. Kuprov and S. Faulkner, *Inorg. Chem.*, 2010, **49**, 7700.
22 M. Regueiro-Figueroa and C. Platas-Iglesias, *J. Phys. Chem. A*, 2015, **119**, 6436.
23 A. L. Thompson, D. Parker, D. A. Fulton, J. A. K. Howard, S. U. Pandya, H. Puschmann, K. Senanayake, P. A. Stenson, A. Badari, M. Botta, S. Avedano and S. Aime, *Dalton Trans.*, 2006, 5605.
24 D. Esteban-Gomez, A. de Blas, T. Rodriguez-Blas, L. Helm and C. Platas-Iglesias, *ChemPhysChem*, 2012, **13**, 3640.
25 A. Beeby, I. M. Clarkson, R. S. Dickins, S. Faulkner, D. Parker, L. Royle, A. S. de Sousa, J. A. G. Williams and M. Woods, *J. Chem. Soc., Perkin Trans. 2,* 1999, 493.
26 (a) C. Adair, M. Woods, P. Y. Zhao, A. Pasha, P. M. Winters, G. M. Lanza, P. Athey, A. D. Sherry and G. E. Kiefer, *Contrast Media Mol. Imaging,* 2007, **2**, 55. (b) M. Polasek, J. Kotek, P. Hermann, I. Cisarova, K. Binnemans and I. Lukes, *Inorg. Chem.*, 2009, **48**, 466. (c) F. A. Dunand, R. S. Dickins, D. Parker, and A. E. Merbach, *Chem. Eur. J.*, 2001, **7**, 5160. (d) S. Aime, M. G. Botta and G. Ermondi, *Inorg. Chem.*, 1992, **31**, 4291.
27 (a) L. S. Natrajan, A. J. L. Villaraza, A. M. Kenwright and Faulkner, *Chem. Commun.*, 2009, 6020. (b) A. Nonat, M. Regueiro-Figueroa, D. Esteban-Gómez, A. de Blas, T. Rodríguez-Blas, C. Platas-Iglesias and L. J. Charbonniere, *Chem. Eur. J.*, 2012, **18**, 8163.

28 (a) S. Aime, M. Botta and G. Ermondi, *Inorg. Chem.,* 1992**, 31**, 4291. (b) A. Rodriguez-Rodriguez, D. Esteban-Gomez, A. de Blas, T. Rodriguez-Blas, M. Fekete, M. Botta, R. Tripier and C. Platas-Iglesias, *Inorg. Chem.,* 2012, **51**, 2509.

29 (a) J. Vipond, M. Woods, P. Zhao, G. Tircso, J. Ren, S. G. Bott, D. Ogrin, G. E. Kiefer, Z. Kovacs and A. D. Sherry, *Inorg. Chem.,* 2007, **46**, 2584. (b) C. Doffek, N. Alzakhem, C: Bischof, J. Washner, T. Güden-Silber, J. Lügger, C. Platas-Iglesias and M. Seitz, *J. Am. Chem. Soc.,* 2012, **134**, 16413. (c) A. Rodríguez-Rodríguez, D. Esteban-Gómez, R. Tripier, G. Tircsó, Z. Garda, I. Tóth, A. de Blas, T. Rodríguez-Blas and C. Platas-Iglesias, *J. Am. Chem. Soc.,* 2014, **136**, 17954.

30 I. Bertini, C. Luchinat and G. Parigi, *Prog. Nucl. Magn. Reson. Spectrosc.,* 2002, **40**, 249.

31 J. H. Forsberg, R. M. Delaney, Q. Zhao, G. Harakas and R. Chandran, *Inorg. Chem.,* 1995, **34**, 3705.

32 A. Roca-Sabio, C. S. Bonnet, M. Mato-Iglesias, D. Esteban-Gómez, É. Toth, A. de Blas, T. Rodríguez-Blas and C. Platas-Iglesias, *Inorg. Chem.,* 2012, **51**, 10893.

33 A. Wacker, F. Carniato, C. Platas-Iglesias, D. Esteban-Gómez, H.-J. Wester, L. Tei, J. Notni, *Dalton Trans,.* 2017, **46**, 16828.

34 (a) L. N. Goswani, P. J. Kueffer, S. S. Jalisatgi, M. F. Hawthorne, *Molecules,* 2013, **18**, 9034. (b) M. Rohrer, H. Bauer, J. Mintorovitch, M. Requardt, H.-J. Weinmann, *Invest. Radiol.,* 2005, **40**, 715.

35 J. Wahsner, E. M. Gale, A. Rodríguez-Rodríguez and P. Caravan, *Chem. Rev.,* 2019, **119**, 957.

36 S. Aime, M. Botta, D. Esteban-Gómez and C. Platas-Iglesias, *Mol. Phys.,* 2019, doi.org/10.1080/00268976.2018.1516898 .

37 (a) T. J. Swift and R. E. Connick, *J. Chem. Phys.,* 1962, **37**, 307. (b) T. J.Swift and R. E. Connick, Erratum: *J. Chem. Phys.,* 1964, **41**, 2553.

38 (a) I. Solomon, *Phys. Rev.,* 1955, **99**, 559. (b) I. Solomon, N. Bloembergen, *J. Chem. Phys.,* 1956, **25**, 261. (c) N. Bloembergen, *J. Chem. Phys.,* 1957, **27**, 572. (d) N. Bloembergen and L. O. Morgan, *J. Chem. Phys.,* 1961, **34**, 842.

39 J. H. Freed, *J. Chem. Phys.,* 1978, **68**, 4034.

40 D. H. Powell, O. M. Ni Dhubhghaill, D. Pubanz, L. Helm, Y. S. Lebedev, W. Schlaepfer and A. E. Merbach, *J. Am. Chem. Soc.,* 1996, **118**, 9333.

41 R. Mills, *J. Phys. Chem.*, 1973, **77**, 685.

42 (a) V. R. Sheth, Y. Li, L. Q. Chen, C. M. Howison, C. A. Flask and M. D. Pagel, *Magn. Reson. Med.,* 2012, **67**, 760. (b) G. Liu, Y. Li, V. R. Sheth and M. D. Pagel, *Mol. Imaging,* 2012, **11**, 47. (c) G. Liu, Y. Li and M. D. Pagel, *Magn. Reson. Med.,* 2007, **57**, 1249.

43 M. Suchy, M. Milne, A. A. H. Elmehriki, N. McVicar, A. X. Li, R. Bartha and R. H. E. Hudson, *J. Med. Chem.,* 2015, **58**, 6516.

44 M. Zaiss, G. Angelovski, E. Demetriou, M. T. McMahon, X. Golay and K. Scheffler, *Magn. Reson. Med.,* 2018, **79**, 1708.

45 S. J. Ratnakar, S. Viswanathan, Z. Kovacs, A. K. Jindal, K. N. Green and A. D. Sherry, *J. Am. Chem. Soc.,* 2012, **134**, 5798.

46 J. Lisowski, J. L. Sessler, V. Lynch and T. D. Mody, *J. Am. Chem. Soc.,* 1995, **117**, 2273.

47 (a) G. Castro, M. Regueiro-Figueroa, D. Esteban-Gómez, P. Pérez-Lourido, C. Platas-Iglesias, and L. Valencia, *Inorg. Chem.,* 2016, **55**, 3490. (b) A. M. Funk, K.-L. N. A. Finney, P. Harvey, A. M. Kenwright, E. R. Neil, N. J. Rogers, P. K. Senanayake and D. Parker, *Chem. Sci.,* 2015, **6**, 1655.

48 (a) J. H. Forsberg, R. M. Delaney, Q. Zhao, G. Harakas and R. Chandran, *Inorg. Chem.,* 1995, **34**, 3705. (b) I. Bertini, C. Luchinat and G. Parigi, *Prog. Nucl. Magn. Reson. Spectrosc.,* 2002, **40**, 249.

49 A. M. Funk, P. Harvey, K.-L. N. A. Finney, M. A. Fox, A. M. Kenwright,N. J. Rogers, P. K. Senanayake and D. Parker, *Phys. Chem. Chem. Phys.,* 2015, **17**, 16507.

50 H. Kurzen, L. Bovigny, C. Bulloni and C. Daul, *Chem. Phys. Lett.,* 2013, **574**, 129.

51 (a) B. M. Alsaadi, F. J. C. Rossotti and R. J. P Williams, *J. Chem. Soc., Dalton Trans.,* 1980, 2147. (b) I. Bertini, F. Capozzi, C. Luchinat, G. Nicastro and Z. Xia, *J. Phys. Chem.,* 1993, **97**, 6351.

52 APEX3 Version 2016.1 (Bruker AXS Inc., 2016).

53 SAINT Version 8.37A (Bruker AXS Inc., 2015)

54 SADABS Version 2014/5 (Sheldrick, Bruker AXS Inc.)

55 SHELXT Version 2014/5. G. M. Sheldrick, *Acta Cryst.*, 2015, A71, 3-8.

56 SHELXL Version 2014/7. G. M. Sheldrick, *Acta Cryst*., 2008, A64, 112-122.

57 Gaussian 09, Revision A.01, M. J. Frisch, G. W. Trucks, H. B. Schlegel, G. E. Scuseria, M. A. Robb, J. R. Cheeseman, G. Scalmani, V. Barone, B. Mennucci, G. A. Petersson, H. Nakatsuji, M. Caricato, X. Li, H. P. Hratchian, A. F. Izmaylov, J. Bloino, G. Zheng, J. L. Sonnenberg, M. Hada, M. Ehara, K. Toyota, R. Fukuda, J. Hasegawa, M. Ishida, T. Nakajima, Y. Honda, O. Kitao, H. Nakai, T. Vreven, J. A. Montgomery Jr., J. E. Peralta, F. Ogliaro, M. Bearpark, J. J. Heyd, E. Brothers, K. N. Kudin, V. N. Staroverov, R. Kobayashi, J. Normand, K. Raghavachari, A. Rendell, J. C. Burant, S. S. Iyengar, J. Tomasi, M. Cossi, N. Rega, N. J. Millam, M. Klene, J. E. Knox, J. B. Cross, V. Bakken, C. Adamo, J. Jaramillo, R. Gomperts, R. E. Stratmann, O. Yazyev, A. J. Austin, R. Cammi, C. Pomelli, J. W. Ochterski, R. L. Martin, K. Morokuma, V. G. Zakrzewski, G. A. Voth. P. Salvador, J. J. Dannenberg, S. Dapprich, A. D. Daniels, O. Farkas, J. B. Foresman, J. V. Ortiz, J. Cioslowski, D. J. Fox in *Gaussian 09, Revision A.01*; Gaussian, Inc., Wallingford, CT, 2009.

58 J. M. Tao, J. P. Perdew, V. N. Staroverov and G. E. Scuseria, *Phys. Rev. Lett.,* 2003, **91**, 146401.

59 D. Esteban-Gomez, A. de Blas, T. Rodriguez-Blas, L. Helm, and C. Platas-Iglesias, *ChemPhysChem*, 2012, **13**, 3640.

60 J. Tomasi, B. Mennucci and R. Cammi, *Chem. Rev.,* 2005, **105**, 2999.

61 M. Dolg, H. Stoll, A. Savin and H. Preuss, *Theor. Chim. Acta,* 1989, **75**, 173.

Reinforced Ni(II)-cyclam derivatives
as dual ^{1}H/^{19}F MRI Probes
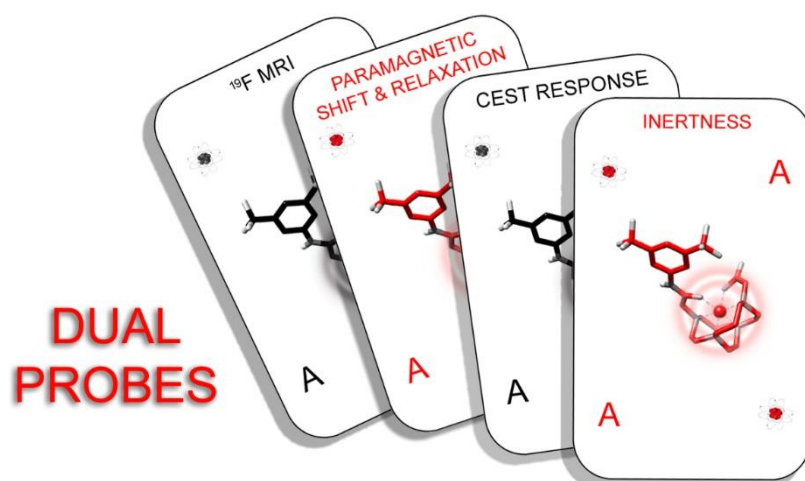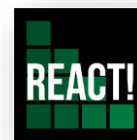
Chapter 6

Reinforced Ni(II)-cyclam derivatives as dual ^{1}H/^{19}F MRI Probes

Reinforced cross-bridged Ni^{2+}-cyclam complexes were functionalised with pendant arms containing both amide protons and CF$_3$ groups that lead to a dual ^{1}H/^{19}F response. The resulting complexes possess very high inertness favourable for MRI applications. The paramangnetism of the Ni^{2+} ion promotes the chemical exchange saturation transfer (CEST) effect at 56 ppm from bulk water and favors shorter adquisition times in the **^{19}F** magnetic resonance imaging (MRI) experiments, thus enhancing signal-to-noise ratios compared to the fluorinated diamagnetic reference.

,

6.1. Introduction

Magnetic resonance imaging (MRI) contrast agents (CAs) are generally paramagnetic metal complexes of Gd^{3+} able to reduce the longitudinal relaxation time (T_1) of protons in their vicinity.[1] These classical CAs are commonly used in clinical practice, although recently there have been some concerns about their toxicity. Indeed, recent studies located Gd^{3+} deposits in the brain and other tissues of patients that received CAs before MRI scans.[2] Furthermore, some patients with renal impairment developed a new disease, nephrogenic systemic fibrosis, associated to the release of toxic Gd^{3+} in vivo.[3] These toxicity issues prompted the European Medicines Agency to restrict in 2017 the use of some non-macrocyclic Gd^{3+} contrast agents and suspend the authorisations for others.[4] Although the use of macrocyclic Gd^{3+}-based contrast agents is thought to be safe and will likely continue in the near future, there is an urgent need to develop alternatives to the classical Gd^{3+}-based CAs.

The toxicity issues abovementioned and some limitations of the Gd^{3+}-based probes triggered the development of different alternatives, including: 1) Developing T_1 shortening agents based on other paramagnetic metal ions such as Mn^{2+};[5] 2) The use of agents that provide contrast following the chemical exchange saturation transfer (CEST) mechanism. CEST agents contain a pool of protons in slow-to-intermediate exchange with bulk water, so that applying a radiofrequency pulse to this proton nuclei results in a decrease of bulk water signal by saturation transfer. Paramagnetic ions such as the Ln^{3+} ions increase the chemical shift difference between the two pools of protons, and consequently the slow-to-intermediate exchange condition can be achieved with faster exchange rates.[6] Furthermore, different CEST agents based on paramagnetic transition metal ions have been also proposed (Fe^{2+}, Co^{2+} and Ni^{2+}).[7] CEST agents can be activated at will by applying a radiofrequency pulse, which opens the possibility of detecting different agents simultaneously. 3) Using ^{19}F-based probes, which represent the best alternative to ^{1}H given the high sensitivity of the ^{19}F nucleus (83% with respect to ^{1}H). ^{19}F-based probes have the advantage of the negligible fluoride concentration in vivo, which eliminates any background signal.[8] However, ^{19}F presents rather long relaxation times, so that paramagnetic metal ions are used to accelerate relaxation times and thus acquisition times. This has been achieved both with transition metal ions[9] or lanthanides.[10]

The combination of CEST ^{1}H and ^{19}F response into a single CA may result in probes that combine the advantages of the two techniques: The generation of on/off response at will by CEST agents and the easier quantification of the MRI signal for ^{19}F probes. Some examples of dual ^{1}H/^{19}F agents based on Ln^{3+} complexes were reported recently in the literature.[11] Given the potential toxicity of probes based on Ln^{3+} ions, it was sought to develop transition metal complexes showing this dual output. Herein it is reported the first generation of these transition metal CA candidates based on Ni^{2+}. Stable complexation of this metal ion was achieved with the use of reinforced (cross-bridged) cyclam derivative, functionalised with a carboxylate pendant arm to ensure a good water solubility, and including a second pendant arm containing an exchangeable amide proton for CEST response and ^{19}F nuclei (Figure 1).

6.2. Results and discussion

6.2.1. Synthesis

The synthesis of the ligands was achieved by sequential alkylation of the commercially available cross-bridged precursor with tert-butyl bromoacetate and the chloroacetamide precursors. Hydrolysis of the tert-butyl groups with formic acid

afforded the HL[1] and HL[2] ligands with fair overall yields (36 and 44%, respectively). The preparation of the Ni^{2+} complexes required harsh conditions due to slow complexation kinetics, using *n*-butanol as a solvent and high temperature.[12]
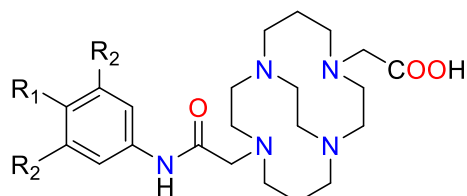
HL[1]: R$_1$= H; R$_2$= CF$_3$
HL[2]: R$_1$= CF$_3$; R$_2$= H

Figure 1. Chemical structures of the ligands reported in this work.

6.2.2. X-ray determination

The structure of both complexes were determined using X-ray diffraction measurements (Figure 2). The [NiL[1]][+] and [NiL[2]][+] complexes were crystallised as the chloride and trifluoromethanesulfonate salts, respectively. The metal ion is directly coordinated to the four N atoms of the macrocyclic unit, with Ni-N distances in the range 2.07-2.10 Å. These distances somewhat shorter than those observed for the few *cross-bridged* Ni^{2+} complexes reported in the literature (2.09-2.20 Å).[13] The oxygen atoms of the pendant arms complete the distorted octahedral coordination around the metal ion in both cases. The Ni-O distance involving the carboxylate oxygen atom (2.026 Å for [NiL[1]][+] and 2.058 Å for [NiL[2]][+]) is slightly shorter than that to the amide oxygen atom (2.075 Å and 2.075 Å for [NiL[2]][+] and [NiL[1]][+], respectively). The macrocyclic unit adopts a cis-V conformation, with the bicyclo[6.6.2] ligand units adopting [2323] conformations, as usually observed for complexes of *cross-bridged* cyclam derivatives with small metal ions.[14]

6.2.3. Dissociation kinetics

The inertness of the [NiL[1]][+] complex was assessed by using spectrophotometric measurements. The absorption spectrum of a 4 M HCl solution of the complex presents a maximum at 248 nm due to the phenylamide chromophore. The absorption spectrum recorded after 24 h is identical to that recorded immediately after dissolving the complex. Furthermore, the mass spectrum of the solution obtained with electrospray ionisation presents the peak of the [NiL[1]][+] entity at *m/z* = 542.19, while the peak of the protonated ligand at *m/z* = 486.26 was not observed (Figure 3). These results confirm that Ni^{2+} ion remains into the macrocyclic cavity, and this no dissociation of the complex takes place under these harsh conditions. For instance, the [Gd(DOTA)][-] complex, which is used as a contrast agent in clinical practice as DOTAREM®, undergoes dissociation under these conditions with a half-live of 144 minutes.[15]
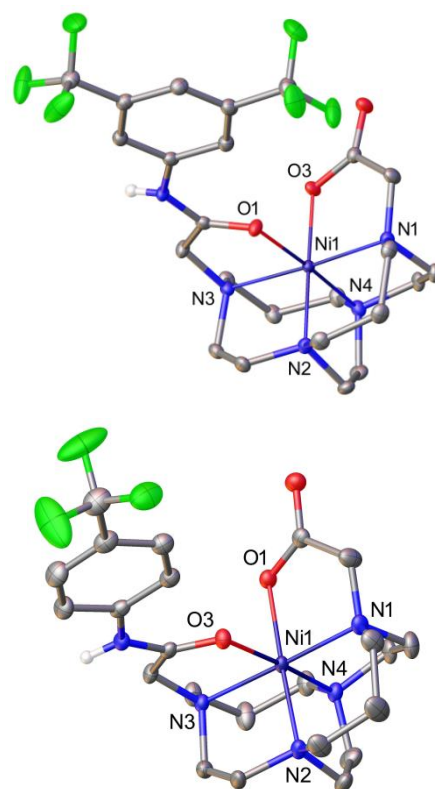
Figure 2. X-ray crystal structure of [NiL[1]][+] and [NiL[2]][+] complexes. Bond distances (Å): [NiL[1]][+] Ni-O1 2.075(2); Ni-O3 2.026(1); Ni-N1 2.084(2); Ni-N2 2.071(2); Ni-N3 2.097(2); Ni-N4 2.070(2). [NiL[2]][+]: Ni-O1 2.0579(18); Ni-O3 2.1103(18); Ni-N1 2.083(2); Ni-N2 2.082(2); Ni-N3 2.096(2); Ni-N4 2.068(2).
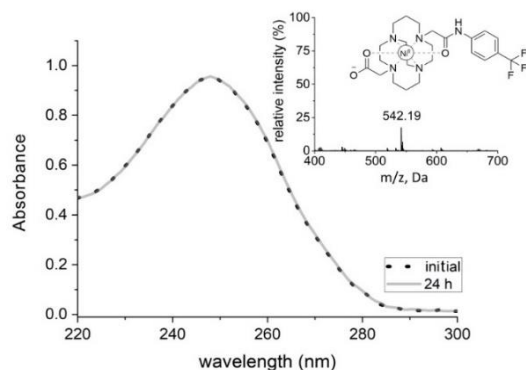
Figure 3. UV-vis spectra of a 5.2×10^{-5} M fresh aqueous solution of **[NiL[2]][+]** and that of the same solution registered 24 h later (25 °C, 4M HCl).

6.2.4. [1]H CEST measurements

The two Ni^{2+} complexes provide moderate CEST effects. The measurements were carried out using 15 mM H$_2$O solutions of the complexes containing 20% acetonitrile due to their low solubility in pure water (Figure 4 and Annexe E). The CEST spectra present prominent CEST peaks at 56 ppm and 25 ºC in both complexes due to the amide proton of the ligands, while the shift reduces to ~52 ppm when the spectra were recorded at 37 ºC. This chemical shift is somewhat smaller than those observed for Ni^{2+} complexes with ligands containing acetamide[7c,16] (typically ~70 ppm) or picolinamide[17] groups (~85 ppm). The CEST spectra obtained using different saturation powers were quantitatively analysed using the standard Bloch-

McConnell equations and 2 exchanging pools (paramagnetically shifted pool and bulk water),[18] providing exchange rates of amide protons of k_{ex} = 10.9 $\pm$ 1.1 and 7.1 $\pm$ 1.7 kHz for [NiL^1]$^+$ and [NiL^2]$^+$, respectively. The highest rate determined for [NiL^1]$^+$ is likely related to the more acidic character of the amide proton due to the combined electron withdrawing effect of two CF$_3$ substituents. However, given the fast exchange rates of both complexes already at 25 ^{o}C, further structural adjustments would be necessary to optimise their properties for potential use as CEST MRI contrast agents.
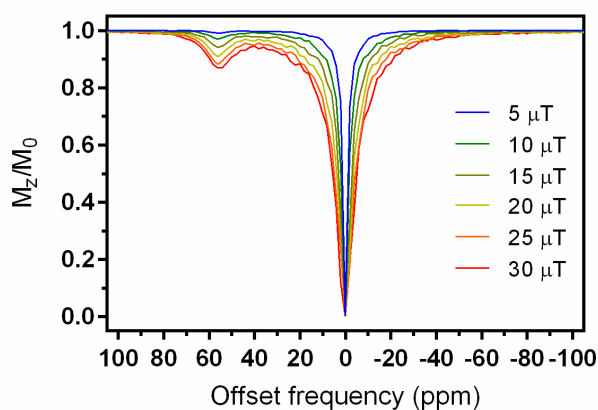
Figure 4. CEST spectra of [NiL^2]$^+$ (15 mM) in H$_2$O containing 20% acetonitrile (pH 7, saturation time 10 s) recorded using different saturation powers.

6.2.5. ^{19}F measurements

The ^{19}F NMR spectra of the two complexes presents a signal at ca. -60 ppm due to the ligand CF$_3$ groups, which in the case of [NiL^1]$^+$ implies that the rotation about the amide N-C bond of the phenyl group is fast on the NMR time scale. The spectra of the two complexes show very different linewidths, which anticipates distinct ^{19}F relaxation rates (Figure 5). This is confirmed by the longitudinal (R_1) and transverse (R_2) relaxation rates, which were measured at three different magnetic fields (Table 1, Figure 5). Both the R_1 and R_2 values remain constant within experimental error at 7, 9.4 and 11.75 T. The two complexes present virtually identical R_1/R_2 ratios (Table 1). Both the R_1 and R_2 values are higher for [NiL^1]$^+$ with respect to [NiL^2]$^+$, which is likely associated to a shorter average Ni···F distance in the former.

Table 1. ^{19}F longitudinal (R_1) and transverse (R_2) relaxation rates obtained from 15 mM aqueous solutions of [NiL^1]$^+$ and [NiL^2]$^+$ containing 20% acetonitrile and signal-to-noise ratios (SNR) obtained with phantom MRI studies (25 °C, 7.05 T).^{a}

Complex	R_1 (s^{-1})	R_2 (s^{-1})	R_1/R_2	SNR^b
[NiL^1]$^+$	99.4(1)	125.0(2)	0.80	136.9 / 47.8^b
[NiL^2]$^+$	34.2(1)	40.8(2)	0.84	98.3 / 30.0^b

^{a} Data obtained at 7.05 T. Standard deviations within parenthesis. ^{b}SNRs obtained for TFA using identical experimental conditions.

6.2.6. Fittings ^{19}F data

The experimental data was analysed by using the standard Solomon-Bloembergen-Morgan theory of paramagnetic relaxation.[19] The ^{19}F relaxation rates at high fields employed in this study were not affected by the relaxation of the Ni^{2+} electron spin. Thus, the analysis of the experimental data required fitting three parameters: The rotational correlation time τ_R^{298}, which was assumed to be identical for the two complexes data of the two complexes, and the Ni···F distances of the two complexes. It was obtained a τ_R^{298} value of the Ni···F vector of 89 $\pm$ 10 ps, which is reasonable considering the size of the complexes. The Ni···F distances were determined to be 7.28 $\pm$ 0.42 and 8.72 $\pm$ 0.5 Å for [NiL^1]$^+$ and [NiL^2]$^+$, respectively. The dipolar paramagnetic relaxation mechanism is proportional to $(1/r_{NiF})^6$, with r_{NiF} being the Ni···F distance. The r_{NiF} distances estimated by averaging the $(1/r_{NiF})^6$ values observed in the X-ray crystal structures of [NiL^1]$^+$ and [NiL^2]$^+$ are 7.01 and 9.3 Å, respectively. Thus, the values obtained from the analysis of relaxation data and those estimated from the X-ray structures are in good mutual agreement.
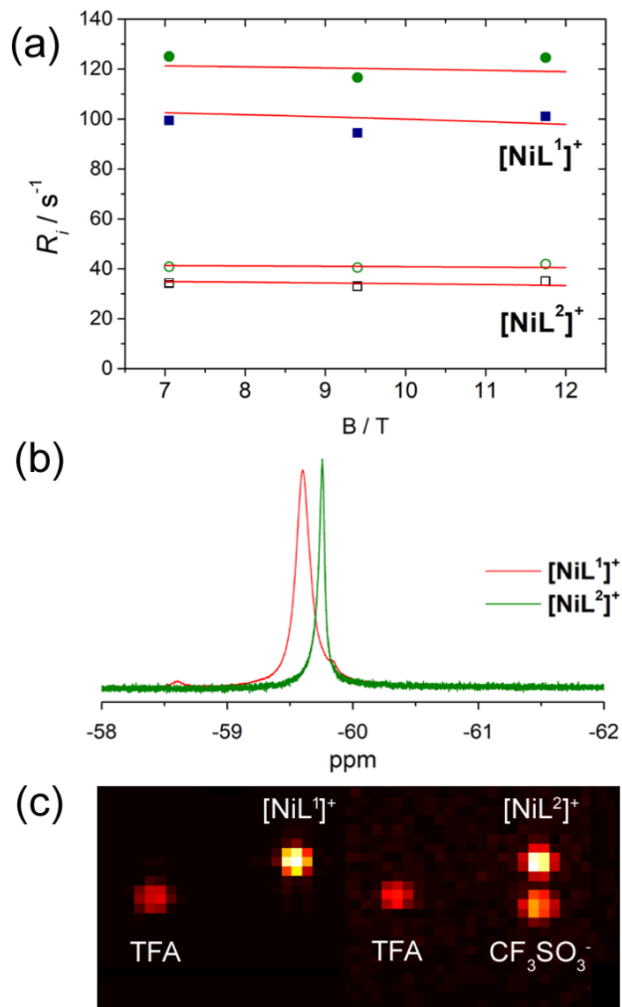
Figure 5. (a) Top: longitudinal (R_1, squares) and transverse (R_2, circles) relaxation rates recorded for [NiL^1]$^+$ and [NiL^2]$^+$ (as the chloride and triflate salts, respectively). The solid lines correspond to the fits of the data using Solomon-Bloembergen-Morgan theory. (b) ^{19}F NMR spectra (7.05 T, 25 ^{o}C) of [NiL^1]$^+$ and [NiL^2]$^+$. (c) ^{19}F MRI on tube phantoms (15 mM complex, 7.05 T, RT) of [NiL^1]$^+$, [NiL^2]$^+$ and TFA (30 mM left tube, 15 mM right tube).

6.2.7. ^{19}F MRI studies

It was also undertook a ^{19}F MRI study on tube phantoms using 15 mM solutions of the two complexes. Tubes containing trifluoroacetic acid (TFA) with equal ^{19}F nuclei concentrations (i.e. 30 and 15 mM of TFA relative to [NiL^1]$^+$ and [NiL^2]$^+$, respectively) were used for comparative purposes. The tube containing [NiL^2]$^+$ resulted in the 'ghost' image arising from the presence of trifluoromethanesulfonate counter anions (see above),[8] which did not affect the SNR for [NiL^2]$^+$ due to sufficient difference in the resonance frequency of fluorine atoms in these two molecules. The resulting ^{19}F MR images confirmed the potential of these complexes as ^{19}F probes. The obtained signal-to-noise ratio (SNR) for [NiL^1]$^+$ after 1 hour acquisition time was 137, which was 2.8 times higher than that of TFA (48). Concurrently, the SNR determined for [NiL^1]$^+$ was 3.3 times higher than that of TFA. Obviously, the paramagnetism of the metal ion affected the ^{19}F relaxation times to a significant extent; however, proportional shortening of both ^{19}F T_1 and T_2 resulted in the values that allow fast repetitions with still sufficient signal, thus giving rise to greater SNR values. In turn, these ^{19}F MRI experiments demonstrated advantageous properties of [NiL^1]$^+$ and [NiL^2]$^+$ over the diamagnetic reference, indicating perspectives for their consideration as ^{19}F MRI contrast agents.

6.3. Experimental section

6.3.1. Materials and methods

Cross-bridged-cyclam was purchased from CheMatech (Dijon, France). All other reagents and solvents were commercial and used without further purification. ^{1}H, ^{19}F and ^{13}C NMR spectra were recorded at 25 ^{o}C or 37 ^{o}C on Bruker Avance 300 MHz, Bruker Avance III HD 400 MHz and Bruker Avance 500 MHz spectrometers. High-resolution electrospray-ionisation time-of-flight (ESI-TOF) mass spectra were obtained in the positive mode using a LC-Q-q-TOF Applied Biosystems QSTAR Elite spectrometer. Elemental analyses were carried out on a ThermoQuest Flash EA 1112 elemental analyser. Medium performance liquid chromatography (MPLC) was carried out using a Puriflash XS 420 instrument equipped with a reverse-phase Puriflash 15C18HP column (60 Å, spherical 15 μm, 20 g) and UV-DAD detection at 210 and 254 nm, and operating at a flow rate of 10 mL/min. Aqueous solutions were lyophilised using a Telstar Cryodos-80 apparatus. Crystal structure determination was analysed using a Bruker D8 Venture diffractometer with a Photon 100 CMOS detector and an Incoatec high brillance microfocus source equipped with Incoatec Helios multilayer optics. Dissociation kinetic assays were performed with a Uvikon-XS (Bio-Tek Instruments) double-beam spectrophotometer with cells of 1 cm path length.

6.3.2. Synthetic procedure

Synthesis of the precursors.

2-chloro-N-(3,5-di-trifluoromethyl-phenyl)acetamide (1a). A solution of chloroacetyl chloride (11.5 mmol) in acetic acid (5 mL) was added dropwise to a mixture of 3,5-bis(trifluoromethyl)aniline (9.78 mmol) in acetic acid (35 mL) at

0 ^{o}C. The reaction mixture was maintained at room temperature for an additional 4 hours. Subsequently it was slowly poured into 100 mL of ice water. The aqueous solution was extracted with CH$_2$Cl$_2$ (4x100 mL). The combined organic phase was dried over anhydrous Na$_2$SO$_4$, filtered and the solvent was evaporated to furnish a solid residue. Yield: 92%. ^{1}H-NMR (solvent CDCl$_3$, 298 K, 400 MHz) δ$_H$ (ppm): 8.52 (s, 1H, NH), 8.07 (s, 2H, CH$_{Ar}$), 7.67 (s, 1H, CH$_{Ar}$), 4.23 (s, 2H, CH$_2$). ^{13}C-NMR (solvent CDCl$_3$, 298 K, 101 MHz) δ$_C$ (ppm): 164.4, (quaternary, CO), 138.1 (quaternary, C$_{Ar}$), 133.1-132.1 (quaternary, CF$_3$), 127.0 (tertiary, CH$_{Ar}$), 124.3 (tertiary, CH$_{Ar}$), 121.6 (quaternary, CH$_{Ar}$), 119.9, 118.9, 118.6, 118.6, 118.6, 42.7 (secondary, CH$_2$). ^{19}F-NMR (solvent CDCl$_3$, 298 K, 376 MHz) δ$_F$ (ppm): -63.09. Mass spectrometry (ESI$^-$) m/z (%BPI): 304.00 (100) ([C$_{10}$H$_5$ClF$_6$NO]$^-$); 339.98 (7) (C$_{10}$H$_6$ClF$_6$NO[Cl]$^-$). HR-MS (ESI$^-$) m/z: [M]$^-$, calculated: 303.9958, found: 303.9959.

Figure 6. Synthetic route for the synthesis of the compounds.

2-chloro-N-(4-(trifluoromethyl)phenyl)acetamide (1b). Chloroacetyl chloride (12.0 mmol) in dry CH$_2$Cl$_2$ (20 mL) was slowly added dropwise to a mixture of 4-(trifluoromethyl)aniline (10.0 mmol) and NaHCO$_3$ (25.5 mmol) in dry CH$_2$Cl$_2$ (30 mL) at 0 ^{o}C. The reaction mixture was stirred at 0 ^{o}C for an additional 4 hours. At a subsequent stage it was slowly poured into 80 mL of water. The aqueous solution was extracted with CH$_2$Cl$_2$ (8x150 mL). The combined organic layer was washed with brine and dried over anhydrous Na$_2$SO$_4$. The solvent was evaporated to dryness to afford a solid residue. Yield: 97%. ^{1}H-NMR (solvent CDCl$_3$, 298 K, 300 MHz) δ$_H$ (ppm): 8.35 (s, 1H, NH), 7.71-7.61 (dd, 4H, CH$_{Ar}$), 4.22 (s, 2H, CH$_2$). ^{13}C-NMR (solvent CDCl$_3$, 298 K, 75 MHz) δ$_C$ (ppm): 164.0 (quaternary, CO), 139.8 (quaternary, C$_{Ar}$), 126.4 (tertiary, C$_{Ar}$), 126.4 (tertiary, CH$_{Ar}$), 119.7 (quaternary, CH$_{Ar}$), 42.8 (secondary, CH$_2$). ^{19}F-NMR (solvent CDCl$_3$, 298 K, 282 MHz) δ$_F$ (ppm): -62.26. Mass spectrometry (ESI$^-$) m/z (%BPI): 236.02 (100) ([C$_9$H$_6$ClF$_3$NO]$^-$); 272.00 (6) (C$_9$H$_7$ClF$_3$NO[Cl]$^-$). HR-MS (ESI$^-$) m/z: [M]$^-$, calculated: 236.0095, found: 236.0099.

Synthesis of the intermediate 2a.

1-*tert*-(butoxycarboxymethyl)- 1,4,8,11-tetraazabicyclo[6.6.2]hexadecane (2a). Cross-bridged cyclam (0.3077 g, 1.36 mmol) was dissolved in CH$_3$CN (25 mL). A solution of *tert*-butyl bromoacetate (201 μL, 1.0 eq) in CH$_3$CN (25 mL) was added slowly dropwise to the suspension. The reaction mixture was stirred at room temperature for 12 hours. The solution was concentrated at low temperature to furnish a yellow oil. The product was washed with diethyl ether and concentrated at low temperature to achieve a white foam. The intermediate was purified by silica chromatography, eluting with CHCl$_3$ in gradient up to 10% in MeOH to yield a crude solid (0.226 g, 49%). ^{1}H NMR (300 MHz, D$_2$O): δ$_H$ (ppm): 3.37 - 1.99 (m, 24H, CH$_2$), 1.73 - 1.23 (m, 11H, CH$_2$ + CH$_3$).^{13}C NMR (75 MHz, D$_2$O) δ$_C$ (ppm): 172.69, 172.02 (quaternary, CO), 86.52, 85.00 (quaternary, CCH$_3$), 71.32, 64.08, 59.65, 59.52, 59.25, 59.16, 59.01, 58.98, 57.84, 57.22, 56.89, 55.60, 55.34, 51.41, 51.17, 50.86, 50.66, 50.30, 49.93, 48.80, 48.63, 43.51, 43.28, 31.26, 29.03, 29.01, 28.91, 22.18 (secondary, CH$_2$)., 21.81, 20.98, 19.92 (primary, CH$_3$). Mass spectrometry (ESI$^+$) m/z (%BPI): 341.29 (100) ([C$_{18}$H$_{37}$N$_4$O$_2$]$^+$); 285.23 (25) ([C$_{14}$H$_{29}$N$_4$O$_2$]$^+$).

Synthesis of the ligands.

General procedure for the preparation of the ligands. Cross-bridged derivative **2a** was dissolved in CH$_3$CN (20 mL) under basic conditions. A solution of the corresponding 2-chloro-*N*-substituted-acetamide in CH$_3$CN (15 mL) was added dropwise to the mixture at room temperature. The reaction was left stirring at room temperature for 18 days, until the alkylation was completed. The reaction mixture was filtered and reduced to dryness in vacuum. Final ligands **HL^1** and **HL^2** were achieved by deprotection of the *tert*-butyl groups with formic acid (5 mL), stirred at reflux for 48 h. Subsequently, the acid was removed and the residue was washed several times with water (5x10 mL). The product was redissolved in water and lyophilised to achieve a yellowish solid.

1-*tert*-(butoxycarboxymethyl)- 8-((3,5-(trifluoromethylphenyl)acetamide)- 1,4,8,11-tetraazabicyclo[6.6.2]hexadecane (3a). Intermediate **2a** (0.113 g, 0.330 mmol), 2-chloro-N-(3,5-(trifluoromethyl)phenyl)acetamide (**1a**, 0.101 g, 0.330 mmol, 1 eq), DIPEA (114 μL, 2 eq). The product was filtered and concentrated under vacuum pressure to afford a yellowish foam. The product was achieved pure with a small fraction of deprotected ligand (0.158 g, 79%). ^{1}H NMR (300 MHz, CDCl$_3$): δ$_H$ (ppm): 11.32 (s, 1H, NH), 10.61 (s, 1H, NH), 8.46 (s, 2H, CH$_{ar}$), 7.52(s, 1H, CH$_{ar}$), 3.99 - 2.74 (m, 26H, CH$_2$), 1.45 (m, 11H, CH$_2$ + CH$_3$). ^{19}F NMR (282 MHz, CDCl$_3$) δ$_F$ (ppm): -63.12. Mass spectrometry (ESI$^+$) m/z (%BPI): 610.32 (100) ([C$_{28}$H$_{42}$F$_6$N$_5$O$_3$]$^+$).

1-carboxymethyl-8-((3,5-(trifluoromethylphenyl)acetamide)- 1,4,8,11-tetraazabicyclo[6.6.2]hexadecane acid (HL^1). Yellowish solid (0.111 g, 45%). ^{1}H NMR (300 MHz, D$_2$O): δ$_H$ (ppm): 8.06 - 7.85 (m, 3H, CH$_{ar}$), 3.99 − 2.42 (m, 26H, CH$_2$), 1.78 (m, 2H, CH$_2$). ^{13}C NMR (75 MHz, D$_2$O) δ$_C$ (ppm): 172.60, 171.45, 168.85 (quaternary), 139.59, 133.26, 132.82, 126.53, 122.84, 120.37 (aromatic), 60.37, 59.51, 59.16, 57.52, 54.76, 53.93, 50.44, 50.02, 49.42, 48.80 (secondary, CH$_2$), 21.28, 20.76 (secondary). ^{19}F NMR (282 MHz, D$_2$O) δ$_F$ (ppm): -62.95. Mass spectrometry (ESI$^+$) m/z (%BPI): 554.25 (100) ([C$_{24}$H$_{34}$F$_6$N$_5$O$_3$]$^+$.

Anal. calcd for (C$_{34}$H$_{48}$F$_{15}$N$_5$O$_4$) 3 TFA·C$_4$H$_{10}$O: C, 42.11; H, 4.78; N, 7.22. Found: C, 41.19; H, 4.73; N, 7.37%.

1-*tert*-(butoxycarboxymethyl)- 8-((4-(trifluoromethylphenyl)acetamide)- 1,4,8,11-tetraazabicyclo[6.6.2]hexadecane (3b). Intermediate **2a** (0.113 g, 0.332 mmol), 2-chloro-N-(4-(trifluoromethyl)phenyl)acetamide (**1b**, 0.0790 g, 0.332 mmol, 1 eq), DIPEA (114 μL, 2 eq). The product was filtered and concentrated under vacuum pressure to afford a yellowish foam. The product was achieved pure with a small fraction of deprotected ligand (0.136 g, 75%). ^{1}H NMR (300 MHz, CDCl$_3$): δ$_H$ (ppm): 10.93 (s, 1H, NH), 10.72 (s, 1H, NH), 8.07 - 8.05 (d, 2H, CH$_{ar}$), 7.52 - 7.50 (d, 2H, CH$_{ar}$), 3.94 - 2.73 (m, 24H, CH$_2$), 1.45 (s, 9H, CH$_2$), 1.25-1.21 (m, 4H, CH$_2$). ^{19}F NMR (282 MHz, CDCl$_3$) δ$_F$ (ppm): -62.51. Mass spectrometry (ESI$^+$) m/z (%BPI): 542.33 (100) ([C$_{27}$H$_{43}$F$_3$N$_5$O$_3$]$^+$).

1-carboxymethyl-8-((4-(trifluoromethylphenyl)acetamide)- 1,4,8,11-tetraazabicyclo[6.6.2]hexadecane acid (HL^2). Deprotected with a mixture CH$_2$Cl$_2$:TFA (1:1) (6 mL). Yellowish solid (0.141 g, 58%). ^{1}H NMR (300 MHz, D$_2$O): δ$_H$ (ppm): 7.76 - 7.69 (m, 4H, CH$_{ar}$), 4.28 - 2.39 (m, 26H, CH$_2$), 1.82 - 1.77 (dd, 2H, CH$_2$). ^{13}C NMR (75 MHz, D$_2$O) δ$_C$ (ppm): 172.92, 168.75, 165.24, 164.76 (quaternary, CO), 164.30, 141.45 (quaternary, CH$_{ar}$), 127.91, 127.86 (tertiary, CH$_{ar}$), 122.24 (quaternary, CF$_3$), 119.89, 116.02 (tertiary, CH$_{ar}$), 60.72, 60.45, 59.80, 59.24, 57.93, 57.74, 54.59, 54.32, 49.91, 49.51, 49.03, 21.24, 21.03 (secondary, CH$_2$). ^{19}F NMR (282 MHz, D$_2$O) δ$_F$ (ppm): -62.05 (HL^2), -75.60 (TFA). Mass spectrometry (ESI$^+$) m/z (%BPI): 486.26 (100) ([C$_{24}$H$_{35}$F$_3$N$_5$O$_3$]$^+$). Anal. calcd for (C$_{34}$H$_{48}$F$_{15}$N$_5$O$_4$)·4H$_2$O 3 TFA·C$_4$H$_{10}$O: C, 40.70; H, 5.69; N, 7.19. Found: C, 41.38; H, 5.23; N, 7.22%.

Synthesis of the complexes.

General procedure for synthesis of the complexes. The corresponding cross-bridged-cyclam ligand derivative was dissolved in *n*-BuOH (10 mL) in the presence of DIPEA (5 eq.) with the assistance of an ultrasound bath. The solution was purged with an argon flow and afterwards the solid nickel salt, Ni(NO$_3$)$_2$·6H$_2$O in HL^1 and Ni(SO$_3$CF$_3$)$_2$ in HL^2, was added. The reaction was maintained at 155 °C for 6 h. The reaction was stopped and allowed to cool down to room temperature. The reaction mixture was concentrated in vacuum and washed with dichloromethane. The pink solid was purified by MPLC using a reverse-phase C18 column. An aqueous solution of the compound in the eluting conditions (CH$_3$CN:H$_2$O, *v:v*, containing 0.1% triethylamine) was prepared and filtered through a cellulose filter (0.20 μm pore size) before injection. The purification method was carried out in gradient of solvent B (CH$_3$CN, 5 to 10%) in solvent A (H$_2$O). The fractions containing the complex were combined and the solvent was removed in vacuum. The final product was redissolved in water and lyophilised to furnish the final complexes.

Synthesis of NiL^1. Light pink solid (0.030 g, 48%). Mass spectrometry (ESI$^+$) *m/z* (%BPI): 610.17 (100) ([C$_{24}$H$_{32}$F$_6$N$_5$NiO$_3$]$^+$). HR-MS (ESI$^+$) *m/z*: [M]$^+$, calculated: 610.1757, found: 610.1753. Anal. calcd for (C$_{25}$H$_{32}$F$_9$N$_5$NiO$_6$S)·0.6 DIPEA: C, 42.72; H, 5.22; N, 9.36. Found: C, 42.27; H, 5.63; N, 9.64%.

Synthesis of NiL². Light pink solid (0.020 g, 30%). Mass spectrometry (ESI⁺) m/z (%BPI): 542.19 (100) ($[C_{23}H_{33}F_3N_5NiO_3]^+$), 564.17 (10) ($[C_{23}H_{32}F_3N_5NaNiO_3]^+$). HR-MS (ESI⁺) m/z: $[M]^+$, calculated: 542.1883, found: 542.1872. Anal. calcd for ($C_{24}H_{33}F_6N_5NiO_6S$)·0.5 C_4H_9OH: C, 42.82; H, 5.25; N, 9.60. Found: C, 42.86; H, 5.04; N, 9.23%.

6.3.3. ¹H CEST experiments

CEST spectra have been recorded at 25 and 37 °C, at diverse radiofrequency fields (B_1 = 2.5, 5, 10, 15, 20, 25 and 30 μT) on a Brucker Advance 300 MHz spectrometer (Tübingen, Germany). Z-spectra of 15 mM complex aqueous solution (with 20% CH_3CN) were performed using a saturation time of 10 s and a 2 ppm frequency resolution. The pH of the solutions was adjust to physiological value ~7 by adding 0.01 to 0.1 M NaOH or HCl solutions. The exact concentration of the solutions was determined by elemental analysis of the complexes.

6.3.4. X-ray crystal structure determination

Single crystals of **[NiL¹]⁺** and **[NiL²]⁺** were analysed by X-ray diffraction and a summary of the crystallographic data and the structure refinement parameters is reported in Table 1. Crystallographic data were collected at 100 K using a Bruker D8 Venture diffractometer with a Photon 100 CMOS detector and Mo-Kα radiation (λ = 0.71073 Å) generated by an Incoatec high brillance microfocus source equipped with Incoatec Helios multilayer optics. The software APEX3[20] was used for collecting frames of data, indexing reflections, and the determination of lattice parameters, SAINT[21] for integration of intensity of reflections, and SADABS[22] for scaling and empirical absorption correction. The structure was solved by dual-space methods using the program SHELXT.[23] All non-hydrogen atoms were refined with anisotropic thermal parameters by full-matrix least-squares calculations on F^2 using the program SHELXL-2014.[24] Hydrogen atoms were inserted at calculated positions and constrained with isotropic thermal parameters. However, the hydrogen atoms from the primary and secondary amine functions in **[NiL¹]⁺**, were located from a Fourier-difference map and refined isotropically. In **[NiL²]⁺**, the unit cell contains a total potential solvent-accessible void volume of 1028 Å³, filled with disordered water molecules. Attempts to model the water molecules did not result in an acceptable model. Therefore, the SQUEEZE[25] function of PLATON[26] was used to eliminate the contribution of the electron density in the solvent region from the intensity data. The use of this strategy and the subsequent solvent-free model produced much better refinement results than the attempt to model the solvent atoms. Therefore, the solvent-free model and intensity data were used for the final results reported. A total of 246 e was found, corresponding to approximately twenty four water molecules.

6.3.5. Magnetic resonance imaging

MRI measurements were performed on Bruker BioSpec 70/30 USR magnet (software version Paravision 5.1) using Bruker surface coil (RF SUC 300 ¹H/¹⁹F_20mm LIN TR). 19F images were acquired using Fast Low Angle Single Shot (FLASH) pulse sequence.

6.3.6. Dissociation kinetics

The dissociation of the **[NiL²]⁺** complex under strong acidic conditions ($[H^+]$= 4M) was investigated at 25 °C by following the changes of the UV absorption spectrum in the range 220-300 nm with a Uvikon-XS (Bio-Tek Instruments) double-beam spectrophotometer with cells of 1 cm path length. The sample was prepared by adding 75μL of a 2.5×10^{-3} M aqueous solution of the complex over 3 mL of HCl (4M) ($[NiL^2]$= 5.2×10^{-5} M).

6.4. Conclusions

In conclusion, they are reported Ni²⁺ cross-bridge derivatives that form extremely inert complexes with great potential for the design of MRI probes. It was demonstrated that the functionalisation of the macrocyclic platform with pendant arms containing amide protons and CF₃ groups provides potential for these systems to be used as ¹H/¹⁹F probes. The paramagnetism of the Ni²⁺ ion allows for a faster ¹⁹F MRI acquisition thanks to the paramagnetic relaxation enhancement effect. The paramagnetically shifted resonance of amide protons promotes the CEST effect safely distant from bulk water. This work further expands the scope of applications of the cyclam-based systems, ensuring exciting forthcoming developments in the field of chemistry of MRI contrast agents.

6.5. Notes

The work presented in this chapter has been submitted for publication as communication in a scientific journal.

6.6. References

1   The Chemistry of Contrast Agents in Medical Magnetic Resonance Imaging, ed. A. E. Merbach, L. Helm and Eva Toth, John Wiley & Sons Ltd, 2nd edn, 2013; (b) L. Helm, J. R. Morrow, C. J. Bond, F. Carniato, M. Botta, M. Braun, Z. Baranyai, R. Pujales-Paradela, M. Regueiro-Figuero, D. Esteban-Gómez, C. Platas-Iglesias and T. J. Scholl, *Contrast Agents for MRI: Experimental Methods*, Eds V.C Pierre and M. J. Allen, The Royal Society of Chemistry, 2017, Chapter 2, pp 121-242.

2   (a) D. R. Roberts, S. M. Lindhorst, C. T. Welsh, K. R. Maravilla, M. N. Herring, K. A. Braun, B. H. Thiers and W. C. Davis, *Invest. Radiol.,* 2016, **51**, 280; (b) M. Birka, K. S. Wentker, E. Lusmöller, B. Arheilger, C. A. Wehe, M. Sperling, R. Stadler and U. Karst, *Anal. Chem.,* 2015, **87**, 3321; (c) T. Kanda, T. Fukusato, M. Matsuda, K. Toyoda, H. Oba, J. Kotoku, T. Haruyama, K. Kitajima and S. Furui, *Radiology,* 2015, **276**, 228; (d) E. Kanal and M. F. Tweedle, *Radiology,* 2015, **275**, 630. (e) T. J. Fraum, D. R. Ludwig, M. R. Bashir and K. J. Fowler, *J. Magn. Reson. Imaging,* 2017, **46**, 338.

3   (a) S. Cheng, L. Abramova, G. Saab, G. Turabelidze, P. Patel, M. Arduino, T. Hess, A. Kallen and M. Jhung, *J. Am. Med. Assoc.,* 2007, **297**, 1542; (b) T. H. Darrah, J. J. Prutsman-Pfeiffer, R. J. Poreda, M. E. Campbell, P. V. Hauschka and R. E. Hannigan, *Metallomics*, 2009, **1**, 479.

4   V. M. Runge, *Invest. Radiol.,* 2018, **53**, 571.

5   E. M. Gale, I. P. Atanasova, F. Blasi, I. Ay and P. Caravan, *J. Am. Chem. Soc.*, 2015, **137**, 15548.

6   (a) S. J. Ratnakar, M. Woods, A. J. M. Lubag, Z. Kovacs and A. D. Sherry, *J. Am. Chem. Soc.,* 2008, **130**, 6; b) S. J. Ratnakar, T.

C. Soesbe, L. L. Lumata, Q. N. Do, S. Viswanathan, C.-Y. Lin, A. D. Sherry and Z. Kovacs, *J. Am. Chem. Soc.,* 2013, **135**, 14904.

7 (a) S. J. Dorazio, P. B. Tsitovich, K. E. Siters, J. A. Spernyak and J. R. Morrow, *J. Am. Chem. Soc.*, 2011, **133**, 14154; (b) P. B. Tsitovich, J. A. Spernyak and J. R. Morrow, *Angew. Chem. Int. Ed.,* 2013, **52**, 13997; (c) A. Olatunde, S. J. Dorazio, J. A. Spernyak and J. R. Morrow, *J Am Chem Soc.,* 2012, **134**, 18503.

8 J. Ruiz-Cabello, B. P. Barnett, P. A. Bottomley and J. W. Bulte, *NMR Biomed.* 2011, **24**, 114.

9 (a) J. Blahut, P. Hermann, A. Gálisová, V. Herynek, I. Císařová, Z. Tošnerc and J. Kotek, *Dalton Trans.*, 2016, **45**, 474; (b) M. Yu, D. Xie, K. P. Phan, J. S. Enriquez, J. J. Luci and E. L. Que, *Chem. Commun.,* 2016, **52**, 13885; (c) J. Blahut, K. Bernasek, A. Galisova, V. Herynek, I. Cisarova, J. Kotek, J. Lang, S. Matejkova and P. Hermann, *Inorg. Chem.,* 2017, **56**, 13337

10 (a) K. L. Peterson, K. Srivastava and V. C Pierre, *Front. Chem.* 2018, **6**, 160; (b) a) K. Srivastava, E. A. Weitz, K. L. Peterson, M. Marjanska and V. C. Pierre, *Inorg. Chem.*, 2017, **56**, 1546–1557. (c) K. H. Chalmers, E. De Luca, N. H. M. Hogg, A. M. Kenwright, I. Kuprov, D. Parker, M. Botta, J. I. Wilson and A. M. Blamire, *Chem. Eur. J.,* 2010, **16**, 134.

11 N. Cakic, T. Savic, J. Stricker-Shaver, V. Truffault, C. Platas-Iglesias, C. Mirkes, R. Pohmann, K. Scheffler and G. Angelovski, *Chem. Commun.,* 2016, **136**, 17954.

12 A. Rodriguez-Rodriguez, D. Esteban-Gomez, R. Tripier, G. Tircso, Z. Garda, I. Toth, A. de Blas, T. Rodriguez-Blas and C. Platas-Iglesias, *J. Am. Chem. Soc.,* 2014, **54**, 10056.

13 (a) R. Smith, D. Huskens, D. Daelemans, R. E. Mewis, C. D. Garcia, A. N. Cain, T. N. C. Freeman, C. Pannecouque, E. De Clercq, D. Schols, T. J. Hubin and S. J. Archibald, *Dalton Trans.,* 2012, **41**, 11369; (b) D. G. Jones, K. R. Wilson, D. J. Cannon-Smith, A. D. Shircliff, Z. Zhang, Z. Chen, T. J. Prior, G. Yin and T. J. Hubin, *Inorg. Chem.,* 2015, **54**, 2221-2234.

14 (a) M. Meyer, V. Dahaoui-Gindrey, C. Lecomte and R. Guilard, *Coord. Chem. Rev.,* 1998, **178–180**, 1313; (b) J. Dale, *Acta Chem. Scand.*, 1973, **27**, 1115.

15 E. Toth, E. Brucher, I. Lazar and I. Toth, *Inorg. Chem.,* 1994, **33**, 4070.

16 A. O. Olatunde, C. J. Bond, S. J. Dorazio, J. M. Cox, J. B. Benedict, M. D. Daddario, J. A. Spernyak and J. R. Morrow, *Chem. Eur. J.,* 2015, **21**, 18290.

17 L. Caneda-Martínez, L. Valencia, I. Fernández-Pérez, M. Regueiro-Figueroa, G. Angelovski, I. Brandariz, D. Esteban-Gómez and C. Platas-Iglesias, *Dalton Trans.,* 2017, **46**, 15095.

18 M. Zaiss, G. Angelovski, E. Demetriou, M. T. McMahon, X. Golay and K. Scheffler, *Magn. Reson. Med.,* 2018, **79**, 1708.

19 (a) I. Solomon and N. Bloembergen, *J. Chem. Phys.,* 1956, **25,** 261; (b) N. Bloembergen and L. O. Morgan, *J. Chem. Phys.*, 1961, **34**, 842.

20 APEX3 Version 2016.1 (Bruker AXS Inc., 2016)

21 SAINT Version 8.37A (Bruker AXS Inc., 2015)

22 SADABS Version 2014/5 (Sheldrick, Bruker AXS Inc.)

23 SHELXT Version 2014/5 (George M. Sheldrick, *Acta Cryst.* (2015). A**71**, 3-8)

24 SHELXL Version 2014/7 (George M. Sheldrick, *Acta Cryst.* (2008). A**64**, 112-122)

25 P. Sluis, A. L. Spek, Acta Cryst. (2015). C**71**, 9–18.

26 A. L. Spek, . Acta Cryst. (2009). D**65**, 148-155.

General conclusions
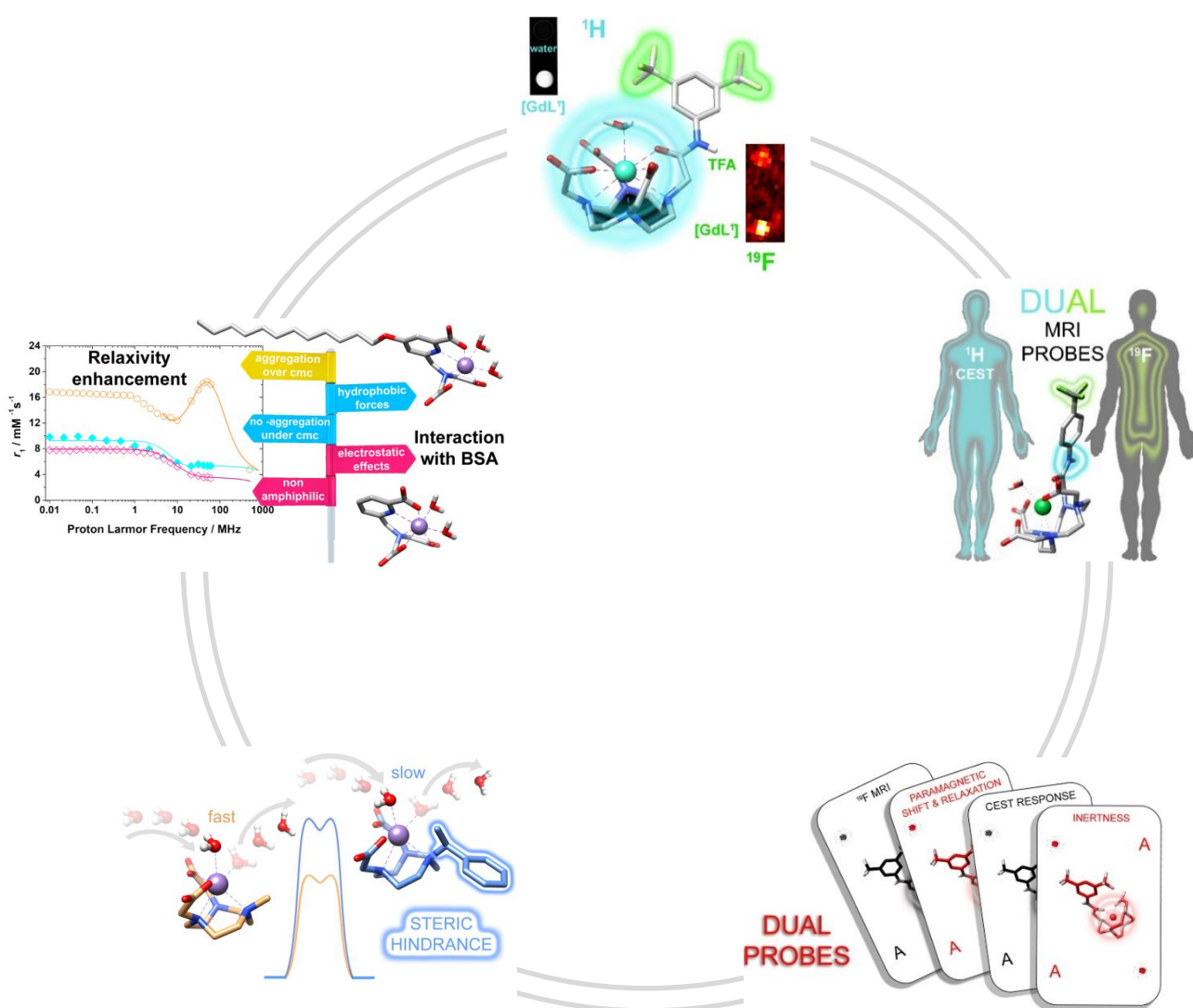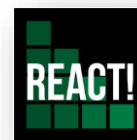
Chapter 7

General conclusions

This doctoral thesis was devoted to the synthesis and characterisation of new coordination compounds with physicochemical properties and structures that were designed for their application as contrast agents in medical imaging, specifically in Magnetic Resonance Imaging (MRI). The work presented in this manuscript comprises the use of different contrast mechanisms: 1) ^1H T_1-based contrast agents based on paramagnetic Mn^{2+} (**Chapters 2** and **3**) or Gd^{3+} (**Chapters 4** and **5**) complexes; 2) Paramagnetic Chemical Exchange Saturation Transfer (paraCEST) agents derived from lanthanide ions (**Chapter 5**) or Ni^{2+} (**Chapter 6**). The systems reported in **Chapters 4-6** were designed to provide dual-frequency response (^1H and ^{19}F). Concerning the nature of the ligands used in this work, **Chapter 2** presents ligands based on the triazacyclononane platform, **Chapters 4** and **5** ligands derived from cyclen and **Chapter 6** macrocycles containing a reinforced (*cross-bridged*) cyclam scaffold. The Mn^{2+} complexes reported in **Chapter 3** are based on non-macrocyclic ligands that contain acetate and picolinate coordinated groups.

The ligands and the corresponding complexes were characterised by using a wide range of techniques, including mass spectrometry (electrospray ionisation), multinuclear (^1H, ^{13}C, ^{19}F, ^{17}O) NMR measurements including variable field and variable temperature studies, luminescence spectroscopy, X-ray diffraction measurements and DFT calculations. The combinations of these techniques provided detailed insight into the mechanisms responsible for contrast enhancement of these complexes.

More specifically, the work presented in this thesis led to the following conclusions:

7.1. Innovative T_1 manganese(II)-based complexes (traditional or longitudinal relaxation agents) as an alternative to the broadly used gadolinium ones.

The studies on Mn^{2+} complexes completed during this doctoral thesis showed that important parameters that govern the relaxivity can be controlled by a judicious ligand design: The water exchange of the coordinated water molecule in monohydrated triazacyclononane derivatives can be modulated by changing the steric hindrance around the water binding site. Bulkier substituents hinder the approach of the entering water molecule, destabilising the seven-coordinated transition state responsible for the associative water exchange mechanism. The relaxivity of Mn^{2+} complexes can be also improved by inserting an aliphatic chain in the ligand scaffold, thanks to the formation of

micelles (above the *cmc*) or the interaction with serum proteins such as Bovine Serum Albumin (BSA). This slows down the rotation of the complex in solution, resulting in higher relaxivities, particularly around 40-60 MHz.
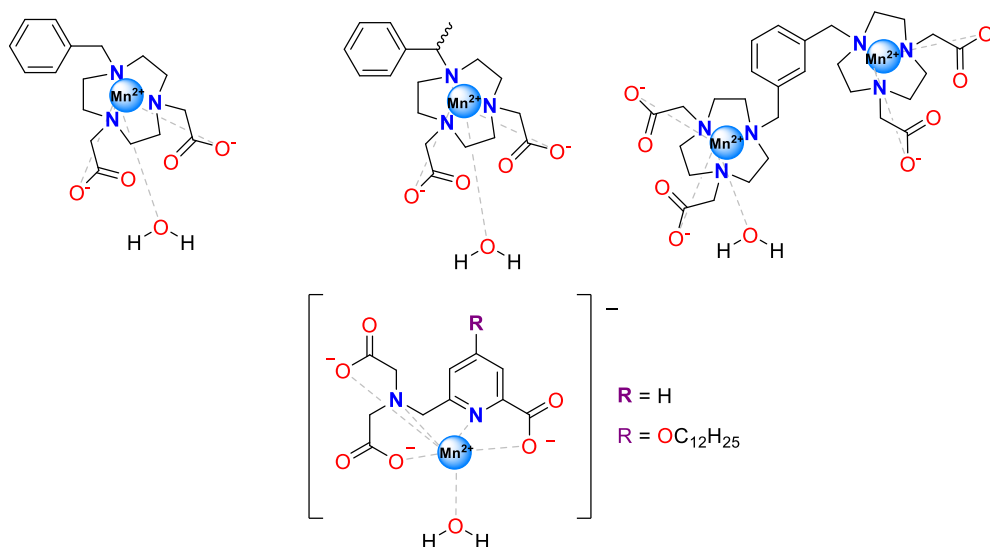
Scheme 7.1. Complexes reported in chapters 2 and 3.

The studies performed on Mn^{2+} complexes contributed to enlarge the range of data available for this type of potential contrast agents, as the number of well-characterised Mn^{2+} complexes reported in the literature is rather limited, particularly if compared to Gd^{3+} analogues. We have found that some Mn^{2+} complexes do not share the same trends for the water exchange reaction as the Gd^{3+} counterparts, as the steric hindrance is observed to have opposite effects on the water exchange rates of each of them. The increase in the relaxivity of the complex upon formation of micelles or binding to BSA represent an interesting approach to improve the efficiency of Mn^{2+} agents.

7.2. Unusual dual-frequency $^1H/^{19}F$ responsive gadolinium(III) complexes.

Two gadolinium(III) systems based on the cyclen platform were designed to provide dual response to the proton and fluorine frequencies. Both systems contain an equivalent amount of fluorine nuclei in the ligand scaffold, but present different Gd···F distances. The paramagnetism of the metal ion enhances the relaxation on the fluorinated groups, allowing shorter acquisition times.
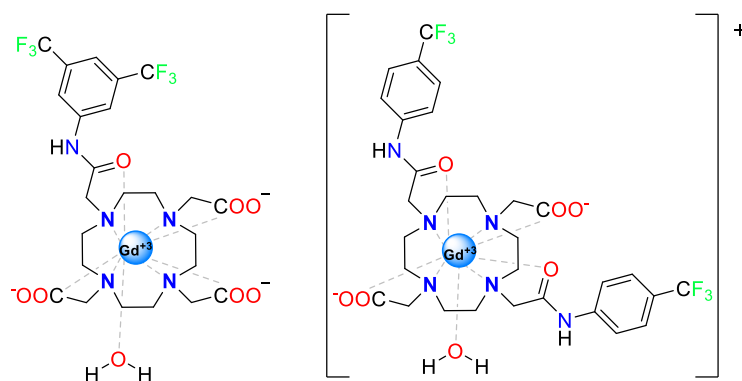
Scheme 7.2. Complexes reported in chapter 4.

The relaxation was shorter for GdL^1 (Gd···F = 7.4 Å) than for [GdL^2]$^+$ (Gd···F = 9.1 Å). However, the short distance also induces short T_2 relaxation for GdL^1, resulting in a weaker MRI signal in the phantom studies. This study established an optimal Gd···F distance for ^{19}F MRI probes in the range 9-10 Å. The hydration numbers determined by luminescence measurements on the Eu(III) and Tb(III) analogues, and a complete ^{1}H and ^{17}O relaxometric study of the gadolinium(III) complexes, confirmed the presence of a coordinated water molecule in these complexes. Proton relaxivities are comparable to those of commercially available contrast agents. The water exchange rate of the coordinated water molecule decreases on increasing the positive charge of the complex, in line with a dissociatively activated mechanism. The results obtained for the GdL^1 and [GdL^2]$^+$ complexes presented in this work represent a promising strategy for the preparation of genuine ^{1}H/^{19}F MRI probes of high stability and inertness.

7.3. Novel multiresponsive lanthanide-based cyclen derivative complexes.

The careful selection of the particular lanthanide(III) ion and the Ln···F distance is critical for the design of efficient MRI probes with dual response as ^{1}H paraCEST and direct detection ^{19}F MRI agents. The properties of the Tm^{3+} complexes are particularly well-suited to provide paraCEST effect, thanks to the large chemical shift difference between the bulk water signal and the resonance of amide protons. The exchange rates of the amide protons are however rather fast due to the electron-withdrawing effect of the CF$_3$ groups, which increase the acidity of the amide protons, facilitating the base-catalised exchange mechanism. The [LnL^1] (Ln = Tm or Tb) complexes were found to be particularly good candidates as ^{19}F probes thanks to an optimal match between the relaxation ability of the metal ions and the Ln···F distance, which was determined to be 7.45 $\pm$ 0.04 Å from ^{19}F relaxation studies. Another advantageous property of the lanthanide complexes described in this Chapter is their presence in solution as a single diastereoisomer, which was shown to present square antiprismatic coordination by analysis of the Yb^{3+}-induced paramagnetic shifts and the X-ray crystal structure of [YbL^3].
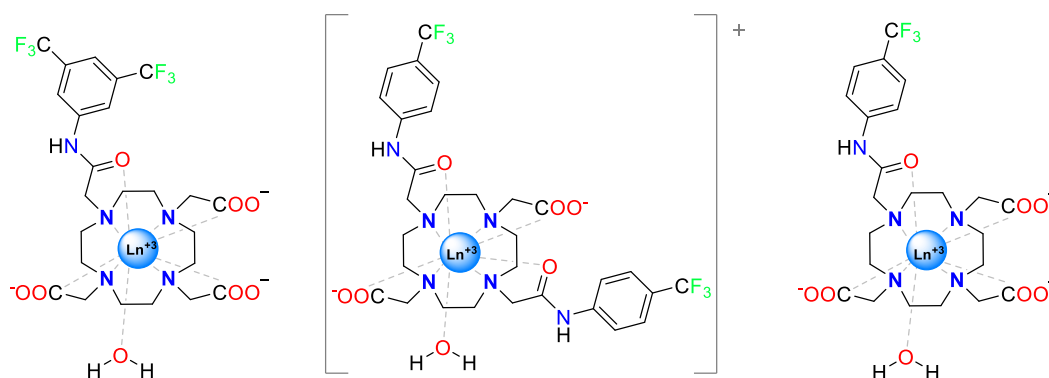
Scheme 7.3. Complexes reported in chapter 5.

7.4. Potential dual-mechanism ^{1}H CEST and ^{19}F direct detection nickel complexes with reinforced stability.

The cross-bridged cyclam platform allows the preparation of highly inert complexes by enclosing the metal ion in its reinforced cavity. The functionalisation of the platform with one acetate and one phenylacetamide pendant arm provides an octahedral coordination for the Ni^{2+} ion, affording extremely inert complexes, which do not experience dissociation even in very harsh conditions,

as in 4 M HCl. The functionalisation of the ligand with a pendant arm containing fluorine nuclei and an amide group provided an interesting dual ^{1}H/^{19}F by CEST and direct fluorine detection, which lays the foundations to develop very efficient MRI probes. The paramagnetism of the nickel(II) ion results in rather fast relaxation enhancements demonstrated by fluorine NMR relaxation studies. Furthermore, the inclusion of an amide group in the pendant arm also provided resonance well-shifted from bulk water, affording a sizeable CEST effect. The Ni···F distances determined in solution using Solomon-Bloembergen-Morgan theory of paramagnetic relaxation are in good agreement with those observed in the X-ray structures of the complexes. The exchange rate of the amide proton was found to be rather fast due to the electron withdrawing effect of the $-CF_3$ groups, and require further optimisation.
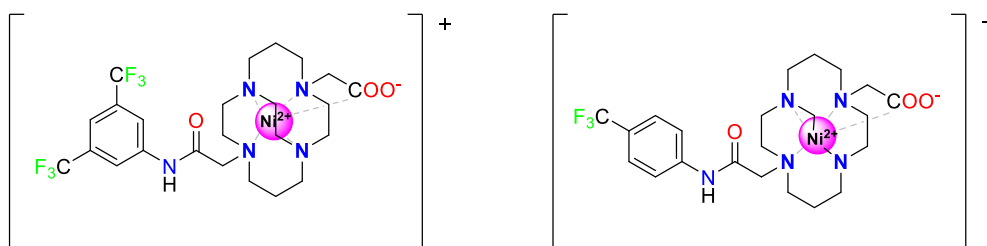
Scheme 7.4. Complexes reported in chapter 6.

In **Conclusion**, this thesis has investigated a series of new compounds that contribute to the goal of obtaining more efficient and safer contrast agents for MRI applications, exploring the use of different paramagnetic metal ions (Gd^{3+} or other lanthanide ions, Mn^{2+} and Ni^{2+}) and contrast mechanisms (^{1}H T$_1$ agents, ^{1}H CEST probes and direct detection ^{19}F systems). All these results provided detailed understanding at the molecular level regarding the parameters and mechanisms involved in the relaxometric properties and other features relevant for the MRI contrast response, setting new horizons in the research of innovative MRI probes in order to provide alternatives to the current medically approved gadolinium(III)-based contrast agents.

Annexe A
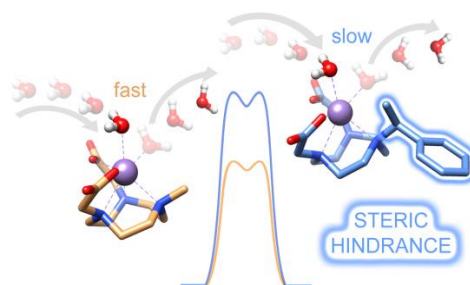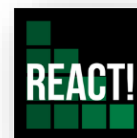
Annexe A

Controlling water exchange rates in potential Mn^{2+}-based MRI agents derived from $NO2A^{2-}$

Annexe A Summary

Figure S1. ^{1}H (300 MHz, 25 °C, top) and ^{13}C (75 MHz, 25 °C, bottom) NMR spectra of compound **2a** recorded in CDCl$_3$ solution.

Figure S2. ESI-MS (positive detection) of intermediate **2a**.
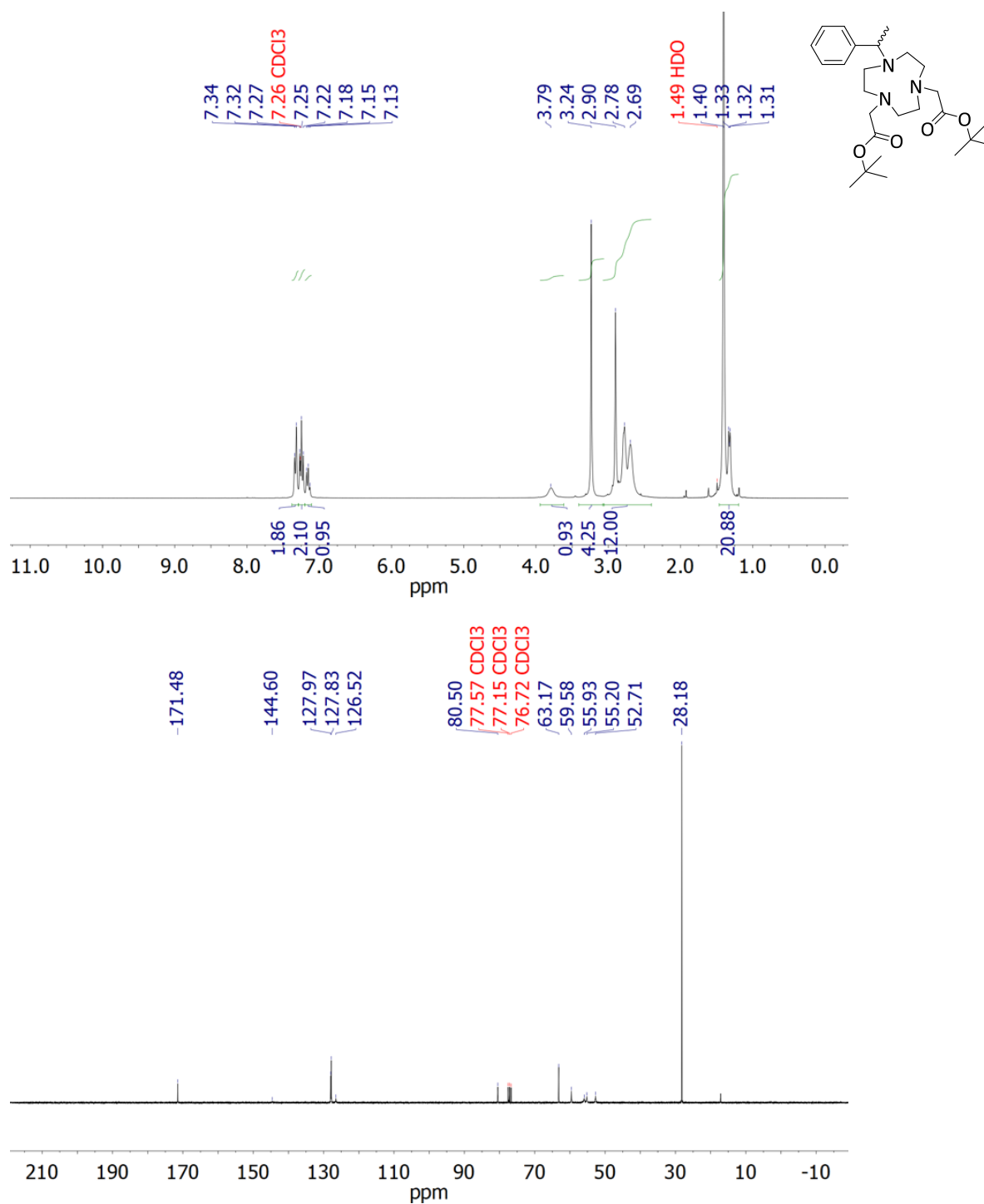
Figure S3. ¹H (300 MHz, 25 °C, top) and ¹³C (75 MHz, 25 °C, bottom) NMR spectra of **2b** recorded in CDCl₃ solution.
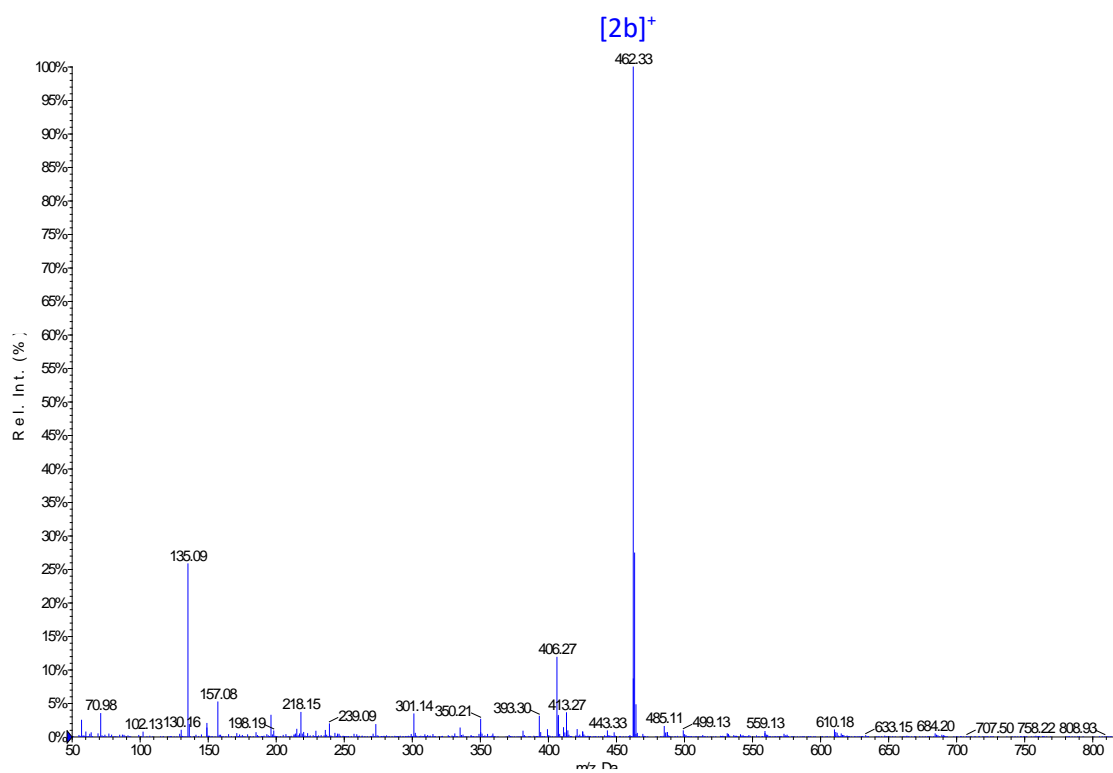
Figure S4. ESI-MS (positive detection) of intermediate **2b**.
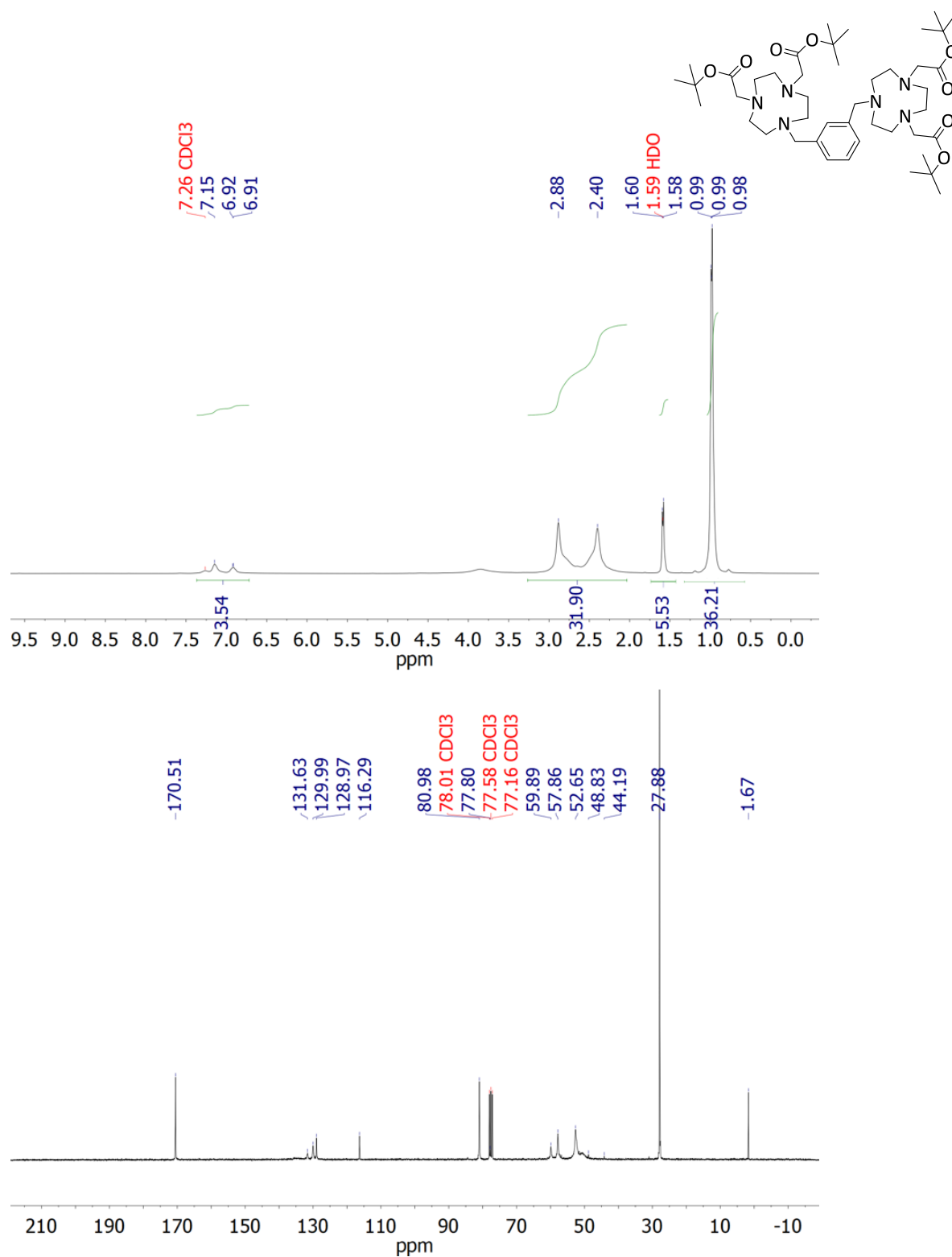
Figure S5. ¹H (300 MHz, 25 °C, top) and ¹³C (75 MHz, 25 °C, bottom) NMR spectra of compound **2c** recorded in CDCl₃ solution.
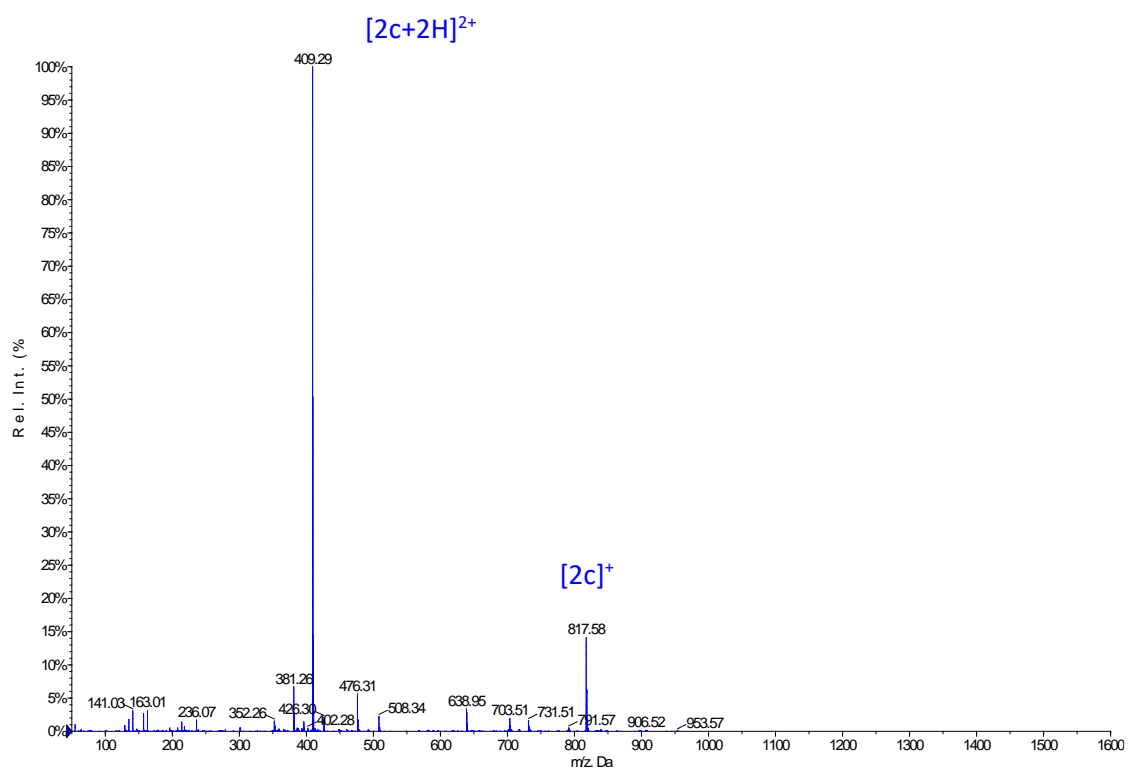
Figure S6. ESI-MS (positive detection) of intermediate **2c**.
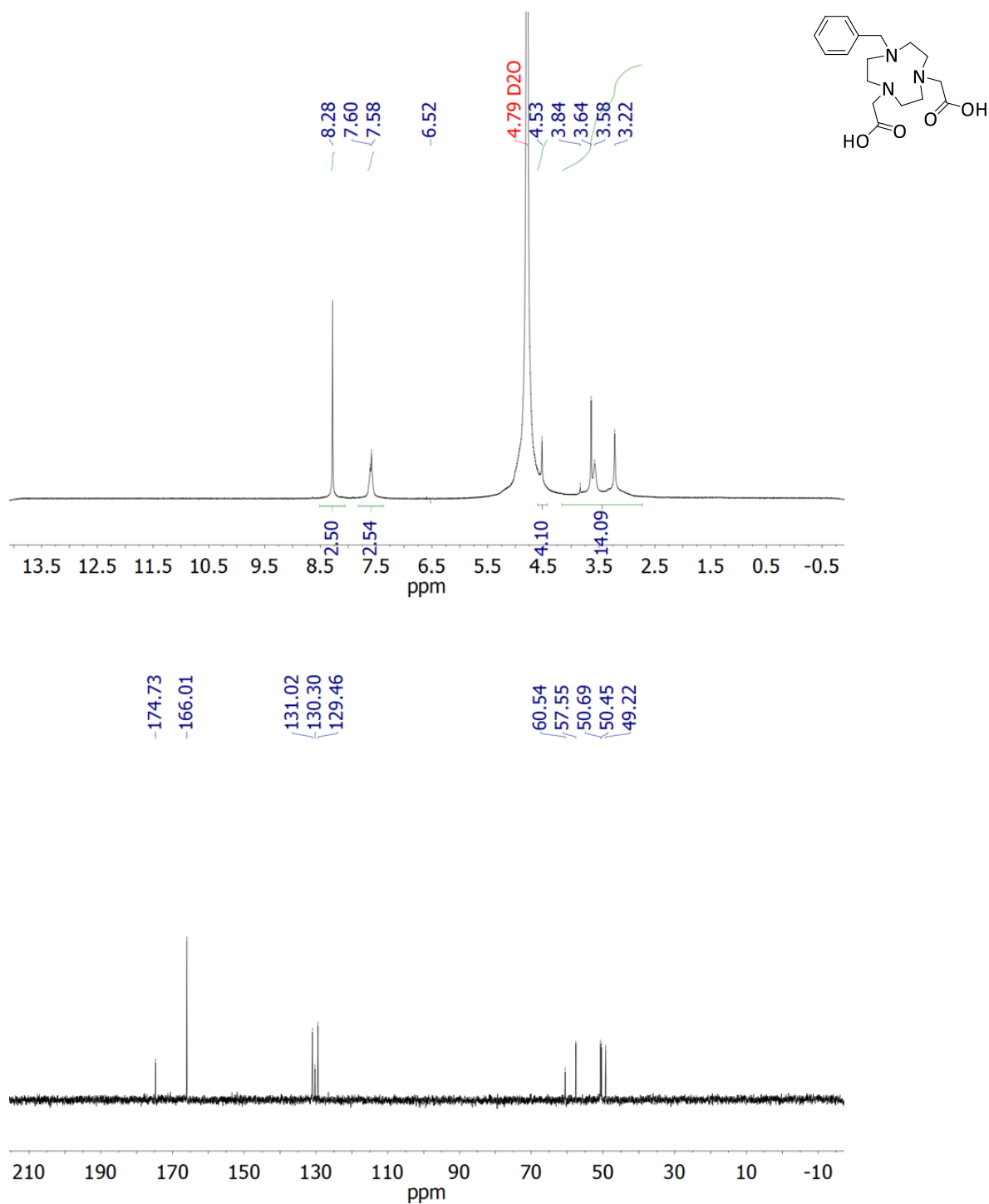
Figure S7. ¹H (300 MHz, 25 °C, top) and ¹³C (75 MHz, 25 °C, bottom) NMR spectra of H₂BzNO2A recorded in D₂O solution.
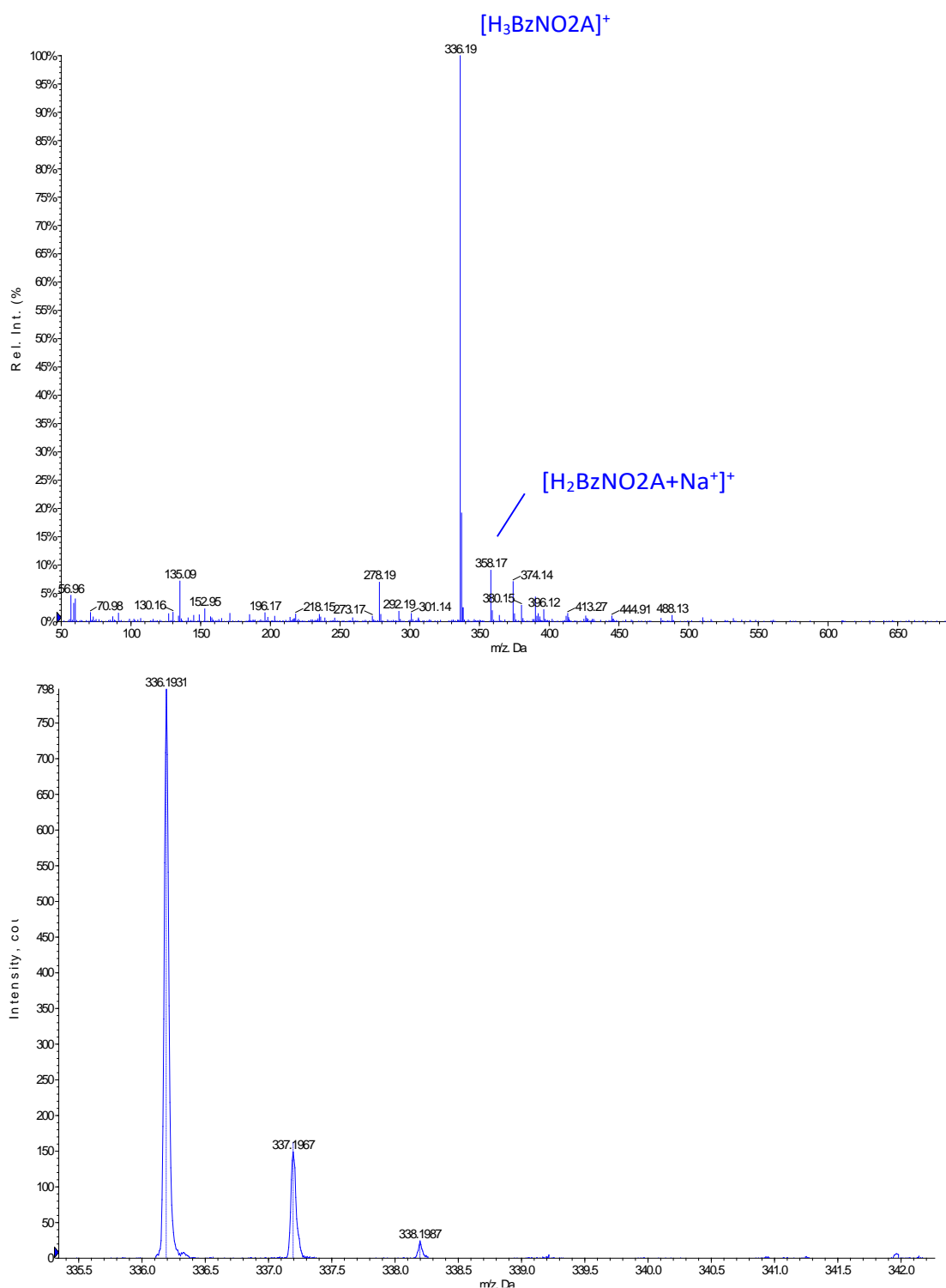
Figure S8. ESI-MS (positive detection) and high resolution mass spectra of ligand H$_2$BzNO2A.
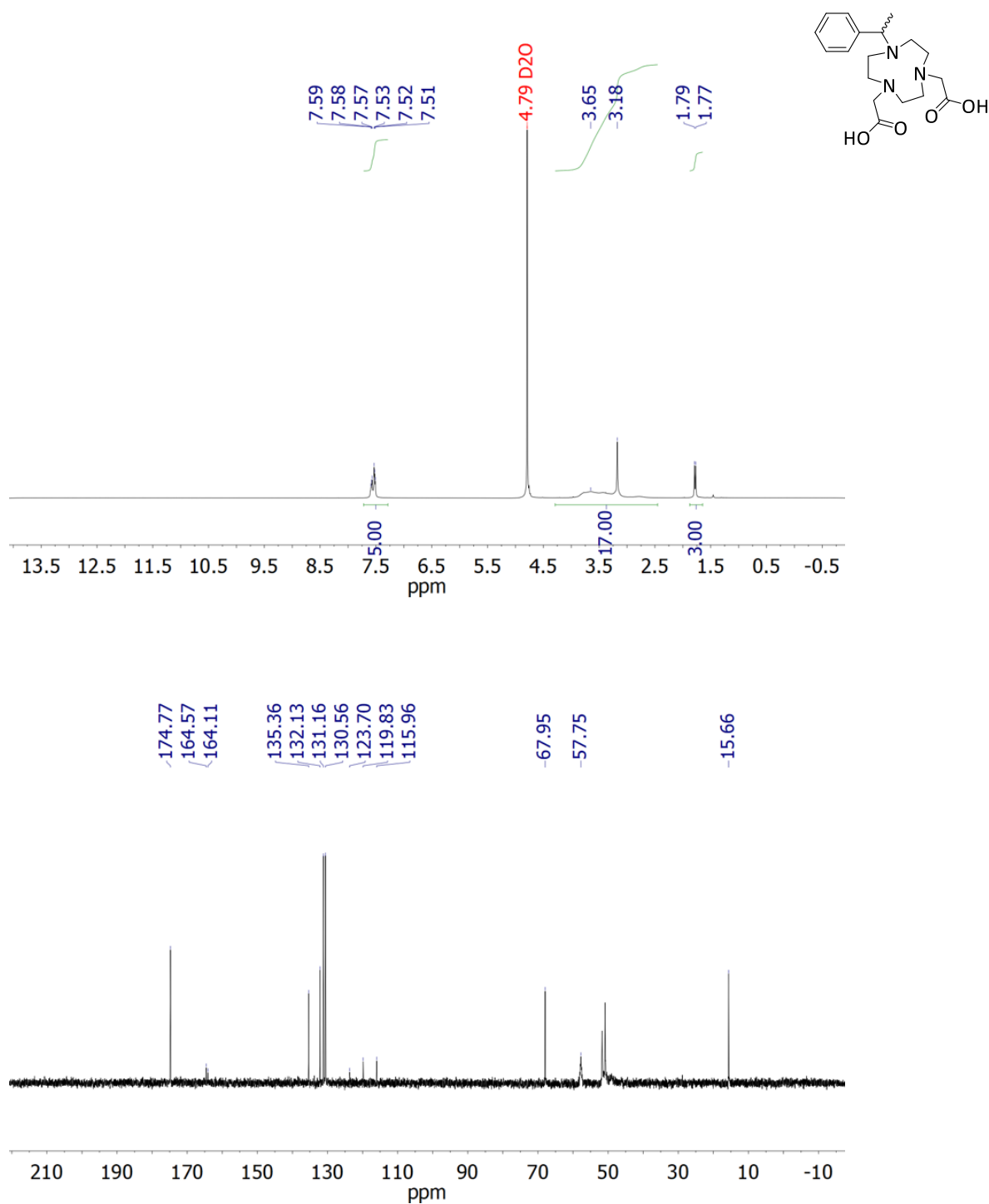
Figure S9. ¹H (300 MHz, 25 °C, top) and ¹³C (75 MHz, 25 °C, bottom) NMR spectra of H₂MeBzNO2A recorded in D₂O solution.
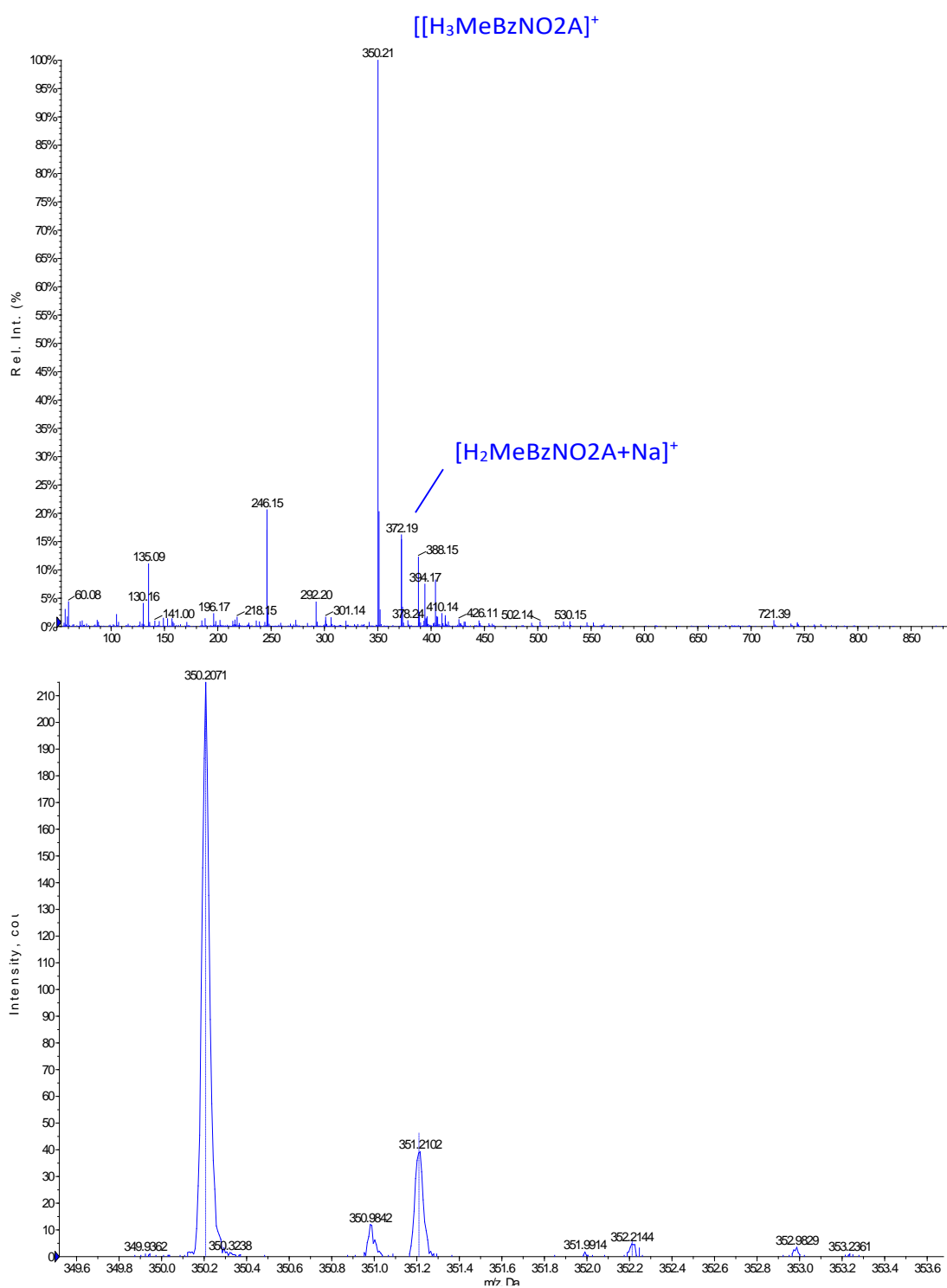
Figure S10. ESI-MS (positive detection) and high resolution mass spectra of ligand H$_2$MeBzNO2A.
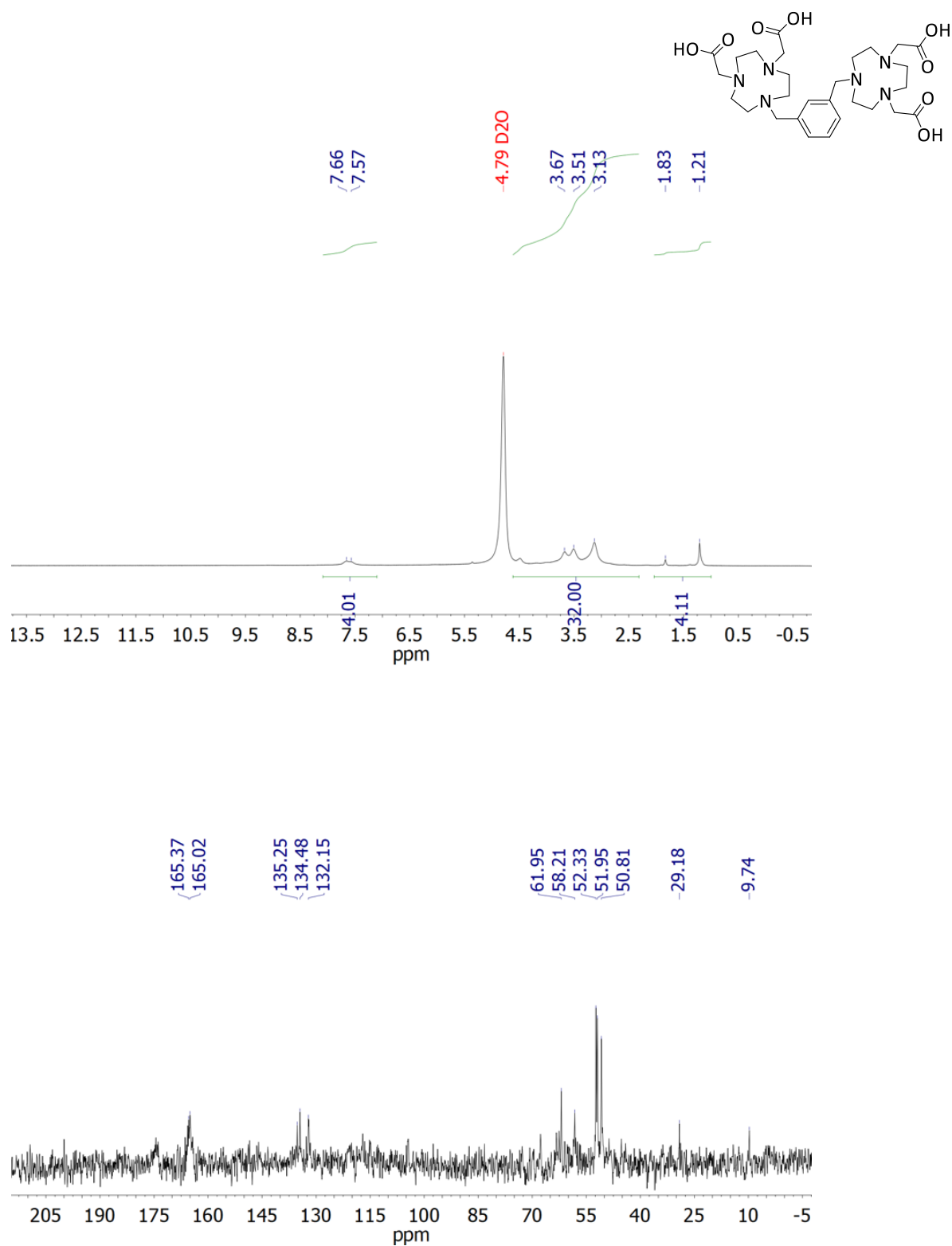
Figure S11. ¹H (300 MHz, 25 °C, top) and ¹³C (75 MHz, 25 °C, bottom) NMR spectra of *m*Bz(H₂NO2A)₂ recorded in D₂O solution.
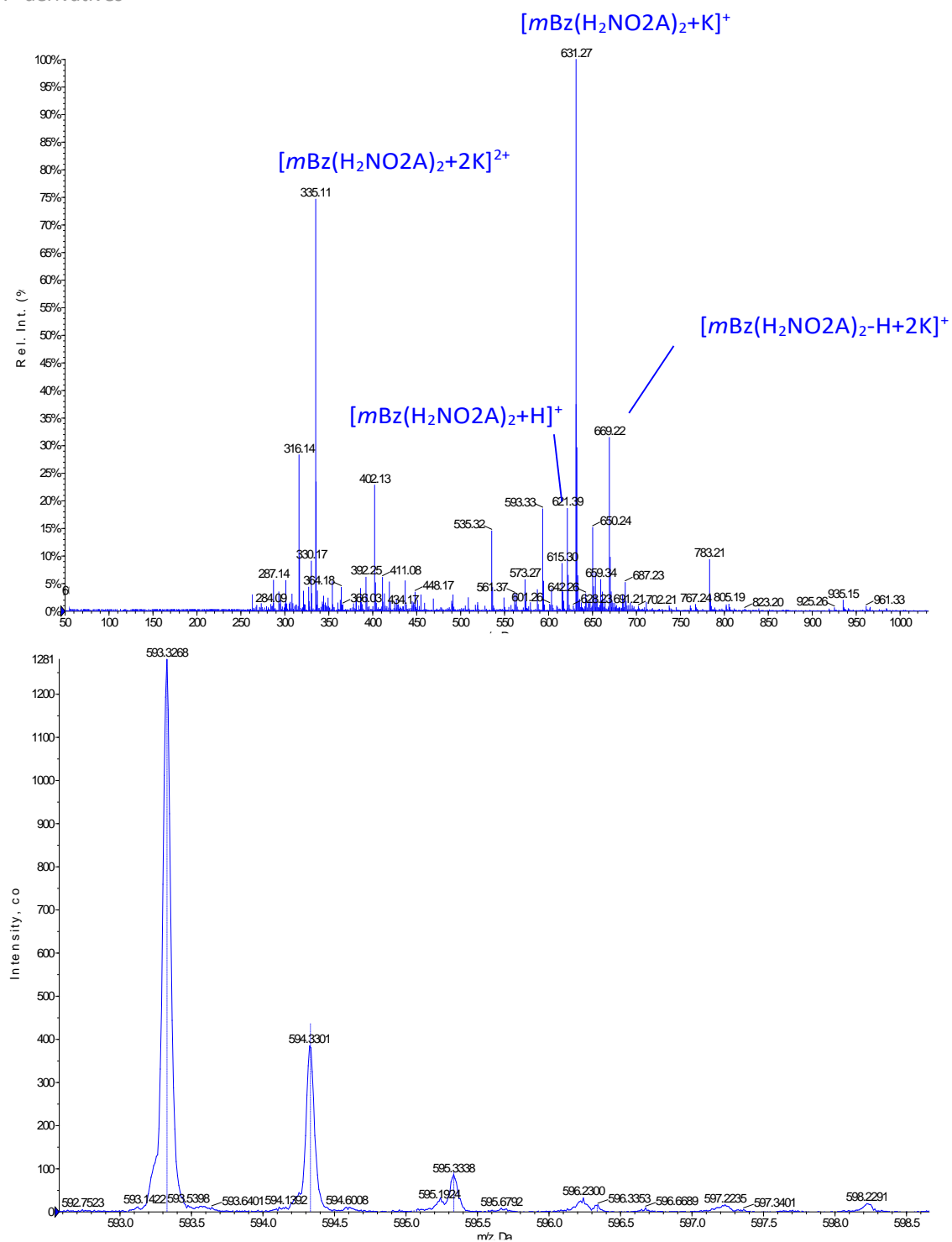
Figure S12. ESI-MS (positive detection) and high resolution mass spectra of ligand *m*Bz(H₂NO2A)₂.
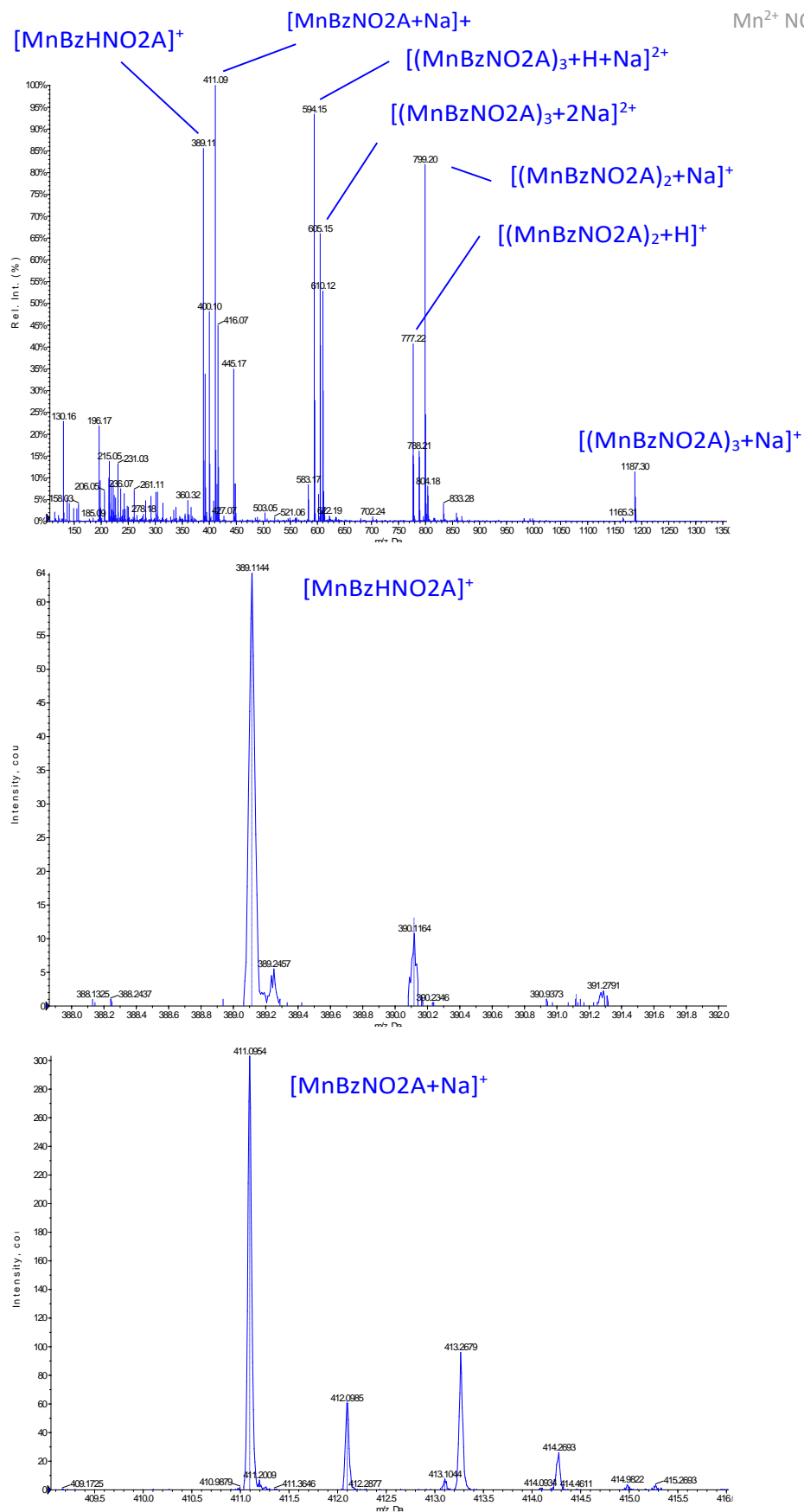
Figure S13. ESI-MS (positive detection) and high resolution mass spectra of the MnBzNO2A complex.
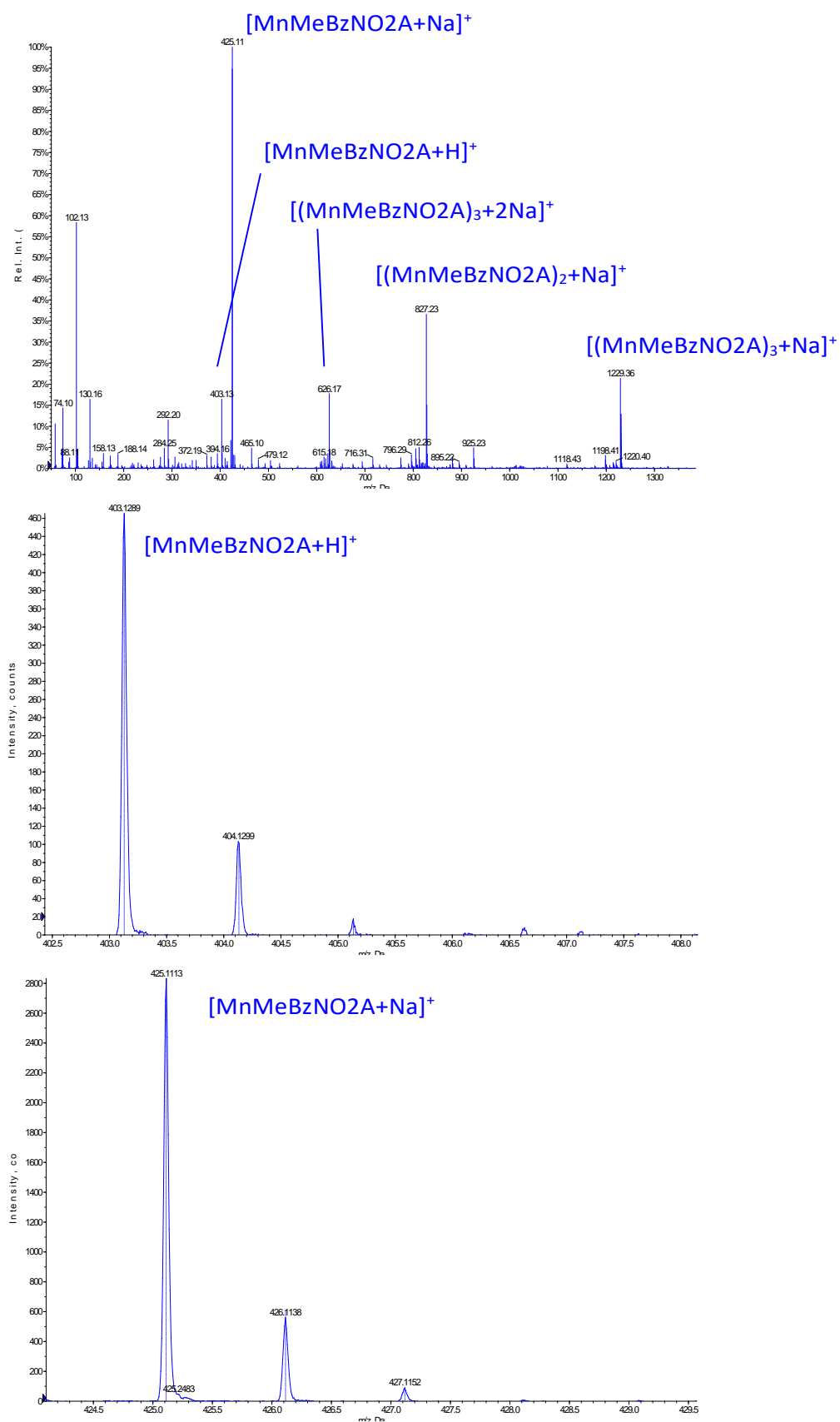
Figure S14. ESI-MS (positive detection) and high resolution mass spectra of the MnMeBzNO2A complex.
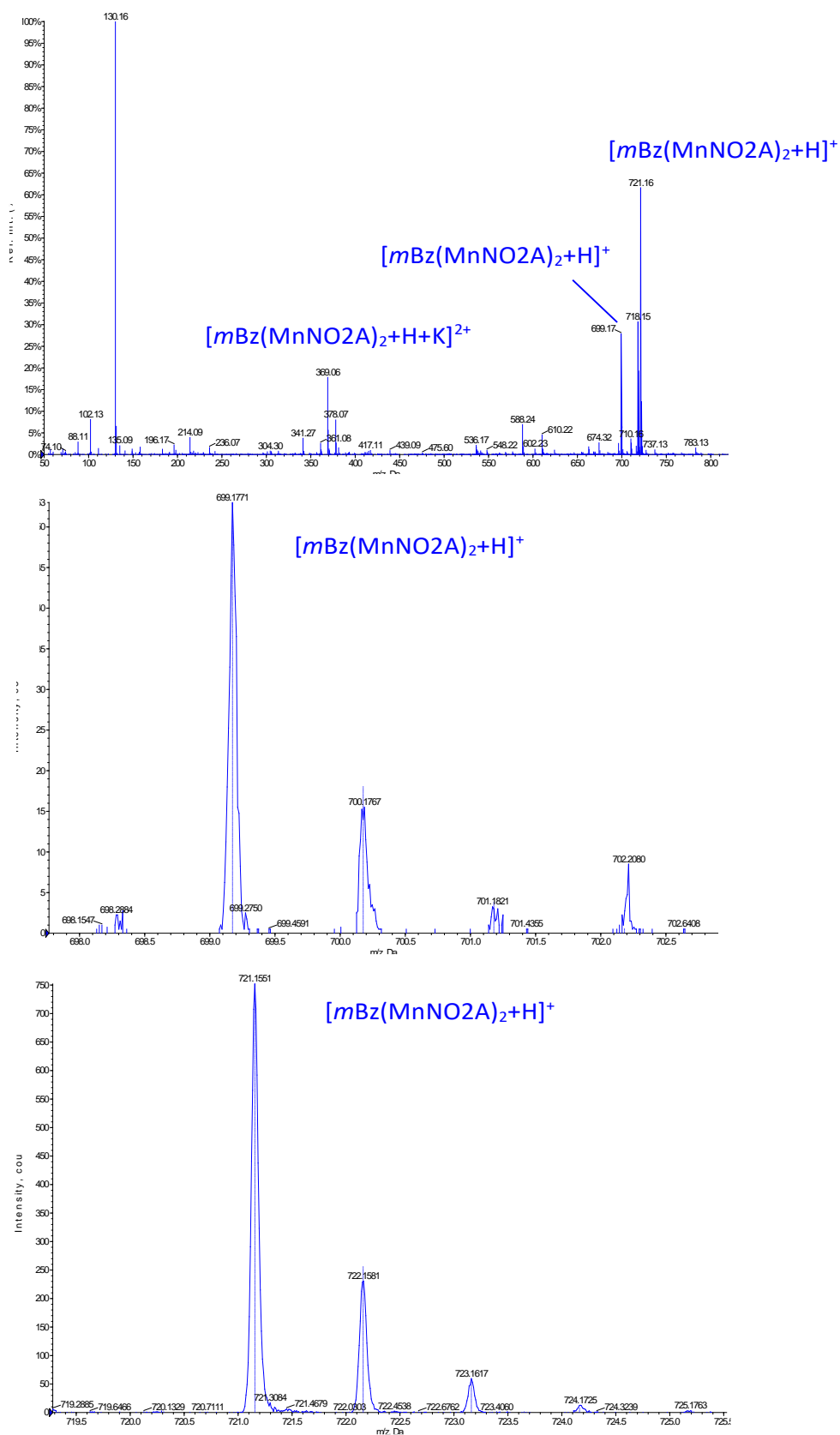
Figure S15. ESI-MS (positive detection) and high resolution mass spectra of the *m*Bz(MnNO2A)$_2$ complex.

Equations used for the analysis of ^{17}O NMR and NMRD data

The reduced relaxation rates, $1/T_{1r}$, $1/T_{2r}$ and reduced chemical shifts (Eqs. (1) – (2)) were obtained from the measured ^{17}O NMR transversal relaxation rates and angular frequencies of the paramagnetic solutions, $1/T_1$, $1/T_2$ and ω, and of the acidified water reference, $1/T_{1A}$, $1/T_{2A}$ and ω_A.

$$\frac{1}{T_{2r}} = \frac{1}{P_m}\left[\frac{1}{T_2} - \frac{1}{T_{2A}}\right] = \frac{1}{\tau_m}\frac{T_{2m}^{-2} + \tau_m^{-1}T_{2m}^{-1} + \Delta\omega_m^2}{\left(\tau_m^{-1} + T_{2m}^{-1}\right)^2 + \Delta\omega_m^2} + \frac{1}{T_{2OS}} \qquad (1)$$

$$\Delta\omega_r = \frac{1}{P_m}(\omega - \omega_A) = \frac{\Delta\omega_m}{(1 + \tau_m T_{2m}^{-1})^2 + \tau_m^2\Delta\omega_m^2} + \Delta\omega_{os} \qquad (2)$$

where $1/T_{2m}$ is the relaxation rate of the bound water and $\Delta\omega_m$ is the chemical shift difference between bound and bulk water, τ_m is the mean residence time of a water molecule in the inner coordination sphere ($\tau_m = 1/k_{ex}$) and P_m is the mole fraction of the bound water.[1,2]

The outer sphere contributions to the ^{17}O relaxation rates and chemical shifts were neglected in the present study. $\Delta\omega_m$ is determined by the hyperfine or scalar coupling constant, $A/\hbar$, which is expressed as in Equation (3).

$$\Delta\omega_m = \frac{g_L\mu_B S(S+1)B}{3k_B T}\frac{A}{\hbar} \qquad (3)$$

where B represents the magnetic field strength, S is the electron spin ($S = 5/2$ for high-spin Mn^{2+} complexes) and g_L is the isotropic Landé g factor.[3]

The exchange rate is assumed to obey the Eyring equation (Eq. (4)):

$$\frac{1}{\tau_m} = k_{ex} = \frac{k_B T}{h}\exp\left\{\frac{\Delta S^\ddagger}{R} - \frac{\Delta H^\ddagger}{RT}\right\} = \frac{k_{ex}^{298}T}{298.15}\exp\left\{\frac{\Delta H^\ddagger}{R}\left(\frac{1}{298.15} - \frac{1}{T}\right)\right\} \qquad (4)$$

where $\Delta S^\ddagger$ and $\Delta H^\ddagger$ are the entropy and enthalpy of activation for the water exchange process, and k_{ex}^{298} is the exchange rate at 298.15 K.

In the transverse relaxation the scalar contribution, $1/T_{2sc}$, is the most important, as given by Eq. (5), with $1/\tau_{s1}$ being the sum of the exchange rate constant and the electron spin relaxation rate.

$$\frac{1}{T_{2m}} \cong \frac{1}{T_{2SC}} = \frac{S(S+1)}{3}\left(\frac{A}{\hbar}\right)^2 \tau_{S1} \qquad (5)$$

$$\frac{1}{\tau_{S1}} = \frac{1}{\tau_m} + \frac{1}{T_{1e}} \qquad (6)$$

The measured longitudinal proton relaxation rate ($R_1{}^{obs)}$ is the sum of the paramagnetic and diamagnetic contributions as given in Eq. (7), where r_{1p} is the proton relaxivity:

$$R_1^{obs} = R_1^d + R_1^p = R_1^d + r_{1p}[Mn(II)] \qquad (7)$$

The relaxivity is the result of both inner- and outer-sphere contributions:

$$r_1 = r_{1is} + r_{1os} \qquad (8)$$

The inner sphere term is given in Eq. (9), where q is the number of inner sphere water molecules.[4]

$$r_{1is} = \frac{1}{1000} \times \frac{q}{55.55} \times \frac{1}{T_{1m}^H + \tau_m} \qquad (9)$$

The longitudinal relaxation rate of proton nuclei of a coordinated water molecule, $1/T_{1m}{}^H$, is given by Eq. (10):

$$\frac{1}{T_{1m}^H} = \frac{2}{15}\left(\frac{\mu_0}{4\pi}\right)^2 \frac{\gamma_I^2 g^2 \mu_B^2}{r_{MnH}^6} S(S+1)\left[\frac{3\tau_{d1}}{1+\omega_I^2\tau_{d1}^2} + \frac{7\tau_{d2}}{1+\omega_S^2\tau_{d2}^2}\right] \qquad (10)$$

where r_{MnH} is the effective distance between the electron charge and the ¹H nucleus, ω_I is the proton resonance frequency and ω_S is the Larmor frequency of the Mn²⁺ electron spin.

$$\frac{1}{\tau_{di}} = \frac{1}{\tau_m} + \frac{1}{\tau_R} + \frac{1}{T_{ie}} \qquad i = 1, 2 \qquad (11)$$

The longitudinal and transverse electronic relaxation rates, $1/T_{1e}$ and $1/T_{2e}$ are approximated by Eqs. (12)-(14),[5] where τ_V is the electronic correlation time for the modulation of the zero-field-splitting interaction, E_V the corresponding activation

energy and Δ^2 is the mean square zero-field-splitting energy. We assumed a simple exponential dependence of τ_V versus $1/T$ as shown in Eq. (14).

$$\frac{1}{T_{1e}} = \frac{1}{25}\Delta^2\tau_V\{4S(S+1)-3\}\left(\frac{1}{1+\omega_s^2\tau_v^2} + \frac{4}{1+4\omega_s^2\tau_v^2}\right) \qquad (12)$$

$$\frac{1}{T_{2e}} = \left(\left(0.02\times(4S^2+4S-3)\times\tau_V\times\Delta^2\times\left(\left(\frac{5}{1+\omega_s^2\tau_V^2}\right)\right)\right) + \left(\frac{2}{1+4\omega_s^2\tau_V^2}\right)+3\right)$$

(13)

$$\tau_v = \tau_v^{298}\exp\left\{\frac{E_v}{R}\left(\frac{1}{T}-\frac{1}{298.15}\right)\right\} \qquad (14)$$

The outer-sphere contribution can be described by Eq. (15) where N_A is the Avogadro constant, and J_{os} is the associated spectral density function.[6,7]

$$r_{1os} = \frac{32N_A\pi}{405}\left(\frac{\mu_0}{4\pi}\right)^2\frac{\hbar^2\gamma_S^2\gamma_I^2}{a_{MnH}D_{MnH}}S(S+1)[3J_{os}(\omega_I;T_{1e})+7J_{os}(\omega_I;T_{2e})] \quad (15)$$

$$J^{OS}(\omega,T_{je}) = \mathrm{Re}\left[\frac{1+\frac{1}{4}\left(i\omega\tau_{MnH}+\frac{\tau_{MnH}}{T_{je}}\right)^{1/2}}{1+\left(i\omega\tau_{MnH}+\frac{\tau_{MnH}}{T_{je}}\right)^{1/2}+\frac{4}{9}\left(i\omega\tau_{MnH}+\frac{\tau_{MnH}}{T_{je}}\right)+\frac{1}{9}\left(i\omega\tau_{MnH}+\frac{\tau_{MnH}}{T_{je}}\right)^{3/2}}\right]$$

(16)

where $j = 1,2$, $\tau_{MnH} = \dfrac{a_{MnH}^2}{D_{MnH}}$.

The diffusion coefficient for the relative diffusion of the complex and water protons away from the Mn^{2+} complex, D_{MnH}, is assumed to obey an exponential law versus the inverse of the temperature, with an activation energy E_{MnH}, as shown in Eq. (17). D_{MnH}^{298} is the diffusion coefficient at 298.15 K.

$$D_{MnH} = D_{MnH}^{298}\exp\left\{\frac{E_{MnH}}{R}\left(\frac{1}{298.15}-\frac{1}{T}\right)\right\} \qquad (17)$$

Table S1. [Mn(MeNO2A)(H₂O)]·2H₂O, M06-2X/TZVP, aqueous solution (0 Imaginary Frequencies).

Center Number	Atomic Number	Coordinates (Angstroms)		
		X	Y	Z
1	7	-1.898472	-0.671549	0.720483
2	6	-2.659757	0.549295	1.054309
3	6	-2.269957	1.757395	0.200775
4	6	-0.228880	2.306797	1.450582
5	6	1.005695	1.471258	1.779444
6	7	0.751017	0.030666	1.617644
7	6	-0.246099	-0.500545	2.567757
8	6	-1.335372	-1.345145	1.899529
9	1	-2.516453	0.776085	2.110141
10	1	-3.732129	0.372866	0.927402
11	1	-2.619794	1.615916	-0.822736
12	1	-2.766351	2.650138	0.602840
13	1	-0.985849	2.188923	2.224568
14	1	0.053572	3.362955	1.465836
15	1	1.803924	1.737269	1.083060
16	1	1.346850	1.718172	2.792608
17	1	-0.699061	0.332376	3.103868
18	1	0.242821	-1.115157	3.329104
19	1	-0.904498	-2.285778	1.557026
20	1	-2.107687	-1.575286	2.644309
21	7	-0.810301	1.955113	0.134407
22	6	-2.654013	-1.564765	-0.157884
23	1	-2.149316	-2.534644	-0.182184
24	1	-3.680106	-1.722970	0.187097
25	6	1.972313	-0.770331	1.572747
26	1	2.273557	-1.136738	2.558987
27	1	2.789688	-0.151376	1.194983
28	6	-2.670796	-1.059283	-1.613546
29	8	-1.616671	-0.450881	-2.005669
30	8	-3.655868	-1.303776	-2.307297
31	8	1.872600	0.560644	-1.360612
32	6	1.895444	-1.956675	0.598603
33	8	0.921639	-1.996369	-0.211137
34	8	2.846654	-2.753927	0.611764
35	25	-0.059252	-0.121813	-0.607333
36	1	2.538572	-0.129932	-1.574862
37	1	2.317915	1.431228	-1.342009
38	6	-0.479781	2.970856	-0.874610
39	1	0.600535	3.113812	-0.901568
40	8	3.594841	-1.524323	-1.817778
41	8	3.049044	3.015703	-1.146599
42	1	3.198825	3.548660	-1.935132
43	1	3.856171	3.087304	-0.625513
44	1	3.486859	-2.145186	-1.073233
45	1	4.541661	-1.380373	-1.912415
46	1	-0.814074	2.627598	-1.854858
47	1	-0.960732	3.930141	-0.649339

E(UM062X) = -2276.2343733 Hartree
Zero-point correction = 0.394609
Thermal correction to Energy = 0.420651
Thermal correction to Enthalpy = 0.421595
Thermal correction to Gibbs Free Energy = 0.338967

```
Sum of electronic and zero-point Energies = -2275.839764
Sum of electronic and thermal Energies = -2275.813722
Sum of electronic and thermal Enthalpies = -2275.812778
Sum of electronic and thermal Free Energies = -2275.895406
```

Table S2. [Mn(BzNO2A)(H₂O)]·2H₂O, M06-2X/TZVP, aqueous solution (0 Imaginary Frequencies).

Center Number	Atomic Number	Coordinates (Angstroms)		
		X	Y	Z
1	7	-1.099756	2.060877	0.822512
2	6	0.274905	2.370484	1.263068
3	6	1.359128	1.659357	0.449478
4	6	1.144814	-0.503779	1.599533
5	6	-0.061741	-1.417468	1.801045
6	7	-1.333462	-0.708697	1.584578
7	6	-1.584414	0.362211	2.570056
8	6	-1.995018	1.689754	1.928111
9	1	0.372821	2.112905	2.316829
10	1	0.459143	3.447153	1.199341
11	1	1.400382	2.079795	-0.557455
12	1	2.326300	1.848058	0.929672
13	1	1.214241	0.221894	2.407951
14	1	2.050199	-1.109115	1.673950
15	1	-0.012893	-2.225563	1.067742
16	1	-0.004840	-1.866936	2.800342
17	1	-0.690057	0.500888	3.176326
18	1	-2.373413	0.061094	3.264981
19	1	-2.995599	1.591380	1.508640
20	1	-2.025693	2.463826	2.705468
21	7	1.101402	0.214024	0.304928
22	6	-1.649420	3.105875	-0.041499
23	1	-2.729239	2.954367	-0.123984
24	1	-1.477228	4.110807	0.354914
25	6	-2.476542	-1.606703	1.422511
26	1	-2.992457	-1.804440	2.367060
27	1	-2.124143	-2.567726	1.041343
28	6	-1.103183	3.015487	-1.478043
29	8	-0.848678	1.837577	-1.904195
30	8	-0.992493	4.051713	-2.130313
31	8	-0.997899	-1.824902	-1.421592
32	6	-3.501111	-1.120019	0.385265
33	8	-3.176420	-0.146395	-0.356786
34	8	-4.551934	-1.773844	0.287813
35	25	-1.059946	0.192444	-0.583891
36	1	-1.849293	-2.213946	-1.724354
37	1	-0.344314	-2.544177	-1.318940
38	6	1.973077	-0.414226	-0.722235
39	1	1.648373	-1.451594	-0.818341
40	1	1.764301	0.093012	-1.668189
41	8	-3.472439	-2.751444	-2.122980
42	8	0.906155	-3.734852	-0.914365
43	1	1.492855	-4.053664	-1.609338
44	1	0.650093	-4.515157	-0.410062
45	1	-4.075254	-2.489218	-1.401845
46	1	-3.631269	-3.687532	-2.280024
47	6	3.456745	-0.383927	-0.434153
48	6	4.086114	-1.495071	0.126373
49	6	4.224843	0.743150	-0.727902
50	6	5.445508	-1.472412	0.415773
51	1	3.507061	-2.390829	0.326297
52	6	5.583272	0.770377	-0.439722
53	1	3.758579	1.602432	-1.196531

```
   54              6                    6.195267   -0.336123    0.138961
   55              1                    5.918577   -2.343033    0.852444
   56              1                    7.254454   -0.316283    0.362772
   57              1                    6.165880    1.652454   -0.674247
   ----------------------------------------------------------------
E(UM062X) = -2507.2648342 Hartree
Zero-point correction = 0.476732
Thermal correction to Energy = 0.507283
Thermal correction to Enthalpy = 0.508227
Thermal correction to Gibbs Free Energy = 0.414728
Sum of electronic and zero-point Energies = -2506.788103
Sum of electronic and thermal Energies = -2506.757551
Sum of electronic and thermal Enthalpies = -2506.756607
Sum of electronic and thermal Free Energies = -2506.850106
```

Table S3. [Mn(MeBzNO2A)(H$_2$O)]·2H$_2$O, M06-2X/TZVP, aqueous solution (0 Imaginary Frequencies).

Center Number	Atomic Number	Coordinates (Angstroms)		
		X	Y	Z
1	7	-1.164424	2.056352	0.870603
2	6	0.215400	2.359812	1.299343
3	6	1.299930	1.652899	0.478918
4	6	1.084852	-0.496602	1.637158
5	6	-0.116717	-1.413890	1.841250
6	7	-1.391632	-0.709120	1.632737
7	6	-1.639833	0.358823	2.622422
8	6	-2.051193	1.687851	1.984462
9	1	0.319065	2.103137	2.352499
10	1	0.401473	3.436096	1.234622
11	1	1.336824	2.089763	-0.519169
12	1	2.261672	1.845645	0.967318
13	1	1.146780	0.237269	2.438048
14	1	1.990935	-1.098417	1.728107
15	1	-0.067854	-2.221118	1.106487
16	1	-0.053987	-1.864931	2.839549
17	1	-0.744334	0.495063	3.227447
18	1	-2.427603	0.055904	3.317802
19	1	-3.055640	1.593018	1.573377
20	1	-2.072076	2.462293	2.761661
21	7	1.055811	0.203558	0.328524
22	6	-1.719855	3.106598	0.016003
23	1	-2.802281	2.965274	-0.047095
24	1	-1.532010	4.109550	0.410156
25	6	-2.532415	-1.611109	1.477888
26	1	-3.036835	-1.817381	2.426753
27	1	-2.179677	-2.568101	1.086417
28	6	-1.202004	3.013139	-1.430478
29	8	-0.949999	1.835019	-1.856604
30	8	-1.110017	4.047690	-2.088522
31	8	-1.060802	-1.805064	-1.398972
32	6	-3.569397	-1.121696	0.454581
33	8	-3.249226	-0.150711	-0.293004
34	8	-4.623624	-1.771600	0.371358
35	25	-1.134924	0.197238	-0.531643
36	1	-1.915874	-2.210479	-1.669365
37	1	-0.398160	-2.517366	-1.298910
38	6	1.969500	-0.472650	-0.649102
39	1	1.684879	-1.525827	-0.589633
40	8	-3.536174	-2.782518	-2.025503
41	8	0.835517	-3.729179	-0.920217
42	1	1.416779	-4.037922	-1.624302
43	1	0.560370	-4.519943	-0.442992
44	1	-4.140822	-2.515557	-1.307997
45	1	-3.683227	-3.723202	-2.165743
46	6	1.731205	-0.015329	-2.084815
47	1	0.700017	-0.183107	-2.394798
48	1	1.963412	1.037654	-2.238206
49	1	2.376364	-0.597744	-2.743553
50	6	3.442768	-0.391814	-0.279712
51	6	4.080472	-1.506066	0.264309
52	6	4.195754	0.763258	-0.498032
53	6	5.427887	-1.465735	0.605184

```
   54           1                      3.516162   -2.421255    0.412487
   55           6                      5.540962    0.809393   -0.155718
   56           1                      3.737443    1.635855   -0.947457
   57           6                      6.160418   -0.304230    0.400692
   58           1                      5.903404   -2.342599    1.026504
   59           1                      6.107848    1.715240   -0.330990
   60           1                      7.209961   -0.268303    0.664594
   ------------------------------------------------------------------
E(UM062X) = -2546.5716587 Hartree
Zero-point correction = 0.505080
Thermal correction to Energy = 0.536918
Thermal correction to Enthalpy = 0.537862
Thermal correction to Gibbs Free Energy = 0.442106
Sum of electronic and zero-point Energies = -2546.066578
Sum of electronic and thermal Energies = -2546.034741
Sum of electronic and thermal Enthalpies = -2546.033796
Sum of electronic and thermal Free Energies = -2546.129553
```

Table S4. [Mn(MeNO2A)(H$_2$O)]·5H$_2$O, M06-2X/TZVP, aqueous solution (0 Imaginary Frequencies).

```
---------------------------------------------------------------------
Center      Atomic                      Coordinates (Angstroms)
Number      Number               X              Y              Z
---------------------------------------------------------------------
   1          7            0.344273      -2.016545      -0.812447
   2          6           -0.036050      -2.910209       0.302440
   3          6           -0.649143      -2.162381       1.488557
   4          6            1.485839      -1.389825       2.423599
   5          6            2.618309      -0.566705       1.813758
   6          7            2.550935      -0.550482       0.342323
   7          6            2.767128      -1.876351      -0.272618
   8          6            1.707494      -2.250764      -1.313788
   9          1            0.843586      -3.465906       0.624607
  10          1           -0.755826      -3.658597      -0.042233
  11          1           -1.640895      -1.788391       1.223850
  12          1           -0.775018      -2.864585       2.322545
  13          1            1.647943      -2.451867       2.247612
  14          1            1.509142      -1.260158       3.508737
  15          1            2.518897       0.467906       2.147125
  16          1            3.578605      -0.952311       2.177080
  17          1            2.796203      -2.628082       0.515113
  18          1            3.746623      -1.914394      -0.757741
  19          1            1.834161      -1.627360      -2.198330
  20          1            1.858101      -3.296639      -1.608320
  21          7            0.158022      -0.998407       1.894589
  22          6           -0.671760      -2.006694      -1.865721
  23          1           -0.263977      -1.493409      -2.740552
  24          1           -0.982954      -3.012053      -2.162255
  25          6            3.377068       0.495174      -0.260301
  26          1            4.392270       0.155156      -0.485767
  27          1            3.463634       1.327290       0.444139
  28          6           -1.891695      -1.198064      -1.412348
  29          8           -1.627099      -0.102800      -0.807845
  30          8           -3.026837      -1.617138      -1.650063
  31          8            0.775745       2.086150       0.939520
  32          6            2.758041       1.112730      -1.524334
  33          8            1.535221       0.870069      -1.756381
  34          8            3.473333       1.883183      -2.180988
  35         25            0.373131       0.213491      -0.074854
  36          1            1.202071       2.777725       0.386624
  37          1            0.009958       2.496003       1.409194
  38          6           -0.574389      -0.181417       2.872414
  39          1            0.033287       0.679540       3.150446
  40          8            2.058479       3.873792      -0.709329
  41          8           -1.463626       2.952259       2.155055
  42          1           -2.188845       2.460472       1.711638
  43          1           -1.701370       3.883614       2.108906
  44          1            2.606457       3.420153      -1.374162
  45          1            2.613783       4.561796      -0.328982
  46          8           -5.220308       1.984494      -1.397978
  47          1           -4.484863       2.264533      -0.837640
  48          1           -5.384215       1.082843      -1.078820
  49          8           -3.218079       1.480144       0.694970
  50          1           -2.669167       0.937154       0.085313
  51          1           -3.954077       0.885490       0.907333
  52          8           -4.993447      -0.534626      -0.115612
  53          1           -5.611370      -1.219650       0.156008
```

```
  54            1                        -4.318753   -0.969047   -0.687665
  55            1                        -0.816369   -0.756492    3.773607
  56            1                        -1.500000    0.182847    2.421938
  ------------------------------------------------------------------
```

E(UM062X) = -2505.5769148 Hartree
Zero-point correction = 0.471142
Thermal correction to Energy = 0.504600
Thermal correction to Enthalpy = 0.505544
Thermal correction to Gibbs Free Energy = 0.406021
Sum of electronic and zero-point Energies = -2505.105773
Sum of electronic and thermal Energies = -2505.072315
Sum of electronic and thermal Enthalpies = -2505.071371
Sum of electronic and thermal Free Energies = -2505.170893

Table S5. [Mn(MeNO2A)(H₂O)₂]·4H₂O, M06-2X/TZVP, aqueous solution (0 Imaginary Frequencies).

Center Number	Atomic Number	Coordinates (Angstroms)		
		X	Y	Z
1	7	0.030978	-2.057941	-0.871424
2	6	-0.260606	-3.018282	0.215692
3	6	-0.751541	-2.375663	1.517307
4	6	1.419087	-1.609806	2.314674
5	6	2.498138	-0.746094	1.673436
6	7	2.307549	-0.640937	0.218916
7	6	2.482216	-1.928742	-0.481497
8	6	1.359504	-2.253119	-1.469031
9	1	0.637221	-3.604554	0.411469
10	1	-1.017955	-3.736233	-0.113362
11	1	-1.778970	-2.038478	1.403747
12	1	-0.733709	-3.139086	2.307248
13	1	1.572287	-2.657543	2.059263
14	1	1.522024	-1.549153	3.401986
15	1	2.428374	0.263087	2.078338
16	1	3.484072	-1.156076	1.929176
17	1	2.563465	-2.723208	0.259295
18	1	3.428104	-1.936955	-1.031545
19	1	1.427997	-1.583432	-2.325012
20	1	1.496025	-3.281351	-1.828768
21	7	0.053475	-1.207284	1.909002
22	6	-1.036742	-2.018319	-1.867438
23	1	-0.677142	-1.486380	-2.752544
24	1	-1.362197	-3.013486	-2.189382
25	6	3.101036	0.429562	-0.377002
26	1	4.096428	0.095944	-0.689039
27	1	3.246792	1.220722	0.363030
28	6	-2.244689	-1.225946	-1.362231
29	8	-2.040366	-0.494363	-0.342868
30	8	-3.309489	-1.280797	-1.990275
31	8	0.797579	1.854975	1.280606
32	6	2.406944	1.104962	-1.567341
33	8	1.189693	0.829976	-1.766080
34	8	3.073366	1.939553	-2.204008
35	25	0.043240	0.183948	-0.034843
36	1	1.234665	2.573247	0.772573
37	1	0.027860	2.257788	1.729164
38	6	-0.614057	-0.470056	2.989563
39	1	0.009616	0.372320	3.288679
40	8	2.085343	3.754948	-0.261122
41	8	-1.672707	2.780515	2.069569
42	1	-2.436002	2.172043	1.928386
43	1	-1.940772	3.446511	2.709510
44	1	2.517107	3.363132	-1.041970
45	1	2.747180	4.313183	0.159316
46	8	-1.265881	2.111748	-0.649432
47	1	-1.440228	2.676262	0.118676
48	1	-2.143859	1.868131	-1.000053
49	8	-3.592569	1.058516	1.254044
50	1	-3.091237	0.408072	0.713870
51	1	-4.120464	1.504758	0.576324
52	8	-3.903909	1.406776	-1.534322
53	1	-4.340943	1.831068	-2.279137

```
  54            1                        -3.861213    0.448777   -1.741499
  55            1                        -0.794996   -1.109225    3.862423
  56            1                        -1.568757   -0.081199    2.629755
 ---------------------------------------------------------------------
 E(UM062X) = -2505.5809106 Hartree
Zero-point correction = 0.473123
 Thermal correction to Energy = 0.505544
 Thermal correction to Enthalpy = 0.506488
 Thermal correction to Gibbs Free Energy = 0.412760
 Sum of electronic and zero-point Energies = -2505.107788
 Sum of electronic and thermal Energies = -2505.075366
 Sum of electronic and thermal Enthalpies = -2505.074422
 Sum of electronic and thermal Free Energies = -2505.168151
```

Table S6. [Mn(MeNO2A)(H$_2$O)$_2$]·4H$_2$O, M06-2X/TZVP, aqueous solution (1 Imaginary Frequency).

Center Number	Atomic Number	Coordinates (Angstroms)		
		X	Y	Z
1	7	0.391628	-1.997165	-0.981805
2	6	0.232976	-3.048568	0.045623
3	6	-0.368739	-2.545804	1.360860
4	6	1.690952	-1.549693	2.240943
5	6	2.629496	-0.493569	1.666996
6	7	2.438133	-0.332876	0.216159
7	6	2.800770	-1.537635	-0.558114
8	6	1.737376	-1.961453	-1.575140
9	1	1.205012	-3.504923	0.231700
10	1	-0.406014	-3.851569	-0.333220
11	1	-1.425344	-2.315611	1.221825
12	1	-0.297738	-3.348771	2.106257
13	1	1.996717	-2.544997	1.922126
14	1	1.784257	-1.543394	3.330271
15	1	2.399201	0.469117	2.126505
16	1	3.665024	-0.755261	1.917493
17	1	2.997044	-2.354226	0.135080
18	1	3.737886	-1.372715	-1.097862
19	1	1.709344	-1.237067	-2.388270
20	1	2.023317	-2.934349	-1.994294
21	7	0.281905	-1.317480	1.849733
22	6	-0.676583	-2.030783	-1.979263
23	1	-0.371527	-1.439447	-2.846730
24	1	-0.902459	-3.042308	-2.330742
25	6	3.057784	0.881116	-0.309949
26	1	4.093217	0.724289	-0.627862
27	1	3.073249	1.641300	0.476527
28	6	-1.960606	-1.375286	-1.464438
29	8	-1.822245	-0.550526	-0.499634
30	8	-3.033123	-1.617155	-2.024102
31	8	0.371670	1.895996	1.297413
32	6	2.266415	1.518984	-1.461749
33	8	1.081265	1.111466	-1.651569
34	8	2.810335	2.453644	-2.068104
35	25	0.129874	0.137776	0.011474
36	1	0.677612	2.691551	0.807987
37	1	-0.471824	2.130973	1.741154
38	6	-0.476100	-0.747197	2.971336
39	1	0.012991	0.167493	3.306199
40	8	1.353168	4.014610	-0.165631
41	8	-2.142144	2.347023	2.219664
42	1	-2.767666	1.603974	2.040821
43	1	-2.432393	2.794522	3.020007
44	1	1.869218	3.737516	-0.943194
45	1	1.884537	4.680135	0.282884
46	8	-2.046983	2.413489	-0.680513
47	1	-2.194810	2.643378	0.246552
48	1	-2.766283	1.802669	-0.914071
49	8	-3.639991	0.325419	1.304763
50	1	-3.006496	-0.069369	0.665247
51	1	-4.339677	0.640807	0.713949
52	8	-4.352141	0.740223	-1.367319
53	1	-4.982756	1.021192	-2.036997

```
    54              1                          -4.007729   -0.133434   -1.652328
    55              1                          -0.537959   -1.449516    3.810887
    56              1                          -1.487375   -0.497878    2.644245
    ----------------------------------------------------------------
E(UM062X) =-2505.5785633 Hartree
Zero-point correction = 0.471389
Thermal correction to Energy = 0.503779
Thermal correction to Enthalpy = 0.504724
Thermal correction to Gibbs Free Energy = 0.410549
Sum of electronic and zero-point Energies = -2505.107175
Sum of electronic and thermal Energies = -2505.074784
Sum of electronic and thermal Enthalpies = -2505.073840
Sum of electronic and thermal Free Energies = -2505.168015
```

References

1. T. J. Swift and R. E. Connick. *J. Chem. Phys.,* 1962, **37**, 307.

2. J. R. Zimmermann and W. E. Brittin, *J. Phys. Chem.,* 1957, **61**, 1328

3. A. D. McLachlan, *Proc. R. Soc. London, A*, 1964, **280**, 271.

4. Z. Luz, and S. Meiboom, *J. Chem. Phys.,* 1964, **40**, 2686.

5. The Chemistry of Contrast Agents in Medical Magnetic Resonance Imaging (Eds: A. E. Merbach and É. Tóth), Wiley, New York, 2001.

6. J. H. Freed, *J. Chem. Phys.,* 1978, **68**, 4034.

7. S. H. Koenig and R. D. Brown III, *Prog. Nucl. Magn. Reson. Spectrosc.,* 1991, **22**, 487.

Annexe B

Annexe B

A Pentadentate Member of the Picolinate Family for Mn(II) Complexation and an Amphiphilic Derivative

Annexe B Summary

Figure S1. ¹H (300 MHz, 25 °C, top) and ¹³C (75 MHz, 25 °C, bottom) NMR spectra of compound **3** recorded in CDCl₃ solution.
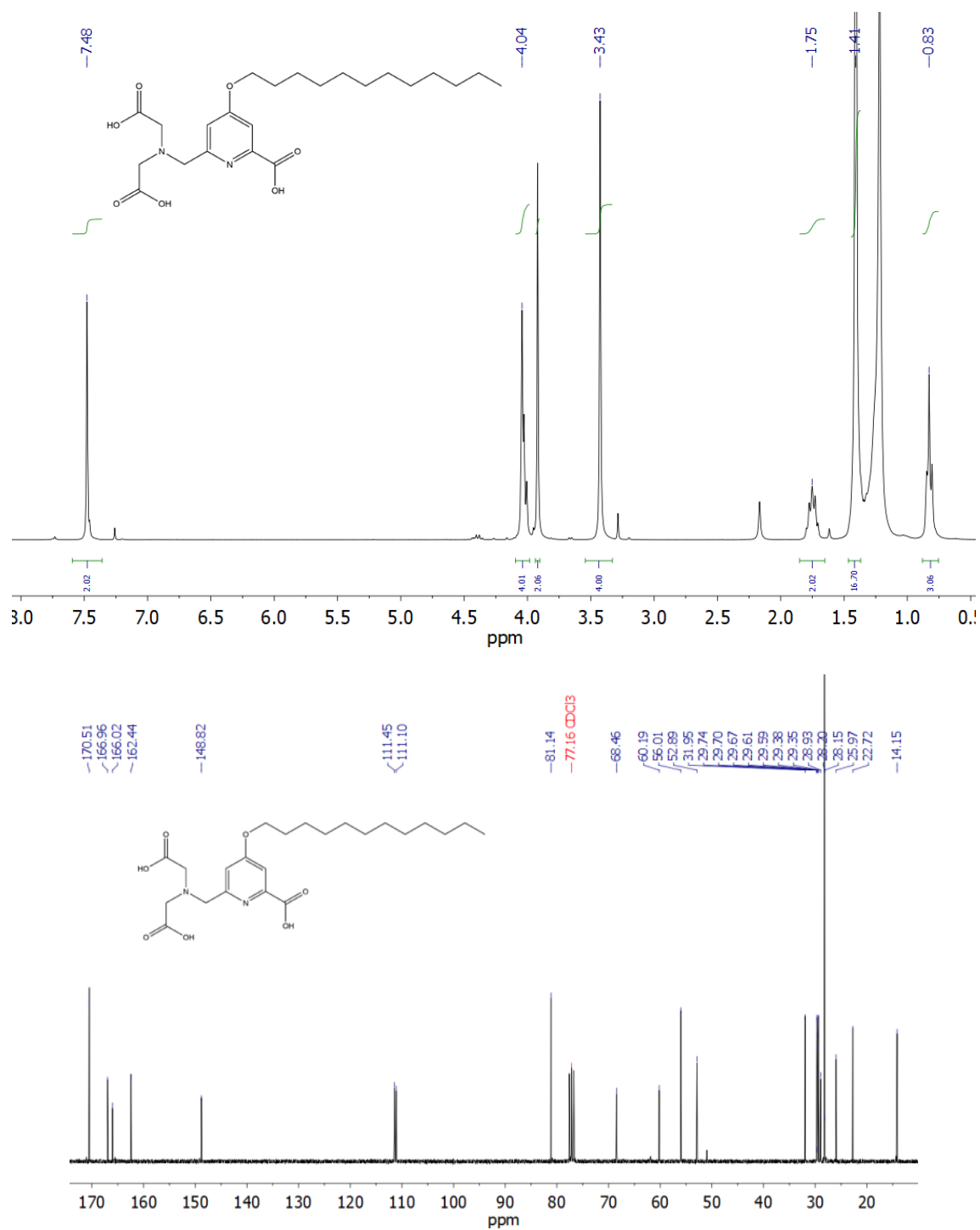
Figure S2. ¹H (300 MHz, 25 °C, top) and ¹³C (75 MHz, 25 °C, bottom) NMR spectra of **H₃C₁₂OPAADA** recorded in CDCl₃ solution.
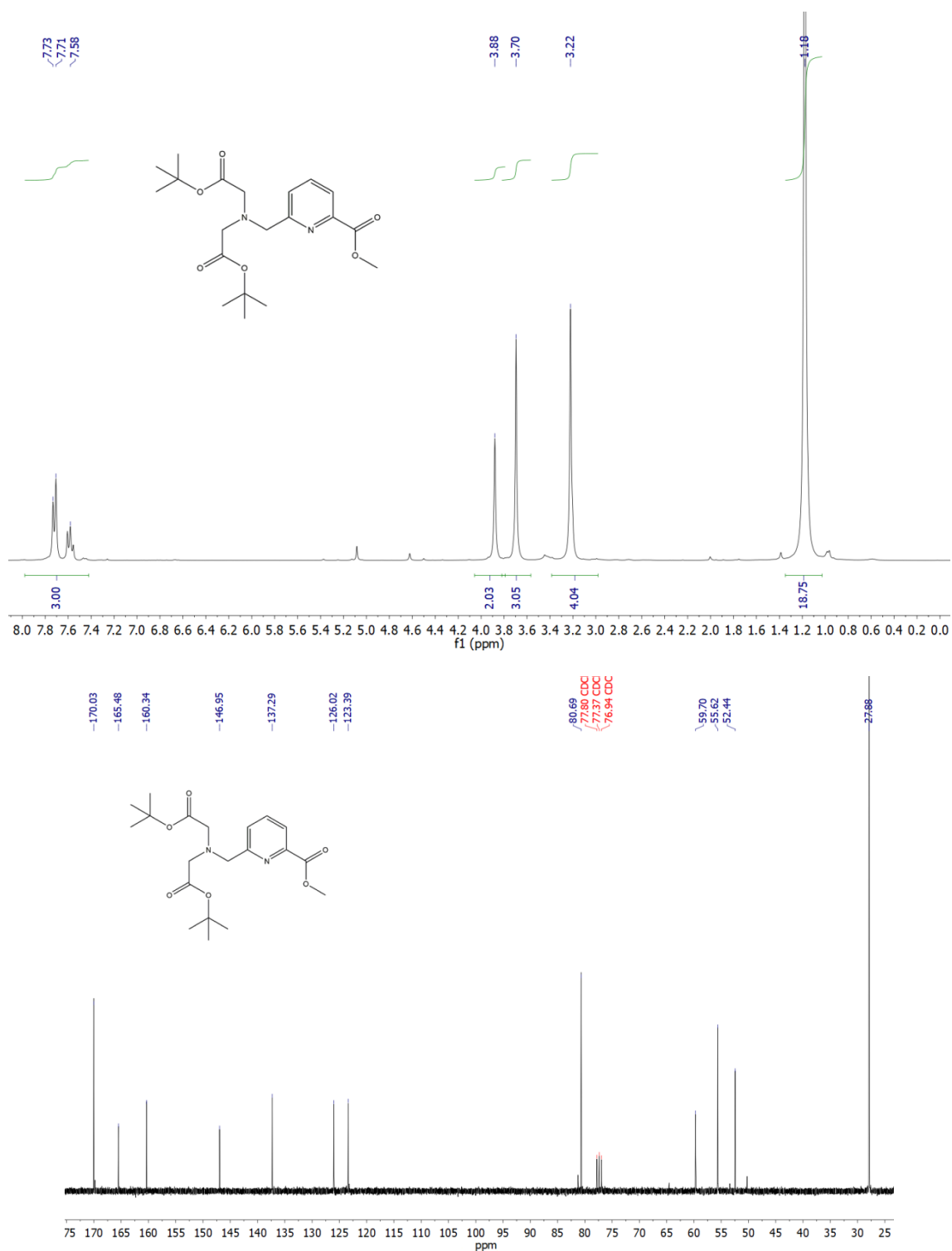
Figure S3. ^{1}H (300 MHz, 25 °C, top) and ^{13}C (75 MHz, 25 °C, bottom) NMR spectra of compound **6** recorded in CDCl$_3$ solution.
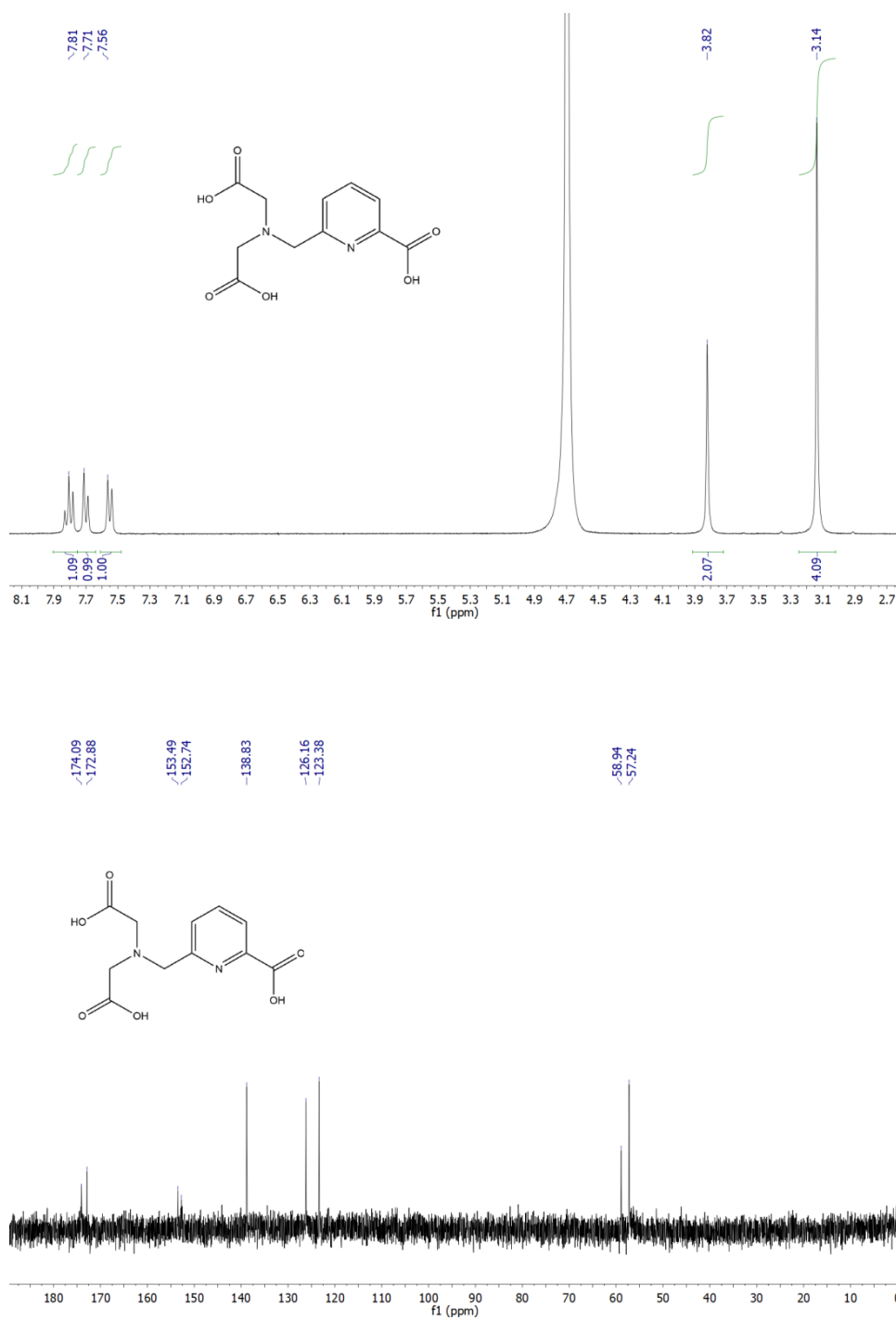
Figure S4. ¹H (300 MHz, 25 °C, top) and ¹³C (75 MHz, 25 °C, bottom) NMR spectra of H₃PAADA recorded in D₂O solution.
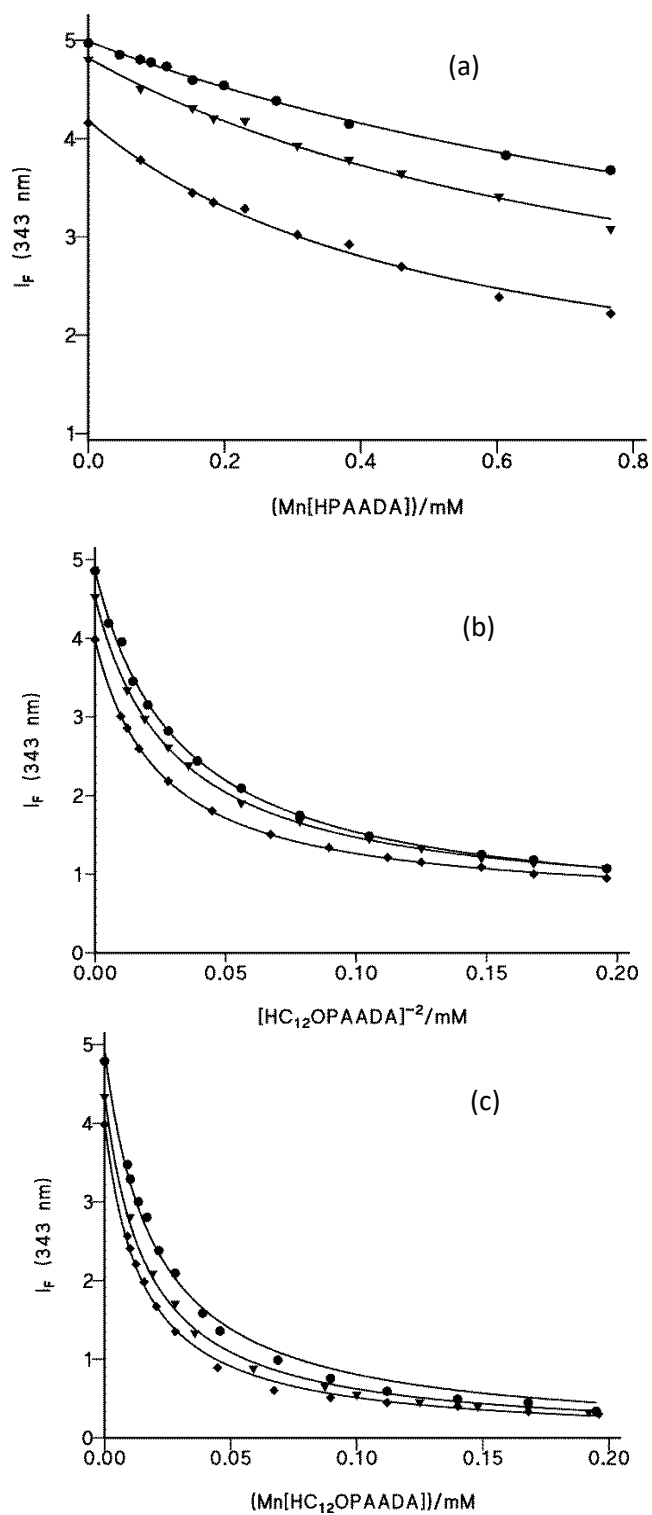
Figure S5. The fluorescence intensity, I_F, of BSA measured as a function of the ligand concentration at three temperatures: (●) 15, (▼)25, and (◆)36 °C. Solid lines represent the fits of the experimental data of I_F-$[L]_o$ to eq. (7).
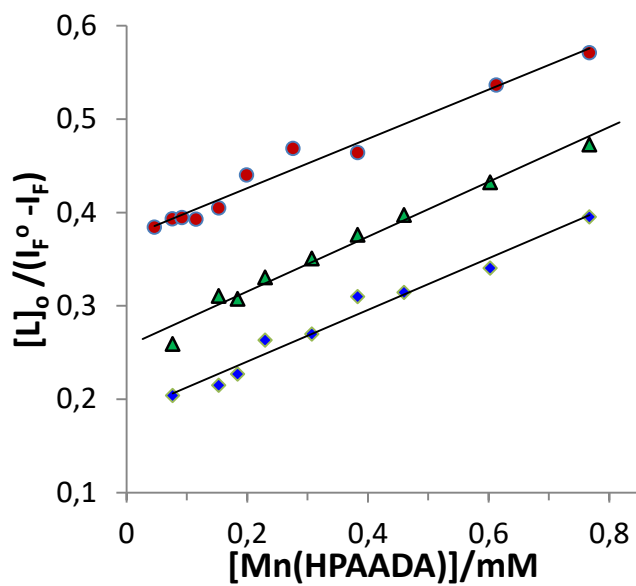
Figure S6. Benessi-Hildebrand plot for the experimental data of Figure S5 (a).
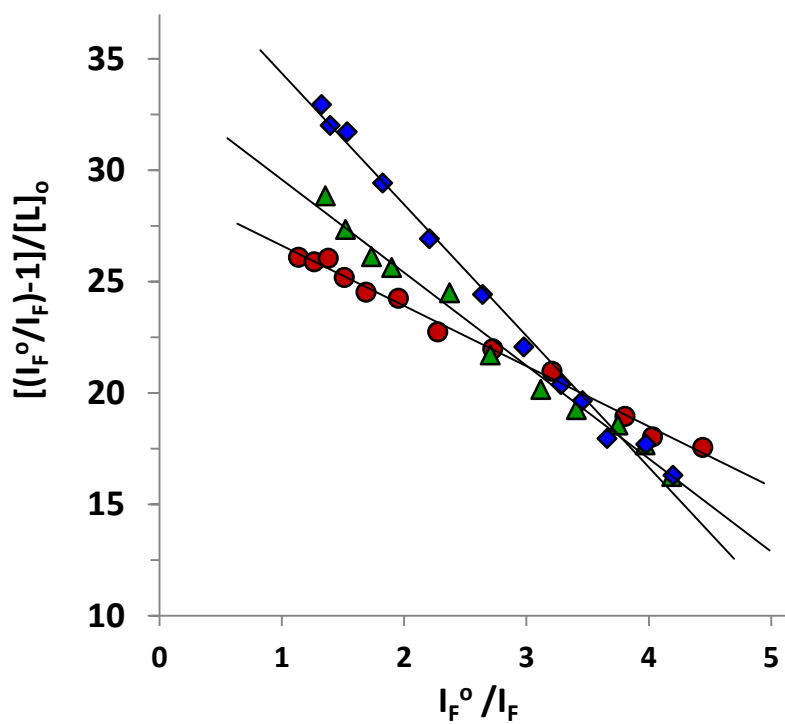
Figure S7. Scatchard plot for the case of BSA fluorescence quenching by the substrate [HC$_{12}$OPAADA]$^-$ using the experimental data of Figure S5(b).
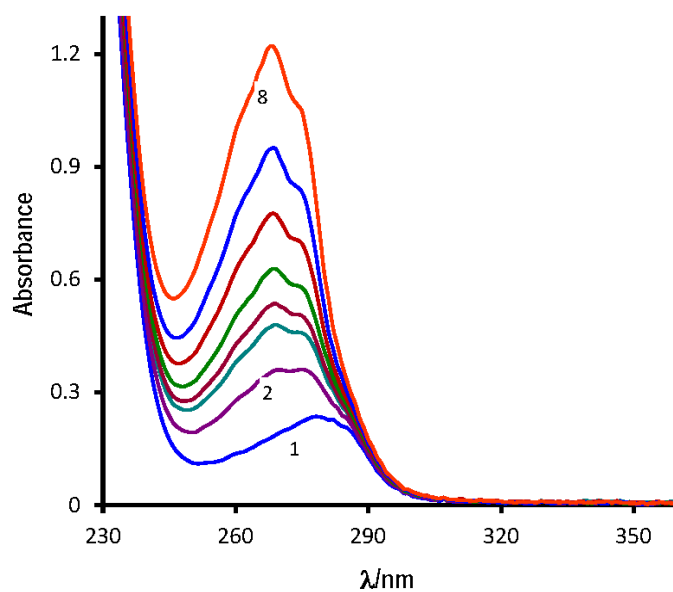
Figure S8. UV-vis absorption spectra of 5.2 μM BSA in 10 mM Tris-HCl buffer at pH 7.4 (1) as a function of increasing concentration of ligand, [HPAADA²⁻] equal to: (1) no ligand; (2) 46 μM to (8) 0.276 mM.
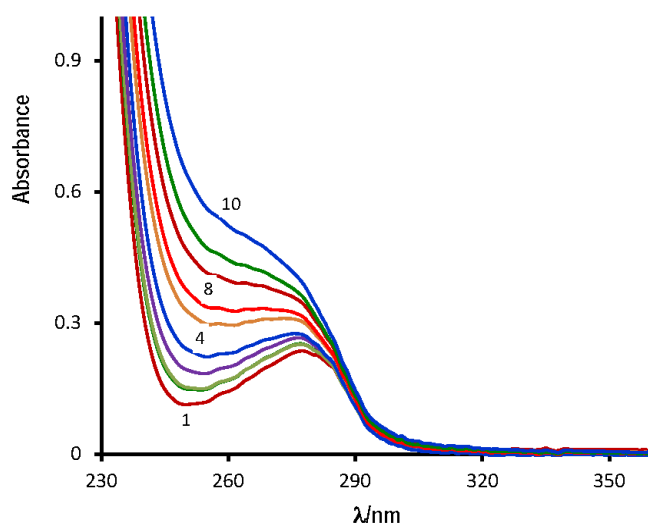
Figure S9. UV-vis absorption spectra of 5.2 µM BSA in 10 mM Tris-HCl buffer at pH 7.4 (1) as a function of increasing concentration of ligand [HC$_{12}$OPAADA]$^{2-}$ at: [1] 0; [4] 28; [8] 112, and [10] 168 µM. The absorbance values at 290 nm are: [1] 0.108; [4] 0.113; [8] 0.134, and [10] 0.145.
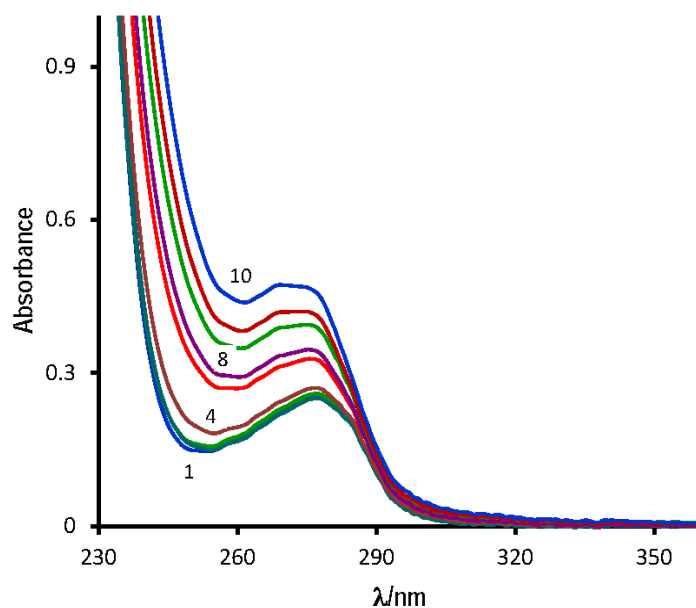
Figure S10. UV-vis absorption spectra of 5.2 µM BSA in 10 mM Tris-HCl buffer at pH 7.4 (1) as a function of increasing concentration of both ligand [HC$_{12}$OPAADA]$^{2-}$ and Mn^{+2} (Mn:L 1:1) at: [1] 0; [4] 28; [8] 112, and [10] 168 µM. The absorbance values at 290 nm are: [1] 0.108; [4] 0.111; [8] 0.140, and [10] 0.148.
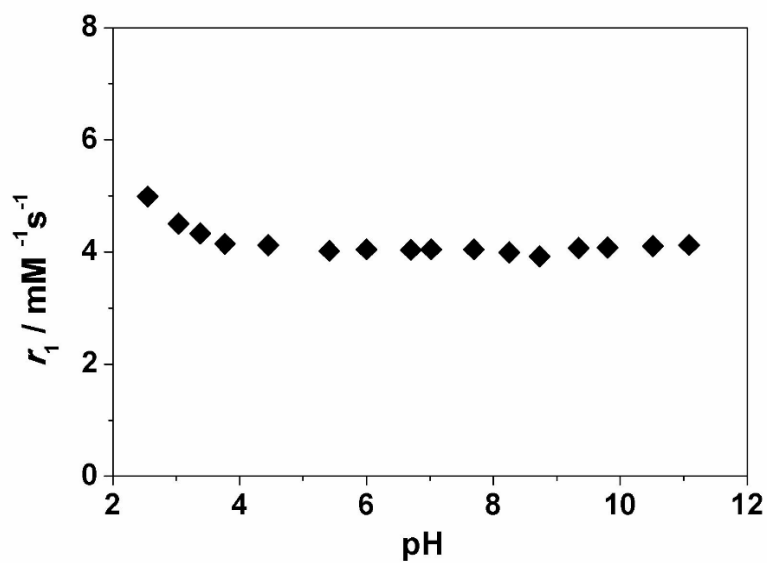
Figure S11. pH dependence of the proton relaxivity (r_1) for [Mn(PAADA)]⁻ measured at 20 MHz and 298 K.
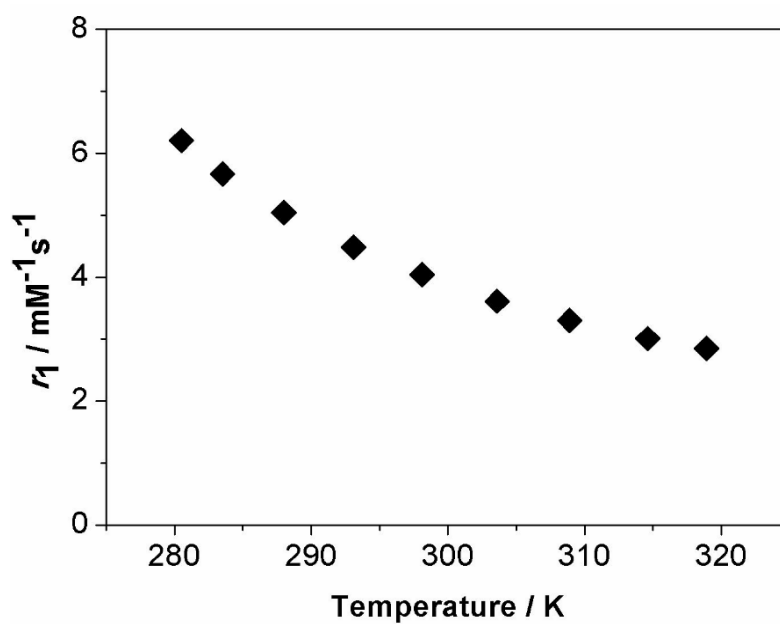
Figure S12. Temperature dependence of the proton relaxivity values at 20 MHz for [Mn(PAADA)]⁻ (pH = 7.5).

Table S1. [Mn(NTA)(H$_2$O)$_2$]$^-$·4H$_2$O, M06-2X/Def2-TZVP, aqueous solution (0 Imaginary Frequencies).

```
---------------------------------------------------------------------
Center      Atomic                      Coordinates (Angstroms)
Number      Number                 X              Y              Z
---------------------------------------------------------------------
   1           7                -2.071818      -0.168555      -0.244522
   2           6                -2.810124       0.497967       0.823999
   3           6                -2.374189      -1.592204      -0.341282
   4           6                -1.149457      -2.467786      -0.643583
   5           8                -0.017397      -2.005499      -0.271153
   6           8                -1.334056      -3.563396      -1.166614
   7           6                -1.331579       1.850969      -1.486674
   8           6                -2.132040       0.538147      -1.516757
   9           8                -0.489582       1.982254      -0.533093
  10           8                -1.530087       2.667049      -2.382881
  11           1                -3.847468       0.156692       0.885443
  12           1                -2.828415       1.571938       0.626328
  13           1                -2.742222      -1.936638       0.629086
  14           1                -3.156710      -1.801936      -1.076118
  15           1                -3.158183       0.752123      -1.835946
  16           1                -1.669890      -0.087902      -2.286076
  17           8                 2.110719      -0.010019       1.390204
  18           1                 2.622651       0.820093       1.368007
  19           8                 1.327502       0.114610      -1.626011
  20           1                 1.922746      -0.654601      -1.714039
  21           1                 2.740042      -0.737094       1.228460
  22           1                 1.831751       0.947069      -1.688883
  23           6                -2.134439       0.332077       2.196275
  24           8                -0.879698       0.121444       2.191211
  25           8                -2.841377       0.456285       3.198146
  26           8                 2.021990       2.768187      -1.319647
  27           8                 2.393743      -2.419402      -1.469232
  28           1                 1.085233       2.722455      -1.037909
  29           1                 2.532993       2.801003      -0.496439
  30           1                 3.031731      -2.447120      -0.740764
  31           1                 1.516043      -2.498986      -1.039188
  32           8                 3.952276      -2.082499       0.929028
  33           8                 3.431446       2.456831       1.191683
  34           1                 3.957180      -2.790534       1.583198
  35           1                 4.867133      -1.788204       0.851711
  36           1                 4.392820       2.430267       1.121563
  37           1                 3.236466       3.083499       1.898068
  38          25                 0.183839       0.071839       0.327606
---------------------------------------------------------------------
E(UM062X) = -2348.4253432 Hartree
Zero-point correction = 0.284542
Thermal correction to Energy = 0.313633
Thermal correction to Enthalpy = 0.314577
Thermal correction to Gibbs Free Energy = 0.222716
Sum of electronic and zero-point Energies = -2348.140801
Sum of electronic and thermal Energies = -2348.111710
Sum of electronic and thermal Enthalpies = -2348.110766
Sum of electronic and thermal Free Energies = -2348.202628
```

Table S2. [Mn(PAADA)(H₂O)₂]⁻·4H₂O, M06-2X/Def2-TZVP, aqueous solution (0 Imaginary Frequencies).

```
-----------------------------------------------------------------------
Center      Atomic                     Coordinates (Angstroms)
Number      Number                 X           Y           Z
-----------------------------------------------------------------------
    1           8              -0.858200    2.074649    0.633369
    2           7              -1.827685   -0.044040   -0.579101
    3           8              -2.787060    3.180579    0.424322
    4           6              -2.260713   -1.206965   -1.051625
    5           7              -0.042326   -2.139212   -0.534010
    6           6              -4.061163    0.759918   -0.442668
    7           1              -4.727744    1.570526   -0.186708
    8           6              -2.086863    2.179759    0.307386
    9           6               1.204229   -2.527694   -1.180589
   10           1               1.216880   -2.141328   -2.201082
   11           1               1.333976   -3.614558   -1.245403
   12           6              -2.695298    0.914241   -0.271158
   13           6              -1.187015   -2.193186   -1.439996
   14           1              -1.609015   -3.202264   -1.511121
   15           1              -0.846643   -1.913182   -2.439391
   16           6              -3.615895   -1.457911   -1.229113
   17           1              -3.945943   -2.419868   -1.597919
   18           6              -4.524786   -0.456110   -0.924279
   19           1              -5.585813   -0.625902   -1.053622
   20           8               1.264165    0.917840   -1.474354
   21           1               2.234144    0.783351   -1.536904
   22           1               1.101427    1.866852   -1.664457
   23           6              -0.280805   -2.902697    0.695534
   24           1              -0.863857   -3.805992    0.492689
   25           1               0.685691   -3.216497    1.096790
   26           8               0.966012    3.624749   -1.839149
   27           1               0.939488    3.943354   -0.915662
   28           1               0.145723    3.922747   -2.244825
   29           8               4.025852    0.482817   -1.596280
   30           1               4.310086    0.766786   -0.712698
   31           1               4.052229   -0.488958   -1.528597
   32           6              -0.947146   -2.122493    1.843204
   33          25               0.318780    0.159105    0.381885
   34           8              -1.691278   -2.755140    2.596410
   35           8              -0.621982   -0.902113    1.974176
   36           6               2.429733   -1.928293   -0.494776
   37           8               2.223171   -1.105978    0.449474
   38           8               3.542371   -2.242288   -0.939366
   39           8               1.654392    1.453909    1.690022
   40           1               1.541148    2.409095    1.546683
   41           1               2.609419    1.263164    1.644673
   42           8               0.795580    4.028927    0.890643
   43           8               4.192891    0.460646    1.224241
   44           1               4.846641    0.165281    1.864600
   45           1               3.605911   -0.307824    1.005410
   46           1              -0.007286    3.436706    0.884762
   47           1               0.591148    4.813455    1.407832
-----------------------------------------------------------------------
E(UM062X) = -2595.5407108 Hartree
Zero-point correction = 0.354360
Thermal correction to Energy = 0.387126
Thermal correction to Enthalpy = 0.388070
Thermal correction to Gibbs Free Energy = 0.288586
Sum of electronic and zero-point Energies = -2595.186350
Sum of electronic and thermal Energies = -2595.153585
Sum of electronic and thermal Enthalpies = -2595.152641
Sum of electronic and thermal Free Energies = -2595.252124
```

Annexe C

Annexe C Summary

Figure S1. High-resolution mass spectrum of [**EuL^1**].

Figure S2. High-resolution mass spectrum of [**GdL¹**].
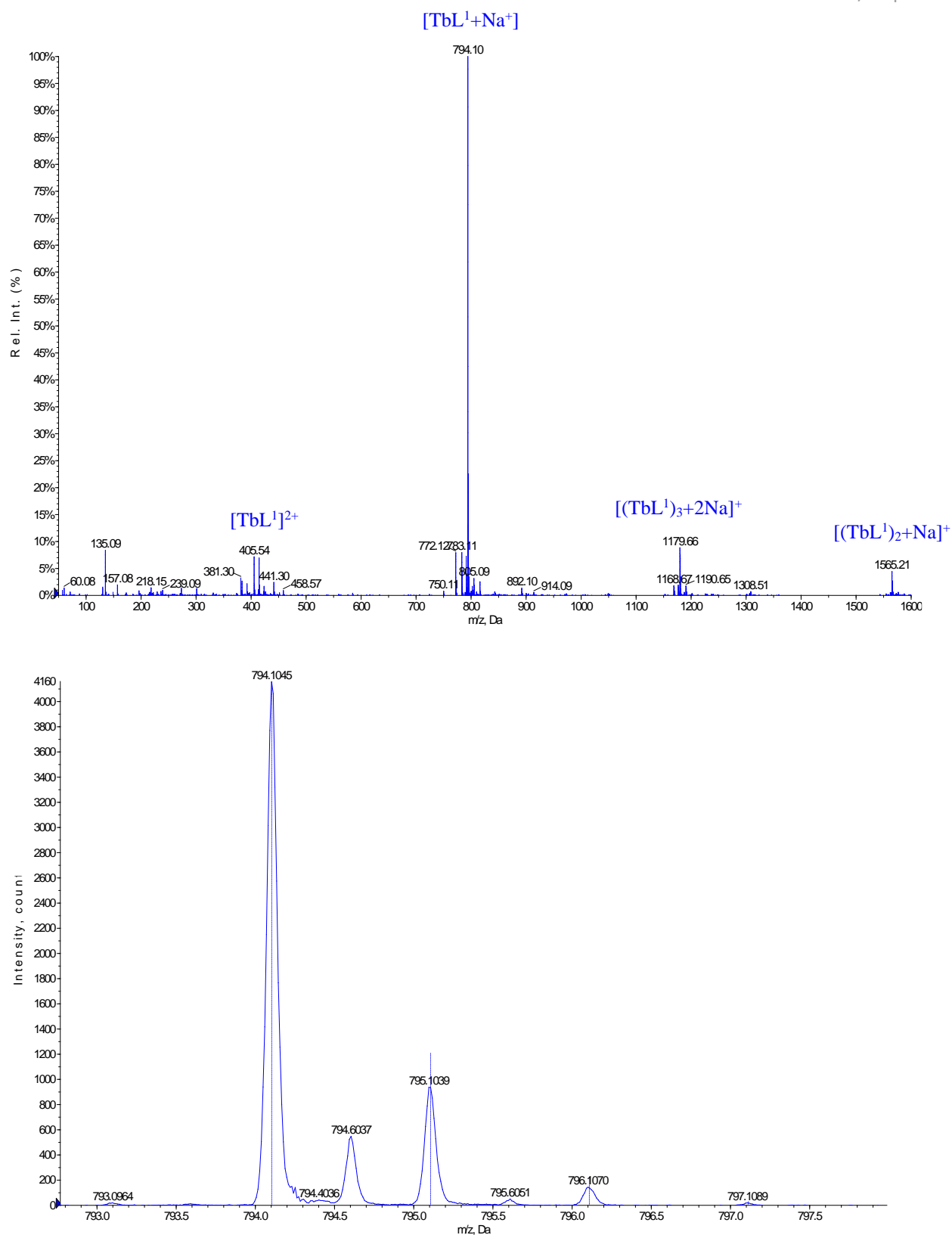
Figure S3. High-resolution mass spectrum of [**TbL¹**].
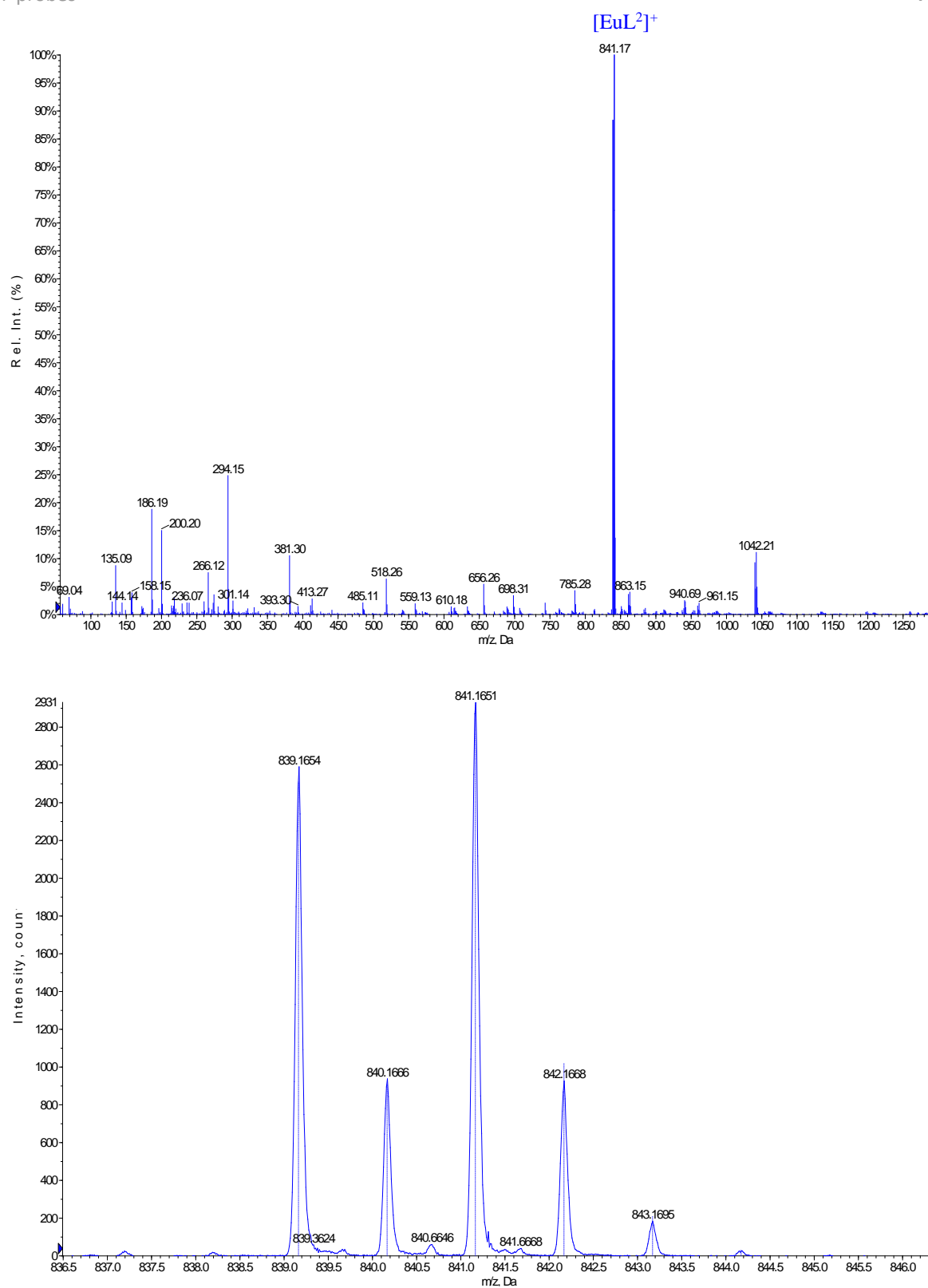
Figure S4. High-resolution mass spectrum of [**EuL²**].

Figure S5. High-resolution mass spectrum of [**GdL²**].
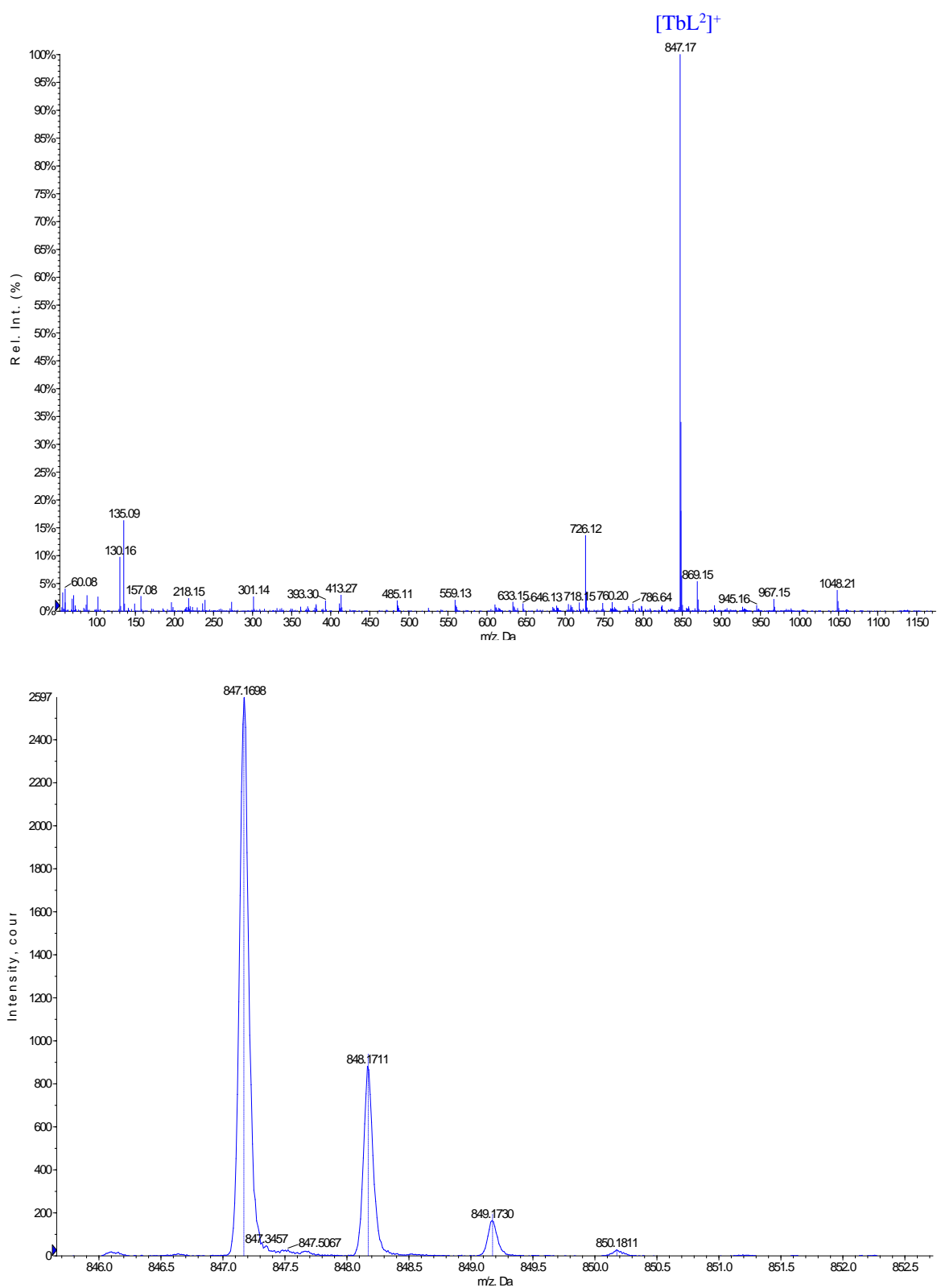
Figure S6. High-resolution mass spectrum of [**TbL²**].
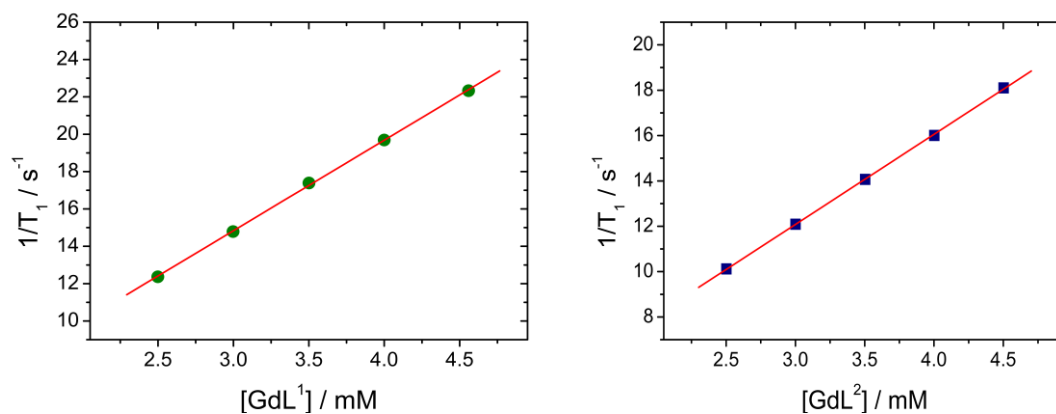
Figure S7. Proton relaxivities (r_{1p}, mM^{-1}s^{-1}) of **GdL^1** (green circles) and **GdL^2** (blue squares) as a function of gadolinium complex concentration (measured on 2.5-4.5 mM solutions, at 298 K and 300 MHz).
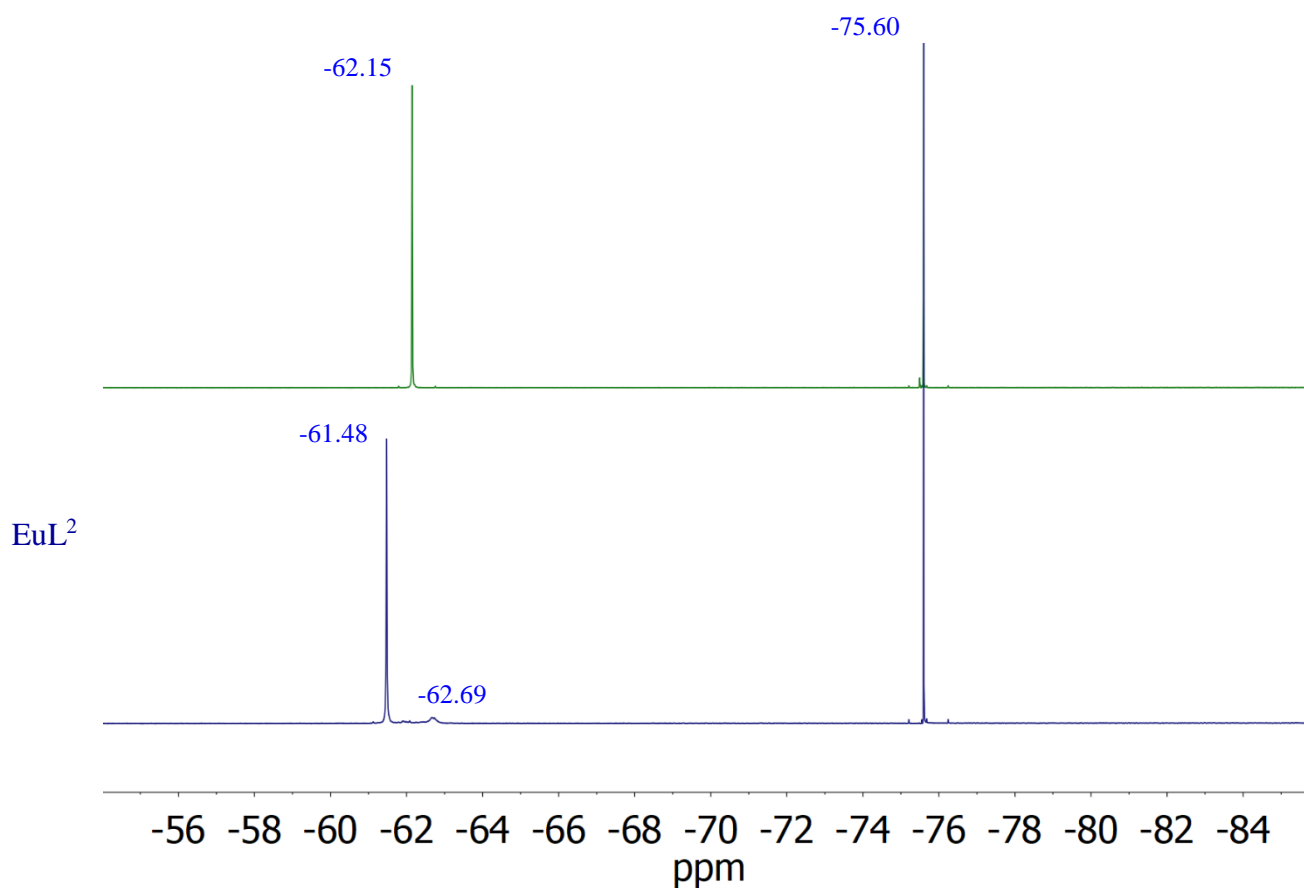
Figure S8. ^{19}F NMR spectra (7.05 T, 25 °C) of 5 mM **EuL^1** and **EuL^2** aqueous solutions buffered at pH 7.4 (0.05 M HEPES). The experiments were performed using a capillary with 125 mM TFA solution as reference (-75.60 ppm).
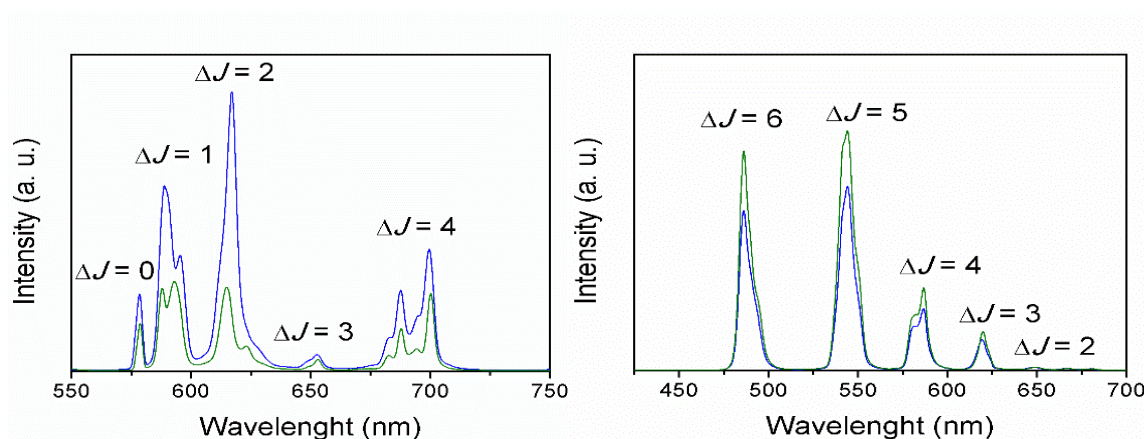
Figure S9. Emission spectra of **LnL¹** (green) and **LnL²** (blue) (Ln = Eu, Tb) recorded in H_2O. The emission wavelengths were set to 258.75 and 267.3 nm, for Eu^{3+} complexes, respectively, and the slits were set at 6 nm for EuL^1 and 7 nm for EuL^2. For Tb^{3+} complexes, the emission wavelengths were set to 257.0 and 267.5 nm, respectively. Slits were set at 6 nm for TbL^1 and 7 nm for TbL^2.
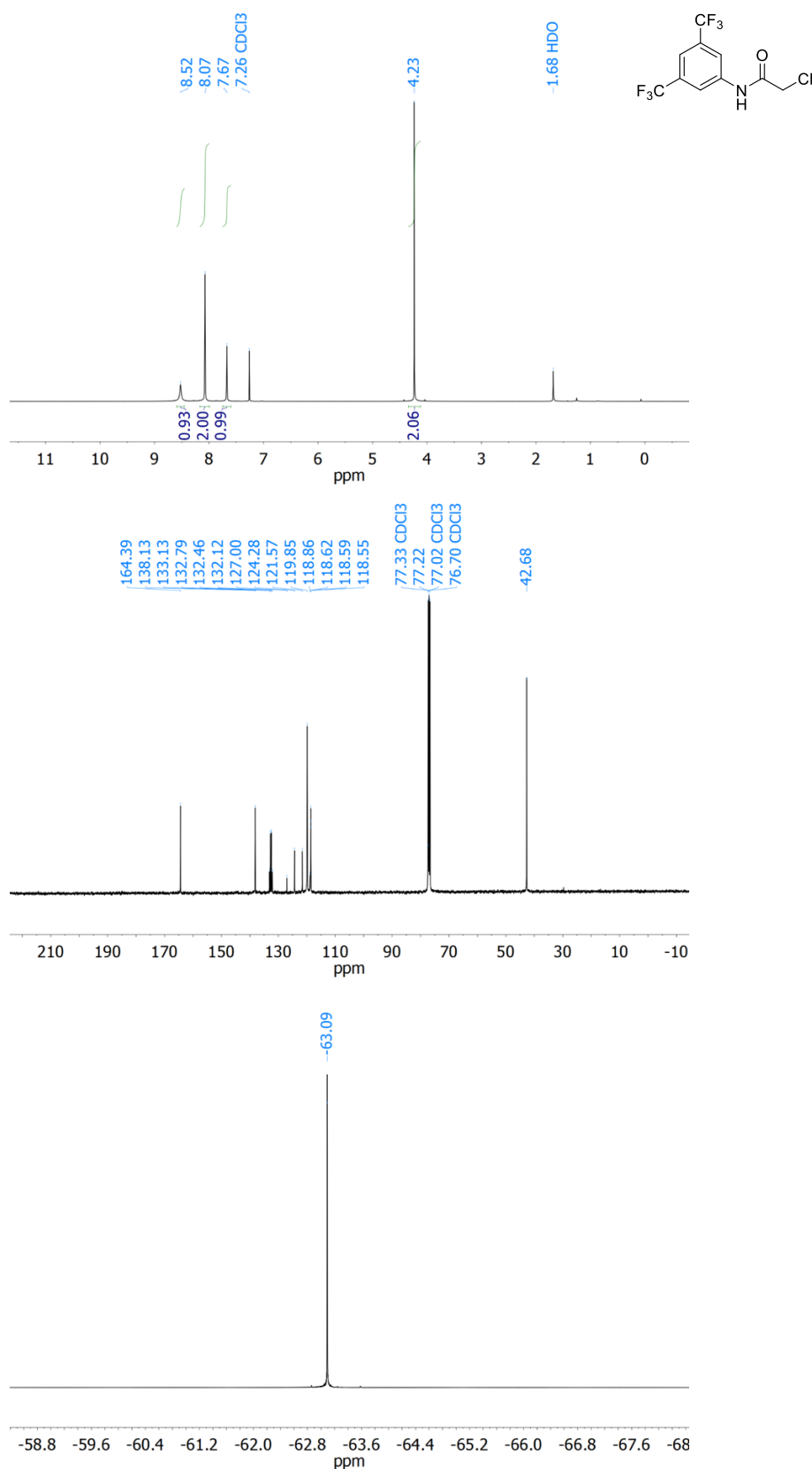
Figure S10. ^{1}H, ^{13}C and ^{19}F NMR spectra (9.40 T, 25 ^{o}C) of precursor **1a** in CDCl$_3$.
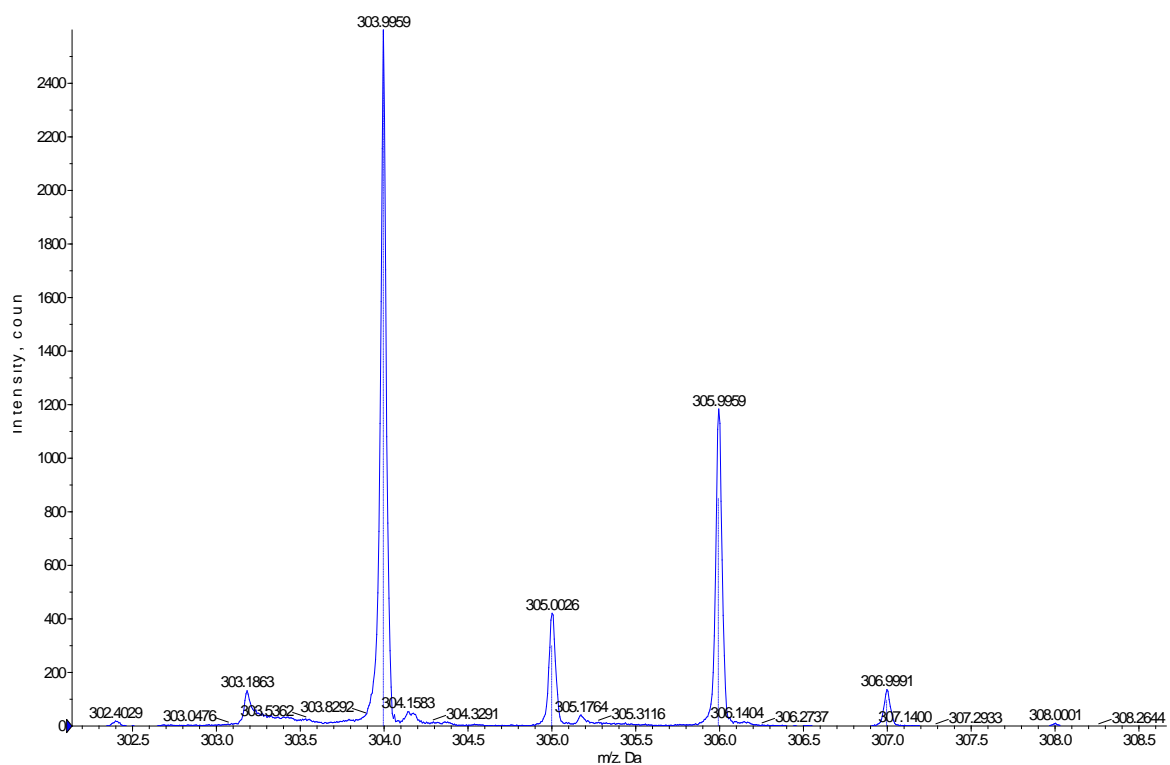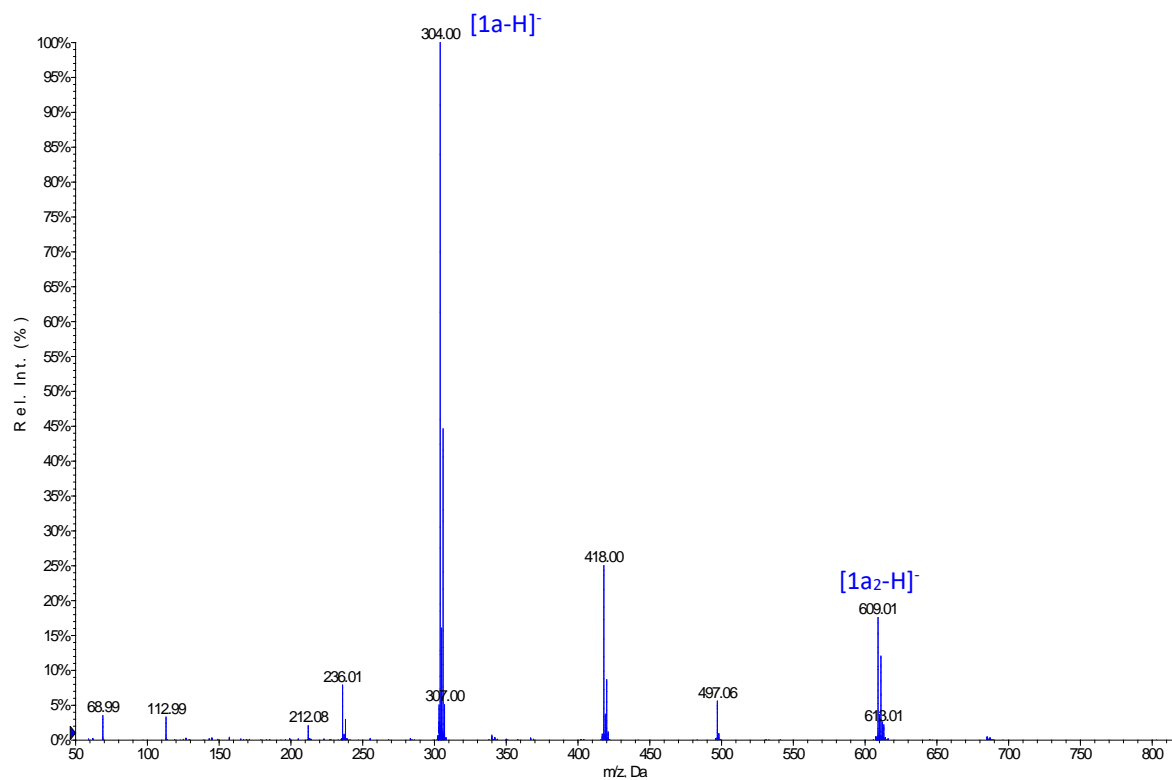
Figure S11. Experimental mass spectrum and high resolution mass spectrum of precursor [**1a**].
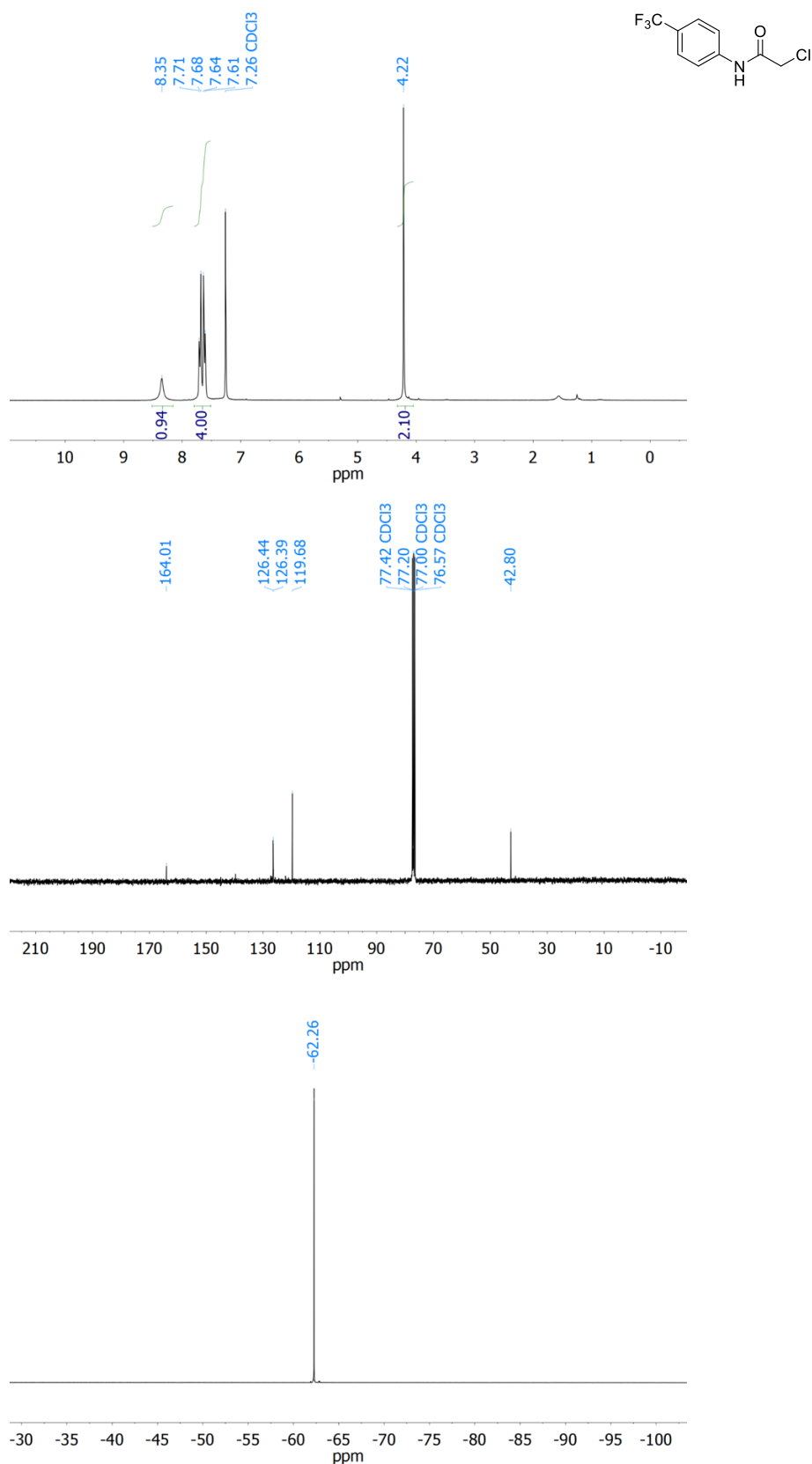
Figure S12. ^{1}H, ^{13}C and ^{19}F NMR spectra (7.05 T, 25 ^{o}C) of precursor **1b** in CDCl$_3$.
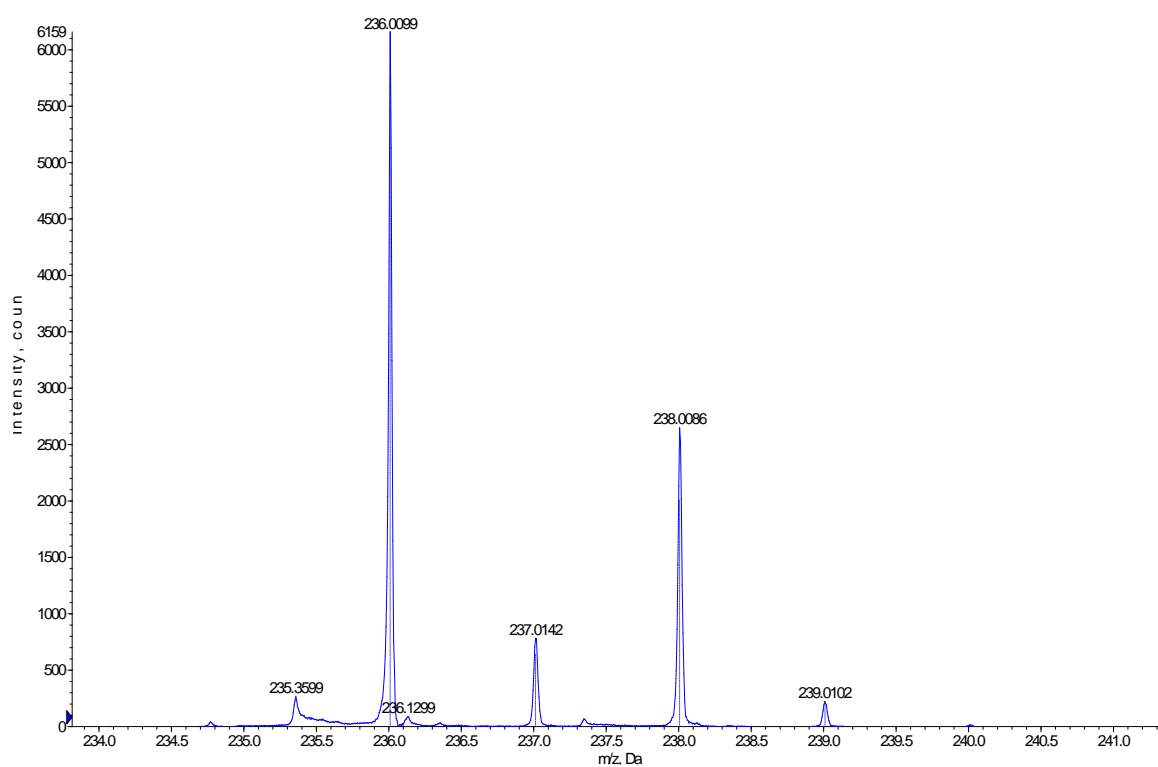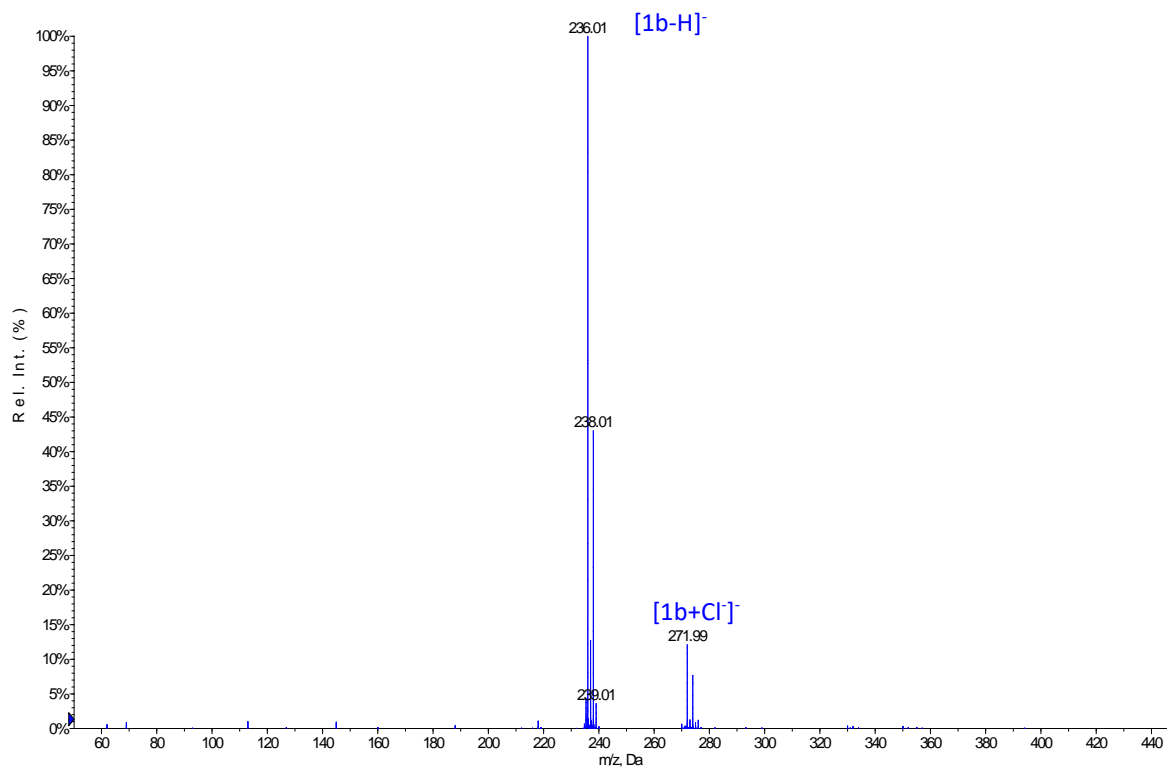
Figure S13. Experimental mass spectrum and high resolution mass spectrum of precursor [**1b**].
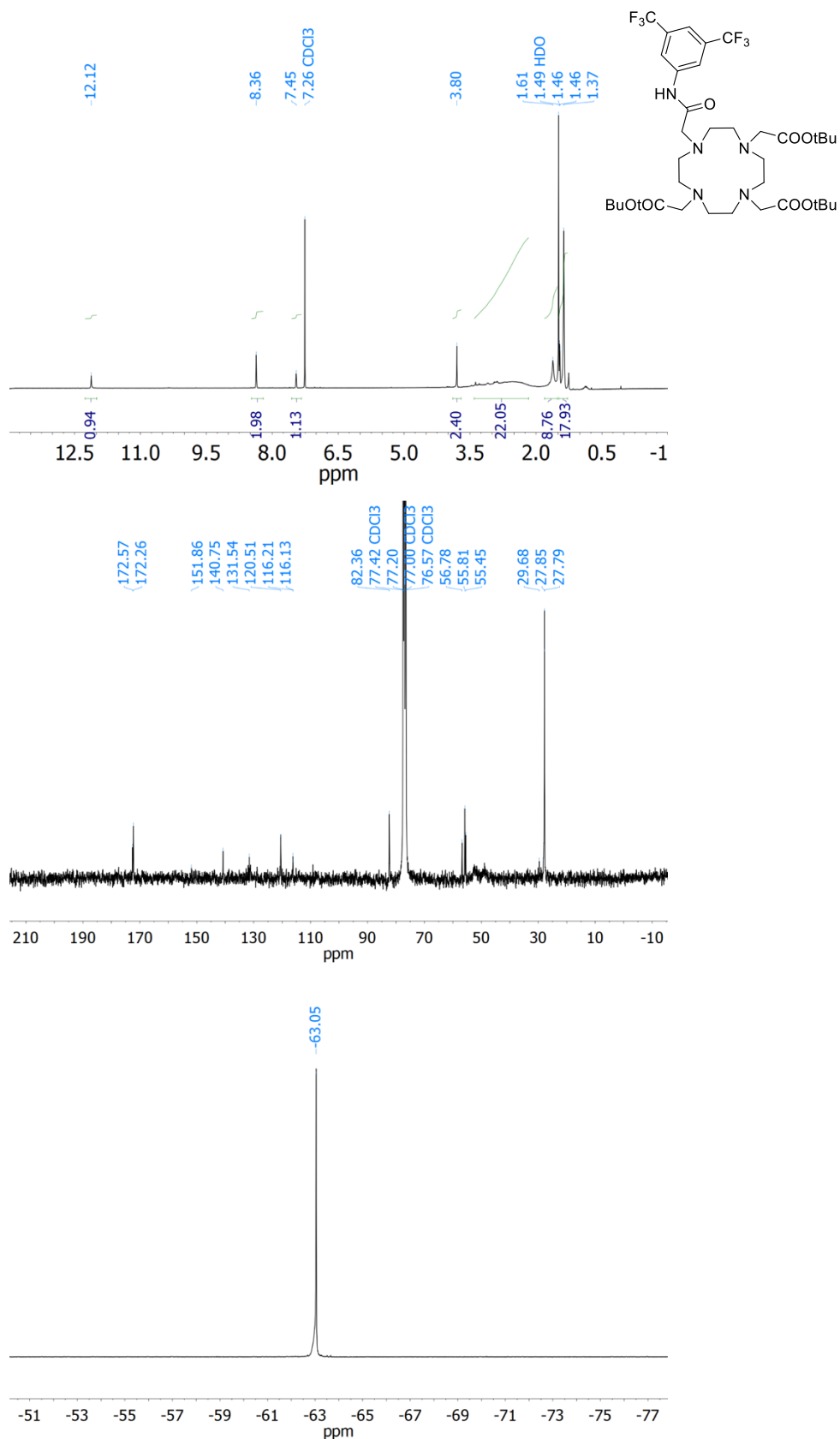
Figure S14. ^{1}H, ^{13}C and ^{19}F NMR spectra (7.05 T, 25 °C) of intermediate **2a** in CDCl$_3$.
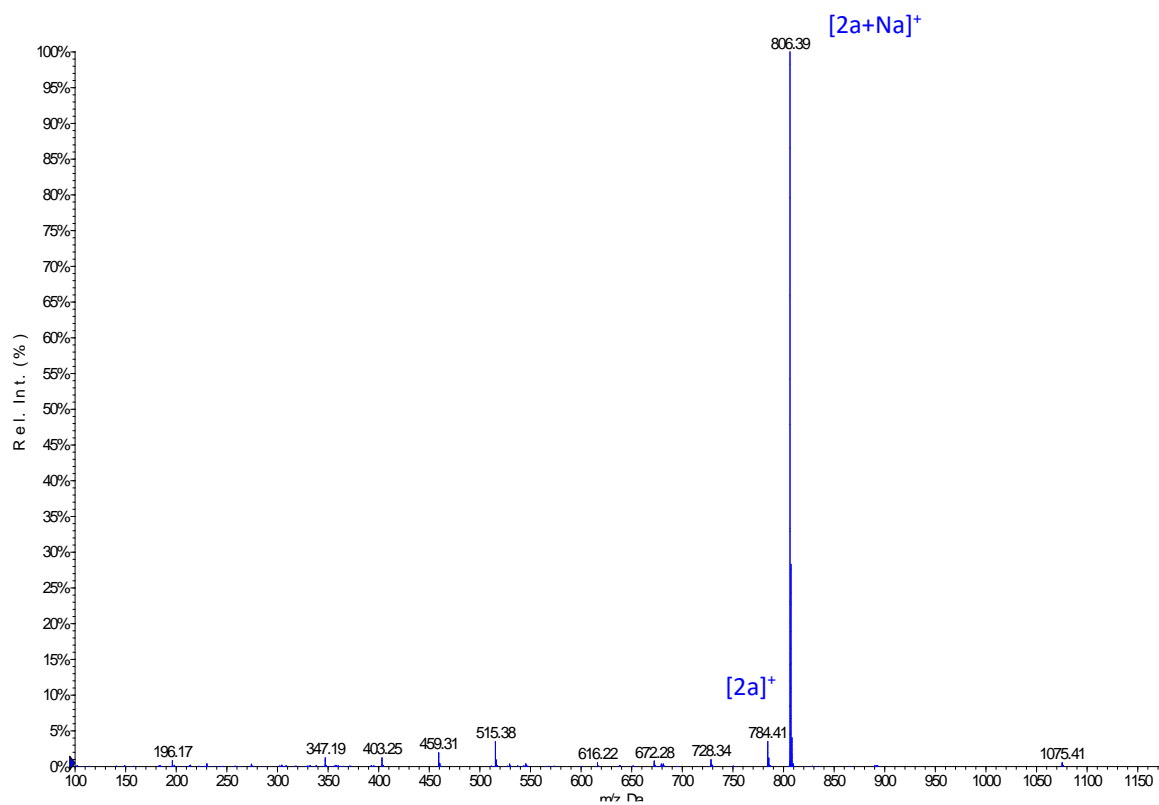
Figure S15. Experimental mass spectrum of intermediate [**2a**].

Figure S16. ¹H, ¹³C and ¹⁹F NMR spectra (7.05 T, 25 °C) of ligand **H₃L¹** in D₂O.
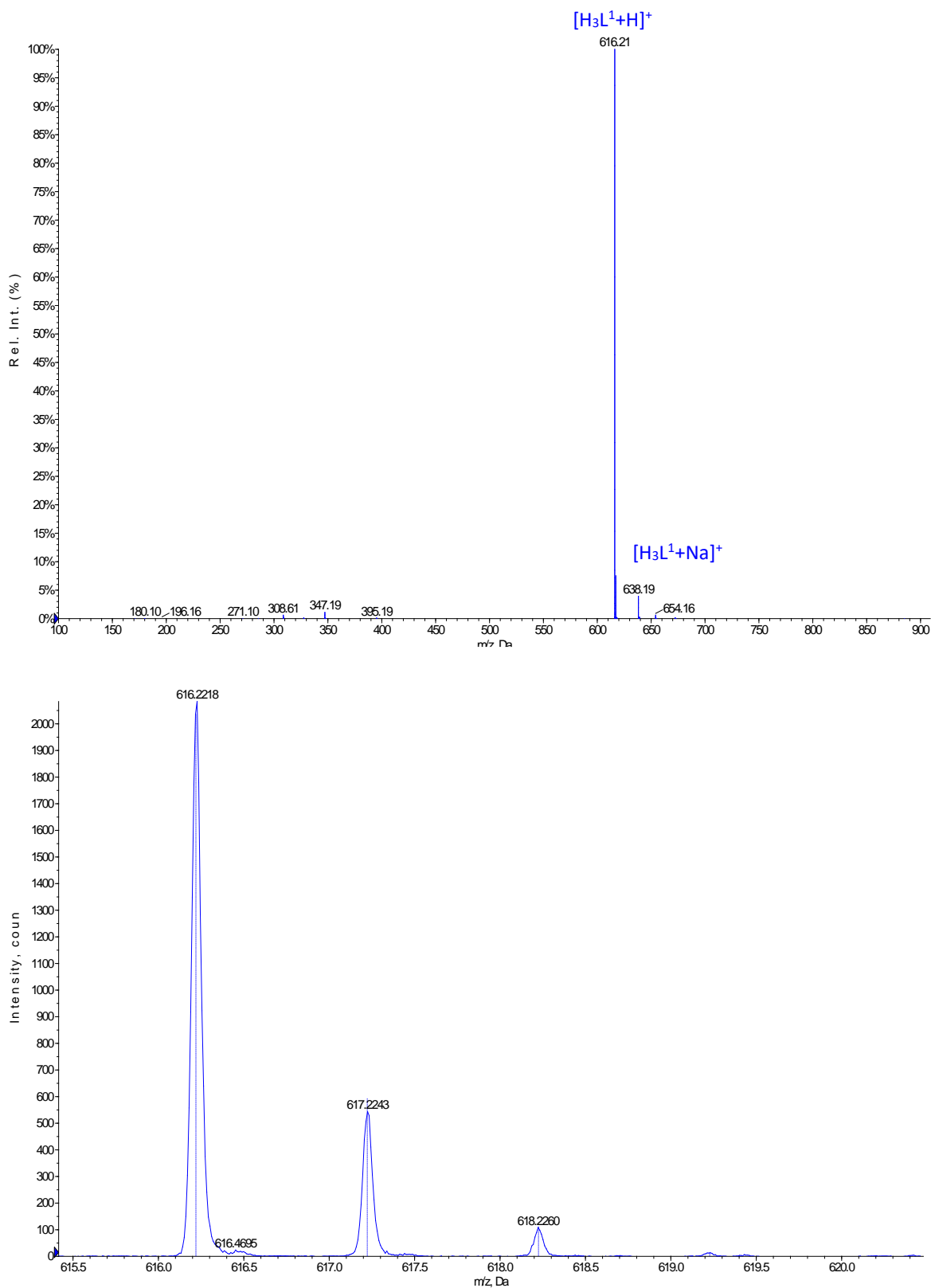
Figure S17. Experimental mass spectrum and high resolution mass spectrum of ligand [**H₃L¹**].

Figure S18. ¹H, ¹³C and ¹⁹F NMR spectra (7.05 T, 25 °C) of intermediate **2b** in CDCl₃.
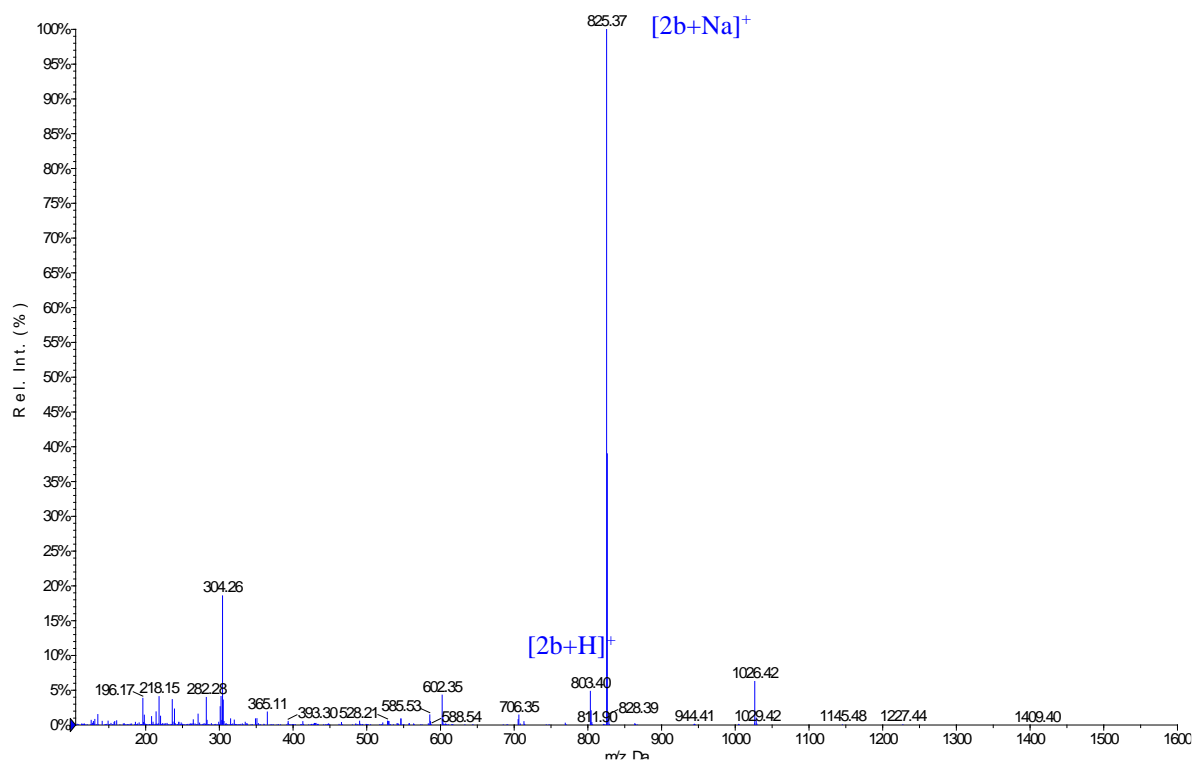
Figure S19. Experimental mass spectrum of the intermediate [**2b**].
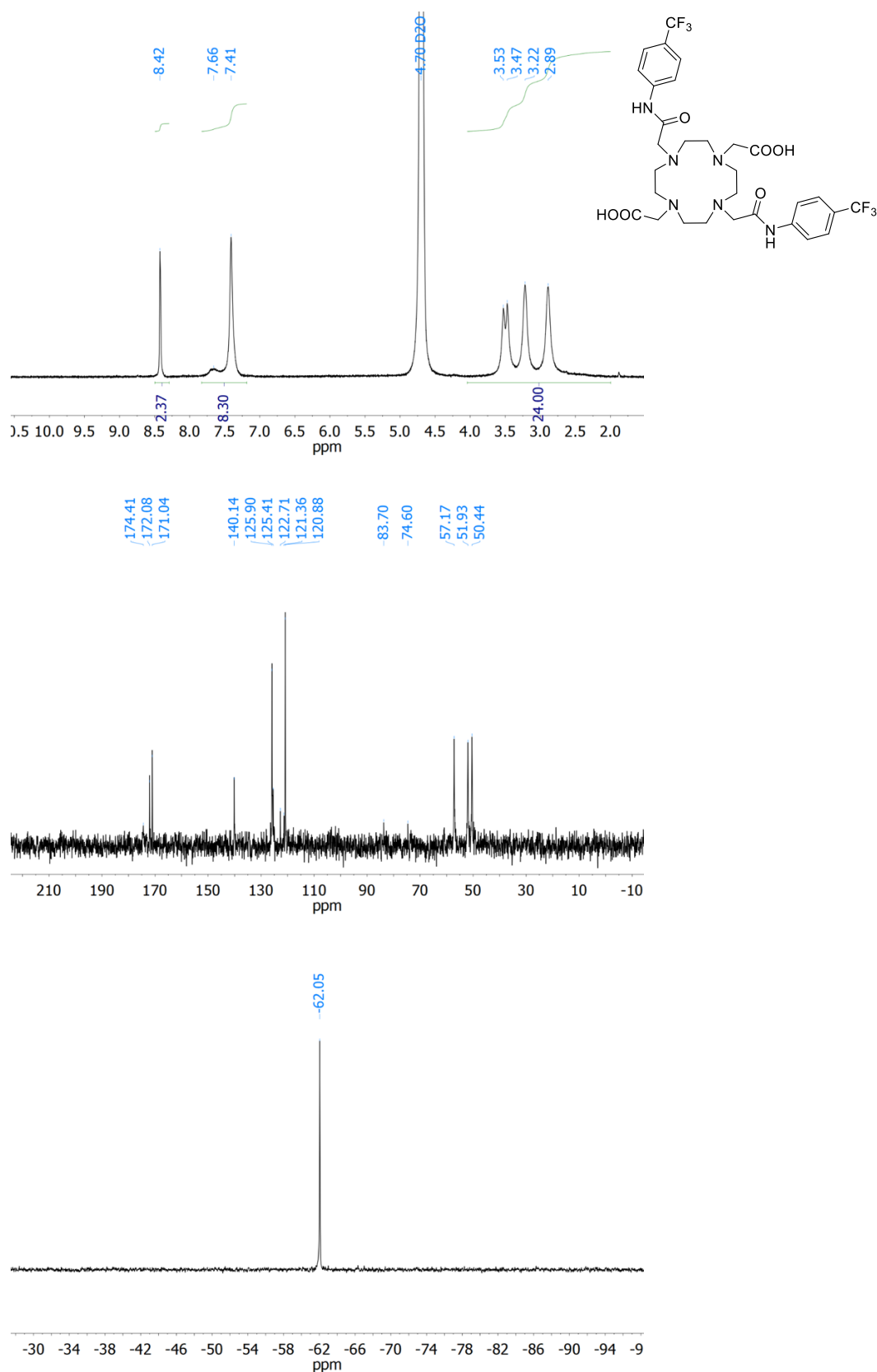
Figure S20. ¹H, ¹³C and ¹⁹F NMR spectra (7.05 T, 25 °C) of ligand **H₂L²** in D₂O.
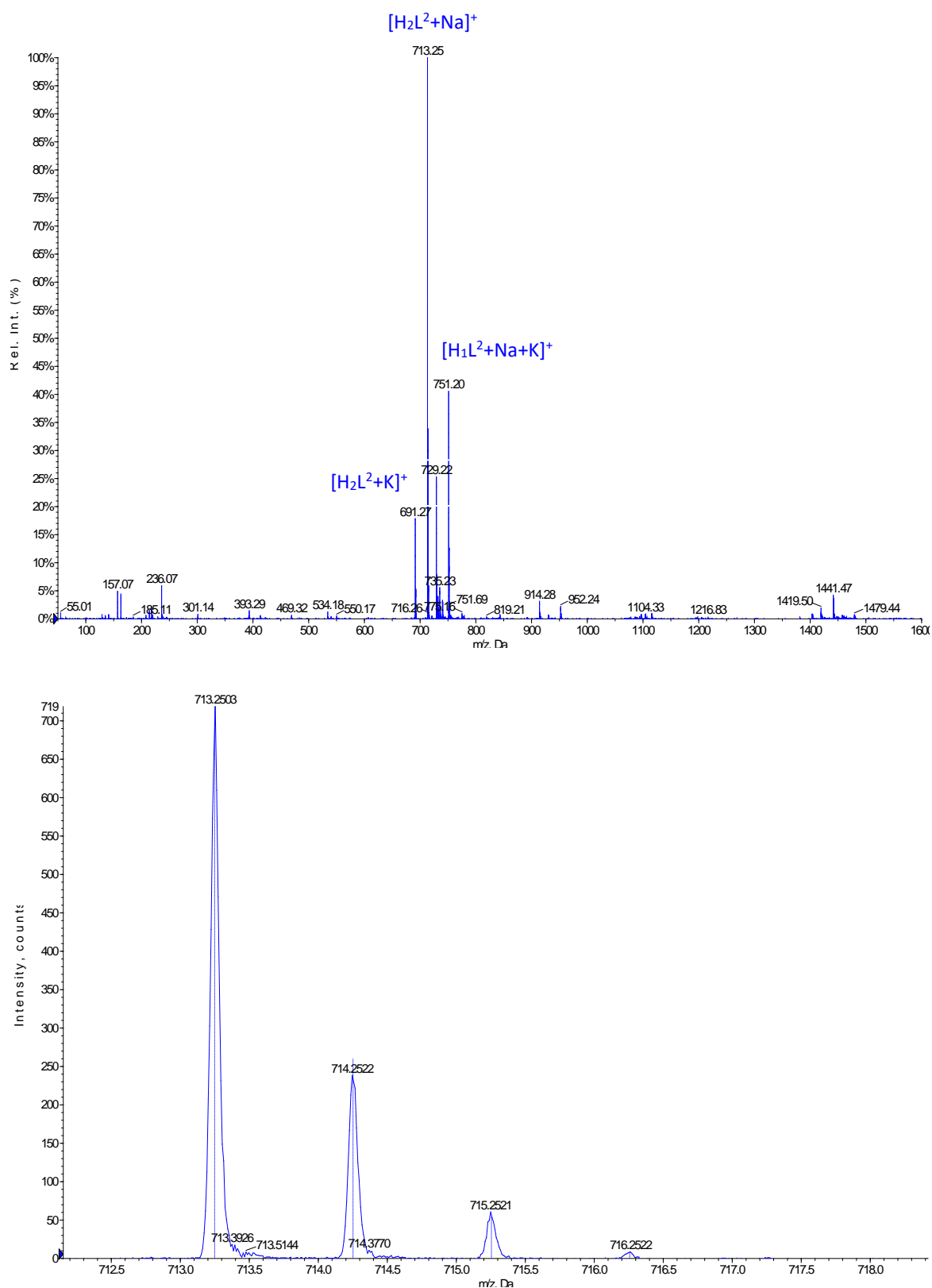
Figure S21. Experimental mass spectrum and high resolution mass spectrum of ligand [**H$_2$L^2**].
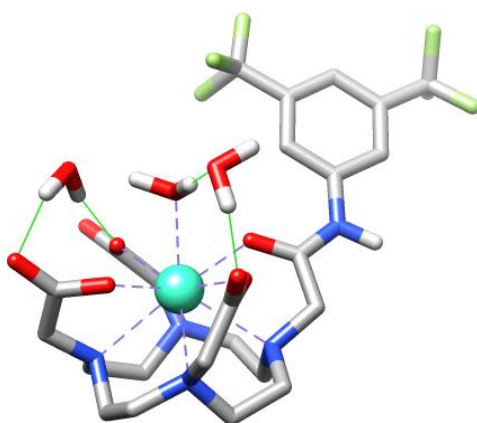
Figure S22. Optimised geometry for [GdL^1(H$_2$O)]·2H$_2$O SAP isomer with DFT calculations (0 imaginary frequencies).
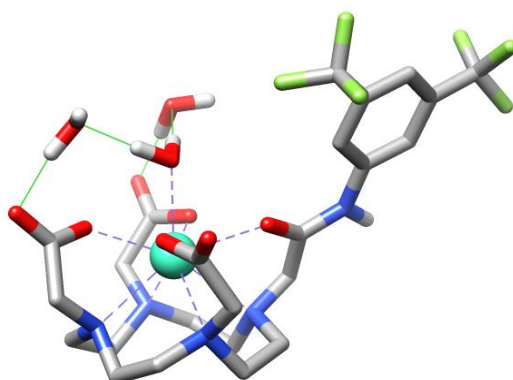
Figure S23. Optimised geometry for [GdL^1(H$_2$O)]·2H$_2$O TSAP isomer with DFT calculations (0 imaginary frequencies).
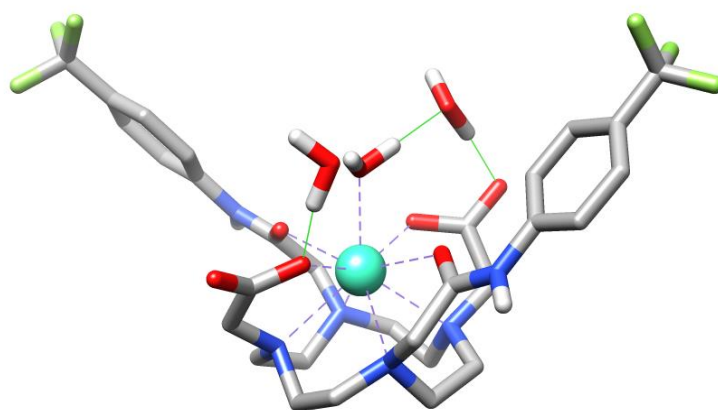
Figure S24. Optimised geometry for [GdL^2(Cl)(H$_2$O)]·2H$_2$O SAP isomer with DFT calculations (0 imaginary frequencies).
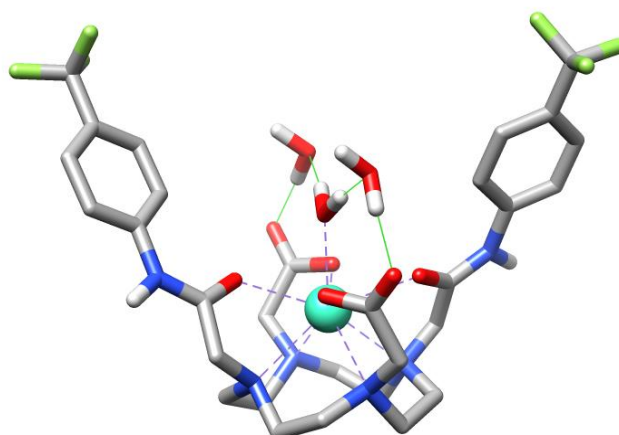
Figure S25. Optimised geometry for [GdL^2(Cl)(H$_2$O)]·2H$_2$O TSAP isomer with DFT calculations (0 imaginary frequencies).

Table S1. Optimised Cartesian coordinates obtained for [GdL¹(H₂O)]·2H₂O SAP isomer with DFT calculations (0 imaginary frequencies).

Center Number	Atomic Number	Coordinates (Angstroms)		
		X	Y	Z
1	7	-3.733106	-1.789873	0.407525
2	6	-5.009983	-1.126854	0.016475
3	6	-4.895836	-0.352925	-1.291175
4	7	-3.898879	0.750635	-1.240405
5	6	-3.511965	1.133329	-2.626969
6	6	-2.522260	0.152402	-3.244881
7	7	-1.237682	0.043576	-2.498571
8	6	-0.511709	-1.174478	-2.960155
9	6	-1.080648	-2.463880	-2.368904
10	7	-1.075000	-2.495067	-0.879362
11	6	-2.064871	-3.495388	-0.378601
12	6	-3.498124	-2.983209	-0.445640
13	6	-3.777872	-2.162170	1.849249
14	6	-2.471526	-1.887829	2.606947
15	8	-1.437165	-1.582201	1.908510
16	8	-2.499300	-1.956961	3.855135
17	6	-4.440056	1.928326	-0.511354
18	6	-4.027486	2.001629	0.966218
19	8	-4.303366	3.046721	1.588108
20	8	-3.384642	0.993811	1.445633
21	6	-0.403656	1.251171	-2.731148
22	6	-0.762492	2.450280	-1.836790
23	8	-0.510649	3.591274	-2.234681
24	8	-1.263068	2.147008	-0.673333
25	6	0.259217	-2.845687	-0.355588
26	6	1.178476	-1.637010	-0.311287
27	8	0.711549	-0.485550	-0.210031
28	1	-4.556642	-1.578258	2.342956
29	1	-4.046793	-3.220089	1.976265
30	1	-5.535983	1.970847	-0.580894
31	1	-4.057352	2.837434	-0.979364
32	1	-0.429103	1.560328	-3.784055
33	1	0.630981	0.994211	-2.482418
34	1	0.138626	-3.152552	0.688572
35	1	0.716315	-3.679140	-0.907396
36	1	-5.274097	-0.439590	0.820862
37	1	-5.820613	-1.864390	-0.079575
38	1	-5.888473	0.047196	-1.546921
39	1	-4.614729	-1.025458	-2.105066
40	1	-4.395603	1.191864	-3.279405
41	1	-3.075830	2.132836	-2.592898
42	1	-2.325461	0.457736	-4.283651
43	1	-2.969281	-0.843345	-3.290668
44	1	-0.544561	-1.254989	-4.056445
45	1	0.538249	-1.061872	-2.685415
46	1	-2.114393	-2.595879	-2.695259
47	1	-0.514171	-3.315768	-2.772825
48	1	-1.805903	-3.719442	0.657318
49	1	-1.993010	-4.430731	-0.951287
50	1	-3.751824	-2.721465	-1.475525
51	1	-4.174155	-3.801150	-0.153550
52	8	-1.464652	3.648763	1.610316
53	1	-1.398044	3.356465	0.668989
54	1	-2.425468	3.582215	1.793717
55	1	-0.623307	0.727738	2.839399
56	8	-0.513853	1.131720	1.934468
57	1	-0.843764	2.069600	1.985647
58	8	-0.730494	0.047378	4.428920
59	1	0.148105	-0.324180	4.597050
60	1	-1.310678	-0.748330	4.287690

```
61            7                    2.505334    -1.901212    -0.322151
62            1                    2.762935    -2.875343    -0.436858
63            6                    3.586595    -1.008793    -0.150206
64            6                    4.877941    -1.560548    -0.169410
65            6                    3.419401     0.367767     0.042315
66            6                    5.985489    -0.736198     0.006587
67            1                    5.016120    -2.627170    -0.311792
68            6                    4.549424     1.172458     0.218826
69            1                    2.427878     0.795988     0.058467
70            6                    5.836310     0.640849     0.204358
71           64                   -1.717382    -0.040276     0.139659
72            1                    6.700126     1.277398     0.350252
73            6                    7.371345    -1.321349    -0.060836
74            6                    4.327193     2.648645     0.418619
75            9                    5.478050     3.315624     0.655124
76            9                    3.748740     3.214994    -0.670188
77            9                    3.496189     2.889879     1.463216
78            9                    8.199344    -0.750256     0.845677
79            9                    7.374534    -2.654742     0.167038
80            9                    7.934848    -1.126651    -1.279487
```

E(RTPSSh) = -2596.47784152 Hartree
·Zero-point correction = 0.615849 (Hartree/Particle)
Thermal correction to Energy = 0.662166
Thermal correction to Enthalpy = 0.663110
Thermal correction to Gibbs Free Energy = 0.533229
Sum of electronic and zero-point Energies = -2595.861992
Sum of electronic and thermal Energies = -2595.815676
Sum of electronic and thermal Enthalpies = -2595.814732
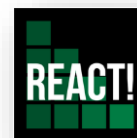Sum of electronic and thermal Free Energies = -2595.944613

Table S2. Optimised Cartesian coordinates obtained for [GdL^{1}(H$_2$O)]·2H$_2$O TSAP isomer with DFT calculations (0 imaginary frequencies).

```
--------------------------------------------------------------------
Center      Atomic                   Coordinates (Angstroms)
Number      Number              X            Y            Z
--------------------------------------------------------------------
   1           7             4.240356     0.529197    -0.533808
   2           6             4.490935     0.538364    -1.994689
   3           6             3.323665     1.151343    -2.755338
   4           7             2.042086     0.431697    -2.511474
   5           6             1.980877    -0.779221    -3.364188
   6           6             0.931645    -1.766908    -2.874935
   7           7             1.156928    -2.161641    -1.455054
   8           6             2.231228    -3.184954    -1.381962
   9           6             2.792651    -3.334744     0.023763
  10           7             3.355408    -2.061792     0.549637
  11           6             4.728271    -1.861332     0.027587
  12           6             5.170392    -0.410468     0.150080
  13           6             4.428552     1.872015     0.056380
  14           6             3.733070     1.952570     1.419721
  15           8             3.000510     0.943091     1.742921
  16           6             0.931803     1.365145    -2.814005
  17           6             0.821206     2.446184    -1.723382
  18           8             1.380406     2.140615    -0.591807
  19           6            -0.102827    -2.687081    -0.902502
  20           6            -1.054653    -1.517783    -0.708960
  21           8            -0.607615    -0.359467    -0.582187
  22           6             3.332998    -2.119446     2.027827
  23           6             1.900898    -1.913608     2.538527
  24           8             1.031005    -1.559919     1.656108
  25           1             4.650361    -0.494579    -2.315669
  26           1             5.411862     1.089967    -2.234946
  27           1             3.182795     2.187269    -2.439881
  28           1             3.552484     1.170657    -3.830607
  29           1             2.968273    -1.247632    -3.353359
  30           1             1.767497    -0.514384    -4.409936
  31           1            -0.061403    -1.316871    -2.948558
  32           1             0.928030    -2.652988    -3.525445
  33           1             3.021858    -2.877158    -2.070197
  34           1             1.865817    -4.160024    -1.735686
  35           1             2.005312    -3.659329     0.706435
  36           1             3.559813    -4.122521     0.022684
  37           1             4.736187    -2.169638    -1.021497
  38           1             5.449033    -2.506710     0.550899
  39           1             5.205925    -0.125302     1.203387
  40           1             6.188708    -0.301748    -0.250921
  41           1             5.491485     2.134632     0.153785
  42           1             3.957074     2.620544    -0.584150
  43           1             1.056355     1.838850    -3.797362
  44           1            -0.011228     0.811177    -2.827223
  45           1            -0.547436    -3.464405    -1.540589
  46           1             0.087156    -3.113948     0.086350
  47           1             3.740125    -3.065975     2.410745
  48           1             3.939218    -1.304380     2.429550
  49           8             0.231736     1.051948     1.693075
  50           1             0.640617     1.858313     2.104368
  51           1            -0.011317     0.472712     2.461489
  52           8             3.873770     2.986576     2.105170
  53           8             1.666928    -2.061448     3.756129
  54           8             0.210394     3.491031    -1.975095
  55           8            -0.493347    -0.392043     3.955212
  56           1             0.234148    -1.069732     3.944489
  57           1            -1.273134    -0.888853     3.666525
  58           8             1.295251     3.236668     2.991539
  59           1             2.265364     3.148349     2.799449
  60           1             1.034653     4.038859     2.515445
```

```
  61            7               -2.372172   -1.818166   -0.675847
  62            1               -2.604418   -2.797293   -0.802326
  63            6               -3.472533   -0.965156   -0.438040
  64            6               -4.730164   -1.569392   -0.295185
  65            6               -3.351438    0.428323   -0.352302
  66            6               -5.854513   -0.780096   -0.060407
  67            1               -4.831553   -2.647489   -0.365781
  68            6               -4.493704    1.195320   -0.112868
  69            1               -2.385194    0.896420   -0.466726
  70            6               -5.750959    0.609778    0.036184
  71           64                1.715199   -0.004003    0.090872
  72            1               -6.628144    1.217696    0.221275
  73            6               -4.358970    2.695143   -0.076018
  74            6               -7.190835   -1.440656    0.153182
  75            9               -8.210108   -0.663240   -0.280644
  76            9               -7.419984   -1.689884    1.466956
  77            9               -7.278683   -2.627218   -0.492100
  78            9               -5.310168    3.269548    0.696362
  79            9               -3.153964    3.082436    0.405375
  80            9               -4.477666    3.237267   -1.314317
 --------------------------------------------------------------
·E(RTPSSh) = -2596.47793437 Hartree
·Zero-point correction = 0.615063 (Hartree/Particle)
 Thermal correction to Energy = 0.661674
 Thermal correction to Enthalpy = 0.662618
 Thermal correction to Gibbs Free Energy = 0.534064
 Sum of electronic and zero-point Energies = -2595.862871
 Sum of electronic and thermal Energies = -2595.816260
 Sum of electronic and thermal Enthalpies = -2595.815316
 Sum of electronic and thermal Free Energies = -2595.943870
```

Table S3. Optimised Cartesian coordinates obtained for [GdL^2(H$_2$O)]·2H$_2$O SAP isomer with DFT calculations (0 imaginary frequencies).

```
------------------------------------------------------------------------
Center      Atomic                 Coordinates (Angstroms)
Number      Number              X              Y              Z
------------------------------------------------------------------------
   1          7            1.878373      -2.944027      -1.413071
   2          6            2.923618      -3.517182      -0.519782
   3          6            2.345650      -4.007422       0.800713
   4          7            1.692216      -2.925216       1.582742
   5          6            0.790544      -3.524716       2.602619
   6          6           -0.526592      -3.986450       1.996172
   7          7           -1.298484      -2.887571       1.352563
   8          6           -2.361191      -3.493585       0.502900
   9          6           -1.813429      -3.998631      -0.829716
  10          7           -1.125050      -2.941585      -1.619829
  11          6           -0.224773      -3.563051      -2.634439
  12          6            1.085507      -4.042064      -2.023556
  13          6            2.513261      -2.099833      -2.459377
  14          6            1.714332      -0.837853      -2.801091
  15          8            0.576571      -0.689444      -2.222818
  16          8            2.227397      -0.016764      -3.591527
  17          6            2.707379      -2.058994       2.236261
  18          6            3.035270      -0.782845       1.452377
  19          8            2.471568      -0.643241       0.302839
  20          6           -1.904222      -2.014907       2.390949
  21          6           -0.960396      -0.925025       2.923498
  22          8           -1.169055      -0.445294       4.041866
  23          8           -0.021220      -0.547789       2.104305
  24          6           -2.104540      -2.080168      -2.310939
  25          6           -2.647534      -1.015027      -1.374358
  26          8           -1.956189      -0.606759      -0.419838
  27          1            3.484748      -1.760275      -2.095070
  28          1            2.697767      -2.671271      -3.379732
  29          1            3.637467      -2.610200       2.433086
  30          1            2.321747      -1.731478       3.203868
  31          1           -2.293949      -2.600742       3.233392
  32          1           -2.746508      -1.485271       1.935357
  33          1           -1.575830      -1.534798      -3.098931
  34          1           -2.912165      -2.662938      -2.775986
  35          1            3.653941      -2.730185      -0.328084
  36          1            3.447852      -4.349488      -1.012075
  37          1            3.151870      -4.468987       1.390434
  38          1            1.604915      -4.790191       0.621093
  39          1            1.269411      -4.381500       3.098810
  40          1            0.603798      -2.774568       3.372625
  41          1           -1.133592      -4.459921       2.782385
  42          1           -0.340532      -4.752532       1.239554
  43          1           -2.845311      -4.333307       1.021983
  44          1           -3.134623      -2.741769       0.338171
  45          1           -1.093372      -4.800838      -0.654418
  46          1           -2.637564      -4.438532      -1.410390
  47          1           -0.021436      -2.811075      -3.398071
  48          1           -0.721097      -4.410840      -3.127187
  49          1            0.885404      -4.787104      -1.249686
  50          1            1.671915      -4.549530      -2.804382
  51          8            1.463886       1.770386       2.206388
  52          1            0.928756       0.978150       2.452095
  53          1            1.645583       2.184717       3.076091
  54          1            0.659830       1.471102      -0.979308
  55          8            0.278187       1.083203      -0.146634
  56          1            0.779351       1.469559       0.618697
  57          8            1.235145       2.261793      -2.439533
  58          1            0.412896       2.513938      -2.885290
  59          1            1.560354       1.479197      -2.959295
  60          7           -3.869663      -0.522177      -1.675901
```

```
61        1              -4.337739   -0.960343   -2.461811
62        6              -4.583559    0.542984   -1.078452
63        6              -5.830175    0.860399   -1.644456
64        6              -4.104759    1.274429    0.020765
65        6              -6.593707    1.896862   -1.119239
66        1              -6.198242    0.299165   -2.498102
67        6              -4.878815    2.312406    0.537881
68        1              -3.146681    1.035718    0.458034
69        6              -6.118644    2.628914   -0.024873
70        1              -7.551182    2.140063   -1.566090
71        1              -4.505704    2.881313    1.382405
72        6              -6.963562    3.714201    0.574688
73        9              -6.215322    4.674892    1.170025
74        9              -7.806989    3.236266    1.529146
75        9              -7.741936    4.324836   -0.352805
76       64               0.319441   -1.314542   -0.037974
77        7               3.814735    0.082914    2.014779
78        6               4.110535    1.354145    1.338485
79        6               4.951204    2.287832    1.945094
80        6               3.550884    1.626908    0.090311
81        6               5.231565    3.494272    1.303905
82        1               5.391650    2.072818    2.929481
83        6               3.832017    2.833249   -0.551651
84        1               2.888427    0.891052   -0.388016
85        6               4.672096    3.766962    0.054965
86        1               5.893679    4.230530    1.782262
87        1               3.390942    3.047862   -1.535962
88        6               4.981931    5.099138   -0.652785
89        9               6.101022    5.639340   -0.125229
90        9               5.168414    4.875620   -1.971028
91        9               3.947964    5.950269   -0.482529
92        1               4.216065   -0.112606    2.909601
       --------------------------------------------------------------
```

·E(RTPSSh) = -2808.10636071 Hartree
·Zero-point correction = 0.721143 (Hartree/Particle)
 Thermal correction to Energy = 0.773138
 Thermal correction to Enthalpy = 0.774082
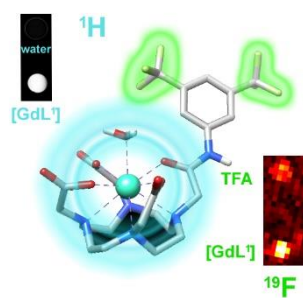 Thermal correction to Gibbs Free Energy = 0.631030
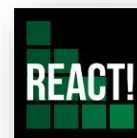 Sum of electronic and zero-point Energies = -2807.428380
 Sum of electronic and thermal Energies = -2807.376386
 Sum of electronic and thermal Enthalpies = -2807.375442
 Sum of electronic and thermal Free Energies = -2807.518493

Table S4. Optimised Cartesian coordinates obtained for [GdL²(H₂O)]·2H₂O TSAP isomer with DFT calculations (0 imaginary frequencies).
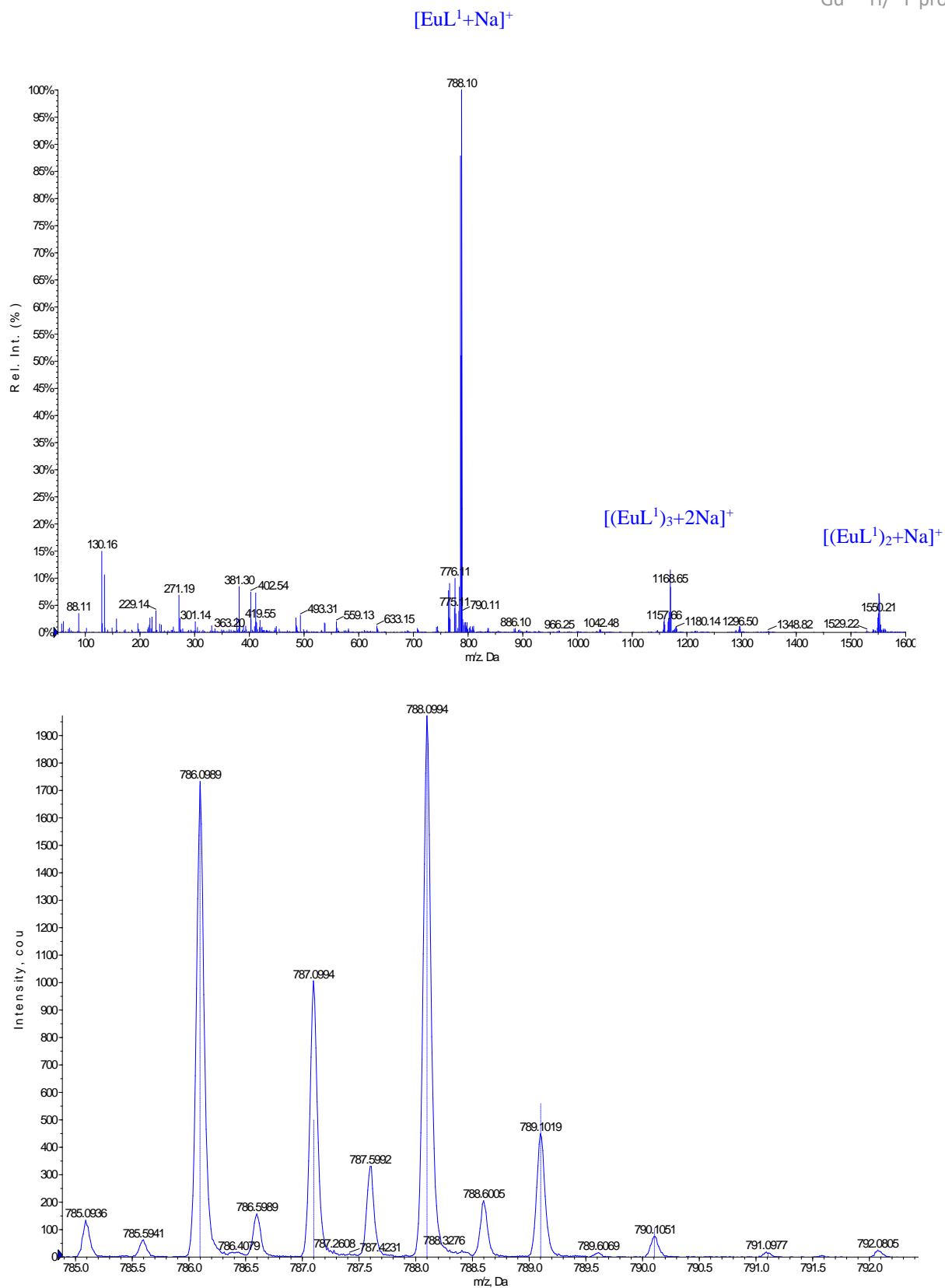
Center Number	Atomic Number	Coordinates (Angstroms)		
		X	Y	Z
1	7	-1.779337	-3.013426	1.135780
2	6	-1.095414	-4.049621	1.956543
3	6	0.114892	-3.506659	2.706689
4	7	1.162347	-2.950165	1.802847
5	6	1.955833	-4.051166	1.199746
6	6	2.720154	-3.607298	-0.042587
7	7	1.831833	-3.014270	-1.090390
8	6	1.181166	-4.095844	-1.880470
9	6	-0.044910	-3.609742	-2.643728
10	7	-1.104396	-3.054906	-1.755200
11	6	-1.867014	-4.150825	-1.105208
12	6	-2.649661	-3.663992	0.109418
13	6	-2.613934	-2.139793	1.984383
14	6	-3.033178	-0.931457	1.158043
15	8	-2.317417	-0.561536	0.197404
16	6	2.009005	-2.017704	2.585902
17	6	1.286320	-0.675267	2.792862
18	8	0.142954	-0.549944	2.209454
19	6	2.644750	-2.146614	-1.967082
20	6	3.066531	-0.926903	-1.157672
21	8	2.375822	-0.566109	-0.179242
22	6	-1.990106	-2.187061	-2.570046
23	6	-1.347773	-0.811121	-2.806393
24	8	-0.195629	-0.618851	-2.261942
25	1	-0.790257	-4.850890	1.280240
26	1	-1.793764	-4.496459	2.678227
27	1	-0.192432	-2.705535	3.381100
28	1	0.537002	-4.309724	3.327733
29	1	1.265113	-4.857889	0.943251
30	1	2.670021	-4.467119	1.924510
31	1	3.463252	-2.856487	0.234421
32	1	3.272493	-4.463193	-0.453496
33	1	0.904487	-4.889046	-1.182280
34	1	1.894339	-4.537672	-2.590347
35	1	0.239896	-2.818235	-3.339630
36	1	-0.444905	-4.441617	-3.241106
37	1	-1.157432	-4.926798	-0.808285
38	1	-2.566012	-4.618042	-1.813270
39	1	-3.398855	-2.933356	-0.205606
40	1	-3.196244	-4.508012	0.552233
41	1	-3.483722	-2.670674	2.396026
42	1	-2.009488	-1.768836	2.817980
43	1	2.297630	-2.444754	3.556371
44	1	2.927571	-1.809764	2.032159
45	1	3.514737	-2.675095	-2.382106
46	1	2.025672	-1.794287	-2.798749
47	1	-2.244724	-2.654417	-3.531613
48	1	-2.926543	-2.018930	-2.033963
49	8	0.059337	1.075415	-0.080557
50	1	0.203204	1.613412	0.743680
51	1	-0.461358	1.584982	-0.756433
52	8	-1.987088	0.039015	-3.458269
53	8	1.846526	0.216949	3.459707
54	8	-1.369238	2.316146	-2.042414
55	1	-1.546267	1.551923	-2.651772
56	1	-0.773968	2.896068	-2.539716
57	8	0.668608	2.409194	2.207194
58	1	1.041597	1.665249	2.746991
59	1	1.424488	2.990903	2.038486
60	7	4.184286	-0.290776	-1.558795

```
61           1              4.657224    -0.695190    -2.359984
62           6              4.791370     0.877081    -1.036733
63           6              5.915564     1.360082    -1.724415
64           6              4.332156     1.537006     0.116148
65           6              6.578742     2.496715    -1.271065
66           1              6.271400     0.846481    -2.612554
67           6              5.004075     2.673478     0.559541
68           1              3.473558     1.163740     0.654311
69           6              6.123778     3.157678    -0.126630
70           1              7.447108     2.864017    -1.805158
71           1              4.651721     3.179916     1.452307
72           6              6.811723     4.391386     0.380575
73           9              7.946946     4.670266    -0.301205
74           9              7.148850     4.275669     1.691376
75           9              6.014759     5.488780     0.291716
76           7             -4.164432    -0.308971     1.528297
77           6             -4.765894     0.866236     1.001496
78           6             -6.017613     1.219075     1.530862
79           6             -4.168603     1.661201     0.011224
80           6             -6.672030     2.360492     1.070079
81           1             -6.475589     0.601353     2.298624
82           6             -4.839662     2.801656    -0.437876
83           1             -3.203953     1.400879    -0.398688
84           6             -6.086960     3.158264     0.081131
85           1             -7.639694     2.623006     1.485927
86           1             -4.368072     3.410645    -1.203110
87           1             -4.672769    -0.740467     2.292913
88          64              0.013768    -1.338942    -0.012737
89           6             -6.811005     4.418406    -0.428184
90           9             -6.013071     5.494426    -0.260902
91           9             -7.100597     4.272302    -1.738638
92           9             -7.954060     4.593160     0.268512
--------------------------------------------------------------
```
·E(RTPSSh) = -2808.14647851 Hartree
·Zero-point correction = 0.721257 (Hartree/Particle)
 Thermal correction to Energy = 0.772982
 Thermal correction to Enthalpy = 0.773926
 Thermal correction to Gibbs Free Energy = 0.632565
 Sum of electronic and zero-point Energies = -2807.429080
 Sum of electronic and thermal Energies = -2807.377354
 Sum of electronic and thermal Enthalpies = -2807.376410
 Sum of electronic and thermal Free Energies = -2807.517772

Annexe D
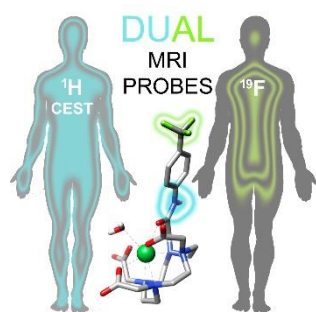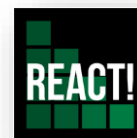
Annexe D

Lanthanide complexes with ^{1}H paraCEST and ^{19}F Response for MRI Applications

Annexe D Summary

Figure S1. High-resolution mass spectrum of [**EuL³**].

Figure S2. High-resolution mass spectrum of [**GdL³**].

Figure S3. High-resolution mass spectrum of [**LuL³**].
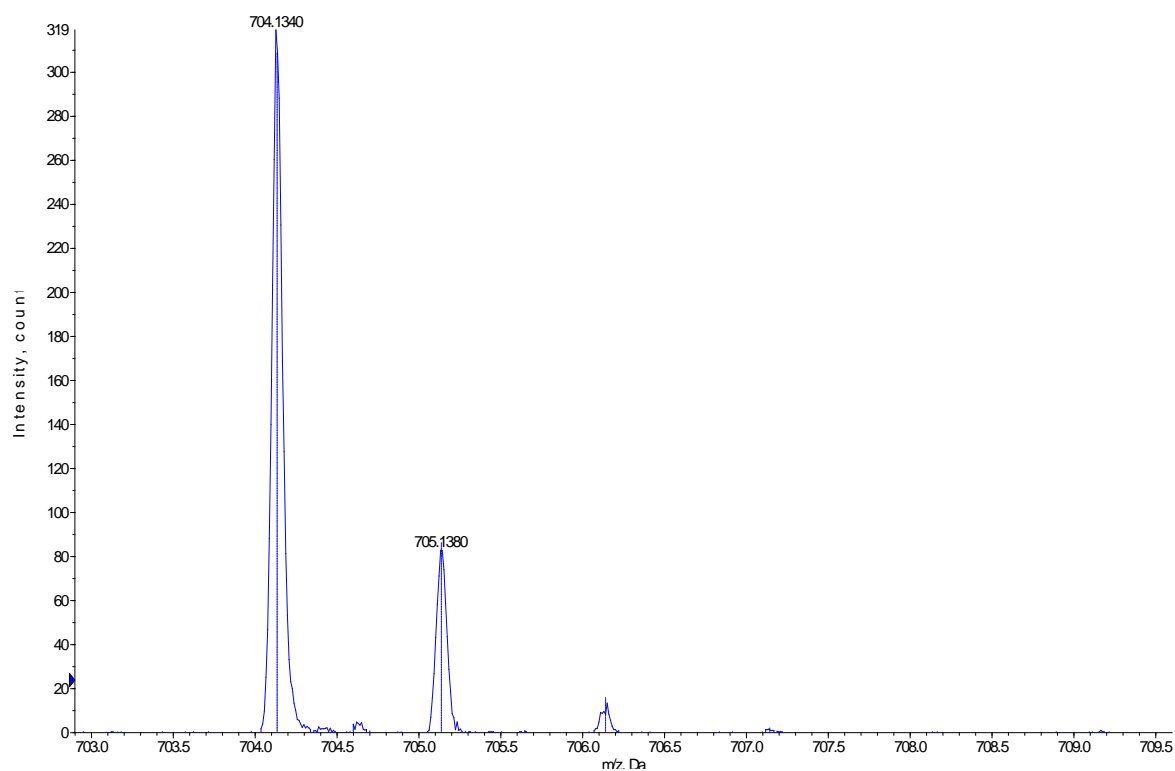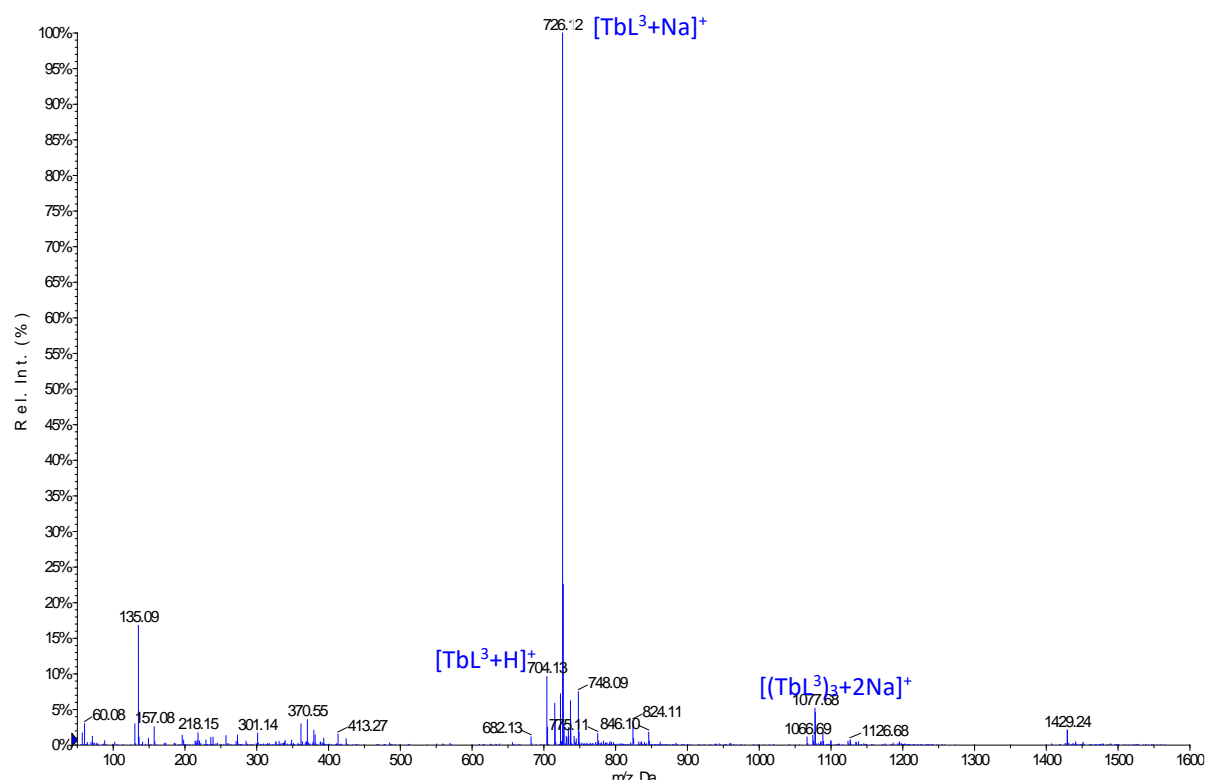
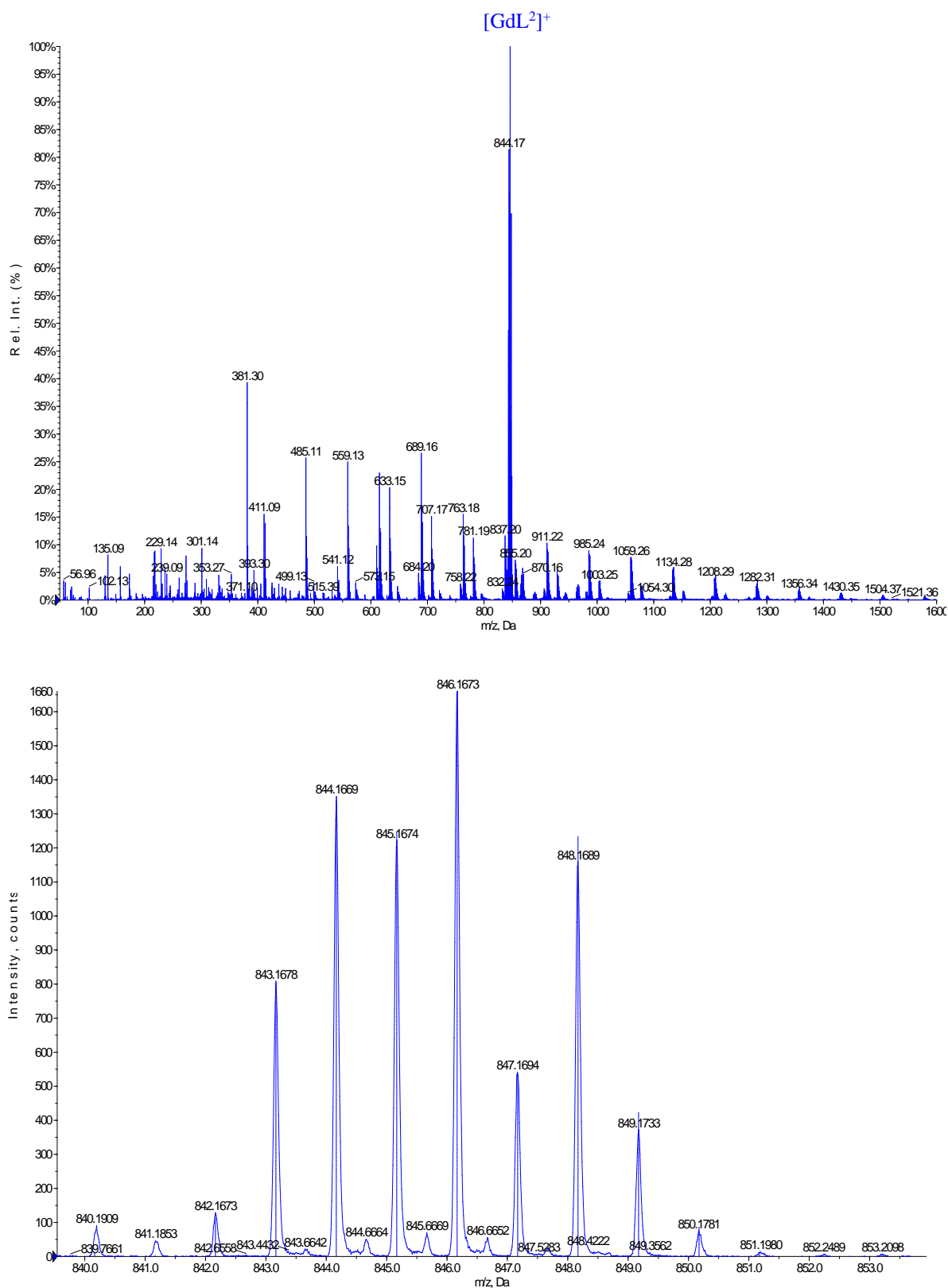**Figure S4.** High-resolution mass spectrum of [**TbL^3**].
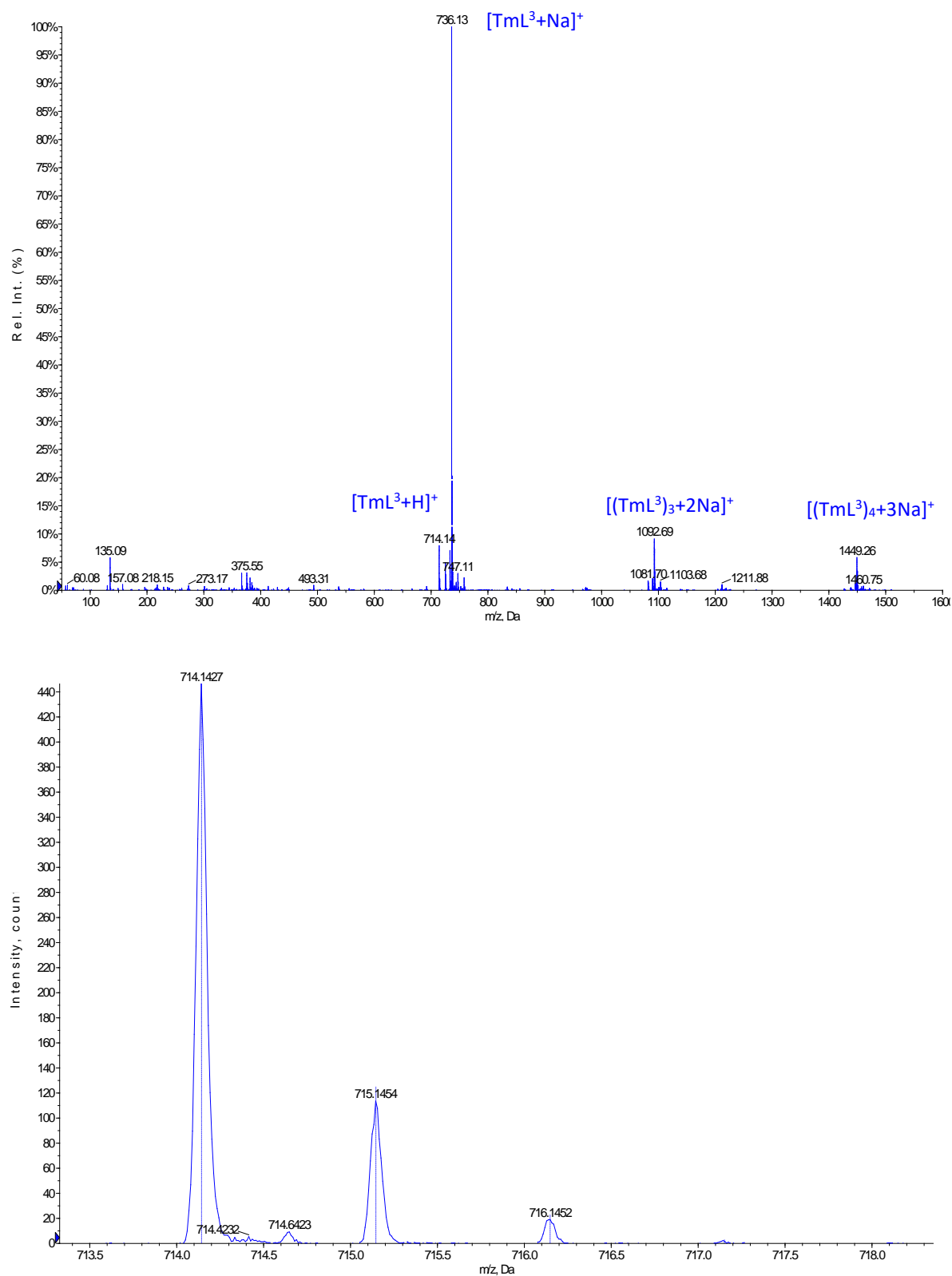
Figure S5. High-resolution mass spectrum of [**TmL³**].
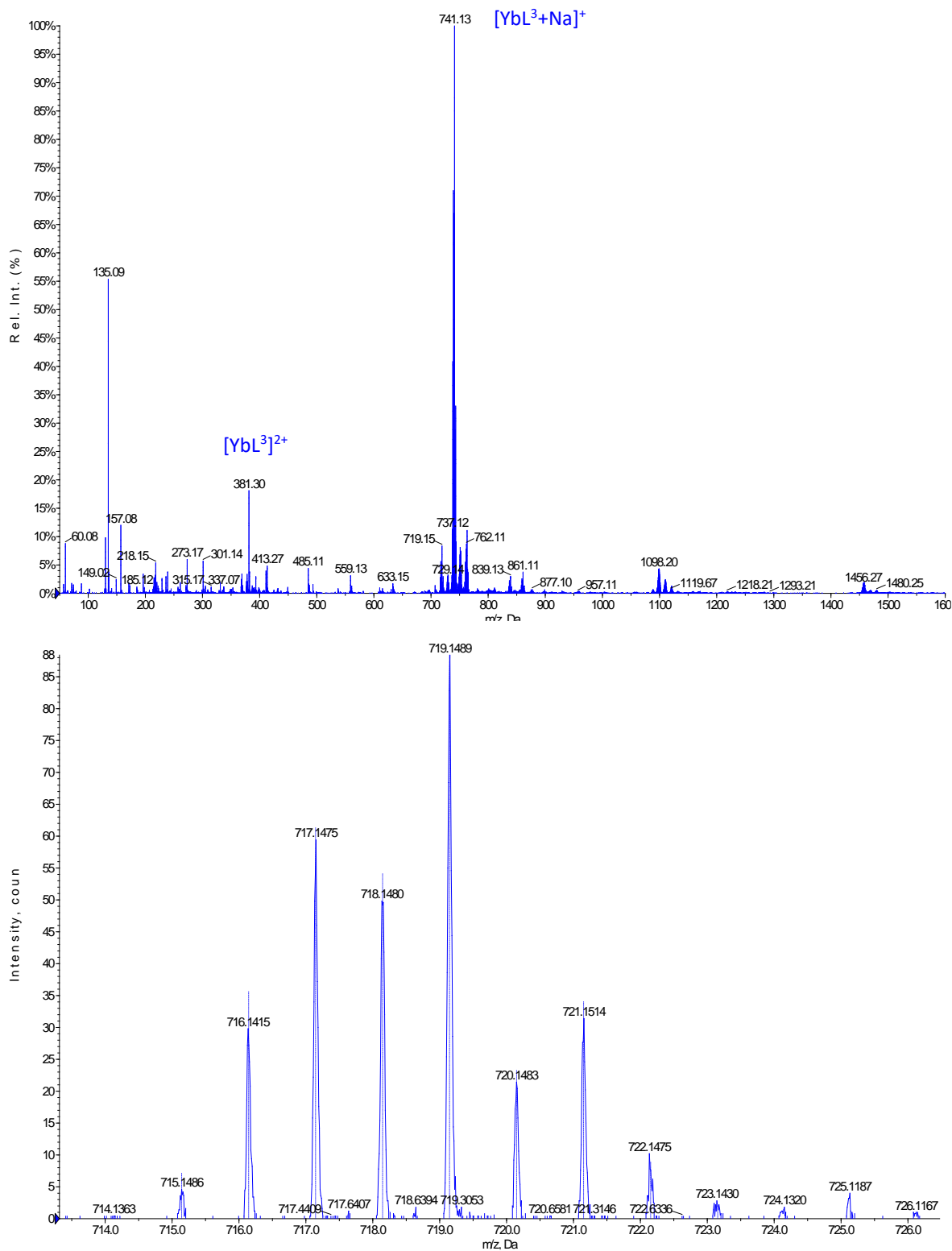
Figure S6. High-resolution mass spectrum of [**YbL³**].
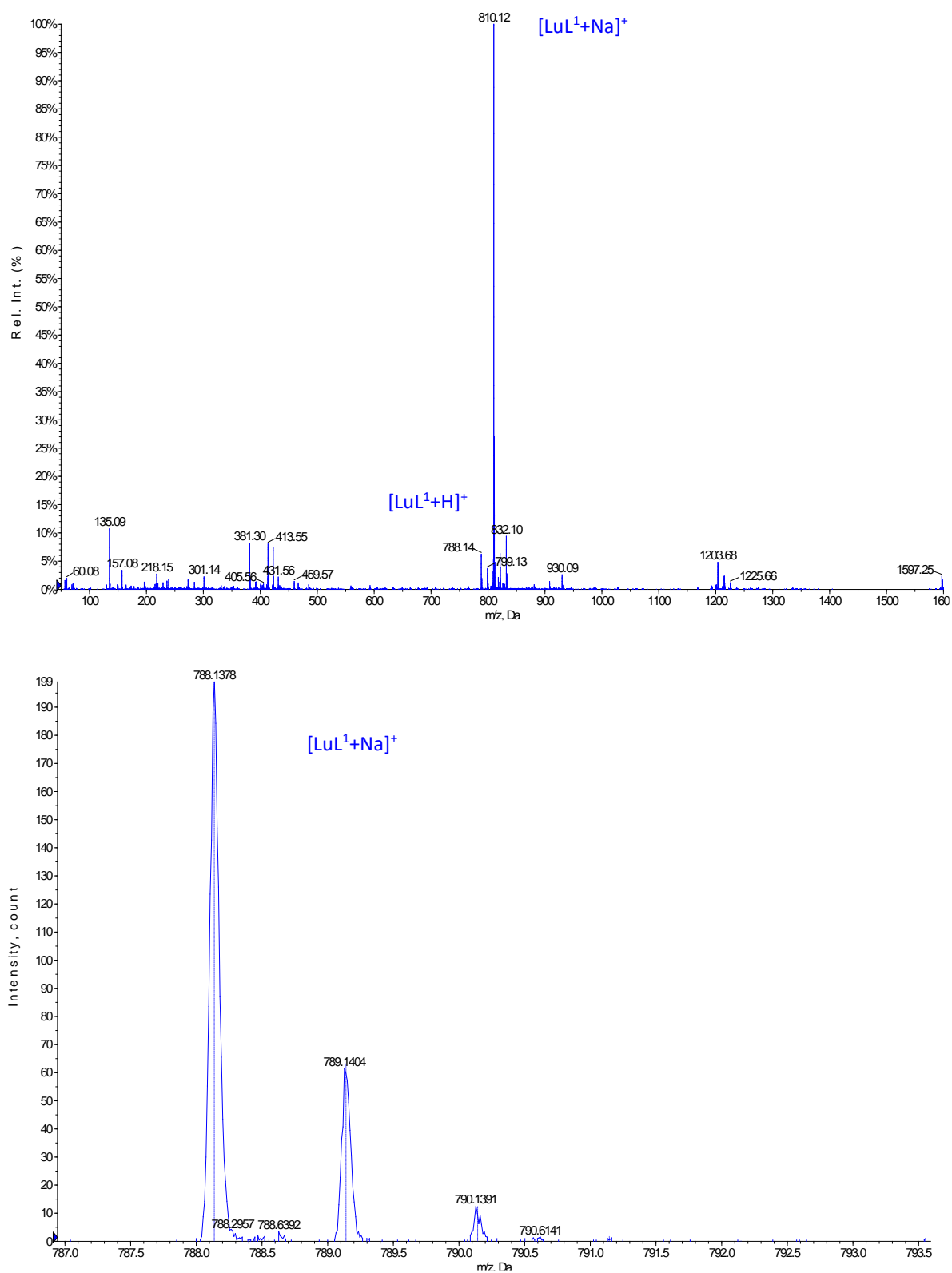
Figure S7. High-resolution mass spectrum of [**LuL¹**].
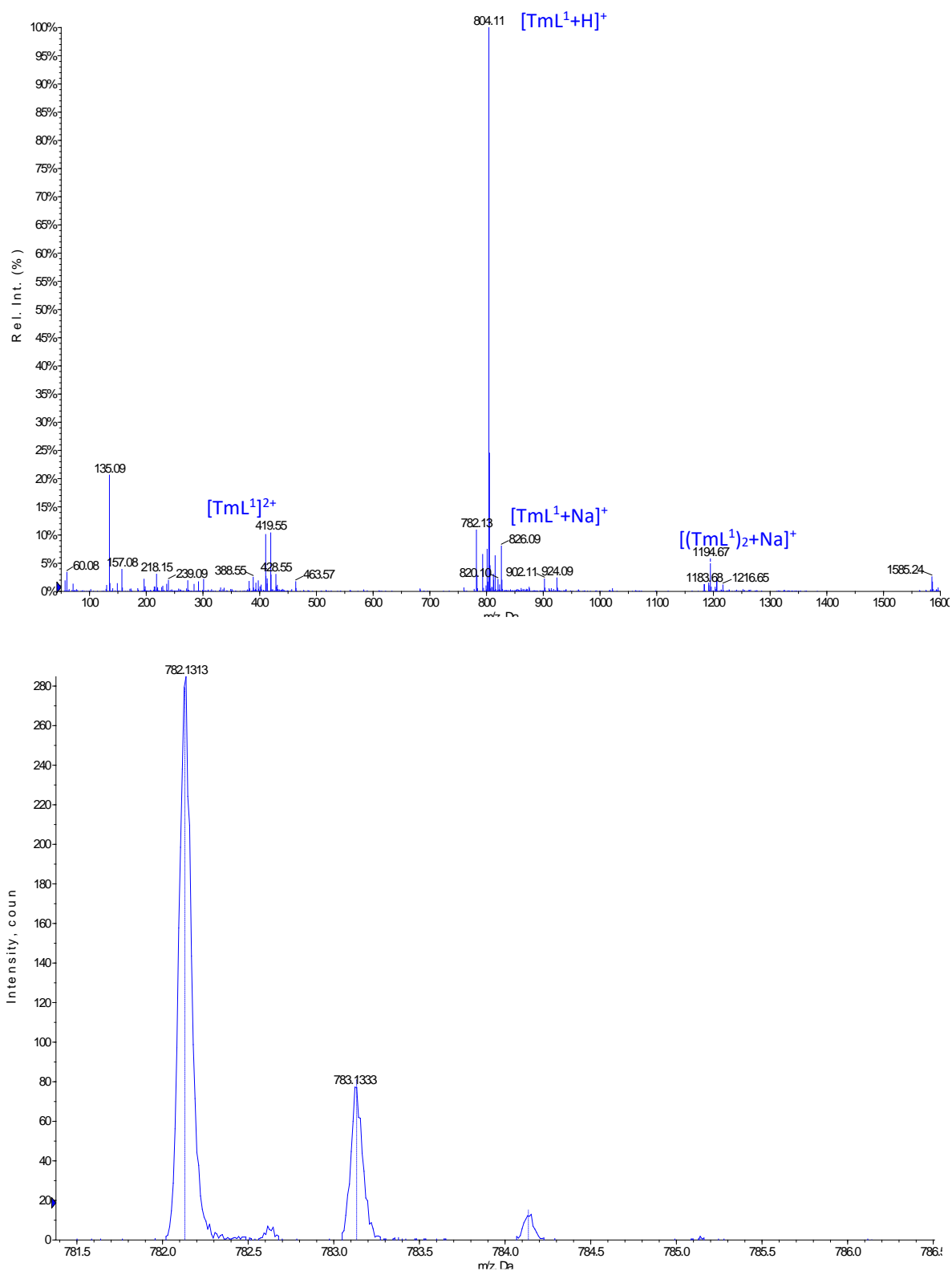
Figure S8. High-resolution mass spectrum of [**TmL^1**].
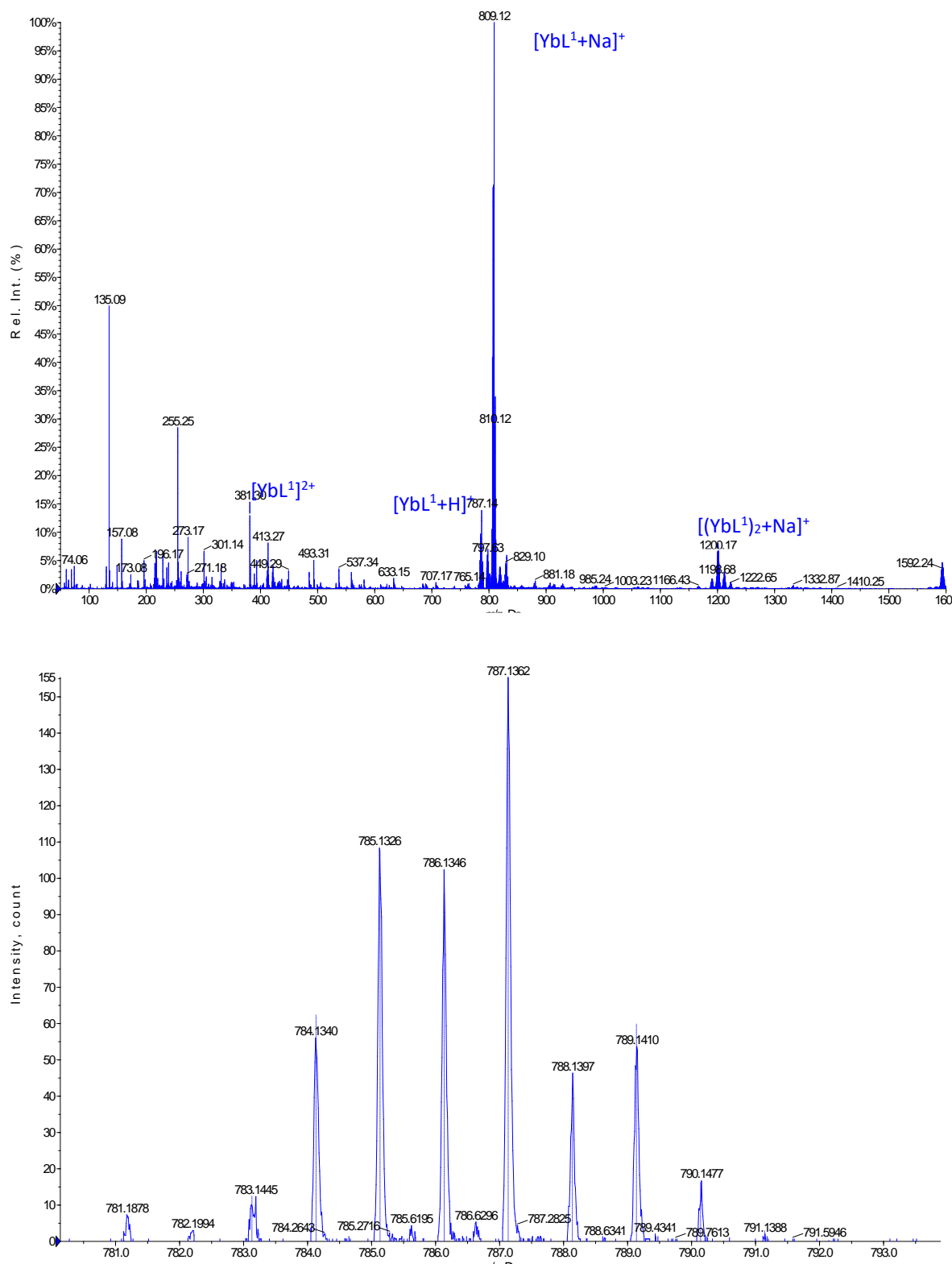
Figure S9. High-resolution mass spectrum of [**YbL²**].
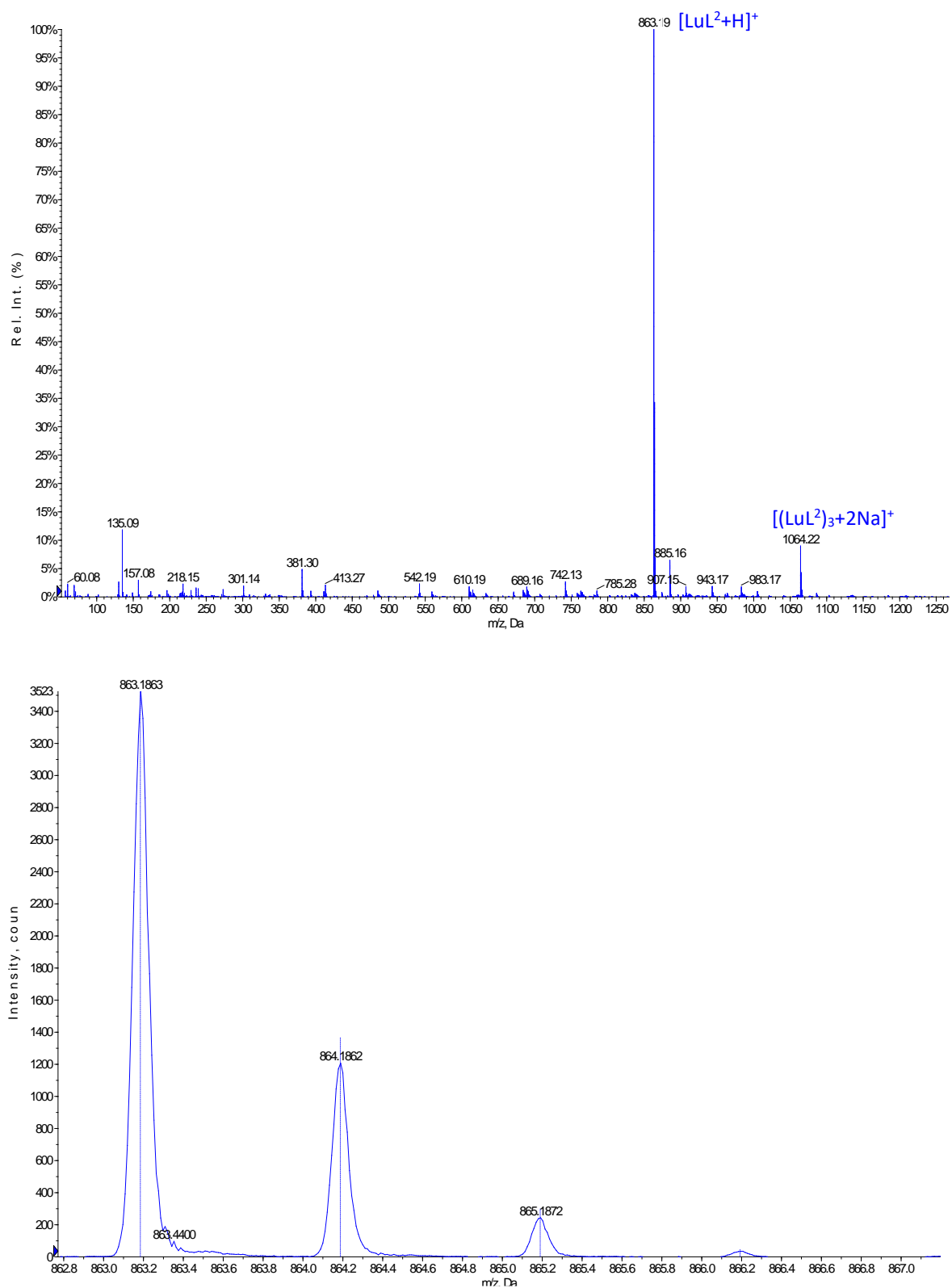
Figure S10. High-resolution mass spectrum of [**LuL^2**].
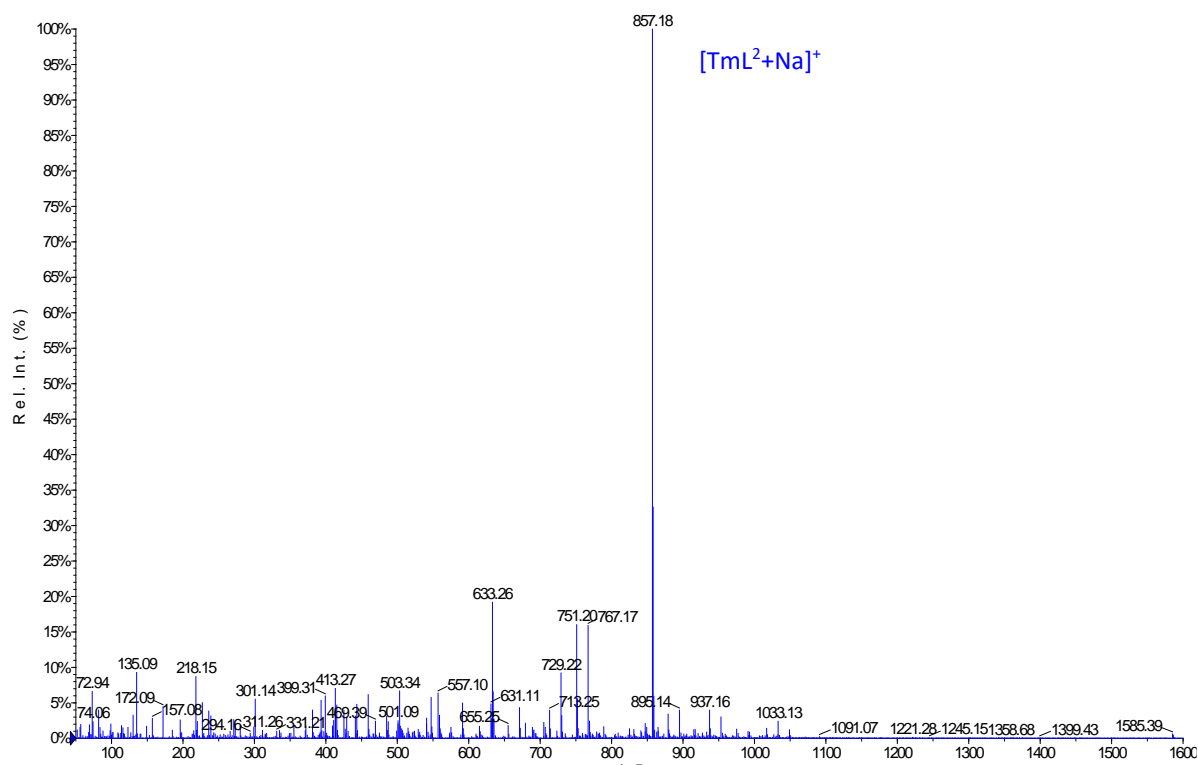
Figure S11. Mass spectrum of [**TmL²**].
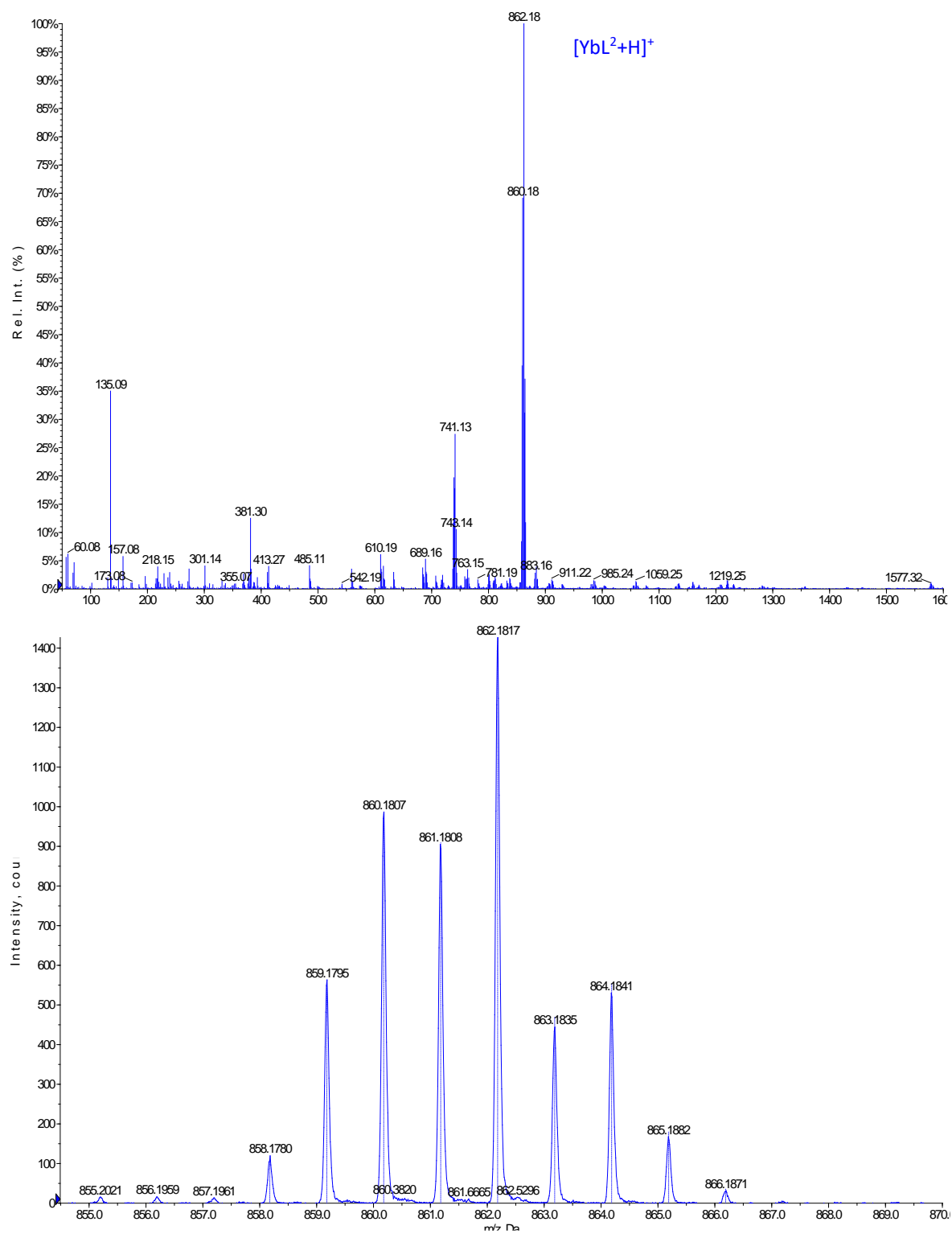
Figure S12. High-resolution mass spectrum of [**YbL^2**].
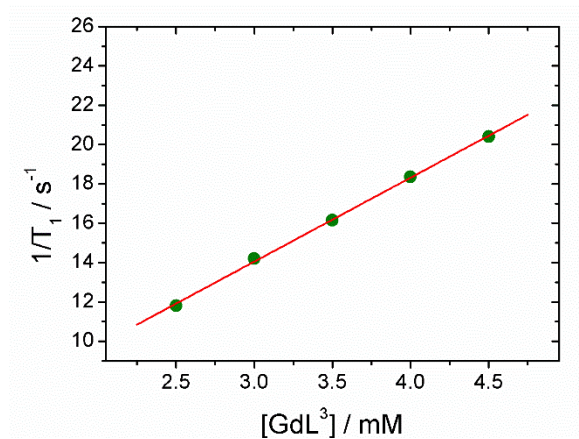
Figure S13. Proton relaxivities (r_{1p}, mM^{-1}s^{-1}) of **GdL^3** (green circles) as a function of gadolinium complex concentration (measured on 2.5-4.5 mM solutions, at 298 K and 300 MHz).
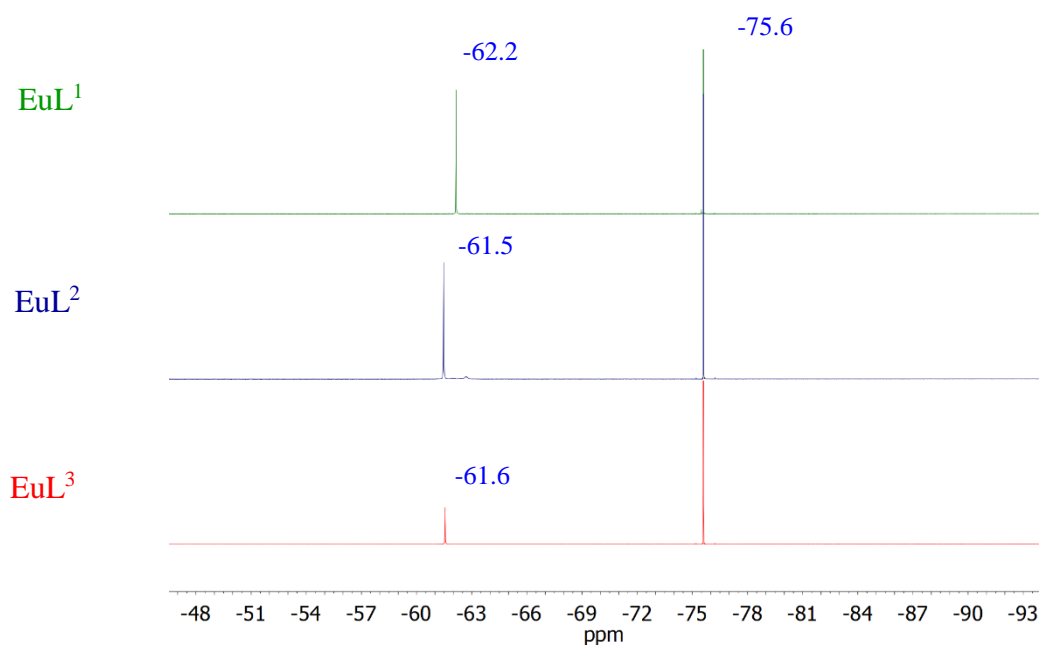
Figure S14. ^{19}F NMR spectra (7.05 T, 25 ºC) of 5 mM **EuL^1**, **EuL^2** and **EuL^3** aqueous solutions buffered at pH 7.4 (0.05 M HEPES). The experiments were performed using a capillary with 125 mM TFA solution as reference (-75.6 ppm).
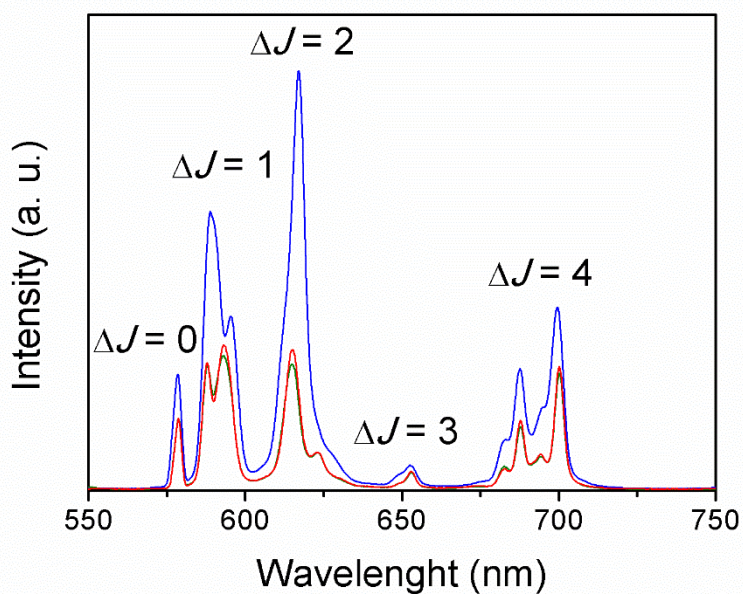
Figure S15. Emission spectra of **EuL^1** (green), **EuL^2** (blue) and **EuL^3** (orange) recorded in H$_2$O. The emission wavelengths were set to 258.75, 267.3 and 262.5 nm, respectively. Slits were set at 6 nm for EuL^1, 7 nm for EuL^{2}and 6 nm for EuL^3.
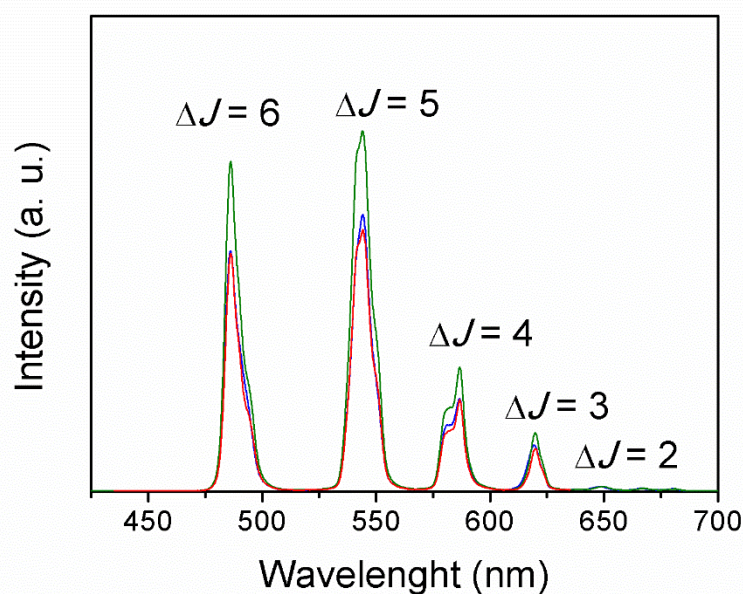
Figure S16. Emission spectra of **TbL^1** (green), **TbL^2** (blue) and **TbL^3** (orange) recorded in H$_2$O. The emission wavelengths were set to 257.0, 267.5 and 263.25 nm, respectively. Slits were set at 6 nm for TbL^1, 7 nm for TbL^2 and 6 nm for TbL^3.
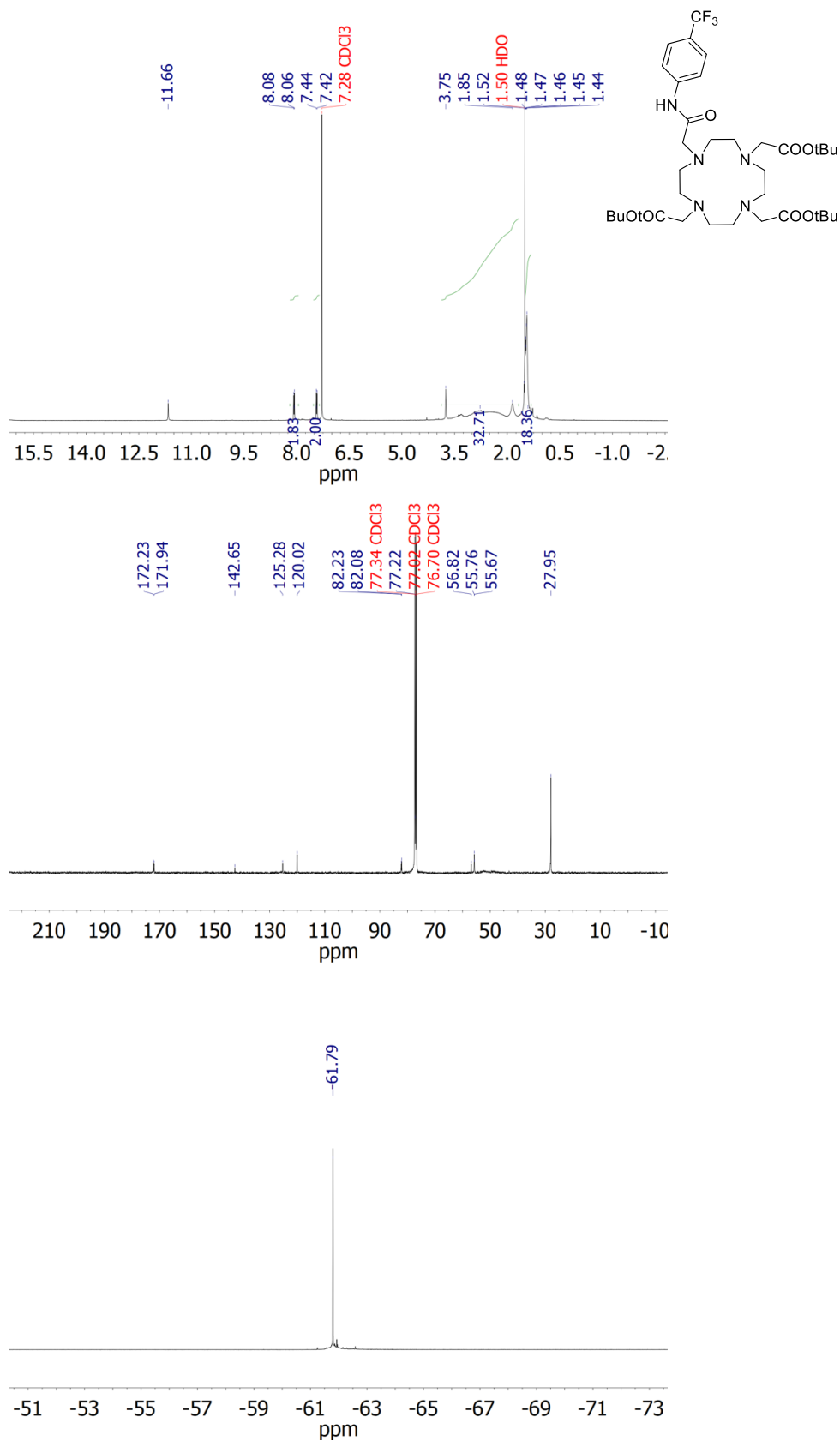
Figure S17. ¹H, ¹³C and ¹⁹F NMR spectra (7.05 T, 25 °C) of intermediate **1** in CDCl₃.
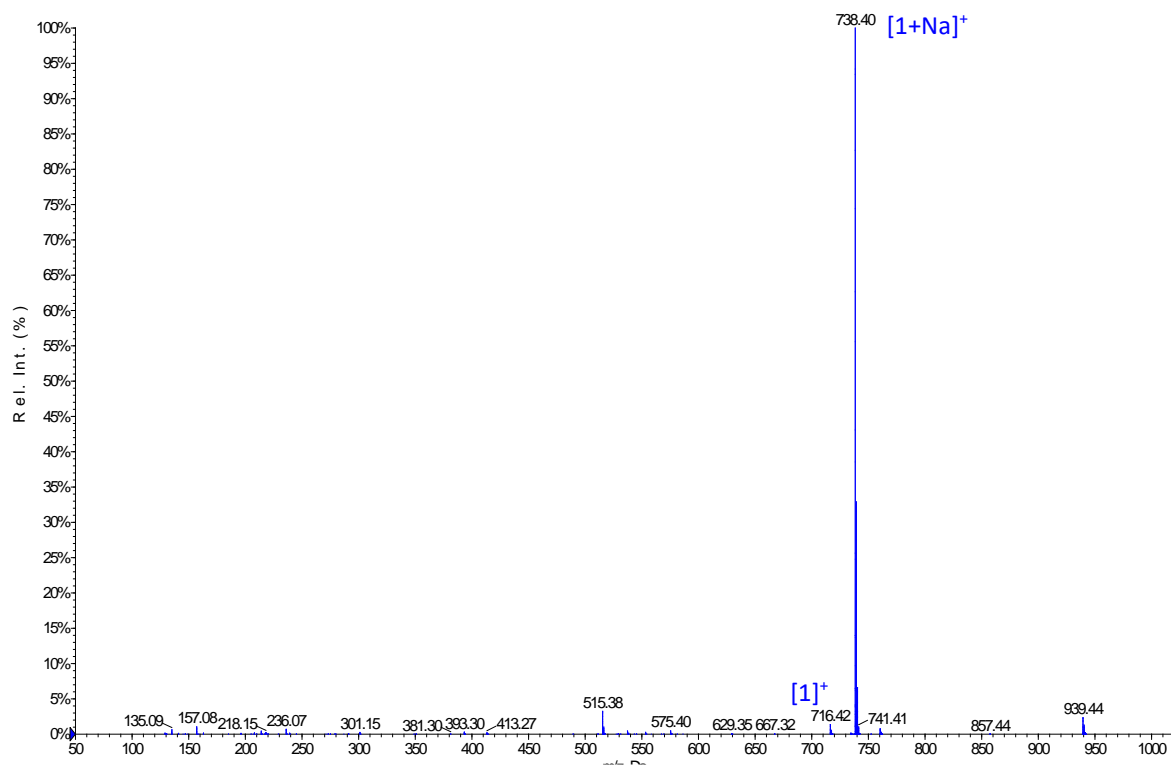
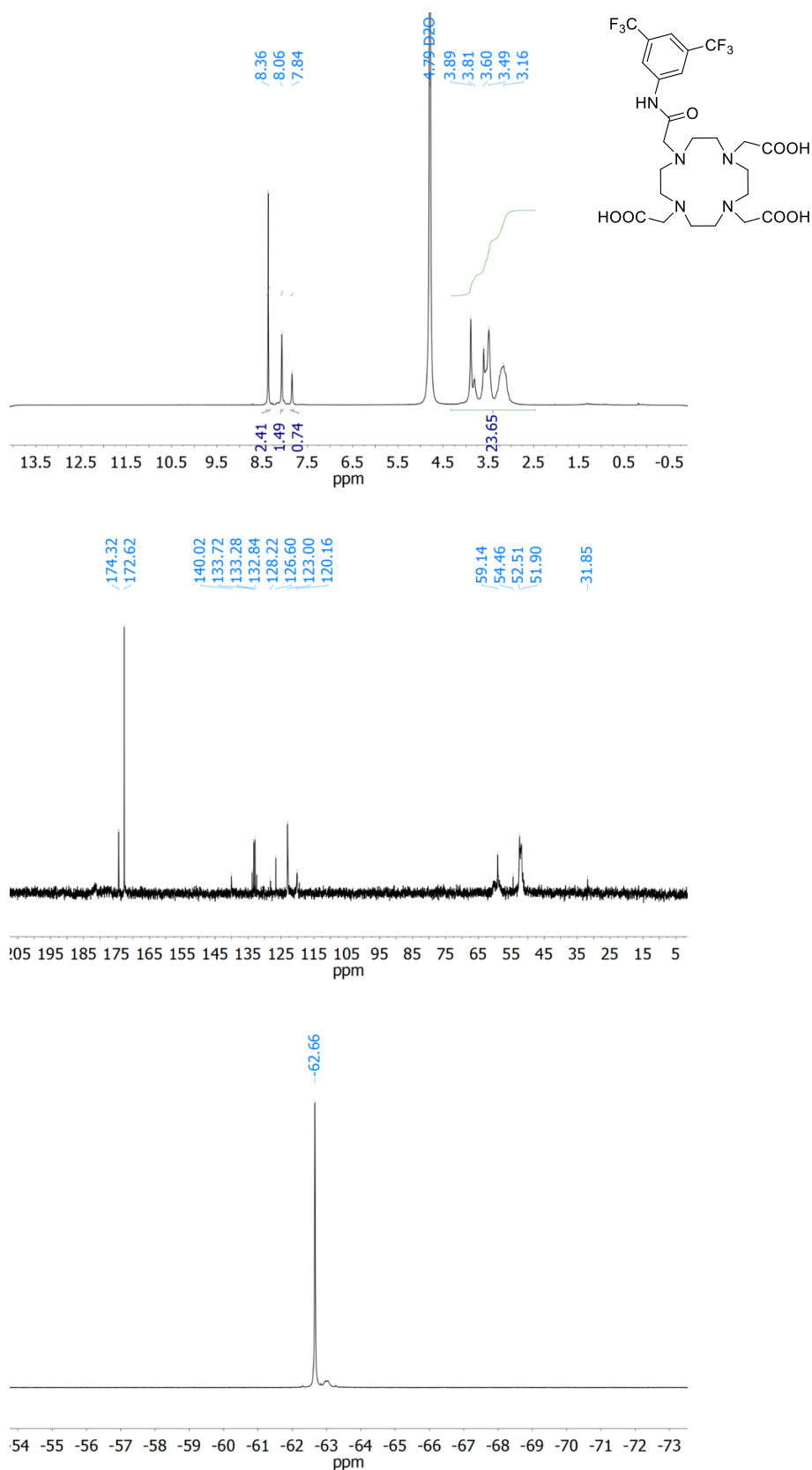**Figure S18.** Experimental mass spectrum of intermediate 1.
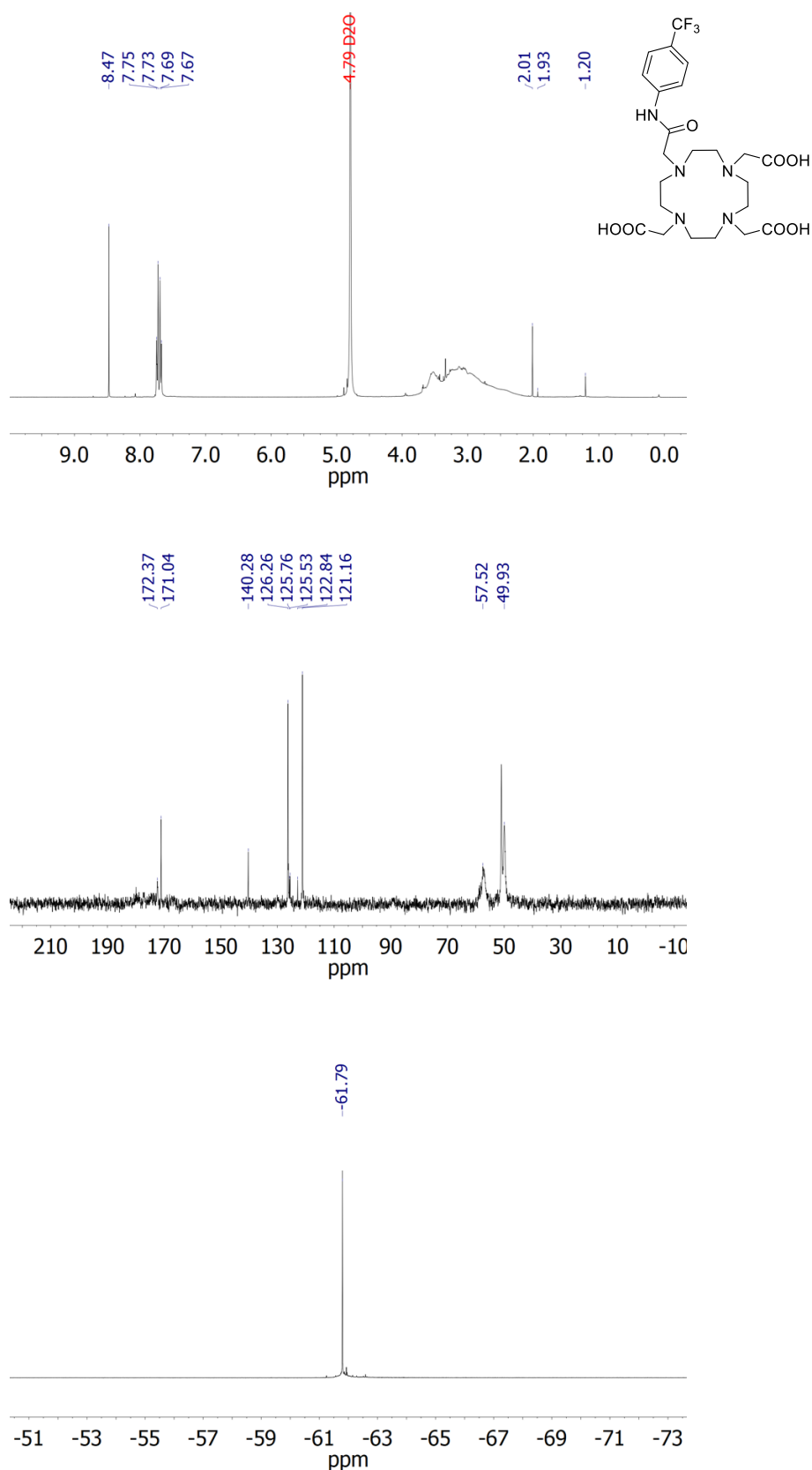
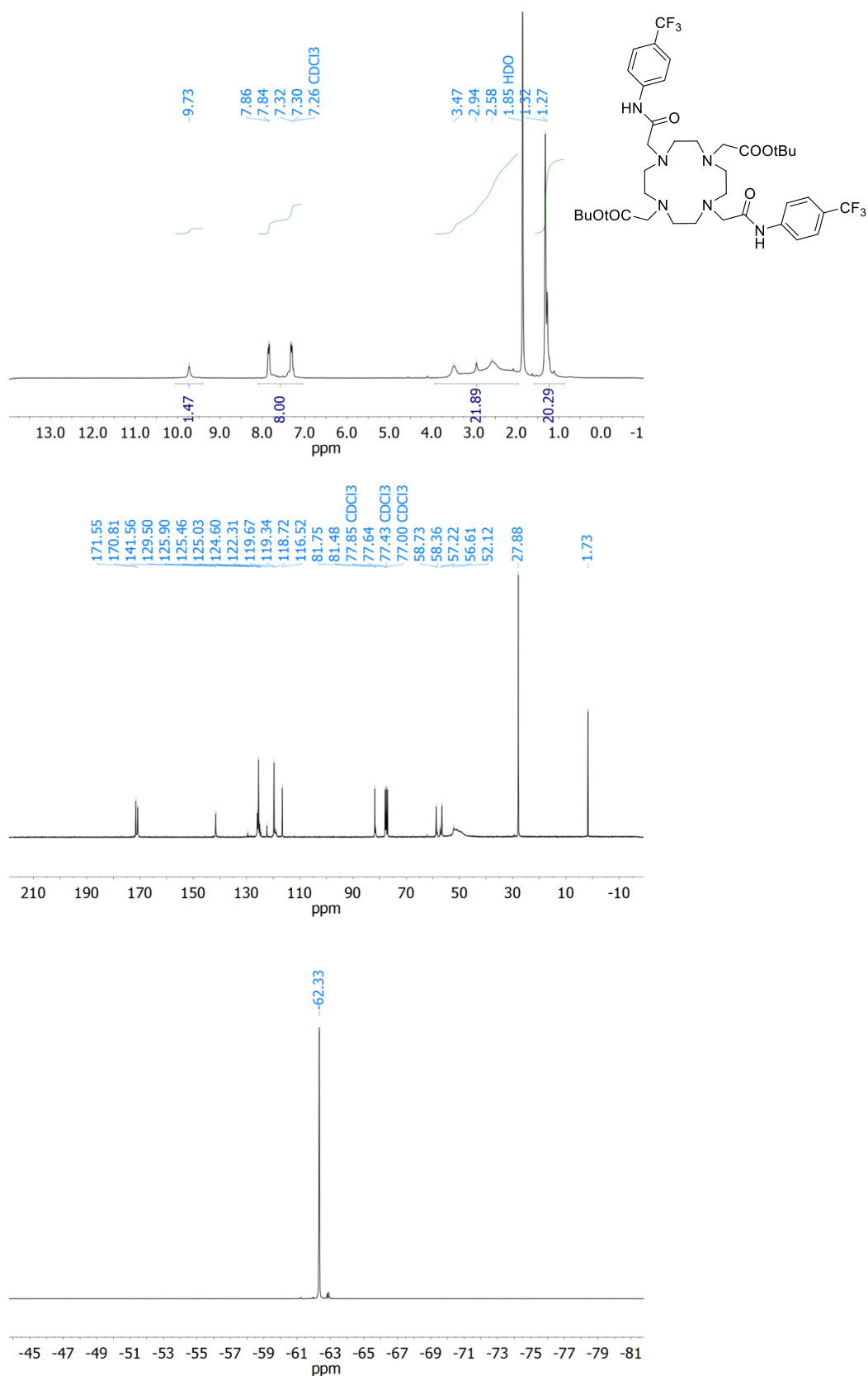**Figure S19.** ^{1}H, ^{13}C and ^{19}F NMR spectra (7.05 T, 25 ^{o}C) of ligand **H$_3$L^3** in D$_2$O.
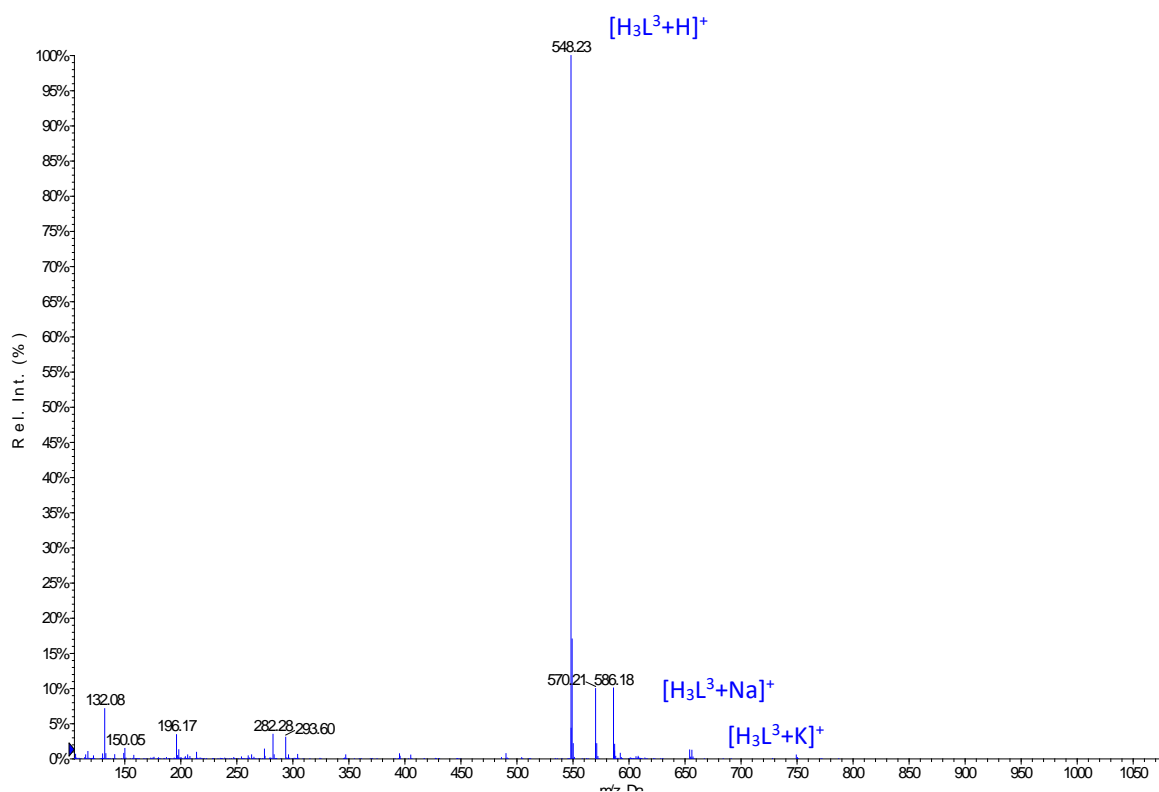
Figure S20. Experimental mass spectrum of ligand [**H₃L³**].
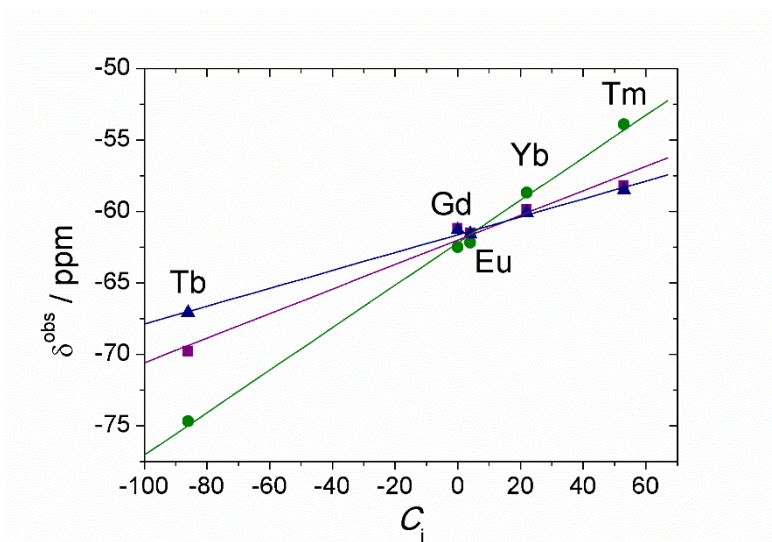
Figure S21. Plot of the observed ^{19}F chemical shifts vs. the Bleaney factors (pH 7.4, 298 K).
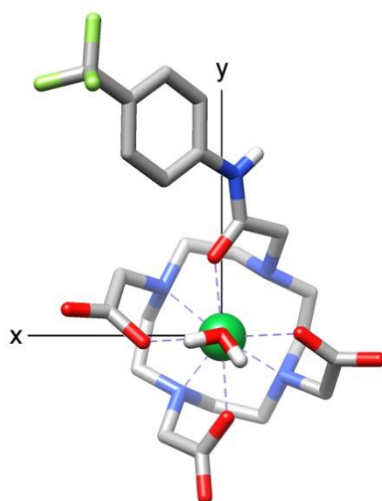
Figure S22. View of the orientation of the magnetic susceptibility tensor obtained by analysing the pseudocontact shifts of YbL^3.
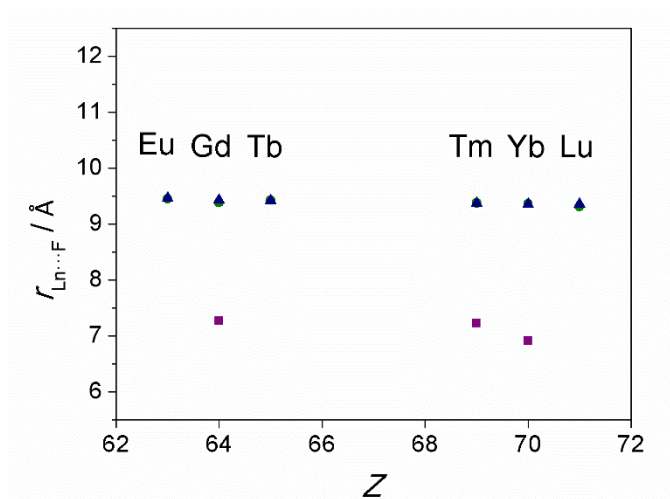
Figure S23. Plot of the distances Ln⋯F obtained by analysing the optimased geometries calculated by DFT calculations of several complexes vs. the atomic number of the lanthanide metal ion.
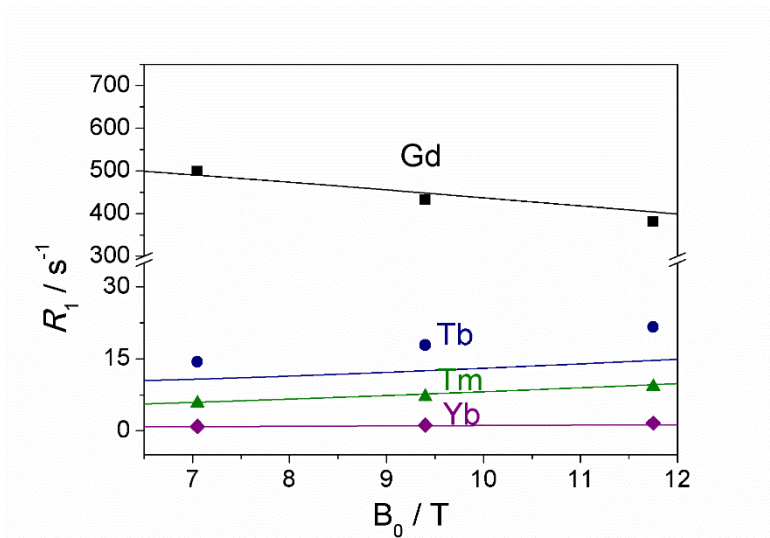
Figure S24. ^{19}F relaxation rates as a function of the magnetic field strength showing the fits and the experimental data points obtained for LnL^2 (5 mM in H_2O:D_2O, 9:1 v:v, pH = 7.4, 50 mM HEPES buffer).
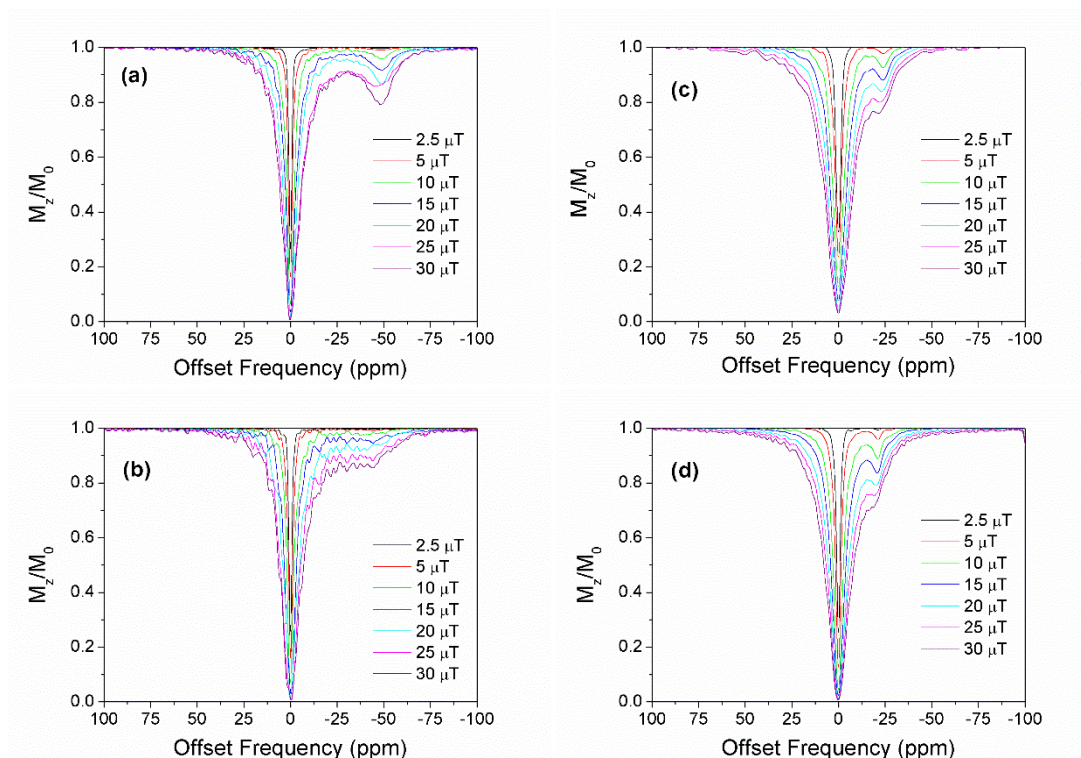
Figure S25. Z-spectra (saturation time 10 s) recorded for (a) TmL^1 (15 mM in H$_2$O) at 25 ^{o}C, (b) TmL^1 (15 mM in H$_2$O) at 37 ^{o}C. (c) TmL^2 (8 mM in H$_2$O) at 25 ^{o}C and (d) TmL^2 (8 mM in H$_2$O) at 37 ^{o}C.
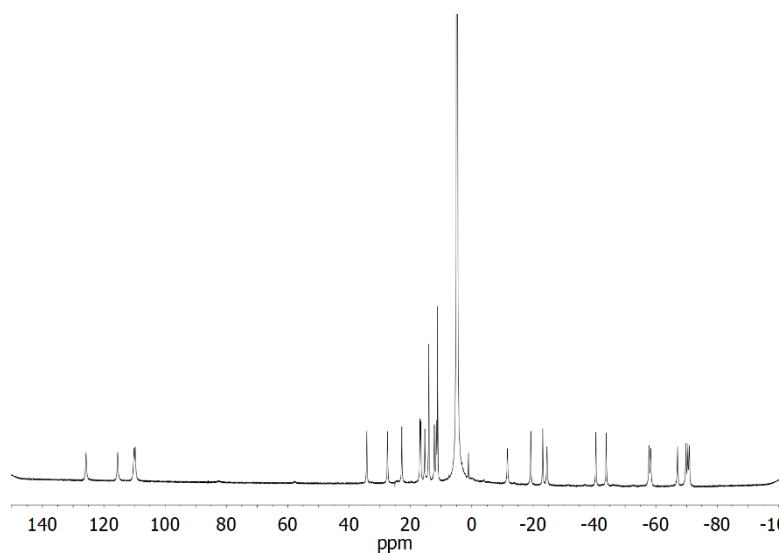
Figure S26. ^{1}H NMR spectra (7.05 T, 25 ^{o}C) of complex YbL^3 in H$_2$O.
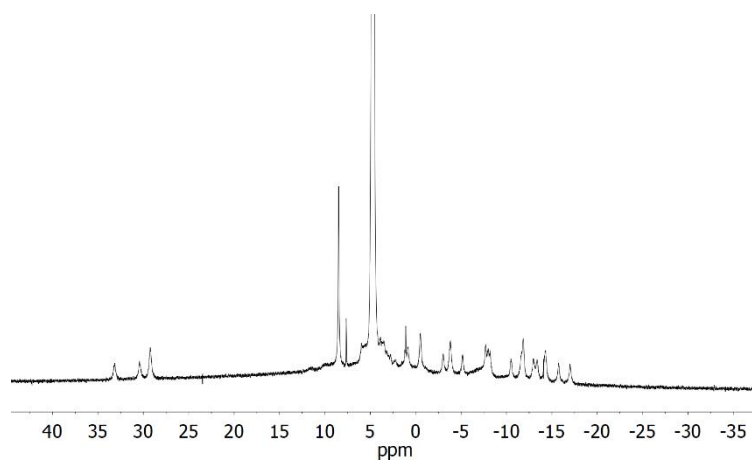
Figure S27. ^{1}H NMR spectrum (7.05 T, 25 ^{o}C) of complex EuL^3 in H$_2$O.

Table S1. MRI parameters ^{19}F.

Sample/parameter	FA / ^{0}	TR / ms	NEX
GdL^1	78	3.2	35156
TbL^1	19	3.6	31250
YbL^1	8	5.6	20089
EuL^1	6	4.2	26785

Table S2. SNR values LnL^1.

Sample SNR	GdL^1 / TFA	TbL^1 / TFA	YbL^1 / TFA	EuL^1 / TFA
^{19}F	102.63 / 66.75	34.08 / 29.60	16.35 / 18.87	14.30 / 19.90

Table S3. Optimised Cartesian coordinates obtained for [GdL^1(H$_2$O)]·2H$_2$O SAP isomer with DFT calculations (0 imaginary frequencies).

Center Number	Atomic Number	X	Y	Z
1	7	−3.733106	−1.789873	0.407525
2	6	−5.009983	−1.126854	0.016475
3	6	−4.895836	−0.352925	−1.291175
4	7	−3.898879	0.750635	−1.240405
5	6	−3.511965	1.133329	−2.626969
6	6	−2.522260	0.152402	−3.244881
7	7	−1.237682	0.043576	−2.498571
8	6	−0.511709	−1.174478	−2.960155
9	6	−1.080648	−2.463880	−2.368904
10	7	−1.075000	−2.495067	−0.879362
11	6	−2.064871	−3.495388	−0.378601
12	6	−3.498124	−2.983209	−0.445640
13	6	−3.777872	−2.162170	1.849249
14	6	−2.471526	−1.887829	2.606947
15	8	−1.437165	−1.582201	1.908510
16	8	−2.499300	−1.956961	3.855135
17	6	−4.440056	1.928326	−0.511354
18	6	−4.027486	2.001629	0.966218
19	8	−4.303366	3.046721	1.588108
20	8	−3.384642	0.993811	1.445633
21	6	−0.403656	1.251171	−2.731148
22	6	−0.762492	2.450280	−1.836790
23	8	−0.510649	3.591274	−2.234681
24	8	−1.263068	2.147008	−0.673333
25	6	0.259217	−2.845687	−0.355588
26	6	1.178476	−1.637010	−0.311287
27	8	0.711549	−0.485550	−0.210031
28	1	−4.556642	−1.578258	2.342956
29	1	−4.046793	−3.220089	1.976265
30	1	−5.535983	1.970847	−0.580894
31	1	−4.057352	2.837434	−0.979364
32	1	−0.429103	1.560328	−3.784055
33	1	0.630981	0.994211	−2.482418
34	1	0.138626	−3.152552	0.688572
35	1	0.716315	−3.679140	−0.907396
36	1	−5.274097	−0.439590	0.820862
37	1	−5.820613	−1.864390	−0.079575
38	1	−5.888473	0.047196	−1.546921
39	1	−4.614729	−1.025458	−2.105066
40	1	−4.395603	1.191864	−3.279405
41	1	−3.075830	2.132836	−2.592898
42	1	−2.325461	0.457736	−4.283651
43	1	−2.969281	−0.843345	−3.290668
44	1	−0.544561	−1.254989	−4.056445
45	1	0.538249	−1.061872	−2.685415
46	1	−2.114393	−2.595879	−2.695259
47	1	−0.514171	−3.315768	−2.772825
48	1	−1.805903	−3.719442	0.657318
49	1	−1.993010	−4.430731	−0.951287
50	1	−3.751824	−2.721465	−1.475525
51	1	−4.174155	−3.801150	−0.153550
52	8	−1.464652	3.648763	1.610316
53	1	−1.398044	3.356465	0.668989
54	1	−2.425468	3.582215	1.793717
55	1	−0.623307	0.727738	2.839399
56	8	−0.513853	1.131720	1.934468
57	1	−0.843764	2.069600	1.985647
58	8	−0.730494	0.047378	4.428920
59	1	0.148105	−0.324180	4.597050
60	1	−1.310678	−0.748330	4.287690

61	7	2.505334	-1.901212	-0.322151
62	1	2.762935	-2.875343	-0.436858
63	6	3.586595	-1.008793	-0.150206
64	6	4.877941	-1.560548	-0.169410
65	6	3.419401	0.367767	0.042315
66	6	5.985489	-0.736198	0.006587
67	1	5.016120	-2.627170	-0.311792
68	6	4.549424	1.172458	0.218826
69	1	2.427878	0.795988	0.058467
70	6	5.836310	0.640849	0.204358
71	64	-1.717382	-0.040276	0.139659
72	1	6.700126	1.277398	0.350252
73	6	7.371345	-1.321349	-0.060836
74	6	4.327193	2.648645	0.418619
75	9	5.478050	3.315624	0.655124
76	9	3.748740	3.214994	-0.670188
77	9	3.496189	2.889879	1.463216
78	9	8.199344	-0.750256	0.845677
79	9	7.374534	-2.654742	0.167038
80	9	7.934848	-1.126651	-1.279487

·E(RTPSSh) = -2596.47784152 Hartree
·Zero-point correction = 0.615849 (Hartree/Particle)
 Thermal correction to Energy = 0.662166
 Thermal correction to Enthalpy = 0.663110
 Thermal correction to Gibbs Free Energy = 0.533229
 Sum of electronic and zero-point Energies = -2595.861992
 Sum of electronic and thermal Energies = -2595.815676
 Sum of electronic and thermal Enthalpies = -2595.814732
 Sum of electronic and thermal Free Energies = -2595.944613

Table S4. Optimised Cartesian coordinates obtained for [TmL^1(H$_2$O)]·2H$_2$O SAP isomer with DFT calculations (0 imaginary frequencies).

```
-----------------------------------------------------------------------
Center     Atomic                     Coordinates (Angstroms)
Number     Number                  X            Y            Z
-----------------------------------------------------------------------
    1         7              -3.765241    -1.673793     0.354021
    2         6              -5.002108    -1.001291    -0.135908
    3         6              -4.778446    -0.279212    -1.457758
    4         7              -3.751034     0.791204    -1.363855
    5         6              -3.285987     1.152690    -2.730238
    6         6              -2.305221     0.131348    -3.291189
    7         7              -1.083336    -0.037687    -2.455691
    8         6              -0.397840    -1.294880    -2.866574
    9         6              -1.053579    -2.532868    -2.259403
   10         7              -1.104515    -2.503772    -0.771226
   11         6              -2.128953    -3.470594    -0.276051
   12         6              -3.545806    -2.928647    -0.410392
   13         6              -3.884986    -1.952098     1.811002
   14         6              -2.573527    -1.778593     2.584478
   15         8              -1.522792    -1.490815     1.903111
   16         8              -2.610837    -1.891299     3.828746
   17         6              -4.293651     1.988925    -0.670796
   18         6              -3.942470     2.059954     0.820609
   19         8              -4.239040     3.103241     1.435093
   20         8              -3.323858     1.047652     1.322719
   21         6              -0.178392     1.126466    -2.638139
   22         6              -0.539816     2.340697    -1.768481
   23         8              -0.191040     3.467296    -2.133592
   24         8              -1.155951     2.064179    -0.655292
   25         6               0.204503    -2.861647    -0.190165
   26         6               1.133620    -1.662263    -0.164846
   27         8               0.669462    -0.507274    -0.099774
   28         1              -4.591416    -1.241863     2.244878
   29         1              -4.285449    -2.958466     1.996314
   30         1              -5.384066     2.058904    -0.787850
   31         1              -3.867775     2.884750    -1.127307
   32         1              -0.123969     1.433674    -3.690472
   33         1               0.824776     0.822520    -2.323525
   34         1               0.044756    -3.128002     0.859394
   35         1               0.664219    -3.720953    -0.698058
   36         1              -5.304846    -0.281290     0.625220
   37         1              -5.821014    -1.725340    -0.256839
   38         1              -5.736562     0.142062    -1.797607
   39         1              -4.459290    -0.988186    -2.225656
   40         1              -4.134084     1.243106    -3.424661
   41         1              -2.810752     2.133249    -2.676140
   42         1              -2.022066     0.434981    -4.310118
   43         1              -2.790778    -0.843511    -3.379523
   44         1              -0.398716    -1.401921    -3.960791
   45         1               0.648196    -1.227016    -2.562842
   46         1              -2.080439    -2.622025    -2.620390
   47         1              -0.518579    -3.428023    -2.608744
   48         1              -1.909180    -3.672198     0.773091
   49         1              -2.057244    -4.422897    -0.820013
   50         1              -3.769962    -2.729560    -1.460857
   51         1              -4.250707    -3.706435    -0.080482
   52         8              -1.392311     3.654065     1.577784
   53         1              -1.302561     3.342015     0.645569
   54         1              -2.359593     3.606062     1.729134
   55         1              -0.655579     0.688842     2.803331
   56         8              -0.538034     1.089795     1.900353
   57         1              -0.837976     2.035458     1.954333
   58         8              -0.741834     0.021767     4.423429
   59         1               0.124182    -0.398315     4.532902
   60         1              -1.363688    -0.741040     4.282982
```

```
61          7                    2.459834   -1.930471   -0.164170
62          1                    2.714120   -2.907962   -0.254866
63          6                    3.544335   -1.033610   -0.042201
64          6                    4.835932   -1.582179   -0.099164
65          6                    3.379964    0.345480    0.134243
66          6                    5.946507   -0.751479    0.018580
67          1                    4.972662   -2.650648   -0.228416
68          6                    4.513104    1.156707    0.250840
69          1                    2.388187    0.771015    0.181157
70          6                    5.800300    0.628668    0.195330
71         69                   -1.705232   -0.043961    0.124945
72          1                    6.666949    1.270449    0.293685
73          6                    7.330644   -1.333679   -0.093772
74          6                    4.293991    2.635536    0.434030
75          9                    5.452487    3.312044    0.594629
76          9                    3.653980    3.178050   -0.632220
77          9                    3.520218    2.893127    1.517574
78          9                    8.193912   -0.738299    0.762648
79          9                    7.348855   -2.661321    0.165187
80          9                    7.841269   -1.166485   -1.339641
    -------------------------------------------------------------
·E(RTPSSh) = =-2599.3991954 Hartree
```

Table S5. Optimised Cartesian coordinates obtained for [YbL^1(H$_2$O)]·2H$_2$O SAP isomer with DFT calculations (0 imaginary frequencies).

```
---------------------------------------------------------------------
Center    Atomic                   Coordinates (Angstroms)
Number    Number               X            Y            Z
---------------------------------------------------------------------
   1         7            -3.748605    -1.346132     0.958237
   2         6            -4.989053    -0.809269     0.331226
   3         6            -4.826045    -0.595224    -1.167773
   4         7            -3.748542     0.374042    -1.497427
   5         6            -3.359516     0.211564    -2.925692
   6         6            -2.451137    -0.993365    -3.137850
   7         7            -1.188046    -0.927455    -2.352288
   8         6            -0.566595    -2.281729    -2.332159
   9         6            -1.225429    -3.207730    -1.312633
  10         7            -1.192719    -2.670804     0.075043
  11         6            -2.226850    -3.344103     0.912843
  12         6            -3.624951    -2.795730     0.658609
  13         6            -3.775142    -1.104767     2.426149
  14         6            -2.408459    -0.743406     3.018365
  15         8            -1.401394    -0.751192     2.220345
  16         8            -2.359774    -0.428721     4.226948
  17         6            -4.195232     1.769194    -1.240871
  18         6            -3.748684     2.328578     0.115372
  19         8            -3.971748     3.532578     0.346665
  20         8            -3.130157     1.518701     0.904158
  21         6            -0.255895     0.051280    -2.968766
  22         6            -0.531171     1.508923    -2.570416
  23         8            -0.173042     2.418782    -3.324072
  24         8            -1.089413     1.669273    -1.404867
  25         6             0.133548    -2.871143     0.688048
  26         6             1.082137    -1.748480     0.312297
  27         8             0.644202    -0.645008    -0.063541
  28         1            -4.430203    -0.255042     2.628533
  29         1            -4.189374    -1.966134     2.968267
  30         1            -5.286656     1.861449    -1.327553
  31         1            -3.760318     2.424186    -1.998491
  32         1            -0.247385    -0.034593    -4.062904
  33         1             0.751649    -0.172296    -2.604545
  34         1             0.021238    -2.803013     1.774665
  35         1             0.560233    -3.855956     0.450534
  36         1            -5.212444     0.143287     0.813450
  37         1            -5.841437    -1.481627     0.507049
  38         1            -5.785570    -0.253955    -1.584504
  39         1            -4.591707    -1.542462    -1.659318
  40         1            -4.247034     0.098537    -3.565230
  41         1            -2.850888     1.122987    -3.243282
  42         1            -2.221522    -1.080943    -4.210400
  43         1            -2.976937    -1.907938    -2.853943
  44         1            -0.628818    -2.753345    -3.323417
  45         1             0.495368    -2.163510    -2.110133
  46         1            -2.271965    -3.371203    -1.579886
  47         1            -0.733773    -4.190754    -1.356800
  48         1            -1.957020    -3.186616     1.957836
  49         1            -2.230687    -4.428209     0.731225
  50         1            -3.903186    -2.951250    -0.386388
  51         1            -4.340602    -3.373100     1.263342
  52         8            -1.100237     3.940923     0.146031
  53         1            -1.091545     3.319878    -0.621224
  54         1            -2.054373     4.002983     0.360668
  55         1            -0.372111     1.528333     2.266150
  56         8            -0.298996     1.593481     1.276395
  57         1            -0.563669     2.516698     1.023313
  58         8            -0.379283     1.460016     4.025671
  59         1             0.475161     1.054898     4.235756
  60         1            -1.037222     0.732416     4.186130
```

```
   61           7              2.403359    -1.993497    0.466028
   62           1              2.666501    -2.947874    0.684768
   63           6              3.468178    -1.073638    0.320164
   64           6              4.755763    -1.596146    0.133589
   65           6              3.273928     0.312432    0.386059
   66           6              5.839921    -0.730314    0.005082
   67           1              4.911021    -2.668665    0.088472
   68           6              4.377058     1.157771    0.243353
   69           1              2.284461     0.720818    0.542854
   70           6              5.663870     0.655520    0.052295
   71          70             -1.654524    -0.000679    0.077422
   72           1              6.508502     1.325343   -0.055222
   73           6              7.217838    -1.284287   -0.243076
   74           6              4.159965     2.643943    0.357539
   75           9              5.128078     3.347650   -0.273313
   76           9              2.971498     3.021351   -0.173324
   77           9              4.154992     3.052005    1.651563
   78           9              8.157958    -0.619639    0.470447
   79           9              7.308795    -2.593848    0.083051
   80           9              7.572160    -1.174054   -1.548070
   ---------------------------------------------------------------
 E(RTPSSh) = -2599.98257217 Hartree
·Zero-point correction = 0.616460 (Hartree/Particle)
 Thermal correction to Energy = 0.662615
 Thermal correction to Enthalpy = 0.663559
 Thermal correction to Gibbs Free Energy = 0.535498
 Sum of electronic and zero-point Energies = -2599.366112
 Sum of electronic and thermal Energies = -2599.319957
 Sum of electronic and thermal Enthalpies = -2599.319013
 Sum of electronic and thermal Free Energies = -2599.447074
```

Table S6. Optimised Cartesian coordinates obtained for [EuL²(H₂O)]·2H₂O SAP isomer with DFT calculations (0 imaginary frequencies).

```
-----------------------------------------------------------------------
Center      Atomic                      Coordinates (Angstroms)
Number      Number                  X             Y             Z
-----------------------------------------------------------------------
 1           7               1.541798     -2.702557     -1.471898
 2           6               2.564054     -3.348912     -0.599858
 3           6               1.993894     -3.822480      0.734377
 4           7               1.353540     -2.740438      1.539544
 5           6               0.427060     -3.349383      2.541786
 6           6              -0.894866     -3.789790      1.920840
 7           7              -1.688386     -2.676614      1.329338
 8           6              -2.745211     -3.246185      0.442727
 9           6              -2.207050     -3.691341     -0.916717
10           7              -1.510676     -2.612189     -1.677069
11           6              -0.599063     -3.212166     -2.698194
12           6               0.685508     -3.754369     -2.085358
13           6               2.208490     -1.876894     -2.518713
14           6               1.528754     -0.523603     -2.767899
15           8               0.360689     -0.348043     -2.258049
16           8               2.160927      0.328870     -3.426179
17           6               2.372081     -1.932730      2.242657
18           6               2.970954     -0.880725      1.322009
19           8               2.296440     -0.412698      0.378754
20           6              -2.313150     -1.860661      2.403008
21           6              -1.392883     -0.788217      3.003051
22           8              -1.637924     -0.343358      4.125575
23           8              -0.428315     -0.375469      2.223756
24           6              -2.478652     -1.731992     -2.362911
25           6              -3.069100     -0.710164     -1.405565
26           8              -2.393745     -0.287792     -0.441333
27           1               3.232620     -1.662732     -2.207647
28           1               2.276598     -2.422389     -3.469718
29           1               3.148542     -2.559219      2.702467
30           1               1.870116     -1.374484      3.039471
31           1              -2.712051     -2.490828      3.207740
32           1              -3.152090     -1.313435      1.961941
33           1              -1.928718     -1.148183     -3.109151
34           1              -3.259036     -2.305507     -2.881931
35           1               3.364824     -2.627085     -0.432730
36           1               3.018734     -4.214018     -1.103901
37           1               2.800327     -4.295972      1.312296
38           1               1.240797     -4.594319      0.564076
39           1               0.895574     -4.221981      3.017399
40           1               0.249878     -2.613729      3.327446
41           1              -1.486455     -4.303347      2.692881
42           1              -0.707699     -4.522484      1.132371
43           1              -3.228758     -4.110514      0.919848
44           1              -3.518919     -2.487390      0.315953
45           1              -1.496591     -4.509610     -0.783342
46           1              -3.040315     -4.095278     -1.508851
47           1              -0.361122     -2.431895     -3.422275
48           1              -1.106517     -4.025037     -3.235604
49           1               0.449228     -4.490114     -1.313520
50           1               1.245881     -4.288563     -2.866972
51           8               0.604956      2.081196      2.490146
52           1               0.206558      1.184461      2.642738
53           1              -0.026195      2.706406      2.876174
54           1               0.601232      1.832645     -0.763310
55           8               0.052482      1.403627     -0.046738
56           1               0.292615      1.820582      0.824196
57           8               1.528643      2.558368     -1.992625
58           1               0.955368      3.168151     -2.480004
59           1               1.711890      1.815708     -2.627723
60           7              -4.306220     -0.268099     -1.708454
```

```
61            1                    -4.747082    -0.720999    -2.501658
62            6                    -5.074113     0.762559    -1.116644
63            6                    -6.321373     1.026795    -1.706440
64            6                    -4.645684     1.507966    -0.006828
65            6                    -7.138155     2.028017    -1.194114
66            1                    -6.647648     0.452821    -2.568648
67            6                    -5.473173     2.510682     0.497203
68            1                    -3.685577     1.307963     0.446408
69            6                    -6.714576     2.775444    -0.089272
70            1                    -8.096565     2.231789    -1.658102
71            1                    -5.141299     3.093225     1.349564
72            6                    -7.614856     3.823603     0.496802
73            9                    -6.915681     4.832001     1.072757
74            9                    -8.426431     3.316457     1.463149
75            9                    -8.427552     4.376329    -0.436762
76            7                     4.214461    -0.460893     1.628429
77            6                     4.976797     0.590216     1.063700
78            6                     6.236372     0.825969     1.639283
79            6                     4.533689     1.378969    -0.010339
80            6                     7.048372     1.843577     1.151457
81            1                     6.578975     0.213533     2.468030
82            6                     5.355981     2.398055    -0.488857
83            1                     3.569973     1.201123    -0.463514
84            6                     6.609420     2.634553     0.083360
85            1                     8.021653     2.016085     1.596822
86            1                     5.012846     3.004918    -1.319625
87            6                     7.461529     3.765289    -0.414196
88            9                     8.783322     3.523911    -0.234328
89            9                     7.270376     4.003893    -1.734830
90            9                     7.191457     4.931826     0.230776
91            1                     4.662544    -0.943596     2.399969
92           63                    -0.058329    -1.029540    -0.034829
---------------------------------------------------------------------
E(RTPSSh) = -2807.55912756 Hartree
·Zero-point correction = 0.721262 (Hartree/Particle)
 Thermal correction to Energy = 0.773193
 Thermal correction to Enthalpy = 0.774137
 Thermal correction to Gibbs Free Energy = 0.631761
 Sum of electronic and zero-point Energies = -2806.838056
 Sum of electronic and thermal Energies = -2806.786125
 Sum of electronic and thermal Enthalpies = -2806.785180
 Sum of electronic and thermal Free Energies = -2806.927556
```

Table S7. Optimised Cartesian coordinates obtained for [GdL^2(H$_2$O)]·2H$_2$O SAP isomer with DFT calculations (0 imaginary frequencies).
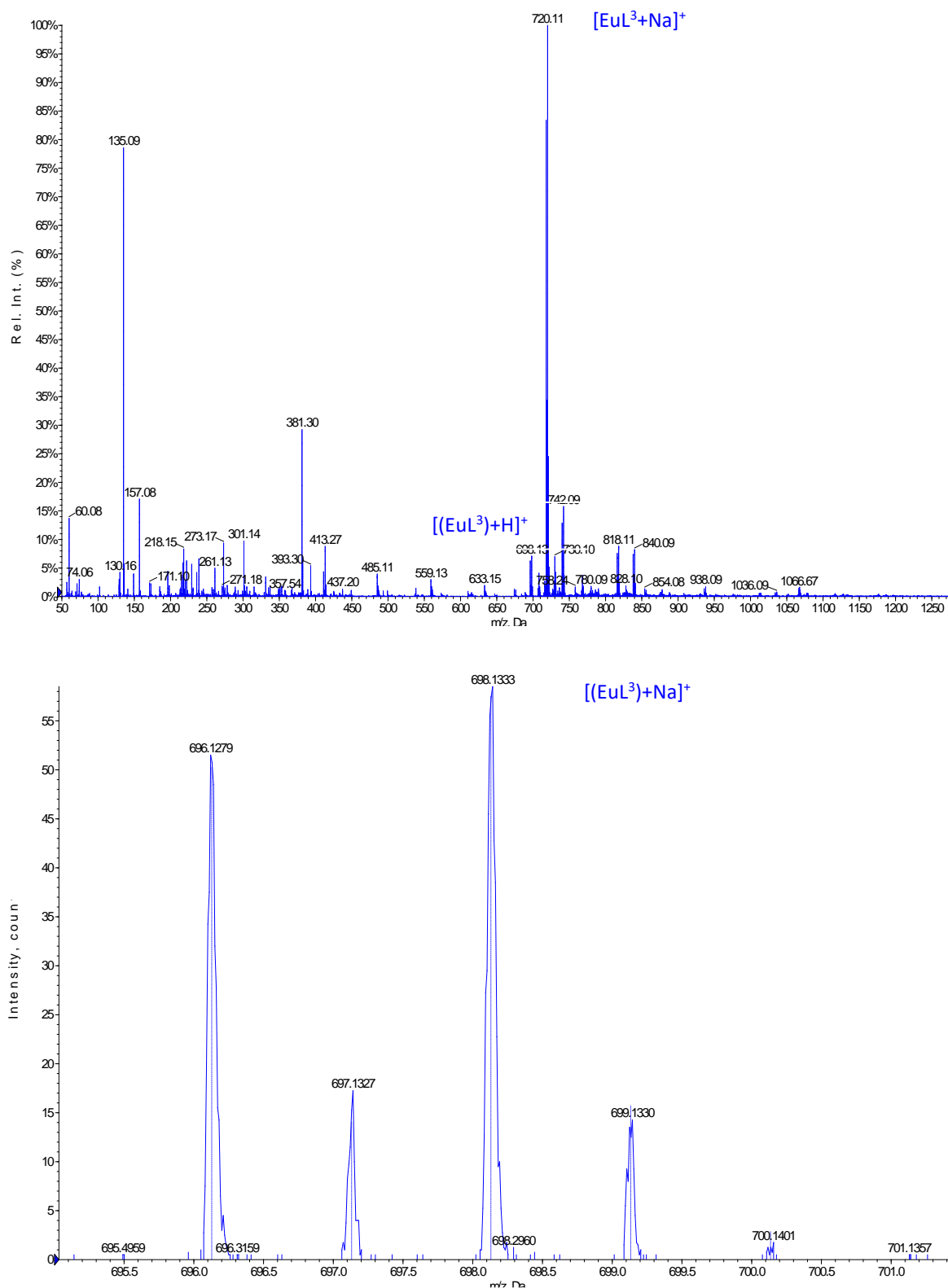
```
---------------------------------------------------------------------
Center      Atomic                  Coordinates (Angstroms)
Number      Number              X             Y             Z
---------------------------------------------------------------------
   1          7            1.547086     -2.698970     -1.473949
   2          6            2.568689     -3.350241     -0.604357
   3          6            1.996073     -3.832657      0.725754
   4          7            1.354848     -2.754916      1.535799
   5          6            0.430956     -3.368218      2.537372
   6          6           -0.891439     -3.807423      1.916949
   7          7           -1.681506     -2.693134      1.322262
   8          6           -2.736149     -3.263716      0.433150
   9          6           -2.193955     -3.703704     -0.926352
  10          7           -1.502203     -2.618776     -1.682238
  11          6           -0.590044     -3.210116     -2.708249
  12          6            0.699242     -3.749046     -2.102203
  13          6            2.213285     -1.859840     -2.509211
  14          6            1.512395     -0.519198     -2.764836
  15          8            0.349566     -0.352540     -2.240702
  16          8            2.125251      0.334414     -3.439693
  17          6            2.372340     -1.946443      2.238929
  18          6            2.958748     -0.884906      1.321701
  19          8            2.278177     -0.421886      0.380450
  20          6           -2.308168     -1.876443      2.394064
  21          6           -1.386459     -0.804683      2.991681
  22          8           -1.632359     -0.352607      4.111196
  23          8           -0.418025     -0.400245      2.213063
  24          6           -2.473260     -1.737297     -2.361254
  25          6           -3.056225     -0.716360     -1.399009
  26          8           -2.379193     -0.306087     -0.430978
  27          1            3.227817     -1.625879     -2.181096
  28          1            2.307127     -2.401997     -3.459914
  29          1            3.155423     -2.571021      2.689942
  30          1            1.871918     -1.396801      3.042554
  31          1           -2.707720     -2.505670      3.199162
  32          1           -3.146447     -1.329399      1.951795
  33          1           -1.927543     -1.152714     -3.109896
  34          1           -3.257697     -2.308976     -2.876143
  35          1            3.368665     -2.629077     -0.430572
  36          1            3.025177     -4.211403     -1.113302
  37          1            2.801117     -4.310369      1.302170
  38          1            1.242288     -4.602417      0.548989
  39          1            0.900939     -4.241745      3.009833
  40          1            0.253873     -2.634950      3.325279
  41          1           -1.484921     -4.316929      2.690156
  42          1           -0.706241     -4.543016      1.130853
  43          1           -3.217603     -4.130436      0.907864
  44          1           -3.512157     -2.507176      0.306777
  45          1           -1.478680     -4.517926     -0.793584
  46          1           -3.024058     -4.110713     -1.520823
  47          1           -0.358124     -2.426011     -3.430018
  48          1           -1.094812     -4.023310     -3.247686
  49          1            0.469019     -4.496719     -1.340256
  50          1            1.264031     -4.268108     -2.890720
  51          8            0.626947      2.047482      2.496740
  52          1            0.223901      1.152257      2.645696
  53          1            0.004400      2.674100      2.894211
  54          1            0.585646      1.803122     -0.754182
  55          8            0.042976      1.370437     -0.035989
  56          1            0.292267      1.783674      0.833735
  57          8            1.506702      2.552070     -1.981650
  58          1            0.931105      3.169915     -2.455900
  59          1            1.683457      1.817861     -2.627945
  60          7           -4.288461     -0.261174     -1.702572
```

```
61         1              -4.731395   -0.706317   -2.499016
62         6              -5.047157    0.775586   -1.109820
63         6              -6.291865    1.051500   -1.699672
64         6              -4.611775    1.516693    0.000154
65         6              -7.098876    2.060785   -1.187785
66         1              -6.623674    0.480234   -2.561568
67         6              -5.429500    2.527673    0.503717
68         1              -3.653778    1.306998    0.453559
69         6              -6.668020    2.804557   -0.083255
70         1              -8.055210    2.273743   -1.651948
71         1              -5.092176    3.107266    1.355929
72         6              -7.557969    3.862182    0.501564
73         9              -6.849146    4.861300    1.081826
74         9              -8.379084    3.362906    1.463960
75         9              -8.360724    4.426092   -0.433959
76        64              -0.057644   -1.055020   -0.033491
77         7               4.197812   -0.452112    1.628240
78         6               4.948516    0.607769    1.064413
79         6               6.213177    0.845536    1.627715
80         6               4.488538    1.403913    0.003007
81         6               7.013819    1.872006    1.139533
82         1               6.568901    0.227644    2.446782
83         6               5.299515    2.431631   -0.476128
84         1               3.520197    1.225071   -0.439614
85         6               6.558400    2.669778    0.083436
86         1               7.991227    2.046071    1.575106
87         1               4.942718    3.043783   -1.297222
88         6               7.398613    3.809010   -0.414904
89         9               8.723222    3.578428   -0.241935
90         9               7.199145    4.049319   -1.734077
91         9               7.121606    4.971689    0.234094
92         1               4.652983   -0.933697    2.396349
---------------------------------------------------------------
E(RTPSSh) = -2808.14952375 Hartree
·Zero-point correction = 0.721143 (Hartree/Particle)
Thermal correction to Energy = 0.773138
Thermal correction to Enthalpy = 0.774082
Thermal correction to Gibbs Free Energy = 0.631030
Sum of electronic and zero-point Energies = -2807.428380
Sum of electronic and thermal Energies = -2807.376386
Sum of electronic and thermal Enthalpies = -2807.375442
Sum of electronic and thermal Free Energies = -2807.518493
```

Table S8. Optimised Cartesian coordinates obtained for [LuL^2(H$_2$O)]·2H$_2$O SAP isomer with DFT calculations (0 imaginary frequencies).

Center Number	Atomic Number	Coordinates (Angstroms)		
		X	Y	Z
1	7	1.606822	-2.718595	-1.260180
2	6	2.544677	-3.370397	-0.303116
3	6	1.847544	-3.780151	0.988546
4	7	1.173091	-2.643687	1.680895
5	6	0.179387	-3.183991	2.655185
6	6	-1.102230	-3.631292	1.964457
7	7	-1.794115	-2.532846	1.231794
8	6	-2.792290	-3.132361	0.300115
9	6	-2.142002	-3.634382	-0.985588
10	7	-1.366197	-2.581491	-1.703177
11	6	-0.414976	-3.223733	-2.658590
12	6	0.817247	-3.772450	-1.954660
13	6	2.363482	-1.898908	-2.245771
14	6	1.655623	-0.597616	-2.634316
15	8	0.486044	-0.394240	-2.138498
16	8	2.268798	0.199820	-3.373206
17	6	2.160354	-1.809841	2.401007
18	6	2.807120	-0.812590	1.455899
19	8	2.175286	-0.406048	0.456202
20	6	-2.474946	-1.633132	2.199156
21	6	-1.554443	-0.563108	2.793950
22	8	-1.863381	-0.009208	3.850442
23	8	-0.500134	-0.274248	2.077874
24	6	-2.270090	-1.690150	-2.462614
25	6	-2.877707	-0.646775	-1.543507
26	8	-2.230811	-0.244316	-0.551894
27	1	3.320071	-1.608243	-1.806376
28	1	2.592078	-2.472597	-3.153873
29	1	2.906865	-2.416828	2.930448
30	1	1.619886	-1.207655	3.138539
31	1	-2.954153	-2.198245	3.008183
32	1	-3.256800	-1.087695	1.662310
33	1	-1.664024	-1.135168	-3.185902
34	1	-3.037086	-2.252652	-3.011639
35	1	3.356011	-2.671635	-0.093338
36	1	3.007411	-4.262138	-0.748949
37	1	2.579813	-4.252870	1.658232
38	1	1.086248	-4.532651	0.773687
39	1	0.600770	-4.036183	3.205404
40	1	-0.037049	-2.404414	3.386220
41	1	-1.776126	-4.063014	2.718267
42	1	-0.880873	-4.426315	1.249390
43	1	-3.319005	-3.970716	0.776645
44	1	-3.548203	-2.377104	0.080468
45	1	-1.452925	-4.448960	-0.754004
46	1	-2.917605	-4.053127	-1.641874
47	1	-0.120044	-2.468323	-3.387809
48	1	-0.909046	-4.038409	-3.205367
49	1	0.527307	-4.524539	-1.217254
50	1	1.444625	-4.287523	-2.696703
51	8	0.585860	2.154588	2.417830
52	1	0.154682	1.273963	2.564738
53	1	-0.056517	2.803321	2.741572
54	1	0.654958	1.731348	-0.816416
55	8	0.078919	1.334913	-0.106534
56	1	0.303916	1.782043	0.750758
57	8	1.647611	2.480399	-2.016360
58	1	1.090187	3.095308	-2.515431
59	1	1.831925	1.732141	-2.642719
60	7	-4.095109	-0.177241	-1.882187

```
61           1                        -4.523127   -0.615567   -2.690776
62           6                        -4.884657    0.819852   -1.259961
63           6                        -6.171151    1.018399   -1.787096
64           6                        -4.441212    1.591355   -0.173491
65           6                        -7.015187    1.972799   -1.230103
66           1                        -6.510613    0.425389   -2.630922
67           6                        -5.296216    2.545234    0.376273
68           1                        -3.449602    1.446804    0.229672
69           6                        -6.579805    2.739362   -0.143484
70           1                        -8.006134    2.122640   -1.643270
71           1                        -4.953093    3.145124    1.212137
72           6                        -7.504771    3.730947    0.499793
73           9                        -6.838420    4.806846    0.986421
74           9                        -8.179965    3.190956    1.549703
75           9                        -8.440938    4.191567   -0.365035
76           7                         4.036121   -0.369356    1.784895
77           6                         4.821532    0.636178    1.168492
78           6                         6.117092    0.821183    1.678199
79           6                         4.360908    1.434764    0.109140
80           6                         6.948110    1.796524    1.137507
81           1                         6.474458    0.201036    2.494650
82           6                         5.202487    2.409470   -0.423790
83           1                         3.368060    1.301766   -0.292594
84           6                         6.492819    2.594564    0.081671
85           1                         7.949196    1.929762    1.531641
86           1                         4.841761    3.021773   -1.243076
87           6                         7.365994    3.682073   -0.472460
88           9                         8.684246    3.402778   -0.326243
89           9                         7.141190    3.891935   -1.792968
90           9                         7.152624    4.873683    0.147573
91           1                         4.461094   -0.808687    2.594647
92          71                        -0.050055   -1.023279   -0.030993
-----------------------------------------------------------------
E(RTPSSh) = -2812.20742053 Hartree
·Zero-point correction = 0.722318 (Hartree/Particle)
Thermal correction to Energy = 0.773837
Thermal correction to Enthalpy = 0.774781
Thermal correction to Gibbs Free Energy = 0.633893
Sum of electronic and zero-point Energies = -2811.485102
Sum of electronic and thermal Energies = -2811.433583
Sum of electronic and thermal Enthalpies = -2811.432639
Sum of electronic and thermal Free Energies = -2811.573527
```

Table S9. Optimised Cartesian coordinates obtained for [TbL^2(H$_2$O)]·2H$_2$O SAP isomer with DFT calculations (0 imaginary frequencies).

```
------------------------------------------------------------------------
Center      Atomic                    Coordinates (Angstroms)
Number      Number              X              Y              Z
------------------------------------------------------------------------
   1          7          1.550475     -2.704431     -1.456513
   2          6          2.570678     -3.353278     -0.584479
   3          6          1.992588     -3.830230      0.744239
   4          7          1.344038     -2.748174      1.542175
   5          6          0.417298     -3.359446      2.541975
   6          6         -0.899779     -3.800789      1.913318
   7          7         -1.685113     -2.685712      1.314394
   8          6         -2.739628     -3.255087      0.425164
   9          6         -2.194086     -3.697905     -0.931467
  10          7         -1.489556     -2.616663     -1.680867
  11          6         -0.576860     -3.215605     -2.701095
  12          6          0.705272     -3.756840     -2.083929
  13          6          2.218815     -1.867444     -2.492187
  14          6          1.520550     -0.525901     -2.747059
  15          8          0.356426     -0.359449     -2.225020
  16          8          2.134595      0.328135     -3.419949
  17          6          2.356002     -1.933460      2.246213
  18          6          2.944792     -0.877718      1.324459
  19          8          2.267135     -0.422019      0.377440
  20          6         -2.311689     -1.865746      2.383813
  21          6         -1.390088     -0.791707      2.976043
  22          8         -1.636108     -0.331900      4.092333
  23          8         -0.419378     -0.393801      2.196588
  24          6         -2.450445     -1.728982     -2.366463
  25          6         -3.035061     -0.708271     -1.405712
  26          8         -2.361312     -0.303163     -0.433071
  27          1          3.233907     -1.635338     -2.164433
  28          1          2.311436     -2.409689     -3.442964
  29          1          3.137892     -2.553807      2.704995
  30          1          1.849934     -1.379566      3.043391
  31          1         -2.709639     -2.492195      3.191860
  32          1         -3.151241     -1.321274      1.940964
  33          1         -1.895158     -1.145796     -3.109135
  34          1         -3.233662     -2.295667     -2.888584
  35          1          3.370471     -2.631950     -0.410394
  36          1          3.028259     -4.215710     -1.090200
  37          1          2.795047     -4.301809      1.329141
  38          1          1.242059     -4.603217      0.567773
  39          1          0.886331     -4.230897      3.019012
  40          1          0.234931     -2.624624      3.327222
  41          1         -1.498698     -4.311522      2.681453
  42          1         -0.708192     -4.534955      1.127327
  43          1         -3.224348     -4.119695      0.900346
  44          1         -3.513402     -2.496849      0.295641
  45          1         -1.485895     -4.517839     -0.795793
  46          1         -3.023516     -4.097642     -1.531679
  47          1         -0.337826     -2.435759     -3.425168
  48          1         -1.083055     -4.028261     -3.239889
  49          1          0.466965     -4.499019     -1.318952
  50          1          1.274434     -4.282405     -2.864993
  51          8          0.588993      2.071727      2.496538
  52          1          0.203002      1.169325      2.644315
  53          1         -0.064056      2.685831      2.863666
  54          1          0.583367      1.793754     -0.756339
  55          8          0.045963      1.356351     -0.037091
  56          1          0.282238      1.780773      0.830674
  57          8          1.484924      2.554128     -1.990897
  58          1          0.881098      3.142200     -2.468054
  59          1          1.675620      1.813709     -2.626254
  60          7         -4.264842     -0.249539     -1.713571
```

```
61          1                  -4.704002   -0.690787   -2.514251
62          6                  -5.027081    0.783496   -1.118996
63          6                  -6.268417    1.062690   -1.714412
64          6                  -4.598947    1.516985   -0.001280
65          6                  -7.079451    2.067474   -1.200029
66          1                  -6.594558    0.497239   -2.582303
67          6                  -5.420611    2.523463    0.504801
68          1                  -3.643591    1.304710    0.456433
69          6                  -6.655942    2.803423   -0.087481
70          1                  -8.033242    2.282934   -1.668220
71          1                  -5.088971    3.097050    1.363301
72          6                  -7.550399    3.855613    0.500259
73          9                  -6.845819    4.853595    1.087671
74          9                  -8.372697    3.349174    1.457897
75          9                  -8.352115    4.422229   -0.434474
76          7                   4.182515   -0.442326    1.632186
77          6                   4.935489    0.614060    1.064933
78          6                   6.191261    0.864380    1.642701
79          6                   4.487155    1.394147   -0.013125
80          6                   6.994151    1.888333    1.153280
81          1                   6.538034    0.258021    2.474182
82          6                   5.300232    2.419959   -0.493112
83          1                   3.526721    1.204435   -0.468485
84          6                   6.549730    2.671219    0.081447
85          1                   7.964633    2.072148    1.600236
86          1                   4.952953    3.020492   -1.326746
87          6                   7.391927    3.808722   -0.417542
88          9                   8.715834    3.578283   -0.238504
89          9                   7.197886    4.045004   -1.738127
90          9                   7.112948    4.973360    0.227099
91          1                   4.633434   -0.916506    2.407353
92         65                  -0.055405   -1.053079   -0.032550
```

```
E(RTPSSh) = -2808.73842926 Hartree
·Zero-point correction = 0.721424 (Hartree/Particle)
Thermal correction to Energy = 0.773303
Thermal correction to Enthalpy = 0.774248
Thermal correction to Gibbs Free Energy = 0.631961
Sum of electronic and zero-point Energies = -2808.017005
Sum of electronic and thermal Energies = -2807.965126
Sum of electronic and thermal Enthalpies = -2807.964182
Sum of electronic and thermal Free Energies = -2808.106469
```

Table S10. Optimised Cartesian coordinates obtained for [TmL^2(H$_2$O)]·2H$_2$O SAP isomer with DFT calculations (0 imaginary frequencies).

```
--------------------------------------------------------------------
Center    Atomic                      Coordinates (Angstroms)
Number    Number              X              Y              Z
--------------------------------------------------------------------
    1        7            1.562805      -2.714277      -1.420452
    2        6            2.577402      -3.365678      -0.544885
    3        6            1.983276      -3.843249       0.775016
    4        7            1.320317      -2.757853       1.555104
    5        6            0.391402      -3.367878       2.551973
    6        6           -0.916981      -3.811415       1.910475
    7        7           -1.684436      -2.694627       1.291546
    8        6           -2.733767      -3.266454       0.398502
    9        6           -2.172534      -3.711765      -0.949580
   10        7           -1.454485      -2.629443      -1.683529
   11        6           -0.538849      -3.229286      -2.699445
   12        6            0.737823      -3.768284      -2.071633
   13        6            2.236465      -1.862610      -2.438521
   14        6            1.503062      -0.547464      -2.719327
   15        8            0.352008      -0.387216      -2.167274
   16        8            2.078178       0.297487      -3.435992
   17        6            2.319936      -1.929143       2.259728
   18        6            2.894100      -0.871350       1.333334
   19        8            2.214125      -0.441899       0.375844
   20        6           -2.315005      -1.861293       2.347750
   21        6           -1.388364      -0.785725       2.924058
   22        8           -1.636498      -0.294552       4.026540
   23        8           -0.403338      -0.421533       2.146285
   24        6           -2.404719      -1.733087      -2.371757
   25        6           -2.975916      -0.709083      -1.408752
   26        8           -2.304177      -0.333281      -0.423329
   27        1            3.230295      -1.592011      -2.076083
   28        1            2.381335      -2.405006      -3.382546
   29        1            3.109199      -2.537367       2.721918
   30        1            1.804679      -1.378224       3.053119
   31        1           -2.715735      -2.476377       3.163003
   32        1           -3.152111      -1.320433       1.896711
   33        1           -1.843303      -1.155941      -3.114136
   34        1           -3.194653      -2.290890      -2.893096
   35        1            3.376055      -2.645651      -0.360233
   36        1            3.039459      -4.225863      -1.049898
   37        1            2.777446      -4.310041       1.374753
   38        1            1.236851      -4.618147       0.589338
   39        1            0.859544      -4.235922       3.035800
   40        1            0.200023      -2.630921       3.332961
   41        1           -1.531008      -4.311698       2.673346
   42        1           -0.718076      -4.552655       1.133164
   43        1           -3.222632      -4.128693       0.873281
   44        1           -3.506159      -2.508745       0.258708
   45        1           -1.467444      -4.532775      -0.804210
   46        1           -2.993387      -4.108508      -1.563273
   47        1           -0.295986      -2.451762      -3.424642
   48        1           -1.042419      -4.042384      -3.239812
   49        1            0.495079      -4.520745      -1.318225
   50        1            1.323387      -4.279742      -2.849808
   51        8            0.606849       2.041341       2.488840
   52        1            0.222240       1.138610       2.632392
   53        1           -0.054858       2.652041       2.846131
   54        1            0.555236       1.721363      -0.762970
   55        8            0.034133       1.281926      -0.034897
   56        1            0.281353       1.713132       0.825041
   57        8            1.429114       2.524552      -2.006851
   58        1            0.799759       3.099872      -2.466221
   59        1            1.617054       1.788936      -2.647790
   60        7           -4.190878      -0.217911      -1.724786
```

```
61          1                -4.630151   -0.639628   -2.535895
62          6                -4.938508    0.822586   -1.124948
63          6                -6.172741    1.126625   -1.723003
64          6                -4.502842    1.540067    0.000130
65          6                -6.969209    2.140532   -1.203883
66          1                -6.504887    0.572784   -2.596098
67          6                -5.309987    2.555850    0.511046
68          1                -3.552984    1.308104    0.459783
69          6                -6.538113    2.860690   -0.083900
70          1                -7.917525    2.375222   -1.673971
71          1                -4.972590    3.117323    1.375253
72          6                -7.417911    3.922785    0.508122
73          9                -6.700433    4.899072    1.115891
74          9                -8.260562    3.420372    1.450109
75          9                -8.198250    4.517095   -0.427589
76          7                 4.119669   -0.406068    1.645229
77          6                 4.855309    0.659106    1.071788
78          6                 6.110876    0.927493    1.641683
79          6                 4.388968    1.432271   -0.003459
80          6                 6.895715    1.962827    1.146892
81          1                 6.471855    0.326199    2.470766
82          6                 5.183802    2.469682   -0.488792
83          1                 3.428342    1.228646   -0.452188
84          6                 6.433237    2.739027    0.077828
85          1                 7.866267    2.160876    1.587551
86          1                 4.821741    3.065030   -1.319850
87          6                 7.255570    3.888714   -0.426311
88          9                 8.583618    3.679229   -0.252312
89          9                 7.052518    4.119888   -1.746469
90          9                 6.961106    5.049931    0.217658
91          1                 4.575161   -0.864075    2.427414
92         69                -0.052196   -1.089485   -0.029145
----------------------------------------------------------------
```

E(RTPSSh) = -2811.07064790 Hartree
·Zero-point correction = 0.721356 (Hartree/Particle)
Thermal correction to Energy = 0.773351
Thermal correction to Enthalpy = 0.774295
Thermal correction to Gibbs Free Energy = 0.630596
Sum of electronic and zero-point Energies = -2810.349292
Sum of electronic and thermal Energies = -2810.297297
Sum of electronic and thermal Enthalpies = -2810.296353
Sum of electronic and thermal Free Energies = -2810.440052

Table S11. Optimised Cartesian coordinates obtained for [YbL^2(H$_2$O)]·2H$_2$O SAP isomer with DFT calculations (0 imaginary frequencies).

Center Number	Atomic Number	Coordinates (Angstroms)		
		X	Y	Z
1	7	1.565137	-2.718457	-1.409425
2	6	2.578477	-3.368976	-0.532094
3	6	1.980732	-3.845333	0.786246
4	7	1.313252	-2.758593	1.560312
5	6	0.382529	-3.367453	2.555778
6	6	-0.923100	-3.811225	1.909691
7	7	-1.686052	-2.693841	1.286217
8	6	-2.734594	-3.265901	0.392699
9	6	-2.169836	-3.713641	-0.952720
10	7	-1.446821	-2.632633	-1.683480
11	6	-0.529984	-3.234858	-2.696557
12	6	0.743960	-3.773542	-2.063570
13	6	2.240245	-1.866118	-2.425464
14	6	1.500263	-0.556926	-2.714085
15	8	0.353095	-0.395523	-2.154313
16	8	2.066418	0.283839	-3.442538
17	6	2.309167	-1.925913	2.265413
18	6	2.881187	-0.868966	1.337214
19	8	2.201669	-0.446724	0.376170
20	6	-2.317181	-1.856981	2.339176
21	6	-1.388909	-0.781393	2.911554
22	8	-1.637088	-0.282693	4.010665
23	8	-0.400587	-0.425623	2.134115
24	6	-2.393271	-1.734311	-2.374237
25	6	-2.961435	-0.708478	-1.411874
26	8	-2.290590	-0.339358	-0.423370
27	1	3.229370	-1.587279	-2.056253
28	1	2.395862	-2.410243	-3.366736
29	1	3.099391	-2.530808	2.730277
30	1	1.790628	-1.374438	3.056313
31	1	-2.718826	-2.469093	3.156189
32	1	-3.153460	-1.316704	1.886044
33	1	-1.829391	-1.159731	-3.116611
34	1	-3.184656	-2.290054	-2.895507
35	1	3.376381	-2.648508	-0.345851
36	1	3.042065	-4.229041	-1.035831
37	1	2.773219	-4.309312	1.390317
38	1	1.236179	-4.621767	0.599387
39	1	0.849511	-4.234736	3.042018
40	1	0.188500	-2.629704	3.335342
41	1	-1.541321	-4.310059	2.670069
42	1	-0.721204	-4.553106	1.133762
43	1	-3.225456	-4.126612	0.868102
44	1	-3.505715	-2.507544	0.249664
45	1	-1.466885	-4.535908	-0.804140
46	1	-2.988964	-4.108960	-1.569577
47	1	-0.284609	-2.459147	-3.422845
48	1	-1.033039	-4.048358	-3.236740
49	1	0.498101	-4.525457	-1.310561
50	1	1.333246	-4.285175	-2.838790
51	8	0.618731	2.033345	2.483631
52	1	0.230353	1.132427	2.627049
53	1	-0.040047	2.646650	2.841879
54	1	0.549751	1.704688	-0.767858
55	8	0.031846	1.266859	-0.036861
56	1	0.284590	1.698791	0.820803
57	8	1.419171	2.513486	-2.014910
58	1	0.787138	3.088020	-2.471559
59	1	1.605354	1.778186	-2.656478
60	7	-4.172366	-0.209086	-1.730305

```
61              1                  -4.611670   -0.625972   -2.543905
62              6                  -4.916479    0.832888   -1.128637
63              6                  -6.149332    1.142742   -1.726572
64              6                  -4.478764    1.546208   -0.001712
65              6                  -6.942458    2.158196   -1.205360
66              1                  -6.483119    0.592018   -2.601011
67              6                  -5.282604    2.563547    0.511340
68              1                  -3.529944    1.309791    0.457812
69              6                  -6.509390    2.874085   -0.083388
70              1                  -7.889742    2.397333   -1.675293
71              1                  -4.943657    3.121775    1.377029
72              6                  -7.385922    3.937677    0.510794
73              9                  -6.665706    4.908325    1.124286
74              9                  -8.233177    3.435140    1.448588
75              9                  -8.161339    4.539209   -0.424419
76              7                   4.103514   -0.396321    1.650521
77              6                   4.835433    0.670296    1.074944
78              6                   6.092270    0.941092    1.640840
79              6                   4.363744    1.443172    0.001842
80              6                   6.873187    1.978421    1.143963
81              1                   6.457411    0.340110    2.468307
82              6                   5.154704    2.482483   -0.485687
83              1                   3.401877    1.238009   -0.443473
84              6                   6.405510    2.754142    0.076826
85              1                   7.844769    2.178371    1.581473
86              1                   4.788427    3.077500   -1.315123
87              6                   7.223578    3.905899   -0.429516
88              9                   8.552545    3.700416   -0.257901
89              9                   7.017349    4.135698   -1.749442
90              9                   6.926893    5.066654    0.214281
91              1                   4.559710   -0.850099    2.434759
92             70                  -0.051822   -1.096117   -0.028424
---------------------------------------------------------------------
E(RTPSSh) = -2811.65381840 Hartree
·Zero-point correction = 0.721358 (Hartree/Particle)
Thermal correction to Energy = 0.773368
Thermal correction to Enthalpy = 0.774312
Thermal correction to Gibbs Free Energy = 0.630300
Sum of electronic and zero-point Energies = -2810.932461
Sum of electronic and thermal Energies = -2810.880451
Sum of electronic and thermal Enthalpies = -2810.879507
Sum of electronic and thermal Free Energies = -2811.023519
```

Table S12. Optimised Cartesian coordinates obtained for [EuL³(H₂O)]·2H₂O SAP isomer with DFT calculations (0 imaginary frequencies).

```
-----------------------------------------------------------------------
Center      Atomic                    Coordinates (Angstroms)
Number      Number              X              Y              Z
-----------------------------------------------------------------------
   1          7          -3.547235      -1.388427      -0.412433
   2          6          -4.723039      -0.483682      -0.557246
   3          6          -4.389671       0.774938      -1.351625
   4          7          -3.314394       1.595585      -0.730460
   5          6          -2.780287       2.560858      -1.729750
   6          6          -1.843874       1.897632      -2.733632
   7          7          -0.647597       1.263340      -2.110514
   8          6          -0.053292       0.302783      -3.083974
   9          6          -0.806746      -1.026056      -3.133985
  10          7          -0.868070      -1.734070      -1.825085
  11          6          -1.964525      -2.747772      -1.835773
  12          6          -3.348003      -2.127772      -1.688986
  13          6          -3.753278      -2.325498       0.725421
  14          6          -2.474695      -2.632654       1.518322
  15          8          -1.367064      -2.182853       1.049091
  16          8          -2.594728      -3.272316       2.586178
  17          6          -3.855703       2.330653       0.439401
  18          6          -3.923447       1.474441       1.712696
  19          8          -4.837605       1.656746       2.523732
  20          8          -2.927897       0.646565       1.865649
  21          6           0.350005       2.303149      -1.744349
  22          6           0.082484       2.998827      -0.398647
  23          8           0.517904       4.138850      -0.216923
  24          8          -0.548690       2.278044       0.484786
  25          6           0.403471      -2.423392      -1.532308
  26          6           1.439670      -1.464067      -0.971159
  27          8           1.084223      -0.467385      -0.310971
  28          1          -4.453981      -1.873784       1.430428
  29          1          -4.203626      -3.269948       0.389119
  30          1          -4.841531       2.761631       0.222703
  31          1          -3.164046       3.149443       0.662599
  32          1           0.445863       3.061645      -2.531875
  33          1           1.320768       1.809488      -1.633632
  34          1           0.213839      -3.147897      -0.733390
  35          1           0.785868      -2.969798      -2.406004
  36          1          -5.068198      -0.213431       0.442016
  37          1          -5.556520      -1.001129      -1.054565
  38          1          -5.305750       1.374774      -1.460970
  39          1          -4.070336       0.506431      -2.361257
  40          1          -3.599087       3.045028      -2.282008
  41          1          -2.253121       3.345598      -1.184464
  42          1          -1.527278       2.649530      -3.471528
  43          1          -2.382167       1.124576      -3.287282
  44          1          -0.045132       0.731375      -4.096524
  45          1           0.989912       0.142940      -2.807709
  46          1          -1.834667      -0.850215      -3.458360
  47          1          -0.341610      -1.667960      -3.896598
  48          1          -1.781448      -3.430848      -1.006001
  49          1          -1.939004      -3.334015      -2.765720
  50          1          -3.538098      -1.436182      -2.513198
  51          1          -4.095060      -2.930752      -1.778723
  52          8          -0.952338       2.399104       3.171824
  53          1          -0.754682       2.616819       2.226585
  54          1          -1.819407       1.959299       3.095252
  55          1          -0.269257      -0.784886       2.940480
  56          8          -0.064824      -0.014578       2.338302
  57          1          -0.246888       0.817383       2.844156
  58          8          -0.557908      -2.111301       3.995963
  59          1           0.237339      -2.659288       3.920471
  60          1          -1.256659      -2.627098       3.509458
```

```
    61            63                    -1.329730    0.042089    0.208701
    62             7                     2.731451   -1.799435   -1.188530
    63             1                     2.880815   -2.609232   -1.780608
    64             6                     3.912940   -1.190046   -0.705751
    65             6                     5.128631   -1.706285   -1.183125
    66             6                     3.912396   -0.131271    0.218049
    67             6                     6.336287   -1.169642   -0.748233
    68             1                     5.128827   -2.528345   -1.892642
    69             6                     5.128056    0.396166    0.648224
    70             1                     2.979357    0.264523    0.591786
    71             6                     6.339551   -0.115298    0.170565
    72             1                     7.270871   -1.574798   -1.118696
    73             1                     5.127823    1.207714    1.368114
    74             6                     7.630276    0.505248    0.618120
    75             9                     7.620936    0.791721    1.944650
    76             9                     7.879427    1.679143   -0.022165
    77             9                     8.696124   -0.297942    0.386957
    ---------------------------------------------------------------------
    E(RTPSSh) = -2258.858775 Hartree
   ·Zero-point correction = 0.611529 (Hartree/Particle)
    Thermal correction to Energy = 0.654424
    Thermal correction to Enthalpy = 0.655368
    Thermal correction to Gibbs Free Energy = 0.535133
    Sum of electronic and zero-point Energies = -2258.247246
    Sum of electronic and thermal Energies = -2258.204351
    Sum of electronic and thermal Enthalpies = -2258.203407
    Sum of electronic and thermal Free Energies = -2258.323642
```

Table S13. Optimised Cartesian coordinates obtained for [GdL^3(H$_2$O)]·2H$_2$O SAP isomer with DFT calculations (0 imaginary frequencies).

Center Number	Atomic Number	Coordinates (Angstroms)		
		X	Y	Z
1	7	-3.541087	-1.492103	0.006239
2	6	-4.724658	-0.616550	-0.228852
3	6	-4.480957	0.424733	-1.315375
4	7	-3.383001	1.374007	-0.989811
5	6	-2.908776	2.038166	-2.235455
6	6	-2.004463	1.138300	-3.069183
7	7	-0.763838	0.710039	-2.364743
8	6	-0.162120	-0.432272	-3.109079
9	6	-0.886003	-1.752964	-2.845681
10	7	-0.927671	-2.137431	-1.407175
11	6	-2.024756	-3.122387	-1.165228
12	6	-3.400506	-2.467261	-1.106023
13	6	-3.671581	-2.184343	1.316906
14	6	-2.360300	-2.272885	2.110016
15	8	-1.282384	-1.914374	1.510184
16	8	-2.425418	-2.661077	3.296975
17	6	-3.830303	2.390480	-0.000675
18	6	-3.444078	2.071293	1.450815
19	8	-3.621483	2.964784	2.302765
20	8	-2.924747	0.915237	1.678096
21	6	0.198484	1.838704	-2.283177
22	6	-0.051955	2.808790	-1.113856
23	8	0.353063	3.971150	-1.208661
24	8	-0.634535	2.293663	-0.068861
25	6	0.353935	-2.737681	-0.982647
26	6	1.392052	-1.671280	-0.670301
27	8	1.037606	-0.546766	-0.262449
28	1	-4.376045	-1.630018	1.939813
29	1	-4.083566	-3.195721	1.193554
30	1	-4.916620	2.547465	-0.055752
31	1	-3.359571	3.346100	-0.239558
32	1	0.232861	2.406436	-3.222040
33	1	1.194235	1.417201	-2.112047
34	1	0.181144	-3.259152	-0.035648
35	1	0.728781	-3.467835	-1.713802
36	1	-4.942873	-0.112271	0.713295
37	1	-5.605493	-1.215111	-0.505093
38	1	-5.418127	0.975867	-1.486205
39	1	-4.234177	-0.066248	-2.259513
40	1	-3.757459	2.352131	-2.860960
41	1	-2.371389	2.943704	-1.950398
42	1	-1.742729	1.667127	-3.998106
43	1	-2.548051	0.237786	-3.364403
44	1	-0.176421	-0.242300	-4.192215
45	1	0.887147	-0.507860	-2.819464
46	1	-1.917365	-1.686245	-3.198258
47	1	-0.403380	-2.542958	-3.439814
48	1	-1.814556	-3.615820	-0.215284
49	1	-2.031596	-3.893047	-1.948794
50	1	-3.606147	-1.945593	-2.043733
51	1	-4.158305	-3.260402	-1.016257
52	8	-0.753390	3.186218	2.527623
53	1	-0.686326	3.131777	1.543775
54	1	-1.722407	3.184045	2.679760
55	1	-0.250385	-0.023882	2.991231
56	8	-0.080372	0.582569	2.219033
57	1	-0.316494	1.506152	2.506155
58	8	-0.456592	-1.081548	4.355736
59	1	0.374181	-1.577322	4.403426
60	1	-1.117623	-1.743972	4.018618

```
        61           7                    2.685285   -2.041438   -0.801519
        62           1                    2.842338   -2.972687   -1.171470
        63           6                    3.860532   -1.327776   -0.467290
        64           6                    5.081950   -1.982693   -0.701003
        65           6                    3.851279   -0.034056    0.079710
        66           6                    6.283395   -1.353285   -0.395787
        67           1                    5.089728   -2.985898   -1.116513
        68           6                    5.062744    0.586700    0.382150
        69           1                    2.915974    0.472689    0.266381
        70           6                    6.277609   -0.063551    0.148656
        71           1                    7.220934   -1.868419   -0.573009
        72           1                    5.054757    1.583192    0.809817
        73           6                    7.575352    0.635279    0.429601
        74           9                    7.454011    1.568342    1.404923
        75           9                    8.054079    1.282703   -0.666864
        76           9                    8.545619   -0.229917    0.816265
        77          64                   -1.339866    0.037497    0.175152
     -----------------------------------------------------------------
     E(RTPSSh) = -2259.4519863 Hartree
    ·Zero-point correction = 0.611626 (Hartree/Particle)
     Thermal correction to Energy = 0.654102
     Thermal correction to Enthalpy = 0.655046
     Thermal correction to Gibbs Free Energy = 0.537125
     Sum of electronic and zero-point Energies = -2258.840360
     Sum of electronic and thermal Energies = -2258.797884
     Sum of electronic and thermal Enthalpies = -2258.796940
     Sum of electronic and thermal Free Energies = -2258.914861
```

Table S14. Optimised Cartesian coordinates obtained for [LuL^3(H$_2$O)]·2H$_2$O SAP isomer with DFT calculations (0 imaginary frequencies).

Center Number	Atomic Number	X	Y	Z
1	7	−3.515266	−1.405720	0.060769
2	6	−4.696366	−0.525581	−0.160790
3	6	−4.451423	0.491645	−1.265757
4	7	−3.307230	1.393781	−0.971830
5	6	−2.852927	2.040791	−2.231613
6	6	−1.993376	1.104908	−3.067690
7	7	−0.766357	0.646327	−2.359711
8	6	−0.195666	−0.507844	−3.108523
9	6	−0.943897	−1.805144	−2.815422
10	7	−0.977977	−2.144424	−1.366352
11	6	−2.083269	−3.109067	−1.093892
12	6	−3.438723	−2.419388	−1.022390
13	6	−3.616600	−2.058985	1.392836
14	6	−2.272555	−2.197034	2.114386
15	8	−1.224600	−1.809165	1.480151
16	8	−2.277581	−2.644165	3.281439
17	6	−3.693285	2.425126	0.026374
18	6	−3.306733	2.073436	1.467408
19	8	−3.497269	2.938224	2.344920
20	8	−2.767409	0.920015	1.661262
21	6	0.223020	1.752856	−2.291306
22	6	0.008005	2.712918	−1.111233
23	8	0.450986	3.863035	−1.184017
24	8	−0.596066	2.201780	−0.077219
25	6	0.299594	−2.747592	−0.938706
26	6	1.336059	−1.675534	−0.653089
27	8	0.977773	−0.537891	−0.288046
28	1	−4.250111	−1.446160	2.036960
29	1	−4.092340	−3.046933	1.320849
30	1	−4.770057	2.640214	−0.015929
31	1	−3.174082	3.356196	−0.209710
32	1	0.251541	2.326563	−3.226564
33	1	1.212553	1.310454	−2.141358
34	1	0.129723	−3.252648	0.017270
35	1	0.668946	−3.489013	−1.661090
36	1	−4.894351	−0.004923	0.776845
37	1	−5.587935	−1.119502	−0.409950
38	1	−5.369392	1.078547	−1.418796
39	1	−4.247396	−0.018354	−2.210224
40	1	−3.709072	2.371347	−2.837516
41	1	−2.284877	2.934589	−1.969013
42	1	−1.718165	1.613242	−4.003886
43	1	−2.569220	0.219793	−3.348642
44	1	−0.224382	−0.323668	−4.192034
45	1	0.856636	−0.603342	−2.836488
46	1	−1.977133	−1.723423	−3.159732
47	1	−0.484702	−2.621542	−3.391863
48	1	−1.867554	−3.597161	−0.142510
49	1	−2.117641	−3.889431	−1.866917
50	1	−3.653468	−1.920311	−1.970462
51	1	−4.217020	−3.185369	−0.886471
52	8	−0.615756	3.188581	2.495566
53	1	−0.583270	3.117891	1.511788
54	1	−1.578654	3.188486	2.679087
55	1	−0.139056	−0.054147	2.860441
56	8	−0.010416	0.563174	2.091391
57	1	−0.222197	1.480295	2.407556
58	8	−0.223175	−1.119368	4.257574
59	1	0.605633	−1.617764	4.202946
60	1	−0.914695	−1.766370	3.955308

61	7	2.629241	-2.052097	-0.767673
62	1	2.781980	-2.997742	-1.101106
63	6	3.808386	-1.335284	-0.457096
64	6	5.024488	-2.014832	-0.642529
65	6	3.807468	-0.014313	0.019764
66	6	6.229617	-1.383353	-0.356377
67	1	5.025364	-3.038288	-1.005462
68	6	5.022231	0.608003	0.304510
69	1	2.875427	0.511182	0.165871
70	6	6.232260	-0.067449	0.120615
71	1	7.163220	-1.916842	-0.495425
72	1	5.020972	1.625689	0.679211
73	6	7.533400	0.632590	0.381693
74	9	7.419504	1.581923	1.342454
75	9	8.006087	1.262296	-0.727722
76	9	8.504465	-0.227679	0.776501
77	71	-1.314968	0.040078	0.155328

```
----------------------------------------------------------------
E(RTPSSh) = -2263.5103742 Hartree
·Zero-point correction = 0.612591 (Hartree/Particle)
Thermal correction to Energy = 0.654813
Thermal correction to Enthalpy = 0.655757
Thermal correction to Gibbs Free Energy = 0.538755
Sum of electronic and zero-point Energies = -2262.897783
Sum of electronic and thermal Energies = -2262.855561
Sum of electronic and thermal Enthalpies = -2262.854617
Sum of electronic and thermal Free Energies = -2262.971619
```

Table S15. Optimised Cartesian coordinates obtained for [TbL^3(H$_2$O)]·2H$_2$O SAP isomer with DFT calculations (0 imaginary frequencies).

```
----------------------------------------------------------------------
Center     Atomic                    Coordinates (Angstroms)
Number     Number                X            Y            Z
----------------------------------------------------------------------
   1         7              -3.537074    -1.477620     0.030309
   2         6              -4.721277    -0.607592    -0.221481
   3         6              -4.475434     0.413762    -1.325501
   4         7              -3.371602     1.361242    -1.015837
   5         6              -2.896904     2.003099    -2.272082
   6         6              -1.996094     1.084542    -3.087792
   7         7              -0.761627     0.662212    -2.369354
   8         6              -0.159024    -0.490751    -3.095796
   9         6              -0.884687    -1.804453    -2.809403
  10         7              -0.929409    -2.157174    -1.362746
  11         6              -2.027520    -3.137167    -1.105042
  12         6              -3.401487    -2.478044    -1.060060
  13         6              -3.668974    -2.142300     1.355304
  14         6              -2.355991    -2.223230     2.144925
  15         8              -1.280288    -1.872606     1.536115
  16         8              -2.416175    -2.597085     3.336430
  17         6              -3.812518     2.394865    -0.042133
  18         6              -3.429608     2.092369     1.413237
  19         8              -3.609668     2.994805     2.254968
  20         8              -2.909857     0.939030     1.653755
  21         6               0.204751     1.789215    -2.301802
  22         6              -0.047191     2.777268    -1.148845
  23         8               0.359006     3.937829    -1.259444
  24         8              -0.632684     2.277661    -0.097975
  25         6               0.349910    -2.750912    -0.923631
  26         6               1.387685    -1.678841    -0.634248
  27         8               1.032786    -0.547103    -0.247041
  28         1              -4.366819    -1.569778     1.969075
  29         1              -4.088756    -3.152936     1.254328
  30         1              -4.897531     2.559768    -0.100409
  31         1              -3.333968     3.343427    -0.293462
  32         1               0.244951     2.341670    -3.249406
  33         1               1.197968     1.366510    -2.119296
  34         1               0.174686    -3.250375     0.034712
  35         1               0.723898    -3.497814    -1.637989
  36         1              -4.941582    -0.086861     0.711107
  37         1              -5.601216    -1.211731    -0.487872
  38         1              -5.409754     0.967206    -1.504094
  39         1              -4.232702    -0.094005    -2.261816
  40         1              -3.744514     2.309483    -2.902750
  41         1              -2.355900     2.911542    -2.003129
  42         1              -1.726516     1.596289    -4.023975
  43         1              -2.543187     0.182381    -3.371495
  44         1              -0.172417    -0.317578    -4.181639
  45         1               0.889955    -0.562372    -2.804351
  46         1              -1.915194    -1.743249    -3.165588
  47         1              -0.402138    -2.607827    -3.385218
  48         1              -1.819409    -3.614957    -0.146656
  49         1              -2.033992    -3.921235    -1.875160
  50         1              -3.606467    -1.976787    -2.009005
  51         1              -4.161727    -3.266416    -0.951822
  52         8              -0.741577     3.230677     2.480967
  53         1              -0.676063     3.161050     1.498224
  54         1              -1.710557     3.226686     2.632923
  55         1              -0.241972     0.018617     2.974220
  56         8              -0.082648     0.615240     2.192757
  57         1              -0.310722     1.542418     2.472270
  58         8              -0.416154    -1.029667     4.355133
  59         1               0.412344    -1.531595     4.362388
  60         1              -1.092797    -1.684392     4.034288
```

```
       61            7                    2.680178    -2.052232    -0.764158
       62            1                    2.833704    -2.988592    -1.122363
       63            6                    3.858995    -1.335656    -0.450350
       64            6                    5.077724    -1.973387    -0.735209
       65            6                    3.854400    -0.056208     0.130465
       66            6                    6.283132    -1.342668    -0.444886
       67            1                    5.081439    -2.963514    -1.181197
       68            6                    5.068192     0.564561     0.418918
       69            1                    2.920312     0.437897     0.353619
       70            6                    6.282178    -0.070119     0.135924
       71            1                    7.219453    -1.843411    -0.662778
       72            1                    5.063340     1.548264     0.876188
       73            6                    7.574001     0.639840     0.416674
       74            9                    7.524031     1.342688     1.576150
       75            9                    7.887628     1.535037    -0.558167
       76            9                    8.620555    -0.215685     0.508599
       77           65                   -1.339027     0.037838     0.170969
    ---------------------------------------------------------------
    E(RTPSSh) = -2260.0408641 Hartree
   ·Zero-point correction = 0.611787 (Hartree/Particle)
    Thermal correction to Energy = 0.654226
    Thermal correction to Enthalpy = 0.655170
    Thermal correction to Gibbs Free Energy = 0.537182
    Sum of electronic and zero-point Energies = -2259.429078
    Sum of electronic and thermal Energies = -2259.386638
    Sum of electronic and thermal Enthalpies = -2259.385694
    Sum of electronic and thermal Free Energies = -2259.503682
```

Table S16. Optimised Cartesian coordinates obtained for [TmL^{3}(H$_2$O)]·2H$_2$O SAP isomer with DFT calculations (0 imaginary frequencies).

Center Number	Atomic Number	Coordinates (Angstroms)		
		X	Y	Z
1	7	−3.524579	−1.425882	0.052127
2	6	−4.704760	−0.544253	−0.170330
3	6	−4.460480	0.480165	−1.270217
4	7	−3.328267	1.395384	−0.969075
5	6	−2.869067	2.047688	−2.224789
6	6	−1.999367	1.122085	−3.063610
7	7	−0.767914	0.667337	−2.360570
8	6	−0.193944	−0.483872	−3.111678
9	6	−0.938374	−1.786419	−2.827217
10	7	−0.971238	−2.141667	−1.381928
11	6	−2.074964	−3.110346	−1.115637
12	6	−3.434965	−2.428462	−1.040544
13	6	−3.630312	−2.089927	1.378405
14	6	−2.291433	−2.217795	2.113358
15	8	−1.237712	−1.837656	1.484128
16	8	−2.307528	−2.651959	3.285397
17	6	−3.728117	2.421171	0.029244
18	6	−3.336554	2.075661	1.471116
19	8	−3.520052	2.946998	2.343853
20	8	−2.802550	0.920747	1.670160
21	6	0.216946	1.777213	−2.287191
22	6	−0.002881	2.737458	−1.106803
23	8	0.435058	3.889366	−1.182604
24	8	−0.603082	2.224929	−0.071109
25	6	0.308117	−2.745556	−0.959430
26	6	1.345689	−1.676041	−0.664641
27	8	0.989363	−0.541946	−0.286969
28	1	−4.279166	−1.491343	2.020602
29	1	−4.091988	−3.083618	1.294046
30	1	−4.808017	2.620552	−0.012536
31	1	−3.222917	3.359785	−0.207288
32	1	0.246848	2.352256	−3.221666
33	1	1.207431	1.337462	−2.134648
34	1	0.139241	−3.258607	−0.007459
35	1	0.678011	−3.481267	−1.687456
36	1	−4.905690	−0.028585	0.769448
37	1	−5.595288	−1.137259	−0.425887
38	1	−5.384117	1.057374	−1.426938
39	1	−4.245656	−0.024580	−2.215051
40	1	−3.723430	2.375691	−2.834837
41	1	−2.307825	2.943711	−1.955297
42	1	−1.728743	1.638235	−3.996963
43	1	−2.568390	0.234321	−3.349999
44	1	−0.221000	−0.296362	−4.194787
45	1	0.858100	−0.577229	−2.837763
46	1	−1.972023	−1.705275	−3.170311
47	1	−0.476726	−2.595485	−3.412173
48	1	−1.857802	−3.602584	−0.166699
49	1	−2.106511	−3.886426	−1.893175
50	1	−3.650536	−1.922125	−1.984535
51	1	−4.207990	−3.201627	−0.915011
52	8	−0.640300	3.180267	2.513502
53	1	−0.601192	3.116672	1.529292
54	1	−1.604697	3.177199	2.690173
55	1	−0.152784	−0.058567	2.886499
56	8	−0.022149	0.560136	2.118352
57	1	−0.235130	1.477403	2.434722
58	8	−0.250061	−1.134967	4.268838
59	1	0.575171	−1.638586	4.207625
60	1	−0.945990	−1.775281	3.961679

```
61          7                    2.638983   -2.051077   -0.783637
62          1                    2.793227   -2.992919   -1.126983
63          6                    3.816553   -1.334692   -0.465442
64          6                    5.034662   -2.007880   -0.661015
65          6                    3.812341   -0.019990    0.028683
66          6                    6.238192   -1.376321   -0.368325
67          1                    5.038344   -3.026626   -1.036930
68          6                    5.025556    0.602482    0.319648
69          1                    2.879044    0.500924    0.182978
70          6                    6.237433   -0.066548    0.125457
71          1                    7.173260   -1.905113   -0.515432
72          1                    5.021540    1.615277    0.707341
73          6                    7.536913    0.633931    0.393582
74          9                    7.419144    1.578946    1.358058
75          9                    8.012423    1.268694   -0.711742
76          9                    8.507737   -0.227058    0.787615
77         69                   -1.322757    0.038882    0.158804
     ---------------------------------------------------------------
E(RTPSSh) = -2262.3736847 Hartree
·Zero-point correction = 0.612405 (Hartree/Particle)
Thermal correction to Energy = 0.654649
Thermal correction to Enthalpy = 0.655593
Thermal correction to Gibbs Free Energy = 0.538713
Sum of electronic and zero-point Energies = -2261.761280
Sum of electronic and thermal Energies = -2261.719036
Sum of electronic and thermal Enthalpies = -2261.718091
Sum of electronic and thermal Free Energies = -2261.834972
```
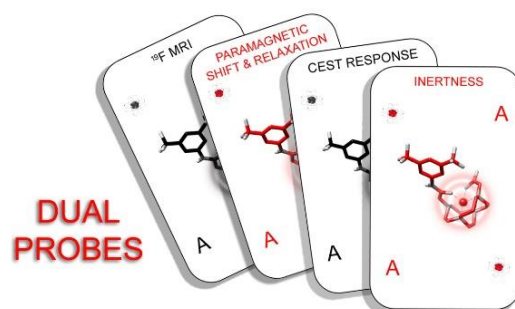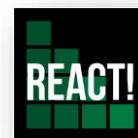
Table S17. Optimised Cartesian coordinates obtained for [YbL³(H₂O)]·2H₂O SAP isomer with DFT calculations (0 imaginary frequencies).

Center Number	Atomic Number	Coordinates (Angstroms)		
		X	Y	Z
1	7	−3.523133	−1.411683	0.053403
2	6	−4.700734	−0.527069	−0.169581
3	6	−4.451843	0.494957	−1.270310
4	7	−3.313565	1.402479	−0.969574
5	6	−2.852205	2.053057	−2.225144
6	6	−1.988176	1.122360	−3.063643
7	7	−0.760460	0.660435	−2.358714
8	6	−0.192018	−0.493252	−3.109985
9	6	−0.942639	−1.791589	−2.823856
10	7	−0.977557	−2.142950	−1.377890
11	6	−2.084377	−3.107024	−1.110191
12	6	−3.440820	−2.418548	−1.035845
13	6	−3.628997	−2.071144	1.381712
14	6	−2.287756	−2.208938	2.109542
15	8	−1.236174	−1.824528	1.479201
16	8	−2.298978	−2.653379	3.277685
17	6	−3.706592	2.429404	0.029895
18	6	−3.319645	2.076761	1.470887
19	8	−3.507252	2.942570	2.348202
20	8	−2.783644	0.921904	1.665039
21	6	0.229949	1.765081	−2.284204
22	6	0.014205	2.722801	−1.101628
23	8	0.460844	3.871746	−1.171398
24	8	−0.593895	2.211391	−0.070071
25	6	0.299780	−2.748869	−0.953220
26	6	1.337509	−1.679455	−0.659922
27	8	0.980734	−0.544063	−0.286634
28	1	−4.267972	−1.463693	2.025544
29	1	−4.100970	−3.060423	1.302930
30	1	−4.784605	2.638384	−0.013070
31	1	−3.192588	3.364062	−0.203464
32	1	0.261903	2.342186	−3.217332
33	1	1.218470	1.320619	−2.133192
34	1	0.129282	−3.260067	−0.000592
35	1	0.669559	−3.486069	−1.679820
36	1	−4.900588	−0.009783	0.769545
37	1	−5.593039	−1.117595	−0.424492
38	1	−5.371853	1.077992	−1.426694
39	1	−4.240751	−0.011624	−2.215029
40	1	−3.705231	2.385944	−2.834347
41	1	−2.285768	2.945864	−1.955792
42	1	−1.713223	1.636646	−3.996738
43	1	−2.562284	0.237980	−3.350423
44	1	−0.218992	−0.305967	−4.193105
45	1	0.859843	−0.591547	−2.837062
46	1	−1.975777	−1.705921	−3.167417
47	1	−0.484794	−2.604203	−3.406891
48	1	−1.869157	−3.599295	−0.160824
49	1	−2.119367	−3.884057	−1.886645
50	1	−3.654966	−1.914179	−1.981230
51	1	−4.217812	−3.187077	−0.906496
52	8	−0.624091	3.177385	2.509821
53	1	−0.586460	3.108565	1.525838
54	1	−1.588044	3.175683	2.688310
55	1	−0.145077	−0.066672	2.872276
56	8	−0.015273	0.554198	2.106030
57	1	−0.225001	1.470451	2.426440
58	8	−0.234523	−1.143437	4.258283
59	1	0.590162	−1.647322	4.192209
60	1	−0.932089	−1.782569	3.952864

61	7	2.630830	-2.055096	-0.776726
62	1	2.784767	-2.998477	-1.115953
63	6	3.808787	-1.337934	-0.461673
64	6	5.026268	-2.014593	-0.648852
65	6	3.805462	-0.018927	0.020768
66	6	6.230113	-1.382300	-0.358936
67	1	5.029258	-3.036482	-1.016143
68	6	5.018921	0.604198	0.309211
69	1	2.872580	0.504634	0.168133
70	6	6.230211	-0.068404	0.123662
71	1	7.164728	-1.913674	-0.499352
72	1	5.015589	1.620331	0.688091
73	6	7.529975	0.632637	0.388922
74	9	7.412549	1.581370	1.349824
75	9	8.005417	1.263220	-0.718824
76	9	8.500623	-0.227058	0.786101
77	70	-1.318773	0.039681	0.156966

```
--------------------------------------------------------------
E(RTPSSh) = -2262.9570523 Hartree
·Zero-point correction = 0.612528 (Hartree/Particle)
Thermal correction to Energy = 0.654751
Thermal correction to Enthalpy = 0.655695
Thermal correction to Gibbs Free Energy = 0.538853
Sum of electronic and zero-point Energies = -2262.344524
Sum of electronic and thermal Energies = -2262.302302
Sum of electronic and thermal Enthalpies = -2262.301358
Sum of electronic and thermal Free Energies = -2262.418199
```

Annexe E

Annexe E

Annexe E Summary

Characterisation of compounds.

Figure S1. ^{1}H, ^{13}C and ^{19}F NMR spectra (9.40 T, 25 ^{o}C) of precursor **1a** in CDCl$_3$.

Figure S2. Experimental ESI-MS and high-resolution spectra of precursor **1a**.

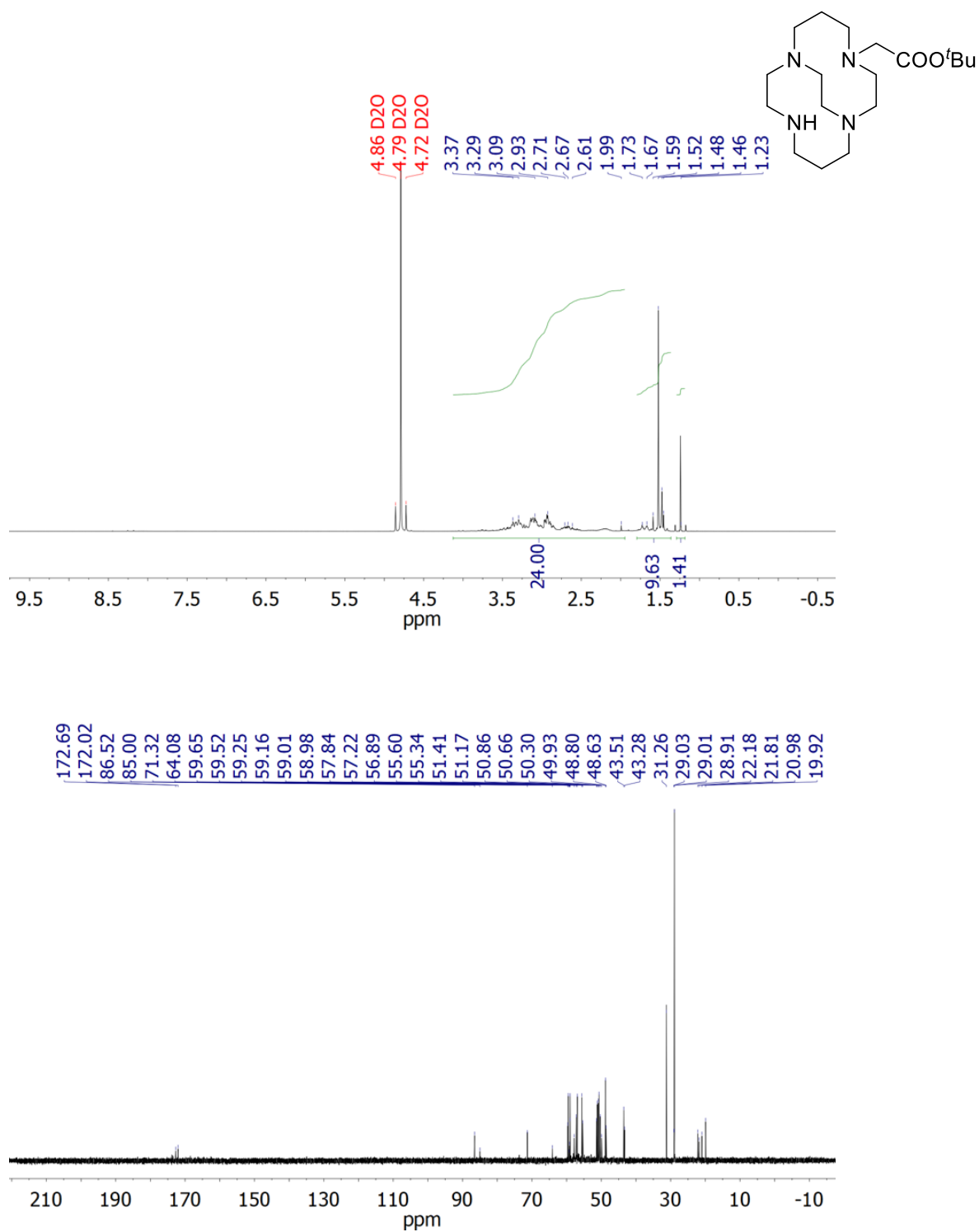**Figure S4.** ^{1}H, ^{13}C and ^{19}F NMR spectra (7.05 T, 25 ^{o}C) of precursor **1b** in CDCl$_3$.
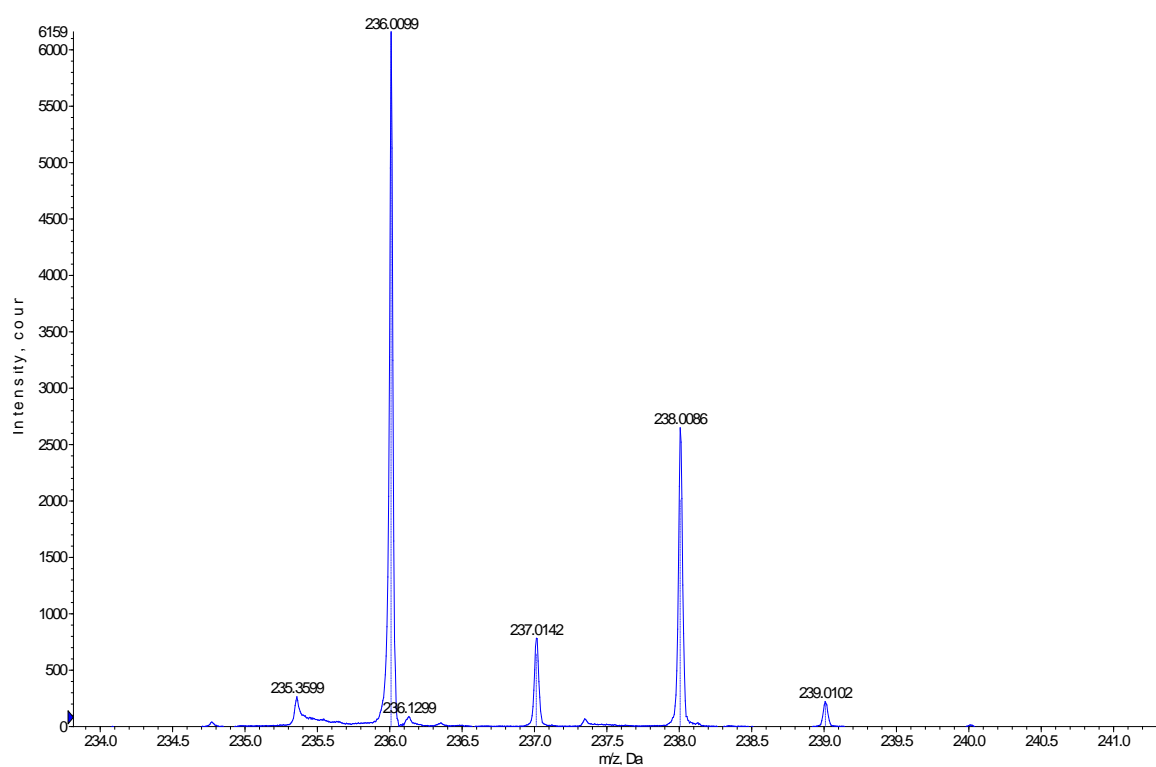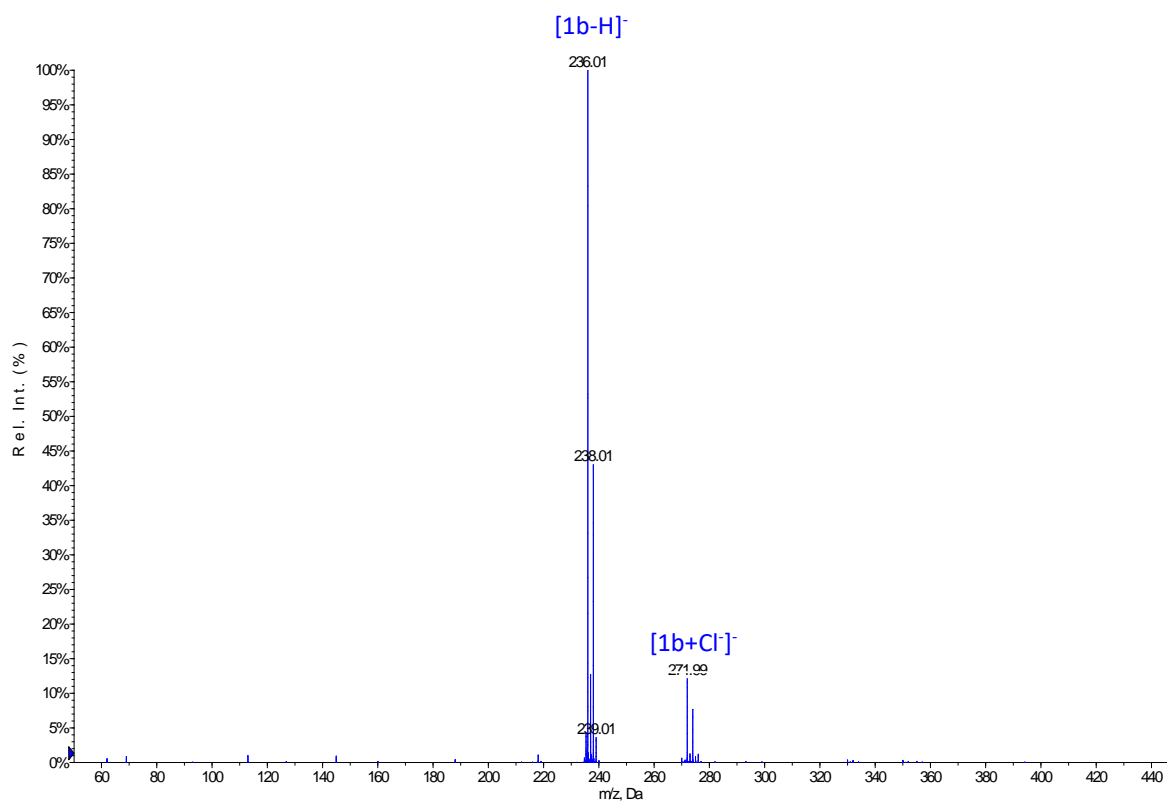
Figure S5. Experimental ESI-MS and high-resolution spectra of precursor **1b**.

Figure S6. ^{1}H and ^{13}C NMR spectra (7.05 T, 25 ^{o}C) of intermediate **2a** recorded in D$_2$O solution.
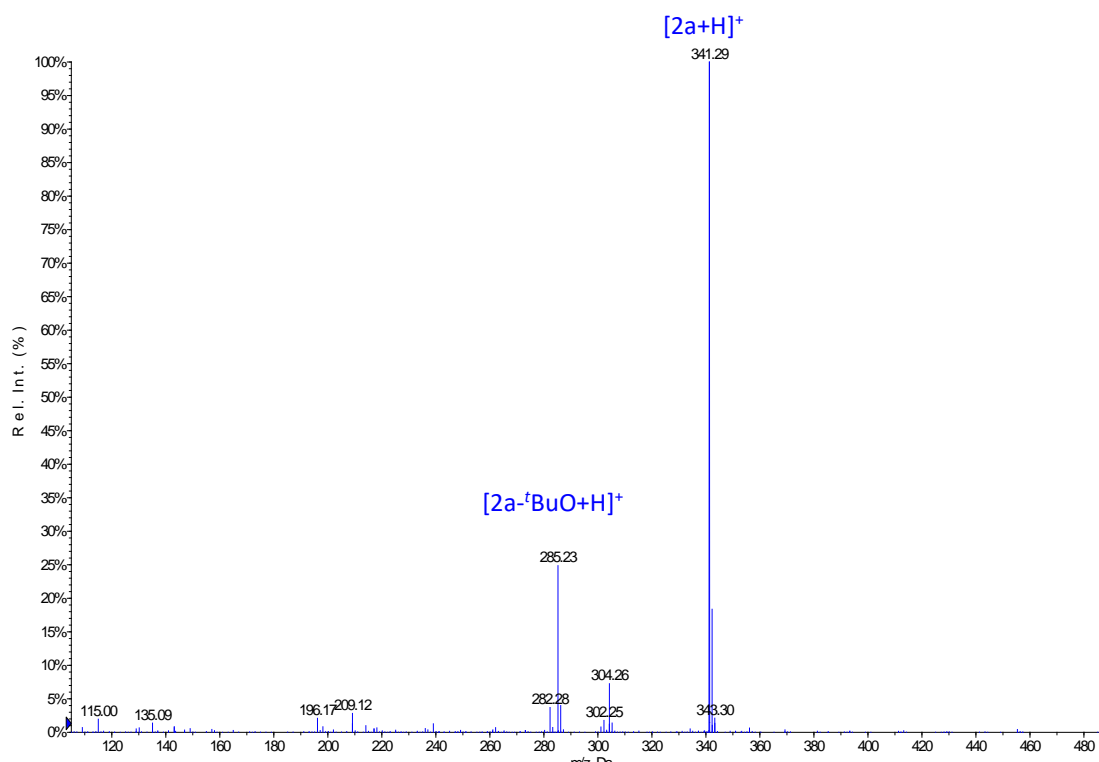
Figure S7. Experimental mass spectrum of intermediate **2a**.
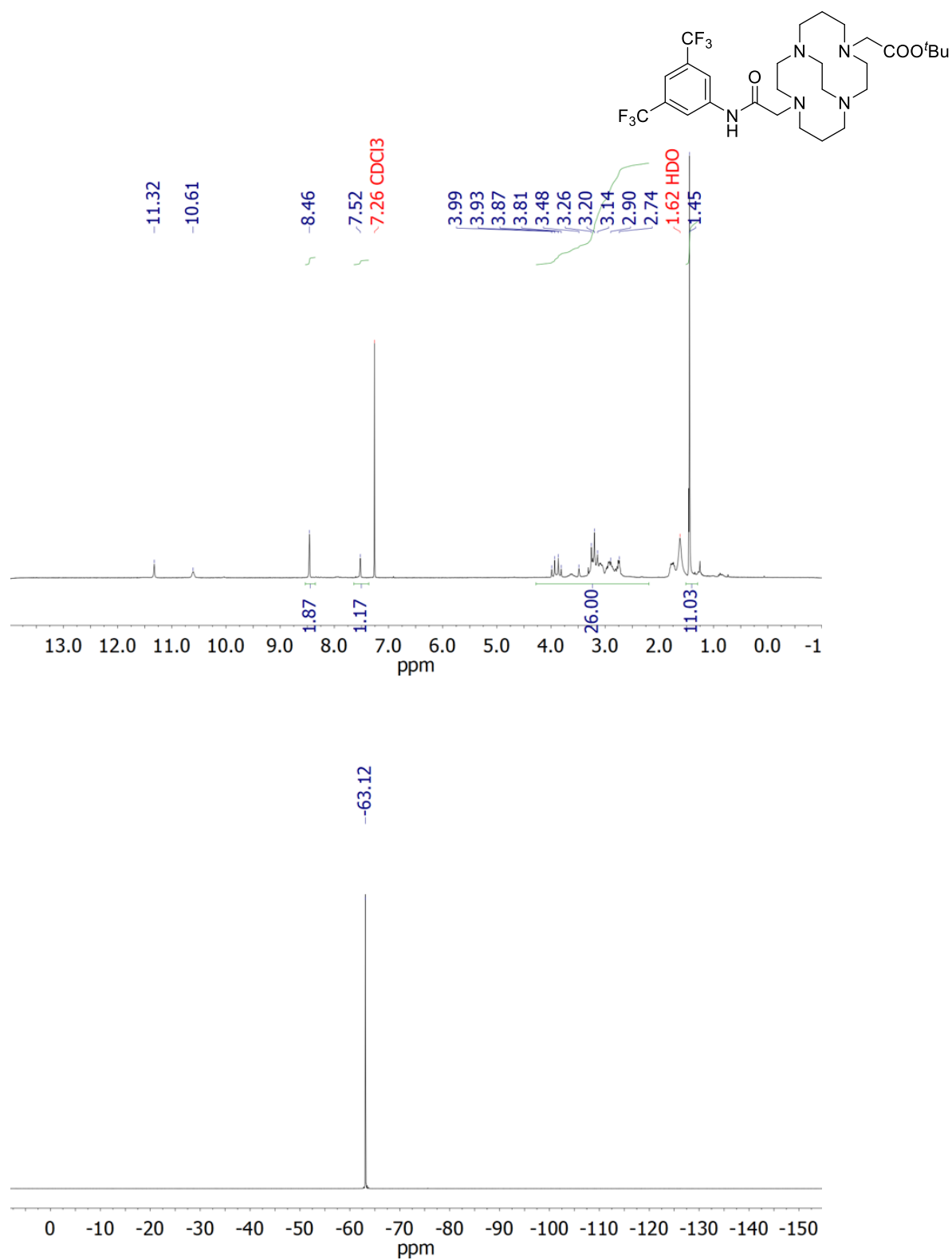
Figure S8. ^{1}H and ^{19}F NMR spectra (7.05 T, 25 °C) of compound **3a** recorded in CDCl$_3$.
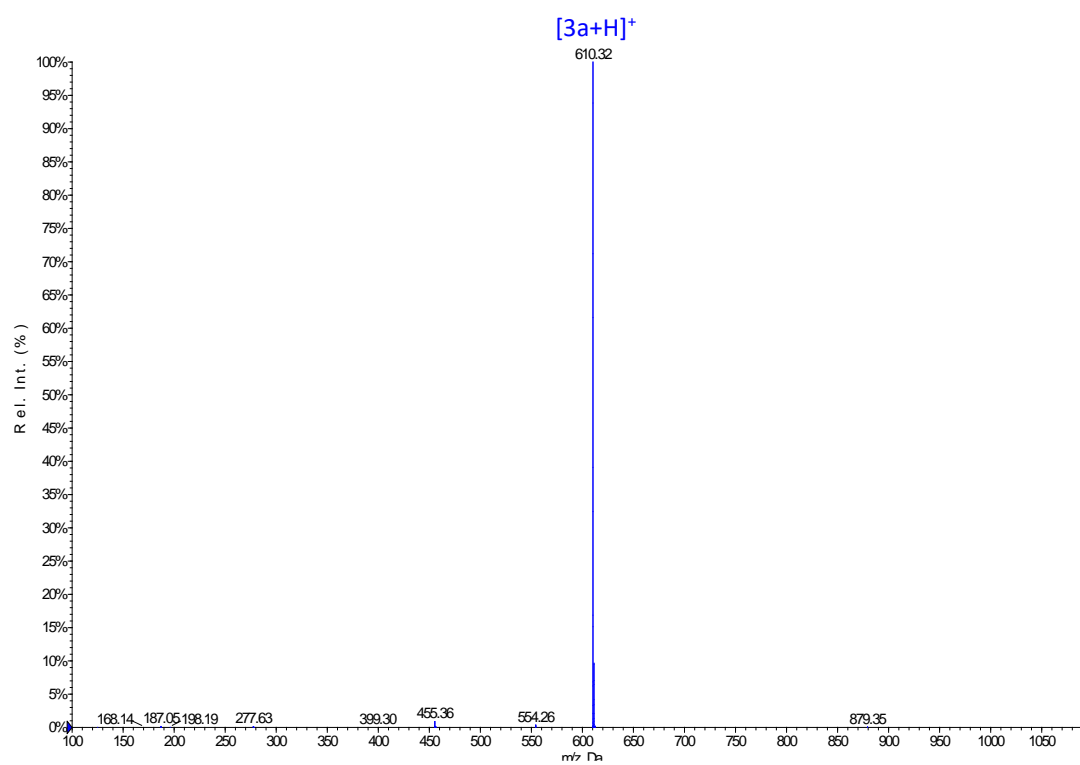
Figure S9. Experimental ESI-MS spectrum of compound **3a**.
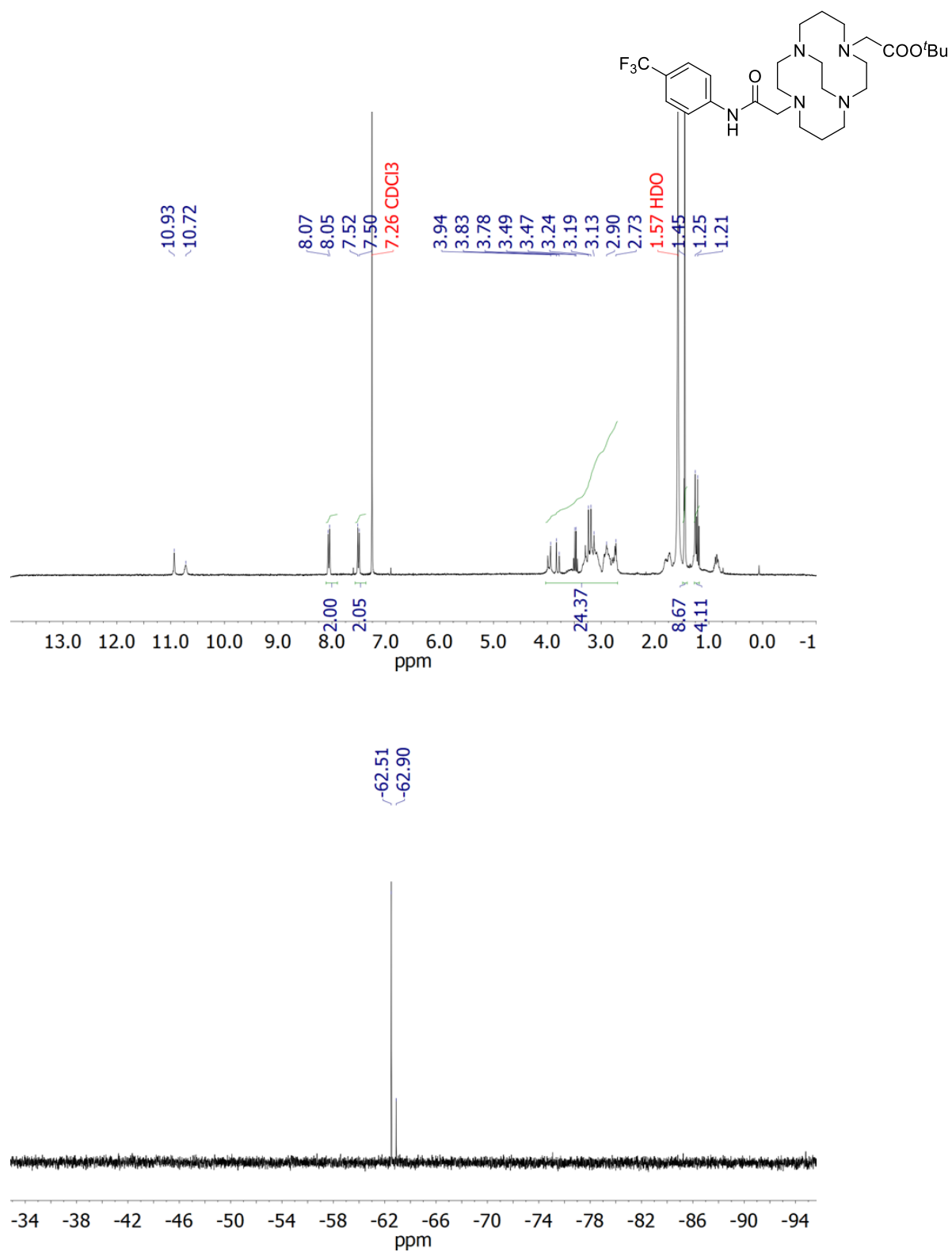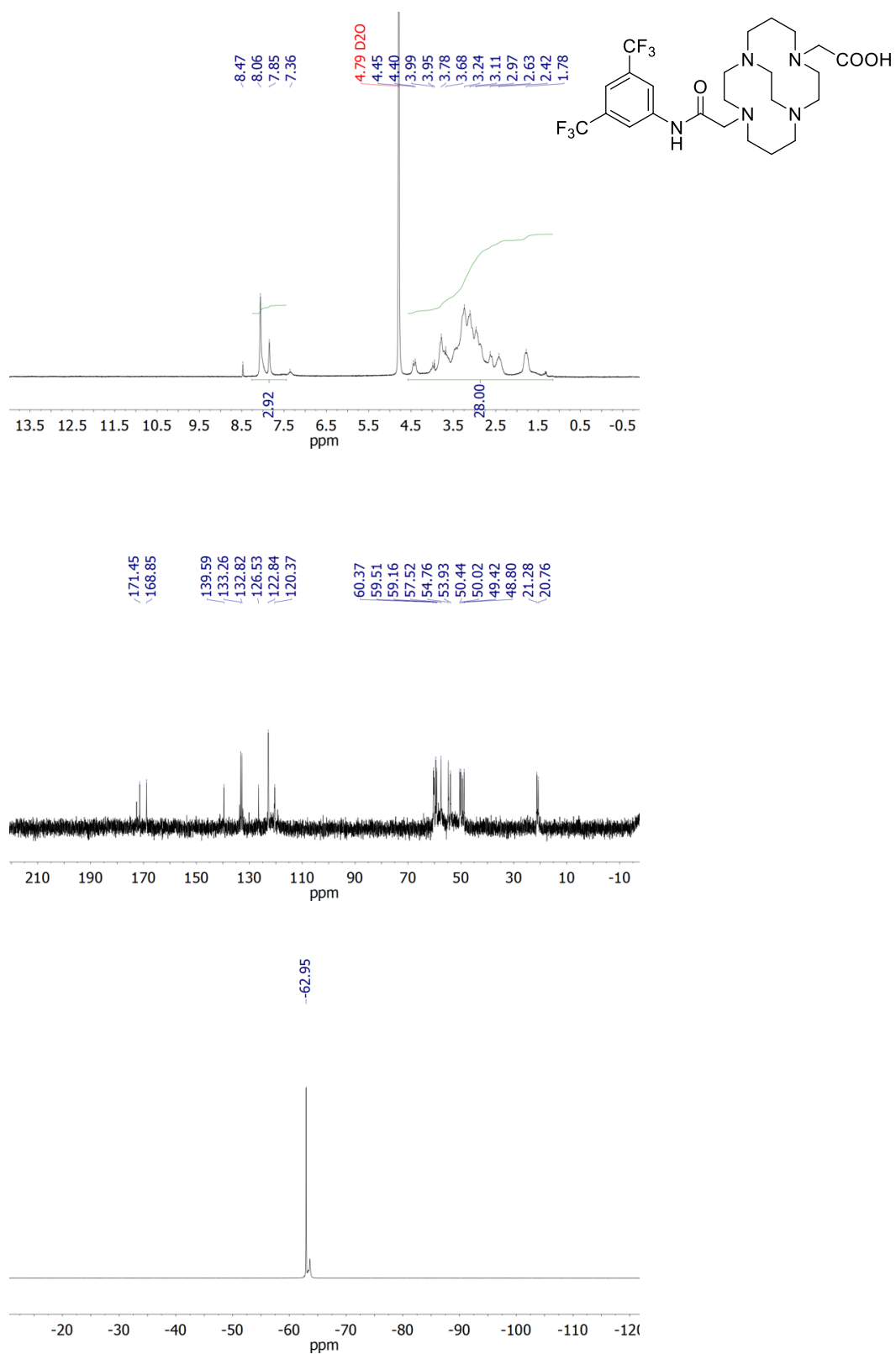
Figure S10. ^{1}H and ^{19}F NMR spectra (7.05 T, 25 ^{o}C) of compound **3b** recorded in CDCl$_3$.
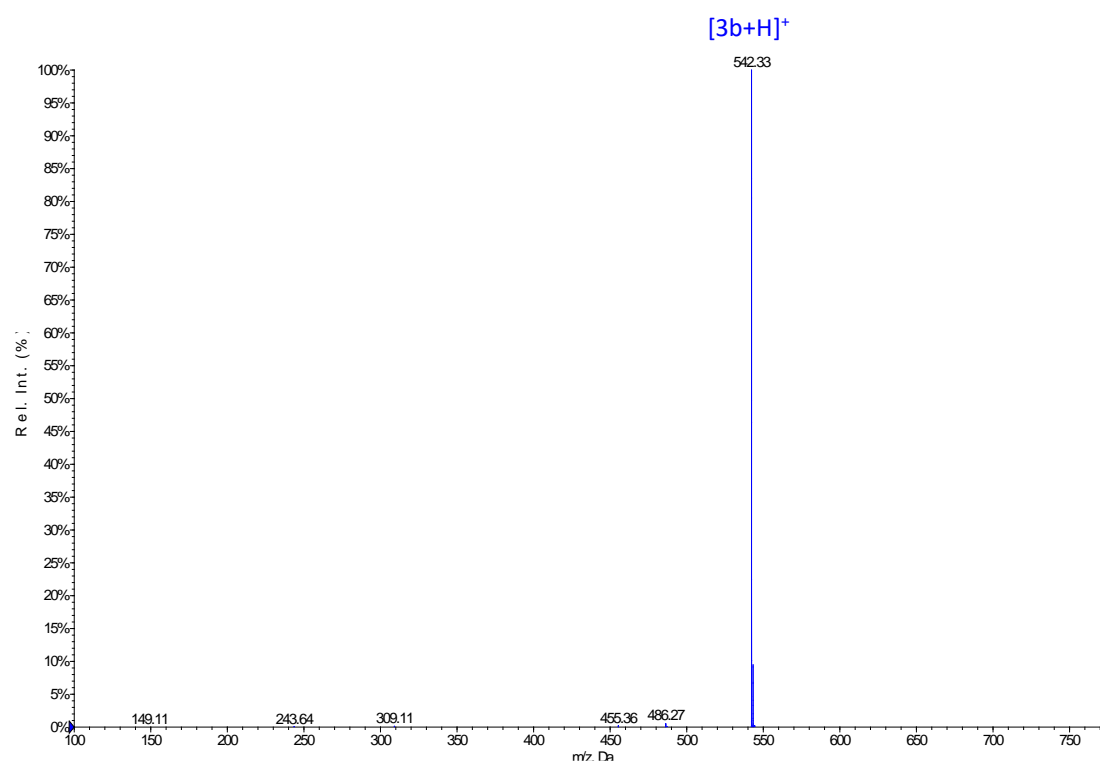
Figure S11. Experimental ESI-MS spectrum of compound **3b**.

Figure S12. ^{1}H, ^{13}C and ^{19}F NMR spectra (7.05 T, 25 °C) of final ligand **HL^1** recorded in D$_2$O.
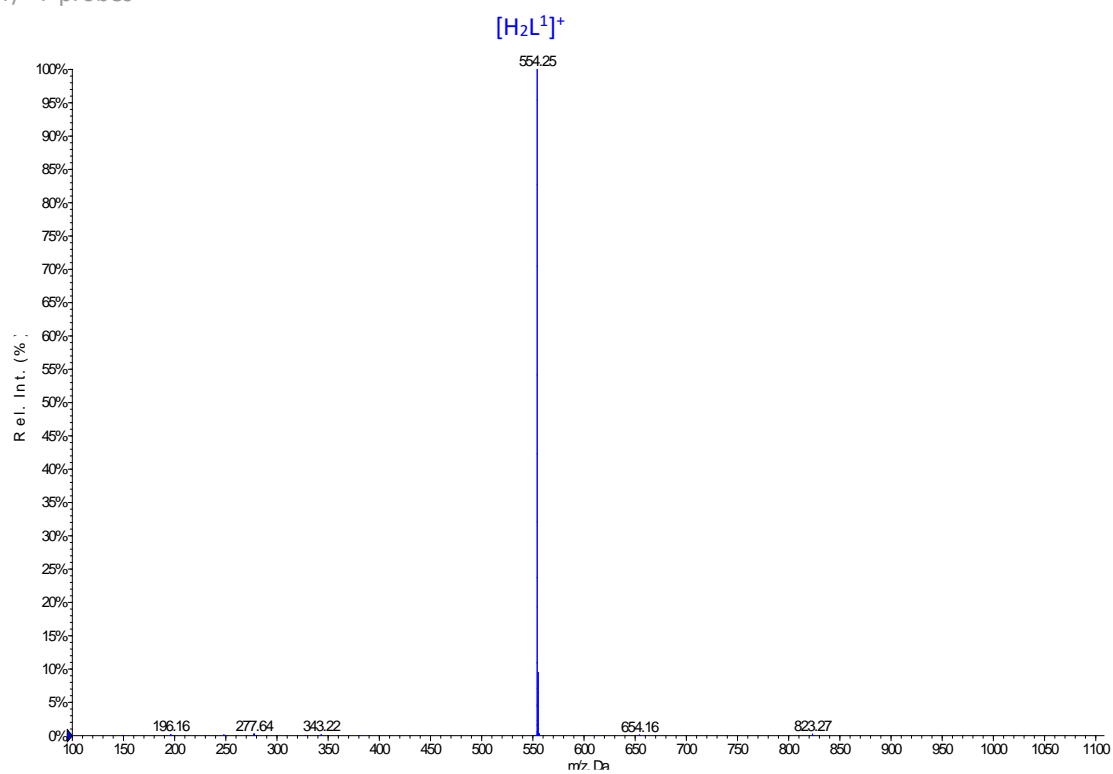
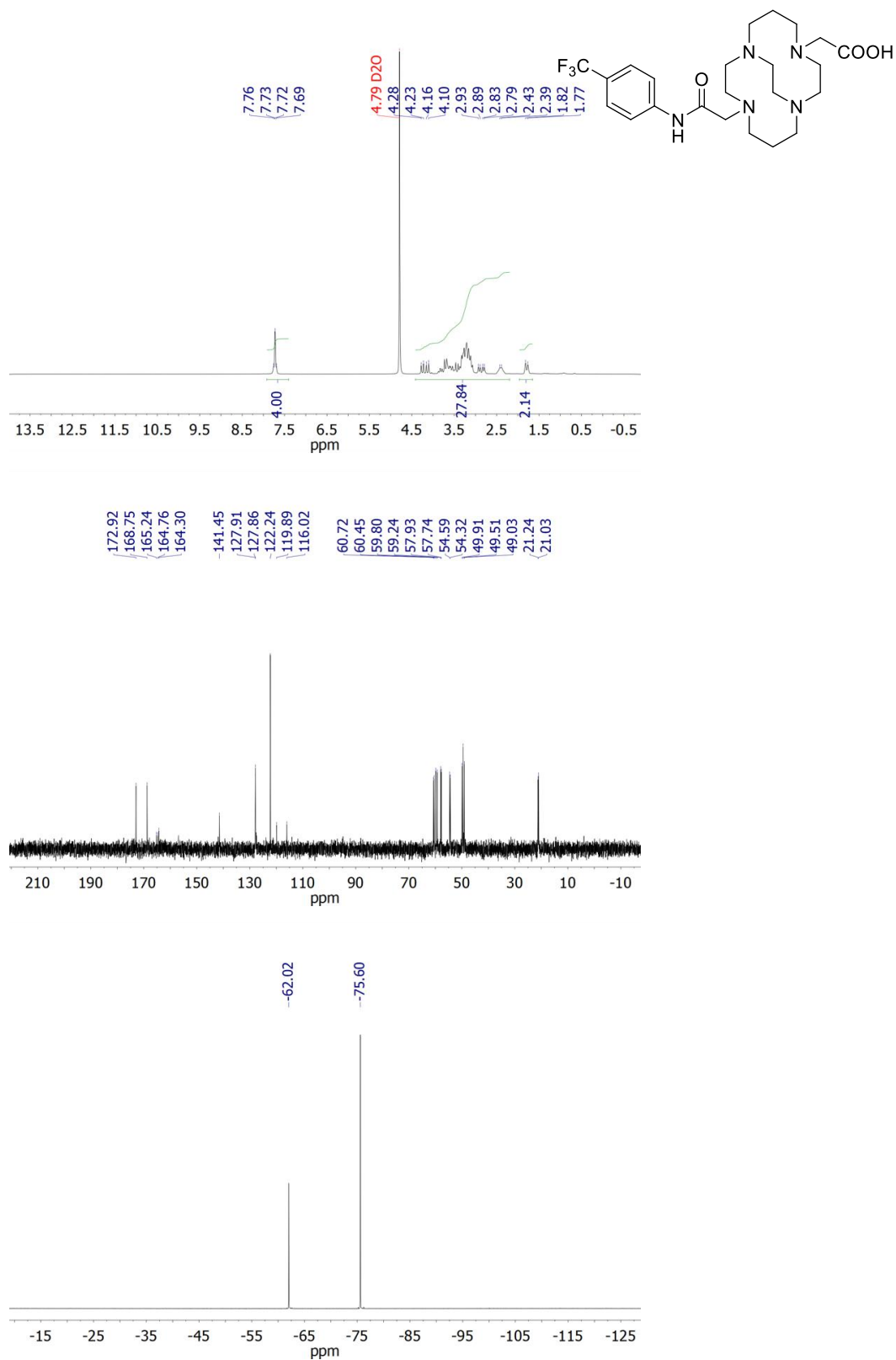**Figure S13.** Experimental ESI-MS spectrum of ligand **HL^1**.

Figure S14. ¹H, ¹³C and ¹⁹F NMR spectra (7.05 T, 25 °C) of final ligand **HL²** recorded in D₂O.
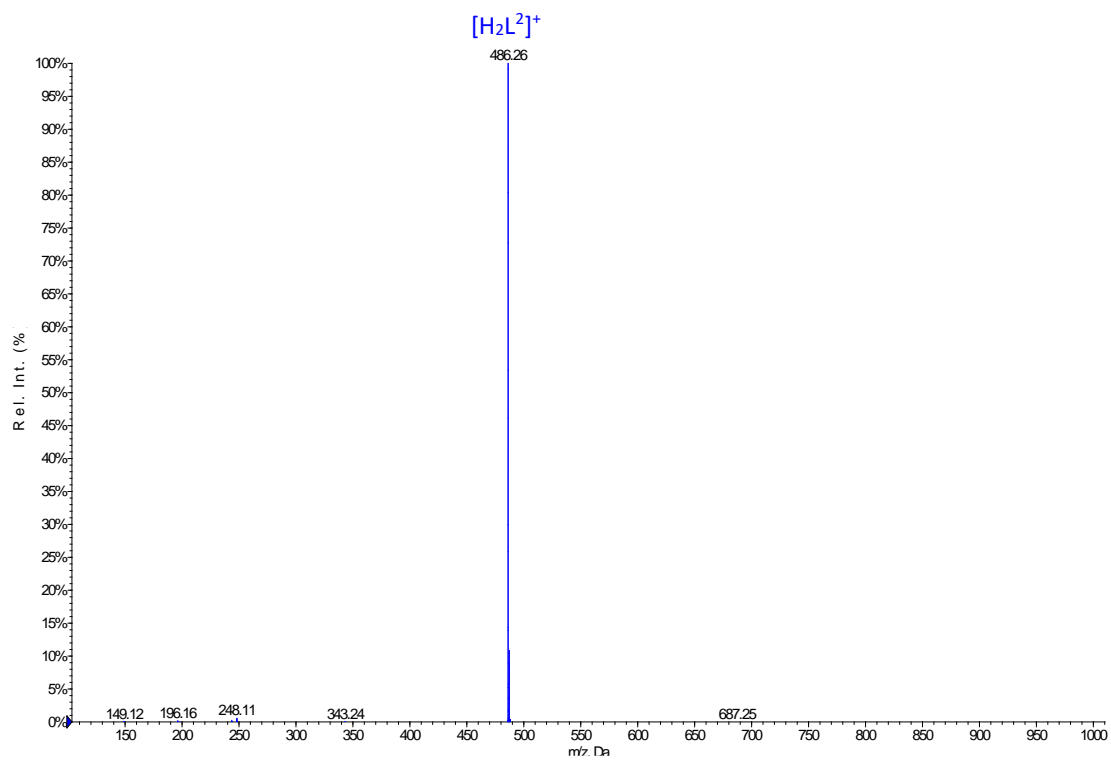
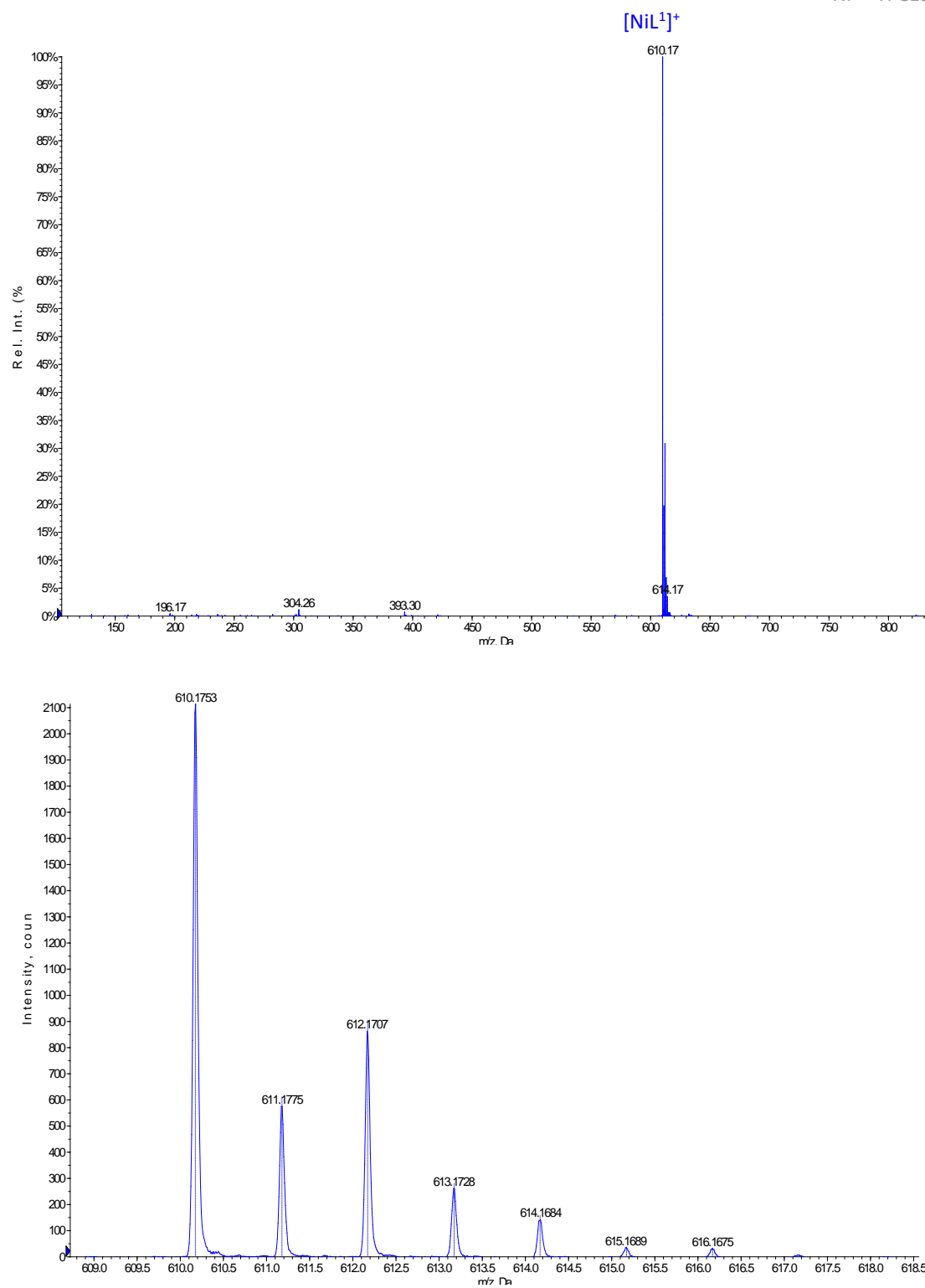**Figure S15.** Experimental ESI-MS spectrum of ligand **HL^2**.

Figure S16. Experimental ESI-MS and high-resolution spectra of **NiL[1]** complex.
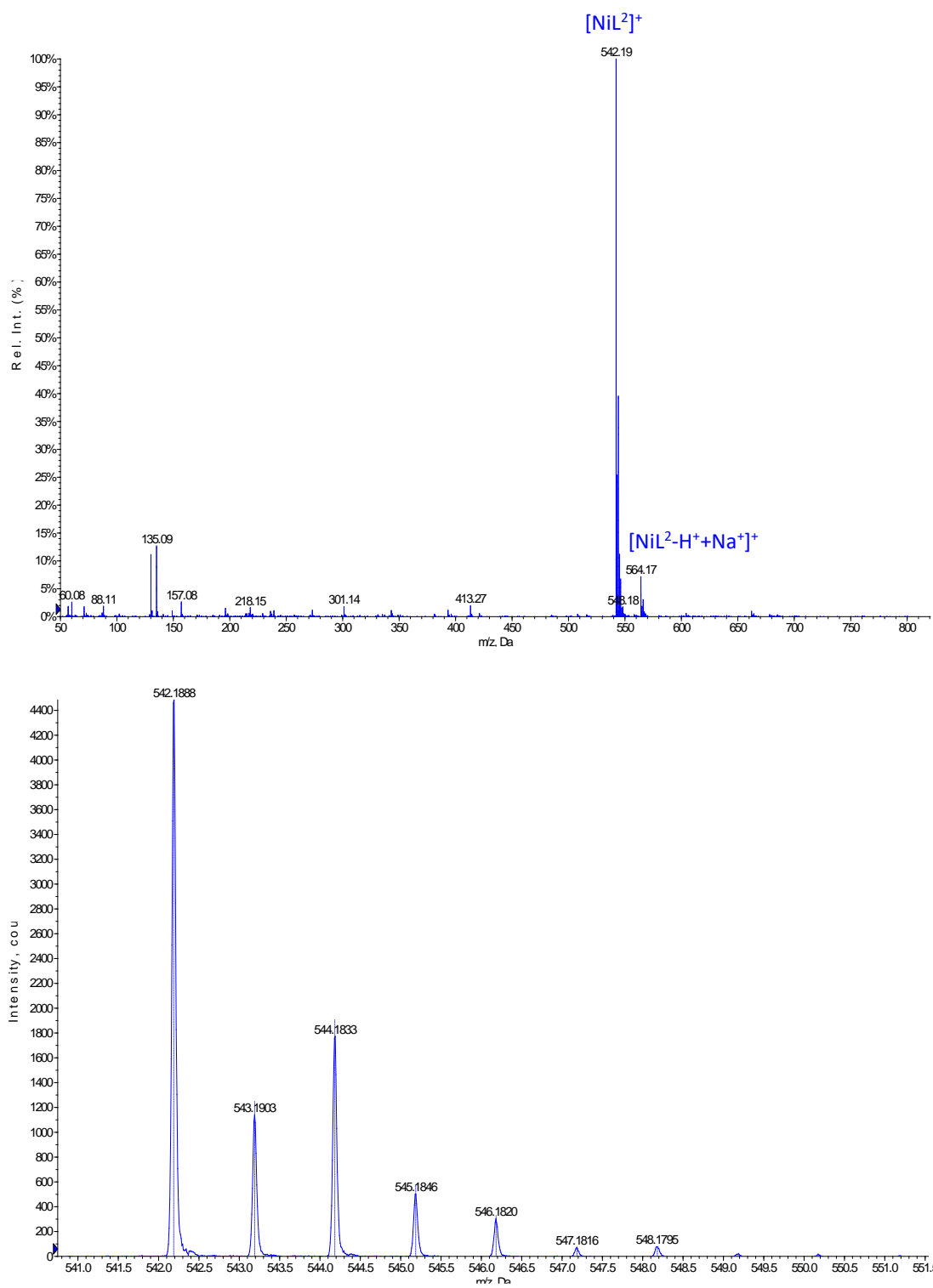
Figure S17. Experimental ESI-MS and high-resolution spectra of **NiL²** complex.

^{19}F MRI studies.

Phantom consisted of a pair of 400 μl vials containing either 15 mM of NiL^{1} or NiL^{2}, respectively with equal concentration of TFA as a reference in all recordings. ^{19}F imaging parameters were: FOV= 32 x 32, MTX 32 x 32, slice thickness 5 mm, the rest of parameters are in Table 1.

Table 1. MRI parameters ^{19}F.

Sample/parameter	Flip angle / ^{0}	TR/TE / ms	NEX	TA / min
NiL^{1}	42	3.20 / 1.01	35156	60
NiL^{2}	29	3.20 / 1.01	35156	60

Crystal structures.

Table 2. Crystal Data and Structure Refinement for **[NiL^1]$^+$** and **[NiL^2]$^+$** complexes.

	[NiL^1]$^+$ (CCDC 1891731)	*[NiL^2]$^+$ (CCDC 1891730)*
formula	C$_{33}$ H$_{37}$ F$_{15}$ N$_6$ O$_6$ Ni	C$_{21}$ H$_{32}$ F$_3$ Cl$_2$ N$_5$ O Ni
mol wt	989.45	557.12
cryst syst	Triclinic	Triclinic
space group	*P-1*	*P-1*
a (Å) α (deg) b (Å)β (deg) c (Å) γ (deg)	11.0932(7) 71.548(2) 12.2717(8) 88.206(2) 15.5846(9) 72.064(2)	11.1218(9) 84.577(2) 15.1505(11) 84.097(2) 20.4174(14) 73.547(2)
V(Å^3)	1909.5(2)	3274.3(4)
Z	2	4
D(calc) (Mg/m^3)	1.721	1.130
μ (mm^{-1})	0.690	0.791
R$_{int}$	0.0663	0.0346
R$_1$^{a}	0.0422	0.0544
wR$_2$ (all data)^b	0.0957	0.1415

^{a} R$_1$ = Σ||F_o|-|F_c||/Σ|F_o|. ^{b} wR$_2$ = {Σ[w(||F_o|^2-|F_c|^2|)^2]/ Σ[w($F_o{}^4$|)]}$^{1/2}$

Table 3. Bond lengths (Å) and angles (deg) of the Nickel(II) coordination environment for **[NiL^1]$^+$** and **[NiL^2]$^+$** complexes.

|	**[NiL^1]$^+$**	**[NiL^2]$^+$**
Ni1-N1	2.0841(17)	2.083(2)
Ni1-N2	2.0709(17)	2.082(2)
Ni1-N3	2.0970(16)	2.096(2)
Ni1-N4	2.0696(17)	2.068(2)
Ni1-O1	2.0260(14)	2.058(2)
Ni1-O3	2.0751(14)	2.110(2)
Ni2-N6		2.086(2)
Ni2-N7		2.079(2)
Ni2-N8		2.094(2)
Ni2-N9		2.067(2)
Ni2-O4		2.040(2)
Ni2-O6		2.083(2)
N1-Ni1-N3	176.70(7)	178.52(9)
N2-Ni1-N1	94.86(7)	93.99(9) .
N2-Ni1-N3	87.35(7)	86.56(8)
N2-Ni1-O3	90.63(6)	92.20(8)
N4-Ni1-N1	87.25(7)	87.21(9)
N4-Ni1-N2	87.46(7)	87.22(9)
N4-Ni1-N3	95.30(6)	94.19(8)
N4-Ni1-O3	177.16(6)	176.73(8)
O1-Ni1-N1	84.28(6) .	83.73(8)
O1-Ni1-N2	179.14(7)	177.71(8)
O1-Ni1-N3	93.51(6)	95.72(8)
O1-Ni1-N4	92.49(6)	92.84(8)
O1-Ni1-O3	89.46(6)	87.87(7)
O3-Ni1-N1	95.02(6)	96.05(8)
O3-Ni1-N3	82.50(6)	82.55(8) .

Table 4. Hydrogen Bond interactions in **[NiL^1]$^+$** complex.

D-H···A	H-A	D-H···A
N(5)-H(5)···O(2)_$1	1.96	168
N(6)-H(6C)···O(1T)_$2	2.27	163
N(6)-H(6D)···O(2T)_$3	2.23	169

$1 –x, -y+1, -z+1; $2 x, +y, +z-1; $3 –x+1, -y+1, -z+1

Annexe F
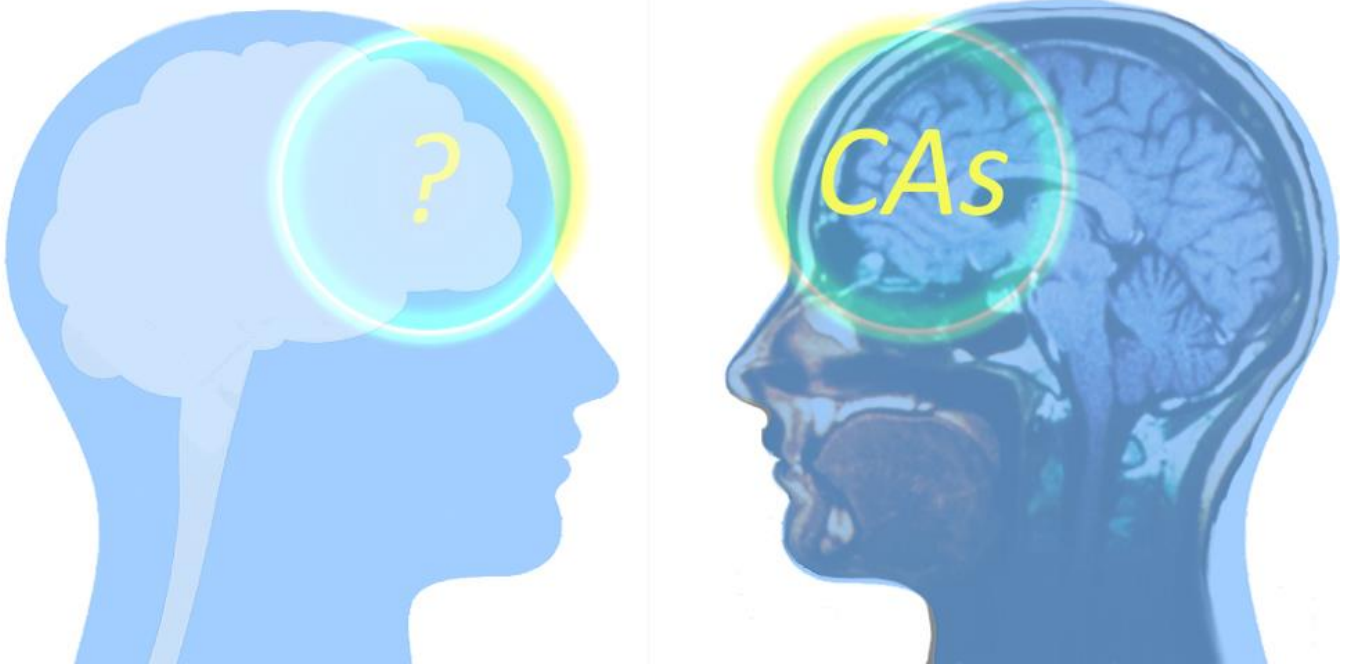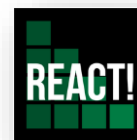
Annexe F

Los avances tecnológicos logrados en las últimas décadas son innegables. Los conocimientos y capacidades acumuladas por la raza humana son casi ilimitados, lo que ha permitido desarrollar con bastante facilidad nuevos métodos, nuevos sistemas, nuevas técnicas e incluso nuevos equipos que satisfacen nuestras necesidades. El objetivo de todos estos desarrollos es principalmente aumentar la comodidad y el bienestar del ser humano. Aunque todos estos esfuerzos están concebidos para mejorar la calidad de vida, las personas deben tener la disponibilidad y las condiciones sanitarias para aprovecharla. A pesar de que el poder adquisitivo en todo el mundo está distribuido de forma desigual,[1] la esperanza media de vida se ha visto aumentada, en términos generales, sin la presencia de guerras mundiales. Aunque la esperanza de vida aumenta, nuevos factores que no existían en el pasado, como por ejemplo los mayores niveles de contaminación, la mayor exposición a la radiación o incluso el estrés, están condicionando la vida y el estilo de vida de las personas.[2] Todos estos nuevos retos a los que la sociedad se enfrenta cada día pueden ser enfrentados a través de diferentes enfoques, pero una de las formas de acción más importantes es mantener y mejorar la salud física y mental, especialmente a través de la prestación de servicios médicos.[3]

Al margen de factores como la situación geográfica, el acceso a la prevención o la calidad del sistema sanitario,[3] la investigación, el desarrollo y la innovación han mejorado el estado de salud medio de las diversas sociedades, llegando a alcanzar el punto en el que, a día de hoy, muchas enfermedades han sido finalmente erradicadas.[4] El apoyo de nuevas técnicas y métodos han convertido lo que anteriormente eran consideradas enfermedades mortales en enfermedades crónicas a través de tratamientos paliativos. Sin embargo, con el fin de dar el tratamiento adecuado a un paciente, se han desarrollado nuevos métodos para detectar y proporcionar un diagnóstico preciso.[5] Según la Organización Mundial de la Salud (OMS),[6] las 10 principales causas de muerte en todo el mundo son: cardiopatías isquémicas, accidentes cerebrovasculares, enfermedades pulmonares obstructivas crónicas, cáncer de pulmón (junto con cánceres de tráquea y bronquios), diabetes, demencias, infecciones de las vías respiratorias inferiores, enfermedades diarreicas, tuberculosis y lesiones en carretera. Cabe destacar que la mayoría de las enfermedades más mortales son prevenibles o tratables. Proporcionar un diagnóstico precoz, la detección, el tratamiento y los cuidados paliativos mejora la probabilidad de supervivencia de estas enfermedades.[7] Además, a lo largo de las últimas décadas y tras constatar su enorme impacto en nuestra sociedad, la comunidad científica ha centrado un gran esfuerzo en el desarrollo de métodos para detectar la presencia de algunas de estas enfermedades más mortales, así como en el seguimiento de los tratamientos o avances de las mismas. La herramienta designada para este propósito es la **imagen médica**, un conjunto de técnicas o modalidades no invasivas que proporcionan imágenes detalladas no sólo con información anatómica, sino también con información de los procesos moleculares y celulares que tienen lugar en el cuerpo.[8] Estas imágenes ayudan a los médicos a dar un diagnóstico exitoso y un tratamiento apropiado.

Las diferentes modalidades de imágenes se pueden clasificar según la radiación utilizada en el examen, que puede tener o no carácter ionizante:[9]

- Técnicas de diagnóstico basadas en radiaciones ionizantes:[10,11] dentro de este grupo se incluyen las técnicas de imagen nuclear como la tomografía computarizada (TC) o tomografía axial computarizada (TAC), tomografía nuclear o tomografía con radionúclidos (TN) y las tomografías de emisión de positrones (TEP) y computarizada de emisión de fotones simples (TCEFS).

- Técnicas de diagnóstico basadas en radiaciones no ionizantes: dentro de este grupo se incluyen las técnicas de ultrasonido o fonografía (US), de imagen por resonancia magnética (IRM) y la imagen óptica (IO).

También se pueden encontrar técnicas de diagnóstico híbridas. Éstas tienen como objetivo combinar los puntos fuertes de dos técnicas diferentes y complementarias. Por ejemplo, la TEP-IRM[12,13] combina la sensibilidad de la TEP con la excelente resolución espacial de la IRM. Las diferentes modalidades de imágenes tienen sus puntos fuertes e inconvenientes asociados, incluyendo la resolución de las imágenes, la sensibilidad de la técnica, su límite de penetración, el tiempo de escaneo y su coste.

Entre los diferentes métodos existentes dentro del campo de la imagen médica, la imagen por resonancia magnética es uno de los métodos más versátiles y prometedores, ya que permite obtener imágenes de tejidos y órganos del cuerpo e identificar anomalías en ellos a nivel anatómico, fisiológico y molecular.[9,10b,14] La IRM proporciona imágenes con una resolución muy alta y una profundidad de penetración ilimitada, lo que hace que esta modalidad de imagen sea ideal para estudiar múltiples enfermedades como cardiopatías isquémicas, accidentes cerebrovasculares, enfermedades crónicas de obstrucción pulmonar, cáncer, infecciones de las vías respiratorias inferiores, esclerosis múltiple, enfermedades del hígado, enfermedades inflamatorias intestinales o malformaciones y anomalías dentro del cuerpo.[15] La IRM tiene un sinfín de aplicaciones, no sólo en el diagnóstico médico, sino también en la investigación biomédica usando modelos animales, y puede ser aplicada en prácticamente cualquier parte del cuerpo.[14b,15] Además, la IRM se puede utilizar para comprobar el estado de salud de los órganos, como la mama, los ovarios, la próstata, el hígado, los riñones, el páncreas...

La IRM se basa en los mismos principios de un espectrómetro de resonancia magnética nuclear (RMN), que registra la señal de resonancia magnética de los núcleos de protones de agua presentes en el cuerpo. J. R. Singer, de la Universidad de Berkeley, fue el primero en proponer en 1959 el uso de la resonancia magnética para medir el flujo sanguíneo *in vivo* [16] y las primeras aplicaciones de la IRM para estudiar tejidos y tumores fueron publicadas por R. Damadian ya en 1971.[17]

Los escáneres de resonancia magnética utilizados en la práctica clínica y la investigación biomédica están equipados con un imán, generalmente de 1,5 ó 3 T, aunque en algunos países se empiezan a introducir también de 7 T.[18] Al contrario de los espectrómetros de resonancia magnética, que se definen por su frecuencia (300, 400, 500 ó 600 MHz, por ejemplo), en el caso de los equipos de imagen, los denominados escáneres, normalmente se utiliza la fortaleza del campo magnético para denominar el tipo de escáner utilizado. Estos imanes componen la parte fundamental de un equipo de resonancia. Además del imán, los escáneres de resonancia magnética incorporan bobinas de radiofrecuencia (para producir y recoger las señales de resonancia magnética), un conjunto de bobinas de gradiente (controladas por secuencias de pulsos, permiten una adquisición rápida y mejorar el contraste en las imágenes registradas), y una consola y un sistema informático (para enviar las instrucciones y recoger los datos).[14] En la actualidad, existen aproximadamente 50.000 escáneres de RMN en todo el mundo,[19] que realizan más de 75 millones de exámenes clínicos al año.[20]

El contraste observado en la IRM se genera aprovechando las diferencias en la densidad de protones (el número de núcleos de protones presentes en una unidad de volumen determinada) de tejidos y órganos, o las diferencias en los tiempos de relajación longitudinal (T_1) y/o transversal (T_2) de los diferentes tejidos.[14] El contenido de agua de la mayoría de los tejidos es bastante similar y, por lo tanto, el contraste logrado al aprovechar las diferencias en las densidades de protones es bastante pobre.[14] Además, el contraste generado

por las diferencias en las densidades de protones requiere el uso de tiempos de repetición largos (el tiempo desde la aplicación de un pulso de excitación hasta la aplicación del siguiente pulso), lo que resulta en tiempos de adquisición más largos.[14a]

Las imágenes generadas por el aprovechamiento de las diferencias en la relajación longitudinal de diversos tejidos se denominan imágenes ponderadas T_1. Las imágenes T_1 se obtienen utilizando tiempos de repetición cortos y, generalmente, proporcionan puntos muy brillantes cuando se trata de tejidos grasos, debido a sus cortos tiempos de relajación, mientras que los tejidos y líquidos basados en agua son de color gris medio y muy oscuro, respectivamente.[14] Por último, las diferencias en T_2 también pueden aprovecharse para generar contraste mediante el uso de secuencias de pulsos adecuadas. En las imágenes T_2, los tejidos con T_2 corto se observan como regiones oscuras en la imagen, en contraste con las imágenes T_1. Las imágenes T_2 generalmente requieren tiempos de repetición y tiempos de eco bastante largos, que intervienen en la secuencia de pulsos de eco de espín comúnmente utilizada.[14]

En los experimentos de resonancia magnética la relajación no es espontánea y necesita ser estimulada. La relajación longitudinal es facilitada por el movimiento de los núcleos vecinos, lo que crea un campo magnético oscilante que genera una distribución de frecuencias y que contiene la frecuencia de resonancia del núcleo excitado.[21] La introducción de especies que contienen electrones no apareados acelera el proceso de relajación. Por lo tanto, ya en los primeros tiempos de la IRM se hizo evidente que el uso de sistemas paramagnéticos puede alterar los tiempos de relajación y así generar contraste en las imágenes registradas. Estos agentes paramagnéticos potencian el efecto de contraste y la intensidad de la región de interés, generalmente induciendo cambios en los tiempos de relajación de los núcleos de agua en su entorno.[14,25] Estos compuestos paramagnéticos se conocen como agentes de contraste (AC).

Actualmente, los agentes de contraste se utilizan en aproximadamente un tercio de las exploraciones clínicas llevadas a cabo mediante esta técnica.[25,26] Estas sustancias químicas se utilizan para mejorar la especificidad, calidad y resolución de las imágenes. Estos agentes exógenos se clasifican según el efecto que producen en la imagen de resonancia magnética. Los AC más comunes son los que producen un acortamiento de los tiempos de relajación.[22-25] Este acortamiento puede afectar a los tiempos de relajación longitudinal (T_1), provocando un aumento de la intensidad de la señal, o alterando los tiempos de relajación transversal (T_2), provocando una disminución de la intensidad de la señal. Los AC basados en la modificación de la T_1 se denominan agentes de contraste tradicionales o agentes T_1, y producen imágenes más brillantes. Típicamente, estos agentes son complejos de iones paramagnéticos, la mayoría de los cuales están basados en el ion gadolinio (Gd^{3+}).[22-28] Estos agentes deben presentar una alta inercia cinética y estabilidad termodinámica para evitar la liberación del ion metálico en el cuerpo, por la toxicidad de éste.[29] A pesar de la gran contribución de estos agentes de contraste a la IRM, presentan importantes limitaciones:

i)   presencia de un importante fondo de imagen debido a su efecto en las moléculas de agua del organismo,

ii) incapacidad para proporcionar una respuesta específica y cuantificable para conocer la concentración del agente,

iii) preocupación en el uso de estos agentes por la toxicidad relacionada con la liberación del ion metálico en el organismo, que se ha vinculado con la aparición de una nueva enfermedad, la fibrosis sistémica nefrógena (FSN), y otros problemas de salud.

Por otro lado, los AC que afectan a T_2 se conocen como agentes T_2 o T_2* (cuando consideran T_2 y la inhomogeneidad del campo magnético), proporcionando imágenes más oscuras.[14a] Estos AC son fundamentalmente partículas superparamagnéticas, más específicamente, partículas de magnetita con un tamaño alrededor de 50-150 nm de diámetro, también conocidas como óxidos de hierro superparamagnéticos (*Superparamagnetic Iron Oxides*, SPIOs por su acrónimo en inglés), y fueron desarrolladas más recientemente

que los agentes clásicos de Gd^{3+}.[14a] Los principales inconvenientes de los agentes T_2 suelen ser la escasa especificidad que presentan y los tiempos de exploración más largos, en comparación con los agentes T_1, aunque el mayor paramagnetismo que poseen afecta a zonas más amplias, por lo que la cantidad de AC necesaria para los exámenes es menor que con el uso de agentes de contraste de gadolinio.[14a] Esto está relacionado con el paramagnetismo más fuerte de las partículas, que propagan la falta de homogeneidad del medio en grandes volúmenes, mientras que los agentes de contraste de gadolinio afectan principalmente a los protones situados a distancias muy cortas.[14a] De hecho, grandes cantidades de SPIOs pueden producir excepcionales acortamientos en la T_2, lo que puede ser problemático para el registro de las imágenes, ya que la intensidad de la señal puede disminuir hasta el punto que apenas se observe.[14a] Además, aunque los SPIOs han mostrado una actividad citotóxica muy baja o inexistente en dosis inferiores al umbral de 100 mg/mL, tanto los SPIOs recubiertos como los no recubiertos han presentado en estudios *in vivo* e *in vitro* algunas modificaciones en el comportamiento celular a través de diversos mecanismos, por ejemplo, disrupción del citoesqueleto, inducción del estrés oxidativo, generación de radicales libres, deterioro de la función mitocondrial, daño del ADN, y alteración de las vías de señalización celular, entre otros.[30]

Otra clase de ACs es aquella que depende de la acumulación de estas sustancias en lugares específicos dentro del cuerpo. Estos agentes o sondas dan una respuesta específica a algunos parámetros de la resonancia magnética, como puede ser la radiofrecuencia, los pulsos de saturación o el campo magnético, o a algunos parámetros fisiológicos como la concentración de sustancias, el pH o la presencia de aniones o cationes endógenos, la actividad enzimática o redox...[22,25,31] Debido a la respuesta específica que proporcionan, es posible localizar estos ACs y adquirir una mejora del contraste para proporcionar un diagnóstico preciso y el adecuado tratamiento posterior.

Algunos de estos agentes de contraste entraron en la práctica clínica hace ya tres décadas, pero todavía se está realizando un gran esfuerzo para encontrar alternativas a los usados en la actualidad (es decir, con mejores perfiles de toxicidad o que proporcionen una respuesta específica). El diseño y preparación de esta nueva generación de agentes de contraste es en gran medida un problema de química de la coordinación que abre nuevas vías para la obtención de complejos metálicos con aplicaciones médicas y que presenten ventajas competitivas con respecto a los compuestos presentemente utilizados. La búsqueda de agentes de contraste para IRM es un campo de investigación puntero internacionalmente en el que hay muchas empresas farmacéuticas interesadas.

Esta tesis doctoral está enfocada en el desarrollo de agentes de contraste novedosos y eficientes para su aplicación en imagen por resonancia magnética. Esta labor ha sido posible haciendo uso del *know-how* y la amplia experiencia en química de la coordinación del grupo de investigación en el que se ha desarrollado este proyecto de tesis doctoral. Sus conocimientos sobre procedimientos sintéticos orgánicos e inorgánicos, han sido fundamentales a la hora de realizar el diseño de los agentes estudiados en la presente tesis para que proveyesen respuesta a los diversos parámetros que afectan a esta técnica de imagen molecular.

Las investigaciones realizadas durante el trabajo de tesis incluyeron la síntesis y caracterización de las sondas, la investigación de las estructuras de los compuestos en disolución y sus propiedades fisicoquímicas, así como la evaluación de su potencial como agentes de contraste en la aplicación de la IRM. Los estudios teóricos realizados con DFT proporcionaron información estructural de las sustancias en solución, así como información a nivel molecular sobre los mecanismos implicados en la respuesta a la IRM.

Los objetivos y resultados científicos específicos se recogen en los diferentes capítulos de esta tesis, distribuidos en función de los diferentes tipos de mecanismos implicados en la formación de contraste:

- En los **capítulos 2** y **3** se describe el desarrollo de agentes de contraste basados en Mn^{2+} y un estudio relaxométrico detallado en el que se estudian los parámetros que rigen la eficiencia de estos sistemas como

posibles agentes de contraste para IRM. En el capítulo 2 se reportan complejos derivados de la plataforma triazaciclononano, mientras que en el capítulo 3 se estudia un ligando derivado del ácido 2,2'-azanodiildiacético funcionalizado con un grupo picolinato en el átomo de nitrógeno (H$_3$paada) y su derivado lipofílico, funcionalizado con un grupo dodeciloxilado en la posición 4 del anillo piridílico (H$_3$C$_{12}$Opaada). En el primer caso, se seleccionaron los diferentes sustituyentes para comprobar la influencia del volumen de la tercera cadena colgante en la aproximación de la molécula de agua entrante durante el mecanismo de intercambio. Este ejemplo fue concebido para estudiar el impedimento estérico y una potencial contribución escalar a la relajatividad a campos magnéticos bajos. En el capítulo 3, se realizó el análisis de dos complejos pentadentados de manganeso(II). En uno de los complejos, se estudió la inserción de una cadena alifática sobre el quelato que, debido a las fuerzas hidrofóbicas, tiende a autoensamblarse formando micelas a una determinada concentración (concentración micelar crítica, *cmc*) en disolución. Este parámetro, *cmc*, fue determinado mediante medidas relaxométricas y confirmado mediante fluorescencia. Estas micelas, que proporcionan un aumento en el volumen que influye en la rotación del distema en el medio, afectan a la relajatividad presentada. Además, se estudió la interacción con la proteína albúmina sérica bovina (ASB) para examinar la fuerza y la afinidad del proceso de unión y mejorar la relajatividad del complejo.

A través de estos estudios se ha podido ampliar el conocimiento referente a los parámetros que afectan a la relajatividad de los complejos basados en manganeso(II) y así poder llevar a cabo mejoras en sus diseños que permitan controlar racionalmente algunos de los parámetros fisicoquímicos fundamentales implicados en la respuesta de IRM. Se observó que los complejos de gadolinio(III) y manganeso(II) no comparten la misma tendencia en el mecanismo de reacción de intercambio de agua y se puede concluir que el obstáculo estérico tiene efectos opuestos en los modos de intercambio de agua de cada uno de ellos. Asimismo, se observó la mejora en la relajación del sistema que formaba micelas y se unía a ASB, siendo contemplada esta modificación como una buena estrategia a considerar para el diseño de nuevos complejos basados en manganeso(II) con aplicación en IRM.

- En el **capítulo 4** se estudian nuevos agentes de contraste basados en el ion Gd^{3+} con detección dual a frecuencias de protón (^{1}H) y flúor (^{19}F). En este capítulo se presenta un estudio completo de los diversos parámetros que afectan a la relajatividad de los protones a diferentes campos magnéticos y temperaturas, así como un análisis de las distancias entre el centro paramagnético y los núcleos fluorados para estimar la distancia óptima necesaria para optimizar la respuesta de ^{19}F.

Se observó un tiempo de relajación más rápido en el sistema con núcleos de flúor a menor distancia (posición 3 y 5 del anillo aromático, GdL^1 (7.4 Å)) que en el sistema con los grupos fluorados ligeramente más separados (posición 4 del anillo aromático, GdL^2 (9.1 Å)). La mayor efectividad del efecto paramagnético sobre el flúor se observó para este último complejo mediante estudios de imagen *phantom*. Esta disertación proporcionó una mejor comprensión del mecanismo de aumento de la velocidad de relajación del flúor y, en comparación con otras plataformas reportadas por otros grupos, establecer una distancia Gd···F óptima en el rango 9-10 Å. Además, se determinó el número de hidratación de los sistemas por medio de mediciones de luminiscencia, de los análogos de Eu(III) y Tb(III), y a través del estudio relaxométrico completo de los complejos de gadolinio(III) usando relaxometría de ^{1}H y ^{17}O. Se confirmó la presencia de una molécula de agua coordinada, que señala relajatividades de protón en el mismo rango, con un intercambio un poco más lento, que los reportados para los agentes de contraste de tamaño similar comercialmente disponibles basados en iones metálicos de gadolinio. Se puede decir que la investigación presentada sobre este tema establece un camino prometedor para la preparación de sondas de IRM ^{1}H/^{19}F genuinas de alta estabilidad e inercia.

- En el **capítulo 5** se presentan agentes de contraste innovadores basados en lantánidos con respuesta múltiple. Se estudiaron tres sistemas diferentes, con diferentes cantidades de núcleos fluorados en su

estructura y a distancias desiguales entre la posición del núcleo fluorado y el centro metálico, para establecer una comparación entre ellos y la influencia del paramagnetismo del ion metálico en su relajatividad. También se estudiaron algunos de los complejos por su potencial como sondas CEST, combinando la señal fluorada con la transferencia de saturación por intercambio químico debido a la presencia del grupo –NH en su estructura y el paramagnetismo del ion lantánido. Los estudios de RMN demonstraron que los complejos presentan un entorno de coordinación de antiprisma cuadrado, con un único diastereoisómero en disolución (el isómero SAP). La estructura cristalina del complejo YbL^3 confirman los resultados del análisis en disolución, en particular mediante el estudio de los desplazamientos paramagnéticos inducidos por el ion Yb^{3+}. Los tiempos de relajación de ^{19}F se analizaron de manera cuantitativa usando la teoría de relajación paramagnética, permitiendo determinar con gran precisión las distancias Ln···F, los tiempos de correlation rotacional asociados y los momentos magnéticos efectivos y los tiempos de relajación electrónicos. Los complejos de Tb^{3+} y Tm^{3+} con L^1 son particularmente eficaces como sondas de ^{19}F, tal y como lo demuestran los estudios de imagen por resonancia magnética.

- En el **capítulo 6** se exponen dos potenciales agentes de contraste de Ni^{2+} derivados de la plataforma *cross-bridged cyclam*, que presentan una respuesta dual a la frecuencia de CEST y ^{19}F, además de una estabilidad extraordinaria. Debido a la preocupación actual con respecto a los problemas de toxicidad de los agentes de contraste basados en Gd^{3+}, los complejos de iones de metales de transición han surgido como una alternativa sólida a ser considerada en el campo de la IRM. El fuerte paramagnetismo del ion Ni^{2+} proporciona un efecto de aumento de la velocidad de relajación que sufren los núcleos fluorados, permitiendo tiempos de adquisición más rápidos de las imágenes de IRM. Además, el uso de una plataforma reforzada como el *cross-bridged cyclam*, ofrece una cavidad estable para el ion metálico evitando la liberación de éste en medios altamente competitivos. Asimismo, la presencia de un grupo -NH como parte de uno de los brazos colgantes fue contemplada por su interesante desplazamiento de la resonancia de la amida, beneficiosa para el mecanismo CEST.

La inercia cinética de los complejos quedó demostrada al seguir el espectro de absorción UV del complejo NiL^2 bajo fuertes condiciones ácidas. La funcionalización del ligando con brazos colgantes proporcionó una interesante respuesta dual mediante el mecanismo CEST y a la detección directa de flúor, lo que sienta las bases de una sonda singular con potencial en el campo de la IRM. Mediante experimentos de RMN de seguimiento de los tiempos de relajación en la frecuencia del flúor se ha podido verificar la influencia del fuerte paramagnetismo del ion níquel(II) sobre la relajación de los núcleos fluorados, presentando tiempos de relajación muy cortos, que benefician el registro de las imágenes, pudiendo aumentar la señal registrada en menores tiempos de adquisición. Además, la inclusión de un grupo amida en uno de los brazos sustituyentes de la plataforma macrocíclica también permitió observar una resonancia desplazada correspondiente a este grupo. Este desplazamiento, considerablemente alejado de la señal del agua, posibilitó el efecto de intercambio de saturación de una manera efectiva, dando lugar al denominado efecto CEST. Además, se lograron aislar dos estructuras cristalinas, que permitieron explorar la disposición de los átomos en estado sólido y conocer las propiedades estructurales y moleculares de estos innovadores sistemas. Estos estudios han mostrado un campo prometedor que aún está por desarrollar.

Para concluir, en el **capítulo 7** se presentan las conclusiones generales extraídas de este trabajo, resumiendo las ideas principales tras la consecución de los objetivos anteriormente mencionados. Del mismo modo, se incluyen los **Anexos A** a **E** para fundamentar la investigación realizada y descrita a lo largo de los capítulos anteriores.

Referencias

1   International Monetary Fund. World Economic Outlook: Challenges to Steady Growth. Washinton DC, October 2018.

2   Y. Li, A. Pan, D. D. Wang, X. Liu, K. Dhana, O. H. Franco, S. Kaptoge, E. Di Angelantonio, M. Stampfer, W. C. Willett and F. B. Hu, *Circulation*, 2018, **138**, 345.

3   (a) F. Carinci, K. Van Gool, J. Mainz, J. Veillard, E. C. Pichora, J. M. Januel, I. Arispe, S. M. Kim and N.S. Klazinga, *International Journal for Quality in Health Care*, 2015, **27**, 137. (b) The psychological and social needs of patients. British Medical Association, Arts & Health South West, Oxford. 2011. Accessed: 15 December 2018. https://www.ahsw.org.uk/userfiles/Other_Resources/Health__Social_Care_Wellbeing/psychologicalsocialneedsofpatients_tcm41-202964_copy.pdf

4   OECD (2017), Health at a Glance 2017: OECD Indicators, OECD Publishing, Paris, https://doi.org/10.1787/health_glance-2017-en. ISBN 978-92-64-28040-3.

5   Diagnostic Imaging. Geneva, World Health Organization, 2018. Accessed: 15 December 2018. https://www.who.int/diagnostic_imaging/en/

6   Global Health Estimates 2016: Deaths by Cause, Age, Sex, by Country and by Region, 2000-2016. Geneva, World Health Organization, 2018.

7   Global Action Plan for Prevention and Control of Noncommunicable diseases 2013-2020. Geneva, World Health Organization, 2018. ISBN 978 92 4 150623 6

8   R. Weissleder, U. Mahmood, Radiology, 2001, 219, 316.

9   (a) L. Fass, *Molecular Oncology 2*, 2008, 115. (b) M. Rudin and R. Weissleder, Nature Reviews Drug Discovery, 2003, 2, 123. (c) R. Weissleder and M. J. Pittet, *Nature*, 2008, **452**, 580. (d) M. A. Stammes, S. L. Bugby, T. Porta, K. Pierzchalski, T. Devling, C. Otto, J. Dijkstra, A. L. Vahrmeijer, L.-F. de Geus-Oei and J. S. D. Mieog, *Br J Surg*, 2018, **105**, e69-e83. (e) Medical Imaging and Technology Alliance 2018, Medical Imaging Modalities, MITA, Arlington, VA, Accessed 28 January 2019, https://www.medicalimaging.org/about-mita/medical-imaging-primer/ (f) World Health Organization 2018, Diagnostic Imaging, WHO, Geneva, Accessed 28 January 2019, https://www.who.int/diagnostic_imaging/imaging_modalities/en/ (g) M. L. Gregory, V. J.Burton, Bruce K. Shapiro, Chapter 3 - Developmental Disabilities and Metabolic Disorders, Neurobiology of Brain Disorders, Biological Basis of Neurological and Psychiatric Disorders, 2015, 18.

10 (a) L. De Chiffre, S. Carmignato, J.-P. Kruth, R. Schmitt, A. Weckenmann, *CIRP Annals - Manufacturing Technology*, 2014, **63**, 655. (b) R. Weissleder, B. D. Ross, A. Rehemtulla and S. S. Gambhir, Molecular imaging: principles and practice, People's Medical Pub. House, Shelton, 2010.

11 (a) H. Jadvar, Cancer Theranostics, Chapter 4, Radionuclide Imaging of Cancer Therapy, 2014, Ed. X. Chen and S. Wong, 45-54. (b) National Cancer Institute at the National Institutes of Health, Diagnosis and Staging, Accessed 14 December 2018, https://www.cancer.gov/about-cancer/diagnosis-staging/diagnosis.

12 (a) M. J. Zigmond, J. T. Coyle and L. P. Rowland, Neurobiology of Brain Disorders: Biological Basis of Neurological and Psychiatric Disorders, San Diego, US, 2015. (b) A. Signore, A. W. J. M. Glaudemans, F. Galli and F. Rouzet, *Biomed Res Int.*, 2015, **2015**, 615150.

13 F. Nensa, F. Bamberg, C. Rischpler, L. Menezes, T. D. Poeppel, C. la Fougère, D. Beitzke, S. Rasul, C. Loewe, K. Nikolaou, J. Bucerius, A. Kjaer, M. Gutberlet, N. H. Prakken, R. Vliegenthart, R. H. J. A. Slart, S. G. Nekolla, M. L. Lassen, B. J. Pichler, T. Schlosser, A. Jacquier, H. H. Quick, M. Schäfers and M. Hacke, *European Journal of Hybrid Imaging*, 2018, **2**, 14.

14 (a) D. W. McRobbie, E. A. Moore, M. J. Graves and M. R. Prince, MRI: from picture to proton, 2nd Edition, Cambridge, 2007. (b) A. Merbach, L. Helm and É. Tóth, The Chemistry of Contrast Agents in Medical Magnetic Resonance Imaging, 2nd Edition, West Sussex, 2013.

15 P. Lam, Medical News Today. MediLexicon, Intl.,"What to know about MRI scans." 24 July 2018. Accessed 24 December. 2018, https://www.medicalnewstoday.com/articles/146309.php

16 J. R. Singer, *Science*, 1959, **130**, 1652.

17 R. Damadian, *Science*, 1971, **171**, 1151.

18 A. Nowogrodzki, *Nature*, 2018, **563**, 24.

19 OECD (2019), Magnetic Resonance Imaging exams, total. Definitions, Sources and Methods per country. Accessed 29 January 2019, http://stats.oecd.org/wbos/fileview2.aspx?IDFile=8d3b4c1f-0ccd-4d36-954a-9a81bea235d0

20 OECD (2019), Magnetic resonance imaging (MRI) units (indicator). doi: 10.1787/1a72e7d1-en. Accessed 24 December 2018.

21 F. Bloch, *Phys. Rev.*, 1946, **70**, 460.

22 C. F. G. C. Geraldes and S. Laurent, *Contrast Media Mol. Imaging*, 2009, **4**, 1.

23 J. Lohrke, T. Frenzel, J. Endrikat, F. Caseiro-Alves, T. M. Grist, M. Law, J. M. Lee . T. Leiner, K.-C. Li, K. Nikolaou, M. R. Prince, H. H. Schild, J. C. Weinreb, K. Yoshikawa and H. Pietsch, *Adv. Ther.*, 2016, **33**, 1.

24 Y.-D. Xiao, R. Paudel, J. Liu, C. Ma, Z.-S. Zhang, S.-K. Zhou, *Inter. J. Mol. Med.*, 2016, **38**, 1319.

25 J. Wahsner, E. M. Gale, A. Rodríguez-Rodríguez and P. Caravan, *Chem. Rev.*, 2019, **119**, 957.

26 N. Ferris, S. Goergen, Gadolinium Contrast Medium (MRI Contrast agents), InsideRadiology, The Royal Australian and New Zealand College of Radiologist, Sydney, Accessed 24 December 2018, https://www.insideradiology.com.au/gadolinium-contrast-medium/

27 J. Kurhanewicz, D. Vigneron, P. Carroll and F. Coakley, Current Opinion in Urology, 2008, 18, 71.

28 D. Gaynor and D. M. Griffith, *Dalton Trans.*, 2012, **41**, 13239.

29 (a) M. Rogosnitzky, S. Branch, *Biometals*, 2016, **29**, 365. (b) L. Caschera, A. Lazzara, L. Piergallini, D. Ricci, B. Tuscano, A. Vanzulli, *Pharmacol. Res.*, 2016, **110**, 65.

30 R. A. Revia and M. Zhang, *Materials Today*, 2016, **19**, 157.

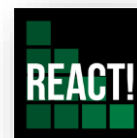31 S. Sinharay and M. D. Pagel, *Annu. Rev. Anal. Chem.*, 2016, **9**, 95

Annexe G

ResearcherID

A-8781-2017

ORCiD

0000-0002-9540-3966

Annexe G

PERSONAL INFORMATION

Work Address:	CICA (Advanced Scientific Research Center), As Carballeiras, s/n Campus de Elviña 15071 Universidade da Coruña, A Coruña - Spain
✉ :	rosa.pujales@udc.es
☎ office/ mobile:	+34 881 01 5597/ + 34 670 98 7106
Birthday/ Birthplace:	25th April 1987/ A Coruña, Spain
Nationality	Spanish

EDUCATION

2014 Nov.- Present	**Ph.D. candidate** in Fundamental Environmental Chemistry, University of Coruña, Spain
2013- 2014	**M.Sc.** in Material Science and Technology, University of Santiago de Compostela, A Coruña, Spain. **(Grade: 8.96/10**)
2009-2013	**B. S.** in Chemistry (4-years degree), University of Coruña, Spain (**Grade: 8.47/10; 1st of the Promotion**) Majors: Physics 2; Experimentation in Physical Chemistry; Experimentation in Organic Chemistry; Project design, writing and management; Laboautomation; Industrial Chemistry; Bachelor Thesis.

LANGUAGES

Spanish (**Native**), Galician (**Native**), English (**C1**)

RESEARCH EXPERIENCE

2014 Nov.-Present

Ph.D. student
Faculty of Science/ Advanced Scientific Research Center (CICA), University of Coruña, A Coruña, Spain
Project title: *Innovative Smart Probes for Molecular Imaging.*

2014 Jan –Jul.

Postgraduate research scientist
Physics of the Condensed Matter of Colloids and Polymers Group, Faculty of Physics, University of Santiago de Compostela, A Coruña, Spain
Project title: *Optimization of Synthesis Parameters in the Obtaining of Magnetic Nanocubes* (**Grade: 9.5/10**)

2011 Apr–Sep.

Undergraduate research scientist
Solid State Chemistry Group
Project Title: *Synthesis and Characterisation of Biocompatible Magnetic Nanoparticles* (**Grade: 9.8/10**)

SCIENTIFIC STAYS IN FOREIGN R&D CENTRES

2018 May- Jul.

Guest Scientist Researcher
Chemprobes Group,
Dipartimento di Scienze e Innovazione Tecnologica (DiSIT), Università del Piemonte Orientale "Amedeo Avogadro", Alessandria, Italy

2017 Apr- Aug.

Guest Scientist Researcher
MR Neuroimaging Agents Group,
Max Planck Institute for Biological Cybernetics, Tübingen, Germany

SCIENTIFIC PROJECTS

2016 Dec – 2019 Dec	**New Generation of Contrast Agents for Magnetic Resonance Imaging (MRI) Alternative to Gadolinium Derivatives** CTQ2016-76756-P, Ministry of Economy and Competitiveness, Spain
2014 Jan- 2016 Dec	**Innovative Smart Probes for Molecular Imaging Applications** CTQ2013-43243-P Ministry of Economy and Competitiveness, Spain

PROFESSIONAL EXPERIENCE

2015 Apr- Present	**Research Scientist** Chemistry Department, Faculty of Science/Advanced Scientific Research Center (CICA), University of Coruña, A Coruña, Spain
2018 Sep- 2019 Jan	**Graduate teacher in Laboratory of Chemistry 1** Bachelor Degree, Chemistry, Faculty of Sciences, First year, University of Coruña, Spain
2018 Apr-May	**Graduate teacher assistant in Inorganic Chemistry 4** Bachelor Degree, Chemistry, Faculty of Sciences, Third year, University of Coruña, Spain

SCHOLARSHIPS/GRANTS/AWARDS

2018	**Predoctoral mobility fellowships for short stays in foreign R & D centres** (EEBB-I-18-13075). Ministry of Economy and Competitiveness, Spain.
2017	**Predoctoral mobility fellowships for short stays in foreign R & D centres** (EEBB-I-17-12213). Ministry of Economy and Competitiveness, Spain.

2015	**Predoctoral contract for doctoral training** (BES2014-068399). Ministry of Economy and Competitiveness, Spain.
2012-2013	**MECD Fellowship in Collaboration with Phys. Chemistry and Chem. Engineering Department.** Ministry of Education, Culture and Sports, Spain.
2011-2012	**UDC Fellowship in Laboratory Training.** University of Coruña, Spain.

PROFESSIONAL MEMBERSHIPS

2017-Present	ESMI – European Society for Molecular Imaging

PUBLICATIONS

- Articles: 7 (accepted)
  - Derived from the doctoral thesis: 3
  - As part of training in techniques applied during the doctoral thesis: 4
- Book chapters: 2
- Conference Talks: 2
- Conference Posters: 6
- Patents: 1

PUBLICATIONS

Articles (7)

- **Derived from the doctoral thesis:**

  1. **R. Pujales-Paradela,** F. Carniato, D. Esteban-Gomez, M. Botta and C. Platas-Iglesias. Controlling water exchange rates in potential Mn^{2+}-based MRI agents derived from $NO2A^{2-}$, *Dalton Trans.*, 2019, Accepted Author Manuscript.

  2. **R. Pujales-Paradela**, T. Savić, D. Esteban-Gomez, G. Angelovski, F. Carniato, M. Botta and C. Platas-Iglesias, Gadolinium(III)-based Dual $^1H/^{19}F$ MRI Probes, *Chem. Eur. J.*, 2019, Accepted Author Manuscript. doi:10.1002/chem.201806192.

  3. **R. Pujales-Paradela**, F. Carniato, R. Uzal-Varela, I. Brandariz, E. Iglesias, C. Platas-Iglesias, M. Botta and David Esteban-Gómez, A pentadentate member of the picolinate family for Mn(II) complexation and an amphiphilic derivative, *Dalton Trans.*, 2019, **48**, 696.

- **As part of training in techniques applied during the doctoral thesis:**

  4. R. N. Pradhan, S. M. Hossain, A. Lakma, D. D. Stojkov, T. Ž. Verbić, G. Angelovski, **R. Pujales–Paradela**, C. Platas–Iglesias and A. K. Singh, Water soluble Eu(III) complexes of macrocyclic triamide ligands: Structure, stability, luminescence and redox properties, *Inorganica Chimica Acta*, 2019, **486**, 252.

  5. **R. Pujales-Paradela**, A. Rodríguez-Rodríguez, A. Gayoso-Padula, I. Brandariz, L. Valencia, D. Esteban-Gómez and C. Platas-Iglesias, On the consequences of the stereochemical activity of the Bi(III) 6s2 lone pair in cyclen-based complexes. The [Bi(DO3A)] case, *Dalton Trans.*, 2018, **47**, 13830.

  6. A. Forgács, **R. Pujales-Paradela**, M. Regueiro-Figueroa, L. Valencia, D. Esteban-Gómez, M. Botta and C. Platas-Iglesias, Developing the family of picolinate ligands for Mn2+ complexation, *Dalton Trans.*, 2017, **46**, 1546.

  7. M. Regueiro-Figueroa, D. Esteban-Gómez, R. Pujales-Paradela, L. Caneda-Martínez, A. de Blas and C. Platas-Iglesias, Water exchange rates and mechanisms in tetrahedral [Be(H2O)4]2+ and [Li(H2O)4]+ complexes using DFT methods and cluster-continuum models, *Int. J. Quantum Chem.,* 2016, **116**, 1388.

Book Chapters (2)

  1. L. Helm, J. R. Morrow, C. J. Bond, F. Carniato, M. Botta, M. Braun, Z. Baranyai, **R. Pujales-Paradela**, M. Regueiro-Figueroa, D. Esteban-Gómez, C. Platas-Iglesias and T. J. Scholl, Gadolinium-based Contrast Agents. Ed: V. C. Pierre and M. J. Allen. Contrast Agents for MRI: Experimental Methods (Chapter 2). Royal Society of Chemistry, 2018, Croydon, UK.*

2. **R. Pujales-Paradela**, M. Regueiro-Figueroa, D. Esteban-Gómez and C. Platas-Iglesias. Transition Metal-based T1 Contrast Agents. Ed: V. C. Pierre and M. J. Allen. Contrast Agents for MRI: Experimental Methods (Chapter 5). Royal Society of Chemistry, 2018, Croydon, UK.*

Conference Talks (2)

1. **R. Pujales-Paradela,** T. Savić, D. Esteban-Gomez, G. Angelovski, F. Carniato, M. Botta and C. Platas-Iglesias, Gadolinium(III)-based Dual ^{1}H/^{19}F MRI Probes, 2nd Workshop of Nuclear Magnetic Resonance Relaxometry CA-15209 (Prague, Czech Republic).

2. **R. Pujales-Paradela**, F. Carniato, D. Esteban-Gómez, M. Botta and C. Platas-Iglesias (Jan-2018): Relaxometric Characterization of Potential Mn(II)-based MRI Contrast Agents, 1st Workshop of Nuclear Magnetic Resonance Relaxometry CA-15209 (Torino, Italy).

Conference Posters (6)

1. F. Carniato, **R. Pujales-Paradela**, C. Platas-Iglesias, M. Botta, D. Esteban-Gómez (Feb-2019): Relaxometric characterization of novel Mn(II) picolinate derivatives for MRI applications, 2nd Workshop of Nuclear Magnetic Resonance Relaxometry CA-15209 (Prague, Czech Republic).

2. **R. Pujales-Paradela**, D. Esteban-Gómez, T. Savić, G. Angelovski, L. Valencia and C. Platas-Iglesias (Dec-2017): Fluorinated lanthanide probes for bimodal 19F/1H MRI application, Is Multimodal Imaging an Invention with a Future? The Input of Chemistry (Orleans - France).

3. **R. Pujales-Paradela**, D. Esteban-Gómez, T. Savić, G. Angelovski, L. Valencia and C. Platas-Iglesias (Dec-2017): Fluorinated nickel probes for bimodal 19F/1H MRI application, Is Multimodal Imaging an Invention with a Future? The Input of Chemistry (Orleans - France).

4. D. Esteban-Gómez, A. Forgács, **R. Pujales-Paradela**, M. Regueiro-Figueroa, L. Valencia, M. Botta, and C. Platas-Iglesias. (Jul-2017): Expandiendo la familia de ligandos picolinato para el desarrollo de agentes de contraste basados en manganeso (II), X Reunión Científica de Bioinorgánica (BioBilbao, Bilbao - Spain).*

5. **R. Pujales-Paradela**, M. Regueiro-Figueroa, A. de Blas, D. Esteban-Gómez and C. Platas-Iglesias (Jul-2016): Lanthanide Complexes as Potential Bimodal 19F/1H MRI Probes, 42nd International Conference on Coordination Chemistry (ICCC 2016 - Brest, France).

6. **R. Pujales-Paradela**, M. Regueiro-Figueroa, T. Rodríguez-Blas, A. de Blas, D. Esteban-Gómez and C. Platas-Iglesias (Jul-2016): Lanthanide complexes derived from macrocyclic platforms for Molecular Imaging Applications, XXXV Bienal Conference Spanish Royal Society of Chemistry (A Coruña, Spain).

* As part of collaboration and training in techniques applied during the doctoral thesis.

Patents (1)

1. Inventors: C. Platas-Iglesias, D. Esteban-Gómez, **R. Pujales-Paradela**, "Ligandos Tetraazamacrocíclicos y los Correspondientes Complejos de Níquel Útiles como Agentes de Contraste" ("Tetraazamacrocyclic Ligands and their corresponding Nickel complexes Useful as Contrast Agents"), Application Number: P201831074. Country of priority: Spain. Entity: University of Coruña. Countries to which it has been extended: Spain.